TECHNISCHE
UNIVERSITÄT
DARMSTADT

RADIO RESOURCE MANAGEMENT FOR MILLIMETER-WAVE NETWORKS: MODELING AND DESIGN

Vom Fachbereich Informatik
der Technischen Universität Darmstadt
genehmigte

DISSERTATION

zur Erlangung des akademischen Grades
Doktor-Ingenieur (Dr.-Ing.)
von

LUIS FERNANDO ABANTO LEON

Erstreferent: Prof. Dr.-Ing. Matthias Hollick
Korreferent: Prof. Dr.-Ing. Jörg Widmer

Darmstadt 2023
Hochschulkennziffer D17

Luis Fernando Abanto Leon, *Radio Resource Management for Millimeter-wave Networks: Modeling and Design*, Dissertation, Technische Universität Darmstadt, 2024.

Fachgebiet Sichere Mobile Netze
Fachbereich Informatik
Technische Universität Darmstadt
Jahr der Veröffentlichung: 2024
Tag der mündlichen Prüfung: 16. November 2023
URN: urn:nbn:de:tuda-tuprints-263639

ABSTRACT

Radio resource management (RRM) plays a critical role in modern wireless communications networks. RRM's ultimate goal is to devise strategies to efficiently manage the network's radio resources, e.g., infrastructure and spectrum, and thus coordinate interference and ensure quality-of-service (QoS) requirements for the user equipments (UEs). RRM has undergone a tremendous transformation from initially being limited to solely the physical layer with fixed policies to presently incorporating dynamic cross-layer algorithms that allow controlling multiple characteristics of the physical and higher layers.

Each succeeding generation of wireless mobile technology has contributed to expanding the network capabilities but has also posed new challenges for RRM in coordinating more radio spectrum, e.g., millimeter-wave spectrum, and more radio infrastructure, e.g., coordinated multi-point operation (CoMP) and integrated access-backhaul (IAB). Therefore, as wireless technologies evolve, RRM strategies must also adapt to account for emerging radio infrastructure and spectrum, ensuring their efficient utilization along with the existing resources.

This thesis proposes several RRM strategies and algorithms to improve radio resource utilization, addressing challenges intrinsic to the evolution of wireless mobile technologies. Different RRM research problems are investigated considering diverse radio resources, such as precoding, admission control, and discrete rate allocation, focusing on various use cases, such as Industry 4.0.

The strategies and algorithms developed herein not only target networks deployed using space-division multiple access (SDMA), adopted as *de facto* multiple access scheme, but also target emerging multiple access schemes, such as layered-division multiple access (LDMA) and rate-splitting multiple access (RSMA). In addition, the strategies and algorithms are not limited to access networks only, but also include backhaul networks, specifically IAB technology.

ZUSAMMENFASSUNG

Radio resource management (RRM) spielt eine entscheidende Rolle in modernen drahtlosen Kommunikationsnetzen. Ziel des RRM ist es, Strategien zur effizienten Verwaltung der Funkressourcen des Netzes, z. B. der Infrastruktur und des Spektrums, zu entwickeln und so Interferenzen zu koordinieren und quality-of-service (QoS)-Anforderungen für das Endgerät zu gewährleisten. RRM hat eine enorme Entwicklung durchgemacht: War es anfangs nur auf die physikalische Schicht mit festen Richtlinien beschränkt, so umfasst es heute dynamische, schichtübergreifende Algorithmen, die die Steuerung mehrerer Merkmale der physikalischen und höherer Schichten ermöglichen.

Jede nachfolgende Generation der drahtlosen Mobilfunktechnologie hat dazu beigetragen, die Netzkapazitäten zu erweitern, hat aber auch neue Herausforderungen für das RRM mit sich gebracht, da mehr Funkspektrum, z. B. im Millimeterwellenbereich, und mehr Funkinfrastruktur, z. B. coordinated multi-point operation (CoMP) und integrated access-backhaul (IAB), koordiniert werden müssen. Da sich die drahtlosen Technologien weiterentwickeln, müssen sich die RRM-Strategien auch an die neu entstehende Funkinfrastruktur und das Spektrum anpassen, um deren effiziente Nutzung zusammen mit den vorhandenen Ressourcen zu gewährleisten.

In dieser Arbeit werden mehrere RRM-Strategien und -Algorithmen vorgeschlagen, um die Nutzung von Funkressourcen zu verbessern und die mit der Entwicklung der drahtlosen Mobilfunktechnologien verbundenen Herausforderungen zu bewältigen. Verschiedene RRM-Forschungsprobleme werden unter Berücksichtigung verschiedener Funkressourcen untersucht, wie z. B. Vorcodierung, Zulassungskontrolle und diskrete Ratenzuweisung, wobei der Schwerpunkt auf verschiedenen Anwendungsfällen, wie z. B. Industrie 4.0, liegt.

Die hier entwickelten Strategien und Algorithmen zielen nicht nur auf Netze ab, die space-division multiple access (SDMA) als de facto-Mehrfachzugriffsverfahren verwenden, sondern auch auf neue Mehrfachzugriffsverfahren wie layered-division multiple access (LDMA) und rate-splitting multiple access (RSMA). Darüber hinaus sind die Strategien und Algorithmen nicht nur auf Zugangsnetze beschränkt, sondern umfassen auch Backhaul-Netze, insbesondere die IAB-Technologie.

ACKNOWLEDGMENTS

I thank Prof. Dr. Matthias Hollick and Dr. Allyson Sim for accepting me at SEEMOO to work towards my doctoral degree under their supervision.

I would also like to thank my colleagues, Arash Asadi, Andreas Bäuml, Mikhail Fomichev, Dingwen Yuan, Luis Alves, Lu Wang, Waqar Ahmed, and Leon Würsching, with whom I have collaborated during my doctoral journey and who have allowed me to grow personally and professionally. I also thank all my SEEMOO and WISE colleagues for the great times together, for their helpfulness, and consideration.

También agradezco inmensamente el apoyo de mis padres, quienes siempre creyeron en mí y que nunca me negaron su apoyo cuando se trató de mi educación. A mi hermano Kike por su constante aliento, a Dunkelcito por ser una motivación y a Aissita. Doy las gracias a Alessita, que ha estado presente desde el inicio de mi doctorado, por haberse convertido en una motivación más para seguir adelante. A Mirtha por estar siempre pendiente de Alessita, permitiéndome concentrarme en mis estudios. Enorme gratitud a mi mamita Maribel, quien es una segunda mamá, y a mi mamita Grande que siempre me nutrió con mucho amor. Agradezco a mis primos y tíos de las familias Abanto y León por estar pendientes de mis logros, especialmente a mi tío Cayo por su ayuda y por ser un ejemplo académico en la familia. Por último, quiero dar las gracias al profesor Kemper por toda la ayuda que me brindó y por haberme dado la oportunidad de iniciarme en la investigación.

Specjalne podziękowania dla Izuchny za zachęcanie do ciągłego doskonalenia się i za towarzyszenie mi w części tej podróży.

Besonderer Dank gilt dem Sonderforschungsbereich (SFB) 1053 "MAKI - Multi-Mechanismen-Adaption für das künftige Internet" (Projekte A3 und B5G-Cell) und der Deutschen Forschungsgemeinschaft (DFG) (Projekt 455077022) für die Förderung meiner Forschung.

CONTENTS

LIST OF FIGURES

LIST OF TABLES

ACRONYMS

2G	2nd generation mobile network
3GPP	the 3rd Generation Partnership Project
4G	4th generation mobile network
5G	5th generation mobile network
ADMM	alternating direction method of multipliers
AO	alternating optimization
B5G	beyond 5G
BCD	block coordinate descent
BER	bit error rate
BLER	block error rate
BnB	branch-and-bound
BnC	branch-and-cut
BS	base station
CMD	Cholesky matrix decomposition
CoMP	coordinated multi-point operation
CQI	channel quality indicator
DPC	dirty paper coding
DPC-RSMA	dirty paper coding rate-splitting multiple access
EE	energy efficiency
ESINR	equalized signal-to-interference-plus-noise ratio
FDMA	frequency-division multiple access
GP	geometric programming
IAB	integrated access-backhaul
IIoT	industrial IoT
ILP	integer linear program

IoT	Internet of Things
IPM	interior-point method
KKT	Karush-Kuhn-Tucker
LDMA	layered-division multiple access
LOS	line-of-sight
LP	linear program
MBS	macro base station
MCS	modulation and coding scheme
MIMO	multiple-input multiple output
MINLP	mixed-integer nonlinear program
MISDP	mixed-integer semidefinite program
MISOCP	mixed-integer second-order cone program
MM	minorization-maximization
MMSE	minimum mean square error
MSE	mean square error
MUST	multi-user superposition transmission
NLOS	non-line-of-sight
NOMA	non-orthogonal multiple access
NOUM	non-orthogonal unicast and multicast
PDD	penalty dual decomposition
QCQP	quadratically constrained quadratic program
QoS	quality-of-service
RF	radiofrequency
RRM	radio resource management
RSMA	rate-splitting multiple access
SBS	small base station
SCA	successive convex approximation
SDMA	space-division multiple access
SDP	semidefinite programming
SDR	semidefinite relaxation

SE	spectral efficiency
SIC	successive interference cancellation
SINR	signal-to-interference-plus-noise ratio
SLA	successive linear approximation
SNR	signal-to-noise ratio
SOCP	second-order cone program
SPO	sequential parametric optimization
SR	sum rate
STBC	space-time block codes
TDMA	time-division multiple access
UE	user equipment
WEE	weighted energy efficiency
WMMSE	weighted minimum mean square error
WSR	weighted sum rate
ZF	zero-forcing

LIST OF PUBLICATIONS

Throughout my doctoral studies, I have co-authored several articles, which are listed below.

[A] **L. F. Abanto-Leon** and G. H. Sim. "Learning-based Max-Min Fair Hybrid Precoding for mmWave Multicasting." In: *Proceedings of the IEEE International Conference on Communications (IEEE ICC)*. 2020, pp. 1–7. **Part of this thesis**.

[B] **L. F. Abanto-Leon**, M. Hollick, and G. H. Sim. "Hybrid Precoding for Multi-Group Multicasting in mmWave Systems." In: *Proceedings of the IEEE Global Communications Conference (IEEE GLOBECOM)*. 2019, pp. 1–7. **Part of this thesis**.

[C] **L. F. Abanto-Leon** and G. H. Sim. "Fairness-Aware Hybrid Precoding for mmWave NOMA Unicast/Multicast Transmissions in Industrial IoT." In: *Proceedings of the IEEE International Conference on Communications (IEEE ICC)*. 2020, pp. 1–7. **Part of this thesis**.

[D] **L. F. Abanto-Leon**, M. Hollick, Bruno Clerckx, and G. H. Sim. "Sequential Parametric Optimization for Rate-Splitting Precoding in Non-Orthogonal Unicast and Multicast Transmissions." In: *Proceedings of the IEEE International Conference on Communications (IEEE ICC)*. 2022, pp. 3904–3910. **Part of this thesis**.

[E] **L. F. Abanto-Leon**, M. Hollick, and G. H. Sim. "HydraWave: Multi-group Multicast Hybrid Precoding and Low-Latency Scheduling for Ubiquitous Industry 4.0 mmWave Communications." In: *Proceedings of the IEEE International Symposium on A World of Wireless, Mobile and Multimedia Networks (IEEE WoWMoM)*. 2020, pp. 98–107. **Part of this thesis**.

[F] **L. F. Abanto-Leon**, M. Hollick, and G. H. Sim. "BeamWave: Cross-layer Beamforming and Scheduling for Superimposed Transmissions in Industrial IoT mmWave Networks." In: *Proceedings of the International Symposium on Modeling and Optimization in Mobile, Ad hoc, and Wireless Networks (WiOpt)*. 2021, pp. 1–8. **Part of this thesis**.

[G] **L. F. Abanto-Leon**, A. Asadi, A. Garcia-Saavedra, G. H. Sim, and M. Hollick. "RadiOrchestra: Proactive Management of Millimeter-wave Self-backhauled Small Cells via Joint Opti-

mization of Beamforming, User Association, Rate Selection, and Admission Control." In: *IEEE Transactions on Wireless Communications* 22.1 (2022), pp. 153–173. **Part of this thesis**.

[H] **L. F. Abanto-Leon**, A. Krishnamoorthy, G. H. Sim, A. Garcia-Saavedra, R. Schober, and M. Hollick. "Radio Resource Management Design for RSMA: Optimization of Beamforming, User Admission, and Discrete/Continuous Rates with Imperfect SIC." In: *IEEE Transactions on Mobile Computing (Under Review)* (2023). **Part of this thesis**.

[I] M. Fomichev, **L. F. Abanto-Leon**, M. Stiegler, A. Molina, J. Link, and M. Hollick. "Next2You: Robust Copresence Detection Based on Channel State Information." In: *ACM Transactions on Internet of Things* 3.2 (2022), pp. 1–31.

[J] **L. F. Abanto-Leon**, G. H. Sim, M. Hollick, A. Boonkajay, and F. Adachi. "SWAN: Swarm-Based Low-Complexity Scheme for PAPR Reduction." In: *Proceedings of the IEEE Global Communications Conference (IEEE GLOBECOM)*. 2020, pp. 1–7.

[K] **L. F. Abanto-Leon**, G. H. Sim A. Bäuml, M. Hollick, and A. Asadi. "Stay Connected, Leave No Trace: Enhancing Security and Privacy in WiFi via Obfuscating Radiometric Fingerprints." In: *Proceedings of the ACM on Measurement and Analysis of Computing Systems (ACM SIGMETRICS)*. Vol. 4. 3. 2021, pp. 1–31.

[L] L. Wang, **L. F. Abanto-Leon**, and A. Asadi. "Joint Communication and Sensing in RIS-enabled mmWave Networks." In: *IEEE Transactions on Vehicular Technology (Under Review)* (2023).

[M] D. Yuan, **L. F. Abanto-Leon**, and M. Hollick. "Scheduling Mechanisms in Wireless Sensor-Actuator Networks for Multi-rate Periodic Control in Industry 4.0." In: *IEEE Transactions on Green Communications and Networking (Under Review)* (2023).

COLLABORATIONS AND MY CONTRIBUTIONS

I have been privileged to collaborate with exceptional individuals who have greatly enriched my knowledge. I am thankful to my co-authors, Matthias Hollick, Allyson Sim, Arash Asadi, Andres Garcia-Saavedra, Bruno Clerckx, Robert Schober, Aravindh Krishnamoorthy, Mikhail Fomichev, Andreas Bäuml, Lu Wang, Dingwen Yuan, Amnart Boonkajay, and Fumiyuki Adachi, for their invaluable input to my research and for allowing me to contribute to theirs.

My research has resulted in a patent[1] and multiple publications, spanning a wide range of topics, such as precoding, scheduling, resource allocation, privacy and security, among others. Several of these publications, i.e., [A, B, C, D, E, F, G, H], are featured in this thesis under the umbrella of RRM, while others, i.e., [I, J, K, L, M], have not been included. In particular, all co-authors contributed to the conception and discussions that led to our publications. However, only the contributions of my co-authors and my own regarding the publications included in this thesis are detailed in the following.

The publications [A, B, C, D] focus on the precoding design for millimeter-wave communications systems. These publications cover different use cases, such as precoding for single-group and multi-group multicast transmissions [A, B], as well as precoding for non-orthogonal unicast and multicast transmissions [C, D].

[A]	**Learning-based Max-Min Fair Hybrid Precoding for mmWave Multicasting**	Part of this thesis
Luis F. Abanto-Leon	He defined the research problem, formulated it, and solved it. He implemented the scripts and performed the simulations. He collected the data, analyzed them, and prepared the figures. Additionally, he finalized the first version of the paper.	
Allyson Sim	She contributed to reorganize the introduction section of the paper and to make the contributions and conclusions clearer. She also collaborated in the proofreading and preparation of the paper.	

1 A patent application was filed on the idea that led to publication [K]. The patent has not been granted yet. The application code is "EP20187873.3".

[B]	**Hybrid Precoding for Multi-Group Multicasting in mmWave Systems**	Part of this thesis
Luis F. Abanto-Leon	He defined the research problem, formulated it, and solved it. He implemented the scripts and performed the simulations. He collected the data, analyzed them, and prepared the figures. Additionally, he finalized the first version of the paper.	
Matthias Hollick	He contributed with the proofreading and preparation of the paper.	
Allyson Sim	She contributed with the proofreading, preparation of the paper, and improving the quality of the figures.	

[C]	**Fairness-Aware Hybrid Precoding for mmWave NOMA Unicast / Multicast Transmissions in Industrial IoT**	Part of this thesis
Luis F. Abanto-Leon	He defined the research problem, formulated it, and solved it. He implemented the scripts and performed the simulations. He collected the data, analyzed them, and prepared the figures. Additionally, he finalized the first version of the paper.	
Allyson Sim	She contributed by reorganizing the simulation results. She was also responsible for the proofreading and preparation of the paper.	

[D]	**Sequential Parametric Optimization for Rate-Splitting Precoding in Non-Orthogonal Unicast and Multicast Transmissions**	Part of this thesis
Luis F. Abanto-Leon	He defined the research problem, formulated it, and solved it. He implemented the scripts and performed the simulations. He collected the data, analyzed them, and prepared the figures. Additionally, he finalized the first version of the paper.	
Matthias Hollick	He contributed with the proofreading and preparation of the paper.	
Bruno Clerkx	He contributed with technical comments on the explanation of rate-splitting multiple access. He also identified mathematical proofs that needed improvement. He introduced the topic of rate-splitting multiple access to Luis F. Abanto-Leon and contributed with the proofreading and preparation of the paper.	
Allyson Sim	She contributed with the proofreading and preparation of the paper.	

The publications [E, F] focus on the design of precoding and admission control for millimeter-wave communications systems, specifically for multi-group multicast in [E] and for non-orthogonal unicast and multicast transmissions in [F]. The contributions of my co-authors and my own concerning these publications are the shown below.

[E]	**HydraWave: Multi-group Multicast Hybrid Precoding and Low-Latency Scheduling for Ubiquitous Industry 4.0 mmWave Communications**	Part of this thesis
Note: This paper was honored with the Best Paper Award at WoWMoM 2020.		

Luis F. Abanto-Leon	He defined the research problem, formulated it, and solved it. He implemented the scripts and performed the simulations. He collected the data, analyzed them, and prepared the figures. Additionally, he finalized the first version of the paper.
Matthias Hollick	He contributed with the proofreading and preparation of the paper.
Allyson Sim	She contributed by proposing to include scheduling in the problem. She was also responsible for the proofreading and preparation of the paper, as well as for the design of figures in the introduction section.

[F]	**BeamWave: Cross-layer Beamforming and Scheduling for Superimposed Transmissions in Industrial IoT mmWave Networks**	Part of this thesis

Luis F. Abanto-Leon	He defined the research problem, formulated it, and solved it. He implemented the scripts and performed the simulations. He collected the data, analyzed them, and prepared the figures. Additionally, he finalized the first version of the paper.
Matthias Hollick	He contributed with the proofreading and preparation of the paper.
Allyson Sim	She contributed by designing figures for the introduction section and improving the quality of figures for the simulations section. She was also responsible for the proofreading and preparation of the paper.

The publications [G, H] focus on the design of precoding, admission control, and discrete-rate allocation for millimeter-wave communications systems. A first use case using IAB is investigated in [G], where multicast transmissions are used for the backhaul network and unicast transmissions for the access network. A second use case using RSMA is investigated in [H], which leverages non-orthogonal unicast and multicast transmissions. The contributions of my co-authors and my own concerning these publications are the shown below.

[G]	**RadiOrchestra: Proactive Management of Millimeter-wave Self-backhauled Small Cells via Joint Optimization of Beamforming, User Association, Rate Selection, and Admission Control**	Part of this thesis

Luis F. Abanto-Leon	He defined the research problem, formulated it and solved it. He implemented the scripts and performed the simulations. He collected the data, analyzed them, and prepared the figures. Additionally, he finalized the first version of the article.
Arash Asadi	He contributed to the initial discussions to define the system model and suggested additional scenarios to be simulated. He was also responsible for proofreading the article as well as improving the introduction section and discussions derived from the simulation results.
Andres Garcia-Saavedra	He contributed to the initial discussions to define the system model and assisted in writing parts of the article to justify the feasibility of channel estimation in integrated access-backhaul networks. He was also responsible for the proofreading and preparation of the article.
Allyson Sim	She contributed to the initial discussions, as well as with proofreading and preparation of the article.
Matthias Hollick	He contributed with the proofreading and preparation of the article.

[H]	**Radio Resource Management Design for RSMA: Optimization of Beamforming, User Admission, and Discrete/Continuous Rates with Imperfect SIC**	Part of this thesis

Luis F. Abanto-Leon	He defined the research problem, formulated it and solved it. He implemented the scripts and performed the simulations. He collected the data, analyzed them, and prepared the figures. Additionally, he finalized the first version of the article.
Aravindh Krishnamoorthy	He contributed with technical comments and organizational aspects. He helped to improve the explanation of several parts of the article, in particular the discussion of simulation results, and suggested improvements for several proofs.
Andres Garcia-Saavedra	He contributed to proofreading, preparing the article, and improving the introduction.
Allyson Sim	She contributed with the proofreading and preparation of the article.
Robert Schober	He contributed with technical comments, specifically with the improvement and formalization of several proofs, as well as with the explanation of the system model and the discussion of the simulation results. He simplified the explanation of several parts of the article and made it more understandable. He provided ideas on how to structure the introduction and the abstract. Finally, he contributed with the proofreading and preparation of the article.
Matthias Hollick	He contributed with the proofreading and preparation of the article.

1 INTRODUCTION

This chapter provides the context and motivation for the investigated radio resource management (RRM) research problems in [A, B, C, D, E, F, G, H], included in this thesis.

1.1 OVERVIEW

RRM has long been recognized as a crucial component of wireless communications networks. RRM is an umbrella term that encompasses a set of strategies and algorithms designed to optimize the utilization of the networks' radio resources, i.e., infrastructure, spectrum, and transmission characteristics. The utilization of the radio resources is optimized through intelligent management and coordination, resulting in reduced interference and improved quality-of-service (QoS) for user equipments (UEs) [1–3].

Traditional RRM in legacy technologies, such as the 2nd generation mobile network (2G), consisted primarily of physical layer strategies in which resources were statically allocated, i.e., unable to adapt to environmental changes and limited to only a small set of possible choices, such as frequency channels [4, 5]. In contrast, contemporary mobile technologies, such as the 4th generation mobile network (4G) and 5th generation mobile network (5G), have evolved to the point that it is feasible to dynamically control a broader range of radio resources, even beyond the physical layer [6].

In 2G, static channel assignment was used, which consisted of assigning a certain number of manually selected channels to every cell.

Thus, RRM has evolved from static and confined solely to the physical layer to dynamic and spanning multiple layers, allowing for unified control of physical and higher layers. Nowadays, RRM can be designed to control a wider variety of characteristics, such as transmit power, modulation and coding scheme (MCS), admission control, UE association, antenna and subcarrier assignment, as well as allowing a choice between fixed or adaptive precoding.

Each generation of mobile technology has contributed tremendous advancements. For instance, 4G introduced coordinated multi-point operation (CoMP) [7–9], whereas 5G incorporated millimeter-wave spectrum and integrated access-backhaul (IAB) [10–12]. Specifically, CoMP has made it possible to serve UEs through multiple cooperating distributed base stations (BSs), while millimeter-wave spectrum has

facilitated the decongestion of data traffic, and IAB has bonded the access and backhaul networks to more closely orchestrate the use of resources, allowing for higher capacity and throughput. However, the introduction of these new radio resource has also posed challenges for RRM. Specifically, integrating and managing new radio resources and infrastructure alongside the existing ones is becoming increasingly complex, thus posing a threat to maintaining high network performance and optimal resource utilization. Furthermore, the increasing QoS requirements and the proliferation of Internet of Things (IoT) devices have further compounded the situation, calling for sophisticated strategies and algorithms to efficiently manage a constantly evolving constellation of radio resources, be it infrastructure, spectrum, or transmission characteristics.

1.2 MOTIVATION AND CHALLENGES

As wireless technologies continue to evolve, so must the algorithms and strategies used to manage the network's radio resources. This thesis proposes several novel RRM strategies and algorithms to tackle many inherent challenges of modern wireless communication networks, aiming to ensure the QoS requirements of UEs and the optimal use of the networks' radio resources. The following discussion focuses on various challenges that are investigated in this thesis.

New infrastructure and spectrum. As new generations of mobile technologies emerge, more advanced infrastructure is developed and integrated with the existing ones. An example is CoMP [7–9], which was introduced in 4G, and allows for higher throughput but requires coordination between BS and UE association to manage inter-user interference effectively, thus requiring more elaborated RRM strategies for proper operation. Similarly, 5G introduced IAB [10–12] as a cutting-edge technology for unified control of access and backhaul networks. IAB promises savings in deployment and maintenance costs compared to traditional fiber optic backhauling but requires optimizing the radio resources for both access and backhaul in tandem, resulting in greater complexity for RRM design. Besides, the use of millimeter-wave spectrum [13–15] was incorporated in 5G as a means to alleviate network congestion caused by the limited bandwidth available in the sub-6GHz spectrum. In particular, adopting the millimeter-wave spectrum in 5G has helped expand network capacity and attend to the increasing throughput demands. However, it has also presented technical challenges, such as high power consumption due to the severe path loss and the need for dedicated hardware, i.e., hybrid precoders, to exploit the spectrum. *Consequently, incorporating new infrastructure and spectrum requires renovated RRM strategies and algorithms tailored to*

exploit the unique attributes of these radio resources and enable their optimal utilization.

Remark: The RRM design considering new spectrum resources, i.e., millimeter-wave spectrum, was investigated in [A, B, C, D, E, F, G, H], and considering new infrastructure, i.e., IAB technology, was investigated in [G].

Hybrid precoders. Analog-digital precoders, also known as hybrid precoders [16–18], were introduced to take early advantage of the available millimeter-wave spectrum. Hybrid precoders provide an acceptable compromise between costs and performance by requiring a high-dimensional network of cost-efficient analog phase shifters and a low-dimensional network of more expensive radiofrequency (RF) chains, thus overall maintaining costs affordable at the tradeoff of a penalty on performance. In contrast, fully-digital precoders, typically used for the sub-6GHz spectrum, are more versatile and perform better than hybrid precoders. However, fully-digital precoders still need to be more affordable to manufacture before they can be used in the millimeter-wave spectrum. Specifically, they require a dedicated RF chain per antenna, substantially increasing costs. *While hybrid precoders are an excellent solution to exploit the millimeter-wave spectrum at a low cost, the couplings between the analog and digital components, which are intrinsic to hybrid precoder architectures, make their design more complex. In particular, these complicating couplings result in nonconvex functions and need to be adequately addressed by the RRM design and thus utilize the radio resources more efficiently.*

The terms precoder/precoding and beamformer/beamforming are used interchangeably.

Remark: The RRM design considering hybrid precoders was investigated in [A, B, C, D, E].

Admission control. Owing to physical constraints, such as a limited number of RF chains, network operators typically devise policies to accommodate a fixed number of UEs per channel use, especially when using hybrid precoders, which have fewer RF chains than their fully-digital counterparts. Specifically, each RF chain can only handle a single data stream. As a result, when the number of UEs exceeds the number of RF chains, some form of regulation, i.e., admission control, is required to decide which UEs are served [19–21]. *Despite the importance of admission control in wireless communications systems, it is usually not accounted for in the literature. With the adoption of hybrid precoders to exploit the millimeter-wave spectrum, the importance of admission control becomes more prominent. Therefore, admission control must be included in the RRM design to depict realistic characteristics of modern wireless communications systems.*

In this thesis, the terms admission control, UE admission, UE scheduling or simply scheduling are used interchangeably although they may have a different connotation in other contexts.

Remark: The RRM design considering admission control was investigated in [E, F, G, H].

UE association. Most works in the literature assume that UEs are served by a single BS or all BSs within a given range, imposing a pre-association for service. Typically, these extreme strategies, i.e., assuming that UEs be served by one or all BSs, are a way of circumventing integer variables that would be used to represent the connectivity between UEs and BSs. Despite this assumption greatly simplifying the RRM design, it is not realistic nor optimal from a practical perspective. In practice, each UE may be served by some BSs, but likely not all in a given range. Again, this may be due to a limited number of RF chains at each BS or a policy imposed by the network operator. Particularly, radio infrastructure, such as BSs, must be exploited intelligently to guarantee the continued sustainability of wireless communications systems. *Thus, to improve radio resource utilization, the RRM design must allow flexible association between BSs and the UEs.*

Remark: The RRM design considering UE association was investigated in [G].

Discrete rates. Shannon capacity provides an information-theoretic upper limit for the rate, which in reality cannot be achieved. Still, Shannon capacity is commonly adopted in most literature, as it facilitates relating signal-to-interference-plus-noise ratios (SINRs) and rates. A more realistic representation of the rate is using MCSs, which yield a limited number of discrete rates. However, relating rates and their corresponding MCSs is more complex and usually disregarded. In particular, continuous rates obtained by Shannon capacity are not achievable and must be approximated or rounded to the nearest feasible discrete rate, resulting in power and/or rate losses [22]. *Therefore, incorporating the use of discrete rates in the RRM design is necessary for efficient use of radio resources, thereby avoiding losses.*

Remark: The RRM design considering discrete rates was investigated in [G, H].

New multiple access schemes. The 3rd Generation Partnership Project (3GPP) standardized multi-user superposition transmission (MUST) in 4G, which is a type of non-orthogonal multiple access scheme. Recently, other forms of non-orthogonal multiple access, such as layered-division multiple access (LDMA) [23, 24] and rate-splitting multiple access (RSMA) [25, 26] have emerged but are not standardized. However, LDMA and RSMA have demonstrated advantages compared to space-division multiple access (SDMA), making it possible for these technologies to be adopted in beyond 5G (B5G) mobile technologies[1]. However, adopting a new multiple access scheme would

1 A variant of LDMA has been standardized for digital terrestrial television, allowing to transmit multimedia content with different qualities overlaid over the same spectrum band. In addition, RSMA has recently been subject of discussion at 3GPP standardization meetings and is strongly supported by the BBC [27].

require restructuring current RRM strategies and algorithms. In particular, this would impact the design of precoding, admission control, UE association as well as discrete and continuous rate allocation. *In particular, investigating RRM design for emerging multiple access is of great relevance. It can help to understand the advantages of these new developments compared to the mainstream ones, which are the basis of today's mobile technologies.*

Remark: The RRM design considering new multiple access schemes was investigated in [C, D, F, H]. Specifically, in [C, F] for LDMA and in [D, H] for RSMA.

Imperfect successive interference cancellation. Non-orthogonal multiple access schemes, such as LDMA and RSMA, rely on successive interference cancellation (SIC) in order to decode the received signals. The efficacy of LDMA and RSMA is directly linked to the success of SIC, which is usually assumed to be perfect in most of the literature. However, SIC is prone to errors that can produce residuals of previously decoded signals, leading to unmitigated self-interference that can negatively affect performance [28, 29]. *Thus, it is essential to take into account possible SIC imperfections in the RRM design of LDMA and RSMA in order to guarantee the efficient use of radio resources.*

Remark: The RRM design considering imperfect SIC was investigated in [H].

Optimization. One of the major challenges faced in RRM is its appropriate design. Specifically, one way to perform the RRM design is to formulate it as an optimization problem and solve it using mathematical programming, also known as optimization theory, the methodology mainly adopted in this thesis. However, other methods exist, such as machine learning and game theory. In the RRM design, various types of radio resources can be considered. For instance, power allocation is one of the most commonly optimized resources, and therefore abundant literature exists on the topic. However, the amount of literature decreases significantly when other radio resources are accounted for, such as precoding, admission control, UE association, discrete rates, IAB, and CoMP. In particular, with more radio resources to consider, the RRM design becomes more complex. In this thesis, RRM designs of varying degrees of difficulty are investigated, ranging from precoding alone to the joint design of precoding, admission control, UE association, and discrete or continuous rate allocation. Depending on the use case and the resources considered, the RRM design can result in optimization problems of different natures, from simple linear programs (LPs) to challenging nonconvex mixed-integer nonlinear programs (MINLPs). Thus, several techniques were employed to solve the optimization problems that

resulted from the RRM designs, for instance, alternating optimization (AO), semidefinite relaxation (SDR), successive convex approximation (SCA), sequential parametric optimization (SPO), Cholesky matrix decomposition (CMD), minorization-maximization (MM), interior-point methods (IPMs), among others. *Knowledge of a wide range of optimization techniques is essential to deal with problems of different natures arising from RRM designs. In general, no one-fits-all technique exists to solve all optimization problems.*

RRM is a crucial component of modern wireless communications networks. RRM is responsible for efficiently managing the networks' radio resources, i.e., infrastructure, spectrum, and transmission characteristics, to meet UEs' connectivity requirements. RRM can be conceptualized as radio resource orchestrator that balances the demands of different UEs, ensuring that each UE meets its individual needs while promoting an efficient use of radio resources. RRM can be designed to support a wide range of use cases and services, from video games to industrial communications. For each case, a different goal is pursued, e.g., maximizing throughput would be of more significant relevance for video gaming while minimizing latency would be more natural to adopt for industrial communications. As wireless networks evolve and new needs and use cases emerge, effective RRM designs that achieve seamless connectivity and high resource utilization efficiency become indispensable.

1.3 OUTLINE

The thesis consists of ten chapters organized as follows. Chapter 1 gives an introduction of the RRM problem investigated in this thesis. Chapter 2, Chapter 3, Chapter 4, and Chapter 5 investigate the design of hybrid precoding for millimeter-wave wireless communications networks, considering several use cases and various multiple access schemes, such as SDMA, LDMA, and RSMA. Chapter 6 and Chapter 7 investigate the joint design of hybrid precoding and admission control for millimeter-wave wireless communications networks, considering SDMA and LDMA. Chapter 8 and Chapter 9 investigate the joint design of precoding, admission control, and discrete rate allocation for millimeter-wave wireless communications networks, considering SDMA and RSMA. In addition, Chapter 8 includes the design of UE association since a CoMP network with multiple BSs is considered, whereas Chapter 9 accounts for imperfect SIC, which may be caused by hardware malfunctioning at the receiving UEs. Finally, Chapter 10 summarizes the conclusion of this thesis. The chapters are briefly summarized in the following.

- Chapter 1 provides an overview of RRM and establishes the need for developing novel RRM strategies and algorithms to address challenges of modern wireless communication networks. Additionally, it provides the outline of this thesis.

- Chapter 2 builds on [A], which is included in Appendix A. In particular, Chapter 2 investigates the design of hybrid precoding for single-group multicast transmissions based on SDMA. The chapter proposes a learning-based algorithm based on AO and the gradient descent method to maximize the rate fairness among all UEs. It is demonstrated that the proposed algorithm can perform close to that of fully-digital precoders.

- Chapter 3 builds on [B], which is included in Appendix B. In particular, Chapter 3 investigates the design of hybrid precoding for multi-group multicast transmissions based on SDMA. The chapter proposes an algorithm based on SDR, AO, and CMD with the objective of minimizing the transmit power. Despite the more constrained architecture of hybrid precoders, it is shown that the proposed hybrid precoder design performs very similarly to its fully-digital counterpart even under challenging scenarios, where fully-digital precoders are known to excel.

- Chapter 4 builds on [C], which is included in Appendix C. In particular, Chapter 4 investigates the design of hybrid precoding for non-orthogonal unicast and multicast (NOUM) transmissions based on LDMA in the context of Industry 4.0. The chapter proposes an algorithm based on SCA with the aim of maximizing the rate fairness among all industrial IoT (IIoT) devices. It is demonstrated that the proposed algorithm outperforms other competing schemes.

- Chapter 5 builds on [D], which is included in Appendix D. In particular, Chapter 5 investigates the design of hybrid precoding for NOUM transmissions based on RSMA. The chapter proposes an algorithm based on level sets, SCA, and SDR with the objective of maximizing the sum rate (SR) among all UEs. It is shown that the proposed algorithm converges to a local optimum and is able to find solutions in more instances than the state-of-the-art algorithm.

- Chapter 6 builds on [E], which is included in Appendix E. In particular, Chapter 6 investigates the joint design of hybrid precoding and admission control for multi-group multicast transmissions based on SDMA in the context of Industry 4.0. The chapter proposes an algorithm using integer linear programs (ILPs), SDR, CMD, and the bisection method with the aim of minimizing data transmission latency. It is demonstrated that the

proposed algorithm can yield high quality solutions compared to the optimal, which requires an exhaustive search to test all possible combinations.

- Chapter 7 is builds on [F], which is included in Appendix F. In particular, Chapter 7 investigates the joint design of hybrid precoding and admission control for NOUM transmissions based on LDMA in the context of Industry 4.0. The chapter proposes an algorithm based on ILPs and SCA with the objective of maximizing the rate fairness among the admitted IIoT devices. It is shown that the proposed algorithm can produce near-optimal solutions compared to the optimal exhaustive search, and significantly outperforms other multiple access schemes, such as time-division multiple access (TDMA) and frequency-division multiple access (FDMA).

- Chapter 8 builds on [G], which is included in Appendix G. In particular, Chapter 8 investigates the joint design of precoding, admission control, rate allocation, and UE association for IAB systems based on SDMA. The chapter proposes a first algorithm based on the convexification of MINLPs and a second algorithm based on MM, both aiming to maximize the SR. It is demonstrated that under specific settings the proposed algorithms can achieve near-optimality, a conclusion obtained by noting a minimum gap with respect to an upper bound.

- Chapter 9 builds on [H], which is included in Appendix H. In particular, Chapter 9 investigates the joint design of precoding, admission control, discrete rates allocation and considering imperfect SIC for networks based on RSMA. The chapter proposes an algorithm based on the convexification of MINLPs with the objective of maximizing the weighted sum rate (WSR) and weighted energy efficiency (WEE). The proposed algorithm provides revealing results on the performance of WSR and WEE when discrete or continuous rates are used, as well as when optimal or random UE admission is employed.

- Chapter 10 provides a summary of the outcomes and contributions of the thesis. This chapter also gives an insight into open research problems and future extensions of the publications presented herein.

2

PRECODING FOR SINGLE-GROUP MULTICAST BASED ON SDMA

This chapter gives an overview of the research problem investigated in [A], which is included in Appendix A. In the following, the motivation is given, the goal is stated, the related work is reviewed, the contributions are summarized, the research problem is formulated, and selected results are discussed.

2.1 MOTIVATION

Wireless multicasting is a favorable transmission strategy for distributing the same content to multiple user equipments (UEs). In particular, the precoding design is crucial for multicast applications as it allows the realization of flexible radiation patterns, leading to enhanced radio resource utilization. Despite the benefits of precoding for better exploiting the radio resources, additional spectrum will be needed to support the increasing throughput demands of emerging high-end applications, such as virtual reality. As a result, the millimeter-wave spectrum has gained momentum as a solution since it offers larger bandwidths [30]. Thanks to recent developments in analog-digital antenna array architectures, the millimeter-wave spectrum can be exploited cost-effectively using analog-digital precoders, also known as hybrid precoders, thus opening an opportunity to realize high-throughput multicasting in the millimeter-wave spectrum. However, designs involving multicast precoding are generally challenging, as they are NP-hard, even for simple cases. Adding to this the complexity of designing hybrid precoders, which have complicating analog-digital couplings, the design becomes even more challenging. This requires novel and performant solutions that can address the inherent difficulties in designing hybrid precoders for multicast purposes.

2.2 GOAL

The goal is to design a hybrid precoder to maximize the minimum signal-to-noise ratio (SNR), subject to transmit power and constant-modulus phase rotation constraints. Specifically, constant-modulus phase rotations are inherent to hybrid precoders and are challenging to design. The minimum SNR maximization is adopted since the weakest SNR dictates the system's performance in multicast applications. Here,

a low-complexity algorithm is proposed to design a hybrid precoder, specifically for single-group multicasting. The proposed algorithm is inspired by machine learning ideas, specifically gradient-based updates, exploration, exploitation, and low-complexity matrix operations. Only a few works exist in this research direction, but none of them for hybrid precoders. Also, most works have employed semidefinite relaxation (SDR), whose complexity is usually very high. In addition, compared to previous works, the proposed algorithm can be applied to any hybrid precoder architecture and to fully-digital precoders.

2.3 RELATED WORK

Precoding for single-group multicasting has been investigated with fully-digital precoders in several works [31–58] and with hybrid precoders in only a few [59–66]. In single-group multicasting, all UEs are interested in the same information. This causes the achievable throughput to be tied to the minimum SNR of all UEs. Therefore, maximizing the minimum SNR is an important criterion in the multicast precoding design, which has been adopted in the research problem investigated in this chapter. However, other criteria have also been used, such as transmit power minimization. The following gives an overview of several works on single-group multicast precoding design.

An initial work on the precoder design for single-group multicasting is [31], where the authors investigated respectively the maximization of the minimum SNR and minimization of the transmit power. The authors showed that multicast precoding yields nonconvex quadratically constrained quadratic programs (QCQPs), which are NP-hard, and proposed algorithms for addressing this difficulty. In particular, the authors employed SDR to recast the the nonconvex QCQPs as semidefinite programmings (SDPs) with relaxed rank-one constraints, thus eliminating the nonconvexities. They showed that the relaxed SDPs yield solutions that are not necessarily feasible to the original optimization problems. This occurs because the relaxation of rank-one constraints enlarges the feasible set, and therefore, the relaxed SDPs can produce solutions outside the original feasible sets. To find feasible solutions, the authors computed the best rank-one approximation of the relaxed SDP solution and perturbed the outcome using randomization to improve its quality. This process can produce high-quality solutions, but not always guarantees that the perturbed solution is feasible.

An algorithm based on SDR, convex projections, and perturbations was proposed in [42] to minimize the transmit power, showing higher performance compared to the algorithm proposed in [31] but with higher computational complexity. Besides, a high-complexity optimal

algorithm for transmit power minimization was developed in [53], showing substantial gains over SDR-based algorithms.

In [54], the authors proposed an iterative algorithm based on convex inner approximations using successive convex approximation (SCA) to minimize the transmit power. The algorithm proved to be less complex than existing SDR-based algorithms and capable of producing high-quality solutions. Besides, a precoder design for the maximization of the minimum SNR was proposed in [55]. In particular, the authors devised an iterative algorithm based on SCA and proposed multiplicative and additive update policies to optimize the precoder iteratively, demonstrating that their proposed algorithm has higher performance than other algorithms based on SDR. Similar algorithms were proposed in [56] based on iterative updates to either maximize the minimum SNR or minimize the transmit power.

The authors of [57] proposed to maximize the weighted sum rate (WSR) of all UEs since they found that the WSR can be used to maximize the minimum SNR if the weights assigned to each UE are chosen suitably. Compared to SDR-based algorithms, their proposed algorithm was shown to be superior. Besides, the authors of [32, 58] employed machine learning to identify the UEs most likely to affect the maximization of the minimum SNR and tailored the precoder design to specifically prioritize those UEs.

An iterative algorithm to maximize the minimum SNR was proposed in [33]. Specifically, the authors leveraged the channel correlation among UEs to guide the precoder design, achieving acceptable performance at low computational complexity. The authors of [34] proposed an algorithm based on subgradient descent for maximizing the minimum SNR. Their algorithm demonstrated high performance and affordable computational complexity compared to competing algorithms. An algorithm based on alternating direction method of multipliers (ADMM) was proposed in [35], which demonstrated similar performance to the algorithm proposed in [34] but with reduced computational complexity.

Several other algorithms have been developed, for instance, based on proximal projections [36, 37], machine learning [38, 39], and switched beams [40, 67]. Other variants of single-group multicast precoding have been studied jointly with space-time block codes (STBC) in [41, 43–47] and multiple-input multiple output (MIMO) transceivers in [49]. Besides, single-group multicast precoding has also been investigated for relaying in [48] and for secrecy maximization in [50–52].

The works mentioned above assumed fully-digital precoders, impractical for the millimeter-wave spectrum due to high fabrication costs. Specifically, the literature on multicast precoding with hybrid

precoders is much scarcer than with fully-digital precoders, partly because hybrid architectures are more recent and partly because they are more challenging to design due to couplings between analog and digital components.

An iterative algorithm for maximizing the minimum SNR was proposed in [59]. The author employed alternating optimization (AO) based on matrix and vector multiplications without resorting to optimization solvers, making the algorithm attractive for fast optimization. The authors of [63] investigated the maximization of the minimum SNR and proposed a low-complexity algorithm, which employed a codebook to design the analog precoder and eigendecomposition to design the digital precoder. In [64], the authors proposed algorithms to maximize the minimum SNR, relying on SDR and genetic algorithms. Besides, the authors of [65] proposed an algorithm based on AO for minimizing the transmit power. The authors of [66] investigated the maximization of the minimum SNR, ensuring secure communications in the presence of non-legitimate UEs. In particular, they proposed an algorithm based on the error minimization between the fully-digital precoder and the hybrid precoder. Security was also the focus of [60], where the authors investigated the maximization of the secrecy rate and proposed an algorithm based on the penalty dual decomposition (PDD) method. In [61] the minimization of the outage probability was considered, and an algorithm based on stochastic optimization was proposed. In [62], a simple heuristic for designing fully-analog precoders was proposed to maximize the minimum SNR.

Multi-group multicasting with hybrid precoders is a more general case, which has also been investigated, e.g., in [68–70]. In particular, the precoder design for multi-group multicasting remains nonconvex and is subject to the same challenges as in single-group multicasting.

2.4 CONTRIBUTIONS

The contributions of this chapter are summarized in the following.

- A low-complexity learning-based algorithm is proposed, employing gradient descent with momentum and AO to optimize the digital and analog precoders of the hybrid precoder at the base station (BS) and the analog combiners at each UE.
- The proposed learning-based algorithm is less complex than other existing solutions, which primarily utilize SDR. In particular, SDR-based algorithms involve vector-lifting, which can be costly as it expands the dimensionality of the decision variables, increasing complexity. Further, SDR-based solutions expand the feasible set of the decision variables, yielding solutions that are

not necessarily feasible for the original problem, thus necessitating a subsequent rank-one projection. This projection may affect the solution found and degenerate its optimality. In contrast, the proposed algorithm involves only matrix multiplications, additions, low-dimensional matrix inversions, and simple projections.

- In contrast to existing solutions, which only allow a limited number of phase rotation values to design the analog precoder, the proposed algorithm can handle an arbitrary number of constant-modulus phase rotations. Similarly, the proposed algorithm is extended to design the analog combiners, which are subject to the same constant-modulus phase rotation constraints.
- The proposed algorithm features exploration and exploitation stages that help to find high-quality solutions avoiding stagnation at low-quality local optima.
- The proposed algorithm is evaluated in various scenarios, showing that it can perform similarly to a fully-digital precoder.

2.5 INVESTIGATED PROBLEM

Consider a millimeter-wave system, where a BS serves several UEs, as shown in Figure 1.

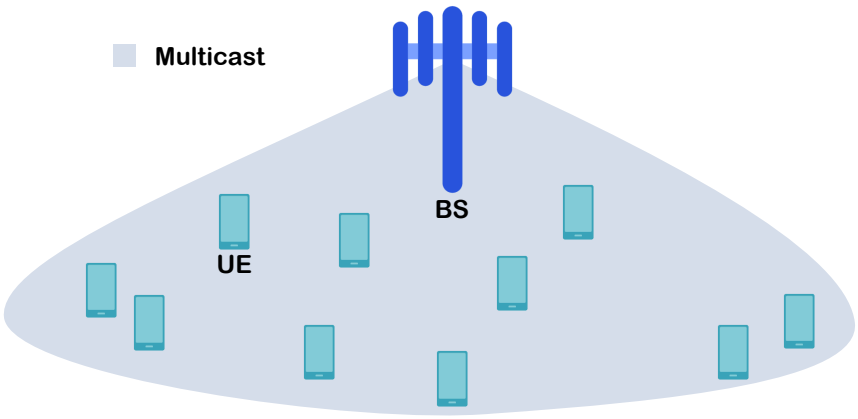

Figure 1: SDMA-based multicast system consisting of a BS and several UEs.

Generalities

The number of UEs is K and they are indexed by set $\mathcal{K} = \{1, 2, \ldots, K\}$. In particular, all UEs are served with the same information by means of a multicast signal.

The BS is equipped with N_{tx} transmit antennas and N_{tx}^{RF} radiofrequency (RF) chains, such that $N_{tx}^{RF} \leqslant N_{tx}$. The downlink signal transmitted from the BS to UEs is represented by $\mathbf{x} = \mathbf{F}\mathbf{m}s$, where $\mathbf{F} \in \mathbb{C}^{N_{tx} \times N_{tx}^{RF}}$ and $\mathbf{m} \in \mathbb{C}^{N_{tx}^{RF} \times 1}$ denote respectively the analog and digital precoders constituting the hybrid precoder. The multicast data symbol $s \in \mathbb{C}$, transmitted from the BS, has unit power on average, i.e., $\mathbb{E}\{ss^*\} = 1$. Every element of the analog precoder is a phase rotation, denoted by $[\mathbf{F}]_{q,r}$ and controlled by an independent phase shifter that selects a value from set $\mathcal{F} = \left\{\sqrt{\delta_{tx}}, \ldots, \sqrt{\delta_{tx}} e^{j\frac{2\pi(L_{tx}-1)}{L_{tx}}}\right\}$, where $\sqrt{\delta_{tx}}$ is the phase modulus, L_{tx} is the number of allowed phase rotations, $q \in \mathcal{Q} = \{1, \ldots, N_{tx}\}$, and $r \in \mathcal{R} = \left\{1, \ldots, N_{tx}^{RF}\right\}$.

Each UE is equipped with N_{rx} receive antennas and a single RF chain, i.e., $N_{rx}^{RF} = 1$. The analog combiner at each UE is denoted by $\mathbf{w}_k \in \mathbb{C}^{N_{rx} \times 1}$, and each of its elements $[\mathbf{w}_k]_l$ can take values from set $\mathcal{W} = \left\{\sqrt{\delta_{rx}}, \ldots, \sqrt{\delta_{rx}} e^{j\frac{2\pi(L_{rx}-1)}{L_{rx}}}\right\}$, where $\sqrt{\delta_{rx}}$ is the phase modulus, L_{rx} is the number of allowed phase rotations, and $l \in \mathcal{L} = \{1, \ldots, N_{rx}\}$.

Under the assumption of narrowband flat-fading, the signal received by the k-th UE is given by

$$y_k = \underbrace{\mathbf{w}_k^H \mathbf{H}_k \mathbf{F}\mathbf{m}s}_{\text{multicast signal}} + \underbrace{\mathbf{w}_k^H \mathbf{n}_k}_{\text{noise}}, \tag{1}$$

where $\mathbf{H}_k \in \mathbb{C}^{N_{rx} \times N_{tx}}$ denotes the channel between the BS and the k-th UE, whereas $\mathbf{n}_k \sim \mathcal{CN}\left(\mathbf{0}, \sigma^2 \mathbf{I}\right)$ denotes circularly symmetric Gaussian noise. The SNR at the k-th UE is given by

$$\gamma_k = \frac{\left|\mathbf{w}_k^H \mathbf{H}_k \mathbf{F}\mathbf{m}\right|^2}{\sigma^2 \left\|\mathbf{w}_k\right\|_2^2}. \tag{2}$$

Problem formulation

The goal is to design the hybrid precoder and analog combiners that maximize the minimum SNR among all UEs, subject to transmit power and constant-modulus phase rotation constraints. The maximization of the minimum SNR is chosen as the objective function because, in multicast applications, the UE with the weakest link dic-

tates the performance for the rest of UEs. The optimization problem is defined as,

$$\mathcal{P}: \max_{\mathbf{F},\mathbf{m},\{\mathbf{w}_k\}_{k=1}^{K}} \min_{k\in\mathcal{K}} \quad \frac{\left|\mathbf{w}_k^H \mathbf{H}_k \mathbf{F}\mathbf{m}\right|^2}{\sigma^2 \left\|\mathbf{w}_k\right\|_2^2} \tag{3a}$$

$$\text{s.t.} \quad \|\mathbf{F}\mathbf{m}\|_2^2 = P_{tx}^{max}, \tag{3b}$$

$$\|\mathbf{F}\|_F^2 = 1, \tag{3c}$$

$$[\mathbf{F}]_{q,r} \in \mathcal{F}, q \in \mathcal{Q}, r \in \mathcal{R}, \tag{3d}$$

$$\|\mathbf{w}_k\|_2^2 = P_{rx}^{max}, k \in \mathcal{K}, \tag{3e}$$

$$[\mathbf{w}_k]_l \in \mathcal{W}, l \in \mathcal{L}, \forall k \in \mathcal{K}, \tag{3f}$$

where (3a) aims to maximize the minimum SNR, (3b) restricts the transmit power of the hybrid precoder to P_{tx}^{max}, (3c) imposes a power normalization on the phase rotations, (3d) enforces every phase rotation of the analog precoder to belong to set $\mathcal{F}$, (3e) restrains the power of the analog combiners to P_{rx}^{max}, and (3f) constrains the phase rotations of the combiners to $\mathcal{W}$.

Constraints (3d) and (3f) define nonconvex sets on $\mathbf{F}$ and $\mathbf{w}_k$ due to their combinatorial nature. Also, (3b) is nonconvex as it exhibits a multiplicative coupling between $\mathbf{F}$ and $\mathbf{m}$. The objective function (3a) is defined as the ratio of two quadratic expressions, where the numerator exhibits a coupling of three different decision variables, making it nonconvex. Besides, nonconvex constraints (3c) and (3e) can be circumvented as the phase rotations have constant modulus, which results in $\delta_{tx} = \frac{1}{N_{tx}^{RF} N_{tx}}$ and $\delta_{rx} = \frac{P_{rx}^{max}}{N_{rx}}$. However, the problem remains nonconvex and challenging to solve.

Note: *For details on the proposed algorithm to solve $\mathcal{P}$, the reader is referred to [A], which can also be found in Appendix A.*

2.6 SELECTED RESULTS

In the following, simulation results of a specific scenario in [A] are discussed. Figure 2 shows the minimum SNR, i.e., the objective of problem $\mathcal{P}$, achieved by the proposed algorithm applied to hybrid and fully-digital precoders.

Figure 2 is taken from [A], but the layout has been slightly modified.

At the BS, the number of antennas is $N_{tx} = 15$ and the number of RF chains is $N_{tx}^{RF} = 6$. At the UEs, the number of antennas is $N_{tx} = 2$ and the number of RF chains is $N_{rx}^{RF} = 1$. The number of UEs is $K = 30$, and $N_{xpr} = \{1, \ldots, 100\}$ and $N_{xpl} = \{1, \ldots, 100\}$ denote respectively the number of exploration and exploitation instances.

The results in Figure 2 show that the proposed algorithm attains significantly higher gains for various numbers of UEs in the system,

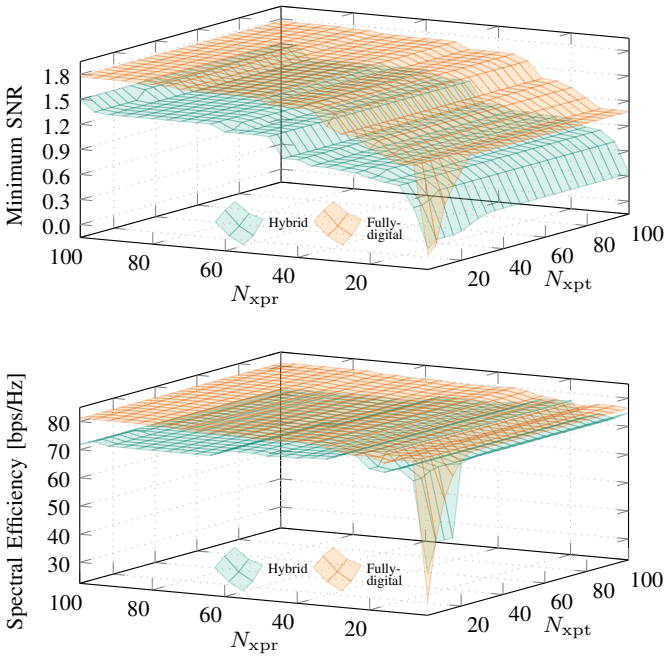

Figure 2: Minimum SNR achieved.

showing its superiority compared to the SDR-based algorithm. Also, it is observed that the minimum SNR decreases as the number of UEs increases, since the limited transmit power must be shared among more UEs, thus decreasing the power contributions for each UE.

The results in Figure 2 show that the minimum SNR improves for increasing values of N_{xpr} and N_{xpt} for both precoding architectures. In addition, N_{xpr} is more relevant than N_{xpt} in improving this metric for the particular realization shown in Figure 2. Nevertheless, both phases are critical. Exploration is the capability of effectively scanning the search space to find potentially fitter solutions, whereas exploitation capitalizes on already known solutions to refine them further. Via these mechanisms, the proposed algorithm avoids getting trapped in local optima. As expected, the fully-digital precede outperforms its hybrid counterpart because it has a larger number of RF chains and is not constrained to constant-modulus phase shifts. The performance gap between the precoders is small. The fully-digital precoder attains a minimum SNR of 1.77, whereas the hybrid precoder achieves 1.49. While the minimum SNR increases monotonically for both precoders, the spectral efficiency (SE), defined as the sum of all rates, does not exhibit the same behavior. This occurs because the optimization criterion of the algorithm is to enhance the minimum SNR and does not consider the SE.

3

PRECODING FOR MULTI-GROUP MULTICAST BASED ON SDMA

This chapter gives an overview of the research problem investigated in [B], which is included in Appendix B. In the following, the motivation is given, the goal is stated, the related work is reviewed, the contributions are summarized, the research problem is formulated, and selected results are discussed.

3.1 MOTIVATION

In today's wireless networks, multicasting has found multiple applications, e.g., for video streaming and conferencing. Most studies have investigated precoding designs for multicasting using fully-digital precoders in the sub-6GHz spectrum. However, as the sub-6GHz spectrum continues to be over-utilized, the millimeter-wave spectrum has emerged as an alternative, requiring hybrid precoders for cost-effective operation [30]. However, the benefits and challenges of multicasting with hybrid precoders in the millimeter-wave spectrum still need to be further explored, especially when considering multiple groups of user equipments (UEs), known as multi-group multicasting. Multi-group multicasting involves sending simultaneously different data streams, each targeting a specific group of UEs. Due to the spatial reuse of spectrum resources, interference arises, and therefore its mitigation through precoding becomes crucial. However, hybrid precoders are less effective than fully-digital precoders in mitigating interference, as the former have fewer radiofrequency (RF) chains, making the design of performant hybrid precoders challenging. Thus, it is of significant interest to investigate hybrid precoder designs for multi-group multicasting to support future applications that can benefit from the millimeter-wave spectrum.

3.2 GOAL

The goal is to design a hybrid precoder for transmit power minimization, subject to satisfying constant-modulus phase rotation constraints and target quality-of-service (QoS) requirements for each multicast group. In particular, it is of great interest to guarantee the QoS requirements for the UEs with minimal transmit power. This is especially desirable when using hybrid precoders, which consume more power

than fully-digital precoders. Specifically, hybrid precoders have much more limited capability to mitigate interference due to having fewer RF chains and thus they compensate for this lack of flexibility by consuming more power. This limitation is more significant in multi-group multicasting, where interference is significantly high, and the UEs with the worst channel conditions dictate the performance of the system. Thus, an algorithm is proposed to design multi-group multicast hybrid precoders. The proposed algorithm is based on semidefinite relaxation (SDR), alternating optimization (AO), and Cholesky matrix decomposition (CMD). Compared to previous works, the proposed algorithm does not need a customized network of phase shifters, nor is limited to a particular set of phase rotations.

3.3 RELATED WORK

Precoding for multi-group multicasting has been investigated with fully-digital precoders in [71–83] and with hybrid precoders in [68–70, 84, 85]. In multi-group multicasting, several data streams are transmitted using the same frequency resources, giving rise to interference. Consequently, the precoding design is paramount to combat interference and thus deliver the transmitted information with the desired QoS requirements. The following provides an overview of several works on multi-group multicast precoding design.

Precoding for multi-group multicasting with fully-digital precoders was first investigated in [71] for respectively minimizing the transmit power and maximizing the minimum signal-to-interference-plus-noise ratio (SINR). The authors showed the NP-hardness of these problems and proposed an algorithm to solve them using SDR and randomization, as an extension of their previous work [31]. In [76], the authors extended their previous work in [71] and gave insight into the relation between the maximization of the minimum SINR and the minimization of the transmit power, allowing them to develop more cost-effective algorithms. A similar work by the same authors is [77], in which Vandermonde channels were assumed to respectively minimize the transmit power and maximize the minimum SINR. The authors showed that the considered problems have rank-one solutions for Vandermonde channels and therefore can be solved optimally via SDR and eigendecomposition.

The authors of [78] proposed algorithms for maximizing the minimum SINR, inspired by the literature on multi-user precoding. In particular, the authors proposed extensions for multicast precoding based on multi-user precoding techniques, such as zero-forcing (ZF) and minimum mean square error (MMSE). Besides, the authors of [79] investigated the minimization of the transmit power and proposed an iterative algorithm based on second-order cone programs (SOCPs).

The authors showed that their SOCP-based reformulation is an inner approximation of the original nonconvex problem. The proposed algorithm was shown to perform relatively well compared to a lower bound obtained using SDR. The authors of [80] proposed an algorithm based on successive convex approximation (SCA) to maximize the minimum SINR, and showed that their algorithm can achieve very good performance compared to an SDR-based upper bound. In [81], an iterative algorithm was proposed for the maximization of the minimum SINR. The authors divided the problem into four simpler subproblems and solved them iteratively, achieving lower computation complexity than SDR-based algorithms and slightly better performance.

Other works on multi-group multicasting precoding with minor variations have been investigated, such as including transmit power constraints per antenna, [82, 83], incorporating energy harvesting [72], with multi-cell systems [73], for relaying purposes [74], and with power control for massive multiple-input multiple output (MIMO) [75].

Considering hybrid precoders, multigroup multicasting has been studied in fewer works. For instance, the authors of [84] investigated the maximization of the minimum SINR, and proposed an algorithm based on the penalty dual decomposition (PDD) method. The authors showed that the performance of the proposed algorithm was generally comparable to that of fully-digital precoders but only for a small number of UEs. The authors of [68] proposed a hybrid precoder architecture based on an especially connected network of phase shifters to maximize the minimum SINR or minimize the transmit power, showing performance close to that of fully-digital precoders. The authors of [69] proposed an algorithm based on SCA and AO to minimize the transmit power subject to energy harvesting constraints. The authors of [85] also investigated the transmit power minimization assuming outage probability constraints, and proposed an algorithm based on AO, SCA, and SDR. In [70], the phase shifters of the hybrid precoder were replaced by high-resolution lens arrays with adjustable magnitude and phase, which resulted in an architecture similar to that of a fully-digital precoder. Doing so removed the complicating constant-modulus phase rotation constraints, making the solution not applicable to usual hybrid precoder architectures.

3.4 CONTRIBUTIONS

The contributions of this chapter are summarized in the following.

- An algorithm is proposed, which leverages SDR, AO, and CMD, to sequentially optimize the digital and analog precoders at the base station (BS) and the fully-digital combiners at each UE.

In particular, the investigated problem is divided into multiple subproblems, each of which is tackled at a time until convergence is achieved.

- Unlike other works, the proposed algorithm can handle phase rotations with an arbitrary resolution for the analog precoder design. Also, the proposed algorithm introduces for the first time the use of CMD to design hybrid precoders, leading to increased flexibility for meeting the QoS requirements of the UEs. Specifically, the use of CMD in this work is in the same spirit as randomization but the difference is the echelon structure of the upper and lower triangular matrices that result from CMD. This allows to limit the randomization to only a subset of elements at a time.

- Simulation results show that the proposed algorithm can design hybrid precoders and successfully deliver a large number of packets to UEs, with similar performance to that of fully-digital precoders, at the expense of additionally larger transmit power.

3.5 INVESTIGATED PROBLEM

Consider a millimeter-wave system, where a BS serves UEs clustered into several groups, as shown in Figure 3.

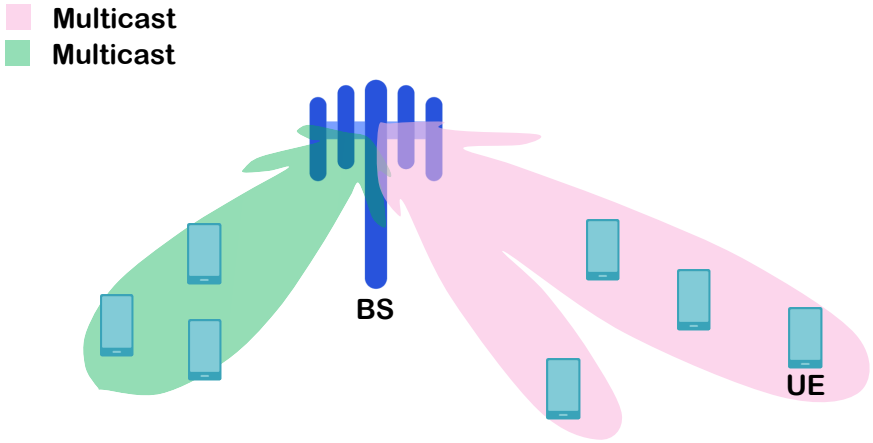

Figure 3: SDMA-based multicast system consisting of a BS and two groups of UEs.

Generalities

The number of UEs is K, which are evenly distributed into G different multicast groups. The UEs are indexed by set $\mathcal{K} = \{1, 2, \ldots, K\}$ and the multicast groups are indexed by set $\mathcal{I} = \{1, 2, \ldots, G\}$. The i-th

multicast group is denoted by $\mathcal{G}_i$ ($i \in \mathcal{I}$) and contains the indices of the UEs that constitute it. The number of UEs in each multicast group is represented by $|\mathcal{G}_i| = \frac{K}{G}$. In addition, it is assumed that $\sum_{i=1}^{G} |\mathcal{G}_i| = K$ and $\mathcal{G}_i \cap \mathcal{G}_j = \{\emptyset\}, \forall i \neq j$, forcing each UE to belong to only one group.

The BS is equipped with N_{tx} transmit antennas and N_{tx}^{RF} RF chains, such that $G \leqslant N_{tx}^{RF} \leqslant N_{tx}$. The downlink signal transmitted from the BS to the UEs is represented by $\mathbf{x} = \mathbf{FMs}$, where $\mathbf{F} \in \mathbb{C}^{N_{tx} \times N_{tx}^{RF}}$ is the analog precoder and $\mathbf{M} = [\mathbf{m}_1, \ldots, \mathbf{m}_G] \in \mathbb{C}^{N_{tx}^{RF} \times G}$ is the digital precoding matrix, which collects the digital precoders for all the multicast groups. The data symbols for the multicast groups are denoted by $\mathbf{s} = [s_1, s_2, \ldots, s_G]^T \in \mathbb{C}^{G \times 1}$, where the entries have unit powers on average and are statistically independent from one another, i.e., $\mathbb{E}\{\mathbf{ss}^H\} = \mathbf{I}$. Every element of the analog precoder, denoted by $[\mathbf{F}]_{q,r}$, is controlled by a phase shifter that sets a phase rotation with constant modulus $\sqrt{\delta_{tx}}$, i.e., $[\mathbf{F}]_{q,r} \in \mathcal{F} = \left\{\sqrt{\delta_{tx}}, \ldots, \sqrt{\delta_{tx}} e^{j\frac{2\pi(L_{tx}-1)}{L_{tx}}}\right\}$, where $q \in \mathcal{Q} = \{1, \ldots, N_{tx}\}$, $r \in \mathcal{R} = \{1, \ldots, N_{tx}^{RF}\}$, and L_{tx} is the number of allowed phase rotations.

Each UE is endowed with N_{rx} receive antennas and N_{rx}^{RF} RF chains, where $N_{rx}^{RF} = N_{rx}$, thus resulting in fully-digital combiners. This is assumed to be possible because N_{rx} is in general small. The combiner at each UE is denoted by $\mathbf{w}_k \in \mathbb{C}^{N_{rx} \times 1}$, such that $\|\mathbf{w}_k\|_2^2 = P_{rx}^{max}$.

Under the assumption of narrowband flat-fading, the signal received by the k-th UE, with $k \in \mathcal{G}_i$, is given by

$$y_k = \underbrace{\mathbf{w}_k^H \mathbf{H}_k \mathbf{F} \mathbf{m}_i s_i}_{\text{desired multicast signal}} + \underbrace{\mathbf{w}_k^H \mathbf{H}_k \sum_{\substack{j=1 \\ j \neq i}}^{G} \mathbf{F} \mathbf{m}_j s_j}_{\text{interference}} + \underbrace{\mathbf{w}_k^H \mathbf{n}_k}_{\text{noise}}, \tag{4}$$

where i is the index of group $\mathcal{G}_i$. In addition, $\mathbf{H}_k \in \mathbb{C}^{N_{rx} \times N_{tx}}$ denotes the channel between the BS and the k-th UE, whereas $\mathbf{n}_k \sim \mathcal{CN}(\mathbf{0}, \sigma^2 \mathbf{I})$ denotes circularly symmetric Gaussian noise. The SINR at the k-th UE is defined as

$$\text{SINR}_k = \frac{\left|\mathbf{w}_k^H \mathbf{H}_k \mathbf{F} \mathbf{m}_i\right|^2}{\sum_{j \neq i} \left|\mathbf{w}_k^H \mathbf{H}_k \mathbf{F} \mathbf{m}_j\right|^2 + \sigma^2 \|\mathbf{w}_k\|_2^2}. \tag{5}$$

Problem formulation

The objective is to design the hybrid precoder and fully-digital combiners, such that the transmit power expenditure at the BS is minimized while satisfying a QoS requirement per multicast group.

The latter constraint means that each UE in a group must achieve a minimum target SINR. Thus, the optimization problem is defined as

$$\mathcal{P}: \min_{\mathbf{F},\{\mathbf{m}_i\}_{i=1}^{G},\{\mathbf{w}_k\}_{k=1}^{K}} \quad \sum_{i=1}^{G} \|\mathbf{F}\mathbf{m}_i\|_2^2 \tag{6a}$$

$$\text{s.t.} \quad \frac{\left|\mathbf{w}_k^H \mathbf{H}_k \mathbf{F}\mathbf{m}_i\right|^2}{\sum_{j\neq i}\left|\mathbf{w}_k^H \mathbf{H}_k \mathbf{F}\mathbf{m}_j\right|^2 + \sigma^2 \|\mathbf{w}_k\|_2^2} \geqslant \gamma_i, \tag{6b}$$

$$\|\mathbf{w}_k\|_2^2 = P_{rx}^{max}, \tag{6c}$$

$$\|\mathbf{F}\|_F^2 = N_{tx}^{RF}, \tag{6d}$$

$$[\mathbf{F}]_{q,r} \in \mathcal{F}, q \in \mathcal{Q}, r \in \mathcal{R}, \tag{6e}$$

where (6a) aims to minimize the transmit power used by the hybrid precoder at the BS. Constraint (6b) imposes specific QoS requirements for each multicast group $\mathcal{G}_i$ in terms of a target SINR denoted by γ_i. Constraint (6c) enforces a power expenditure equal to P_{rx}^{max} for the combiner of each UE. Constraint (6d) limits the power of the analog precoder, which is fixed because of the constant modulus of the phase rotations. In addition, (6e) enforces every phase rotation to belong to set $\mathcal{F}$.

Constraint (6a) is nonconvex due to multiplicative coupling between $\mathbf{F}$ and $\mathbf{m}_i$. Constraint (6b) is nonconvex since it is defined as the ratio of two nonconvex expressions. On the other hand, (6c) is quadratic and nonconvex on $\mathbf{w}_k$. Constraint (6e) is inherently of combinatorial nature, therefore nonconvex. Thus, (6d) is also nonconvex due to its dependence on (6e). As a result, $\mathcal{P}$ is nonconvex and challenging to solve.

Note: *For details on the proposed algorithm to solve $\mathcal{P}$, the reader is referred to [B], which can also be found in Appendix B.*

3.6 SELECTED RESULTS

In the following, simulation results of a specific scenario in [B] are discussed. Figure 4 shows the transmit power, i.e., the objective of $\mathcal{P}$, needed by the proposed hybrid precoder and a fully-digital precoder.

Figure 4 is taken from [B], but the layout has been slightly modified.

At the BS, the number of antennas is $N_{tx} = 12$ and the number of RF chains is $N_{tx}^{RF} = 8$. At the UEs, the number of antennas is $N_{tx} = 2$ and the number of RF chains is $N_{rx}^{RF} = 2$. The number of UEs is $K = 60$, the number of multicast groups is $G = 4$, and the number of randomizations is $N_{rand} = \{1, 10, 25, 50, 75, 100, 500, 1000\}$. Specifically, randomization is used to mitigate the performance loss caused by rank-one projections. In general, the performance tends to improve for higher values of N_{rand}. The target SINR $\gamma_i = 5$ dB is set the same for

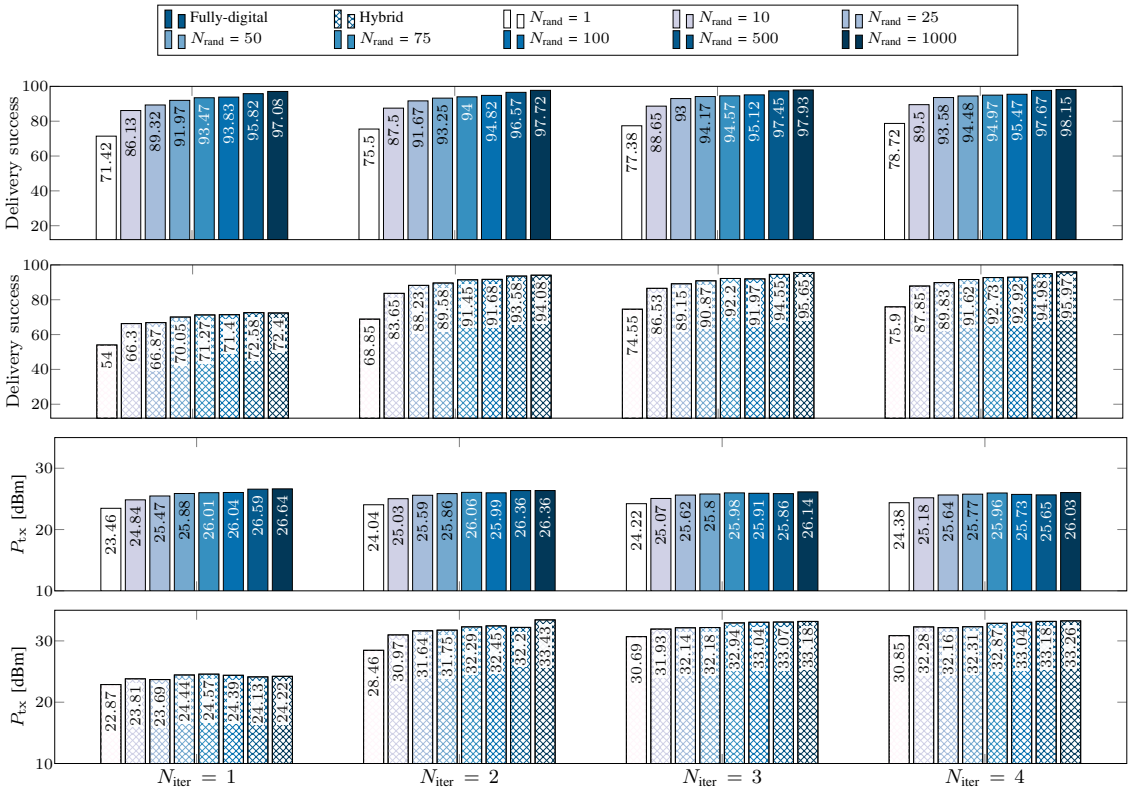

Figure 4: Delivery success and transmit power in a multi-group multicast system.

all multicast groups. Besides, $N_{iter} = \{1, 2, 3, 4\}$ represents the number of iterations needed by the proposed algorithm.

The results show that the proposed hybrid precoder improves the delivery success, i.e., the percentage of successfully received packets by the UEs, as the number of iterations N_{iter} increases. In fact, beyond $N_{iter} = 4$ the results do not change substantially, showing that the algorithm converges quickly. It is also noted that the performance of the fully-digital precoder does not change significantly as the number of iterations increases. This occurs because it converges much quicker since it has fewer variables to optimize. In contrast, the analog phase rotations in the hybrid precoder pose a difficulty for optimization, and therefore its convergence is slower. Also, as the packet delivery success increases with every iteration, the hybrid precoder consumes more transmit power. Specifically, to satisfy the QoS requirements for more UEs, an increment in the transmit power is needed.

4

PRECODING FOR UNICAST AND MULTICAST BASED ON LDMA

This chapter gives an overview of the research problem investigated in [C], which is included in Appendix C. In the following, the motivation is given, the goal is stated, the related work is reviewed, the contributions are summarized, the research problem is formulated, and selected results are discussed.

4.1 MOTIVATION

Modern production factories consist of several industrial IoT (IIoT) devices, such as sensors, actuators, programmable logic devices, and robotic arms, interconnected by redundant wiring to ensure safety and reliable communications during the various manufacturing stages [86]. However, wires limit automation and restrict the mobility of robotics. As a result, wireless technologies are a promising alternative for replacing wires, which are undesirable for future intelligent factories, also known as Industry 4.0 [87].

Recent studies have highlighted the importance of leveraging non-orthogonal multiple access to improve wireless networks' capacity and spectral efficiency [88, 89]. In addition, the millimeter-wave spectrum is considered a key driver to meet the high throughput requirements of future wireless networks [13–15]. Therefore, non-orthogonal multiple access and millimeter-wave spectrum together are expected to support many use cases, including Industry 4.0 scenarios [90–92].

Layered-division multiple access (LDMA) is a non-orthogonal multiple access variant that allows the simultaneous transmission of different signals by overlaying them on the same radio resources [23, 24]. This characteristic makes LDMA attractive, for instance, for transmitting common information via multicast signals and private information via unicast signals, known as non-orthogonal unicast and multicast (NOUM). In particular, using LDMA for implementing NOUM is advantageous as it eliminates the need to resort to time-division multiple access (TDMA) or frequency-division multiple access (FDMA) to switch between unicast and multicast traffic transmission, thus improving resource utilization. However, LDMA requires user equipments (UEs) to perform successive interference cancellation (SIC) to decode the multicast signal before accessing the

unicast signals. Therefore, the precoding design is relevant to ensure adequate signal-to-interference-plus-noise ratios (SINRs) to differentiate multicast from the unicast signals. In addition, the integration of NOUM with LDMA and the millimeter-wave spectrum has not been studied in depth. Furthermore, hybrid precoders are preferable for exploiting the millimeter-wave spectrum, but their design poses challenges owing to digital-analog couplings. Consequently, further research in this direction is needed.

4.2 GOAL

The goal is to design a hybrid precoder to maximize the unicast and multicast sum rate (SR) of NOUM transmissions based on LDMA, subject to transmit power and constant-modulus phase rotation constraints. Investigating the precoding design for LDMA-based NOUM is essential, especially for future wireless network deployments, where multicast and unicast signals are expected to coexist. Thus, two algorithms are proposed, which leverage successive convex approximation (SCA) and alternating optimization (AO). As a potential application of NOUM, an industrial setting is considered. Specifically, the base station (BS) transmits two types of overlapping signals. The first type is comprised of a single multicast signal carrying common control information with superlative importance (e.g., critical control packets) and targeting all IIoT devices. The second type is comprised of a set of unicast signals carrying less critical private information (e.g., routine updates) for the IIoT device. It is worth mentioning that only a few works have investigated the hybrid precoder design for NOUM transmissions based on LDMA.

4.3 RELATED WORK

The design of precoders for NOUM transmissions based on LDMA has been investigated for several purposes, with fully-digital precoders in [93–103] and with hybrid precoders in [104–107]. Since NOUM includes a multicast signal, the precoder design for NOUM is NP-hard [31]. In addition, due to the mutual interference caused by resource sharing of unicast and multicast signals, and the complicated analog-digital couplings of the hybrid precoder, a proper precoder design is required. The following provides an overview of several works investigating the precoding design for LDMA-based NOUM.

The authors of [93] investigated the precoder design for transmit power minimization and proposed two algorithms based on SCA and semidefinite relaxation (SDR). The authors showed that LDMA can outperform TDMA, as LDMA reuses the same radio resources without resorting to time sharing. The authors extended their work in [96],

assuming an imperfect channel. A work similar to [96] is [97], where an application to satellite communications was considered.

The transmit power minimization was also investigated in [98], where two algorithms based on SCA and branch-and-bound (BnB) were proposed. Besides, the authors of [99] proposed an algorithm based on SCA in order to minimize the transmit power considering a system with cooperative BSs, which were subject to backhaul capacity constraints. The work was extended in [100], where BS clustering was included, and a BnB algorithm was proposed for its solution.

The energy efficiency (EE) maximization was investigated in [101], where the authors proposed an algorithm based on SCA. Specifically, the authors showed that LDMA has higher EE than TDMA. The EE maximization was also investigated in [102], assuming a cell-free network. The authors proposed an algorithm based on SCA for the solution. The same authors extend their work in [103], including energy harvesting constraints. Besides, a learning-based algorithm was proposed in [94] to maximize the weighted sum rate (WSR) of unicast and multicast signals. The authors of [95] also investigated the WSR maximization of unicast and multicast signals. They proposed an algorithm based on SCA and a statistical description of the channel.

Considering hybrid precoders, LDMA-based NOUM has been studied in fewer works. For instance, the authors of [104] investigated the WSR maximization of unicast and multicast signals. The authors designed the analog precoder using a heuristic method and the digital precoder using zero-forcing (ZF) technique. In addition, the authors used SCA to optimize the power allocation of the digital precoder. In [105, 106], the EE maximization with energy harvesting constraints was investigated. The authors proposed an algorithm based on SCA and the bisection method to solve the investigated problems. A system with cooperative BSs was envisaged in [107] for the WSR maximization of unicast and multicast signals. The authors proposed a framework based on several techniques including Bayesian learning.

4.4 CONTRIBUTIONS

The contributions of this chapter are summarized in the following.

- Two novel algorithms based on SCA and AO are proposed to accomplish the design of hybrid precoders at the BS and analog combiners at the UEs.
- This is the first study that prioritizes multicast over unicast signals in LDMA-based NOUM transmissions by proposing a power-splitting mechanism. The power splitting ensures that the multicast signal is received with a higher power than the power

of all unicast signals together, which enables the SIC decoder to operate correctly.

- A fairness constraint is included to guarantee ubiquitous multicast service. Specifically, it guarantees the delivery of critical control packets that ensure that multicast information is received and decoded on all IIoT devices.
- Two algorithms are proposed. The first one designs independently the multicast precoder from the unicast precoders. Specifically, the unicast precoders are pre-designed as the unit-norm ZF precoding vectors and their powers are optimized. In the second algorithm, the multicast precoder is designed as a conic combination of the unicast unit-norm ZF precoding vectors.
- The proposed algorithms are compared against a benchmark algorithm in terms of SR and bit error rate (BER). It is shown that one of the proposed algorithms outperforms the benchmark in terms of SR while the other proposed algorithm is slightly outperformed. However, the two proposed algorithms exhibit a higher BER compared to the existing benchmark, demonstrating the importance of prioritizing the multicast signals in LDMA-based NOUM transmissions, where overlapping signals may interfere with each other.

4.5 INVESTIGATED PROBLEM

Consider a millimeter-wave system, where a BS serves multiple IIoT devices, as shown in Figure 5.

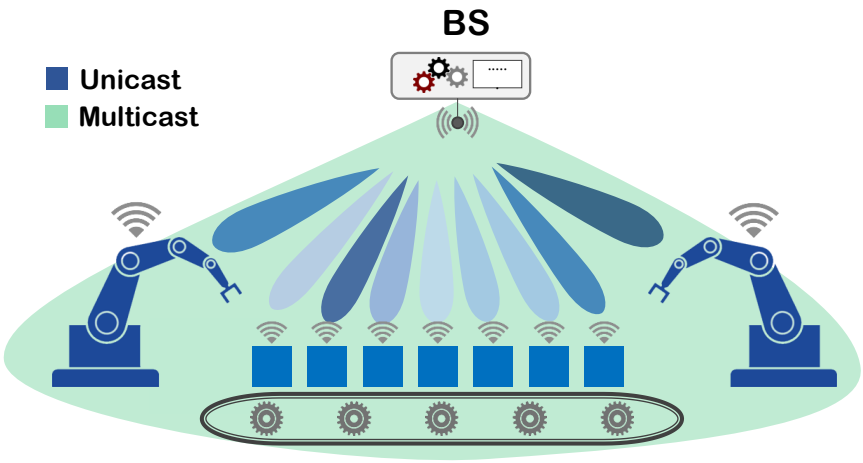

Figure 5: LDMA-based NOUM industrial system consisting of a BS and several IIoT devices.

Generalities

The number of IIoT devices is K and they are indexed by set $\mathcal{K} = \{1, \ldots, K\}$. All the IIoT devices is served by the same multicast signal, which carries common information. In addition, the IIoT devices receive unicast signals, which convey private information for each of them.

The BS is equipped with a hybrid precoder consisting of N_{tx} transmit antennas and N_{tx}^{RF} radiofrequency (RF) chains, where $N_{tx}^{RF} \leqslant N_{tx}$. Without loss of generality, it is assumed that $N_{tx}^{RF} = K$. The downlink signal, transmitted from the BS to the IIoT devices, is represented by $\mathbf{x} = \mathbf{F}[\mathbf{B}|\mathbf{m}][\mathbf{s}|z]^T$, where $\mathbf{F} = [\mathbf{f}_1, \ldots, \mathbf{f}_K] \in \mathbb{C}^{N_{tx} \times K}$ is the analog precoder, $\mathbf{B} = [\mathbf{b}_1, \ldots, \mathbf{b}_K] \in \mathbb{C}^{K \times K}$ is the unicast precoding matrix formed by all unicast precoding vectors $\mathbf{b}_k$, and $\mathbf{m} \in \mathbb{C}^{K \times 1}$ is the multicast digital precoder. In addition, $\mathbf{s} = [s_1, \ldots, s_K]^T \in \mathbb{C}^{K \times 1}$ denotes the unicast data symbols for the K IIoT devices and $z \in \mathbb{C}$ represents the multicast symbol, where $\mathbb{E}\left\{[\mathbf{s}^T z]^H [\mathbf{s}^T z]\right\} = \mathbf{I}$. Every element $[\mathbf{F}]_{q,r}$ of the analog precoder is controlled by a phase shifter that chooses a phase rotation from set $\mathcal{F} = \left\{1/\sqrt{N_{tx}}, \ldots, 1/\sqrt{N_{tx}} e^{j\frac{2\pi(L_{tx}-1)}{L_{tx}}}\right\}$, where $q \in \mathcal{Q} = \{1, \ldots, N_{tx}\}$ and $r \in \mathcal{R} = \left\{1, \ldots, N_{tx}^{RF}\right\}$. In addition, L_{tx} denotes the number of phase rotations in $\mathcal{F}$.

Each IIoT device is equipped with N_{rx} receive antennas and a single RF chain, i.e., $N_{rx}^{RF} = 1$. Further, $\mathbf{w}_k \in \mathbb{C}^{N_{rx} \times 1}$ represents the analog combiner of the k-th IIoT device. Every element $[\mathbf{w}_k]_n$ of the analog combiners is restricted to $\mathcal{W} = \left\{1/\sqrt{N_{rx}}, \ldots, 1/\sqrt{N_{rx}} e^{j\frac{2\pi(L_{rx}-1)}{L_{rx}}}\right\}$, where $n \in \mathcal{N} = \{1, \ldots, N_{rx}\}$. Also, L_{rx} denotes the number of phase rotations in $\mathcal{W}$.

Under the assumption of narrowband flat-fading, the signal received by the k-th IIoT device is given by

$$y_k = \underbrace{\mathbf{w}_k^H \mathbf{H}_k \mathbf{F} \mathbf{m} z}_{\text{common multicast signal}} + \underbrace{\mathbf{w}_k^H \mathbf{H}_k \mathbf{F} \mathbf{b}_k s_k}_{\text{unicast signal for the } k\text{-th device}} + \underbrace{\mathbf{w}_k^H \mathbf{H}_k \mathbf{F} \sum_{j \neq k} \mathbf{b}_j s_j}_{\text{interference at the } k\text{-th device}} + \underbrace{\mathbf{w}_k^H \mathbf{n}_k}_{\text{noise}}, \tag{7}$$

where $\mathbf{H}_k \in \mathbb{C}^{N_{rx} \times N_{tx}}$ denotes the channel between the BS and the k-th IIoT device, whereas $\mathbf{n}_k \sim \mathcal{CN}\left(\mathbf{0}, \sigma^2 \mathbf{I}\right)$ denotes circularly symmetric Gaussian noise.

At each IIoT device, SIC is employed to obtain the multicast and unicast information transmitted from the BS. The multicast symbol z is decoded first by treating all unicast signals as interference. Afterwards, the multicast signal is reconstructed using the already decoded symbol

z and is subtracted from y_k. After removing the multicast signal, the remaining signal consists only of unicast components and noise, from where each IIoT device can decode its intended unicast symbol s_k.

The SINR of the multicast and unicast signals are, respectively, defined as

$$\mathrm{SINR}_k^{\mathrm{multicast}} = \frac{\left|\mathbf{w}_k^H \mathbf{H}_k \mathbf{F}\mathbf{m}\right|^2}{\sum_j \left|\mathbf{w}_k^H \mathbf{H}_k \mathbf{F}\mathbf{b}_j\right|^2 + \sigma^2 \left\|\mathbf{w}_k\right\|_2^2} \tag{8}$$

$$\mathrm{SINR}_k^{\mathrm{unicast}} = \frac{\left|\mathbf{w}_k^H \mathbf{H}_k \mathbf{F}\mathbf{b}_k\right|^2}{\sum_{j\neq k} \left|\mathbf{w}_k^H \mathbf{H}_k \mathbf{F}\mathbf{b}_j\right|^2 + \sigma^2 \left\|\mathbf{w}_k\right\|_2^2}. \tag{9}$$

Problem formulation

The objective is to design the hybrid precoder and analog combiners that maximize the SR of the system, subject to transmit power, constant-modulus phase rotations, and fairness constraints. Thus, the optimization problem is defined as,

$$\begin{aligned}
\mathcal{P}: \max_{\substack{\{\mathbf{w}_k\}_{k=1}^K, \\ \{\mathbf{f}_k\}_{k=1}^K, \\ \{\mathbf{b}_k\}_{k=1}^K, \mathbf{m}, \Delta}} \quad & \sum_{k=1}^{K} \log_2\left(1+\mathrm{SINR}_k^{\mathrm{multicast}}\right) \\
& + \sum_{k=1}^{K} \log_2\left(1+\mathrm{SINR}_k^{\mathrm{unicast}}\right) - C\Delta && \text{(10a)} \\
\text{s.t.} \quad & \left|\mathrm{SINR}_k^{\mathrm{multicast}} - \gamma_{\min}\right| \leqslant \Delta, \forall k \in \mathcal{K}, && \text{(10b)} \\
& \left\|\mathbf{F}\mathbf{m}\right\|_2^2 / \sum_k \left\|\mathbf{F}\mathbf{b}_k\right\|_2^2 \geqslant \beta, && \text{(10c)} \\
& \left\|\mathbf{F}\mathbf{m}\right\|_2^2 + \sum_k \left\|\mathbf{F}\mathbf{b}_k\right\|_2^2 \leqslant P_{\mathrm{tx}}^{\max}, && \text{(10d)} \\
& [\mathbf{F}]_{q,r} \in \mathcal{F}, q \in \mathcal{Q}, r \in \mathcal{R}, && \text{(10e)} \\
& [\mathbf{w}_k]_n \in \mathcal{W}, n \in \mathcal{N}, \forall k \in \mathcal{K}, && \text{(10f)} \\
& \Delta \geqslant 0, && \text{(10g)}
\end{aligned}$$

where (10a) maximizes the overall SR of the unicast and multicast signals. In addition, the objective contains penalty function $C\Delta$, where C is a very large value that promotes minimization of Δ and helps to improve multicast fairness. Constraint (10b) aims to minimize the multicast SINR deviation from a target $\gamma_{\min}$. Constraint (10c) splits the power among multicast and unicast signals with the aim of giving higher priority to multicast information and thus ensure successful SIC decoding. Constraint (10d) limits the transmit power to $P_{\mathrm{tx}}^{\max}$. Constraints (10e) and (10f) limits the phase rotations to sets $\mathcal{F}$ and

$\mathcal{W}$, respectively, ensuring the constant-modulus characteristics of the analog components. Finally, (10g) enforces the positiveness of Δ. All constraints as well as the objective are nonconvex, which makes it difficult to solve problem $\mathcal{P}$.

Note: *For details on the proposed algorithm to solve $\mathcal{P}$, the reader is referred to [C], which can also be found in Appendix C.*

4.6 SELECTED RESULTS

In the following, simulation results of a specific scenario in [C] are discussed. Figure 6 shows the SR and BER achieved by the proposed algorithms and a existing benchmark.

Figure 6 is taken from [C], but the layout has been slightly modified.

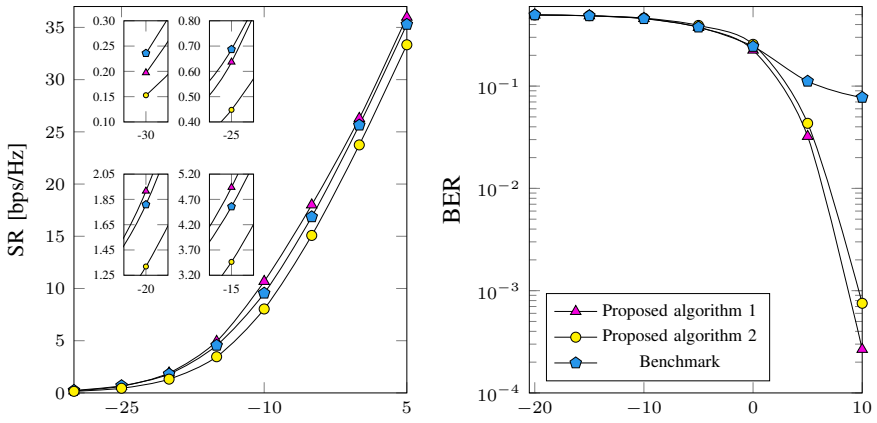

Figure 6: SR and BER of LDMA-based NOUM.

At the BS, the number of antennas is $N_{tx} = 64$ and the number of RF chains is $N_{tx}^{RF} = 6$. At the UEs, the number of antennas is $N_{tx} = 4$ and the number of RF chains is $N_{rx}^{RF} = 1$. The number of UEs is $K = 6$ whereas the number of allowed phase rotations at the BS and IIoT devices are $L_{tx} = 32$ and $L_{tx} = 4$, respectively. In addition, $P_{tx}^{max} = 1$ W, $\beta = 1$ and $\gamma_{min} = 5$ dB.

It is observed that the three algorithms perform similarly in terms of SR but greatly differ in terms of BER. In particular, the multicast BER is seldom satisfied by the existing algorithm, as multicast information is not prioritized and therefore unsuccessfully decoded, which leads to severely degraded BER. On the other, the proposed algorithms ensure the multicast quality-of-service (QoS) and therefore maintains a high unicast and multicast BER.

5

PRECODING FOR UNICAST AND MULTICAST BASED ON RSMA

This chapter gives an overview of the research problem investigated in [D], which is included in Appendix D. In the following, the motivation is given, the goal is stated, the related work is reviewed, the contributions are summarized, the research problem is formulated, and selected results are discussed.

5.1 MOTIVATION

The increase in wireless applications and the growing number of Internet of Things (IoT) devices are expected to aggravate the scarcity of radio resources. This problem is compounded by the need to support multiple services simultaneously, such as unicast and multicast. As a result, much attention has been devoted to studying non-orthogonal unicast and multicast (NOUM) transmissions, which can improve spectral efficiency (SE) by allowing unicast and multicast services to reuse the same radio resources. In addition, exploiting the millimeter-wave spectrum is expected to help alleviate the scarcity of radio resources in the sub-6GHz spectrum. Although previous works have shown that layered-division multiple access (LDMA) is an effective means of implementing NOUM, a more comprehensive multiple access scheme, called rate-splitting multiple access (RSMA), has recently emerged as an alternative technology [25]. In particular, RSMA has been shown to outperform non-orthogonal multiple access (NOMA) and space-division multiple access (SDMA) due to its capability to partially decode interference and partially treat remaining interference as noise. In contrast, SDMA fully treats interference as noise, whereas NOMA aims to fully decode interference. RSMA splits the signals for the user equipments (UEs) into private and common portions. The common portions are encoded into a single message, which is precoded and then transmitted in a multicast manner to all UEs. The private portions are encoded into independent messages and are precoded before being transmitted to the intended UEs. Therefore, in RSMA-based NOUM, the multicast signal transmitted to all UEs carries common information, such as video content, in addition to the common portions resulting from information splitting. The unicast signals only carry the private portions resulting from information splitting.

Given the rise of coexisting unicast and multicast services, investigating RSMA-based NOUM transmissions in the millimeter-wave spectrum is of timely interest. However, hybrid precoders will be required to exploit the millimeter-wave spectrum, posing difficulties owing to analog-digital couplings inherent to hybrid precoders. In fact, few studies have considered using hybrid precoders for NOUM transmissions based on RSMA, and therefore, this should be further investigated. Besides, the literature on RSMA has mainly focused on using weighted minimum mean square error (WMMSE) as a predominant means for RSMA precoding design. However, a disadvantage of WMMSE is that it strongly depends on the quality of the initial feasible points, which can lead to varying performance levels and high inconsistency. Also, existing studies have not compared RSMA against LDMA but only against NOMA and SDMA.

5.2 GOAL

The goal is to design a hybrid precoder to maximize the weighted sum rate (WSR) for NOUM transmissions based on RSMA, subject to transmit power limitations, constant-modulus phase rotations, and a minimum signal-to-interference-plus-noise ratio (SINR) requirement for the multicast signal. Thus, a new algorithm is proposed to design hybrid precoders. In particular, the proposed algorithm leverages successive convex approximation (SCA) and semidefinite relaxation (SDR) and is compared against the state-of-the-art WMMSE. In addition, the performance of RSMA and LDMA are compared.

5.3 RELATED WORK

The design of fully-digital precoders for RSMA-based NOUM has been investigated in [108–112]. In particular, the authors of [108] were the first to investigate this research problem. The authors studied the WSR maximization and proposed an algorithm leveraging WMMSE and alternating optimization (AO). The authors showed in multiple settings that RSMA outperforms NOMA and SDMA. The authors extended their work [108] and further investigated the energy efficiency (EE) maximization in [109]. They proposed an algorithm based on SCA and showed that RSMA can achieve higher EE than NOMA and SDMA. The authors of [110] investigated the precoding design to study the EE. The authors considered the minimization of the weighted sum of the transmit power and the rate mean square error (MSE), computed with respect to a desired rate value. In particular, the authors proposed a low-complexity algorithm based on fractional programming. Besides, the authors of [111, 112] combined dirty paper coding (DPC) and RSMA, referred to as dirty paper coding rate-splitting multiple access (DPC-RSMA). They investigated the WSR maximization and showed

that DPC-RSMA can attain higher SE than DPC or RSMA alone. To solve the investigated research problem, the authors developed an algorithm based on WMMSE and AO.

With hybrid precoders, RSMA-based NOUM was only investigated in [113]. Specifically, the authors investigated the transmit power minimization and proposed an algorithm based on SDR. The hybrid precoder design for NOUM using LDMA, a similar multiple access scheme to RSMA, was investigated in [104–107], as already revisited in Chapter 4.

Besides, literature that has addressed similar problems to WSR maximization for RSMA-based NOUM are, for example, [114–118]. In these works, however, there was no common information to transmit to the UEs except for the common portions resulting from rate-splitting.

5.4 CONTRIBUTIONS

The contributions of this chapter are summarized in the following.

- An algorithm is proposed based on sub-level and super-level sets, allowing to establish parametric convex upper bounds that can be adapted iteratively. In addition, the algorithm leverages sequential parametric optimization (SPO), SDR, and SCA, which provide desirable characteristics for precoder design in RSMA.
- The proposed algorithm converges to a local optimum of the nonconvex WSR maximization problem.
- The proposed algorithm does not rely on carefully selected initial feasible points, as WMMSE does, in order to guarantee high performance, thus facilitating its applicability.
- The proposed algorithm is compared against the optimal DPC, revealing a small optimality gap between the two algorithms.
- Quantizing the phase rotations of the hybrid precoder with 4 bits is sufficient for the proposed algorithm to achieve the same performance as fully-digital precoders under specific settings.
- The proposed algorithm is less prone than WMMSE to return infeasible solutions due to not strongly depending on initial feasible points. Nevertheless, the proposed algorithm has higher computational complexity per iteration but needs fewer number of iterations to converge. Overall, the time complexity of the proposed algorithm is much lower than that of WMMSE.

Consider a millimeter-wave system, where a base station (BS) serves several UEs, as shown in Figure 7

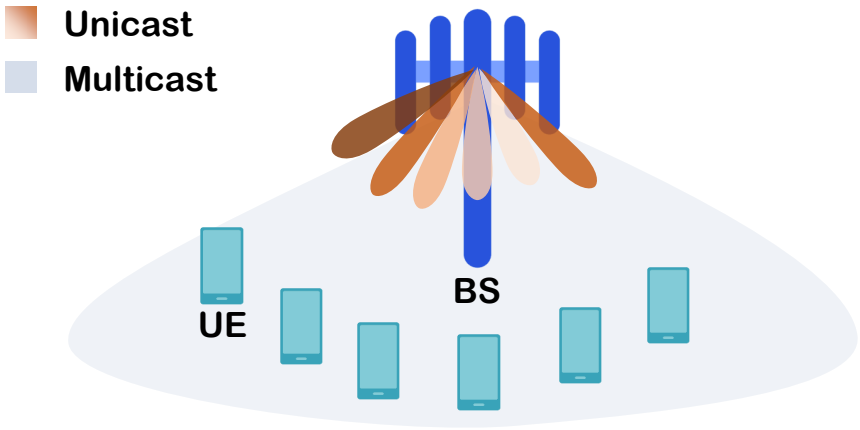

Figure 7: RSMA-based NOUM system consisting of a BS and several UEs.

Generalities

The number of UEs is K and they are indexed by set $\mathcal{K} = \{1, \ldots, K\}$. Each of the UEs expects to receive two messages from the BS, transmitted in a non-orthogonal manner, particularly a multicast message destined for all UEs and an unicast message intended only for a given UE. The multicast message is denoted by $W^{(m)}$ and the unicast message of the k-th UE is denoted by $W_k^{(u)}$.

The BS is equipped with a hybrid precoder consisting of N_{tx} transmit antennas and N_{tx}^{RF} radiofrequency (RF) chains, where $K \leqslant N_{tx}^{RF} \leqslant N_{tx}$. Without loss of generality, it is assumed that $N_{tx}^{RF} = K$. Every unicast message $W_k^{(u)}$ is decomposed into $W_k^{(u,c)}$ and $W_k^{(u,p)}$, which are known as the common and private portions of $W_k^{(u)}$, respectively. The multicast message together with the common parts of the unicast messages are jointly encoded into a common macro-stream as $\left\{W_1^{(u,c)}, \ldots, W_K^{(u,c)}, W^{(m)}\right\} \mapsto \widetilde{\mathbf{z}} = [\widetilde{z}_1, \widetilde{z}_2, \ldots]^T$. The unicast private portions are encoded into independent streams as $W_k^{(u,p)} \mapsto \widetilde{\mathbf{s}}_k = [\widetilde{s}_{k,1}, \widetilde{s}_{k,2}, \ldots]^T$, $\forall k \in \mathcal{K}$. Then, the encoded streams are precoded by the digital precoder $[\mathbf{B}|\mathbf{m}] = [\mathbf{b}_1, \ldots, \mathbf{b}_K, \mathbf{m}] \in \mathbb{C}^{K \times (K+1)}$. Let z and $\mathbf{s} = [s_1, \ldots, s_K]^T$ denote the instantaneous symbol and vector symbol of the common macro-stream and private streams, respectively, such that $\mathbb{E}\left\{\left[\mathbf{s}^T|z\right]^H \left[\mathbf{s}^T|z\right]\right\} = \mathbf{I}$. Thus, the downlink signal from the BS is $\mathbf{x} = \mathbf{F}\left[\mathbf{B}|\mathbf{m}\right]\left[\mathbf{s}^T|z\right]^T \in \mathbb{C}^{N_{tx} \times 1}$, where $\mathbf{F} = [\mathbf{f}_1, \ldots, \mathbf{f}_K] \in \mathbb{C}^{N_{tx} \times K}$ represents the analog precoder.

Under flat fading, the signal received by the k-th UE is

$$y_k = \underbrace{\mathbf{h}_k^H \mathbf{F} \mathbf{m} z}_{\substack{\text{common signal} \\ y_k^{(c)}}} + \underbrace{\mathbf{h}_k^H \mathbf{F} \mathbf{b}_k s_k}_{\substack{\text{private signal for the k-th UE} \\ y_k^{(p)}}} + \underbrace{\mathbf{h}_k^H \mathbf{F} \sum_{j \neq k} \mathbf{b}_j s_j}_{\substack{\text{interference at the k-th UE} \\ y_k^{(i)}}} + \underbrace{n_k}_{\text{noise}},$$

where $n_k \sim \mathcal{CN}\left(0, \sigma^2\right)$ denotes circularly symmetric Gaussian noise and $\mathbf{h}_k \in \mathbb{C}^{N_{tx} \times 1}$ is the channel between the BS and the k-th UE.

To decode the non-orthogonal signals transmitted by the BS, each UE relies on successive interference cancellation (SIC), which consists in decoding and removing one signal after the other. Specifically, the k-th UE decodes the common macro-stream symbol z (in term $y_k^{(c)}$) by treating the rest of signals as noise. Then, the common signal $y_k^{(c)}$ is reconstructed and subtracted from y_k. The remaining signal $\tilde{y}_k = y_k - y_k^{(c)}$ consists solely of private unicast components $\left\{y_k^{(p)}, y_k^{(i)}\right\}$ and noise n_k, from where the k-th UE decodes symbol s_k.

The SINR of the common macro-stream and private streams are denoted by $\text{SINR}_k^{(c)}$ and $\text{SINR}_k^{(p)}$, respectively.

$$\text{SINR}_k^{(c)} = \frac{\left|\mathbf{h}_k^H \mathbf{F} \mathbf{m}\right|^2}{\sum_{j \in \mathcal{K}} \left|\mathbf{h}_k^H \mathbf{F} \mathbf{b}_j\right|^2 + \sigma^2} \tag{11}$$

$$\text{SINR}_k^{(p)} = \frac{\left|\mathbf{h}_k^H \mathbf{F} \mathbf{b}_k\right|^2}{\sum_{j \neq k} \left|\mathbf{h}_k^H \mathbf{F} \mathbf{b}_j\right|^2 + \sigma^2} \tag{12}$$

Based on the SINRs in (11) and (12), the rates are defined as $R_k^{(c)} = \log_2\left(1 + \text{SINR}_k^{(c)}\right)$ and $R_k^{(p)} = \log_2\left(1 + \text{SINR}_k^{(p)}\right)$. In addition, $\bar{R}^{(c)}$ is defined as the maximal rate at which all UEs can decode the common symbol z. Therefore, the common macro-stream must be encoded at a rate $\bar{R}^{(c)} \leqslant R_{min}^{(c)}$, where $R_{min}^{(c)} = \min_{k \in \mathcal{K}} \left\{R_1^{(c)}, \ldots, R_K^{(c)}\right\}$. This holds true because the lowest rate dictates the performance in a multicast transmission.

Recall that z results from jointly encoding multiple components, i.e., the common portions $W_k^{(u,c)}$ resulting from rate-splitting and the common message $W^{(m)}$ which, for example, could be video content. Thus, let C_0 denote the fraction of $\bar{R}^{(c)}$ that carries the multicast message $W^{(m)}$, and C_k the fraction of $\bar{R}^{(c)}$ that carries the unicast common part $W_k^{(u,c)}$, such that $C_0 + \sum_{k \in \mathcal{K}} C_k = \bar{R}^{(c)}$. Upon decoding

the received signals, the k-th UE acquires $W_1^{(u,c)}, \ldots, W_K^{(u,c)}, W^{(m)}$, and $W_k^{(u,p)}$, from where the unicast message $W_k^{(u)}$ can be recomposed.

Problem formulation

The objective is to design a hybrid precoder that maximizes the WSR, subject to constraints on the transmit power and constant modulus of the phase rotations. The optimization problem is defined as,

$$\mathcal{P}: \max_{\substack{C_0, C_k, \\ \mathbf{F}, \mathbf{b}_k, \mathbf{m}}} \quad \sum_{k\in\mathcal{K}} \mu_k \left(C_k + \log_2\left(1 + \mathrm{SINR}_k^{(p)}\right)\right) \tag{13a}$$

$$\text{s.t.} \quad C_0 + \sum_{j\in\mathcal{K}} C_j \leqslant \min_{k\in\mathcal{K}} \left\{ R_1^{(c)}, \ldots, R_K^{(c)} \right\}, \tag{13b}$$

$$C_0 \geqslant C_0^{th}, \tag{13c}$$

$$C_k \geqslant 0, \forall k \in \mathcal{K}, \tag{13d}$$

$$\|\mathbf{Fm}\|_2^2 + \sum_{k\in\mathcal{K}} \|\mathbf{Fb}_k\|_2^2 \leqslant P_{tx}^{max}, \tag{13e}$$

$$[\mathbf{F}]_{n_1,n_2} \in \mathcal{F}, n_1 \in \mathcal{N}_1, n_2 \in \mathcal{N}_2, \tag{13f}$$

where $\mu_k > 0$ in (13a) is the weight assigned to the k-th UE and (13b) is used to enforce that the sum of common rate portions is at most $\min_{k\in\mathcal{K}} \left\{ R_1^{(c)}, \ldots, R_K^{(c)} \right\}$. Constraint (13c) imposes a minimum rate requirement C_0^{th} for decoding the common message whereas (13d) imposes a non-negativity restriction on the rates C_k. Constraint (13e) restricts the transmit power to P_{tx}^{max} while (13f) enforces the analog precoder characteristics. Concretely, every phase rotation $[\mathbf{F}]_{n_1,n_2}$ is constrained to set $\mathcal{F} = \left\{ \delta_{tx}, \ldots, \delta_{tx} \exp\left(j\frac{2\pi(L_{tx}-1)}{L_{tx}}\right)\right\}$, where L_{tx} is the number of allowed constant-modulus phase rotations, $\delta_{tx} = \sqrt{1/N_{tx}^{RF}}$, $n_1 \in \mathcal{N}_1 = \{1, \ldots, N_{tx}\}$, and $n_2 \in \mathcal{N}_2 = \left\{1, \ldots, N_{tx}^{RF}\right\}$. Note that the aggregate unicast rate of UE k is given by

$$R_k^{(u)} = C_k + \log_2\left(1 + \mathrm{SINR}_k^{(p)}\right). \tag{14}$$

Note: *For details on the proposed algorithm to solve $\mathcal{P}$, the reader is referred to [D], which can also be found in Appendix D.*

5.6 SELECTED RESULTS

In the following, simulation results of a specific scenario in [D] are discussed. Figure 8 shows the rates achieved by the proposed algorithm. The proposed algorithm was used for both LDMA and RSMA due to their similarity.

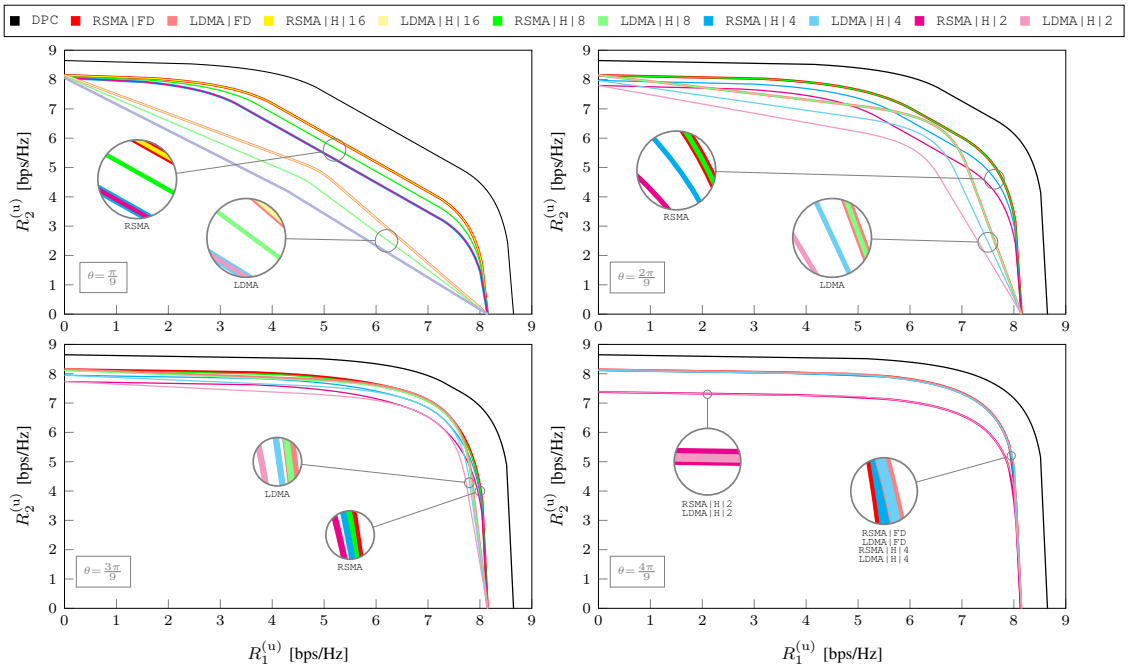

Figure 8: Rate performance of LDMA and RSMA.

Figure 8 show four scenarios, where $N_{tx} = 4$ and $K = 2$. The rates $R_1^{(u)}$ and $R_2^{(u)}$ are computed according to (14). The noise power is set to $\sigma^2 = 30$ dBm and the UE channels are defined as $\mathbf{h}_1 = [1, 1, 1, 1]^H$, $\mathbf{h}_2 = \left[1, e^{j\theta}, e^{j2\theta}, e^{j3\theta}\right]^H$, where the channel correlation between $\mathbf{h}_1$ and $\mathbf{h}_2$ is controlled by $\theta = \left\{\frac{\pi}{9}, \frac{2\pi}{9}, \frac{3\pi}{9}, \frac{4\pi}{9}\right\}$. Specifically, a small value, such as $\theta = \frac{\pi}{9}$ implies that the channels are highly correlated (nearly parallel) while a large value, such as $\theta = \frac{4\pi}{9}$ implies that the channels are highly uncorrelated (nearly orthogonal).

In the legend of Figure 8, "FD" and "H" are used to respectively identify the fully-digital and hybrid precoders. The values next to "FD" and "H", i.e., $L_{tx} = \{2, 4, 8, 16\}$, denote the number of allowed phase rotations, which are linked to phase resolution. For instance, $L_{tx} = 2$ implies that only two phase rotations are used, i.e., $\mathcal{F} = \{0, \pi\}$, whereas $L_{tx} = 8$ implies that $\mathcal{F} = \{0, \pi/8, \pi/4, 3\pi/8, \pi/2, 5\pi/8, 3\pi/4, 7\pi/8\}$.

One first observation from Figure 8 is that performance generally improves for an increasing value of L_{tx}. This is especially true when $\theta = \frac{\pi}{9}$. On the other hand, a higher L_{tx} is less relevant when $\theta = \frac{4\pi}{9}$. This occurs because interference is significant when the channels are highly correlated, e.g., $\theta = \frac{\pi}{9}$, posing an obstacle for rate improvement. As a result, a higher L_{tx} makes more phase rotations available that can improve decorrelation among channels. When $\theta = \frac{4\pi}{9}$, the channels are already nearly orthogonal, thus interference is not substantially significant. Thus, a lower L_{tx} is sufficient to achieve high performance.

Another observation is that RSMA outperforms LDMA. The most significant difference is observed when $\theta = \frac{\pi}{9}$ whereas the smallest difference occurs when $\theta = \frac{4\pi}{9}$. Specifically, when $\theta = \frac{\pi}{9}$, interference is very high for the unicast signals due to high channel correlation. This scenario is, in fact, more suitable for the multicast signal. Therefore, RSMA splits the unicast messages, so that most of the information for the UEs is transmitted through the multicast signal, avoiding the high interference that would have resulted from transmitting via unicast signals alone as LDMA does. On the other hand, LDMA cannot split the unicast messages for the UEs into unicast and multicast, and transmits only via unicast. Recall that, LDMA also transmits a multicast messages, e.g., video content, which generates high interference and affects rates. When $\theta = \frac{4}{9}$, the channels are highly uncorrelated, making the multicast signal unsuitable and the unicast signals more preferable. Therefore, RSMA does not split the information for UEs into unicast and multicast in this case, and chooses to transmit only using unicast signals. As a result, RSMA collapses to LDMA, as a particular case, and both perform similarly.

6

PRECODING AND ADMISSION CONTROL FOR MULTI-GROUP MULTICAST BASED ON SDMA

This chapter gives an overview of the research problem investigated in [E], which is included in Appendix E. In the following, the motivation is given, the goal is stated, the related work is reviewed, the contributions are summarized, the research problem is formulated, and selected results are discussed.

6.1 MOTIVATION

Industry 4.0 represents the next generation of smart factories, where all components of the production chain, including industrial equipment, logistics, and processes, will be interconnected. Given the high degree of connectivity expected in Industry 4.0, wired connections become less desirable since they may hinder automation and limit the movement of industrial robotics. Therefore, wireless technologies are considered a solution to overcome hard wiring.

Besides, the millimeter-wave spectrum offers wide bandwidth and requires small antennas that can be easily embedded into miniature industrial machinery/devices. Thus, the millimeter-wave spectrum is advantageous to support future industrial networks, benefiting dense deployments due to low interference resulting from high path loss.

Multicasting will be necessary in industrial settings since several industrial IoT (IIoT) devices, such as sensor and actuators, will need to receive common information, e.g., control signaling. In particular, multicasting with multiple groups of IIoT devices can increase spectral efficiency and reduce latency. Also, to exploit the millimeter-wave spectrum, hybrid precoders will be needed. However, hybrid precoders have a limited number of radiofrequency (RF) chains, which allows transmitting only a few data streams simultaneously. Thus, admission control, i.e., scheduling of multiple multicast groups, must also be considered. Specifically, the joint design of hybrid precoding and admission control for multi-group multicasting has not been explored in depth, yet.

6.2 GOAL

The objective is to design hybrid precoders for several multicast groups and their corresponding scheduling in order to achieve low-latency communications, subject to transmit power limitations and phase rotation constraints. Each multicast group consists of several IIoT devices. Additionally, due to the small number of RF chains available at the base station (BS), the multicast groups cannot be served all at the same time. Therefore, they must be served in smaller groups such that the total latency of serving them all is minimized. However, finding such groupings and the precoders for each of them is not trivial. In particular, unsuitable groupings can lead to high interference and, consequently, very low throughput and high communications latency. Thus, a new algorithm is proposed to design the hybrid precoders and the admission control for multi-group multicasting. Precisely, the proposed algorithm consists of two phases, i.e., admission control and hybrid precoding, which are devised taking advantage of integer linear programs (ILPs), semidefinite relaxation (SDR), and the bisection method.

6.3 RELATED WORK

The precoder design for multi-group multicasting has been investigated with fully-digital precoders in [71–83] and with hybrid precoders in [68–70, 84, 85], as already revisited in Appendix B. However, the joint design of precoding and admission control for multi-group multicasting has not been investigated in many works.

The works [119–124] studied the precoding and admission control for single-group multicasting. Specifically, only [119–122] considered the precoder design, whereas [123, 124] employed physical layer abstractions of the multicast beams to simplify the design. In particular, the authors of [119] proposed an algorithm consisting of two stages. In the first stage, the total number of user equipments (UEs) was partitioned into several disjoint groups using a similarity metric based on the channels of the UEs. Only one group was served at a time, and therefore, interference was not generated. In the second stage, a fully-digital precoder for each group was designed to maximize the minimum signal-to-noise ratio (SNR). The precoder for each group was designed using linear combinations of the channels of the UEs in each group. In [120], a similar scenario as in [119] was studied. In particular, the UEs were divided into several groups and the groups were assigned to different orthogonal frequency channels. Thus, all the UE groups could be served simultaneously without interference. The authors proposed a first algorithm based on SDR and randomization followed by a power allocation stage, and a second algorithm based

on gradient descent. Specifically, the proposed algorithms aimed at minimizing the transmit power. A similar scenario was investigated in [121], where the authors distributed the multicast groups among different subcarriers and then optimized the transmit power to maximize the sum rate (SR) using an algorithm based on geometric programming (GP). Besides, the authors of [122] investigated the precoding design for transmit power minimization under the condition of admitting a fixed number of UEs. The authors proposed an algorithm based on the outer approximation of a mixed-integer semidefinite programs (MISDPs), which was recast as a sequence of mixed-integer second-order cone programs (MISOCPs).

The authors of [123] considered mutually orthogonal beams to serve a number of UEs, which were partitioned into disjoint groups. The authors proposed an optimal and a suboptimal greedy algorithm to form subsets of beams in order to serve all groups at maximum rate. A similar problem was considered in [124], where the authors proposed an algorithm closely related to the bin-packing problem.

Besides, the works [125–128] investigated the joint design of multi-group multicasting and admission control. However, none of these works considered hybrid precoders. Further, none of them investigated the admission control to minimize the total communications latency. In particular, the authors of [125] investigated the maximization of the number of UEs served. Specifically, as many UEs as possible were assigned to every multicast group, subject to satisfying transmit power and signal-to-interference-plus-noise ratio (SINR) constraints. The authors proposed an algorithm based on SDR, randomization, and deflation. In [126], a problem similar to that of [125] was investigated. The authors proposed three algorithms, two based on branch-and-bound (BnB) and a third based on heuristics. Besides, the authors of [127, 128] investigated UE grouping and precoding for SR [128] and energy efficiency (EE) [127] maximization. In both cases, an algorithm based on successive convex approximation (SCA) was proposed.

6.4 CONTRIBUTIONS

The contributions of this chapter are summarized in the following.

- Three propositions are introduced to guide the design of the precoders. The first proposition explains the relationship between SINR and latency. Exploiting this result, the second proposition reveals that latency minimization is promoted if the equalized signal-to-interference-plus-noise ratio (ESINR) is maximized. The third proposition takes advantage of the latter result to formulate the problem of joint precoding and admission control for multi-group multicasting for latency minimization.

- Due to the complexity of addressing the joint precoding and admission control, which is a mixed-integer nonlinear program (MINLP), its design is divided into two subproblems, i.e., admission control and precoding. Admission control is accomplished by proposing an algorithm that is formulated as an ILP, which co-schedules the multicast groups by minimizing the number of scheduling windows and the channel correlation between the served IIoT devices. To achieve this, a new metric is designed which is shown to be well suited.

- The multi-group multicast precoding problem is nonconvex. Thus, an algorithm based on SDR and alternating optimization (AO) is proposed, where the analog and digital precoders are optimized sequentially and iteratively.

- Compared to prior works on multi-group multicast precoding, the IIoT devices are assumed to have multiple antennas, which is feasible in the millimeter-wave spectrum due to the small size of the antennas.

- The proposed admission control algorithm is not only evaluated with hybrid precoders, but also with fully-digital and fully-analog precoders, demonstrating that it is effective in scheduling several multicast groups and achieving low latency. Furthermore, it is demonstrated via simulations that the proposed admission control algorithm achieves performance close to that of exhaustive search and is significantly more efficient than random admission.

6.5 INVESTIGATED PROBLEM

Consider a millimeter-wave system, where a BS serves IIoT devices clustered into several groups, as shown in Figure 9. In particular, the BS has a limited number of RF chains and it cannot serve all multicast groups at the same time. Therefore, the BS splits the groups and serves them in smaller groups. The groups must be scheduled such that the overall latency of serving all groups is minimized.

Generalities

The number of IIoT devices is K_T and they are indexed by set $\mathcal{K} = \{1, \ldots, K_T\}$. The number of multicast groups is G_T and they are indexed by set $\mathcal{I} = \{1, \ldots, G_T\}$. In addition, $\mathcal{G}_i$ represents the set of IIoT devices in multicast group $i \in \mathcal{I}$ and $|\mathcal{G}_i|$ represents the number of IIoT devices in that group. Furthermore, it is assumed that $\mathcal{G}_i \cap \mathcal{G}_{i'} = \{\emptyset\}, \forall i \neq i'$.

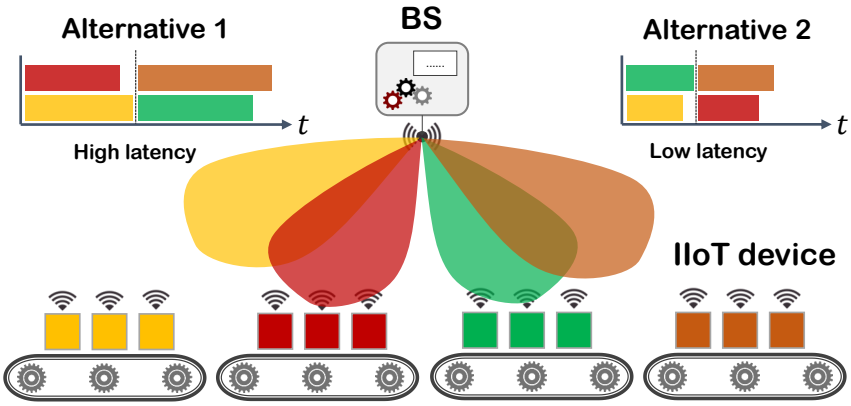

Figure 9: SDMA-based multi-group multicast industrial system consisting of a BS and several groups of IIoT devices.

The BS is equipped with a sub-connected hybrid precoder consisting of N_{tx} transmit antennas and N_{tx}^{RF} RF chains. Specifically, each RF chain is connected to a sub-array of $L_{tx} = N_{tx}/N_{tx}^{RF}$ antennas. Besides, each IIoT device is equipped with analog combiners that have N_{rx} antennas and a single RF chain, i.e., $N_{rx}^{RF} = 1$. Since $G_T \geqslant N_{tx}^{RF}$, admission control is necessary. In particular, N_{tx}^{RF} determines the maximum number of groups that can be simultaneously served.

Let T_s be the number of scheduling windows needed to serve all groups, assuming exclusive subsets of multicast groups across all scheduling windows, i.e., each group is served only once within T_s scheduling windows. The number of scheduling windows T_s depends on both N_{tx}^{RF} and G_T, i.e., $\lceil \frac{G_T}{N_{tx}^{RF}} \rceil \leqslant T_s \leqslant G_T$. Specifically, T_s is maximum when only one multicast group is served at each scheduling window. Similarly, T_s is minimum when the BS serves N_{tx}^{RF} multicast groups simultaneously at each window (except for at most one window, in case G_T is not a multiple of N_{tx}^{RF}).

Let ordered set $\mathcal{V}_t$ contain the indices of the multicast groups scheduled in window t. In addition, let set $\mathcal{U}_t$ denote the IIoT devices served in window t, i.e., $\mathcal{U}_t = \{k \mid k \in \mathcal{G}_i, i \in \mathcal{V}_t\}$. Besides, let $\{\mathcal{V}_t\}_{t=1}^{T_s}$ and $\{\mathcal{U}_t\}_{t=1}^{T_s}$ denote the collection of multicast groups and IIoT devices served over all T_s windows, respectively. Since each multicast group is served only once within T_s windows, then $\mathcal{V}_t \cap \mathcal{V}_{t' \neq t} = \{\emptyset\}$, $\mathcal{U}_t \cap \mathcal{U}_{t' \neq t} = \{\emptyset\}$.

Since multicasting is considered, all IIoT devices in the same group require the same length-B_i bit stream $\mathbf{b}_i = [b_{i_1}, \ldots b_{i_{B_i}}]^T$. Thus, the amount of bits required by IIoT device k is $B_k = B_i, \forall k \in \mathcal{G}_i$. At the BS, each bit stream $\mathbf{b}_i$ is encoded at a suitable rate π_i that allows successful decoding at the intended IIoT devices. As a result, streams $\tilde{\mathbf{s}}_i = [\tilde{s}_{i_1}, \tilde{s}_{i_2}, \ldots]^T$ $(i \in \mathcal{I})$ are simultaneously transmitted, each having

symbol-wise unit power on average, i.e., $\mathbb{E}\left\{\tilde{\mathbf{s}}_i \tilde{\mathbf{s}}_i^H\right\} = \mathbf{I}$. The symbol streams are arranged in matrix $\mathbf{S} = [\tilde{\mathbf{s}}_1, \ldots, \tilde{\mathbf{s}}_{G_T}]^T$, which is padded with zeroes where necessary, as the length of each stream $\tilde{\mathbf{s}}_i$ depends on B_i and π_i. Note that the non-zero entries of $\mathbf{S}$ represent the data that needs to be delivered to all the groups.

Let $\hat{\mathbf{S}}_t = \mathbf{V}_t \mathbf{S}$ denote the symbol streams transmitted in the t-th scheduling window. Here, $\mathbf{V}_t \in \{0,1\}^{|\mathcal{V}_t| \times G_T}$ is a binary scheduling matrix that filters the symbol streams from $\mathbf{S}$ that are to be transmitted in window t. The latency associated to delivering $\hat{\mathbf{S}}_t$ is $\xi_t = \max_{i \in \mathcal{V}_t} \frac{B_i}{\pi_i}$, which represents the minimal time interval required by the IIoT devices in window t to receive the intended data.

Let $\mathbf{F}_t \in \mathbb{C}^{N_{tx} \times N_{tx}^{RF}}$ and $\mathbf{M}_t \in \mathbb{C}^{N_{tx}^{RF} \times |\mathcal{V}_t|}$ denote, respectively, the analog and digital precoders in window t. Each element (q, r) of the analog precoder is a constant-modulus phase rotation. Thus, $[\mathbf{F}_t]_{q,r} \in \mathcal{F}$, where $q \in \mathcal{Q} = \{(r-1)L_{tx} + l \mid 1 \leqslant l \leqslant L_{tx}\}$, $r \in \mathcal{R} = \left\{1, \ldots, N_{tx}^{RF}\right\}$, and $\mathcal{F} = \left\{\sqrt{\delta_F} \ldots, \sqrt{\delta_F} e^{j\frac{2\pi(D_F-1)}{D_F}}\right\}$. Specifically, D_F is the number of allowed phase shifts and δ_F is a scaling factor. Thus, the downlink signal transmitted from the BS at window t is given by $\mathbf{x}_t = \mathbf{F}_t \mathbf{M}_t \tilde{\mathbf{s}}$.

Let $\mathbf{w}_k \in \mathbb{C}^{N_{rx} \times 1}$ be the combiner of the k-th IIoT device, where $[\mathbf{w}_k]_l \in \mathcal{W}$, $l \in \mathcal{L} = \{1, \ldots, N_{rx}\}$, $\mathcal{W} = \left\{\sqrt{\delta_W}, \ldots, \sqrt{\delta_W} e^{j\frac{2\pi(D_W-1)}{D_W}}\right\}$. Here, D_W is the number of phase shifts allowed and δ_W is a scaling factor.

Under the assumption of narrowband flat-fading, the signal received by the k-th IIoT device is

$$y_k = \underbrace{\mathbf{w}_k^H \mathbf{H}_k \mathbf{F}_t \mathbf{M}_t \mathbf{s}_{i_t}}_{\text{desired multicast signal}} + \underbrace{\mathbf{w}_k^H \mathbf{H}_k \sum_{j_t=1, j_t \neq i_t}^{|\mathcal{V}_t|} \mathbf{F}_t \mathbf{M}_t \mathbf{s}_{j_t}}_{\text{interference}} + \underbrace{\mathbf{w}_k^H \mathbf{n}_k}_{\text{noise}}, \quad (15)$$

where $\mathbf{H}_k \in \mathbb{C}^{N_{rx} \times N_{tx}}$ is the channel between the BS and the k-th IIoT device, whereas $\mathbf{n}_k \sim \mathcal{CN}\left(\mathbf{0}, \sigma^2 \mathbf{I}\right)$ denotes circularly symmetric Gaussian noise. Also, $i_t \in \{1, \ldots, |\mathcal{V}_t|\}$ is a relative index that represents the elements of $\mathcal{V}_t$, whereas $\mathbf{s}_{i_t} = \tilde{\mathbf{s}} - \mathbf{s}_{j_t}$ is a vector padded with zeroes except for the i_t-th position and contains the i_t-th element of $\tilde{\mathbf{s}}$. The SINR at IIoT device k is defined as

$$\text{SINR}_k = \frac{\left|\mathbf{w}_k^H \mathbf{H}_k \mathbf{F}_t \mathbf{M}_t \mathbf{e}_{i_t}\right|^2}{\sum_{j_t=1, j_t \neq i_t}^{|\mathcal{V}_t|} \left|\mathbf{w}_k^H \mathbf{H}_k \mathbf{F}_t \mathbf{M}_t \mathbf{e}_{j_t}\right|^2 + \sigma^2 \left\|\mathbf{w}_k\right\|_2^2}, \quad (16)$$

In (16), vector $\mathbf{e}_{i_t}$ has a 1 in the i_t-th position if $k \in \mathcal{V}_t\{i_t\}$ and 0 otherwise. Note that in (15) and (16), the subscript t has been dropped for the combiner $\mathbf{w}_k$. The reason is that each combiner $\mathbf{w}_k$ is designed using only its corresponding $\mathbf{H}_k$. In particular, the design of $\mathbf{w}_k$ is based on the maximization of the effective channel gain between the BS and the k-th IIoT device, and therefore does depend on the rest of channels. This allows each device to be capable to optimize its own combiner.

Problem formulation

The joint design of precoding and admission control is challenging to address. Thus, the problem is split into two subproblems. The first problem, $\mathcal{S}$, aims to minimize the number of scheduling windows and the channel correlation of the admitted IIoT devices. Reducing the number of scheduling windows naturally results in lower latency, especially when a switching delay is considered. Besides, seeking the reduction of the overall correlation of the scheduled devices allows for lower interference and, therefore, higher rates, thus promoting latency minimization.

$$\mathcal{S}: \min_{\mu_{i,i},\tau_{i,j,l}} \quad \underbrace{\sum_{i=1}^{G_T} \mu_{i,i}}_{\text{first term}} + \omega \underbrace{\sum_{i=1}^{G_T-1} \sum_{j\geqslant i}^{G_T-1} \sum_{l>j}^{G_T} \rho_{j,l} \cdot \tau_{i,j,l}}_{\text{second term}} \tag{17a}$$

$$\text{s.t.} \quad \sum_{i\leqslant j<l} \rho_{j,l} \cdot \tau_{i,j,l} \leqslant \lambda \cdot \mu_{i,i}, \forall i, \tag{17b}$$

$$\sum_{i\leqslant j} \mu_{i,j} = 1, \forall j, \tag{17c}$$

$$\sum_{j\geqslant i} \mu_{i,j} \leqslant N_{tx}^{RF}, \forall i, \tag{17d}$$

$$\mu_{i,j} \leqslant \mu_{i,i}, \forall i < j, \tag{17e}$$

$$\mu_{i,j} + \mu_{i,l} \leqslant 1 + \tau_{i,j,l}, \forall i \leqslant j < l, \tag{17f}$$

$$\mu_{i,j} \in \{0,1\}, \tag{17g}$$

$$\tau_{i,j,l} \in \{0,1\}. \tag{17h}$$

In $\mathcal{S}$, binary variable $\mu_{i,j}$ indicates with 1 that multicast group j is scheduled in the i-th window and with 0 otherwise. Binary variable $\tau_{i,j,l}$ is 1 if multicast groups j and l are co-scheduled in the i-th window. Besides, $\rho_{j,l} = \frac{|\mathbf{h}_j^H \mathbf{h}_l|}{\|\mathbf{h}_j\|_2 \|\mathbf{h}_l\|_2}$ is the metric used to capture the channel correlation between the co-scheduled IIoT devices. In particular, $\rho_{j,l}$ measures the inter-group correlation between groups j and l, where $\mathbf{h}_j = \frac{1}{|\mathcal{G}_j|} \sum_{k\in\mathcal{G}_j} \text{vec}(\mathbf{H}_k)$ is the mean channel of all IIoT devices in group j.

The first term in the objective (17a) is the number of scheduling windows. The second term is the aggregate channel correlation, which is computed pair-wise for all multicast groups. Further, ω in (17a) is a penalty factor used to balance the importance of the two terms. Constraint (17b) restricts, for every window i, the aggregate channel correlation of the admitted groups to be below a certain threshold λ. Constraint (17c) enforces every group j to be scheduled only once, whereas constraint (17d) restricts the number of groups per window to be at most N_{tx}^{RF}, i.e., it cannot exceed the number of RF chains. Constraint (17e) reduces the search space by pruning redundant variables, allowing to decrease the computational complexity of $\mathcal{S}$, without affecting the solution. Constraint (17f) links variables $\mu_{i,j}$ and $\tau_{i,j,l}$, ensuring consistency. Constraints (17g) and (17h) define $\mu_{i,i}$ and $\tau_{i,j,l}$ as binary.

Having found a suitable scheduling after solving $\mathcal{S}$, then $\mathcal{V}_t$ becomes available. Therefore, a hybrid precoder and analog combiners for every window t can be designed based on $\mathcal{P}$.

$$\mathcal{P}: \max_{\substack{\mathbf{F}_t, \mathbf{M}_t, \\ \{\mathbf{w}_k\}_{k\in\mathcal{U}_t}}} \quad \min_{k\in\mathcal{U}_t} \frac{\frac{1}{B_k}\left|\mathbf{w}_k^H \mathbf{H}_k \mathbf{F}_t \mathbf{M}_t \mathbf{e}_{i_t}\right|^2}{\sum_{\substack{j_t=1 \\ j_t\neq i_t}}^{|\mathcal{V}_t|} \left|\mathbf{w}_k^H \mathbf{H}_k \mathbf{F}_t \mathbf{M}_t \mathbf{e}_{j_t}\right|^2 + \sigma^2 \|\mathbf{w}_k\|_2^2} \tag{18a}$$

$$\text{s.t.} \quad \|\mathbf{F}_t \mathbf{M}_t\|_F^2 \leqslant P_{tx}^{max}, \tag{18b}$$

$$\|\mathbf{w}_k\|_2^2 \leqslant P_{rx}^{max}, k \in \mathcal{U}_t, \tag{18c}$$

$$[\mathbf{F}_t]_{q,r} \in \mathcal{F}, q \in \mathcal{Q}, r \in \mathcal{R}, \tag{18d}$$

$$[\mathbf{w}_k]_l \in \mathcal{W}, l \in \mathcal{L}. \tag{18e}$$

The objective (18a) is to maximize of the minimum ESINR. Constraint (18b) limits the transmit power of the hybrid precoder and (18c) limits the receive power of each IIoT device. Further, (18d) and (18e) enforce constant-modulus phase rotations for the analog precoder $\mathbf{F}_t$ and analog combiners $\{\mathbf{w}_k\}_{k\in\mathcal{U}_t}$, respectively. Note that the objective is fractional and therefore nonconvex. Also, the coupling $\mathbf{F}_t\mathbf{M}_t$ adds nonconvexity to constraint (18b) and the objective. Constraints (18d) and (18e) are nonconvex since $[\mathbf{F}_t]_{q,r}$ and $[\mathbf{w}]_l$ are limited to nonconvex sets $\mathcal{F}$ and $\mathcal{W}$, respectively. Thus, (18) is nonconvex.

Note: *For details on the proposed algorithm to solve $\mathcal{P}$, the reader is referred to [E], which can also be found in Appendix E.*

6.6 SELECTED RESULTS

In the following, simulation results of a specific scenario in [E] are discussed. Figure 10 shows the latency achieved by the proposed

algorithm alongside with other benchmarks. In the legend of Figure 10, HYDRAWAVE denotes the proposed algorithm. Benchmarks XHAUS and RAND denote exhaustive and random search, respectively. In particular, XHAUS considers all possible combinations of scheduling whereas RAND considers random co-scheduling of groups. Additionally, benchmark SING is included, representing single-group multicasting, i.e., only one group is served at a time.

Figure 10 is taken from [E], but the layout has been slightly modified.

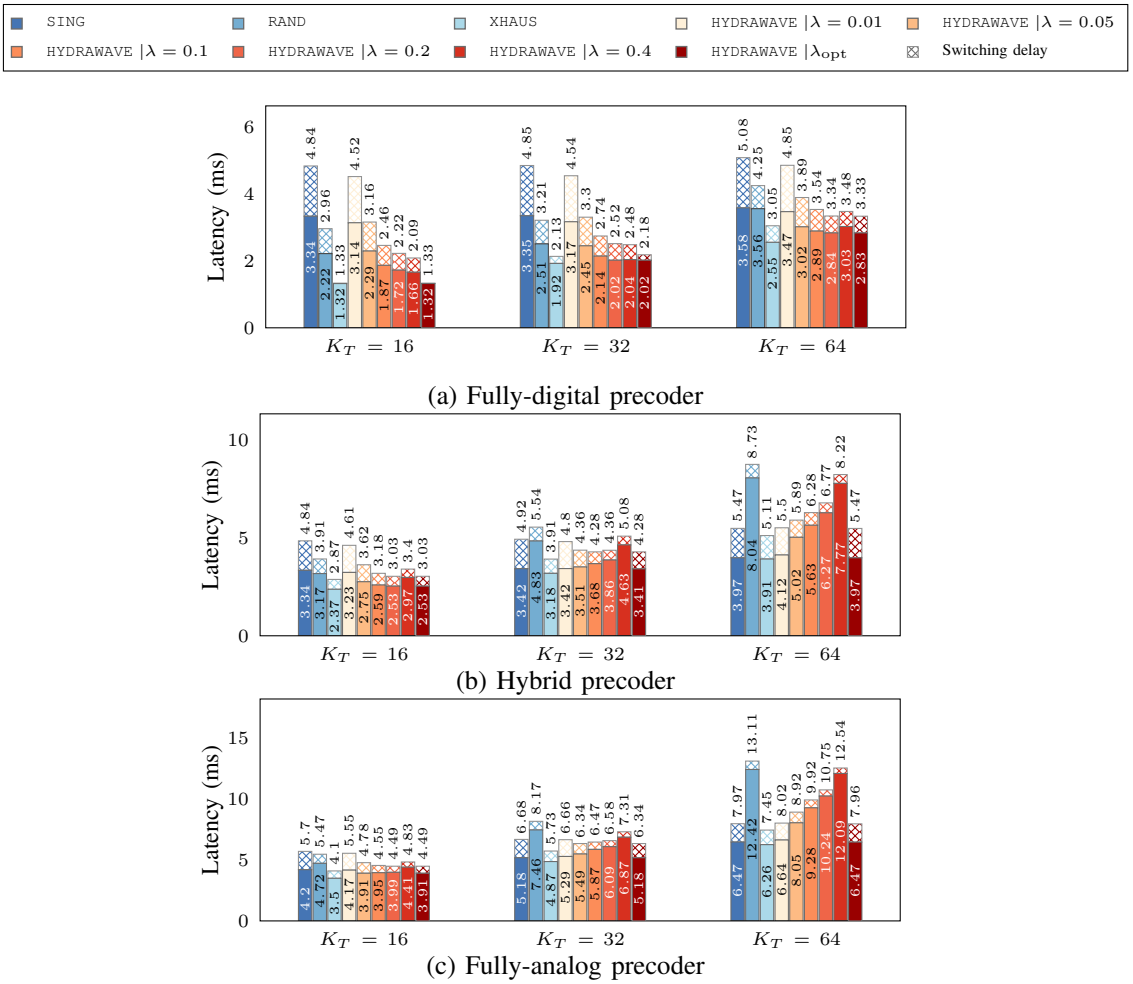

Figure 10: Latency of several algorithms with fully-digital, hybrid, and fully-analog precoders.

Figure 10 shows the performance of the proposed algorithm using fully-digital, hybrid, and fully-analog precoders. Solid colors represent the latency without switching delay whereas dashed colors represent the latency with switching delay. The switching delay increases proportionally to the number of scheduling windows, since it is assumed that the configuration of the precoders from one time window to another requires some processing time. The parameter λ is left for the design, as it regulates the amount of interference supported in each

time window, thus also affecting latency. Finding an optimal value for λ is not trivial, in general, as it involves an additional search.

In Figure 10, the number of antennas and RF chains at the BS are $N_{tx} = 24$ and $N_{tx}^{RF} = 4$, respectively. Each IIoT device has $N_{rx} = 2$ antennas and $N_{rx}^{RF} = 1$ RF chains. The maximum transmit power at the BS is $P_{tx}^{max} = 20$ dBm. The number of multicast groups is $G_T = 4$ and the number of IIoT devices is $K_T = \{16, 32, 64\}$. The length of the bit-streams for all multicast groups are considered the same, i.e., $B_1 = B_2 = B_3 = B_4 = 4$ Mbits. The switching is denote by $\delta_{SW} = \{0.0, 0.5\}$ ms.

When $K_T = 16$, `SING` generally produces the highest latency whereas `XHAUS` produces the lowest. Further, `RAND` exhibits an intermediate performance between `SING` and `XHAUS`. When, $K_T = 64$, the performance gap between `SING` and `XHAUS` reduces considerably since interference becomes more difficult to manage, making `SING` optimal in some realizations. Specifically, when K_T is large, interference is higher and, therefore, it is more suitable to schedule less groups simultaneously. As a result, `RAND` deteriorates markedly due to inadequate co-scheduling of the multicast groups which causes mutual high interference, allowing only very low rates and, therefore, resulting in high latency. Note that when a switching delay is assumed, similar behavior is observed in all results except for `SING`, which is more severely penalized because it serves only one group at a time, incurring more overall switching delay due to needing more scheduling windows. Considering the fully-digital precoder with $K_T = 16$, the performance of `HYDRAWAVE` is close to that of `XHAUS`. Besides, for $K_T = \{32, 64\}$, its performance is within 11% of `XHAUS` when $\delta_{SW} = 0.0$ ms and within 9% when $\delta_{SW} = 0.5$ ms. Considering the hybrid and fully-analog precoders, the performance of `HYDRAWAVE` is within $1.5 - 9.5\%$ and $3.4 - 11.7\%$ of `XHAUS`, respectively. With the hybrid precoder, `HYDRAWAVE` exhibits gains up 32% higher than `SING` and up to 102% compared to `RAND` when $\delta_{SW} = 0$ ms. Besides, when $\delta_{SW} = 0.5$ ms, the gains are up to 60% and 59%, respectively.

Finding an optimal value of λ for `HYDRAWAVE` is generally time-consuming. The results with λ_{opt}, i.e., optimal value of λ, are shown only for the purpose of serving as a performance benchmark. Generally, `HYDRAWAVE` performs acceptably well for $\lambda = \{0.2, 0.4\}$, which can be adopted for the considered scenario. Besides, λ is related to the amount of interference allowed per scheduling window. For the fully-digital precoder, a larger λ can be tolerated due to the versatility of these precoders to manage interference better. For hybrid precoders, smaller λ values are more suitable due to the limited number of RF chains available.

7

PRECODING AND ADMISSION CONTROL FOR UNICAST AND MULTICAST BASED ON LDMA

This chapter gives an overview of the research problem investigated in [F], which is included in Appendix F. In the following, the motivation is given, the goal is stated, the related work is reviewed, the contributions are summarized, the research problem is formulated, and selected results are discussed.

7.1 MOTIVATION

Industry 4.0 envisions fully automated factories with a vast network of interconnected industrial IoT (IIoT) devices, such as sensors, actuators, programmable logic devices, and access points. This high degree of interconnectivity is expected to provide ultra-precise control and seamless coordination, resulting in incredibly efficient and reliable production processes. However, most IIoT devices in today's industrial environments are interconnected via hard wiring to ensure reliable communications.

As the number of IIoT devices in industrial settings increases, wires will face the following challenges: intricate deployment complexity, increased operational costs, limited maneuverability of articulated robots, and difficulty to communicate with autonomous mobile robots. On the other hand, wireless technologies can significantly reduce deployment and maintenance costs while promoting more flexible mechanics for robotics. Consequently, transitioning from wired to wireless technology is an attractive option for industrial evolution.

High spectral efficiency has been demonstrated by exploiting the millimeter-wave spectrum and massive multiple-input multiple output (MIMO). Specifically, the millimeter-wave spectrum is an attractive substitute for the saturated sub-6GHz spectrum because of its high bandwidth availability. In addition, due to its shorter wavelength, the millimeter-wave spectrum requires smaller antennas that can be embedded into small IIoT devices. Furthermore, the millimeter-wave spectrum exhibits high spatial reuse due to significant path loss and sparse propagation. These characteristics make it excellent for short-range communications in highly congested scenarios, such as industrial environments. In addition, thanks to the superior degrees

of freedom of massive MIMO, improved interference mitigation can be achieved, enabling greater spectral efficiency (SE) and multiplexing capability, both desirable attributes to support the future industrial landscape.

Future industries will need two forms of information: shared control messages, i.e., multicast signals, and private communications, i.e., unicast signals. Orthogonal multiple access schemes can meet this requirement, transmitting multicast and unicast signals on separate time or frequency resources. However, as the number of IIoT devices increases, orthogonal multiple access schemes will struggle to accommodate a large number of devices on separate radio resources. As a result, non-orthogonal multiple access is being considered, as it allows the same resources to be reused to serve multiple devices. Non-orthogonal multiple access schemes can improve SE by enabling overlapping transmissions on the same radio resources. Specifically, layered-division multiple access (LDMA) is a non-orthogonal multiple access scheme, which is promising among many existing variants. LDMA can transmit multiple layers of information simultaneously using the same radio resources. For instance, with LDMA, multicast and unicast information can be transmitted simultaneously, which is known as non-orthogonal unicast and multicast (NOUM).

Several non-orthogonal multiple access schemes have recently been applied to the millimeter-wave spectrum and massive MIMO, demonstrating excellent synergy in various applications. Furthermore, research on exploiting non-orthogonal multiple access and the millimeter-wave spectrum for industrial settings has also yielded promising results. Based on these outcomes, combining the millimeter-wave spectrum, massive MIMO, and LDMA is expected to bring further benefits for future industrial ecosystems. However, intertwining these technologies raises questions requiring further research in two critical aspects, as explained in the following.

Admission control. Generally, the number of radiofrequency (RF) chains in the base station (BS) limits the number of IIoT devices that can be simultaneously served with individual signals. Most works on precoding consider sufficient RF chains to serve all IIoT devices, making admission control unnecessary. However, as wireless networks become denser, admission control will be essential in order to maintain high performance.

Precoding. In NOUM-based LDMA, overlapping unicast and multicast transmissions are employed. However, multicast and unicast have opposite objectives. In particular, multicast precoding aims to exploit the channel similarities to design the precoder. On the contrary, unicast precoding aims to design the precoders exploiting the channel

dissimilarities. Therefore, the precoding performance will depend on admission control, i.e., the IIoT devices admitted for service.

7.2 GOAL

The goal is to design the precoding and admission control for NOUM transmissions based on LDMA. In particular, the investigated research problem aims to serve a subset of IIoT devices for which unicast and multicast precoders are designed to maximize unicast signal-to-interference-plus-noise ratio (SINR) fairness. Due to safety reasons, the multicast signal, which carries control information, is not subject to admission control or scheduling. Thus, it is always present and must be received by all IIoT devices. In contrast, the unicast signals, which carry non-critical information, are conveyed to only a subset of devices, subject to the availability of RF chains. Thus, two superimposed signals are transmitted by the BS.

7.3 RELATED WORK

The precoding design for NOUM transmissions based on LDMA has been studied for different purposes. For instance, the precoding design for transmit power minimization was investigated in [93, 96, 98]. In particular, the authors of [93, 96] proposed two algorithms based on successive convex approximation (SCA) and semidefinite relaxation (SDR) and showed that LDMA consistently outperforms time-division multiple access (TDMA) as it requires less power to fulfill the same given task. Besides, the authors of [98] proposed algorithms based on branch-and-bound (BnB) and successive linear approximation (SLA), which exhibited similar performance.

Also, the precoding design for energy efficiency (EE) maximization was investigated in [101, 105, 106]. In [101], the authors studied the EE of LDMA for the first time and proposed an algorithm based on first-order Taylor approximations. The authors revealed that LDMA can also improve EE compared to TDMA. The authors of [105, 106] further included energy harvesting constraints into the NOUM system and proposed two algorithms to solve the investigated problem. The first algorithm proposed was based on the bisection method and SCA, whereas the second low-complexity algorithm on zero-forcing (ZF) precoding.

In addition, the joint precoding and base station clustering design for weighted sum rate (WSR) maximization was investigated in [99, 100]. The authors of these works proposed algorithms based on BnB and SCA and confirmed the higher versatility of LDMA compared to TDMA.

Although some works have investigated the precoding design for LDMA-based NOUM transmissions, e.g., [93, 96, 98–101, 105, 106], the joint design of precoding and admission control has not yet been studied. In addition, the combination of the millimeter-wave spectrum, massive MIMO, and LDMA has neither been investigated for industrial environments.

7.4 CONTRIBUTIONS

The contributions of this chapter are summarized in the following.

- The investigated research problem is formulated as mixed-integer nonlinear program (MINLP), which jointly optimizes the precoding and admission control in LDMA-based NOUM systems. In particular, a minimum SINR target is imposed on the multicast signal, which carries the ubiquitous control message, to ensure that all IIoT devices receive the signal.

- An algorithm called `BEAMWAVE` is proposed, which decomposes the MINLP into two subproblems, i.e., admission control and precoding. To design the admission control, an integer linear program (ILP) is formulated, which uses pairwise metrics named `PAWN`, `ROOK`, `KING` to guide the decision of admitting IIoT devices. Essentially, these metrics represent the discordance of serving two devices together, and therefore, the goal is to minimize such discordance. To design the precoding, an algorithm based on SCA is proposed. Through simulations, it is shown that `BEAMWAVE` can attain near-optimality when compared to a benchmark based on exhaustive search.

- The need for admission control is motivated in the context of LDMA-based NOUM transmissions, especially when the number of RF chains is insufficient to serve a large number of IIoT devices, expected in future industrial settings. It is shown through simulations the importance of designing the admission control compared to adopting trivial criteria, such as random admission.

7.5 INVESTIGATED PROBLEM

Consider a millimeter-wave system, where a BS serves multiple IIoT devices, as shown in Figure 11. The BS transmits common and private information leveraging multicast and unicast precoding, respectively. The BS has a limited number of RF chains and, therefore, not all devices can be serviced simultaneously with unicast and multicast information. All devices receive shared information via multicast but only a subset of devices is chosen to receive private signals via unicast.

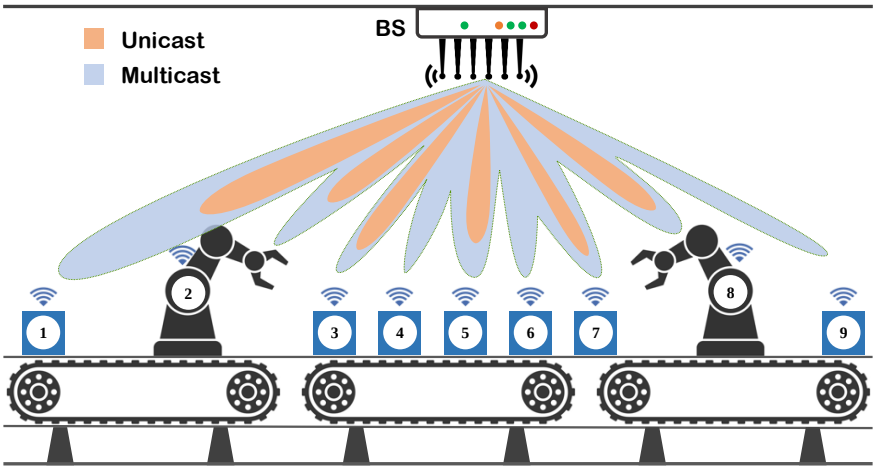

Figure 11: LDMA-based NOUM industrial system consisting of a BS and several IIoT devices.

Generalities

The number of IIoT devices is K and they are indexed by set $\mathcal{K} = \{1, 2, \ldots, K\}$. All the IIoT devices are served by the multicast signal, which carries common information. However, onlya subset of IIoT devices receive their corresponding unicast signals, each of which conveys private information. Thus, the BS transmits two types of non-orthogonal signals: multicast and unicast. The multicast signal is intended for every device $k \in \mathcal{K}$. Besides, a composite signal is transmitted to only a subset of devices $\mathcal{K}' \subseteq \mathcal{K}$, where $|\mathcal{K}'| = K'$. Devices served only with the multicast signal are called single-layer device, whereas devices that are served with both signals are called dual-layer devices. Thus, K' dual-layer devices are served with both unicast and multicast information, whereas $K - K'$ single-layer devices are served with multicast information only.

The BS is equipped with N_{tx} antennas and N_{tx}^{RF} RF chains. It is assumed that $N_{tx}^{RF} = K'$. The unicast and multicast precoders are denoted by $\mathbf{B} \in \mathbb{C}^{N_{tx} \times K'}$ and $\mathbf{m} \in \mathbb{C}^{N_{tx} \times 1}$, respectively. The unicast and multicast symbols are denoted by $\mathbf{s} \in \mathbb{C}^{K' \times 1}$ and $z \in \mathbb{C}$, respectively, assuming $\mathbb{E}\left\{ \left[\mathbf{s}^T, z\right]^H \left[\mathbf{s}^T, z\right] \right\} = \mathbf{I}$. The downlink signal from the BS is $\mathbf{x} = [\mathbf{B}|\mathbf{m}] \left[\mathbf{s}^T | z\right]^T$. Here, $\mathbf{B} = \widetilde{\mathbf{B}}\mathbf{U}$, where $\widetilde{\mathbf{B}} = [\mathbf{b}_1, \ldots, \mathbf{b}_K] \in \mathbb{C}^{N_{tx} \times K}$ and $\mathbf{U} \in \mathbb{B}^{K \times K'}$ is a binary matrix used to select the dual-layer devices. Also, $\mathbf{s} = \mathbf{U}^T \widetilde{\mathbf{s}}$, where $\widetilde{\mathbf{s}} = [s_1, \ldots, s_K]^T \in \mathbb{C}^{K \times 1}$. It must also hold $\mathbf{1}^T \mathbf{U} \mathbf{1} = K'$, $\mathbf{U}\mathbf{1} \preccurlyeq \mathbf{1}$ and $\mathbf{U}^T \mathbf{1} \preccurlyeq \mathbf{1}$, which yields that $\mathbf{U}\mathbf{U}^T = \mathrm{diag}\left([\mu_1, \cdots, \mu_K]\right)$ is a square matrix. In particular, the k-th diagonal element is 1 when k is a dual-layer device and 0 otherwise.

Besides, each IIoT device is equipped with N_{rx} antennas and $N_{rx}^{RF} = 1$ RF chains. To design the combiner $\mathbf{w}_k$ for each IIoT device,

only a small number of L_{rx} constant-modulus phase rotations are allowed. Every element $[\mathbf{w}_k]_l$ is a constant-modulus phase rotation limited to $\mathcal{W} = \left\{\delta_{rx}, \ldots, \delta_{rx} e^{j\frac{2\pi(L_{rx}-1)}{L_{rx}}}\right\}$, $l \in \mathcal{L} = \{1, \ldots, N_{rx}\}$, where $\delta_{rx} = \sqrt{P_{rx}^{max}/N_{rx}}$ and P_{rx}^{max} is the receive power for each IIoT device.

Assuming flat fading, the signal received by the k-th IIoT device is given by

$$y_k = \underbrace{\mathbf{w}_k^H \mathbf{H}_k \mathbf{m} z}_{y_k^M\text{: multicast signal}} + \underbrace{\mathbf{w}_k^H \mathbf{H}_k \sum_{j \in \mathcal{K}'} \mathbf{b}_j s_j}_{y_k^U\text{: aggregate unicast signal}} + \underbrace{\mathbf{w}_k^H \mathbf{n}_k}_{\eta_k\text{:noise}}, \tag{19}$$

where $\mathbf{H}_k \in \mathbb{C}^{N_{rx} \times N_{tx}}$ denotes the channel between the BS and the k-th device and $\mathbf{n}_k \sim \mathcal{CN}\left(\mathbf{0}, \sigma^2 \mathbf{I}\right)$ is circularly symmetric Gaussian noise. Note that the unicast signal for single-layer devices will be zero.

Since unicast and multicast signals are transmitted in a non-orthogonal manner, successive interference cancellation (SIC) is performed by the dual-layer devices to extract the information from both received signals. Each device $k \in \mathcal{K}$ decodes the multicast symbol by treating the aggregate unicast signal as noise. In addition, if device k is a dual-layer device, then it applies SIC to decode the unicast signal. The k-th device reconstructs the multicast signal y_k^M using the decoded symbol z, and then subtracts y_k^M from y_k. The remaining signal only contains unicast components and noise, from where the device can decode symbol s_k.

The SINR for the multicast and unicast signals at the k-th device are defined as

$$\text{SINR}_k^M = \frac{\left|\mathbf{w}_k^H \mathbf{H}_k \mathbf{m}\right|^2}{\sum_{j \in \mathcal{K}'} \left|\mathbf{w}_k^H \mathbf{H}_k \mathbf{b}_j\right|^2 + \sigma^2 \left\|\mathbf{w}_k\right\|_2^2}, \forall k \in \mathcal{K}, \tag{20}$$

$$\text{SINR}_k^U = \frac{\left|\mathbf{w}_k^H \mathbf{H}_k \mathbf{b}_k\right|^2}{\sum_{j \neq k, j \in \mathcal{K}'} \left|\mathbf{w}_k^H \mathbf{H}_k \mathbf{b}_j\right|^2 + \sigma^2 \left\|\mathbf{w}_k\right\|_2^2}, \forall k \in \mathcal{K}'. \tag{21}$$

Problem formulation

The objective is to design the precoder and admission control as well as the combiners with the aim of maximizing the minimum SINR, as shown in the following.

$$
\begin{aligned}
\mathcal{P}: \max_{\substack{\mathbf{W},\mathbf{m},\\ \widetilde{\mathbf{B}},\boldsymbol{\mu}}} \quad & \min_{k\in\mathcal{K}} \frac{\left|\mathbf{w}_k^H \mathbf{H}_k \mathbf{b}_k\right|^2 g(\mu_k)}{\sum_{j\neq k, j\in\mathcal{K}} \left|\mathbf{w}_k^H \mathbf{H}_k \mathbf{b}_j\right|^2 \mu_j + \sigma^2 \left\|\mathbf{w}_k\right\|_2^2} \\
\text{s.t.} \quad & C_1: \frac{\left|\mathbf{w}_k^H \mathbf{H}_k \mathbf{m}\right|^2}{\sum_{j\in\mathcal{K}} \left|\mathbf{w}_k^H \mathbf{H}_k \mathbf{b}_j\right|^2 \mu_j + \sigma^2 \left\|\mathbf{w}_k\right\|_2^2} \geqslant \gamma_{\min}, \forall k \in \mathcal{K}, \\
& C_2: \sum_{k\in\mathcal{K}} \left\|\mathbf{b}_k\right\|_2^2 \mu_k + \left\|\mathbf{m}\right\|_2^2 \leqslant P_{tx}^{max}, \\
& C_3: \sum_{k\in\mathcal{K}} \mu_k = K', \\
& C_4: [\mathbf{w}_k]_l \in \mathcal{W}, l \in \mathcal{L}, \forall k \in \mathcal{K}, \\
& C_5: \mu_k \in \{0, 1\},
\end{aligned}
$$

where $g(\chi)$ is defined as

$$
g(\chi) = \begin{cases} 1, & \text{if } \chi = 1, \\ \infty, & \text{if } \chi = 0. \end{cases}
$$

and $\mathbf{W} = [\mathbf{w}_1, \cdots, \mathbf{w}_K]$, $\widetilde{\mathbf{B}} = [\mathbf{b}_1, \cdots, \mathbf{b}_K]$, $\boldsymbol{\mu} = [\mu_1, \cdots, \mu_K]$.

The objective function of $\mathcal{P}$ aims to find a subset $\mathcal{K}' \subseteq \mathcal{K}$ that maximizes the minimum SINR_k^U of the admitted IIoT devices. Constraint C_1 in nonconvex and enforces the multicast SINR to be above a target SINR $\gamma_{\min}$ for all devices. Constraint C_2 is convex and limits the transmit power to P_{tx}^{max}. Constraint C_3 selects K' dual-layer devices while C_4 imposes restrictions on the combiners design. Both C_3 and C_3 are of combinatorial nature. Finally, C_5 enforces μ_k to be binary. Problem $\mathcal{P}$ is a nonconvex MINLP that is generally difficult to solve.

Note: *For details on the proposed algorithm to solve $\mathcal{P}$, the reader is referred to [F], which can also be found in Appendix F.*

7.6 SELECTED RESULTS

In the following, simulation results of a specific scenario in [F] are discussed. Figure 12 shows the fairness in terms of the minimum SINR achieved by the admitted IIoT devices. In the legend of Figure 12, `XHAUS` denotes the algorithm that employs exhaustive search for admission control. Thus, it is used as an upper bound for the achievable fairness. Besides, `RANDOM` denotes the algorithm that employs random selection for admission control and, therefore, it is used as a performance lower bound. In addition, `BEAMWAVE-PAWN`, `BEAMWAVE-ROOK`, and `BEAMWAVE-KING` represent the proposed algorithm using three different metrics, `PAWN`, `ROOK`, and `KING`, respectively. Each of these metrics lever-

Figure 12 is taken from [F], but the layout has been slightly modified.

age different characteristics of the channels to select the IIoT devices to be admitted.

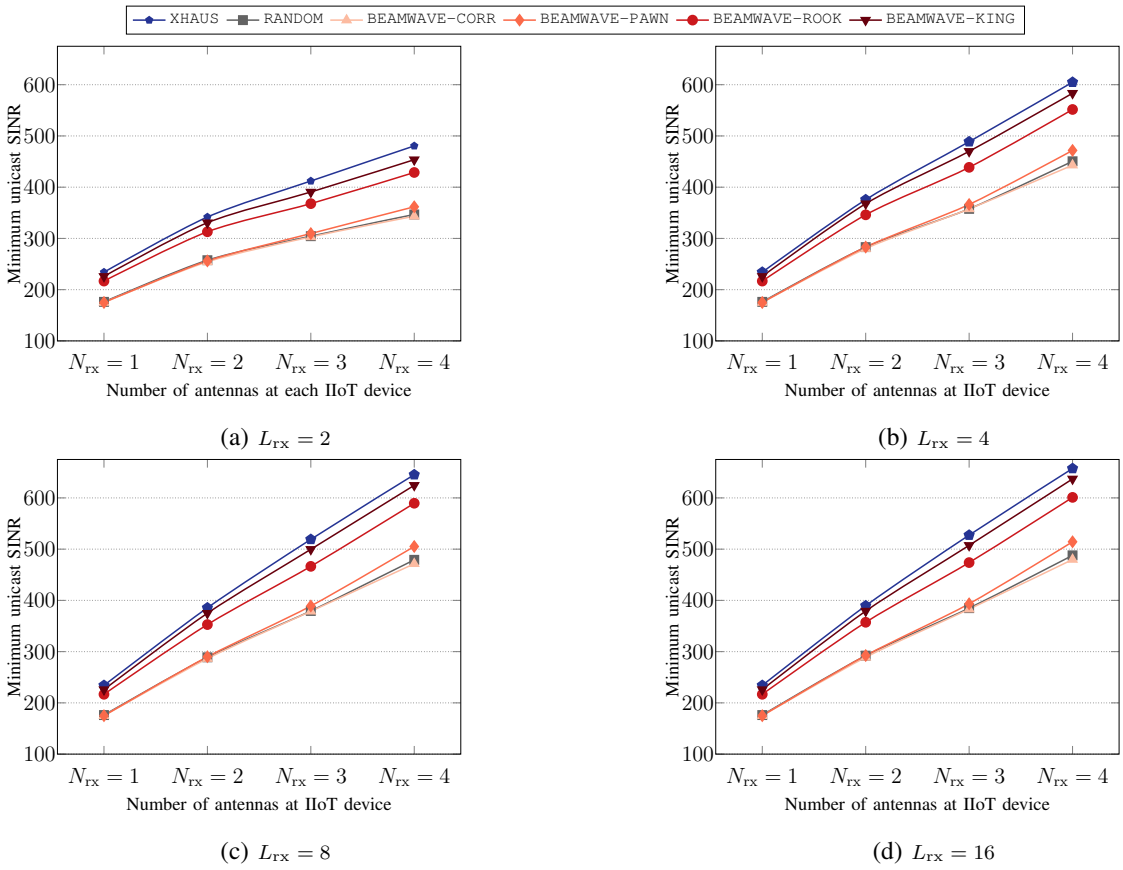

(a) $L_{rx} = 2$

(b) $L_{rx} = 4$

(c) $L_{rx} = 8$

(d) $L_{rx} = 16$

Figure 12: Minimum unicast SINR.

At the BS, the number of antennas is $N_{tx} = 16$ and the number of RF chains is $N_{tx}^{RF} = 5$. The transmit power at the BS is $P_{tx}^{max} = 35$ dBm. At the IIoT devices, the number of antennas is $N_{tx} = \{1, \ldots, 4\}$ and the number of RF chains is $N_{rx}^{RF} = 1$. The number of IIoT devices is $K = 6$, and the number of allowed phase rotations at each combiner is $L_{rx} = \{2, 4, 8, 16\}$. The power assigned to the combiners is $P_{rx}^{max} = 0$ dBm. The target SINR for the multicast signal is $\gamma_{min} = 6$ dB.

Figure 12 shows the impact of N_{rx} and L_{rx} on the unicast SINR fairness. It is observed that the fairness improves for all algorithms as the number of receive antennas N_{rx} increases. With larger N_{rx}, the IIoT devices can devise more directional reception beampatterns to mitigate undesired unicast signals from other devices. A larger number of antennas at the IIoT devices also facilitates the task of the multicast precoder, whose design alone is NP-hard. Specifically, endowing IIoT devices with multiple antennas saves extra power at the BS that can be used to improve the unicast SINR fairness of the admitted devices. For instance, up to 60% gain can be achieved with

$L_{rx} = 4$ when varying the number of receive antennas from $N_{tx} = 1$ to $N_{tx} = 2$. On the other hand, it is also observed that a larger number of allowed phase rotations at the IIoT devices has a beneficial effect on fairness. In particular, gains up to 16.00%, 30.70%, and 49.47% are achieved when increasing from $L_{rx} = 2$ to $L_{rx} = 4$, from $L_{rx} = 4$ to $L_{rx} = 8$, and from $L_{rx} = 8$ to $L_{rx} = 16$, respectively.

Comparing the performance of the algorithms, `BEAMWAVE-KING` attains superior performance, close to that of `XHAUS`, and at a fraction of the computational complexity of `XHAUS`. In particular, `BEAMWAVE-KING` is outperformed by 5.60% compared to `XHAUS`.

8

PRECODING, ADMISSION CONTROL, AND RATE ALLOCATION FOR UNICAST AND MULTICAST BASED ON SDMA

This chapter gives an overview of the research problem investigated in [G], which is included in Appendix G. In the following, the motivation is given, the goal is stated, the related work is reviewed, the contributions are summarized, the research problem is formulated, and selected results are discussed.

8.1 MOTIVATION

Next-generation wireless communications networks will incorporate millimeter-wave integrated access-backhaul (IAB) leveraging macro base stations (MBSs) and small base stations (SBSs) as critical infrastructure for the rollout. However, achieving efficient operation of millimeter-wave IAB technology is a major challenge. In particular, to guarantee efficient operation, the joint radio resource management (RRM) design of access and backhaul networks is essential. In addition, several practical challenges must be overcome to ensure smooth operation and high radio resource utilization efficiency, as explained in the following.

Scalable self-backhauling design. Most previous studies considered point-to-point backhaul links between an MBS and SBSs, which is impractical, making it unscalable in dense SBS deployments since MBSs cannot spatially multiplex a large number of streams at the same time. Some studies have proposed that MBSs employ multicasting and SBSs employ multi-layer successive interference cancellation (SIC) to partially alleviate the scalability issue. However, multi-layer SIC requires considerable processing time and is prone to errors that depend on the decoding order of the received signals, making it unsuitable. Therefore, novel backhauling strategies need to be developed to enable scalable IAB.

Adaptive backhaul capacity. Although IAB relies on wireless media sensitive to noise and interference and has, therefore, a highly variable capacity, many previous studies assumed that backhaul capacity is unlimited or constant. However, it is critical to account for variations and limitations in backhaul link capacity, even though backhaul links are more stable than access links.

UE association. A typical assumption is that user equipments (UEs) are served by one SBS or all SBSs within a certain distance. Although this assumption simplifies the RRM design, it is not optimal. Therefore, a more comprehensive strategy is needed that flexibly allows connectivity between UEs and several SBSs, enabling the full multi-connectivity potential of dense SBSs.

Admission control. Numerous studies have assumed that all UEs in a network can be served simultaneously, which is not always possible due to power limitation, insufficient number of antennas, or radiofrequency (RF) chains. Thus, admission control is critical to ensure that at least a fraction of the UEs have granted access. However, the selection of such set of UEs is not trivial and should be investigated further.

Discrete data rates. Many works have assumed that data rates are continuous. In reality, they are discrete since they result from a limited number of modulation and coding schemes (MCSs). Considering the discrete nature of the rates is critical since continuous-valued solutions cannot be applied in real wireless communications systems and are unlikely to work as intended.

The performance of IAB technology depends largely on considering the above practical challenges in the RRM design. It is important to note that there exist few studies addressing these challenges.

8.2 GOAL

The goal is to propose an RRM design that maximizes the weighted sum rate (WSR) in IAB systems while addressing the above practical challenges. The RRM design includes optimizing precoding, rate allocation, UE association, and admission control in the access network and precoding, and rate allocation in the backhaul network. In particular, the RRM design for the considered system results in a nonconvex mixed-integer nonlinear program (MINLP), which is difficult to solve. Therefore, three algorithms that balance complexity and optimality are proposed. The first algorithm is based on the convexification of the nonconvex MINLP, while the second and third algorithms are based on successive convex approximation (SCA), minorization-maximization (MM), and the penalty method. The proposed algorithms are evaluated in several scenarios, demonstrating that it is possible to deploy a practical IAB system in future millimeter-wave networks.

8.3 RELATED WORK

There is a large body of literature on RRM for IAB. However, much of this literature have considered the sub-6GHz spectrum, e.g., [129–131], assuming signal properties that do not necessarily apply to the

millimeter-wave spectrum. Furthermore, many works have focused on the RRM design of either the backhaul, e.g., [132–134] or the access network, e.g., [127, 135] alone. However, the evolution of mobile networks demands integrating the RRM design of both access and backhaul. In particular, precoding is a key aspect to improve the throughput in IAB. Considering linear antenna arrays, many works have optimized the precoding, e.g., [129, 136]. However, precoding with planar arrays for IAB has been seldom investigated, even though planar arrays allow beampattern control in elevation and azimuth, making them more suitable for dense deployments.

Precoding is not the only aspect that needs consideration in IAB. In particular, UE association, admission control, and discrete rate allocation should also be accounted for in the RRM. In particular, their joint design generally requires solving complicated nonconvex MINLPs. Thus, many papers facing these challenges divide the RRM design into subproblems and solve them separately. For instance, integer variables are first eliminated by assuming a given set of admitted UEs, e.g., [136, 137]. Next, the underlying problem is solved in the continuous domain. Although simpler to solve, dividing the RRM design into subproblems affects optimality due to removing interdependencies between variables. To meet the continuously growing throughput demands, radio resources have to be exploited more efficiently. Therefore, RRM designs must be addressed holistically rather than dividing them into subproblems, which results in inefficient use of radio resources.

The works most related to the one summarized in this chapter are [130, 138]. Similar to [G], the authors of [138] considered a multicast topology for the backhaul links. In particular, the MBS was tasked with the transmission of multiple signals to various SBSs employing multi-group multicast precoding. Each transmitted signal from the MBS carried the data of one UE. Further, since each SBS was allowed to serve several UEs, SBSs were required to employ multi-layer SIC to decode the different signals for the UEs they served, increasing the computational burden for low-cost SBSs. The decoding order of signals in multi-layer SIC is known to affect performance and lead to high decoding errors but this was not considered in [138]. The authors investigated the maximization of the WSR and proposed an algorithm based on the successive lower-bound maximization, for which a new concave lower-bound approximation for the achievable rate was introduced. Besides, the authors of [130] considered multiple SBS groups served in a multicast manner using time-division multiple access (TDMA), thus generating zero interference for the backhaul links since only one multicast stream was active at a time. However, using TDMA affects the scalability of the adopted system. Specifically, as the number of clusters increases, a larger latency is generated, mak-

ing it only practical for small systems. The authors investigated the WSR maximization and proposed an algorithm based on semidefinite relaxation (SDR), SCA, and second-order cone program (SOCP). Furthermore, [130, 138] did not consider discrete rates, admission control, millimeter-wave spectrum, and planar arrays.

Other related works on RRM for IAB or similar systems, such as cloud RAN and relay networks, can be found in the literature [100, 122, 127, 130–133, 135–137, 139–152]. However, these works are fundamentally different from [G]. The resemblance is minimal with respect to these works, since they generally address only one of the aforementioned challenges and focus on the RRM for only the access or backhaul links but not both.

8.4 CONTRIBUTIONS

The contributions of this chapter are summarized in the following.

- To address the scalability issue in IAB, a clustering strategy is proposed for grouping SBSs and UEs, which generates several disjoint clusters. This enables the use of multi-group multicast precoding to transmit backhaul traffic. Thus, the proposed clustering strategy simplifies backhaul design by requiring only a few RF chain at the MBS and eliminating the need for SIC at the SBSs.

- To address the remaining challenges, a joint formulation is proposed that includes the optimization of the precoding, UE association, rate allocation, and admission control in the access network and the precoding and rate allocation in the backhaul network. The resulting RRM design yields a nonconvex MINLP, which is novel and has not been investigated before.

- Three algorithms are proposed to solve the aforementioned nonconvex MINLP. The first algorithm consists in convexifying the nonconvex MINLP by using convex transformations to recast the problem as a mixed-integer second-order cone program (MISOCP) that can be solved optimally via branch-and-cut (BnC). This is achieved by eliminating additive binary couplings and multiplicative couplings of mixed integers, and reducing the search space by adding custom cutting planes. However, the BnC is overly expensive due to the large number of integer variables. Thus, a second algorithm is proposed that solves iteratively a sequence of SOCPs, obtained upon relaxing and penalizing the integrality constraints. The third algorithm is based on the second algorithm but reduces the complexity further by optimizing only the precoder gains, resulting in fewer variables.

- An upper bound is derived to assess the performance differences and trade-offs of the proposed algorithms. In addition, a simple lower bound is included to mark the worst-case performance.

8.5 INVESTIGATED PROBLEM

Consider a millimeter-wave system, where data is transported from the core network to the UEs via a MBS and several SBSs as shown in Figure 13. It is assumed that the backhaul and access networks operate in non-overlapping bands. The system model assumptions are described below in more detail.

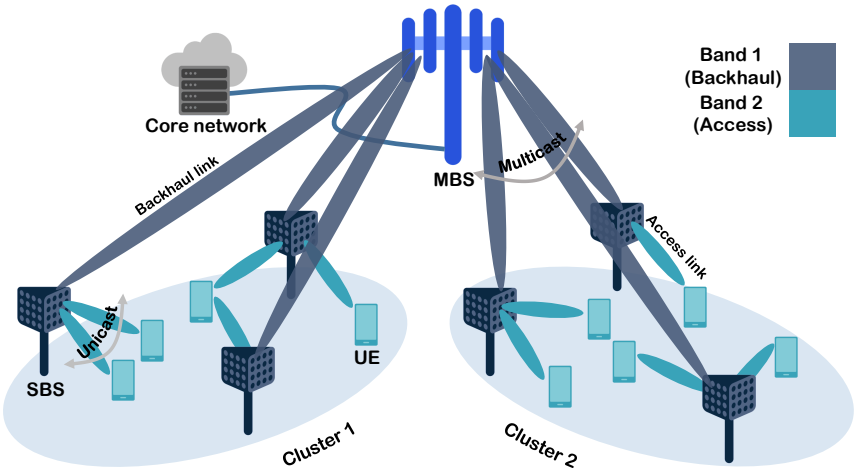

Figure 13: SDMA-based IAB system consisting of multiple clustered SBSs and UEs.

Generalities

The MBS is equipped with a planar array of N_{tx}^{MBS} transmit antennas, each SBS is equipped with a planar array of N_{tx}^{SBS} transmit antennas and $N_{rx}^{SBS} = 1$ receive antenna, and each UE has $N_{rx}^{UE} = 1$ receive antenna. The transmit antennas at the MBS and the receive antennas at the SBSs operate in Band 1, whereas the transmit antennas at SBSs and the receive antennas at the UEs operate in Band 2. Since Band 1 and Band 2 are non-overlapping, this system is called out-of-band full-duplex IAB.

Backhaul model: The SBSs are divided into L non-overlapping clusters, each consisting of B SBSs. In this way, data streams sent from the MBS to an SBS cluster contain the aggregated content for all UEs served in that cluster. The SBSs are clustered based on their proximity.

Access model: Depending on geographical distance or operator policy, each UE is pre-assigned to an SBS cluster. It is assumed that

each cluster has U UEs. As a result, the SBSs in a cluster only transmit collaboratively to the UEs in that cluster. However, not all SBSs are required to serve a given UE, and not all UEs may be served. All SBSs co-process information for all served UEs, allowing for more efficient interference management.

Channel model: The access and backhaul networks operate on disjoint frequencies. For the backhaul network, channels with line-of-sight (LOS) are assumed since the MBS and SBSs are usually strategically placed in the planning phase. For the access network, channels with multipath scattering and containing both LOS and non-line-of-sight (NLOS) components are assumed. Access and backhaul channels are modeled according to [153].

Optimization model: It is assumed that the MBS has knowledge of the access channels between the SBSs and UEs. This is possible since the 3rd Generation Partnership Project (3GPP) specifies channel training procedures in the access network. In addition, the MBS also knows the backhaul channels, i.e., between itself and the SBSs. Estimating the backhaul channels demand less overhead since they are more stable and have small variability compared to the access channels. Thus, the MBS collects knowledge of all the wireless channels and, accordingly, can manage the radio resources of the system.

Backhaul Network

In the backhaul network, two important aspects are dealt with: rate allocation and precoding, as explained in the following.

Precoding: The MBS transmits as many streams as there are clusters. Each stream contains the aggregated data of the UEs that will be served in their respective clusters. The instantaneous multicast symbol for the SBSs in cluster $\mathcal{B}_l$ is denoted by z_l, with $\mathbb{E}[z_l] = 0$ and $\mathbb{E}\left[|z_l|_2^2\right] = 1$. The precoding vector conveying z_l is denoted by $\mathbf{m}_l$. The composite signal transmitted from the MBS to all SBS clusters is $\mathbf{x}^{\text{MBS}} = \sum_{l\in\mathcal{L}} \mathbf{m}_l z_l$. The received signal at SBS $b \in \mathcal{B}_l$ is expressed as

$$y_b^{\text{SBS}} = \mathbf{g}_b^H \mathbf{x}^{\text{MBS}} + n_b = \underbrace{\mathbf{g}_b^H \mathbf{m}_l z_l}_{\text{signal for SBS } b} + \underbrace{\sum_{l'\in\mathcal{L}, l'\neq l} \mathbf{g}_b^H \mathbf{m}_{l'} z_{l'}}_{\text{interference}} + \underbrace{n_b}_{\text{noise}},$$

where $\mathbf{g}_b$ is the channel between SBS $b \in \mathcal{B}_l$ and the MBS whereas $n_b \sim \mathcal{CN}\left(0, \sigma_{\text{SBS}}^2\right)$ represents circularly symmetric Gaussian noise. The signal-to-interference-plus-noise ratio (SINR) at SBS b is given by

$$\text{SINR}_b^{\text{SBS}} = \frac{\left|\mathbf{g}_b^H \mathbf{m}_l\right|^2}{\sum_{l'\in\mathcal{L}, l'\neq l} \left|\mathbf{g}_b^H \mathbf{m}_{l'}\right|^2 + \sigma_{\text{SBS}}^2}. \tag{23}$$

Since all SBSs within a cluster receive the same stream, the performance of each cluster is determined by the SBS with the weakest channel conditions in that cluster. Consequently, a more sensible way to characterize the performance of each cluster is to use the minimum SINR, i.e., $\widetilde{\text{SINR}}_l^{\text{SBS}} = \min_{b \in \mathcal{B}_l} \left\{ \text{SINR}_b^{\text{SBS}} \right\}, \forall l \in \mathcal{L}$.

Rate allocation: The set of feasible data rates is finite in practical wireless communications systems [22, p. 64]. These predefined rates are uniquely identified by their associated channel quality indicator (CQI), and each corresponds to a specific MCS. In addition, for each rate, a minimum target SINR is required in order to guarantee the block error rate (BLER) [154]. The following target SINRs in [155] are considered.

Table 1: Rates and target SINR values

Coding rate	120/1024	308/1024	602/1024	466/1024	948/1024
Rate [bps/Hz]	$R_1^{\text{SBS}} = 0.2344$	$R_2^{\text{SBS}} = 0.6016$	$R_3^{\text{SBS}} = 1.1758$	$R_4^{\text{SBS}} = 2.7305$	$R_5^{\text{SBS}} = 5.5547$
SINR	$\Gamma_1^{\text{SBS}} = 0.2159$	$\Gamma_2^{\text{SBS}} = 0.6610$	$\Gamma_3^{\text{SBS}} = 1.7474$	$\Gamma_4^{\text{SBS}} = 10.6316$	$\Gamma_5^{\text{SBS}} = 95.6974$

To allocate rate R_j^{SBS} to the SBSs in the l-th cluster, it is needed that $\widetilde{\text{SINR}}_l^{\text{SBS}} \geqslant \Gamma_j^{\text{SBS}}$, $j \in \mathcal{J}^{\text{SBS}}$, where $\mathcal{J}^{\text{SBS}}$ is the set of possible rates. To represent the rate allocation, binary variables $\beta_{l,j} \in \{0, 1\}$ are introduced, where $\beta_{l,j} = 1$ denotes that the SBSs in $\mathcal{B}_l$ are served at rate R_j^{SBS}. Also, it is assumed that all SBS clusters are served, which is ensured via $\sum_{j \in \mathcal{J}^{\text{SBS}}} \beta_{l,j} = 1, \forall l \in \mathcal{L}$ and $N_{\text{streams}}^{\text{MBS}} \geqslant L$. To guarantee the predefined target BLER for cluster $\mathcal{B}_l$, it must hold that $\widetilde{\text{SINR}}_l^{\text{SBS}} \geqslant \sum_{j \in \mathcal{J}^{\text{SBS}}} \beta_{l,j} \Gamma_j^{\text{SBS}}$.

Access Network

In the access network, two important aspects are dealt with: admission control, rate allocation, UE association, and precoding, as explained in the following.

Precoding and UE association: A SBS $b \in \mathcal{B}_l$ serving a subset of UEs in $\mathcal{U}_l$ transmits several unicast signals simultaneously, where each signal aims to serve a specific UE. The instantaneous unicast symbol for UE $u \in \mathcal{U}_l$ is denoted by $s_{l,u}$, with $\mathbb{E}[s_{l,u}] = 0$ and $\mathbb{E}\left[|s_{l,u}|_2^2\right] = 1$. In addition, the precoder designed by SBS $b \in \mathcal{B}_l$ to transmit $s_{l,u}$ to UE $u \in \mathcal{U}_l$ is denoted by $\mathbf{w}_{b,u}$. Thus, the composite signal that SBS b in $\mathcal{B}_l$ sends to all UEs in $\mathcal{U}_l$ is given by $\mathbf{x}_b^{\text{SBS}} = \sum_{u \in \mathcal{U}_l} \mathbf{w}_{b,u} s_{l,u} \kappa_{b,u}$. Here, $\kappa_{b,u}$ represents a binary variable whose value is 1 when SBS $b \in \mathcal{B}_l$ serves UE $u \in \mathcal{U}_l$ and is 0 otherwise. Further, an admitted UE

$u \in \mathcal{U}_l$ is served by at least $B_{min} = 1$ and at most $B_{max} = B$ SBSs in $\mathcal{B}_l$. Specifically, the signal received by UE u in $\mathcal{U}_l$ is given by

$$y_u^{UE} = \underbrace{\sum_{b \in \mathcal{B}_l} \mathbf{h}_{b,u}^H \mathbf{w}_{b,u} s_{l,u} \kappa_{b,u}}_{\text{signal for UE } u \text{ in cluster } \mathcal{U}_l} + \underbrace{\sum_{b \in \mathcal{B}_l} \sum_{\substack{u' \in \mathcal{U}_l \\ u' \neq u}} \mathbf{h}_{b,u}^H \mathbf{w}_{b,u'} s_{l,u'} \kappa_{b,u'}}_{\text{interference originated in cluster } \mathcal{U}_l} + \underbrace{\sum_{\substack{l' \in \mathcal{L} \\ l' \neq l}} \sum_{b' \in \mathcal{B}_{l'}} \sum_{u' \in \mathcal{U}_{l'}} \mathbf{h}_{b',u}^H \mathbf{w}_{b',u'} s_{l',u'} \kappa_{b',u'} + \underbrace{n_u}_{\text{noise}}}_{\text{aggregate interference originated in clusters } \mathcal{U}_{l' \neq l}} \quad (24)$$

where $n_u \sim \mathcal{CN}\left(0, \sigma_{UE}^2\right)$ and $\mathbf{h}_{b,u}$ is the channel between SBS b and UE u. Note that UEs receive interference from within its own cluster and from neighboring clusters since the access network reuses the same frequency band to serve all UEs. The SINR at UE u in $\mathcal{U}_l$ is defined as

$$SINR_u^{UE} = \frac{P_u^{des}}{P_u^{intra} + P_u^{inter} + \sigma_{UE}^2}.$$

where

$$P_u^{des} = \left| \sum_{b \in \mathcal{B}_l} \mathbf{h}_{b,u}^H \mathbf{w}_{b,u} \kappa_{b,u} \right|^2$$

$$P_u^{intra} = \sum_{\substack{u' \in \mathcal{U}_l \\ u' \neq u}} \left| \sum_{b \in \mathcal{B}_l} \mathbf{h}_{b,u}^H \mathbf{w}_{b,u'} \kappa_{b,u'} \right|^2$$

$$P_u^{inter} = \sum_{\substack{l' \in \mathcal{L} \\ l' \neq l}} \sum_{u' \in \mathcal{U}_{l'}} \left| \sum_{b' \in \mathcal{B}_{l'}} \mathbf{h}_{b',u}^H \mathbf{w}_{b',u'} \kappa_{b',u'} \right|^2$$

Rate allocation and admission control: The rate allocated to an admitted UE can only be from a set of predefined values. Thus, to depict this rate allocation, binary variables $\alpha_{u,j} \in \{0, 1\}$ are introduced. In particular, these variables are used for both admission control and rate allocation. This is ensured by including $\sum_{j \in \mathcal{J}^{UE}} \alpha_{u,j} \leqslant 1, \forall l \in \mathcal{L}, u \in \mathcal{U}_l$, where $\mathcal{J}^{UE}$ represents the set of possible rate values. An UE u is served when $\sum_{j \in \mathcal{J}^{UE}} \alpha_{u,j} = 1$, indicating that one rate has been allocated. Otherwise, when $\sum_{j \in \mathcal{J}^{UE}} \alpha_{u,j} = 0$, the UE is not admitted. The rates and target SINRs for UEs are denoted by R_j^{UE} and Γ_j^{UE}, respectively. To allocate rate R_j^{UE} to UE u, it must be satisfied that $SINR_u^{UE} \geqslant \Gamma_j^{UE}$, $j \in \mathcal{J}^{UE}$. Specifically, for the access network, we assume the same values shown in Table 1. Note that not all UEs are necessarily admitted since each SBS can transmit at most $N_{streams}^{SBS}$ streams simultaneously.

Problem formulation

The objective is to design the precoding, UE association, rate allocation, and admission control in the access network, and precoding, rate selection in the backhaul network in order to maximize the WSR at the access network. Thus, the optimization problem is defined as,

$$
\begin{aligned}
\mathcal{P}' : \max_{\substack{\mathbf{m}_l, \mathbf{w}_{b,u}, \\ \alpha_{u,j}, \beta_{l,j}, \kappa_{b,u}}} \quad & R^{\text{access}}_{w-\text{sum}}(\boldsymbol{\alpha}) \equiv \sum_{l \in \mathcal{L}} \sum_{u \in \mathcal{U}_l} \omega_u \sum_{j \in \mathcal{J}^{\text{UE}}} \alpha_{u,j} R^{\text{UE}}_j \\
\text{s.t.} \quad & C_1 : \alpha_{u,j} = \{0,1\}, \forall l \in \mathcal{L}, u \in \mathcal{U}_l, j \in \mathcal{J}^{\text{UE}}, \\
& C_2 : \sum_{j \in \mathcal{J}^{\text{UE}}} \alpha_{u,j} \leqslant 1, \forall l \in \mathcal{L}, u \in \mathcal{U}_l, \\
& C_3 : \sum_{l \in \mathcal{L}} \|\mathbf{m}_l\|_2^2 \leqslant P^{\text{MBS}}_{\text{tx}}, \\
& \overline{C}_4 : \sum_{u \in \mathcal{U}_l} \|\mathbf{w}_{b,u} \kappa_{b,u}\|_2^2 \leqslant P^{\text{SBS}}_{\text{tx}}, \forall l \in \mathcal{L}, b \in \mathcal{B}_l, \\
& \overline{C}_5 : \text{SINR}^{\text{UE}}_u \geqslant \sum_{j \in \mathcal{J}^{\text{UE}}} \alpha_{u,j} \Gamma^{\text{UE}}_j, \forall l \in \mathcal{L}, u \in \mathcal{U}_l, \\
& C_6 : \kappa_{b,u} = \{0,1\}, \forall l \in \mathcal{L}, b \in \mathcal{B}_l, u \in \mathcal{U}_l, \\
& C_7 : \sum_{u \in \mathcal{U}_l} \kappa_{b,u} \leqslant N^{\text{SBS}}_{\text{streams}}, \forall l \in \mathcal{L}, b \in \mathcal{B}_l, \\
& C_8 : \sum_{u \in \mathcal{U}_l} \kappa_{b,u} \geqslant 1, \forall l \in \mathcal{L}, b \in \mathcal{B}_l, \\
& C_9 : \sum_{b \in \mathcal{B}_l} \kappa_{b,u} \leqslant B_{\max} \sum_{j \in \mathcal{J}^{\text{UE}}} \alpha_{u,j}, \forall l \in \mathcal{L}, u \in \mathcal{U}_l, \\
& C_{10} : \sum_{b \in \mathcal{B}_l} \kappa_{b,u} \geqslant B_{\min} \sum_{j \in \mathcal{J}^{\text{UE}}} \alpha_{u,j}, \forall l \in \mathcal{L}, u \in \mathcal{U}_l, \\
& C_{11} : \beta_{l,j} = \{0,1\}, \forall l \in \mathcal{L}, j \in \mathcal{J}^{\text{SBS}}, \\
& C_{12} : \sum_{j \in \mathcal{J}^{\text{SBS}}} \beta_{l,j} = 1, \forall l \in \mathcal{L}, \\
& C_{13} : W^{\text{access}}_{\text{BW}} \sum_{u \in \mathcal{U}_l} \sum_{j \in \mathcal{J}^{\text{UE}}} \alpha_{u,j} R^{\text{UE}}_j \leqslant W^{\text{backhaul}}_{\text{BW}} \sum_{j \in \mathcal{J}^{\text{SBS}}} \beta_{l,j} R^{\text{SBS}}_j, \forall l \in \mathcal{L}, \\
& C_{14} : \sum_{u \in \mathcal{U}_l} \sum_{j \in \mathcal{J}^{\text{UE}}} \alpha_{u,j} = U_{\text{served}}, \forall l \in \mathcal{L}, \\
& \bar{C}_{15} : \widetilde{\text{SINR}}^{\text{SBS}}_l \geqslant \sum_{j \in \mathcal{J}^{\text{SBS}}} \beta_{l,j} \Gamma^{\text{SBS}}_j, \forall l \in \mathcal{L},
\end{aligned}
$$

The weight associated with UE u is represented by ω_u, which can be adjusted to enforce different priorities between UEs. Thus, $R^{\text{access}}_{w-\text{sum}}(\boldsymbol{\alpha})$ represents the WSR achieved by all UEs. Constraints $C_1 - C_2$ ensure rate selection for all UEs. Constraint C_3 limits the transmit power of the MBS to $P^{\text{MBS}}_{\text{tx}}$, whereas constraint $\overline{C}_4$ limits the transmit

power of the SBS to P_{tx}^{SBS}. To guarantee the allocated rate for a UE, the UE's SINR must to be larger than the target SINR corresponding to the allocated rate (see Table 1), which is enforced via constraint $\overline{C}_5$. To ensure that each SBS serves at least one UE and that each SBS cannot serve more UEs than the number of streams supported, constraints $C_6 - C_8$ are included. Each admitted UE is served by at least B_{min} and by at most B_{max} SBSs, therefore, constraints $C_9 - C_{10}$ are considered. Constraints $C_{11} - C_{12}$ together select a rate for the SBS clusters. Besides, to guarantees that the access throughput in a cluster does not exceed the backhaul throughput for that cluster, constraint C_{13} is included. Constraint C_{14} ensures that U_{served} UEs are served per cluster. To guarantee the allocated rate for the SBS clusters, the SINR of the SBS cluster needs to be larger than the target SINR corresponding to the allocated rate (see Table 1). As a result, constraint $\overline{C}_{15}$ is included.

Note: *For details on the proposed algorithm to solve $\mathcal{P}'$, the reader is referred to [G], which can also be found in Appendix G.*

8.6 SELECTED RESULTS

Figure 14 is taken from [G], but the layout has been slightly modified.

In the following, simulation results of a specific scenario in [G] are discussed. Figure 14 shows the throughput achieved by the proposed algorithms, which are denoted by `BnC-MISOCP`, `RnP-SOCP-1`, and `RnP-SOCP-2`. In addition, the proposed upper and lower bounds are denoted by `UB` and `LB`, respectively.

Figure 14 shows three scenarios where the transmit power of the SBSs is $P_{tx}^{SBS} = \{6, 10, 14\}$ dBm and the transmit power of the MBS is $P_{tx}^{MBS} = \{9, 12, \ldots, 36\}$ dBm. In addition, the number of antennas of the MBS and SBSs are $N_{tx}^{MBS} = 64$ and $N_{tx}^{SBS} = 16$, respectively. The number of clusters is $L = 2$, the number of SBSs per cluster is $B = 3$, the number of UEs per cluster is $U = 6$, and the number of admitted UEs per cluster is $U_{served} = 3$.

Figure 14 shows that `RnP-SOCP-1` and `RnP-SOCP-2` are 5.1% and 9.7% below `BnC-MISOCP`, respectively, when $P_{tx}^{SBS} = 14$ dBm. This indicates that `RnP-SOCP-1` and `RnP-SOCP-2` can achieve relatively high performance at much lower complexity than `BnC-MISOCP`. Specifically, `BnC-MISOCP` attains near-optimality but demands high computational complexity.

On the other hand, it is observed that the performance gap between `UB` and `BnC-MISOCP` reduces when increasing P_{tx}^{SBS}, showing only 9.6% difference when $P_{tx}^{SBS} = 14$ dBm. However, the difference between `UB` and `BnC-MISOCP` is large when the transmit power of the SBS is $P_{tx}^{SBS} = 6$ dBm. This occurs because the SBSs can only serve UEs at

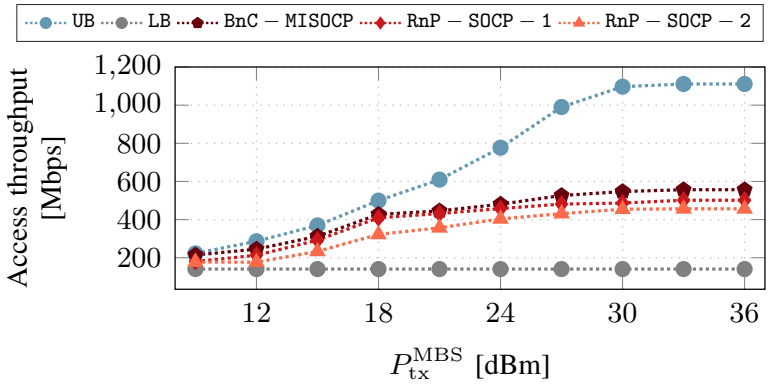

(a) Varying $P_{\text{tx}}^{\text{MBS}}$ when $P_{\text{tx}}^{\text{SBS}} = 6$ dBm

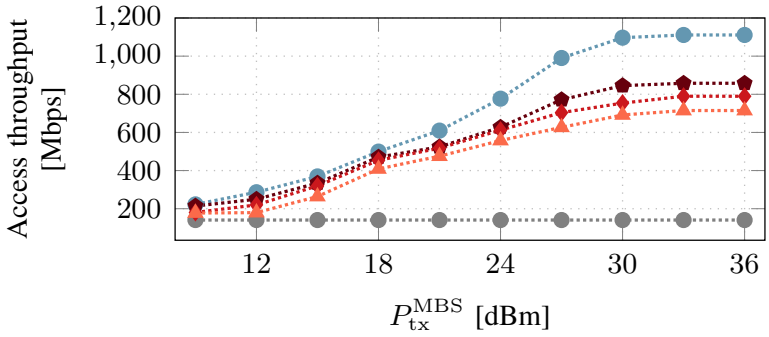

(b) Varying $P_{\text{tx}}^{\text{MBS}}$ when $P_{\text{tx}}^{\text{SBS}} = 10$ dBm

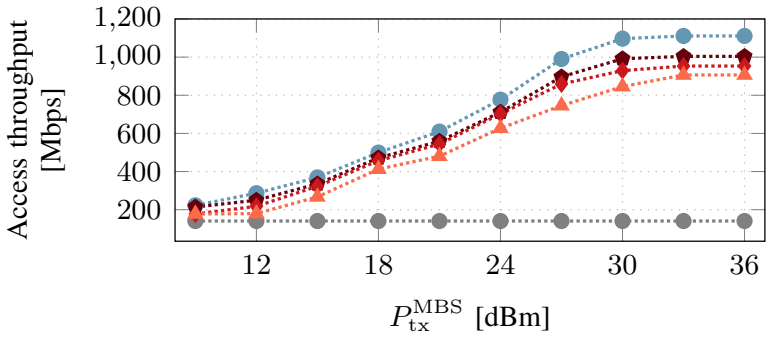

(c) Varying $P_{\text{tx}}^{\text{MBS}}$ when $P_{\text{tx}}^{\text{SBS}} = 14$ dBm

Figure 14: Rate performance of the proposed algorithms.

very low rates when $P_{\text{tx}}^{\text{SBS}} = 6$ dBm, producing a large difference with respect to UB. When $P_{\text{tx}}^{\text{SBS}} = 14$ dBm, the SBSs have sufficient transmit power and therefore can guarantee higher rates for the served UEs, thus showing little difference with respect to UB.

9

PRECODING, ADMISSION CONTROL, AND RATE ALLOCATION FOR UNICAST AND MULTICAST BASED ON RSMA

This chapter gives an overview of the research problem investigated in [H], which is included in Appendix H. In the following, the motivation is given, the goal is stated, the related work is reviewed, the contributions are summarized, the research problem is formulated, and selected results are discussed.

9.1 MOTIVATION

Due to its enhanced ability to cope with multi-user interference, rate-splitting multiple access (RSMA) is capable of outperforming non-orthogonal multiple access (NOMA) and space-division multiple access (SDMA). To date, several studies have demonstrated in several use cases that RSMA has superior capabilities compared to SDMA and NOMA, thus positioning RSMA as a formidable multiple access scheme candidate with great potential to meet the stringent connectivity requirements of next-generation wireless communications systems.

Radio resource management (RRM) design is critical to ensure suitable RSMA performance. In particular, precoding and power are the most commonly optimized resources in RSMA, and their design has been examined in a variety of RRM designs and for a variety of purposes. For instance, the precoding design was investigated in [156, 157] for fairness maximization, in [158–162] for weighted sum rate (WSR) and WSR maximization, and in [160–163] for weighted energy efficiency (WEE) maximization. Besides, power allocation was investigated in [118, 164–167].

Although the literature on RSMA continues to grow and show promising results, questions arise as to whether the observed results remain equally valid when accounting for frequently overlooked practical characteristics, such as discrete rates, admission control, and imperfect successive interference cancellation (SIC). It is expected that by accounting for these practical characteristics of wireless communications systems, the true potential of RSMA can be revealed compared to SDMA and NOMA.

In fact, the full extent of the impact of these practical characteristics on RSMA performance remains largely unexplored, as most works have assumed continuous rates, perfect SIC, and have not included admission control in the RRM design. Motivated by this, the RRM design for RSMA is investigated, considering discrete rates, admission control, and imperfect SIC, together with the precoding. In particular, the maximization of the WSR and WEE are investigated, which are two key indicators to quantify spectral efficiency (SE) and energy efficiency (EE) performance.

9.2 GOAL

The goal is to design the RRM to maximize the WSR and WEE of RSMA accounting for practical characteristics of real wireless communications systems, such as discrete rate, admission control, and imperfect SIC. A first algorithm is proposed to design the precoders, discrete rate allocation and admission control, accounting for potentially imperfect SIC. In particular, the proposed algorithm is based on the convexification of nonconvex mixed-integer nonlinear programs (MINLPs). Given the wide adoption of Shannon capacity to model rates, a second algorithm for continuous rates is proposed, which is also a nonconvex MINLPs.

9.3 RELATED WORK

Most studies have assumed continuous rates based on Shannon capacity. This assumption contravenes the predominant use of discrete rates in real wireless communications systems, and raises questions as to whether the advantages of RSMA will still hold when discrete rates are considered. Transmission rates are discrete in practice and are governed by a set of modulation and coding schemes (MCSs) [22], resulting in a finite number of discrete rates. Shannon capacity, on the other hand, is a continuous-rate information-theoretic upper bound that cannot be achieved in practice, but is often used because dealing directly with MCSs is impractical. Thus, it is common practice to use Shannon capacity and project the continuous rates, i.e., round them to the closest discrete rate, to meet the MCS specifications. However, rate projection may lead to performance degradation. Therefore, rate discretization must be properly accounted for in the RRM design to exploit the full potential of RSMA. A first study to investigate the impact of discrete rates in RSMA is [168]. The authors considered the precoding design and discrete rate allocation to maximize the sum rate (SR) of RSMA. The authors demonstrated that RSMA outperforms SDMA when discrete rates are considered. However, the proposed design does not allow handling predefined MCSs, as the authors assumed continuous rates. Specifically, the authors customized

the MCSs to achieve a SR close to the ensemble average, obtained over multiple realizations of the channel. In addition, a number of works have investigated the impact of precoding and discrete rates on SDMA performance. The joint design of precoding and discrete rate allocation was investigated in [139, 144, 169] for SR and WSR maximization, where algorithms based on convexification of nonconvex MINLPs were proposed. However, the findings in these works are not applicable to RSMA, as RSMA is a more general framework that includes SDMA as a particular case.

Due to the availability of a limited number of radiofrequency (RF) chains, wireless communications systems typically limit the number of user equipments (UEs) served per time slot. This is generally true for SDMA since each RF chain only support one UE. When the number of UEs exceeds the maximum number supported, some form of control is required. Although RSMA can serve multiple UEs using the multicast signal, RSMA's multicast signal degrades rapidly as the number of UEs increases, defeating the purpose of the service and necessitating selective admission control. Particularly, the impact of admission control has not yet been studied for RSMA but has been studied for SDMA and NOMA. For instance, the precoding design and admission control for SDMA was investigated in [170] to minimize the transmit power, where the authors proposed an algorithm based on mixed-integer semidefinite program (MISDP). The precoding design and admission control for SDMA was also investigated in [171], where the authors proposed an algorithm based on successive convex approximation (SCA) to maximize the SR. The maximization of the number of UEs served was investigated in [172] for SDMA. To this purpose the authors proposed algorithms based on semidefinite relaxation (SDR) and second-order cone programs (SOCPs) to design the precoding and admission control. The power allocation and admission control were designed in [173] for NOMA in order maximize the number of UEs served. In particular, an algorithm based on matching theory and linear programming was proposed. Besides, the design of precoding, admission control, and discrete rate allocation for SR maximization of SDMA was investigated in [G]. The authors proposed algorithms based on the convexification of nonconvex MINLPs and minorization-maximization (MM). The algorithms developed in the preceding studies, in particular, do not apply to RSMA. First, RSMA admission control differs significantly from SDMA and NOMA because RSMA delivers information to users through overlapping multicast and unicast precoders. Unicast precoders benefit from UEs with uncorrelated channels because interference is easier to mitigate, while multicast precoders benefit from UEs with correlated channels as this facilitates transmitting shared information. Given these competing objectives, it is critical to incorporate admission control into the RRM design of RSMA.

The success of SIC has a significant impact on RSMA performance. In practice, SIC is rarely perfect, which can result in unmanaged self-interference that can impair performance. Despite the importance of accounting for an imperfect SIC in the RRM design of RSMA, most RSMA literature has assumed perfect SIC, with the exception of a few studies. For instance, the authors of [174] proposed a block coordinate descent (BCD) algorithm to investigate the precoding design and subcarrier allocation for SR maximization, assuming imperfect SIC. The proposed algorithm, however, assumed continuous rates and did not account for admission control. The SR maximization of RSMA with imperfect SIC was also investigated in [175], where the authors derived criteria for power allocation but did not account for admission control or discrete rates. Since NOMA also depends on SIC, imperfect SIC in NOMA systems has been investigated in a few works. In particular, the power allocation with imperfect SIC for NOMA was investigated in [176–178] for SR maximization, and in [179] for EE maximization.

9.4 CONTRIBUTIONS

The contributions of this chapter are summarized in the following.

- Two novel RRM problems are formulated, whose objective is to maximize the WSR and WEE of RSMA via the joint optimization of the precoding, admission control, and private and common discrete rates, while accounting for imperfect SIC. The resulting WSR and WEE problems, denoted by $\mathcal{P}'_{\text{DWSR}}$ and $\mathcal{P}'_{\text{DWEE}}$, are nonconvex MINLPs and challenging to solve. In addition, nonconvex MINLPs $\mathcal{Q}'_{\text{CWSR}}$ and $\mathcal{Q}'_{\text{CWEE}}$ are also formulated, which represent the continuous-rate counterparts of $\mathcal{P}'_{\text{DWSR}}$ and $\mathcal{P}'_{\text{DWEE}}$ based on Shannon capacity.

- A first algorithm is proposed to solve nonconvex MINLPs $\mathcal{P}'_{\text{DWSR}}$ and $\mathcal{P}'_{\text{DWEE}}$. The algorithm proposed is referred to as optimal mixed-integer second-order cone program (`OPT-MISOCP`), which tackles the nonconvexities of $\mathcal{P}'_{\text{DWSR}}$ and $\mathcal{P}'_{\text{DWEE}}$ through applying a series of convex transformations. `OPT-MISOCP` approximates $\mathcal{P}'_{\text{DWSR}}$ and $\mathcal{P}'_{\text{DWEE}}$ as convex MINLPs $\mathcal{P}_{\text{DWSR}}$ and $\mathcal{P}_{\text{DWEE}}$, instead of treating $\mathcal{P}'_{\text{DWSR}}$ and $\mathcal{P}'_{\text{DWEE}}$ as general nonconvex MINLPs. This allows to solve $\mathcal{P}_{\text{DWSR}}$ and $\mathcal{P}_{\text{DWEE}}$ in a globally optimal manner. However, getting rid of the nonconvexities of $\mathcal{P}'_{\text{DWSR}}$ and $\mathcal{P}'_{\text{DWEE}}$ carries the risk of reducing the feasible set, possibly resulting in a loss of optimality. Thus, to assess the loss of optimality, an upper bound is derived, showing that globally optimal solutions for $\mathcal{P}_{\text{DWSR}}$ and $\mathcal{P}_{\text{DWEE}}$ result in near-optimal solutions for $\mathcal{P}'_{\text{DWSR}}$ and $\mathcal{P}'_{\text{DWEE}}$ with negligible degradation.

- A second algorithm is proposed to solve nonconvex MINLPs $\mathcal{Q}'_{\text{CWSR}}$ and $\mathcal{Q}'_{\text{CWEE}}$. The algorithm proposed is based on binary enumeration and convex transformations. Enumeration is utilized to list all possible combinations of admission control, which results in multiple subproblems where binary variables are known. To solve each of the resulting subproblems, the optimal successive convex approximation with semidefinite relaxation (`OPT-SCA-SDR`) algorithm is proposed, which converges to a Karush-Kuhn-Tucker (KKT) point. To enforce compliance with the finite set of discrete rates, the continuous rates obtained by `OPT-SCA-SDR` are projected, i.e., rounded to the closest feasible discrete rates.

- Compared to projecting continuous rates, RSMA designed for discrete rates achieves gains of up to 89.7% (WSR) and 21.5% (WEE). Besides, admission control for RSMA yields additional gains of up to 15.3% (WSR) and 11.4% (WEE) compared to random admission control when discrete rates are considered. Also, self-interference can be successfully mitigated by accounting for imperfect SIC in the RRM design.

- In general, simulation results show that incorporating characteristics of practical wireless systems in the RRM design of RSMA leads to improved exploitation of the radio resources and, therefore, to higher WSR and WEE.

9.5 INVESTIGATED PROBLEM

Consider a millimeter-wave system, where a base station (BS) serves multiple UEs, as shown in Figure 15.

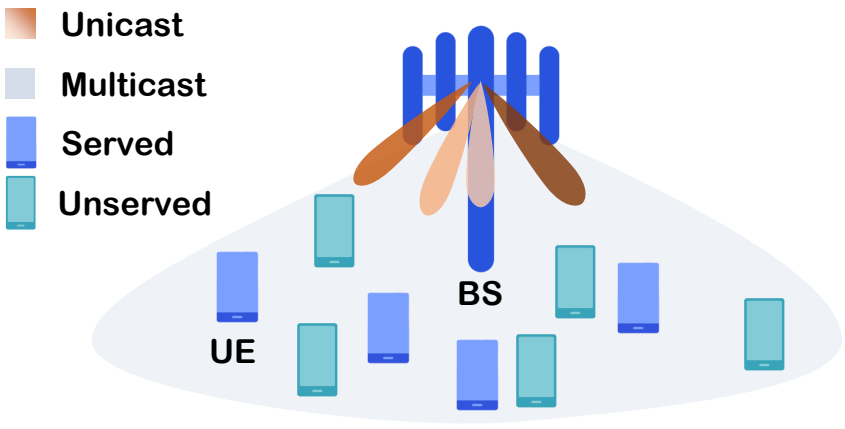

Figure 15: RSMA-based system consisting of a BS and multiple UEs.

Generalities

The number of UEs is U and they are indexed by set $\mathcal{U} = \{1, \ldots, U\}$. It is assumed that the UEs have one antenna and one RF chain, i.e., $N_{rx} = 1$ and $N_{rx}^{RF} = 1$. The BS is equipped with an antenna array with N_{tx} elements and N_{tx}^{RF} RF chains. The maximum transmit power that the BS can use for downlink is P_{tx}^{max}. In addition, the BS admits K of the U UEs, where $K \leqslant U$. In the following, the system model and constraints for the RRM design are introduced and discussed.

RSMA principle: The following explains RSMA's principle but excludes admission control for the sake of simplicity. However, admission control is considered in the RRM design, described afterwards. It is assumed that the BS has messages for all UEs, denoted by $\widetilde{W}_u$, $u \in \mathcal{U}$. However, only K out of U UE are served with their respective messages. Since admission control is disregarded for this explanation, the set of admitted UEs is assumed to be known beforehand, which is denoted by $\mathcal{U}'$, such that $|\mathcal{U}'| = K$. Let UE_u denote the u-th UE in $\mathcal{U}'$. To differentiate the UEs served from those not served, the messages for the served UEs are denoted by W_u, $u \in \mathcal{U}'$. Based on the rate-splitting concept, message W_u, $u \in \mathcal{U}'$ is decomposed into two parts as $W_u \triangleq \left(W_u^{(p)}, W_u^{(c)}\right)$, where $W_u^{(p)}$ and $W_u^{(c)}$ are respectively referred to as the private and common portions of W_u.

The private portion $W_u^{(p)}$ is encoded into symbol $s_u \in \mathbb{C}$, which is transmitted at a rate $R_u^{(p)}$ to UE_u in an unicast manner. On the other hand, all K common portions, $W_1^{(c)}, \ldots, W_K^{(c)}$, are merged and encoded into symbol $s_0 \in \mathbb{C}$, which is transmitted at rate $R^{(c)}$ in a multicast manner to all UEs. The symbols are assumed to be statistically independent, such that $\mathbb{E}\left\{\mathbf{s}^H\mathbf{s}\right\} = \mathbf{I}$ and $\mathbf{s} = [s_0, s_1, \ldots, s_K]^T \in \mathbb{C}^{(K+1)\times 1}$. Let C_u denote the rate portion of $R^{(c)}$ corresponding to UE_u, such that $R^{(c)} = \sum_u C_u$. Therefore, UE_u is served with an overall rate of $R_u^{(p)} + C_u$, i.e., the private rate transmitted via unicast and a fraction of the common rate transmitted via multicast. Using SIC, as explained in more detail afterwards, each UE is able to recover $W_u^{(c)}$ and $W_u^{(p)}$ after decoding s_0 and s_u, thus allowing to recompose the original message W_u. Furthermore, each UE_u obtains common parts $W_{i\neq u}^{(c)}$, corresponding to the other UEs, which are used for interference decoding and cancellation. *Thus, RSMA can smoothly bridge the two extremes of fully treating the interference as noise and fully decoding it by means of adjusting the partition ratio of the common and private parts of the messages, $W_u^{(p)}$ and $W_u^{(c)}$ [180].*

Discrete rates: Wireless communications systems support only a finite set of data rates [22, p. 64]. Each of these predefined rates is the result of a specific MCS, each of which is identified by its channel

quality indicator (CQI). To enable a given rate, a target signal-to-interference-plus-noise ratio (SINR) is required which ensures a given block error rate (BLER) [154]. Rates and MCSs are usually standardized but the target SINRs depend on the UE's features. Let $\mathcal{J} = \{1, \ldots, J\}$ be the set indexing the MCSs supported by the system and let J be the total number of MCSs. Thus, for a given discrete rate R_j, $j \in \mathcal{J}$, there is a corresponding target SINR Γ_j that must be satisfied to ensure rate R_j. Assuming that $R_{j+1} > R_j$ and $\Gamma_{j+1} > \Gamma_j$, if an UE achieves an SINR of $\overline{\Gamma}$, the BS can allocate any discrete rate $\overline{R}_{\text{dis}} \triangleq \left\{R_j \mid \Gamma_j \leqslant \overline{\Gamma}, j \in \mathcal{J}\right\}$ to the UE. However, when Shannon capacity is employed, the BS allocates the continuous rate $\overline{R}_{\text{con}} \triangleq \log_2\left(1 + \overline{\Gamma}\right)$. The discrete rates and target SINRs used for the RRM design are shown in Table 2

Table 2: Rates and target SINRs for various CQIs.

CQI index j	**Coding rate**	**Rate** R_j [bps/Hz]	**SINR** Γ_j
1	0.0762	0.1523	0.1128
2	0.1172	0.2344	0.2159
3	0.1885	0.3770	0.3892
4	0.3008	0.6016	0.6610
5	0.4385	0.8770	1.0962
6	0.5879	1.1758	1.7474
7	0.3691	1.4766	2.8113
8	0.4785	1.9141	4.3321
9	0.6016	2.4063	7.0081
10	0.4551	2.7305	10.6316
11	0.5537	3.3223	16.6648
12	0.6504	3.9023	25.8345
13	0.7539	4.5234	38.4503
14	0.8525	5.1152	60.0620
15	0.9258	5.5547	95.6974

Admission control

To indicate whether a given UE_u is admitted or not, constraint $\overline{C}_1 : \chi_u \in \{0, 1\}, \forall u \in \mathcal{U}$ is introduced. Specifically, $\chi_u = 1$ indicates that the BS serves UE_u, and $\chi_u = 0$ otherwise. Constraint $\overline{C}_2 : \sum_{u \in \mathcal{U}} \chi_u = K$ is included to enforce admission control, i.e., the number of admitted UEs must be K, which are chosen out of U. An admitted UE can be served via the common signal only, the private signal only, or both. Therefore, to indicate whether an admitted UE_u is served via the private signal, constraint $\overline{C}_3 : \mu_u \in \{0, 1\}, \forall u \in \mathcal{U}$ is introduced, i.e., $\mu_u = 1$ indicates that UE_u is served via the private signal, and $\mu_u = 0$ otherwise. Constraint $\overline{C}_4 : \mu_u \leqslant \chi_u, \forall u \in \mathcal{U}$ is included to ensure that non-admitted UEs are not served by a private signal. Obviously, non-admitted UEs are neither served by the common signal but this aspect is addressed by constraint $\overline{C}_{12}$, discussed later. Constraint

$\overline{C}_5 : \psi \in \{0, 1\}$ is incorporated to specify whether the common signal is employed or not.

Precoding

For each UE, the BS employs a private precoder $\mathbf{w}_u \mu_u \in \mathbb{C}^{N_{tx} \times 1}$, $u \in \mathcal{U}$. Also, the BS employs common precoder $\mathbf{m}\psi \in \mathbb{C}^{N_{tx} \times 1}$ for the common signal serving all the admitted UEs. In particular, the private precoder is $\mathbf{o}$ when UE_u is not admitted. Every private symbol s_u is precoded by its corresponding $\mathbf{w}_u \mu_u$. Similarly, the common symbol s_0 is precoded by $\mathbf{m}\psi$. Therefore, the downlink signal transmitted from the BS to the UEs is given by $\mathbf{x} = \sum_{u \in \mathcal{U}} \mathbf{w}_u \mu_u s_u + \mathbf{m}\psi s_0$. Since the BS has limited power for precoding, the following constraint is included $\overline{C}_6 : \sum_{u \in \mathcal{U}} \|\mathbf{w}_u \mu_u\|_2^2 + \|\mathbf{m}\psi\|_2^2 \leqslant P_{tx}^{max}$.

Imperfect SIC

The signal received by UE_u is expressed as

$$y_u = \mathbf{h}_u^H \mathbf{x} + n_u = \underbrace{\mathbf{h}_u^H \mathbf{m}\psi s_0}_{\substack{\text{common signal} \\ y_u^{(c)}}} + \underbrace{\mathbf{h}_u^H \mathbf{w}_u \mu_u s_u}_{\substack{\text{private signal for } \mathsf{UE}_u \\ y_u^{(p)}}} + \underbrace{\mathbf{h}_u^H \sum_{i \neq u} \mathbf{w}_i \mu_i s_i}_{\substack{\text{interference at } \mathsf{UE}_u \\ y_u^{(int)}}} + \underbrace{n_u}_{\text{noise}}. \tag{26}$$

In (26), terms $y_u^{(c)}$, $y_u^{(p)}$, and $y_u^{(int)}$ represent the received common signal, private signal, and interference at UE_u. Circularly symmetric Gaussian noise is denoted by $n_u \sim \mathcal{CN}(0, \sigma^2)$ whereas the channel between the BS and UE_u is represented by $\mathbf{h}_u \in \mathbb{C}^{N_{tx} \times 1}$. Obviously, only admitted UE_u utilize SIC to recover the message s_u from y_u. Thus, an admitted UE UE_u decodes first the common symbol s_0 from y_u by treating signals terms $y_u^{(p)}$ and $y_u^{(int)}$ as noise. Afterwards, UE_u reconstructs the received common signal $y_u^{(c)}$ using the decoded symbol s_0 and subtracts $y_u^{(c)}$ from y_u, yielding $y_u^{SIC} = y_u^{(p)} + y_u^{(int)} + n_u$. From y_u^{SIC}, UE_u can decode private symbol s_u. However, removal of $y_u^{(c)}$ is not perfect, which may be caused, e.g., by hardware impairments [175, 176]. Hence, the resulting signal after imperfect SIC can be expressed as $y_u^{iSIC} = \Delta_{SIC} y_u^{(c)} + y_u^{(p)} + y_u^{(int)} + n_u$, where $0 \leqslant \Delta_{SIC} \leqslant 1$ represents the percentage of the common signal that was not canceled. In particular, $\Delta_{SIC} = 0$ indicates that SIC is perfect.

From (26), the SINRs of the common and private signals at UE_u are obtained and defined as

$$SINR_u^{(c)} = \frac{\left|\mathbf{h}_u^H \mathbf{m} \psi\right|^2}{\sum_{i \in \mathcal{U}} \left|\mathbf{h}_u^H \mathbf{w}_i \mu_i\right|^2 + \sigma^2}, \tag{27}$$

$$SINR_u^{(p)} = \frac{\left|\mathbf{h}_u^H \mathbf{w}_u \mu_u\right|^2}{\left|\Delta_{SIC} \mathbf{h}_u^H \mathbf{m} \psi\right|^2 + \sum_{i \neq u} \left|\mathbf{h}_u^H \mathbf{w}_i \mu_i\right|^2 + \sigma^2}. \tag{28}$$

The exact value of Δ_{SIC} is usually not known by the BS. Therefore, it must be set properly to avoid performance degradation, and thus guarantee the target SINRs that enable the allocated rates. Typical values for Δ_{SIC} are in the range of 4% and 10% [176].

Rate allocation for the private signals

An UE_u that receives its private signal at a rate R_j, can only decode the message if its SINR satisfies $SINR_u^{(p)} \geqslant \Gamma_j$. Here, Γ_j is the target SINR that guarantees R_j. In particular, Table 2 defines the target SINRs Γ_j for every rate supported by the system. Constraint $\overline{C}_7 : \alpha_{u,j} \in \{0,1\}, \forall u \in \mathcal{U}, j \in \mathcal{J}$, is introduced to depict the assignment of private rates. Specifically, $\alpha_{u,j} = 1$ indicates that UE_u is served by a private signal transmitted at rate R_j. Constraint $\overline{C}_8 : \sum_{j \in \mathcal{J}} \alpha_{u,j} = \mu_u, \forall u \in \mathcal{U}$, is also included to ensure that a rate is allocated to UE_u, if UE_u is served by a private signal. Constraint $\overline{C}_9 : SINR_u^{(p)} \geqslant \sum_{j \in \mathcal{J}} \alpha_{u,j} \Gamma_j, \forall u \in \mathcal{U}$, is included in order to relate each discrete rate and its corresponding target SINR. Thus, $\overline{C}_9$ ensures for UE_u a private rate of $\sum_{j \in \mathcal{J}} \alpha_{u,j} R_j$, if $\mu_u = 1$. In particular, $\mu_u = 0$ does not indicate that UE_u is not admitted since UE_u can also be served by the common signal when $C_u > 0$.

Rate allocation for the common signal

An UE_u that is admitted can decode the common message, which is transmitted at rate R_j, only if $SINR_u^{(c)} \geqslant \Gamma_j$. Thus, to depict the rate allocation for the common signal, constraint $\overline{C}_{10} : \kappa_j \in \{0,1\}$, $j \in \mathcal{J}$, is introduced, where $\kappa_j = 1$ indicates that rate R_j is chosen. Furthermore, constraint $\overline{C}_{11} : \sum_{j \in \mathcal{J}} \kappa_j = \psi$ is introduced to enable the possibility that the common rate is 0. In order to combine admission control and the allocation of the common rate, constraint $\overline{C}_{12} : SINR_u^{(c)} \geqslant \chi_u \sum_{j \in \mathcal{J}} \kappa_j \Gamma_j, \forall u \in \mathcal{U}$ is included. This, results in common rate $\sum_{j \in \mathcal{J}} \kappa_j R_j$ for all admitted UEs. Note that rate portions C_u are not continuous. However, these rates have very fine granularity since rate-splitting can divide messages W_u into portions of

any size. Therefore, rate portions C_u are regarded as continuous-valued, and constraint $\overline{C}_{13} : C_u \geqslant 0, \forall u \in \mathcal{U}$ is included. Constraint $\overline{C}_{14} : C_u \leqslant \chi_u \sum_{j\in\mathcal{J}} \kappa_j R_j, \forall u \in \mathcal{U}$, is included in order to enforce consistency with admission control, i.e., $C_u = 0$ in two possible cases: when the common rate is zero or when referring to non-admitted UEs. Also, constraint $\overline{C}_{15} : \sum_u C_u = \sum_{j\in\mathcal{J}} \kappa_j R_j$ is added in order to guarantee that the sum of all C_u is equal to the overall common rate. To enforce a minimum rate R_{min} for each admitted UE, constraint $\overline{C}_{16} : \sum_{j\in\mathcal{J}} \alpha_{u,j} R_j + C_u \geqslant R_{min}\chi_u$ is included.

Problem formulation

Two objectives are considered, namely WSR and WEE maximization. Thus, the optimization problems are $\mathcal{P}'_{DWSR}$ and $\mathcal{P}'_{DWEE}$, which are defined as follows

$$
\begin{aligned}
\mathcal{P}'_{DWSR} : \mathcal{P}'_{DWEE} : \max_{\mathbf{W},\mathbf{m},\mathbf{c},\boldsymbol{\chi},\boldsymbol{\mu},\boldsymbol{\alpha},\boldsymbol{\kappa},\psi} \quad & \begin{cases} f_{DWSR}(\mathbf{c},\boldsymbol{\alpha}) & \text{(linear)} \\ f_{DWEE}(\mathbf{W},\mathbf{m},\mathbf{c},\boldsymbol{\mu},\boldsymbol{\alpha},\psi) & \text{(nonconvex)} \end{cases} \\
\text{s.t.} \quad & \overline{C}_1 : \chi_u \in \{0,1\}, \forall u \in \mathcal{U}, && \text{(binary)} \\
& \overline{C}_2 : \sum_{u\in\mathcal{U}} \chi_u = K, && \text{(linear)} \\
& \overline{C}_3 : \mu_u \in \{0,1\}, \forall u \in \mathcal{U}, && \text{(binary)} \\
& \overline{C}_4 : \mu_u \leqslant \chi_u, \forall u \in \mathcal{U}, && \text{(linear)} \\
& \overline{C}_5 : \psi \in \{0,1\}, && \text{(binary)} \\
& \overline{C}_6 : \sum_{u\in\mathcal{U}} \|\mathbf{w}_u\mu_u\|_2^2 + \|\mathbf{m}\psi\|_2^2 \leqslant P_{tx}^{max}, && \text{(nonconvex)} \\
& \overline{C}_7 : \alpha_{u,j} \in \{0,1\}, \forall u \in \mathcal{U}, j \in \mathcal{J}, && \text{(binary)} \\
& \overline{C}_8 : \sum_{j\in\mathcal{J}} \alpha_{u,j} = \mu_u, \forall u \in \mathcal{U}, && \text{(linear)} \\
& \overline{C}_9 : SINR_u^{(p)} \geqslant \sum_{j\in\mathcal{J}} \alpha_{u,j}\Gamma_j, \forall u \in \mathcal{U}, && \text{(nonconvex)} \\
& \overline{C}_{10} : \kappa_j \in \{0,1\}, \forall j \in \mathcal{J}, && \text{(binary)} \\
& \overline{C}_{11} : \sum_{j\in\mathcal{J}} \kappa_j = \psi, && \text{(linear)} \\
& \overline{C}_{12} : SINR_u^{(c)} \geqslant \chi_u \sum_{j\in\mathcal{J}} \kappa_j\Gamma_j, \forall u \in \mathcal{U}, && \text{(nonconvex)} \\
& \overline{C}_{13} : C_u \geqslant 0, \forall u \in \mathcal{U}, && \text{(linear)} \\
& \overline{C}_{14} : C_u \leqslant \chi_u \sum_{j\in\mathcal{J}} \kappa_j R_j, \forall u \in \mathcal{U}, && \text{(nonconvex)} \\
& \overline{C}_{15} : \sum_{u\in\mathcal{U}} C_u = \sum_{j\in\mathcal{J}} \kappa_j R_j, && \text{(linear)} \\
& \overline{C}_{16} : \sum_{j\in\mathcal{J}} \alpha_{u,j} R_j + C_u \geqslant R_{min}\chi_u, \forall u \in \mathcal{U}, && \text{(linear)}
\end{aligned}
$$

where the objectives are $f_{DWSR}(\mathbf{c},\boldsymbol{\alpha}) \triangleq \sum_{u\in\mathcal{U}} \omega_u \Big(\sum_{j\in\mathcal{J}} \alpha_{u,j} R_j + C_u \Big)$ and $f_{DWEE}(\mathbf{W},\mathbf{m},\mathbf{c},\boldsymbol{\mu},\boldsymbol{\alpha},\psi) \triangleq \frac{\sum_{u\in\mathcal{U}} \omega_u \left(\sum_{j\in\mathcal{J}} \alpha_{u,j} R_j + C_u\right)}{\frac{1}{\eta_{eff}}\left(\sum_{u\in\mathcal{U}} \|\mathbf{w}_u \mu_u\|_2^2 + \|\mathbf{m}\psi\|_2^2\right) + P_{cir}}$. Here, ω_u is the weight assigned to UE_u, which may be adjusted by the network operator. Besides, $\mathbf{W} = [\mathbf{w}_1,\ldots,\mathbf{w}_U]$, $\mathbf{c} = [C_1,\ldots,C_U]$, $\boldsymbol{\chi} = [\chi_1,\ldots,\chi_U]$, $\boldsymbol{\mu} = [\mu_1,\ldots,\mu_U]$, $\boldsymbol{\alpha} = [\alpha_{1,1},\ldots,\alpha_{U,J}]$, and $\boldsymbol{\kappa} = [\kappa_1,\ldots,\kappa_J]$. Parameter η_{eff} is the amplifier efficiency and $P_{cir} = N_{tx}P_{dyn} + P_{sta}$ is the power consumed by the circuitry at the BS. P_{dyn} and P_{sta} denote the dynamic and static parts of the power, respectively [162].

The continuous-rate counterparts of $\mathcal{P}'_{DWSR}$ and $\mathcal{P}'_{DWEE}$ are $\mathcal{Q}'_{CWSR}$ and $\mathcal{Q}'_{CWEE}$, which are defined as follows,

$$
\begin{aligned}
\mathcal{Q}'_{CWSR}: \max_{\mathbf{W},\mathbf{m},\mathbf{c},\boldsymbol{\chi},\psi} \quad & \begin{cases} f'_{CWSR}(\mathbf{W},\mathbf{m},\mathbf{c}) \triangleq \sum_{u\in\mathcal{U}} \omega_u \left(\log_2\left(1+\mathrm{SINR}_u^{(p)}\right) + C_u\right) & \text{(nonconvex)} \\ f'_{CWEE}(\mathbf{W},\mathbf{m},\mathbf{c}) \triangleq \frac{\sum_{u\in\mathcal{U}} \omega_u \left(\log_2\left(1+\mathrm{SINR}_u^{(p)}\right)+C_u\right)}{\frac{1}{\eta_{eff}}\left(\sum_{u\in\mathcal{U}} \|\mathbf{w}_u\chi_u\|_2^2 + \|\mathbf{m}\psi\|_2^2\right)+P_{cir}} & \text{(nonconvex)} \end{cases} \\
\text{s.t.} \quad & \overline{C}_1: \chi_u \in \{0,1\}, \forall u \in \mathcal{U}, & \text{(binary)} \\
& \overline{C}_2: \sum_{u\in\mathcal{U}} \chi_u = K, & \text{(linear)} \\
& \overline{C}_5: \psi \in \{0,1\}, & \text{(binary)} \\
& \overline{C}_6: \sum_{u\in\mathcal{U}} \|\mathbf{w}_u\chi_u\|_2^2 + \|\mathbf{m}\psi\|_2^2 \leqslant P_{tx}^{max}, & \text{(nonconvex)} \\
& \overline{C}_{13}: C_u \geqslant 0, \forall u \in \mathcal{U}, & \text{(linear)} \\
& \overline{C}_{17}: C_u \leqslant \psi\chi_u S_{max}, \forall u \in \mathcal{U}, & \text{(linear)} \\
& \overline{C}_{18}: \sum_{i\in\mathcal{U}} C_i \leqslant \log_2\left(1+\mathrm{SINR}_u^{(c)}\right) + (1-\chi_u)S_{max}, \forall u \in \mathcal{U}, & \text{(nonconvex)} \\
& \overline{C}_{19}: \log_2\left(1+\mathrm{SINR}_u^{(p)}\right) + C_u \geqslant R_{min}\chi_u, \forall u \in \mathcal{U}. & \text{(nonconvex)}
\end{aligned}
$$

To account for continuous rates, the following changes have been applied to problems $\mathcal{P}'_{DWSR}$ and $\mathcal{P}'_{DWEE}$. The binary variables $\boldsymbol{\alpha},\boldsymbol{\kappa}$ used for discrete rate selection have been eliminated. Also, the number of binary variables has been reduced by dropping variables $\boldsymbol{\mu}$ to only use $\boldsymbol{\chi}$, because $\boldsymbol{\mu} = \boldsymbol{\chi}$. Hence, constraints $\overline{C}_3, \overline{C}_4, \overline{C}_7 - \overline{C}_{12}$ have been removed allowing to employ Shannon capacity to redefine constraints $\overline{C}_{14}, \overline{C}_{15}, \overline{C}_{16}$. Specifically, constraint $\overline{C}_{14}$ was replaced with $\overline{C}_{17}: C_u \leqslant \psi\chi_u S_{max}, \forall u \in \mathcal{U}$, and constraint $\overline{C}_{15}$ with $\overline{C}_{18}: \sum_{i\in\mathcal{U}} C_i \leqslant \log_2\left(1+\mathrm{SINR}_u^{(c)}\right) + (1-\chi_u)S_{max}, \forall u \in \mathcal{U}$, where $S_{max} = \max_{u\in\mathcal{U}} \log_2\left(1 + \frac{P_{tx}^{max}}{\sigma^2}\|\mathbf{h}_u\|_2^2\right)$ is an upper bound for the common rate. Finally, constraint $\overline{C}_{16}$ was replaced with $\overline{C}_{19}: \log_2\left(1+\mathrm{SINR}_u^{(p)}\right) + C_u \geqslant R_{min}\chi_u, \forall u \in \mathcal{U}$, and the objective functions were redefined using Shannon capacity as $f'_{CWSR}(\mathbf{W},\mathbf{m},\mathbf{c}) \triangleq \sum_{u\in\mathcal{U}} \omega_u \left(\log_2\left(1+\mathrm{SINR}_u^{(p)}\right) + C_u\right)$ and $f'_{CWEE}(\mathbf{W},\mathbf{m},\mathbf{c}) \triangleq \frac{\sum_{u\in\mathcal{U}} \omega_u \left(\log_2\left(1+\mathrm{SINR}_u^{(p)}\right)+C_u\right)}{\frac{1}{\eta_{eff}}\left(\sum_{u\in\mathcal{U}} \|\mathbf{w}_u\chi_u\|_2^2 + \|\mathbf{m}\psi\|_2^2\right)+P_{cir}}$.

Note: *For details on the proposed algorithms to solve* $\mathcal{P}'_{\text{DWSR}}$, $\mathcal{P}'_{\text{DWEE}}$, $\mathcal{Q}'_{\text{CWSR}}$, *and* $\mathcal{Q}'_{\text{CWEE}}$ *the reader is referred to [H], which can also be found in Appendix H.*

9.6 SELECTED RESULTS

Figure 16 is taken from [H], but the layout has been slightly modified.

In the following, simulation results of a specific scenario in [H] are discussed. Figure 16 shows the SE achieved by the proposed algorithm `OPT-MISOCP` considering discrete rates. The proposed algorithm was used for both SDMA and RSMA since the latter is a more general case than the former, which occurs when $\psi = 0$. In addition, the performance of dirty paper coding (DPC) with continuous rates is included as a benchmark for reference.

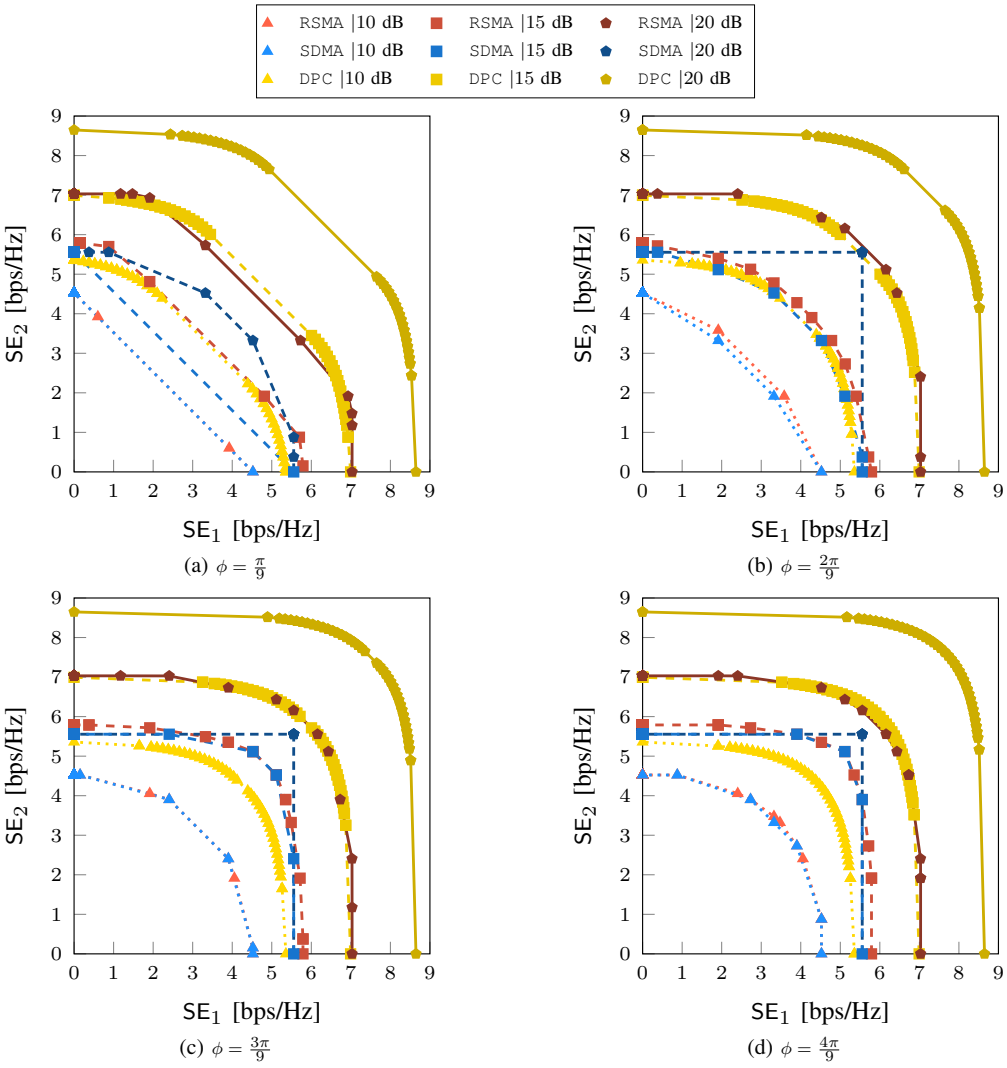

Figure 16: Rate performance of RSMA and SDMA with discrete rates.

Figure 16 shows four scenarios, where $N_{tx} = 4$ and $K = 2$. The noise power is set to $\sigma^2 = 30$ dBm and the UE channels are defined as $\mathbf{h}_1 = [1, 1, 1, 1]^H$, $\mathbf{h}_2 = \left[1, e^{j\phi}, e^{j2\phi}, e^{j3\phi}\right]^H$, where $\phi = \left\{\frac{\pi}{9}, \frac{2\pi}{9}, \frac{3\pi}{9}, \frac{4\pi}{9}\right\}$ varies the similarity between channels $\mathbf{h}_1$ and $\mathbf{h}_2$. Specifically, a small value, such as $\theta = \frac{\pi}{9}$ makes the channels highly correlated (nearly parallel) while a large value, such as $\theta = \frac{4\pi}{9}$ makes the channels highly uncorrelated (nearly orthogonal).

In the legend, different colors are used to depict the performance for several SINR values, i.e., $\frac{P_{tx}^{max}}{\sigma^2} = \{10, 15, 20\}$. It is observed that RSMA and SDMA have almost the same performance when $\frac{P_{tx}^{max}}{\sigma^2} = 10$ dB, for all $\phi = \left\{\frac{\pi}{9}, \frac{2\pi}{9}, \frac{3\pi}{9}, \frac{4\pi}{9}\right\}$. When $\frac{P_{tx}^{max}}{\sigma^2} = 15$ dB, the performance of both RSMA and SDMA is very similar when the channels are sufficiently uncorrelated, i.e., $\phi = \left\{\frac{2\pi}{9}, \frac{3\pi}{9}, \frac{4\pi}{9}\right\}$. However, RSMA outperforms SDMA more evidently when $\frac{P_{tx}^{max}}{\sigma^2} = 20$ dB, for all $\phi = \left\{\frac{\pi}{9}, \frac{2\pi}{9}, \frac{3\pi}{9}, \frac{4\pi}{9}\right\}$. Specifically, SDMA saturates as it is allocated the maximum rate $R_{15} = 5.5547$ bps/Hz, while RSMA can still improve since it can use any surplus power to support a common signal albeit with a small rate.

10

CONCLUSIONS

This thesis contributes to the modeling and design for the efficient management of radio resources in millimeter-wave wireless networks, leading to multiple algorithms formulated as optimization problems. The motifs and scenarios investigated herein are diverse, e.g., maximization of sum rate (SR), weighted sum rate (WSR), weighted energy efficiency (WEE), and fairness or minimization of transmit power, which were studied in settings such as Industry 4.0 and integrated access-backhaul (IAB).

Chapter 2, Chapter 3, Chapter 4, and Chapter 5 focused on the design of hybrid precoding for three types of multiple access schemes: space-division multiple access (SDMA), layered-division multiple access (LDMA), and rate-splitting multiple access (RSMA). These chapters showed that hybrid precoding is more constrained than fully-digital precoding and generally has lower performance due to having a reduced number of radiofrequency (RF) chains, limiting its capability to cope with interference. However, by properly accounting for the limitations of the architecture, performance close to fully-digital precoders can be obtained for specific cases.

Chapter 2 investigated the hybrid precoder design for single-group multicasting in a wireless system based on SDMA. Specifically, a low-complexity algorithm based on gradient descent was proposed, which proved to be capable of realizing high-performance hybrid precoders.

Chapter 3 investigated the hybrid precoder design for multi-group multicasting in a wireless system based on SDMA. An algorithm based on semidefinite relaxation (SDR), alternating optimization (AO), and Cholesky matrix decomposition (CMD) was proposed, showing remarkable flexibility and capability to perform properly despite the limitations of analog phase shifting.

Chapter 4 investigated the hybrid precoder design for non-orthogonal unicast and multicast (NOUM) transmissions in an industrial setting based on LDMA. An algorithm was proposed based on successive convex approximation (SCA) and AO, exhibiting improved performance compared to the considered benchmarks.

Chapter 5 investigated the hybrid precoder design for NOUM transmissions in a wireless system based on RSMA. Notably, an algorithm was proposed based on SCA and SDR, exhibiting substantial performance compared to the state-of-the-art in terms of optimality, convergence, and feasibility performance.

Chapter 6 and Chapter 7 focused on the design of precoding and admission control for two types of multiple access schemes: SDMA and LDMA. Chapter 6 dealt with hybrid precoding whereas Chapter 7 dealt with fully-digital precoding. These chapters showed that admission control is crucial in improving the communications quality and in securing quality-of-service (QoS) requirements for the admitted user equipments (UEs). In particular, failing to account for admission control may result in low rates or fairness, and in infeasible solutions, e.g., due to high QoS requirements, limited transmit power or reduced number of RF chains.

Chapter 6 investigated the design of hybrid precoding and admission control for multi-group multicasting in an industrial setting based on SDMA, where multiple groups of industrial IoT (IIoT) devices were serviced. An algorithm was proposed, which divided the investigated problem into two subproblems: admission control and hybrid precoding. The admission control was formulated as an integer linear program (ILP), whereas the hybrid precoding relied on AO and SDR. It was shown that it is possible to reduce transmission latency by controlling which devices are served since lower interference can be achieved depending on the selection, thus allowing for higher data rates.

Chapter 7 investigated the design of fully-digital precoding and admission control for NOUM transmission in an industrial setting based on LDMA. Similarly to Chapter 6, an algorithm was proposed that decouples the investigated problem into two subproblems, i.e., admission control and precoding. The admission control was formulated as an ILP, whereas SCA was employed for the precoding design. This chapter showed that LDMA outperforms SDMA combined with time-division multiple access (TDMA) or frequency-division multiple access (FDMA), where the latter was employed to schedule unicast and multicast traffic in orthogonal time/frequency resources. In addition, it was shown that admission control is crucial as it allows to select and serve UEs that can mutually benefit when served together.

Chapter 8 and Chapter 9 focused on the design of precoding, admission control, and discrete-rate allocation for two types of multiple access schemes: SDMA and RSMA. Additionally, Chapter 8 included UE association, allowing multiple small base stations (SBSs) to collaboratively serve the admitted UEs, whereas Chapter 9 instead considered imperfect successive interference cancellation (SIC) arising

due to hardware imperfections. These chapters showed the importance of accounting for practical characteristics of wireless systems that can substantially affect their performance.

Chapter 8 investigated the design of precoding, admission control, UE association, and discrete-rate allocation at the access network and the design of precoding and discrete-rate allocation at the backhaul network in an IAB system based on SDMA. Three algorithms with different degrees of computational complexity were proposed to solve the formulated problem. The first algorithm was based on the convexification of nonconvex mixed-integer nonlinear programs (MINLPs), and the second and third algorithms were based on the penalty method and minorization-maximization (MM). Due to the interdependency of backhaul and radio access networks, devising effective and practical solutions for IAB is generally challenging. However, this chapter demonstrated how to cope with this complexity through several system design options and mathematical formulation and optimization of the radio resources.

Chapter 9 investigated the design of precoding, admission control, and discrete- or continuous-rate allocation assuming imperfect SIC in a wireless system based on RSMA. Two algorithms were proposed to solve the formulated problems. The algorithm for discrete rates was based on the convexification of nonconvex MINLPs, whereas the algorithm for continuous rates was based on binary enumeration, SDR, and SCA. This chapter shared insights for the first time on the impact of how practical characteristics such as imperfect SIC, UE admission, and discrete rates can impact the performance of RSMA. Not accounting for these characteristics can result in misleading results concerning the advantages of RSMA over SDMA.

In beyond 5G (B5G), in addition to millimeter-wave, the terahertz spectrum is expected to become part of the radio resource realm. While the proposed algorithms have been developed for millimeter-wave wireless networks, they are not limited to this spectrum. For instance, the hybrid precoder designs investigated in Chapter 2, Chapter 3, Chapter 4, Chapter 5, and Chapter 6 could be used in the terahertz spectrum as it is expected that the first terahertz base stations (BSs) will have hybrid architectures since fully-digital precoders will be too expensive to afford. Also, the algorithms developed in this thesis can be extended to support novel use cases with emerging technologies, such as integrated sensing and communications, non-terrestrial infrastructure, and reflecting intelligent surfaces.

Chapter 6, Chapter 7, Chapter 8, and Chapter 9 investigated UE admission control and showed its importance in dictating the performance of a wireless system. Admission control in these chapters focused on determining whether a UE should be admitted or not.

The admitted UEs would be multiplexed in the spatial domain and served for several slots. The process would then be repeated with the remaining UEs until all UEs were served. The investigated problems in these chapters can be generalized by including the time domain in the admission control, thus determining from the beginning the subset of UEs to be served in each slot without the need to perform the admission control sequentially with the remaining UEs. It is expected that this method would lead to improved performance.

BIBLIOGRAPHY

[A] L. F. Abanto-Leon and G. H. Sim. "Learning-based Max-Min Fair Hybrid Precoding for mmWave Multicasting." In: *Proceedings of the IEEE International Conference on Communications (IEEE ICC)*. 2020, pp. 1–7.

[B] L. F. Abanto-Leon, M. Hollick, and G. H. Sim. "Hybrid Precoding for Multi-Group Multicasting in mmWave Systems." In: *Proceedings of the IEEE Global Communications Conference (IEEE GLOBECOM)*. 2019, pp. 1–7.

[C] L. F. Abanto-Leon and G. H. Sim. "Fairness-Aware Hybrid Precoding for mmWave NOMA Unicast/Multicast Transmissions in Industrial IoT." In: *Proceedings of the IEEE International Conference on Communications (IEEE ICC)*. 2020, pp. 1–7.

[D] L. F. Abanto-Leon, M. Hollick, Bruno Clerckx, and G. H. Sim. "Sequential Parametric Optimization for Rate-Splitting Precoding in Non-Orthogonal Unicast and Multicast Transmissions." In: *Proceedings of the IEEE International Conference on Communications (IEEE ICC)*. 2022, pp. 3904–3910.

[E] L. F. Abanto-Leon, M. Hollick, and G. H. Sim. "HydraWave: Multi-group Multicast Hybrid Precoding and Low-Latency Scheduling for Ubiquitous Industry 4.0 mmWave Communications." In: *Proceedings of the IEEE International Symposium on A World of Wireless, Mobile and Multimedia Networks (IEEE WoWMoM)*. 2020, pp. 98–107.

[F] L. F. Abanto-Leon, M. Hollick, and G. H. Sim. "BeamWave: Cross-layer Beamforming and Scheduling for Superimposed Transmissions in Industrial IoT mmWave Networks." In: *Proceedings of the International Symposium on Modeling and Optimization in Mobile, Ad hoc, and Wireless Networks (WiOpt)*. 2021, pp. 1–8.

[G] L. F. Abanto-Leon, A. Asadi, A. Garcia-Saavedra, G. H. Sim, and M. Hollick. "RadiOrchestra: Proactive Management of Millimeter-wave Self-backhauled Small Cells via Joint Optimization of Beamforming, User Association, Rate Selection, and Admission Control." In: *IEEE Transactions on Wireless Communications* 22.1 (2022), pp. 153–173.

[H] L. F. Abanto-Leon, A. Krishnamoorthy, G. H. Sim, A. Garcia-Saavedra, R. Schober, and M. Hollick. "Radio Resource Management Design for RSMA: Optimization of Beamforming, User

Admission, and Discrete/Continuous Rates with Imperfect SIC." In: *IEEE Transactions on Mobile Computing (Under Review)* (2023).

[1] P. Cheng, Z. Chen, M. Ding, Y. Li, B. Vucetic, and D. Niyato. "Spectrum Intelligent Radio: Technology, Development, and Future Trends." In: *IEEE Communications Magazine* 58.1 (2020), pp. 12–18.

[2] Y. Li, E. Pateromichelakis, B. Vucic, J. Luo, W. Xu, and G. Caire. "Radio Resource Management Considerations for 5G Millimeter Wave Backhaul and Access Networks." In: *IEEE Communications Magazine* 55.6 (2017), pp. 86–92.

[3] Q.-Y. Yu, H.-C. Lin, and H.-H. Chen. "Intelligent Radio for Next Generation Wireless Communications: An Overview." In: *IEEE Wireless Communications* 26.4 (2019), pp. 94–101.

[4] L. P. Petak. "Planning in Support of Spectrum Management." In: *Proceedings of the IEEE Vehicular Technology Conference (IEEE VTC)*. Vol. 32. 1982, pp. 124–128.

[5] M.F.A. Ibrahim. "Radio Planning tools for Mobile Radio Services." In: *Proceedings of the IEE Colloquium on Terrestrial Radio Spectrum Management Tools*. Vol. 9. 1988, pp. 1–4.

[6] H. Zhang, N. Liu, X. Chu, K. Long, A.-H. Aghvami, and V. C. M. Leung. "Network Slicing Based 5G and Future Mobile Networks: Mobility, Resource Management, and Challenges." In: *IEEE Communications Magazine* 55.8 (2017), pp. 138–145.

[7] S. Sun, Q. Gao, Y. Peng, Y. Wang, and L. Song. "Interference Management through CoMP in 3GPP LTE-Advanced Networks." In: *IEEE Wireless Communications* 20.1 (2013), pp. 59–66.

[8] C. Yang, S. Han, X. Hou, and A. F. Molisch. "How Do We Design CoMP to Achieve its Promised Potential?" In: *IEEE Wireless Communications* 20.1 (2013), pp. 67–74.

[9] D. Lee, H. Seo, B. Clerckx, E. Hardouin, D. Mazzarese, S. Nagata, and K. Sayana. "Coordinated Multipoint Transmission and Reception in LTE-Advanced: Deployment Scenarios and Operational Challenges." In: *IEEE Communications Magazine* 50.2 (2012), pp. 148–155.

[10] M. Cudak, A. Ghosh, A. Ghosh, and J. Andrews. "Integrated Access and Backhaul: A Key Enabler for 5G Millimeter-Wave Deployments." In: *IEEE Communications Magazine* 59.4 (2021), pp. 88–94.

[11] G. Y. Suk, S.-M. Kim, J. Kwak, S. Hur, E. Kim, and C.-B. Chae. "Full Duplex Integrated Access and Backhaul for 5G NR: Analyses and Prototype Measurements." In: *IEEE Wireless Communications* 29.4 (2022), pp. 40–46.

[12] Y. Sadovaya, D. Moltchanov, W. Mao, O. Orhan, S.-P. Yeh, H. Nikopour, S. Talwar, and S. Andreev. "Integrated Access and Backhaul in Millimeter-Wave Cellular: Benefits and Challenges." In: *IEEE Communications Magazine* 60.9 (2022), pp. 81–86.

[13] Z. Lin, X. Du, H.-H. Chen, B. Ai, Z. Chen, and D. Wu. "Millimeter-Wave Propagation Modeling and Measurements for 5G Mobile Networks." In: *IEEE Wireless Communications* 26.1 (2019), pp. 72–77.

[14] J. Zhang, X. Ge, Q. Li, M. Guizani, and Y. Zhang. "5G Millimeter-Wave Antenna Array: Design and Challenges." In: *IEEE Wireless Communications* 24.2 (2017), pp. 106–112.

[15] C. Liu, M. Li, S. V. Hanly, P. Whiting, and I. B. Collings. "Millimeter-Wave Small Cells: Base Station Discovery, Beam Alignment, and System Design Challenges." In: *IEEE Wireless Communications* 25.4 (2018), pp. 40–46.

[16] H. Yan, S Ramesh, T. Gallagher, C. Ling, and D. Cabric. "Performance, Power, and Area Design Trade-Offs in Millimeter-Wave Transmitter Beamforming Architectures." In: *IEEE Circuits and Systems Magazine* 19.2 (2019), pp. 33–58.

[17] M. Li, Z. Wang, H. Li, Q. Liu, and L. Zhou. "A Hardware-Efficient Hybrid Beamforming Solution for mmWave MIMO Systems." In: *IEEE Wireless Communications* 26.1 (2019), pp. 137–143.

[18] J. Wang, X. Zhang, X. Shi, and J. Song. "Higher Spectral Efficiency for mmWave MIMO: Enabling Techniques and Precoder Designs." In: *IEEE Communications Magazine* 59.4 (2021), pp. 116–122.

[19] J. Li, D. Della Penda, H. Sahlin, P. Schliwa-Bertling, M. Folke, and M. Stattin. "An Overview of 5G System Accessibility Differentiation and Control." In: *IEEE Communications Standards Magazine* 5.4 (2021), pp. 104–111.

[20] H. Baligh, M. Hong, W.-C. Liao, Z.-Q. Luo, M. Razaviyayn, M. Sanjabi, and R. Sun. "Cross-Layer Provision of Future Cellular Networks: A WMMSE-based Approach." In: *IEEE Signal Processing Magazine* 31.6 (2014), pp. 56–68.

[21] Y. Ai, G. Qiu, C. Liu, and Y. Sun. "Joint Resource Allocation and Admission Control in Sliced Fog Radio Access Networks." In: *China Communications* 17.8 (2020), pp. 14–30.

[22] 3GPP. *5G; NR; Physical Layer Procedures for Data*. Technical Specification (TS) 38.214. Version 16.2.0. 3rd Generation Partnership Project (3GPP), 2020.

[23] L. Zhang et al. “Layered-Division-Multiplexing for High Spectrum Efficiency and Service Flexibility in Next Generation ATSC 3.0 Broadcast System.” In: *IEEE Wireless Communications* 26.2 (2019), pp. 116–123.

[24] L. Zhang et al. “Layered-Division Multiplexing: An Enabling Technology for Multicast/Broadcast Service Delivery in 5G.” In: *IEEE Communications Magazine* 56.3 (2018), pp. 82–90.

[25] B. Clerckx, H. Joudeh, C. Hao, M. Dai, and B. Rassouli. “Rate Splitting for MIMO Wireless Networks: A Promising PHY-layer Strategy for LTE Evolution.” In: *IEEE Communications Magazine* 54.5 (2016), pp. 98–105.

[26] A. S. de Sena, P. H. J. Nardelli, D. B. da Costa, P. Popovski, and C. B. Papadias. “Rate-Splitting Multiple Access and Its Interplay with Intelligent Reflecting Surfaces.” In: *IEEE Communications Magazine* 60.7 (2022), pp. 52–57.

[27] *Rate Splitting Multiple Access (RSMA) for Multi-User MIMO - Enhancement of Unicast and Joint Unicast/Multicast Delivery*. RWS-230044. 3GPP TSG RAN Rel-19. BBC, 2023.

[28] Z. Xiang, X. Tong, and Y. Cai. “Secure Transmission for NOMA Systems with Imperfect SIC.” In: *China Communications* 17.11 (2020), pp. 67–78.

[29] Y. Zhang, H. Cao, M. Zhou, and L. Yang. “Non-Orthogonal Multiple Access in Cell-Free Massive MIMO Networks.” In: *China Communications* 17.8 (2020), pp. 81–94.

[30] A. Biason and M. Zorzi. “Multicast via Point to Multipoint Transmissions in Directional 5G mmWave Communications.” In: *IEEE Communications Magazine* 57.2 (2019), pp. 88–94.

[31] N. D. Sidiropoulos, T. N. Davidson, and Z. Luo. “Transmit Beamforming for Physical-Layer Multicasting.” In: *IEEE Transactions on Signal Processing* 54.6 (2006), pp. 2239–2251.

[32] L. Liu, Y. Wang, C. Hua, and J. Jian. “A Learning Approach for Efficient Multicast Beamforming Based on Determinantal Point Process.” In: *IEEE Transactions on Wireless Communications* 21.9 (2022), pp. 7427–7442.

[33] B. Du, C. Pan, W. Zhang, M. Chen, and H. Lan. “Beamforming for Single Group Multicast Systems to Maximize the Access Rate.” In: *Proceedings of the International Conference on Wireless Communications and Signal Processing (WCSP)*. 2013, pp. 1–6.

[34] R. Jiang, H. Liu, and A. M.-C. So. “LPA-SD: An Efficient First-Order Method for Single-Group Multicast Beamforming.” In: *Proceedings of the IEEE International Workshop on Signal Processing Advances in Wireless Communications (IEEE SPAWC)*. 2018, pp. 1–5.

[35] H. Liu, P. Wang, and A. M.-C. So. "Fast First-order Methods for the Massive Robust Multicast Beamforming Problem with Interference Temperature Constraints." In: *Proceedings of the IEEE International Conference on Acoustics, Speech and Signal Processing (IEEE ICASSP)*. 2019, pp. 4744–4748.

[36] Q. Li, Y. Liu, M. Shao, and W.-K. Ma. "Proximal Distance Algorithm for Nonconvex QCQP with Beamforming Applications." In: *Proceedings of the IEEE International Conference on Acoustics, Speech and Signal Processing (IEEE ICASSP)*. 2020, pp. 5155–5159.

[37] L. Zhou, X. Zhou, J. Chen, W. Jiang, and W. Luo. "Fast Proximal Gradient Algorithm for Single-Group Multicast Beamforming." In: *Proceedings of the International Conference on Wireless Communications & Signal Processing (WCSP)*. 2016, pp. 1–5.

[38] S. Takabe and T. Wadayama. "Deep Unfolded Multicast Beamforming." In: *Proceedings of the IEEE Global Communications Conference (IEEE GLOBECOM)*. 2020, pp. 1–6.

[39] Z. Zhang and M. Tao. "A Learning Based Branch-and-Bound Algorithm for Single-Group Multicast Beamforming." In: *Proceedings of the IEEE Global Communications Conference (IEEE GLOBECOM)*. 2021, pp. 1–6.

[40] G. H. Sim and J. Widmer. "Finite Horizon Opportunistic Multicast Beamforming." In: *IEEE Transactions on Wireless Communications* 16.3 (2017), pp. 1452–1465.

[41] D. Taleb, Y. Liu, and M. Pesavento. "Full-rate General Rank Beamforming in Single-Group Multicasting Networks Using Non-orthogonal STBC." In: *Proceedings of the European Signal Processing Conference (EUSIPCO)*. 2016, pp. 2365–2369.

[42] J. Fink, R. L. G. Cavalcante, and S. Stanczak. "Multicast Beamforming Using Semidefinite Relaxation and Bounded Perturbation Resilience." In: *Proceedings of the IEEE International Conference on Acoustics, Speech and Signal Processing (IEEE ICASSP)*. 2019, pp. 4749–4753.

[43] D. Taleb and M. Pesavento. "Rank Regularized Beamforming in Single Group Multicasting Networks." In: *Proceedings of the IEEE Sensor Array and Multichannel Signal Processing Workshop (IEEE SAM)*. 2020, pp. 1–5.

[44] D. Taleb and M. Pesavento. "General Rank Beamforming Using Full Rate Real-Value OSTBC for Multicasting Networks." In: *Proceedings of the International ITG Workshop on Smart Antennas (WSA)*. 2020, pp. 1–5.

[45] X. Wen, K. L. Law, S. J. Alabed, and M. Pesavento. "Rank-Two Beamforming for Single-Group Multicasting Networks Using OSTBC." In: *Proceedings of the IEEE Sensor Array and Multichannel Signal Processing Workshop (IEEE SAM)*. 2012, pp. 69–72.

[46] S. X. Wu, A. M.-C. So, and W.-K. Ma. "Rank-Two Transmit Beamformed Alamouti Space-Time Coding for Physical-Layer Multicasting." In: *Proceedings of the IEEE International Conference on Acoustics, Speech and Signal Processing (IEEE ICASSP)*. 2012, pp. 2793–2796.

[47] B. Liu, L. Shi, and X.-G. Xia. "Robust Rank-Two Multicast Beamforming Under a Unified CSI Uncertainty Model." In: *IEEE Signal Processing Letters* 23.10 (2016), pp. 1419–1423.

[48] A. Schad, K. L. Law, and M. Pesavento. "A Convex Inner Approximation Technique for Rank-Two Beamforming in Multicasting Relay Networks." In: *Proceedings of the European Signal Processing Conference (EUSIPCO)*. 2012, pp. 1369–1373.

[49] Shuying Shi, M. Schubert, and H. Boche. "Physical Layer Multicasting with Linear MIMO Transceivers." In: *Proceedings of the Annual Conference on Information Sciences and Systems (CISS)*. 2008, pp. 884–889.

[50] S. Fan and J. Xu. "Single-Group Multicast Secure Beamforming via Learning the Eavesdropper's Channel Correlation." In: *Proceedings of the IEEE International Conference on Communications (IEEE ICC)*. 2020, pp. 1–6.

[51] S. Fan, J. Xu, J. Xue, and Y. Zhang. "One-Bit Statistical ECSI Learning for Single-Group Multicast Secure Beamforming." In: *IEEE Communications Letters* 26.11 (2022), pp. 2552–2556.

[52] B. Zhu, J. Ge, Y. Huang, Y. Yang, and M. Lin. "Rank-Two Beamformed Secure Multicasting for Wireless Information and Power Transfer." In: *IEEE Signal Processing Letters* 21.2 (2014), pp. 199–203.

[53] C. Lu and Y.-F. Liu. "An Efficient Global Algorithm for Single-Group Multicast Beamforming." In: *IEEE Transactions on Signal Processing* 65.14 (2017), pp. 3761–3774.

[54] L. Tran, M. F. Hanif, and M. Juntti. "A Conic Quadratic Programming Approach to Physical Layer Multicasting for Large-Scale Antenna Arrays." In: *IEEE Signal Processing Letters* 21.1 (2014), pp. 114–117.

[55] B. Gopalakrishnan and N. D. Sidiropoulos. "High Performance Adaptive Algorithms for Single-Group Multicast Beamforming." In: *IEEE Transactions on Signal Processing* 63.16 (2015), pp. 4373–4384.

[56] R. Hunger, D. A. Schmidt, M. Joham, A. Schwing, and W. Utschick. "Design of Single-Group Multicasting-Beamformers." In: *Proceedings of the IEEE International Conference on Communications (IEEE ICC)*. 2007, pp. 2499–2505.

[57] B. Du, M. Chen, W. Zhang, and C. Pan. "Optimal Beamforming for Single Group Multicast Systems based on Weighted Sum Rate." In: *Proceedings of the IEEE International Conference on Communications (IEEE ICC)*. 2013, pp. 4921–4925.

[58] J. Jian, L. Liu, C. Hua, Y. Wang, and M. Wang. "Efficient Single-Group Multicast Beamforming: A Determinantal Point Process Approach." In: *Proceedings of the IEEE International Conference on Space-Air-Ground Computing (IEEE SAGC)*. 2021, pp. 29–35.

[59] J. Choi. "Iterative Methods for Physical-Layer Multicast Beamforming." In: *IEEE Transactions on Wireless Communications* 14.9 (2015), pp. 5185–5196.

[60] Q. Song, S. Zhao, and Q. Shi. "Secure Satellite-Terrestrial Transmission via Hybrid Analog-Digital Beamforming." In: *Proceedings of the International Conference on Wireless Communications and Signal Processing (WCSP)*. 2018, pp. 1–6.

[61] Y. Shi and Y. Huang. "Hybrid Beamforming for Minimum Outage via Stochastic Approximation." In: *Proceedings of the CIE International Conference on Radar (RADAR)*. 2021, pp. 2238–2242.

[62] Z. Li, C. Qi, and G. Y. Li. "Low-Complexity Multicast Beamforming for Millimeter Wave Communications." In: *IEEE Transactions on Vehicular Technology* 69.10 (2020), pp. 12317–12320.

[63] M. Dai and B. Clerckx. "Hybrid Precoding for Physical Layer Multicasting." In: *IEEE Communications Letters* 20.2 (2016), pp. 228–231.

[64] J. Wang, X. Hu, J. Zhu, C. Zhong, and Z. Zhang. "Hybrid Beamforming for MISO Multicasting with Finite-Resolution Phase Shifters." In: *Proceedings of the International Conference on Wireless Communications and Signal Processing (WCSP)*. 2019, pp. 1–5.

[65] Ö. T. Demir and T. E. Tuncer. "Hybrid Beamforming with Two Bit RF Phase Shifters in Single Group Multicasting." In: *Proceedings of the IEEE International Conference on Acoustics, Speech and Signal Processing (IEEE ICASSP)*. 2016, pp. 3271–3275.

[66] W. Ci, C. Qi, G. Y. Li, and S. Mao. "Hybrid Beamforming Design for Covert Multicast mmWave Massive MIMO Communications." In: *Proceedings of the IEEE Global Communications Conference (IEEE GLOBECOM)*. 2021, pp. 1–6.

[67] H. Park, S. Park, T. Song, and S. Pack. "An Incremental Multicast Grouping Scheme for mmWave Networks with Directional Antennas." In: *IEEE Communications Letters* 17.3 (2013), pp. 616–619.

[68] M. Sadeghi, L. Sanguinetti, and C. Yuen. "Hybrid Precoding for Multi-Group Physical Layer Multicasting." In: *Proceedings of the European Wireless Conference*. 2018, pp. 1–6.

[69] Ö. T. Demir and T. E. Tuncer. "Antenna Selection and Hybrid Beamforming for Simultaneous Wireless Information and Power Transfer in Multi-Group Multicasting Systems." In: *IEEE Transactions on Wireless Communications* 15.10 (2016), pp. 6948–6962.

[70] J. Huang, Z. Cheng, E. Chen, and M. Tao. "Low-Complexity Hybrid Analog/Digital Beamforming for Multicast Transmission in mmWave Systems." In: *Proceedings of the IEEE International Conference on Communications (IEEE ICC)*. 2017, pp. 1–6.

[71] E. Karipidis, N. D. Sidiropoulos, and Z.-Q. Luo. "Transmit Beamforming of Multiple Co-Channel Multicast Groups." In: *Proceedings of the IEEE International Workshop on Computational Advances in Multi-Sensor Adaptive Processing (IEEE CAMSAP)*. 2005, pp. 109–112.

[72] Ö. T. Demir and T. E. Tuncer. "Multi-Group Multicast Beamforming for Simultaneous Wireless Information and Power Transfer." In: *Proceedings of the European Signal Processing Conference (EUSIPCO)*. 2015, pp. 1356–1360.

[73] M. Ashraphijuo, X. Wang, and M. Tao. "Multicast Beamforming Design in Multicell Networks With Successive Group Decoding." In: *IEEE Transactions on Wireless Communications* 16.6 (2017), pp. 3492–3506.

[74] N. Bornhorst, M. Pesavento, and A. B. Gershman. "Distributed Beamforming for Multiuser Peer-to-Peer and Multi-group Multicasting Relay Networks." In: *Proceedings of the IEEE International Conference on Acoustics, Speech and Signal Processing (IEEE ICASSP)*. 2011, pp. 1–4.

[75] M. Sadeghi, E. Björnson, E. G. Larsson, C. Yuen, and T. L. Marzetta. "Max-Min Fair Transmit Precoding for Multi-Group Multicasting in Massive MIMO." In: *IEEE Transactions on Wireless Communications* 17.2 (2018), pp. 1358–1373.

[76] E. Karipidis, N. D. Sidiropoulos, and Z.-Q. Luo. "Quality of Service and Max-Min Fair Transmit Beamforming to Multiple Cochannel Multicast Groups." In: *IEEE Transactions on Signal Processing* 56.3 (2008), pp. 1268–1279.

[77] E. Karipidis, N. D. Sidiropoulos, and Z.-Q. Luo. "Far-Field Multicast Beamforming for Uniform Linear Antenna Arrays." In: *IEEE Transactions on Signal Processing* 55.10 (2007), pp. 4916–4927.

[78] Y. C. B. Silva and A. Klein. "Linear Transmit Beamforming Techniques for the Multigroup Multicast Scenario." In: *IEEE Transactions on Vehicular Technology* 58.8 (2009), pp. 4353–4367.

[79] N. Bornhorst and M. Pesavento. "An Iterative Convex Approximation Approach for Transmit Beamforming in Multi-Group Multicasting." In: *Proceedings of the IEEE International Workshop on Signal Processing Advances in Wireless Communications (IEEE SPAWC)*. 2011, pp. 426–430.

[80] A. Schad and M. Pesavento. "Max-min Fair Transmit Beamforming for Multi-Group Multicasting." In: *Proceedings of the International ITG Workshop on Smart Antennas (WSA)*. 2012, pp. 115–118.

[81] A. Gharanjik, M. R. Bhavani Shankar, M. Soltanalian, and B. Ottersten. "Max-Min Transmit Beamforming via Iterative Regularization." In: *Proceedings of the Asilomar Conference on Signals, Systems and Computers*. 2016, pp. 1437–1441.

[82] D. Christopoulos, S. Chatzinotas, and B. Ottersten. "Weighted Fair Multicast Multigroup Beamforming Under Per-antenna Power Constraints." In: *IEEE Transactions on Signal Processing* 62.19 (2014), pp. 5132–5142.

[83] D. Christopoulos, S. Chatzinotas, and B. Ottersten. "Frame Based Precoding in Satellite Communications: A Multicast Approach." In: *Proceedings of the Advanced Satellite Multimedia Systems Conference and Signal Processing for Space Communications Workshop (ASMS/SPSC)*. 2014, pp. 293–299.

[84] P. Gui, M.-M. Zhao, Q. Shi, and Q. Wu. "Max-Min Hybrid Precoder Design for mmWave Multi-Group Multicasting Systems." In: *Proceedings of the IEEE/CIC International Conference on Communications in China (IEEE ICCC)*. 2017, pp. 1–5.

[85] J. Li, Z. Wang, Y. Zhang, P. Zhu, D. Wang, and X. You. "Robust Hybrid Beamforming for Outage-Constrained Multigroup Multicast mmWave Transmission With Phase Shifter Impairments." In: *IEEE Systems Journal* 17.1 (2023), pp. 869–880.

[86] A. Grau, M. Indri, L. Lo Bello, and T. Sauter. "Robots in Industry: The Past, Present, and Future of a Growing Collaboration With Humans." In: *IEEE Industrial Electronics Magazine* 15.1 (2021), pp. 50–61.

[87] M. Wollschlaeger, T. Sauter, and J. Jasperneite. "The Future of Industrial Communication: Automation Networks in the Era of the Internet of Things and Industry 4.0." In: *IEEE Industrial Electronics Magazine* 11.1 (2017), pp. 17–27.

[88] Y. Huang, C. Zhang, J. Wang, Y. Jing, L. Yang, and X. You. "Signal Processing for MIMO-NOMA: Present and Future Challenges." In: *IEEE Wireless Communications* 25.2 (2018), pp. 32–38.

[89] X. Liu, B. Lin, M. Zhou, and M. Jia. "NOMA-Based Cognitive Spectrum Access for 5G-Enabled Internet of Things." In: *IEEE Network* 35.5 (2021), pp. 290–297.

[90] J. Cui, Y. Liu, Z. Ding, P. Fan, A. Nallanathan, and L. Hanzo. "Next-Generation mm-Wave Small-Cell Networks: Multiple Access, Caching, and Resource Management." In: *IEEE Vehicular Technology Magazine* 15.1 (2020), pp. 46–53.

[91] P. Liu and F. Zhao. "Millimeter-Wave mMIMO-NOMA Communication System Design in a Complex Blocking Environment." In: *IEEE Network* 36.4 (2022), pp. 10–17.

[92] K. Chandra, A. S. Marcano, S. Mumtaz, R. V. Prasad, and H. L. Christiansen. "Unveiling Capacity Gains in Ultradense Networks: Using mm-Wave NOMA." In: *IEEE Vehicular Technology Magazine* 13.2 (2018), pp. 75–83.

[93] J. Zhao, O. Simeone, D. Gunduz, and D. Gomez-Barquero. "Non-Orthogonal Unicast and Broadcast Transmission via Joint Beamforming and LDM in Cellular Networks." In: *Proceedings of the IEEE Global Communications Conference (IEEE GLOBECOM)*. 2016, pp. 1–6.

[94] Z. Zhang, M. Tao, and Y.-F. Liu. "Learning to Beamform in Joint Multicast and Unicast Transmission with Imperfect CSI." In: *IEEE Transactions on Communications* (2023), pp. 1–13.

[95] L. You, J. Xiong, K.-X. Li, W. Wang, and X. Gao. "Non-Orthogonal Unicast and Multicast Transmission for Massive MIMO With Statistical Channel State Information." In: *IEEE Access* 6 (2018), pp. 66841–66849.

[96] J. Zhao, O. Simeone, D. Gunduz, and D. Gomez-Barquero. "Non-Orthogonal Unicast and Broadcast Transmission via Joint Beamforming and LDM in Cellular Networks." In: *IEEE Transactions on Broadcasting* 66.2 (2020), pp. 216–228.

[97] D. Peng, S. Domouchtsidis, S. Chatzinotas, Y. Li, and B. Ottersten. "Non-Orthogonal Multicast and Unicast Robust Beamforming in Integrated Terrestrial-Satellite Networks." In: *Proceedings of the IEEE Global Communications Conference (IEEE GLOBECOM)*. 2022, pp. 2044–2049.

[98] Y.-F. Liu, C. Lu, M. Tao, and J. Wu. "Joint Multicast and Unicast Beamforming for the MISO Downlink Interference Channel." In: *Proceedings of the IEEE International Workshop on Signal Processing Advances in Wireless Communications (IEEE SPAWC)*. 2017, pp. 1–5.

[99] E. Chen and M. Tao. "Backhaul-Constrained Joint Beamforming for Non-Orthogonal Multicast and Unicast Transmission." In: *Proceedings of the IEEE Global Communications Conference (IEEE GLOBECOM)*. 2017, pp. 1–6.

[100] E. Chen, M. Tao, and Y.-F. Liu. "Joint Base Station Clustering and Beamforming for Non-Orthogonal Multicast and Unicast Transmission With Backhaul Constraints." In: *IEEE Transactions on Wireless Communications* 17.9 (2018), pp. 6265–6279.

[101] Y. Li, M. Xia, and Y.-C. Wu. "Energy-Efficient Precoding for Non-Orthogonal Multicast and Unicast Transmission via First-Order Algorithm." In: *IEEE Transactions on Wireless Communications* 18.9 (2019), pp. 4590–4604.

[102] F. Tan, P. Wu, and M. Xia. "Energy-Efficient Power Allocation for Non-Orthogonal Multicast and Unicast Transmission of Cell-Free Massive MIMO Systems." In: *Proceedings of the International Symposium on Networks, Computers and Communications (ISNCC)*. 2020, pp. 1–6.

[103] F. Tan, P. Wu, Y.-C. Wu, and M. Xia. "Energy-Efficient Non-Orthogonal Multicast and Unicast Transmission of Cell-Free Massive MIMO Systems With SWIPT." In: *IEEE Journal on Selected Areas in Communications* 39.4 (2021), pp. 949–968.

[104] J. Wang, H. Xu, B. Zhu, L. Fan, and A. Zhou. "Hybrid Beamforming Design for mmWave Joint Unicast and Multicast Transmission." In: *IEEE Communications Letters* 22.10 (2018), pp. 2012–2015.

[105] W. Hao, Z. Chu, F. Zhou, P. Xiao, V. C. M. Leung, and R. Tafazolli. "Hybrid Precoding Design for SWIPT Joint Multicast-Unicast mmWave System with Subarray Structure." In: *Proceedings of the IEEE International Conference on Communications (IEEE ICC)*. 2019, pp. 1–6.

[106] W. Hao, G. Sun, F. Zhou, D. Mi, J. Shi, P. Xiao, and V. C. M. Leung. "Energy-Efficient Hybrid Precoding Design for Integrated Multicast-Unicast Millimeter Wave Communications With SWIPT." In: *IEEE Transactions on Vehicular Technology* 68.11 (2019), pp. 10956–10968.

[107] M. Jafri, S. Srivastava, N. K. D. Venkategowda, A. K. Jagannatham, and L. Hanzo. "Cooperative Hybrid Transmit Beamforming in Cell-free mmWave MIMO Networks." In: *IEEE Transactions on Vehicular Technology* (2023), pp. 1–16.

[108] Y. Mao, B. Clerckx, and V. O. K. Li. "Rate-Splitting for Multi-Antenna Non-Orthogonal Unicast and Multicast Transmission." In: *Proceedings of the IEEE International Workshop on Signal Processing Advances in Wireless Communications (IEEE SPAWC)*. 2018, pp. 1–5.

[109] Y. Mao, B. Clerckx, and V. O. K. Li. "Rate-Splitting for Multi-Antenna Non-Orthogonal Unicast and Multicast Transmission: Spectral and Energy Efficiency Analysis." In: *IEEE Transactions on Communications* 67.12 (2019), pp. 8754–8770.

[110] R.-J. Reifert, S. Roth, A. A. Ahmad, and A. Sezgin. "Energy Efficiency in Rate-Splitting Multiple Access with Mixed Criticality." In: *Proceedings of the IEEE International Conference on Communications Workshops (IEEE ICC Workshops)*. 2022, pp. 681–686.

[111] Y. Mao and B. Clerckx. "Dirty Paper Coded Rate-Splitting for Non-Orthogonal Unicast and Multicast Transmission with Partial CSIT." In: *Proceedings of the Asilomar Conference on Signals, Systems, and Computers*. 2020, pp. 990–995.

[112] Y. Mao and B. Clerckx. "Beyond Dirty Paper Coding for Multi-Antenna Broadcast Channel With Partial CSIT: A Rate-Splitting Approach." In: *IEEE Transactions on Communications* 68.11 (2020), pp. 6775–6791.

[113] Z. Li, S. Yang, and T. Clessienne. "A General Rate Splitting Scheme for Hybrid Precoding in mmWave Systems." In: *Proceedings of the IEEE International Conference on Communications (IEEE ICC)*. 2019, pp. 1–6.

[114] A. A. Ahmad, Y. Mao, A. Sezgin, and B. Clerckx. "Rate Splitting Multiple Access in C-RAN: A Scalable and Robust Design." In: *IEEE Transactions on Communications* 69.9 (2021), pp. 5727–5743.

[115] A. Mishra, Y. Mao, O. Dizdar, and B. Clerckx. "Rate-Splitting Multiple Access for Downlink Multiuser MIMO: Precoder Optimization and PHY-Layer Design." In: *IEEE Transactions on Communications* 70.2 (2022), pp. 874–890.

[116] J. Park, J. Choi, N. Lee, W. Shin, and H. V. Poor. "Rate-Splitting Multiple Access for Downlink MIMO: A Generalized Power Iteration Approach." In: *IEEE Transactions on Wireless Communications* 22.3 (2023), pp. 1588–1603.

[117] Y. Mao, E. Piovano, and B. Clerckx. "Rate-Splitting Multiple Access for Overloaded Cellular Internet of Things." In: *IEEE Transactions on Communications* 69.7 (2021), pp. 4504–4519.

[118] Z. Yang, M. Chen, W. Saad, and M. Shikh-Bahaei. "Optimization of Rate Allocation and Power Control for Rate Splitting Multiple Access (RSMA)." In: *IEEE Transactions on Communications* 69.9 (2021), pp. 5988–6002.

[119] E. Aryafar, M. A. Khojastepour, K. Sundaresan, S. Rangarajan, and E. Knightly. "ADAM: An Adaptive Beamforming System for Multicasting in Wireless LANs." In: *IEEE/ACM Transactions on Networking* 21.5 (2013), pp. 1595–1608.

[120] L. Zhou, Z. Xu, W. Jiang, and W. Luo. "Joint Multicast Beamforming and User Scheduling in Large-scale Antenna Systems." In: *IET Communications* 12.11 (2018), pp. 1307–1314.

[121] K. Yang, W. Xu, S. Li, and J. Lin. "Distributed Multicast Resource Allocation in OFDM-based Cognitive Radio Networks." In: *Proceedings of the International Conference on Communications and Networking in China (EAI CHINACOM)*. 2013, pp. 57–62.

[122] S. X.-Y. Ni and A. M.-C. So. "Mixed-Integer Semidefinite Relaxation of Joint Admission Control and Beamforming: An SOC-Based Outer Approximation Approach with Provable Guarantees." In: *Proceedings of the IEEE International Workshop on Signal Processing Advances in Wireless Communications (IEEE SPAWC)*. 2018, pp. 1–5.

[123] K. Sundaresan, K. Ramachandran, and S. Rangarajan. "Optimal Beam Scheduling for Multicasting in Wireless Networks." In: *Proceedings of the International Conference on Mobile Computing and Networking (ACM MOBICOM)*. 2009, pp. 205–216.

[124] H. Zhang, Y. Jiang, K. Sundaresan, S. Rangarajan, and B. Zhao. "Wireless Multicast Scheduling With Switched Beamforming Antennas." In: *IEEE/ACM Transactions on Networking* 20.5 (2012), pp. 1595–1607.

[125] E. Matskani, N. D. Sidiropoulos, Z.-Q. Luo, and L. Tassiulas. "Efficient Batch and Adaptive Approximation Algorithms for Joint Multicast Beamforming and Admission Control." In: *IEEE Transactions on Signal Processing* 57.12 (2009), pp. 4882–4894.

[126] B. Hu, C. Hua, C. Chen, and X. Guan. "Transmit Beamforming and Admission Control for Multicast with Uncertain User Partition." In: *Proceedings of the IEEE/CIC International Conference on Communications in China (IEEE ICCC)*. 2014, pp. 16–20.

[127] A. Bandi, M. R. Bhavani Shankar, S. Chatzinotas, and B. Ottersten. "Joint User Grouping, Scheduling, and Precoding for Multicast Energy Efficiency in Multigroup Multicast Systems." In: *IEEE Transactions on Wireless Communications* 19.12 (2020), pp. 8195–8210.

[128] A. Bandi, M. R. Bhavani Shankar, S. Chatzinotas, and B. Ottersten. "Joint User Scheduling and Precoding for Multicast Spectral Efficiency in Multigroup Multicast Systems." In: *Proceedings of the IEEE International Conference on Signal Processing and Communications (IEEE SPCOM)*. 2020, pp. 1–5.

[129] B. Hu, C. Hua, C. Chen, and X. Guan. "Joint Beamformer Design for Wireless Fronthaul and Access Links in C-RANs." In: *IEEE Trans. Wireless Commun.* 17.5 (2018), pp. 2869–2881.

[130] B. Hu, C. Hua, J. Zhang, C. Chen, and X. Guan. "Joint Fronthaul Multicast Beamforming and User-Centric Clustering in Downlink C-RANs." In: *IEEE Trans. Wireless Commun.* 16.8 (2017), pp. 5395–5409.

[131] H. H. M. Tam, H. D. Tuan, D. T. Ngo, T. Q. Duong, and H. V. Poor. "Joint Load Balancing and Interference Management for Small-Cell Heterogeneous Networks With Limited Backhaul Capacity." In: *IEEE Trans. Wireless Commun.* 16.2 (2017), pp. 872–884.

[132] A. Pizzo and L. Sanguinetti. "Optimal Design of Energy-Efficient Millimeter Wave Hybrid Transceivers for Wireless Backhaul." In: *International Symposium on Modeling and Optimization in Mobile, Ad Hoc, and Wireless Networks (WiOpt)*. 2017, pp. 1–8.

[133] S. Hur, T. Kim, D. J. Love, J. V. Krogmeier, T. A. Thomas, and A. Ghosh. "Millimeter Wave Beamforming for Wireless Backhaul and Access in Small Cell Networks." In: *IEEE Trans. Commun.* 61.10 (2013), pp. 4391–4403.

[134] D. Yuan, H.-Y. Lin, J. Widmer, and M. Hollick. "Optimal and Approximation Algorithms for Joint Routing and Scheduling in Millimeter-Wave Cellular Networks." In: *IEEE/ACM Trans. Netw.* 28.5 (2020), pp. 2188–2202.

[135] A. Alizadeh and M. Vu. "Load Balancing User Association in Millimeter Wave MIMO Networks." In: *IEEE Trans. Wireless Commun.* 18.6 (2019), pp. 2932–2945.

[136] T. K. Vu, M. Bennis, S. Samarakoon, M. Debbah, and M. Latva-aho. "Joint Load Balancing and Interference Mitigation in 5G Heterogeneous Networks." In: *IEEE Trans. Wireless Commun.* 16.9 (2017), pp. 6032–6046.

[137] G. Kwon and H. Park. "Joint User Association and Beamforming Design for Millimeter Wave UDN With Wireless Backhaul." In: *IEEE J. Sel. Topics Signal Process.* 37.12 (2019), pp. 2653–2668.

[138] E. Chen, M. Tao, and N. Zhang. "User-Centric Joint Access-Backhaul Design for Full-Duplex Self-Backhauled Wireless Networks." In: *IEEE Trans. Commun.* 67.11 (2019), pp. 7980–7993.

[139] Y. Cheng, A. Philipp, and M. Pesavento. "Dynamic Rate Adaptation and Multiuser Downlink Beamforming Using Mixed Integer Conic Programming." In: *Proceedins of the European Signal Processing Conference (EUSIPCO)*. 2012, pp. 824–828.

[140] M. Tao, E. Chen, H. Zhou, and W. Yu. "Content-Centric Sparse Multicast Beamforming for Cache-Enabled Cloud RAN." In: *IEEE Trans. Wireless Commun.* 15.9 (2016), pp. 6118–6131.

[141] C. Pan, H. Zhu, N. J. Gomes, and J. Wang. "Joint Precoding and RRH Selection for User-Centric Green MIMO C-RAN." In: *IEEE Trans. Wireless Commun.* 16.5 (2017), pp. 2891–2906.

[142] X. Huang, G. Xue, R. Yu, and S. Leng. "Joint Scheduling and Beamforming Coordination in Cloud Radio Access Networks With QoS Guarantees." In: *IEEE Transactions on Vehicular Technology* 65.7 (2016), pp. 5449–5460.

[143] T. H. L. Dinh, M. Kaneko, E. H. Fukuda, and L. Boukhatem. "Energy Efficient Resource Allocation Optimization in Fog Radio Access Networks With Outdated Channel Knowledge." In: *IEEE Trans. Green Commun. Netw.* 5.1 (2021), pp. 146–159.

[144] Y. Cheng and M. Pesavento. "Joint Discrete Rate Adaptation and Downlink Beamforming Using Mixed Integer Conic Programming." In: *IEEE Transactions on Signal Processing* 63.7 (2015), pp. 1750–1764.

[145] L. Chen, F. R. Yu, H. Ji, B. Rong, X. Li, and V. C. M. Leung. "Green Full-Duplex Self-Backhaul and Energy Harvesting Small Cell Networks With Massive MIMO." In: *IEEE J. Sel. Topics Signal Process.* 34.12 (2016), pp. 3709–3724.

[146] H. T. Nguyen, H. D. Tuan, T. Q. Duong, H. V. Poor, and W.-J. Hwang. "Nonsmooth Optimization Algorithms for Multicast Beamforming in Content-Centric Fog Radio Access Networks." In: *IEEE Trans. Signal Process.* 68 (2020), pp. 1455–1469.

[147] Y. Chen, S. He, Y. Huang, J. Ren, and L. Yang. "Robust Multigroup Multicast Beamforming Design for Backhaul-Limited Cloud Radio Access Network." In: *IEEE Signal Processing Letters* 26.1 (2019), pp. 189–193.

[148] L. Lei, E. Lagunas, S. Chatzinotas, and B. Ottersten. "NOMA Aided Interference Management for Full-Duplex Self-Backhauling HetNets." In: *IEEE Communications Letters* 22.8 (2018), pp. 1696–1699.

[149] Y. Cheng, M. Pesavento, and A. Philipp. "Joint Network Optimization and Downlink Beamforming for CoMP Transmissions Using Mixed Integer Conic Programming." In: *IEEE Trans. Signal Process.* 61.16 (2013), pp. 3972–3987.

[150] D. H. N. Nguyen, L. B. Le, and T. Le-Ngoc. "Optimal Dynamic Point Selection for Power Minimization in Multiuser Downlink CoMP." In: *IEEE Trans. Wireless Commun.* 16.1 (2017), pp. 619–633.

[151] M. Sanjabi, M. Razaviyayn, and Z.-Q. Luo. "Optimal Joint Base Station Assignment and Beamforming for Heterogeneous Networks." In: *IEEE Trans. Signal Process.* 62.8 (2014), pp. 1950–1961.

[152] H. Ghauch, M. M. U. Rahman, S. Imtiaz, C. Qvarfordt, M. Skoglund, and J. Gross. "User Assignment in C-RAN Systems: Algorithms and Bounds." In: *IEEE Trans. Wireless Commun.* 17.6 (2018), pp. 3889–3902.

[153] 3GPP. *Study on Channel Model for Frequencies from 0.5 to 100 GHz*. Technical Report (TR) 38.901. Version 14.00. 3rd Generation Partnership Project (3GPP), 2017.

[154] K. K. Leung and W. Li-Chun. "Integrated Link Adaptation and Power Control to Improve Error and Throughput Performance in Broadband Wireless Packet Networks." In: *IEEE Transactions on Wireless Communications* 1.4 (2002), pp. 619–629.

[155] R. Kovalchukov, D. Moltchanov, Y. Gaidamaka, and E. Bobrikova. "An Accurate Approximation of Resource Request Distributions in Millimeter Wave 3GPP New Radio Systems." In: *Proceedings of the International Conference on Next Generation Wired/Wireless Networking (NEW2AN)*. Ed. by O. Galinina, S. Andreev, S. Balandin, and Y. Koucheryavy. Cham: Springer International Publishing, 2019, pp. 572–585.

[156] H. Pang, F. Ji, L. Xu, Y. Liu, and M. Wen. "Resource Allocation for RSMA-Based Coordinated Direct and Relay Transmission." In: *IEEE Wireless Communications Letters* 12.3 (2023), pp. 505–509.

[157] H. Fu, S. Feng, and D. W. K. Ng. "Resource Allocation Design for IRS-Aided Downlink MU-MISO RSMA Systems." In: *Proceedings of the IEEE International Conference on Communications (IEEE ICC Workshops)*. 2021, pp. 1–6.

[158] C. Xu, B. Clerckx, S. Chen, Y. Mao, and J. Zhang. "Rate-Splitting Multiple Access for Multi-Antenna Joint Radar and Communications." In: *IEEE Journal of Selected Topics in Signal Processing* 15.6 (2021), pp. 1332–1347.

[159] S. Naser, L. Bariah, S. Muhaidat, M. Al-Qutayri, M. Uysal, and P. C. Sofotasios. "Interference Management Strategies for Multiuser Multicell MIMO VLC Systems." In: *IEEE Transactions on Communications* 70.9 (2022), pp. 6002–6019.

[160] Y. Mao, B. Clerckx, and V. O. K. Li. "Rate-Splitting for Multi-Antenna Non-Orthogonal Unicast and Multicast Transmission: Spectral and Energy Efficiency Analysis." In: *IEEE Transactions on Communications* 67.12 (2019), pp. 8754–8770.

[161] B. Matthiesen, Y. Mao, A. Dekorsy, P. Popovski, and B. Clerckx. "Globally Optimal Spectrum- and Energy-Efficient Beamforming for Rate Splitting Multiple Access." In: *IEEE Transactions on Signal Processing* 70 (2022), pp. 5025–5040.

[162] G. Zhou, Y. Mao, and B. Clerckx. "Rate-Splitting Multiple Access for Multi-Antenna Downlink Communication Systems: Spectral and Energy Efficiency Tradeoff." In: *IEEE Transactions on Communications* 21.7 (2022), pp. 4816–4828.

[163] A. Rahmati, Y. Yapici, N. Rupasinghe, I. Guvenc, H. Dai, and A. Bhuyan. "Energy Efficiency of RSMA and NOMA in Cellular-Connected mmWave UAV Networks." In: *Proceedings of the IEEE International Conference on Communications (IEEE ICC Workshops)*. 2019, pp. 1–6.

[164] N. Q. Hieu, D. T. Hoang, D. Niyato, and D. I. Kim. "Optimal Power Allocation for Rate Splitting Communications With Deep Reinforcement Learning." In: *IEEE Wireless Communications Letters* 10.12 (2021), pp. 2820–2823.

[165] A. R. Flores and R. C. de Lamare. "Robust and Adaptive Power Allocation Techniques for Rate Splitting Based MU-MIMO Systems." In: *IEEE Transactions on Communications* 70.7 (2022), pp. 4656–4670.

[166] T. Cai, J. Zhang, S. Yan, L. Meng, J. Sun, and N. Al-Dhahir. "Resource Allocation for Secure Rate-Splitting Multiple Access with Adaptive Beamforming." In: *Proceedings of the IEEE International Conference on Communications (IEEE ICC Workshops)*. 2021, pp. 1–6.

[167] N. Q. Hieu, D. T. Hoang, D. Niyato, D. N. Nguyen, D. I. Kim, and A. Jamalipour. "Joint Power Allocation and Rate Control for Rate Splitting Multiple Access Networks with Covert Communications." In: *IEEE Transactions on Communications* (2023), pp. 1–14.

[168] O. Dizdar, Y. Mao, W. Han, and B. Clerckx. "Rate-Splitting Multiple Access for Downlink Multi-Antenna Communications: Physical Layer Design and Link-level Simulations." In: *Proceedings of the IEEE International Symposium on Personal, Indoor and Mobile Radio Communications (IEEE PIMRC)*. 2020, pp. 1–6.

[169] H.-T. Wai, Q. Li, and W.-K. Ma. "Discrete Sum Rate Maximization for MISO Interference Broadcast Channels: Convex Approximations and Efficient Algorithms." In: *IEEE Transactions on Signal Processing* 64.16 (2016), pp. 4323–4336.

[170] S. X.-Y. Ni and A. M.-C. So. "Mixed-Integer Semidefinite Relaxation of Joint Admission Control and Beamforming: An SOC-Based Outer Approximation Approach with Provable Guarantees." In: *Proceedings of the IEEE International Workshop on Signal Processing Advances in Wireless Communications (IEEE SPAWC)*. 2018, pp. 1–5.

[171] A. Bandi, M. R. Bhavani Shankar, S. Chatzinotas, and B. Ottersten. "A Joint Solution for Scheduling and Precoding in Multiuser MISO Downlink Channels." In: *IEEE Transactions on Wireless Communications* 19.1 (2020), pp. 475–490.

[172] E. Matskani, N. D. Sidiropoulos, Z.-Q. Luo, and L. Tassiulas. "Convex Approximation Techniques for Joint Multiuser Downlink Beamforming and Admission Control." In: *IEEE Trans. Wireless Commun.* 7.7 (2008), pp. 2682–2693.

[173] R. Wang, W. Kang, G. Liu, R. Ma, and B. Li. "Admission Control and Power Allocation for NOMA-Based Satellite Multi-Beam Network." In: *IEEE Access* 8 (2020), pp. 33631–33643.

[174] X. Ou, X. Xie, H. Lu, and H. Yang. "Resource Allocation in MU-MISO Rate-Splitting Multiple Access With SIC Errors for URLLC Services." In: *IEEE Transactions on Communications* 71.1 (2023), pp. 229–243.

[175] G. Chopra, A. Chowdary, and A. Kumar. "Bounds on Power and Common Message Fractions for RSMA with Imperfect SIC." In: (2022).

[176] N. Mouni, A. Kumar, and P. K. Upadhyay. "Adaptive User Pairing for NOMA Systems With Imperfect SIC." In: *IEEE Wireless Communications Letters* 10.7 (2021), pp. 1547–1551.

[177] I. A. Mahady, E. Bedeer, S. Ikki, and H. Yanikomeroglu. "Sum-Rate Maximization of NOMA Systems Under Imperfect Successive Interference Cancellation." In: *IEEE Communications Letters* 23.3 (2019), pp. 474–477.

[178] X. Wang, R. Chen, Y. Xu, and Q. Meng. "Low-Complexity Power Allocation in NOMA Systems With Imperfect SIC for Maximizing Weighted Sum-Rate." In: *IEEE Access* 7 (2019), pp. 94238–94253.

[179] H. Wang, Z. Zhang, and X. Chen. "Energy-efficient Power Allocation for Non-orthogonal Multiple Access with Imperfect Successive Interference Cancellation." In: *Proceedings of the International Conference on Wireless Communications and Signal Processing (WCSP)*. 2017, pp. 1–6.

[180] Y. Mao, B. Clerckx, and V. O. K. Li. "Rate-splitting Multiple Access for Downlink Communication Systems: Bridging, Generalizing, and Outperforming SDMA and NOMA." In: *EURASIP Journal on Wireless Communications and Networking* 1.133 (2018).

Part I

APPENDICES

This part of the thesis includes the publications in which this thesis is based.

A

PUBLICATION I.
LEARNING-BASED MAX-MIN FAIR HYBRID PRECODING FOR MMWAVE MULTICASTING

Learning-based Max-Min Fair Hybrid Precoding for mmWave Multicasting

Luis F. Abanto-Leon and Gek Hong (Allyson) Sim
Secure Mobile Networking (SEEMOO) Lab, Technische Universität Darmstadt, Germany
{labanto, asim}@seemoo.tu-darmstadt.de

***Abstract*—This paper investigates the joint design of hybrid transmit precoder and analog receive combiners for single-group multicasting in millimeter-wave systems. We propose `LB-GDM`, a low-complexity learning-based approach that leverages gradient descent with momentum and alternating optimization to design *(i)* the digital and analog constituents of a hybrid transmitter and *(ii)* the analog combiners of each receiver. In addition, we also extend our proposed approach to design fully-digital precoders. We show through numerical evaluation that, implementing `LB-GDM` in either hybrid or digital precoders attains superlative performance compared to competing designs based on semidefinite relaxation. Specifically, in terms of minimum signal-to-noise ratio, we report a remarkable improvement with gains of up to 105% and 101% for the fully-digital and hybrid precoders, respectively.**

***Index Terms*—max-min fairness, hybrid precoding, multicast, millimeter-wave, learning, semidefinite relaxation.**

I. Introduction

Wireless multicasting has a long-standing record for efficient utilization of spectrum resources to disseminate common information. Looking at the unprecedented growth in number and variety of multicast applications (e.g., high-definition video streaming, mobile video, content distribution in autonomous vehicular networks), multicast is outlined as a key player in emerging 5G millimeter-wave (mmWave) networks to sustain these demands [1]. With the recent advancements in antenna arrays architectures (e.g., digital-analog designs), particularly for mmWave systems, continuous investigation on beamforming techniques is crucial to ensure high performance. Indeed, a vital aspect to ensure high spectral efficiency lies in the optimal design of the beamformer or precoder. Nevertheless, the optimization problems derived from this context are at best non-convex quadratically constrained quadratic programs (QCQP), which have been proven NP-hard [2]. Therefore, many ongoing works are devoted to exploring alternative low-complexity schemes that yield near-optimality.

A. Related work

An initial work that addresses the NP-hardness of multicast optimization problems (e.g., quality-of-service (QoS) and max-min fairness (MMF)) in single-group scenarios is [2], where non-convex QCQPs are reformulated as semidefinite relaxation (SDR) programs. It is shown that SDR yields an approximate solution that, if feasible, is not necessarily optimum. To find feasible solutions, three types of Gaussian randomization are evaluated. In [3], an iterative algorithm based on second-order conic programming (SOCP) is proposed for the QoS problem in single-group multicasting. The single-group MMF problem is studied in [4]. Furthermore, the QoS and MMF problems in multi-group multicast contexts are studied in [5]–[11].

The above-mentioned works consider beamforming using fully-digital precoders. In such an architecture, each antenna requires a dedicated baseband and a radio frequency (RF) chain, which is deemed impractical in many multi-antenna systems (e.g., mmWave) due to high design complexity, hardware cost, and power consumption. Consequently, industry and academia scrutinize antenna designs based on a digital-analog (hybrid) architectures which allow the use of a large number of antennas with a limited amount of RF chains [12]. While fully-digital precoders for physical layer multicasting has been widely researched, the design of hybrid precoders remains understudied. The existing literature on hybrid precoding includes investigations on the MMF (in [13], [14]) and QoS (in [15], [16]) problems for single-group and multi-group multicasting. However, the designs proposed therein are either *(i)* constrained due to simplified premises or *(ii)* unimplementable in the existing multi-antenna hardware, for the following reasons. In [14], the propounded solution requires a specially connected network of phase shifters for optimal operation. On the other hand, the proposed scheme in [16] is restricted to implementations with only four different phase shifts. In [15], the analog phase shifters are replaced by high-resolution lens arrays with adjustable power, thus circumventing the actual problem of phase shift selection. Finally, in [13], it is required to test several codewords in order to design the analog precoder, thus demanding additional memory storage that scales with the number of antennas.

Our objective is to provide a low-complexity scheme for already available off-the-shelf devices (e.g., TP-Link TALON AD7200), which reckon with a primitive network of phase shifters, limited memory storage, and moderate computational capabilities [17]. To address all these requirements, we propose a learning-based scheme that only requires matrix multiplications/additions with controllable complexity and performance that depend on customizable input parameters. Furthermore, in contrast to prior literature on multicasting, we include the design of analog multi-antenna combiners at the receivers.

B. Our contributions

We design the first learning-based hybrid precoder for single-group multicasting while considering analog multi-

antenna receivers. The details of our contributions are summarized as follows:

- We investigate the MMF problem subject to power constraints at the transmitter and receivers. Precisely, our solution can handle an arbitrary number of constant-modulus phase shifts for the analog precoder in contrast to the existing designs that only consider a limited number of phase shifts. Moreover, the idea is extended for designing the analog combiners at the receivers.
- Our proposed learning-based scheme has lower complexity than SDR-based approaches. While SDR-based solutions require expensive vector-lifting that expands the variables into higher dimensional spaces, our proposed scheme, namely LB−GDM, only uses matrix multiplications/additions and a number of low-dimensional matrix inversions. Furthermore, the exploration and exploitation phases of our algorithm promote the search for optimal solutions while preventing getting trapped in local optima. Specifically, LB−GDM leverages gradient descent with momentum and alternating optimization.
- We consider analog multi-antenna receivers. We show that, by endowing the receivers with only two antennas, the minimum SNR improves by 75.7% compared to omnidirectional receiving patterns (i.e., single antenna case).
- Since the SDR method in [2] is only applicable to fully-digital implementations, we propose a novel scheme called SDR−C, capable of handling the constant-modulus constraints of the hybrid precoder and analog receivers. Inspired by [18], SDR−C exploits SDR and Cholesky matrix factorization. A similar technique was used by [19] to solve the QoS problem for multi-group multicasting. We extend the idea in [19] to the MMF problem.
- We perform extensive simulations to evaluate the performance of LB−GDM and SDR−C in terms of minimum SNR and spectral efficiency. We provide valuable insights on the fully-digital and hybrid precoders design under various system parameters (i.e., the number of transmit and receive antennas, the number of RF chains, and the number of iterations). We show that LB−GDM substantially outperforms state-of-the-art SDR-based solutions such as SDR−C, achieving up to 105.6% and 101.4% gains in digital and hybrid precoders, respectively.

II. System Model

We consider a mmWave system where a next generation Node B (gNodeB) serves a set of K multicast users denoted by $\mathcal{K} = \{1, 2, \ldots, K\}$. The gNodeB is equipped with N_{tx} transmit antennas and $N_{\mathrm{tx}}^{\mathrm{RF}}$ radio frequency (RF) chains, where $N_{\mathrm{tx}}^{\mathrm{RF}} \leq N_{\mathrm{tx}}$. The downlink signal is represented by $\mathbf{x} = \mathbf{F}\mathbf{m}s$, where $\mathbf{F} \in \mathbb{C}^{N_{\mathrm{tx}} \times N_{\mathrm{tx}}^{\mathrm{RF}}}$ and $\mathbf{m} \in \mathbb{C}^{N_{\mathrm{tx}}^{\mathrm{RF}} \times 1}$ are the analog and digital components of the hybrid precoder. The data symbol s has unit power in average, i.e., $\mathbb{E}\{ss^*\} = 1$. Every element of the analog precoder is a phase rotation with constant modulus, i.e., $[\mathbf{F}]_{q,r} \in \mathcal{F} = \left\{ \sqrt{\delta_{\mathrm{tx}}}, \ldots, \sqrt{\delta_{\mathrm{tx}}} e^{j\frac{2\pi(L_{\mathrm{tx}}-1)}{L_{\mathrm{tx}}}} \right\}$, where $q \in \mathcal{Q} = \{1, \ldots, N_{\mathrm{tx}}\}$, $r \in \mathcal{R} = \{1, \ldots, N_{\mathrm{tx}}^{\mathrm{RF}}\}$ and L_{tx} is the number of allowed phase rotation values. Each user is endowed with $N_{\mathrm{rx}} \ll N_{\mathrm{tx}}$ antennas and an analog combiner $\mathbf{w}_k \in \mathbb{C}^{N_{\mathrm{rx}} \times 1}$ with $N_{\mathrm{rx}}^{\mathrm{RF}} = 1$, such that $[\mathbf{w}_k] \in \mathcal{W} = \left\{ \sqrt{\delta_{\mathrm{rx}}}, \ldots, \sqrt{\delta_{\mathrm{rx}}} e^{j\frac{2\pi(L_{\mathrm{rx}}-1)}{L_{\mathrm{rx}}}} \right\}$, $l \in \mathcal{L} = \{1, \ldots, N_{\mathrm{rx}}\}$ and L_{rx} is the number of allowed phase rotation possibilities at the receivers. Under the assumption of narrowband flat-fading, the signal received by the k-th user is

$$y_k = \underbrace{\mathbf{w}_k^H \mathbf{H}_k \mathbf{F}\mathbf{m}s}_{\text{multicast signal}} + \underbrace{\mathbf{w}_k^H \mathbf{n}_k}_{\text{noise}}, \tag{1}$$

where $\mathbf{H}_k \in \mathbb{C}^{N_{\mathrm{rx}} \times N_{\mathrm{tx}}}$ denotes the channel between the k-th user and the gNodeB, whereas $\mathbf{n}_k \sim \mathcal{CN}(\mathbf{0}, \sigma^2\mathbf{I})$ denotes additive white Gaussian noise. The SNR at user k is given by

$$\gamma_k = \frac{\left|\mathbf{w}_k^H \mathbf{H}_k \mathbf{F}\mathbf{m}\right|^2}{\sigma^2 \left\|\mathbf{w}_k\right\|_2^2}. \tag{2}$$

III. Problem Formulation

The objective is to design a hybrid precoder that maximizes the minimum SNR among all K users, subject to power constraints at the transmitter and receiver. We define

$$\mathcal{P}_0^{\text{hyb}}: \max_{\mathbf{F},\mathbf{m},\{\mathbf{w}_k\}_{k=1}^K} \min_{k\in\mathcal{K}} \quad \frac{\left|\mathbf{w}_k^H \mathbf{H}_k \mathbf{F}\mathbf{m}\right|^2}{\sigma^2 \left\|\mathbf{w}_k\right\|_2^2} \tag{3a}$$

$$\text{s.t.} \quad \|\mathbf{F}\mathbf{m}\|_2^2 = P_{\mathrm{tx}}^{\max}, \tag{3b}$$

$$\|\mathbf{F}\|_{\mathrm{F}}^2 = 1, \tag{3c}$$

$$[\mathbf{F}]_{q,r} \in \mathcal{F}, q \in \mathcal{Q}, r \in \mathcal{R}, \tag{3d}$$

$$\|\mathbf{w}_k\|_2^2 = P_{\mathrm{rx}}^{\max}, k \in \mathcal{K}, \tag{3e}$$

$$[\mathbf{w}_k]_l \in \mathcal{W}, l \in \mathcal{L}, \forall k \in \mathcal{K}, \tag{3f}$$

where (3b) restricts the transmit power of the hybrid precoder, (3c) imposes a power normalization on the phase rotations, (3d) enforces every phase rotation of the analog precoder to be in $\mathcal{F}$, (3e) restrains the receive power whereas (3f) constrains the phase rotations of the combiners to $\mathcal{W}$. The constraints (3d) and (3f) denote non-convex feasible sets due to their combinatorial nature. Also, due to parameter coupling, (3b) is non-convex. The objective function (3a) is defined as the ratio of two quadratic expressions, where the numerator exhibits coupling of three parameters. Thus, $\mathcal{P}_0^{\text{hyb}}$ is a non-convex problem. Note that (3c) and (3e) can be circumvented as they are only employed to calculate $\delta_{\mathrm{tx}} = 1/N_{\mathrm{tx}}^{\mathrm{RF}} N_{\mathrm{tx}}$ and $\delta_{\mathrm{rx}} = P_{\mathrm{rx}}^{\max}/N_{\mathrm{rx}}$.

> *Remark:* When $N_{\mathrm{rx}} = 1$, $\{\mathbf{w}_k\}_{k=1}^K = 1$, and $\mathbf{F} = \mathbf{I}$, $\mathcal{P}_0^{\text{hyb}}$ collapses to the problem investigated in [2], which is known to be NP-hard. Since (3) has additional non-convex constraints, $\mathcal{P}_0^{\text{hyb}}$ is thus NP-hard as well. Additionally, when $N_{\mathrm{rx}} = 1$ and $\{\mathbf{w}_k\}_{k=1}^K = 1$, $\mathcal{P}_0^{\text{hyb}}$ is equivalent to the problem studied in [13].

IV. Proposed Scheme

In order to solve (3), we adopt an alternating optimization approach that allows us to decouple the unknown parameters $\mathbf{F}$, $\mathbf{m}$, and $\{\mathbf{w}_k\}_{k=1}^K$. Thus, $\mathcal{P}_0^{\text{hyb}}$ in (3) is decomposed into three sub-problems $\mathcal{P}_1^{\text{hyb}}$, $\mathcal{P}_2^{\text{hyb}}$, and $\mathcal{P}_3^{\text{hyb}}$ defined in (4), (9), and (11), respectively. Moreover, for each of the sub-problems we propose a learning-based algorithm that leverages gradient

Algorithm 1: Optimization of the analog precoder

Input: The precoders $\mathbf{F}^{(t-1)}$, $\mathbf{m}^{(t-1)}$ and receive combiners $\left\{\mathbf{w}_k^{(t-1)}\right\}_{k=1}^K$

Output: The analog precoder $\mathbf{F}^{(t)}$

Execute:

1: Calculate the weights $c_k^{(t)}, \forall k \in \mathcal{K}$.

2: Compute $\nabla J^F = \sum_{k=1}^K c_k^{(t)} \nabla_{\mathbf{F}} J_k^F / \left\| \nabla_{\mathbf{F}} J_k^F \right\|_{\mathrm{F}}$.

3: Compute the normalized gradient $\nabla \tilde{J}_F^{(t)} = \nabla J^F / \left\| \nabla J^F \right\|_{\mathrm{F}}$.

4: Compute $\mathbf{F}^{(t)} = \mathbf{F}^{(t-1)} + \rho_F \mathbf{F}_{\text{best}}^{(t-1)} + \alpha_F \nabla \tilde{J}_F^{(t)}$.

5: Project $\left[\mathbf{F}^{(t)}\right]_{q,r} \leftarrow \Pi_{\mathcal{F}} \left[\mathbf{F}^{(t)}\right]_{q,r}$ onto $\mathcal{F}$ to satisfy (8b).

Algorithm 2: Optimization of the digital precoder

Input: The precoders $\mathbf{F}^{(t)}$, $\mathbf{m}^{(t-1)}$ and receive combiners $\left\{\mathbf{w}_k^{(t-1)}\right\}_{k=1}^K$

Output: The digital precoder $\mathbf{m}^{(t)}$

Execute:

1: Calculate the weights $d_k^{(t)}, \forall k \in \mathcal{K}$.

2: Compute $\nabla J^M = \sum_{k=1}^K d_k^{(t)} \nabla_{\mathbf{m}} J_k^M / \left\| \nabla_{\mathbf{m}} J_k^M \right\|_2$.

3: Compute the normalized gradient $\nabla \tilde{J}_M^{(t)} = \nabla J^M / \left\| \nabla J^M \right\|_2$.

4: Compute $\mathbf{m}^{(t)} = \mathbf{m}^{(t-1)} + \rho_M \mathbf{m}_{\text{best}}^{(t-1)} + \alpha_M \nabla \tilde{J}_M^{(t)}$.

5: Normalize $\mathbf{m}^{(t)} \leftarrow \sqrt{P_{\text{tx}}^{\max}} \mathbf{m}^{(t)} / \left\| \mathbf{F}\mathbf{m}^{(t)} \right\|_2$.

descent with momentum, i.e., LB-GDM. Conversely to [20], where the momentum term affects the most recent gradient, in our case the momentum is associated with the fittest known solution (at each iteration). Furthermore, we include two parameters, N_{xpr} and N_{xpt}, that control exploration and exploitation of the learning process, respectively.

A. Optimization of the analog precoder $\mathbf{F}$

Assuming that $\mathbf{m}$ and $\{\mathbf{w}_k\}_{k=1}^K$ are known, we optimize $\mathbf{F}$,

$$\mathcal{P}_1^{\text{hyb}}: \max_{\mathbf{F}} \ \min_{k\in\mathcal{K}} \quad \frac{\left|\mathbf{w}_k^H \mathbf{H}_k \mathbf{F}\mathbf{m}\right|^2}{\sigma^2 P_{\text{rx}}^{\max}} \tag{4a}$$

$$\text{s.t.} \quad \|\mathbf{F}\mathbf{m}\|_2^2 = P_{\text{tx}}^{\max}, \tag{4b}$$

$$[\mathbf{F}]_{q,r} \in \mathcal{F}, q \in \mathcal{Q}, r \in \mathcal{R}. \tag{4c}$$

In order to reduce the number of constraints, we incorporate (4b) into the objective function (4a). Specifically, we replace $\frac{\left|\mathbf{w}_k^H \mathbf{H}_k \mathbf{F}\mathbf{m}\right|^2}{\sigma^2 P_{\text{rx}}^{\max}} = \psi \frac{\left|\mathbf{w}_k^H \mathbf{H}_k \mathbf{F}\mathbf{m}\right|^2}{\|\mathbf{F}\mathbf{m}\|_2^2}$, where $\psi = \frac{P_{\text{tx}}^{\max}}{\sigma^2 P_{\text{rx}}^{\max}}$. Notice that ψ can be disregarded as it is constant for all the users. Thus,

$$\overline{\mathcal{P}}_1^{\text{hyb}}: \max_{\mathbf{F}} \ \min_{k\in\mathcal{K}} \quad \frac{\mathbf{m}^H \mathbf{F}^H \mathbf{H}_k^H \mathbf{w}_k \mathbf{w}_k^H \mathbf{H}_k \mathbf{F}\mathbf{m}}{\mathbf{m}^H \mathbf{F}^H \mathbf{F}\mathbf{m}} \tag{5a}$$

$$\text{s.t.} \quad [\mathbf{F}]_{q,r} \in \mathcal{F}, q \in \mathcal{Q}, r \in \mathcal{R}. \tag{5b}$$

Instead of approaching (5), we propose to solve the surrogate problem (6), which consists of a weighted sum of all $\tau_k^F = \frac{\mathbf{m}^H \mathbf{F}^H \mathbf{H}_k^H \mathbf{w}_k \mathbf{w}_k^H \mathbf{H}_k \mathbf{F}\mathbf{m}}{\mathbf{m}^H \mathbf{F}^H \mathbf{F}\mathbf{m}}$, as shown in (6)

$$\widehat{\mathcal{P}}_1^{\text{hyb}}: \max_{\mathbf{F}} \quad \sum_{k=1}^K c_k \frac{\mathbf{m}^H \mathbf{F}^H \mathbf{H}_k^H \mathbf{w}_k \mathbf{w}_k^H \mathbf{H}_k \mathbf{F}\mathbf{m}}{\mathbf{m}^H \mathbf{F}^H \mathbf{F}\mathbf{m}} \tag{6a}$$

$$\text{s.t.} \quad [\mathbf{F}]_{q,r} \in \mathcal{F}, q \in \mathcal{Q}, r \in \mathcal{R}, \tag{6b}$$

where $c_k \geq 0$ denotes the k-th weighting factor. On the other hand, note that τ_k^F is upper-bounded by

$$\begin{aligned} \tau_k^F &\leq \lambda_{\max}\left(\left(\mathbf{F}^H\mathbf{F}\right)^{-1} \mathbf{F}^H \mathbf{H}_k^H \mathbf{w}_k \mathbf{w}_k^H \mathbf{H}_k \mathbf{F}\right) \\ &= \underbrace{\mathbf{w}_k^H \mathbf{H}_k \mathbf{F} \left(\mathbf{F}^H\mathbf{F}\right)^{-1} \mathbf{F}^H \mathbf{H}_k^H \mathbf{w}_k}_{J_k^F}, \end{aligned} \tag{7}$$

where $\lambda_{\max}(\cdot)$ extracts the maximum eigenvalue of matrix $\left(\mathbf{F}^H\mathbf{F}\right)^{-1} \mathbf{F}^H \mathbf{H}_k^H \mathbf{w}_k \mathbf{w}_k^H \mathbf{H}_k \mathbf{F}$. Upon replacing τ_k^F in (6) by its upper bound J_k^F, the problem collapses to

$$\widetilde{\mathcal{P}}_1^{\text{hyb}}: \max_{\mathbf{F}} \quad \sum_{k=1}^K c_k \mathbf{w}_k^H \mathbf{H}_k \mathbf{F} \left(\mathbf{F}^H\mathbf{F}\right)^{-1} \mathbf{F}^H \mathbf{H}_k^H \mathbf{w}_k, \tag{8a}$$

$$\text{s.t.} \quad [\mathbf{F}]_{q,r} \in \mathcal{F}, q \in \mathcal{Q}, r \in \mathcal{R}. \tag{8b}$$

Since (8a) is an upper bound for (6a), an optimal solution to (8), in general, may not be optimal to (6). Notice that the performance of the system in (8) will be determined by the minimum J_k^F, which can be regarded as a utility function of the k-th user. In order to solve (8), we first compute the gradient of $\sum_{k=1}^K c_k J_k^F$ to update $\mathbf{F}$. Then, we scale the modulus of each $[\mathbf{F}]_{q,r}$ and approximate its phase by the closest available option in $\mathcal{F}$ in order to comply with (8b), as detailed in Algorithm 1. The gradient of J_k^F with respect to $\mathbf{F}$ is $\nabla_{\mathbf{F}} J_k^F = \left(\mathbf{I} - \mathbf{F}\mathbf{F}^\dagger\right)^T \left(\mathbf{F}^\dagger \mathbf{H}_k^H \mathbf{w}_k \mathbf{w}_k^H \mathbf{H}_k\right)^T$, where $\mathbf{F}^\dagger = \left(\mathbf{F}^H\mathbf{F}\right)^{-1}\mathbf{F}^H$ (see Appendix for derivation). In *Step 1*, the weights are computed according to $c_k^{(t)} = \left(1 + \xi\left(\gamma_{\max}^{(t-1)} - \gamma_k^{(t-1)}\right)/\gamma_{\max}^{(t-1)}\right)^2$ for each iteration t, where $\gamma_k^{(t)}$ is the SNR attained by user k, $\gamma_{\max}^{(t)} = \max_{k\in\mathcal{K}} \gamma_k^{(t)}$ and $\xi > 0$. In *Step 2*, the weighted sum of the unit-power gradients $\nabla_{\mathbf{F}} J_k^F / \|\nabla_{\mathbf{F}} J_k^F\|_{\mathrm{F}}$ is computed. In *Step 3*, the unit-power aggregate gradient $\nabla \tilde{J}_F^{(t)}$ is obtained. In *Step 4*, the current $\mathbf{F}^{(t-1)}$ is updated using $\nabla \tilde{J}_F^{(t)}$. Also, $\mathbf{F}_{\text{best}}^{(t)}$ represents the best known solution until iteration t, whereas ρ_F and α_F are the momentum and learning factors associated to $\mathbf{F}$, respectively. Finally, *Step 5* enforces (8b). The weights are bounded to $1 \leq c_k^{(t)} \leq (1+\xi)^2$ and increase inversely proportional to the attained SNR $\gamma_k^{(t)}$. Thus, the gradient of the user with minimum SNR is weighted with the largest $c_k^{(t)}$, whereas the gradient of the user with maximum SNR is assigned the smallest $c_k^{(t)} = 1$.

> *Remark:* To motivate the connection between (5) and (6), we assume that (6) can be solved iteratively, and in each iteration we are capable of predicting $k^\star = \arg\min_{k\in\mathcal{K}} \tau_k^F$. Thus, if we assigned binary values $c_{k^\star} = 1$ and $c_{k\neq k^\star} = 0$ at each iteration instance, we would indirectly be solving a problem closely related to (5), where the minimum SNR is maximized. However, due to the intractability of predicting such $k^\star$, we propose to simultaneously maximize a subset of the smallest SNRs by considering non-binary positive weights $c_k^{(t)}$ that can be adapted based on the SNR values (obtained after each iteration), thus controlling the priorities of τ_k^F or J_k^F. This proposed approach also facilitates to keep track of several gradients simultaneously, preventing the search from getting trapped in local optima.

B. Optimization of the digital precoder $\mathbf{m}$

When $\mathbf{F}$ and $\{\mathbf{w}_k\}_{k=1}^K$ are known, the problem collapses to

$$\mathcal{P}_2^{\text{hyb}}: \max_{\mathbf{m}} \ \min_{k\in\mathcal{K}} \quad \left|\mathbf{w}_k^H \mathbf{H}_k \mathbf{F}\mathbf{m}\right|^2 \tag{9a}$$

$$\text{s.t.} \quad \|\mathbf{F}\mathbf{m}\|_2^2 = P_{\text{tx}}^{\max}. \tag{9b}$$

Algorithm 3: Optimization of the k-th combiner

Input: The precoders $\mathbf{F}^{(t)}$, $\mathbf{m}^{(t)}$ and the receive combiner $\mathbf{w}_k^{(t-1)}$
Output: The receive combiner $\mathbf{w}_k^{(t)}$
Execute:
1: Compute $\nabla_{\mathbf{w}_k} J_k^W$.
2: Compute $\nabla_{\mathbf{w}_k} \tilde{J}_W^{(t)} = \nabla_{\mathbf{w}_k} J_k^W / \left\| \nabla_{\mathbf{w}_k} J_k^W \right\|_2$.
3: Compute $\mathbf{w}_k^{(t)} = \mathbf{w}_k^{(t-1)} + \rho_W \mathbf{w}_{\text{best},k}^{(t-1)} + \alpha_W \nabla_{\mathbf{w}_k} \tilde{J}_W^{(t)}$.
4: Project $\left[\mathbf{w}_k^{(t)}\right]_l \leftarrow \Pi_{\mathcal{W}} \left[\mathbf{w}_k^{(t)}\right]_l$ onto $\mathcal{W}$, $\forall l \in \mathcal{L}$ to satisfy (12b).

Similarly as in (5) and (6), we recast (9) as

$$\widetilde{\mathcal{P}}_2^{\text{hyb}} : \max_{\mathbf{m}} \quad \sum_{k=1}^{K} d_k \left| \mathbf{w}_k^H \mathbf{H}_k \mathbf{F} \mathbf{m} \right|^2 \tag{10a}$$

$$\text{s.t.} \quad \|\mathbf{F}\mathbf{m}\|_2^2 = P_{\text{tx}}^{\max}, \tag{10b}$$

where d_k is the weight corresponding to $J_k^M = \left| \mathbf{w}_k^H \mathbf{H}_k \mathbf{F} \mathbf{m} \right|^2$. Compared to $\widetilde{\mathcal{P}}_1^{\text{hyb}}$, where an upper bound J_k^M for τ_k^F was derived, finding such a bound by means of the same procedure is not feasible in this case, as it involves computing the inverse of a rank-1 matrix $M = \mathbf{m}^* \mathbf{m}^T$. Thus, we assume $J_k^M = \tau_k^M$. $\widetilde{\mathcal{P}}_2^{\text{hyb}}$ is iteratively solved employing Algorithm 2, where a similar procedure as in Algorithm 1 is used to compute $\mathbf{m}$. Moreover, we assume that $d_k^{(t)}$ are computed in the same fashion as $c_k^{(t)}$. The gradient of J_k^M with respect to $\mathbf{m}$ is $\nabla_{\mathbf{m}} J_k^M = \mathbf{m}^H \mathbf{F}^H \mathbf{H}_k^H \mathbf{w}_k \mathbf{w}_k \mathbf{H}_k \mathbf{F}$. The main difference between Algorithm 1 and Algorithm 2 is *Step 5*, which restricts the transmit power to $P_{\text{tx}}^{\max}$.

C. Optimization of the combiners $\mathbf{w}_k$

Assuming that $\mathbf{F}$ and $\mathbf{m}$ are given, we optimize $\{\mathbf{w}_k\}_{k=1}^K$

$$\mathcal{P}_3^{\text{hyb}} : \max_{\{\mathbf{w}_k\}_{k=1}^K} \min_{k \in \mathcal{K}} \quad \frac{\left| \mathbf{w}_k^H \mathbf{H}_k \mathbf{F} \mathbf{m} \right|^2}{\sigma^2 \left\| \mathbf{w}_k \right\|_2^2} \tag{11a}$$

$$\text{s.t.} \quad [\mathbf{w}_k]_l \in \mathcal{W}, l \in \mathcal{L}, \forall k \in \mathcal{K}. \tag{11b}$$

Note that (11) can be decomposed into K parallel and independent sub-problems, whereby users will adapt their corresponding $\mathbf{w}_k$ in order to maximize their own SNR. Also, since $\|\mathbf{w}_k\|_2^2$ is an scalar, each sub-problem reduces to

$$\widetilde{\mathcal{P}}_{3,k}^{\text{hyb}} : \max_{\mathbf{w}_k} \quad \left| \mathbf{w}_k^H \mathbf{H}_k \mathbf{F} \mathbf{m} \right|^2 \tag{12a}$$

$$\text{s.t.} \quad [\mathbf{w}_k]_l \in \mathcal{W}, l \in \mathcal{L}, \tag{12b}$$

$\forall k \in \mathcal{K}$. As in $\widetilde{\mathcal{P}}_2^{\text{hyb}}$, we assume $J_k^W = \tau_k^W = \left| \mathbf{w}_k^H \mathbf{H}_k \mathbf{F} \mathbf{m} \right|^2$. Moreover, each sub-problem in (12) is similar to (8) except that each user optimizes their own utility function J_k^W. We employ Algorithm 3 to find $\{\mathbf{w}_k\}_{k=1}^K$, where $\nabla_{\mathbf{w}_k} J_k^W = \mathbf{w}_k^H \mathbf{H}_k \mathbf{F} \mathbf{m} \mathbf{m}^H \mathbf{F}^H \mathbf{H}_k^H$.

For completeness, LB-GDM is summarized in Algorithm 4. The exploration phase is based on randomization of $\mathbf{F}$, $\mathbf{m}$ and $\{\mathbf{w}_k\}_{k=1}^K$ (line 17). The exploitation phase harnesses $\mathbf{F}_{\text{best}}^{(t)}$, $\mathbf{m}_{\text{best}}^{(t)}$, and $\left\{\mathbf{w}_{\text{best},k}^{(t)}\right\}_{k=1}^K$ as the momentum terms, which preserve the fittest known solutions until iteration t and are updated once per exploration instance (line 16). On the other hand, $\mathbf{F}_{\text{opt}}$, $\mathbf{m}_{\text{opt}}$, and $\{\mathbf{w}_{\text{opt},k}\}_{k=1}^K$ retain the fittest solutions after each exploitation instance (line 10). These parameters are updated more frequently since they execute a finer scanning of the search space. Further, to refine the potential solutions in this phase, the learning factors α_F, α_M and α_W are progressively decreased as the exploration phase advances (line 13). However, these learning factors are reset to their original values when a new exploration instance begins (line 18). A proper balance between exploration and exploitation allows LB-GDM to produce more suitable precoders than SDR.

Algorithm 4: Proposed LB-GDM scheme

Initialize:
1: Assign $\left[\mathbf{F}^{(0)}\right]_{q,r} \leftarrow \delta$, $q = \{1, \ldots, N_{\text{tx}}\}$, $r \leftarrow \mod\left(q, N_{\text{tx}}^{\text{RF}}\right) + 1$, $\mathbf{m}^{(0)} \leftarrow \left[1 \; \mathbf{0}_{1\times(N_{\text{tx}}^{\text{RF}}-1)}\right]^T$, $\mathbf{w}_k^{(0)} \leftarrow \left[1 \; \mathbf{0}_{1\times(N_{\text{rx}}-1)}\right]^T$, $\forall k \in \mathcal{K}$.
2: Assign $\mathbf{F}_{\text{best}} \leftarrow \mathbf{0}$, $\mathbf{m}_{\text{best}} \leftarrow \mathbf{0}$ and $\{\mathbf{w}_{\text{best},k}\} \leftarrow \mathbf{0}$.
3: Assign $\alpha_F \leftarrow \alpha_{F_0}$, $\alpha_M \leftarrow \alpha_{M_0}$, $\alpha_W \leftarrow \alpha_{W_0}$.
4: Assign $t \leftarrow 0$, $\gamma_T \leftarrow 0$.
Execute:
5: **for** $i_{\text{xpr}} = 1, \ldots, N_{\text{xpr}}$ **do** (exploration phase)
6: **for** $i_{\text{xpt}} = 1, \ldots, N_{\text{xpt}}$ **do** (exploitation phase)
7: Compute $\mathbf{F}^{(t)}$, $\mathbf{m}^{(t)}$, $\left\{\mathbf{w}_k^{(t)}\right\}_{k=1}^K$ via Algorithms 1, 2, 3.
8: Find the minimum SNR, γ_{min}, among all users.
9: **if** $\gamma_{\text{min}} \geq \gamma_T$
10: Assign $\mathbf{F}_{\text{opt}} \leftarrow \mathbf{F}^{(t)}$, $\mathbf{m}_{\text{opt}} \leftarrow \mathbf{m}^{(t)}$, $\{\mathbf{w}_{\text{opt},k}\}_{k=1}^K \leftarrow \left\{\mathbf{w}_k^{(t)}\right\}_{k=1}^K$.
11: Assign $\gamma_T \leftarrow \gamma_{\text{min}}$.
12: **end if**
13: Update $\alpha_F \leftarrow 0.98\, \alpha_F$, $\alpha_M \leftarrow 0.98\, \alpha_M$, $\alpha_W \leftarrow 0.98\, \alpha_W$.
14: Increment $t \leftarrow t + 1$.
15: **end for**
16: Assign $\mathbf{F}_{\text{best}}^{(t)} \leftarrow \mathbf{F}_{\text{opt}}$, $\mathbf{m}_{\text{best}}^{(t)} \leftarrow \mathbf{m}_{\text{opt}}$, $\left\{\mathbf{w}_{\text{best},k}^{(t)}\right\}_{k=1}^K \leftarrow \{\mathbf{w}_{\text{opt},k}\}_{k=1}^K$.
17: Randomize $\mathbf{F}^{(t)}$, $\mathbf{m}^{(t)}$ and $\left\{\mathbf{w}_k^{(t)}\right\}_{k=1}^K$ enforcing (3b) - (3f).
18: Assign $\alpha_F \leftarrow \alpha_{F_0}$, $\alpha_M \leftarrow \alpha_{M_0}$, $\alpha_W \leftarrow \alpha_{W_0}$.
19: **end for**

V. Simulation Results

We consider the geometric channel model with $N_p = 5$ propagation paths between the transmitter and each user. Also, $P_{\text{tx}}^{\max} = 1$ (30 dBm), $P_{\text{rx}}^{\max} = 0.01$ (10 dBm), $\sigma^2 = 1$ (30 dBm), while $\mathcal{F}$ and $\mathcal{W}$ consist of $L_{\text{tx}} = 8$ and $L_{\text{rx}} = 4$ different phase shifts, respectively. In the following scenarios, we compare the performance of LB-GDM and SDR-C for fully-digital and hybrid precoders in terms of the minimum SNR (among all users) and the spectral efficiency (SE), computed as the sum-capacity of the whole system. We evaluate several configurations of N_{tx}, $N_{\text{tx}}^{\text{RF}}$, N_{rx}, N_{xpr}, N_{xpt}, and K. For LB-GDM, we set $\rho_F = \rho_M = \rho_W = 0.9$, $\alpha_{F_0} = 1$, $\alpha_{M_0} = 1$, $\alpha_{W_0} = 1$ and vary N_{xpr}, N_{xpt} to control the fitness of the solutions. In the case of SDR-C, we control the number of randomizations N_{rand}. Furthermore, the numerical results show the average over 100 channel realizations.

A. Impact of exploration (N_{xpr}) and exploitation (N_{xpt})

In this scenario we evaluate the performance of LB-GDM for different values of N_{xpr} and N_{xpt}, under a particular channel realization. We consider $K = 30$, $N_{\text{tx}} = 15$, $N_{\text{rx}} = 2$, when N_{xpr} and N_{xpt} are varied in the range $[1, 100]$. For the fully-digital and hybrid precoders, we assume $N_{\text{tx}}^{\text{RF}} = N_{\text{tx}} = 15$ and $N_{\text{tx}}^{\text{RF}} = 6$, respectively. We observe in Fig. 1 that the minimum SNR improves for increasing values of N_{xpr} and N_{xpt} in both precoders. Further, N_{xpr} is more relevant than N_{xpt} in improving this metric for this particular realization. Nevertheless, both of these phases are important. Exploration is the capability of effectively sampling/scanning the search space to find potentially fitter solutions, whereas exploitation

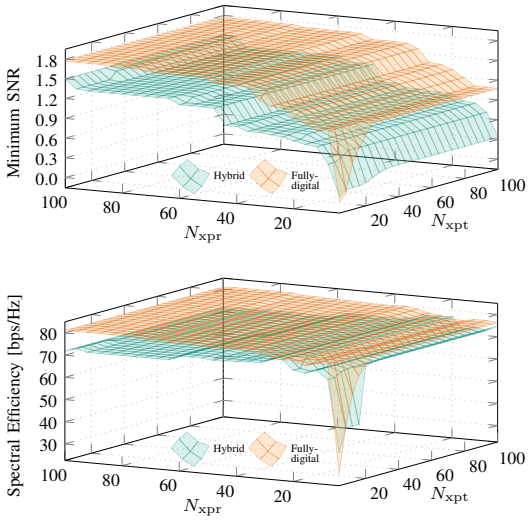

Figure 1: Impact of exploration (N_{xpr}) and exploitation (N_{xpt}) phases on the system performance.

capitalizes on already known solutions to further refine them. By doing so, our proposed LB−GDM avoids getting trapped in local optima. As expected, the fully-digital precoder outperforms its hybrid counterpart due to a larger number of RF chains and less stringent constraints (constant-modulus phase shifts). The former attains a minimum SNR of 1.77 whereas the latter achieves 1.49. Besides, the hybrid precoder attains 11.5% lower SE than that of the fully-digital precoder.

Remark: While the minimum SNR monotonically increases for both precoders, the SE performance does not exhibit the same behavior. This is because the optimization criterion of LB−GDM is to enhance the minimum SNR (MMF), without considering the spectral efficiency. Nevertheless, the general trend shows that higher N_{xpr} and N_{xpt} yield SE improvement.

B. Impact of the number of antennas N_{tx} and N_{rx}

In this scenario, we evaluate the performance of hybrid and fully-digital precoders based on LB−GDM for a different number of transmit and receive antennas. We consider $K = 50$, $N_{\text{tx}} = \{8, 12, 16\}$, and $N_{\text{rx}} = \{1, 2, 3, 4, 5\}$. For the hybrid precoder, we assume $N_{\text{tx}}^{\text{RF}} = 2$. Fig. 2 depicts the improvement of the minimum SNR when increasing N_{tx} and N_{rx}, for both types of precoders. Since the transmit and receive power are limited, endowing users with multiple antennas is beneficial to improve the SNR. In particular, in the fully-digital case, when $N_{\text{tx}} = 8$, the minimum SNR improves from 0.37 to 0.65 when the number of receive antenna increases from $N_{\text{rx}} = 1$ to $N_{\text{rx}} = 2$, which essentially indicates a 75.7% gain. Similarly, the gain for the hybrid precoder is 100%. We also observe a considerable improvement of the minimum SNR as N_{tx} increases from 8 to 16, in which we attain a gain of up to 72.9% and 58.6% for fully-digital and hybrid precoders, respectively. Further, the SE also achieves 25.5% and 32.9% gain, for the fully-digital and hybrid precoders, respectively (when $N_{\text{tx}} = 8$, for $N_{\text{rx}} = 1$ and $N_{\text{rx}} = 2$). In general, the hybrid precoder attains a SE at worst 11.8% lower than its fully-digital counterpart (for

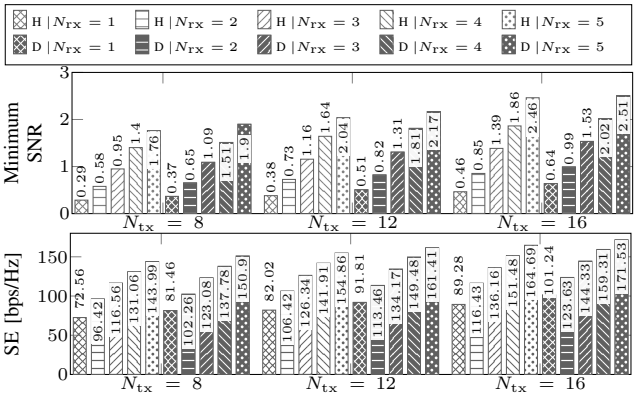

Figure 2: Performance evaluation of LB−GDM for varying N_{tx} and N_{rx} in fully-digital (D) and hybrid (H) precoders.

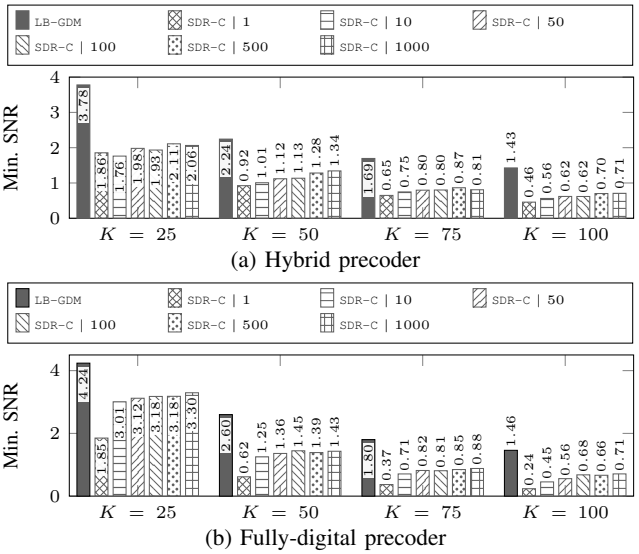

Figure 3: Performance comparison between LB−GDM and SDR−C in terms of the minimum SNR.

all the cases). We also observe that with only $N_{\text{tx}}^{\text{RF}} = 2$, the hybrid transmit precoder is at worst 25.5% below the optimality attained by the fully-digital in terms of the minimum SNR.

Remark: This scenario sheds lights on the relevance of reckoning with multiple antennas at the receivers when constrained by power at both ends. Specifically, we obtain improvements up to 72.9% and 58.6% by increasing the number of receive antennas from $N_{\text{rx}} = 1$ to $N_{\text{rx}} = 2$. On the other hand, in this case where $N_{\text{tx}}^{\text{RF}} = 2$, the complexity of LB−GDM is even more affordable as $\mathbf{F}^{\dagger} = \left(\mathbf{F}^H\mathbf{F}\right)^{-1}\mathbf{F}^H$ requires no actual inversion of $\mathbf{F}^H\mathbf{F}$, since a 2×2 matrix can be inverted directly.

C. Performance comparison with an SDR-based scheme

We compare the performance of LB−GDM and SDR−C, when implemented in fully-digital and hybrid precoders. We consider $N_{\text{tx}} = 20$, $N_{\text{rx}} = 3$, with a wide range of users $K = \{25, 50, 75, 100\}$. For the hybrid precoder $N_{\text{tx}}^{\text{RF}} = 6$, whereas for the fully-digital counterpart $N_{\text{tx}}^{\text{RF}} = N_{\text{tx}}$. For LB−GDM, we assume that $N_{\text{xpt}} = N_{\text{xpr}} = 120$. For SDR−C, the number of randomizations are $N_{\text{rand}} = \{1, 10, 50, 100, 500, 1000\}$. To ensure

a fair comparison, we refine the solutions of SDR−C by optimizing sequentially $\mathbf{F}$, $\mathbf{m}$, and $\{\mathbf{w}_k\}_{k=1}^K$ over $N_{\text{iter}}^{\text{SDR}} = 3$ iterations. In each iteration, N_{rand} randomizations are evaluated. Fig. 3 depicts a notable improvement of LB−GDM over SDR−C in both fully-digital (see Fig. 3b) and hybrid (see Fig. 3a) implementations, for all K. Specifically, the SDR−C results are shown in the format $\langle$SDR−C $\mid N_{\text{rand}}\rangle$. We observe a more prominent improvement for larger K. For instance, in the case of the fully-digital precoder, when $K = 50$, the minimum SNR obtained by LB−GDM is 79.3% higher than that of SDR−C although a wide range of N_{rand} were tested. The gain is even higher (i.e. 105.6%) for $K = 100$. We observe a similar trend for LB−GDM-based hybrid precoder, with gains of up to 101.4%.

VI. Discussion

SDR−C: This scheme is based on the approach in [19], where the QoS problem is researched. We extended the approach therein for the MMF problem. In this paper, SDR−C solves the sub-problems $\mathcal{P}_1^{\text{hyb}}$, $\mathcal{P}_2^{\text{hyb}}$, $\mathcal{P}_3^{\text{hyb}}$ in alternate manner over $N_{\text{iter}}^{\text{SDR}} = 3$ iterations. The initialization of $\mathbf{m}$ and $\{\mathbf{w}_k\}_{k=1}^K$ are the same as for LB−GDM (see line 1 of Algorithm 4). The SDR-C scheme is discussed in Appendix B.

Optimality: The proposed schemes, LB−GDM and SDR−C, cannot ensure global optimality. However, by observing Fig. 1 and Fig. 3 we corroborate that the approaches converge to a local optima for increasing N_{xpr}, N_{xpt} or N_{rand}.

Impact of number of constraints: It is well known that the optimality-gap of SDR degrades with increasing number of constraints (i.e., number of users K). As a result, we observe that for large K, the performance difference between LB−GDM and SDR−C increases, which indicates that LB−GDM is more robust and less sensitive to the number of constraints.

VII. Conclusion

In this paper, we investigated the design of fully-digital and hybrid precoders for single-group multicasting using a learning-based scheme. With the aim of maximizing the minimum SNR, our proposed low-complexity LB−GDM uses only matrix multiplications/additions and low-dimensional matrix inversion operations. We compare the performance of precoders based on SDR−C and LB−GDM under diverse simulation settings. The numerical results show a substantial gain, where LB−GDM outperforms SDR−C by up to 105.6% and 101.4% for digital and hybrid precoders, respectively. In addition, we demonstrate the importance of incorporating more receive antennas, where we achieve 75.7% and 100% gains in terms of the minimum SNR by increasing the number of receive antennas from one to two.

VIII. Acknowledgment

This research was in part funded by the Deutsche Forschungsgemeinschaft (DFG) within the B5G-Cell project as part of the SFB 1053 MAKI.

Appendix A
Gradient of J_k^F in Algorithm 1

Let us define $\mathbf{u} = \mathbf{F}^H\mathbf{H}_k^H\mathbf{w}_k$ and $\mathbf{Y} = \mathbf{F}^H\mathbf{F}$. Then, the following differentials are computed: $d\mathbf{u} = d\mathbf{F}^H\mathbf{H}_k^H\mathbf{w}_k$, $d\mathbf{Y} = \mathbf{F}^H\, d\mathbf{F}$, $d\mathbf{u}^H = \mathbf{w}_k^H\mathbf{H}_k\, d\mathbf{F}$ and $d\mathbf{Y}^{-1} = -\mathbf{Y}^{-1}\, d\mathbf{Y}\mathbf{Y}^{-1}$. Thus, the differential of $J_k^F = \mathbf{u}^H\mathbf{Y}^{-1}\mathbf{u}$ is given by

$$\begin{aligned} dJ_k^F &= \left(d\mathbf{u}^H\right)\mathbf{Y}^{-1}\mathbf{u} + \mathbf{u}^H\left(d\mathbf{Y}^{-1}\right)\mathbf{u} + \mathbf{u}^H\mathbf{Y}^{-1}\left(d\mathbf{u}\right) \\ &= \left(\mathbf{w}_k^H\mathbf{H}_k\, d\mathbf{F}\right)\mathbf{Y}^{-1}\mathbf{u} - \mathbf{u}^H\left(\mathbf{Y}^{-1}\, d\mathbf{Y}\mathbf{Y}^{-1}\right)\mathbf{u} \\ &= \left(\mathbf{w}_k^H\mathbf{H}_k\, d\mathbf{F}\right)\mathbf{Y}^{-1}\mathbf{u} - \mathbf{u}^H\left(\mathbf{Y}^{-1}\mathbf{F}^H\, d\mathbf{F}\mathbf{Y}^{-1}\right)\mathbf{u} \\ &= \mathrm{Tr}\left\{\mathbf{Y}^{-1}\mathbf{u}\mathbf{w}_k^H\mathbf{H}_k\, d\mathbf{F}\right\} - \mathrm{Tr}\left\{\mathbf{Y}^{-1}\mathbf{u}\mathbf{u}^H\mathbf{Y}^{-1}\mathbf{F}^H\, d\mathbf{F}\right\} \\ &= \mathrm{Tr}\left\{\left(\mathbf{Y}^{-1}\mathbf{u}\mathbf{w}_k^H\mathbf{H}_k - \mathbf{Y}^{-1}\mathbf{u}\mathbf{u}^H\mathbf{Y}^{-1}\mathbf{F}^H\right) d\mathbf{F}\right\} \end{aligned}$$

The Frobenius inner product of two matrices $\mathbf{P}$ and $\mathbf{Q}$ is defined as $\mathbf{P} : \mathbf{Q} \equiv \mathrm{Tr}\{\mathbf{P}^T\mathbf{Q}\}$. Thus, $dJ_k^F = \left(\mathbf{Y}^{-1}\mathbf{u}\mathbf{w}_k^H\mathbf{H}_k - \mathbf{Y}^{-1}\mathbf{u}\mathbf{u}^H\mathbf{Y}^{-1}\mathbf{F}^H\right)^T : d\mathbf{F}$. Upon replacing $\mathbf{u}$ in the expression above, we obtain

$$\nabla_{\mathbf{F}} J_k^F = \left(\mathbf{I} - \mathbf{F}\mathbf{F}^\dagger\right)^T\left(\mathbf{F}^\dagger\mathbf{H}_k^H\mathbf{w}_k\mathbf{w}_k^H\mathbf{H}_k\right)^T, \tag{A.1}$$

where $\mathbf{F}^\dagger = \left(\mathbf{F}^H\mathbf{F}\right)^{-1}\mathbf{F}^H$. Note that the Wirtinger derivative of J_k^F with respect to $\mathbf{F}^*$ is zero, i.e., $\nabla_{\mathbf{F}^*} J_k^F = \nabla_{\mathbf{F}^H} J_k^F = \mathbf{0}$.

Appendix B
SDR-C Scheme

B.1. Optimization of $\mathbf{F}$

Assuming that $\{\mathbf{w}_k\}_{k=1}^K$ and $\mathbf{m}$ are known, notice that we can express $\mathbf{F}\mathbf{m} = \mathbf{P}\mathbf{f}$, where $\mathbf{P} = \mathbf{m}^T \otimes \mathbf{I}$ and $\mathbf{f} = \mathrm{vec}\,(\mathbf{F})$. Furthermore, if we assign $t = \min_{k\in\mathcal{K}} \frac{\left|\mathbf{w}_k^H\mathbf{H}_k\mathbf{F}\mathbf{m}\right|^2}{\sigma^2 P_{\text{rx}}^{\max}}$, then $\mathcal{P}_1^{\text{hyb}}$ in (4) can be equivalently expressed as,

$$\begin{aligned} \mathcal{P}_1^{\text{hyb}}: \max_{t,\mathbf{F}} \quad & t && \text{(B.1a)} \\ \text{s.t.} \quad & \left|\mathbf{w}_k^H\mathbf{H}_k\mathbf{P}\mathbf{f}\right|^2 \geq t, && \text{(B.1b)} \\ & \|\mathbf{P}\mathbf{f}\|_2^2 = P_{\text{tx}}^{\max}, && \text{(B.1c)} \\ & [\mathbf{f}]_n \in \mathcal{F}, n \in \mathcal{N}, && \text{(B.1d)} \end{aligned}$$

where $\mathcal{N} = \{1, 2, \ldots, N_{\text{tx}}N_{\text{tx}}^{\text{RF}}\}$. In (B.1), realize that $\|\mathbf{P}\mathbf{f}\|_2^2 = \mathrm{Tr}\,(\mathbf{X}\mathbf{D})$, with $\mathbf{X} = \mathbf{P}^H\mathbf{P}$ and $\mathbf{D} = \mathbf{f}\mathbf{f}^H$. Also, $[\mathbf{D}]_{n,n} = \delta_{\text{tx}}$ since $[\mathbf{f}]_n \in \mathcal{F}$. By noticing that $\left|\mathbf{w}_k^H\mathbf{H}_k\mathbf{P}\mathbf{f}\right|^2 = \mathrm{Tr}\,(\mathbf{R}_k\mathbf{D})$, with $\mathbf{R}_k = \mathbf{P}^H\mathbf{H}_k^H\mathbf{w}_k\mathbf{w}_k^H\mathbf{H}_k\mathbf{P}$, (B.1) can be recast in its SDR form as shown in (B.2)

$$\begin{aligned} \mathcal{P}_{\text{SDR},1}^{\text{hyb}}: \max_{t,\mathbf{D}} \quad & t && \text{(B.2a)} \\ \text{s.t.} \quad & \mathrm{Tr}\,\{\mathbf{R}_k\mathbf{D}\} \geq t, && \text{(B.2b)} \\ & [\mathbf{D}]_{n,n} = \delta_{\text{tx}}, n \in \mathcal{N}, && \text{(B.2c)} \\ & \mathbf{D} \succcurlyeq \mathbf{0}, && \text{(B.2d)} \end{aligned}$$

where the constraint $\mathrm{rank}\,(\mathbf{D}) = 1$ has been dropped. Also, (B.2d) enforces $\mathbf{D}$ to be Hermitian positive semidefinite (PSD). Note that (B.2d) is linear in the PSD domain, and thus can be effectively approached by optimization solvers such as SDPT3. Upon obtaining $\mathbf{D}$, $\mathbf{f}$ is recovered in three stages.

Stage 1: Observe that any element (n_1, n_2) of matrix $\mathbf{D}$ can be represented as $[\mathbf{D}]_{n_1,n_2} = [\mathbf{f}]_{n_1}[\mathbf{f}]_{n_2}^*$. Now, let us define a vector $\mathbf{u} \in \mathbb{C}^{N_{\text{tx}}^{\text{RF}}\times 1}$ such that $\|\mathbf{u}\|_2^2 = \mathbf{u}^H\mathbf{u} = 1$. Thus, we can express $[\mathbf{D}]_{n_1,n_2}$ in terms of $\mathbf{u}$, i.e., $[\mathbf{D}]_{n_1,n_2} =$

$\left([\mathbf{f}]_{n_1}\,\mathbf{u}^T\right)\left([\mathbf{f}]^*_{n_2}\,\mathbf{u}^*\right)$. Assuming that $\mathbf{q}_n = [\mathbf{f}]_n\,\mathbf{u}$, $\mathbf{D}$ can be recast as $\mathbf{D} = \mathbf{Q}^T\mathbf{Q}^*$ with $\mathbf{Q} = \left[\mathbf{q}_1, \mathbf{q}_2, \ldots, \mathbf{q}_{N_{\text{tx}}N_{\text{tx}}^{\text{RF}}}\right]$.

Stage 2: If the solution returned by $\mathcal{P}^{\text{hyb}}_{\text{SDR},1}$ is denoted by $\widehat{\mathbf{D}}$. Then, via Cholesky decomposition we can obtain $\widehat{\mathbf{D}} = \widehat{\mathbf{Q}}^T\widehat{\mathbf{Q}}^*$, where $\widehat{\mathbf{Q}} = \left[\widehat{\mathbf{q}}_1, \widehat{\mathbf{q}}_2, \ldots, \widehat{\mathbf{q}}_{N_{\text{tx}}N_{\text{tx}}^{\text{RF}}}\right]$. In the previous stage, the premise was that each $\mathbf{q}_n$ could be obtained from the same $\mathbf{u}$, since $\mathbf{q}_n = [\mathbf{f}]_n\,\mathbf{u}$. However, we cannot guarantee that every $\widehat{\mathbf{q}}_n$ in $\widehat{\mathbf{D}}$ has the same stem $\widehat{\mathbf{u}}$. Although we have found $\widehat{\mathbf{D}}$, $\mathbf{f}$ and $\widehat{\mathbf{u}}$ remain unknown.

Stage 3: The objective is to find some $\widehat{\mathbf{u}}$ such that it originates the least error in the 2-norm sense, i.e.,

$$\mathcal{P}^{\text{hyb}}_{\text{LS},1}: \min_{\widehat{\mathbf{u}},[\mathbf{f}]_n,\forall n\in\mathcal{N}} \quad \sum_{n=1}^{N_{\text{tx}}N_{\text{tx}}^{\text{RF}}} \left\|\widehat{\mathbf{q}}_n - [\mathbf{f}]_n\,\widehat{\mathbf{u}}\right\|_2^2 \tag{B.3a}$$

$$\text{s.t.} \quad \|\widehat{\mathbf{u}}\|_2^2 = 1, \tag{B.3b}$$

$$[\mathbf{f}]_n \in \mathcal{F}, n \in \mathcal{N}. \tag{B.3c}$$

Minimizing simultaneously over both $\widehat{\mathbf{q}}_n$ and $\widehat{\mathbf{u}}$ is challenging. If we assume that $\widehat{\mathbf{u}}$ is known such that (8b) is satisfied, then we are required to solve

$$\widetilde{\mathcal{P}}^{\text{hyb}}_{\text{LS},1}: \min_{[\mathbf{f}]_n,\forall n\in\mathcal{N}} \quad \sum_{n=1}^{N_{\text{tx}}N_{\text{tx}}^{\text{RF}}} \left\|\widehat{\mathbf{q}}_n - [\mathbf{f}]_n\,\widehat{\mathbf{u}}\right\|_2^2 \tag{B.4a}$$

$$\text{s.t.} \quad [\mathbf{f}]_n \in \mathcal{F}, n \in \mathcal{N}. \tag{B.4b}$$

By expanding (B.4a), we realize that $\left\|\widehat{\mathbf{q}}_n - [\mathbf{f}]_n\,\widehat{\mathbf{u}}\right\|_2^2 = \widehat{\mathbf{q}}_n^H\widehat{\mathbf{q}}_n - 2\Re\mathfrak{e}\left([\mathbf{f}]_n\,\widehat{\mathbf{q}}_n^H\widehat{\mathbf{u}}\right) + \left|[\mathbf{f}]_n\right|^2\widehat{\mathbf{u}}^H\widehat{\mathbf{u}}$. Thus, (B.4) is

$$\widetilde{\mathcal{P}}^{\text{hyb}}_{\text{LS},1}: \max_{[\mathbf{f}]_n,\forall n\in\mathcal{N}} \quad \sum_{n=1}^{N_{\text{tx}}N_{\text{tx}}^{\text{RF}}} \Re\mathfrak{e}\left([\mathbf{f}]_n\,\widehat{\mathbf{q}}_n^H\widehat{\mathbf{u}}\right) \tag{B.5a}$$

$$\text{s.t.} \quad [\mathbf{f}]_n \in \mathcal{F}, n \in \mathcal{N}. \tag{B.5b}$$

Note that (B.5) can be decomposed into $N_{\text{tx}}N_{\text{tx}}^{\text{RF}}$ independent sub-problems. Thus, since $z_n = \widehat{\mathbf{q}}_n^H\widehat{\mathbf{u}}$ is known, we need to select $[\mathbf{f}]_n$ such that the real part of (B.5a) is maximized. This is equivalent to choosing $[\mathbf{f}]_n$ with the closest phase to z_n^*. After finding $\mathbf{f}$, it can be reshaped to obtain $\mathbf{F}$.

B.2. Optimization of $\mathbf{m}$

We assume herein that $\mathbf{F}$ and $\{\mathbf{w}_k\}_{k=1}^K$ are known. Thus, the SDR form of $\mathcal{P}_2^{\text{hyb}}$ is given by

$$\mathcal{P}^{\text{hyb}}_{\text{SDR},2}: \max_{t,\mathbf{M}} \quad t \tag{B.6a}$$

$$\text{s.t.} \quad \text{Tr}\left(\mathbf{Z}_k\mathbf{M}\right) \geq t, \tag{B.6b}$$

$$\text{Tr}\left(\mathbf{Y}\mathbf{M}\right) = P_{\text{tx}}^{\max}, \tag{B.6c}$$

$$\mathbf{M} \succcurlyeq \mathbf{0}, \tag{B.6d}$$

where $\mathbf{Y} = \mathbf{F}^H\mathbf{F}$, $\mathbf{Z}_k = \mathbf{F}^H\mathbf{H}_k^H\mathbf{w}_k\mathbf{w}_k^H\mathbf{H}_k\mathbf{F}$ and $\mathbf{M} = \mathbf{m}\mathbf{m}^H$.

B.3. Optimization of $\mathbf{w}_k$

Now, we assume that $\mathbf{F}$ and $\mathbf{m}$ are given. Therefore, SDR form of $\mathcal{P}_3^{\text{hyb}}$ is

$$\mathcal{P}^{\text{hyb}}_{\text{SDR},3}: \max_{t,\{\mathbf{W}_k\}_{k=1}^K} \quad t \tag{B.7a}$$

$$\text{s.t.} \quad \text{Tr}\left(\mathbf{C}_k\mathbf{W}_k\right) \geq t, \tag{B.7b}$$

$$\text{Tr}\left(\mathbf{W}_k\right) = P_{\text{rx}}^{\max}, \tag{B.7c}$$

$$\mathbf{W}_k \succcurlyeq \mathbf{0}, k \in \mathcal{K}, \tag{B.7d}$$

where $\mathbf{W}_k = \mathbf{w}_k\mathbf{w}_k^H$ and $\mathbf{C}_k = \mathbf{H}_k\mathbf{F}\mathbf{m}\mathbf{m}^H\mathbf{F}^H\mathbf{H}_k^H$. The problems $\mathcal{P}^{\text{hyb}}_{\text{SDR},1}$, $\mathcal{P}^{\text{hyb}}_{\text{SDR},2}$ and $\mathcal{P}^{\text{hyb}}_{\text{SDR},3}$ can be straightforwardly recast as linear programs and can therefore be efficiently solved by numerical solvers. In our case, we employed `CVX` and `SDPT3`.

REFERENCES

[1] A. Biason and M. Zorzi, "Multicast via Point to Multipoint Transmissions in Directional 5G mmWave Communications," *IEEE Communications Magazine*, vol. 57, no. 2, pp. 88–94, February 2019.

[2] N. D. Sidiropoulos, T. N. Davidson, and Z. Luo, "Transmit Beamforming for Physical-Layer Multicasting," *IEEE Transactions on Signal Processing*, vol. 54, no. 6, pp. 2239–2251, June 2006.

[3] L. Tran, M. F. Hanif, and M. Juntti, "A Conic Quadratic Programming Approach to Physical Layer Multicasting for Large-Scale Antenna Arrays," *IEEE Signal Processing Letters*, vol. 21, no. 1, pp. 114–117, January 2014.

[4] B. Gopalakrishnan and N. D. Sidiropoulos, "High Performance Adaptive Algorithms for Single-Group Multicast Beamforming," *IEEE Transactions on Signal Processing*, vol. 63, no. 16, pp. 4373–4384, August 2015.

[5] E. Karipidis, N. D. Sidiropoulos, and Z. Luo, "Quality of Service and Max-Min Fair Transmit Beamforming to Multiple Cochannel Multicast Groups," *IEEE Transactions on Signal Processing*, vol. 56, no. 3, pp. 1268–1279, March 2008.

[6] E. Karipidis, N. D. Sidiropoulos, and Z. Q. Luo, "Transmit Beamforming of Multiple Co-Channel Multicast Groups," in *IEEE CAMSAP*, December 2005, pp. 109–112.

[7] N. Bornhorst and M. Pesavento, "An Iterative Convex Approximation Approach for Transmit Beamforming in Multi-Group Multicasting," in *IEEE SPAWC*, June 2011, pp. 426–430.

[8] A. Schad and M. Pesavento, "Max-min Fair Transmit Beamforming for Multi-Group Multicasting," in *WSA*, March 2012, pp. 115–118.

[9] D. Christopoulos, S. Chatzinotas, and B. Ottersten, "Weighted Fair Multicast Multigroup Beamforming Under Per-antenna Power Constraints," *IEEE Transactions on Signal Processing*, vol. 62, no. 19, pp. 5132–5142, October 2014.

[10] O. T. Demir and T. E. Tuncer, "Multi-Group Multicast Beamforming for Simultaneous Wireless Information and Power Transfer," in *Eusipco*, August 2015, pp. 1356–1360.

[11] M. Sadeghi, E. Björnson, E. G. Larsson, C. Yuen, and T. L. Marzetta, "Max–Min Fair Transmit Precoding for Multi-Group Multicasting in Massive MIMO," *IEEE Transactions on Wireless Communications*, vol. 17, no. 2, pp. 1358–1373, February 2018.

[12] T. Kim, J. Park, J. Seol, S. Joeng, J. Cho, and W. Roh, "Tens of Gbps Support with mmWave Beamforming Systems for Next Generation Communications," in *IEEE GLOBECOM*, December 2013, pp. 3685–3690.

[13] M. Dai and B. Clerckx, "Hybrid Precoding for Physical Layer Multicasting," *IEEE Communications Letters*, vol. 20, no. 2, pp. 228–231, February 2016.

[14] M. Sadeghi, L. Sanguinetti, and C. Yuen, "Hybrid Precoding for Multi-Group Physical Layer Multicasting," in *EW*, May 2018, pp. 1–6.

[15] J. Huang, Z. Cheng, E. Chen, and M. Tao, "Low-Complexity Hybrid Analog/Digital Beamforming for Multicast Transmission in mmWave Systems," in *IEEE ICC*, May 2017, pp. 1–6.

[16] O. T. Demir and T. E. Tuncer, "Antenna Selection and Hybrid Beamforming for Simultaneous Wireless Information and Power Transfer in Multi-Group Multicasting Systems," *IEEE Transactions on Wireless Communications*, vol. 15, no. 10, pp. 6948–6962, October 2016.

[17] J. Palacios, D. Steinmetzer, A. Loch, M. Hollick, and J. Widmer, "Adaptive Codebook Optimization for Beam Training on Off-the-Shelf IEEE 802.11ad Devices," in *ACM MOBICOM*, October 2018, pp. 241–255.

[18] W. K. Ma, P. C. Ching, and Z. Ding, "Semidefinite Relaxation Based Multiuser Detection for M-Ary PSK Multiuser Systems," *IEEE Transactions on Signal Processing*, vol. 52, no. 10, pp. 2862–2872, October 2004.

[19] L. F. Abanto-Leon, M. Hollick, and G. H. Sim, "Hybrid Precoding for Multi-Group Multicasting in mmWave Systems," in *IEEE GLOBECOM*, December 2019.

[20] P. J. Werbos, "Beyond Regression: New Tools for Prediction and Analysis in the Behavioral Sciences," *Ph.D. thesis, Harvard University*, 1974.

B

PUBLICATION II.
HYBRID PRECODING FOR MULTI-GROUP MULTICASTING IN MMWAVE SYSTEMS

Hybrid Precoding for Multi-Group Multicasting in mmWave Systems

Luis F. Abanto-Leon, Matthias Hollick, and Gek Hong (Allyson) Sim
Secure Mobile Networking (SEEMOO) Lab, Technische Universität Darmstadt, Germany
{labanto, mhollick, asim}@seemoo.tu-darmstadt.de

***Abstract*—Multicast beamforming is known to improve spectral efficiency. However, its benefits and challenges for hybrid precoders design in millimeter-wave (mmWave) systems remain understudied. To this end, this paper investigates the first joint design of hybrid transmit precoders (with an arbitrary number of finite-resolution phase shifts) and receive combiners for mmWave multi-group multicasting. Our proposed design leverages semidefinite relaxation (SDR), alternating optimization and Cholesky matrix factorization to sequentially optimize the digital/analog precoders at the transmitter and the combiners at each receiver. By considering receivers with multiple-antenna architecture, our design remarkably improves the overall system performance. Specifically, with only two receive antennas the average transmit power per received message improves by 16.8% while the successful information reception is boosted by 60%. We demonstrate by means of extensive simulations that our hybrid precoder design performs very close to its fully-digital counterpart even under challenging scenarios (i.e., when co-located users belong to distinct multicast groups).**

***Index Terms*—hybrid precoding, millimeter-wave, multicast, semidefinite relaxation, alternating optimization.**

I. Introduction

In recent years, millimeter-wave (mmWave) has emerged as a promising technology to fuel the ever-increasing consumer demands for extremely fast (i.e., up to multi-Gbps) connectivity. In delivering such requirements for dense networks scenarios (due to extreme densification in next-generation networks), a system can leverage the benefits of multicast communications [1]. Indeed, recent studies in [2], [3] demonstrate the potential of multicast to significantly improve the network throughput and spectral efficiency of mmWave systems. To guarantee these performances, an appropriate design for multicast precoders is crucial *(i)* to compensate for severe channel attenuation, and *(ii)* to minimize the interference between simultaneous transmissions.

An early effort on multicast precoder design is presented in [4], where the authors investigated single-group multicast precoding with a multi-antenna base station and several single-antenna receivers. Aiming at minimizing the transmit power subject to predefined quality of service (QoS) requirements (i.e., QoS problem), the problem is formulated as a relaxed semidefinite program (SDP) where befitting solutions are obtained via randomization [5]. Since their work only considers single-group multicast, the problem formulation thus excludes the interference aspect that is relevant in designing multi-group multicast precoders. Expanding on [4], the authors of [6], [7] investigate a scenario with multiple co-channel multicast groups, which allows transmissions of simultaneous multicast signals by exploiting spatial multiplexing. Furthermore, to mitigate the interference between the distinct signals (and thus increase the number of served users), [6], [7] an additional stage of power control is incorporated. The QoS problem is also considered in [8]–[10] with diverse extensions to the formulation. A related formulation known as the max-min fair (MMF) problem is studied in [11]–[13].

The works mentioned above are developed within the framework of fully-digital multicast precoders. Given the affordable hardware and moderate computational complexity of hybrid precoders, a shift of interest has been observed in departing from fully-digital to adopting hybrid antenna arrays architectures. Hybrid precoders are composed of a low-dimensional digital beamformer in cascade with a high-dimensional network of cost-efficient constant-modulus phase shifters that admit a limited number of phase rotations. In general, hybrid precoders are less flexible than their fully-digital counterparts, thus rendering the design of an optimal hybrid precoder a challenging task. Besides, they pose a compromise in terms of beamforming capabilities and interference management. On the other hand, the versatility of digital precoders comes at the expense of highly complicated and expensive hardware, wherein a dedicated radio frequency (RF) chain is required for each antenna element.

To date, the body of works that has studied hybrid precoding for physical layer multicasting includes single-group multicasting (in [14]) and multi-group multicasting (in [15]–[17]). The authors of [14] consider the MMF problem in single-group multicast settings, wherein a codebook-based design is presented. On the other hand, the multi-group multicast QoS and MMF problems are revisited in [15], where the authors propose a customized hybrid architecture with improved performance. In [16], the authors investigate the QoS problem by considering a high-resolution lens array with adjustable power. However, such design circumvents the constant-modulus discrete phase shifts characteristics of analog circuitry components of hybrid precoders. On the contrary, the authors in [17] design an scheme to support joint power and information transfer with hybrid precoders. Their formulation considers discrete phase shifts, but restrains the set of phase shifts to only four choices. In addition, the existing studies on multicast precoders for mmWave systems only consider receivers with single-antenna architecture. This conditioning prevents the mitigation of undesired signals (e.g.,

interference), especially when users from different multicast groups have correlated channel vectors. In particular, endowing receivers with multiple antennas: *(i)* mitigates interference from other sources, *(ii)* reduces the power expenditure from the transmitter, and *(iii)* improves the service ubiquitousness.

To the best of our knowledge, we are the first to investigate the *joint design of hybrid multicast precoders with an arbitrary number of finite-resolution constant-modulus phase shifts at the transmitter while considering multiple antennas at the receivers*. Related art on hybrid precoding for multi-user scenarios (e.g., in [18]) are fundamentally different as each RF chain at the transmitter is matched to the channel of one dedicated user. In the multi-group multicast scenario we consider in this paper—due to the limitation of RF chains—several users with distinct channel conditions need to be served by a single RF unit, thus complicating the design of the hybrid precoder. Our proposed formulation focuses on the QoS problem, for which we present an SDR-based approach to optimize the digital precoder, analog phase shifts and receive combiners. Due to the existence of several design parameters, our proposed formulation is divided into a set of sub-problems that we approach adopting alternating optimization (as in e.g., [19]). Moreover, we incorporate a set of slack parameters to promote coherent parameter binding among the decoupled sub-problems. Since alternating optimization requires each sub-problem to be solvable to guarantee the continuity of the optimization process, such a set of slack parameters ensures that each sub-problem always yields a feasible solution for the succeeding stages. Finally, due to the selection of finite-resolution constant-modulus phase shifts, the problem is inherently of combinatorial nature. To circumvent this matter, we propose a scheme where the phase shifts selection is recast as an SDR program followed by a stage consisting of Cholesky matrix factorization, least squares, and randomization.

The paper is structured as follows. In Section II, we model and elaborate on the problem of multi-group multicast hybrid transmit precoders with finite-resolution phase shifts and multi-antenna receivers in mmWave systems. In Section III, we formulate the problem and present the proposed solution in Section IV. We analyze and compare the performance of our design in Section V. Also, we include an insightful discussion in Section VI. Finally, we conclude with the contributions of this paper in Section VII.

II. System Model

We adopt a mmWave system where a gNodeB serves K users distributed into G different co-channel multicast groups. The sets of users and groups are denoted by $\mathcal{K} = \{1, 2, \ldots, K\}$ and $\mathcal{I} = \{1, 2, \ldots, G\}$, respectively. Each multicast group $\mathcal{G}_i \, (i \in \mathcal{I})$ contains the indices of users that constitute it. The amount of users in each multicast group is represented by $|\mathcal{G}_i|$, such that $\sum_{i=1}^{G} |\mathcal{G}_i| = K$. As in [6], we assume that $\mathcal{G}_i \cap \mathcal{G}_j = \{\emptyset\}, \forall i \neq j$. The gNodeB is equipped with N_{tx} transmit antennas and $N_{\mathrm{tx}}^{\mathrm{RF}}$ RF chains, with $G \leq N_{\mathrm{tx}}^{\mathrm{RF}} \leq N_{\mathrm{tx}}$. The downlink signal is represented by $\mathbf{x} = \mathbf{FMs}$, where $\mathbf{F} \in \mathbb{C}^{N_{\mathrm{tx}} \times N_{\mathrm{tx}}^{\mathrm{RF}}}$ is the analog precoder whereas $\mathbf{M} = [\mathbf{m}_1, \mathbf{m}_2, \ldots, \mathbf{m}_G] \in \mathbb{C}^{N_{\mathrm{tx}}^{\mathrm{RF}} \times G}$ assembles the digital precoders for each of the multicast group. The collection of data symbols for the intended groups is denoted by $\mathbf{s} = [s_1, s_2, \ldots, s_G]^T \in \mathbb{C}^{G \times 1}$, where each entry has unit power on average, i.e., $\mathbb{E}\{\mathbf{s}\mathbf{s}^H\} = \mathbf{I}$. Also, every element (q, r) of the analog precoder is a phase rotation with constant modulus. Therefore, $[\mathbf{F}]_{q,r} \in \mathcal{F}$, where $q \in \mathcal{Q} = \{1, 2, \ldots, N_{\mathrm{tx}}\}$, $r \in \mathcal{R} = \{1, 2, \ldots, N_{\mathrm{tx}}^{\mathrm{RF}}\}$, $\mathcal{F} = \left\{\sqrt{\delta}, \sqrt{\delta}e^{\frac{2\pi}{L}}, \ldots, \sqrt{\delta}e^{\frac{2\pi(L-1)}{L}}\right\}$, L denotes the number of different phase shifts that are allowed, and δ is a scaling factor. Each multicast receiver has a finite number of receive antennas $N_{\mathrm{rx}} \ll N_{\mathrm{tx}}$, and an equal number of RF chains. Under the assumption of narrowband flat-fading, the signal received by the k-th user ($k \in \mathcal{G}_i$) is given by

$$y_k = \underbrace{\mathbf{w}_k^H \mathbf{H}_k \mathbf{F} \mathbf{m}_i s_i}_{\text{desired multicast signal}} + \underbrace{\mathbf{w}_k^H \mathbf{H}_k \sum_{\substack{j=1 \\ j \neq i}}^{G} \mathbf{F} \mathbf{m}_j s_j}_{\text{interference}} + \underbrace{\mathbf{w}_k^H \mathbf{n}_k}_{\text{noise}}, \tag{1}$$

where i is the index of group $\mathcal{G}_i$, and $\mathbf{w}_k \in \mathbb{C}^{N_{\mathrm{rx}} \times 1}$ represents the digital receive beamformer of the k-th user. Also, $\mathbf{H}_k \in \mathbb{C}^{N_{\mathrm{rx}} \times N_{\mathrm{tx}}}$ denotes the channel between the gNodeB and the k-th user, whereas $\mathbf{n}_k \sim \mathcal{CN}(\mathbf{0}, \sigma^2 \mathbf{I})$ denotes additive white Gaussian noise. The signal–to–interference–plus-noise ratio (SINR) at user k is defined as

$$\mathrm{SINR}_k = \frac{\left|\mathbf{w}_k^H \mathbf{H}_k \mathbf{F} \mathbf{m}_i\right|^2}{\sum_{j \neq i} \left|\mathbf{w}_k^H \mathbf{H}_k \mathbf{F} \mathbf{m}_j\right|^2 + \sigma^2 \left\|\mathbf{w}_k\right\|_2^2}. \tag{2}$$

III. Problem Formulation

Aiming to optimize the transmit power, we formulate

$$\mathcal{P}^{\mathrm{hyb}}: \min_{\substack{\mathbf{F}, \{\mathbf{m}_i\}_{i=1}^{G}, \\ \{\mathbf{w}_k\}_{k=1}^{K}}} \quad \sum_{i=1}^{G} \|\mathbf{F}\mathbf{m}_i\|_2^2 \tag{3a}$$

$$\text{s.t.} \quad \frac{\left|\mathbf{w}_k^H \mathbf{H}_k \mathbf{F} \mathbf{m}_i\right|^2}{\sum_{j \neq i} \left|\mathbf{w}_k^H \mathbf{H}_k \mathbf{F} \mathbf{m}_j\right|^2 + \sigma^2 \left\|\mathbf{w}_k\right\|_2^2} \geq \gamma_i, \tag{3b}$$

$$\|\mathbf{w}_k\|_2^2 = P_{\mathrm{rx}}^{\max}, \tag{3c}$$

$$\|\mathbf{F}\|_{\mathrm{F}}^2 = N_{\mathrm{tx}}^{\mathrm{RF}}, \tag{3d}$$

$$[\mathbf{F}]_{q,r} \in \mathcal{F}, q \in \mathcal{Q}, r \in \mathcal{R}, \forall k \in \mathcal{G}_i, i \in \mathcal{I}, \tag{3e}$$

where (3a) targets the minimization of the transmit power. Constraint (3b) imposes specific QoS requirements for each multicast group, whereas (3c) restricts the power expenditure for receive beamforming at each user. Constraint (3d) limits the power associated with the analog precoder. In addition, (3e) enforces every phase shift to belong to $\mathcal{F}$. The target SINR of every group $\mathcal{G}_i$ is denoted by γ_i. Note that (3a) is non-convex due to multiplicative coupling between $\mathbf{F}$ and $\mathbf{m}_i$. Constraint (3b) is non-convex since it is defined as the ratio of two non-convex expressions. On the other hand, (3c) is quadratic and non-convex on $\mathbf{w}_k$. Constraint (3e) is inherently of combinatorial nature, therefore non-convex. Thus, (3d) is also non-convex due to its dependence on (3e). As a result, $\mathcal{P}^{\mathrm{hyb}}$ is classified as a non-convex quadratically constrained quadratic program (QCQP), which is known to be NP-hard.

IV. Proposed Solution

In this section, we propose an approach based on alternating optimization, where the unknown parameters $\mathbf{F}$, $\{\mathbf{m}_i\}_{i=1}^{G}$

and $\{\mathbf{w}_k\}_{k=1}^K$ are optimized sequentially and iteratively. Due to sequential (and independent) parameter optimization, the suitability of the solution can be compromised. Therefore, we include an additional set of slack parameters $\{x_k\}_{k=1}^K$ to reinforce the linkage between $\mathbf{F}$, $\{\mathbf{m}_i\}_{i=1}^G$ and $\{\mathbf{w}_k\}_{k=1}^K$. Thus, the resulting problem formulation is defined as follows,

$$\mathcal{P}_0^{\text{hyb}}: \min_{\substack{\mathbf{F},\{\mathbf{m}_i\}_{i=1}^G,\\ \{\mathbf{w}_k\}_{k=1}^K,\\ \{x_k\}_{k=1}^K}} \quad \sum_{i=1}^G \|\mathbf{F}\mathbf{m}_i\|_2^2 + \beta \sum_{k=1}^K x_k \tag{4a}$$

$$\text{s.t.} \quad \frac{\left|\mathbf{w}_k^H \mathbf{H}_k \mathbf{F}\mathbf{m}_i\right|^2 + x_k}{\sum_{j\neq i}\left|\mathbf{w}_k^H \mathbf{H}_k \mathbf{F}\mathbf{m}_j\right|^2 + \sigma^2 \|\mathbf{w}_k\|_2^2} \geq \gamma_i, \tag{4b}$$

$$\|\mathbf{w}_k\|_2^2 = P_{\text{rx}}^{\max}, \tag{4c}$$

$$\|\mathbf{F}\|_{\text{F}}^2 = N_{\text{tx}}^{\text{RF}}, \tag{4d}$$

$$[\mathbf{F}]_{q,r} \in \mathcal{F}, \tag{4e}$$

$$x_k \geq 0, q \in \mathcal{Q}, r \in \mathcal{R}, \forall k \in \mathcal{G}_i, i \in \mathcal{I}. \tag{4f}$$

Each $x_k \in \mathbb{R}_+$ penalizes the objective function (with a sufficiently large β) whenever $x_k > 0$ needs to be added to the left-hand side numerator of (4b) for the QoS inequality to hold. Thus, an increment of $\sum_{i=1}^G \|\mathbf{F}\mathbf{m}_i\|_2^2$ will be prioritized instead of letting $\sum_{k=1}^K x_k$ augment. This regularization promotes more QoS inequalities to be satisfied by action of $\mathbf{F}$, $\{\mathbf{m}_i\}_{i=1}^G$ and $\{\mathbf{w}_k\}_{k=1}^K$. The slack parameters $\{x_k\}_{k=1}^K$ ensure that a feasible solution always exists as x_k will absorb any surplus that is required for (4b) to hold. In the following we optimize the three sets of parameters by separating $\mathcal{P}_0^{\text{hyb}}$ into 3 sub-problems $\mathcal{P}_1^{\text{hyb}}$, $\mathcal{P}_2^{\text{hyb}}$ and $\mathcal{P}_3^{\text{hyb}}$, which are sequentially and alternately solved.

Observation: Even with fully-digital precoders and single-antenna receivers (i.e., $\mathbf{F} = \mathbf{I}$, $\mathbf{w}_k = 1$), a feasible solution to (4) cannot always be guaranteed. This usually occurs when $N_{\text{tx}} < K$ (as in our case). As a consequence, $\mathcal{P}_1^{\text{hyb}}$, $\mathcal{P}_2^{\text{hyb}}$ or $\mathcal{P}_3^{\text{hyb}}$ may render infeasible, thus interrupting the optimization procedure. To prevent this, we include x_k to ensure the existence of a feasible solution (without raising infeasibility certificates), thereby guaranteeing the continuity of the sequential optimization process.

Observation: In contrast to adaptive hybrid precoding, where the architectures changes dynamically (i.e., some phase shifters activate/deactivate), in our case the fixed fully-connected architecture allows us to determine $\delta = 1/N_{\text{tx}}^{\text{RF}}$ from (4d). Thus, (4d) is removed in the sequel.

A. Optimization of $\mathbf{F}$

Assuming that $\{\mathbf{m}_i\}_{i=1}^G$ and $\{\mathbf{w}_k\}_{k=1}^K$ are known, we optimize over $\mathbf{F}$. Thus,

$$\mathcal{P}_1^{\text{hyb}}: \min_{\mathbf{F},\{x_k\}_{k=1}^K} \quad \sum_{i=1}^G \|\mathbf{F}\mathbf{m}_i\|_2^2 + \beta \sum_{k=1}^K x_k \tag{5a}$$

$$\text{s.t.} \quad \gamma_i \left(\sum_{j\neq i}\left|\mathbf{w}_k^H \mathbf{H}_k \mathbf{F}\mathbf{m}_j\right|^2 + \sigma^2 \|\mathbf{w}_k\|_2^2\right) - \left|\mathbf{w}_k^H \mathbf{H}_k \mathbf{F}\mathbf{m}_i\right|^2 \leq x_k, \tag{5b}$$

$$[\mathbf{F}]_{q,r} \in \mathcal{F}, \tag{5c}$$

$$x_k \geq 0, q \in \mathcal{Q}, r \in \mathcal{R}, \forall k \in \mathcal{G}_i, i \in \mathcal{I}. \tag{5d}$$

Notice that we can express $\mathbf{F}\mathbf{m}_i = \mathbf{J}_i \mathbf{f}$, where $\mathbf{J}_i = \mathbf{m}_i^T \otimes \mathbf{I}$ and $\mathbf{f} = \text{vec}(\mathbf{F})$. With this redefinition, (5) can be equivalently expressed as,

$$\mathcal{P}_1^{\text{hyb}}: \min_{\mathbf{f},\{x_k\}_{k=1}^K} \quad \sum_{i=1}^G \|\mathbf{J}_i \mathbf{f}\|_2^2 + \beta \sum_{k=1}^K x_k \tag{6a}$$

$$\text{s.t.} \quad \gamma_i \left(\sum_{j\neq i}\left|\mathbf{w}_k^H \mathbf{H}_k \mathbf{J}_j \mathbf{f}\right|^2 + \sigma^2 \|\mathbf{w}_k\|_2^2\right) - \left|\mathbf{w}_k^H \mathbf{H}_k \mathbf{J}_i \mathbf{f}\right|^2 \leq x_k, \tag{6b}$$

$$[\mathbf{f}]_n \in \mathcal{F}, \tag{6c}$$

$$x \geq 0, n \in \mathcal{N}, \forall k \in \mathcal{G}_i, i \in \mathcal{I}, \tag{6d}$$

where $\mathcal{N} = \{1, 2, \ldots, N_{\text{tx}}^{\text{RF}} N_{\text{tx}}\}$. Note that $\|\mathbf{J}_i \mathbf{f}\|_2^2 = \text{Tr}(\mathbf{R}_i \mathbf{D})$, with $\mathbf{R}_i = \mathbf{J}_i^H \mathbf{J}_i$ and $\mathbf{D} = \mathbf{f}\mathbf{f}^H$. Also, $[\mathbf{D}]_{n,n} = \delta$ since $[\mathbf{f}]_n \in \mathcal{F}$. Furthermore, since $\left|\mathbf{w}_k^H \mathbf{H}_k \mathbf{J}_i \mathbf{f}\right|^2 = \text{Tr}(\mathbf{V}_{i,k}\mathbf{D})$, with $\mathbf{V}_{i,k} = \mathbf{J}_i^H \mathbf{H}_k^H \mathbf{w}_k \mathbf{w}_k^H \mathbf{H}_k \mathbf{J}_i$, we can recast (6) in its SDP form as,

$$\mathcal{P}_{\text{SDP},1}^{\text{hyb}}: \min_{\mathbf{D},\{x_k\}_{k=1}^K} \quad \sum_{i=1}^G \text{Tr}(\mathbf{D}\mathbf{R}_i) + \beta \sum_{k=1}^K x_k \tag{7a}$$

$$\text{s.t.} \quad \text{Tr}\left(\mathbf{D}\left(\gamma_i \sum_{j\neq i} \mathbf{V}_{j,k} - \mathbf{V}_{i,k}\right)\right) + \sigma^2 \gamma_i \|\mathbf{w}_k\|_2^2 \leq x_k, \tag{7b}$$

$$[\mathbf{D}]_{n,n} = \delta, \tag{7c}$$

$$\text{rank}(\mathbf{D}) = 1, \tag{7d}$$

$$\mathbf{D} \succcurlyeq \mathbf{0}, \tag{7e}$$

$$x_k \geq 0, n \in \mathcal{N}, \forall k \in \mathcal{G}_i, i \in \mathcal{I}. \tag{7f}$$

The SDP program in (7) has a linear objective subject to affine constraints except for the non-convex constraint (7d), which imposes a rank-one condition on $\mathbf{D}$ (as it is originally obtained from $\mathbf{D} = \mathbf{f}\mathbf{f}^H$). Constraint (7e) restricts $\mathbf{D}$ to be Hermitian positive semidefinite. It is worth noticing that (6c) is the only constraint not strongly enforced in (7). Thus, while the constant-modulus requirement of (6c) is satisfied by (7c), its phase has been ignored. Nevertheless, the phase will be optimized through the following procedure [20].

Stage A_1: Notice that any element (n_1, n_2) of matrix $\mathbf{D}$ can be represented as $[\mathbf{D}]_{n_1,n_2} = [\mathbf{f}]_{n_1}[\mathbf{f}]_{n_2}^*$. Now, let us define a vector $\mathbf{u} \in \mathbb{C}^{N_{\text{tx}}^{\text{RF}} N_{\text{tx}} \times 1}$ such that $\|\mathbf{u}\|_2^2 = \mathbf{u}^H\mathbf{u} = 1$. As a consequence, we can express $[\mathbf{D}]_{n_1,n_2}$ in terms of $\mathbf{u}$, i.e., $[\mathbf{D}]_{n_1,n_2} = \left([\mathbf{f}]_{n_1}\mathbf{u}^T\right)\left([\mathbf{f}]_{n_2}^*\mathbf{u}^*\right)$. Assuming that $\mathbf{q}_n = [\mathbf{f}]_n\mathbf{u}$, $\mathbf{D}$ can be recast as $\mathbf{D} = \mathbf{Q}^T\mathbf{Q}^*$ with $\mathbf{Q} = \left[\mathbf{q}_1, \mathbf{q}_2, \ldots, \mathbf{q}_{N_{\text{tx}}^{\text{RF}} N_{\text{tx}}}\right]$.

Stage A_2: In (7), the only non-convex constraint is (7d). Thus, we define $\mathcal{P}_{\text{SDR},1}^{\text{hyb}}$ as the resultant SDR surrogate of (7) obtained upon dropping (7d). The solution returned by $\mathcal{P}_{\text{SDR},1}^{\text{hyb}}$ is denoted by $\widehat{\mathbf{D}}$. Then, via Cholesky matrix factorization we obtain $\widehat{\mathbf{D}} = \widehat{\mathbf{Q}}^T\widehat{\mathbf{Q}}^*$, where $\widehat{\mathbf{Q}} = \left[\widehat{\mathbf{q}}_1, \widehat{\mathbf{q}}_2, \ldots, \widehat{\mathbf{q}}_{N_{\text{tx}}^{\text{RF}} N_{\text{tx}}}\right]$. Although we have derived a relation that associates the unknown phase shifts $\widehat{\mathbf{f}}$ with the known vectors $\{\widehat{\mathbf{q}}_n\}_{n=1}^{N_{\text{tx}}^{\text{RF}} N_{\text{tx}}}$ (via $\widehat{\mathbf{q}}_n = \left[\widehat{\mathbf{f}}\right]_n \widehat{\mathbf{u}}$), the vector $\widehat{\mathbf{u}}$ also remains unknown. Moreover, the initial premise was that every $\widehat{\mathbf{q}}_n$ could be obtained from the same $\widehat{\mathbf{u}}$. However, this cannot be guaranteed as a solution $\left(\widehat{\mathbf{f}}, \widehat{\mathbf{u}}\right)$ for $\widehat{\mathbf{q}}_n = \left[\widehat{\mathbf{f}}\right]_n \widehat{\mathbf{u}}, \forall n \in \mathcal{N}$ may not exist. Thus, we aim at finding approximate $\widehat{\mathbf{f}}$ and $\widehat{\mathbf{u}}$, such that $\widehat{\mathbf{q}}_n \approx \left[\widehat{\mathbf{f}}\right]_n \widehat{\mathbf{u}}$, and whose error

is minimum in the 2-norm sense. Mathematically,

$$\mathcal{P}_{\mathrm{LS}}^{\mathrm{hyb}}: \quad \min_{\widehat{\mathbf{u}},[\widehat{\mathbf{f}}]_n} \quad \sum_{n=1}^{N_{\mathrm{tx}}^{\mathrm{RF}}N_{\mathrm{tx}}} \left\| \widehat{\mathbf{q}}_n - \left[\widehat{\mathbf{f}}\right]_n \widehat{\mathbf{u}} \right\|_2^2 \tag{8a}$$

$$\text{s.t.} \quad \|\widehat{\mathbf{u}}\|_2^2 = 1, \tag{8b}$$

$$\left[\widehat{\mathbf{f}}\right]_n \in \mathcal{F}, n \in \mathcal{N}. \tag{8c}$$

Stage A_3: Minimizing simultaneously over both $\widehat{\mathbf{q}}_n$ and $\widehat{\mathbf{u}}$ is challenging. If we assume that $\widehat{\mathbf{u}}$ is known such that (8b) is satisfied, then we are required to solve

$$\widetilde{\mathcal{P}}_{\mathrm{LS}}^{\mathrm{hyb}}: \quad \min_{[\widehat{\mathbf{f}}]_n} \quad \sum_{n=1}^{N_{\mathrm{tx}}^{\mathrm{RF}}N_{\mathrm{tx}}} \left\| \widehat{\mathbf{q}}_n - \left[\widehat{\mathbf{f}}\right]_n \widehat{\mathbf{u}} \right\|_2^2 \tag{9a}$$

$$\text{s.t.} \quad \left[\widehat{\mathbf{f}}\right]_n \in \mathcal{F}, n \in \mathcal{N} \tag{9b}$$

By expanding (9a), we realize that $\left\| \widehat{\mathbf{q}}_n - \left[\widehat{\mathbf{f}}\right]_n \widehat{\mathbf{u}} \right\|_2^2 = \widehat{\mathbf{q}}_n^H \widehat{\mathbf{q}}_n - 2\Re\mathfrak{e}\left(\left[\widehat{\mathbf{f}}\right]_n \widehat{\mathbf{q}}_n^H \widehat{\mathbf{u}} \right) + \left| \left[\widehat{\mathbf{f}}\right]_n \right|^2 \widehat{\mathbf{u}}^H \widehat{\mathbf{u}}$. Thus, (9) is equivalent to

$$\widetilde{\mathcal{P}}_{\mathrm{LS}}^{\mathrm{hyb}}: \quad \max_{[\widehat{\mathbf{f}}]_n} \quad \sum_{n=1}^{N_{\mathrm{tx}}^{\mathrm{RF}}N_{\mathrm{tx}}} \Re\mathfrak{e}\left(\left[\widehat{\mathbf{f}}\right]_n \widehat{\mathbf{q}}_n^H \widehat{\mathbf{u}} \right) \tag{10a}$$

$$\text{s.t.} \quad \left[\widehat{\mathbf{f}}\right]_n \in \mathcal{F}, n \in \mathcal{N}. \tag{10b}$$

Note that (10) can be decomposed into $N_{\mathrm{tx}}^{\mathrm{RF}}N_{\mathrm{tx}}$ independent sub-problems. Thus, since $z_n = \widehat{\mathbf{q}}_n^H \widehat{\mathbf{u}}$ is known, we need to select $[\mathbf{f}]_n$ such that the real part of (10a) is maximized. This is equivalent to choosing $\left[\widehat{\mathbf{f}}\right]_n \in \mathcal{F}$ with the closest phase to z_n^*. After finding $\widehat{\mathbf{f}}$, it can be reshaped in order to obtain $\widehat{\mathbf{F}}$. As shown in Algorithm 1, N_{rand} candidate vectors $\widehat{\mathbf{u}}$ are generated and the best-performing option is maintained.

B. Optimization of $\mathbf{m}_i$

We assume herein that $\mathbf{F}$ and $\{\mathbf{w}_k\}_{k=1}^K$ are known. Thus, the original problem in (4) collapses to

$$\mathcal{P}_2^{\mathrm{hyb}}: \min_{\substack{\{\mathbf{m}_i\}_{i=1}^G, \\ \{x_k\}_{k=1}^K}} \quad \sum_{i=1}^G \|\mathbf{F}\mathbf{m}_i\|_2^2 + \beta \sum_{k=1}^K x_k \tag{11a}$$

$$\text{s.t.} \quad \gamma_i \left(\sum_{j \neq i} \left| \mathbf{w}_k^H \mathbf{H}_k \mathbf{F} \mathbf{m}_j \right|^2 + \sigma^2 \|\mathbf{w}_k\|_2^2 \right) - \left| \mathbf{w}_k^H \mathbf{H}_k \mathbf{F} \mathbf{m}_i \right|^2 \leq x_k, \tag{11b}$$

$$x_k \geq 0, \forall k \in \mathcal{G}_i, i \in \mathcal{I}. \tag{11c}$$

The SDP equivalent formulation of (11) is expressed as

$$\mathcal{P}_{\mathrm{SDP},2}^{\mathrm{hyb}}: \min_{\substack{\{\mathbf{M}_i\}_{i=1}^G, \\ \{x_k\}_{k=1}^K}} \quad \sum_{i=1}^G \mathrm{Tr}\left(\mathbf{Y}\mathbf{M}_i\right) + \beta \sum_{k=1}^K x_k \tag{12a}$$

$$\text{s.t.} \quad \mathrm{Tr}\left(\mathbf{X}_k \left(\gamma_i \sum_{j \neq i} \mathbf{M}_j - \mathbf{M}_i \right) \right) + \sigma^2 \gamma_i \|\mathbf{w}_k\|_2^2 \leq x_k, \tag{12b}$$

$$\mathbf{M}_i \succcurlyeq \mathbf{0}, \tag{12c}$$

$$\mathrm{rank}\left(\mathbf{M}_i\right) = 1, \tag{12d}$$

$$x_k \geq 0, \forall k \in \mathcal{G}_i, i \in \mathcal{I}, \tag{12e}$$

where $\mathbf{Y} = \mathbf{F}^H\mathbf{F}$, $\mathbf{X}_k = \mathbf{F}^H\mathbf{H}_k^H\mathbf{w}_k\mathbf{w}_k^H\mathbf{H}_k\mathbf{F}$ and $\mathbf{M}_i = \mathbf{m}_i\mathbf{m}_i^H$. Similarly as before, (12) has a linear objective with affine constraints except for (12d). Thus, we define $\mathcal{P}_{\mathrm{SDR},2}^{\mathrm{hyb}}$ as the SDR surrogate of (12), where (12d) is neglected.

C. Optimization of $\mathbf{w}_k$

Now, we assume that $\mathbf{F}$ and $\{\mathbf{m}_i\}_{i=1}^G$ are given. Therefore, we optimize over $\{\mathbf{w}_k\}_{k=1}^K$ as shown in (13)

$$\mathcal{P}_3^{\mathrm{hyb}}: \min_{\substack{\{\mathbf{w}_k\}_{k=1}^K, \\ \{x_k\}_{k=1}^K}} \quad \sum_{k=1}^K x_k \tag{13a}$$

$$\text{s.t.} \quad \gamma_i \left(\sum_{j \neq i} \left| \mathbf{w}_k^H \mathbf{H}_k \mathbf{F} \mathbf{m}_j \right|^2 + \sigma^2 \|\mathbf{w}_k\|_2^2 \right) - \left| \mathbf{w}_k^H \mathbf{H}_k \mathbf{F} \mathbf{m}_i \right|^2 \leq x_k, \tag{13b}$$

$$\|\mathbf{w}_k\|_2^2 = P_{\mathrm{rx}}^{\max}, \tag{13c}$$

$$x_k \geq 0, \forall k \in \mathcal{G}_i, i \in \mathcal{I}, \tag{13d}$$

In SDP form, (13) can be recast as

$$\mathcal{P}_{\mathrm{SDP},3}^{\mathrm{hyb}}: \min_{\substack{\{\mathbf{W}_k\}_{k=1}^K, \\ \{x_k\}_{k=1}^K}} \quad \sum_{k=1}^K x_k \tag{14a}$$

$$\text{s.t.} \quad \mathrm{Tr}\left(\mathbf{W}_k \left(\gamma_i \sum_{j \neq i} \mathbf{Z}_{k,j} - \mathbf{Z}_{k,i} \right) \right) + \sigma^2 \gamma_i \mathrm{Tr}\left(\mathbf{W}_k\right) \leq x_k, \tag{14b}$$

$$\mathrm{Tr}\left(\mathbf{W}_k\right) = P_{\mathrm{rx}}^{\max}, \tag{14c}$$

$$\mathbf{W}_k \succcurlyeq \mathbf{0}, \tag{14d}$$

$$\mathrm{rank}\left(\mathbf{W}_k\right) = 1, \tag{14e}$$

$$x_k \geq 0, \forall k \in \mathcal{G}_i, i \in \mathcal{I}, \tag{14f}$$

where $\mathbf{W}_k = \mathbf{w}_k\mathbf{w}_k^H$ and $\mathbf{Z}_{k,i} = \mathbf{H}_k\mathbf{F}\mathbf{m}_i\mathbf{m}_i^H\mathbf{F}^H\mathbf{H}_k^H$. Now, we define $\mathcal{P}_{\mathrm{SDR},3}^{\mathrm{hyb}}$ as (14) without the non-convex constraint (14e). Furthermore, since the optimization of $\mathbf{W}_k$ only affects SINR_k, then $\mathcal{P}_{\mathrm{SDR},3}^{\mathrm{hyb}}$ can be split into K parallel sub-problems $\mathcal{P}_{\mathrm{SDR},3,k}^{\mathrm{hyb}}$. For completeness, we summarize our proposed scheme in Algorithm 1 with more implementation details. Note that $\mathcal{P}_{\mathrm{SDR},1}^{\mathrm{hyb}}$, $\mathcal{P}_{\mathrm{SDR},2}^{\mathrm{hyb}}$ and $\mathcal{P}_{\mathrm{SDR},3}^{\mathrm{hyb}}$ can be recast as linear programs and can therefore be efficiently solved in polynomial time by numerical solvers. In our case, we employed `CVX` and `SDPT3`. In Algorithm 1, $g^{(t)}$ computes the total transmit power, whereas $\mathcal{K}^{(t)}$ counts the number of users whose QoS requirement has been satisfied at iteration t. In the initialization stage, every $\mathbf{w}_k$ is set in omnidirectional reception mode, i.e., only one antenna is active. Similarly, every multicast precoder $\mathbf{m}_i$ is in omnidirectional mode. Then, $\mathbf{F}$, $\{\mathbf{m}_i\}_{i=1}^G$ and $\{\mathbf{w}_k\}_{k=1}^K$ are alternately optimized for a number of iterations N_{iter}. At each iteration, the SDR-based solutions are used to generate N_{rand} potentially befitting solutions.

V. Simulation Results

To evaluate our proposed design, we consider the geometric channel model with $M_p = 8$ propagation paths between the transmitter and each user. The maximum receive power for all the users is $P_{\mathrm{rx}}^{\max} = 10$ dBm, and $\mathcal{F}$ consists of $L = 8$ different phase shifts equally spaced in a circle with radius $\sqrt{\delta}$. The regularization hyper-parameter in (4) is defined as $\beta = G^3 N_{\mathrm{tx}}^{\mathrm{RF}} N_{\mathrm{tx}} N_{\mathrm{rx}}$. In the following scenarios, we compare the performance of fully-digital and hybrid precoders in terms of the number of decoded packets N_{packets} and the required transmit power P_{tx} for several configurations of γ_i, $N_{\mathrm{tx}}^{\mathrm{RF}}$, N_{tx},

Algorithm 1: Proposed Iterative Approach

Define

Let $g^{(t)} = \sum_{i=1}^{G} \left\| \mathbf{F}^{(t)} \mathbf{m}_i^{(t)} \right\|_2^2$ be the total transmit power.

Let $\mathcal{K}^{(t)}$ be the number of users that satisfy (5b) at iteration t.

Initialize

Set $\mathbf{w}_k^{(0)} \leftarrow [1\ \mathbf{0}]^T, \forall k \in \mathcal{K}$, $\mathbf{m}_i^{(0)} \leftarrow [1\ \mathbf{0}]^T, \forall i \in \mathcal{I}$.

Set $\widetilde{\mathcal{K}} \leftarrow 0$, $\tilde{g} \leftarrow 10^5$, $t \leftarrow 1$.

Iterate

Set $C_1 \leftarrow 0$, $C_2 \leftarrow 0$ and $\{C_{3,k}\}_{k=1}^{K} \leftarrow 0$.

Optimize $\mathbf{F}$:

Solve $\mathcal{P}_{\mathrm{SDR},1}^{\mathrm{hyb}}$ to obtain $\mathbf{D}^{(t)}$.

repeat

Generate $\mathbf{u}$ with uniform distribution in the sphere $\|\mathbf{u}\|_2^2 = 1$.

Solve $\widetilde{\mathcal{P}}_{\mathrm{LS}}^{\mathrm{hyb}}$ and compute $\mathbf{F}^{(t)}$.

if $\mathcal{K}^{(t)} > \widetilde{\mathcal{K}}$ or $\left(\mathcal{K}^{(t)} = \widetilde{\mathcal{K}} \text{ and } g^{(t)} \leq \tilde{g}\right)$

Assign $\mathbf{F} \leftarrow \mathbf{F}^{(t)}$, $\tilde{g} \leftarrow g^{(t)}$, $\widetilde{\mathcal{K}} \leftarrow \mathcal{K}^{(t)}$.

end

Increase the counter C_1, $C_1 \leftarrow C_1 + 1$.

while $C_1 \leq N_{\mathrm{rand}}$

Optimize $\mathbf{m}_i$:

Solve $\mathcal{P}_{\mathrm{SDR},2}^{\mathrm{hyb}}$ and obtain $\left\{\mathbf{M}_i^{(t)}\right\}_{i=1}^{G}$.

repeat

Generate $\widetilde{\mathbf{m}}_i^{(t)} \sim \mathcal{CN}\left(\mathbf{0}, \mathbf{M}_i^{(t)}\right), \forall i \in \mathcal{I}$.

if $\mathcal{K}^{(t)} > \widetilde{\mathcal{K}}$ or $\left(\mathcal{K}^{(t)} = \widetilde{\mathcal{K}} \text{ and } g^{(t)} \leq \tilde{g}\right)$

Assign $\{\mathbf{m}_i\}_{i=1}^{G} \leftarrow \left\{\mathbf{m}_i^{(t)}\right\}_{i=1}^{G}$, $\tilde{g} \leftarrow g^{(t)}$, $\widetilde{\mathcal{K}} \leftarrow \mathcal{K}^{(t)}$.

end

Increase the counter C_2, $C_2 \leftarrow C_2 + 1$.

while $C_2 \leq N_{\mathrm{rand}}$

Optimize $\mathbf{w}_k$:

Solve $\mathcal{P}_{\mathrm{SDR},3}^{\mathrm{hyb}}$ and obtain $\left\{\mathbf{W}_k^{(t)}\right\}_{k=1}^{K}$.

repeat for each k

Generate $\mathbf{w}_k^{(t)} \leftarrow \mathbf{W}_k^{(t)} \mathbf{v}_k, \forall k \in \mathcal{K}$ with $\mathbf{v}_k$ uniformly distributed in the sphere $\|\mathbf{v}_k\|_2^2 = 1$.

if $\mathcal{K}^{(t)} > \widetilde{\mathcal{K}}$ or $\left(\mathcal{K}^{(t)} = \widetilde{\mathcal{K}} \text{ and } g^{(t)} \leq \tilde{g}\right)$

Assign $\mathbf{w}_k \leftarrow \mathbf{w}_k^{(t)}$, $\tilde{g} \leftarrow g^{(t)}$, $\widetilde{\mathcal{K}} \leftarrow \mathcal{K}^{(t)}$

end

Increase the counter $C_{3,k}$, $C_{3,k} \leftarrow C_{3,k} + 1$

while $C_{3,k} \leq \lfloor N_{\mathrm{rand}}/K \rfloor$

Until $t > N_{\mathrm{iter}}$

N_{rx}, N_{rand} and N_{iter}. In the sequel, we consider $K = 60$ users evenly distributed among $G = 4$ multicast groups. All groups have the same SINR requirements, i.e., $\gamma = \gamma_i\,(\forall i \in \mathcal{I})$ and $\sigma^2 = 10$ dBm. All the numerical results show the average over 100 channel realizations.

1) Impact of $N_{\mathrm{tx}}^{\mathrm{RF}}$: The objective of this experiment is to evaluate the performance of the hybrid precoder with respect to its fully-digital counterpart, when $N_{\mathrm{tx}}^{\mathrm{RF}} = \{5, 6, 7, 8, 9, 10, 11\}$ is varied for different $\gamma = \{4, 6, 8\}$. We assume that $N_{\mathrm{tx}} = 12$, $N_{\mathrm{rx}} = 2$, $N_{\mathrm{iter}} = 3$ and $N_{\mathrm{rand}} = 500$. The results for this setting are shown in Fig. 1, where the hybrid precoder is denoted by HY and the fully-digital by FD. We observe that for any specific γ, the number of decoded packets N_{packets} augments when N_{RF} increases. By observing N_{packets}, it is evident that it suffices to only have $N_{\mathrm{tx}}^{\mathrm{RF}} = 8$ to yield a similar performance as that of the fully-digital precoder (which requires $N_{\mathrm{tx}}^{\mathrm{RF}} = 12$). However, due to the reduced

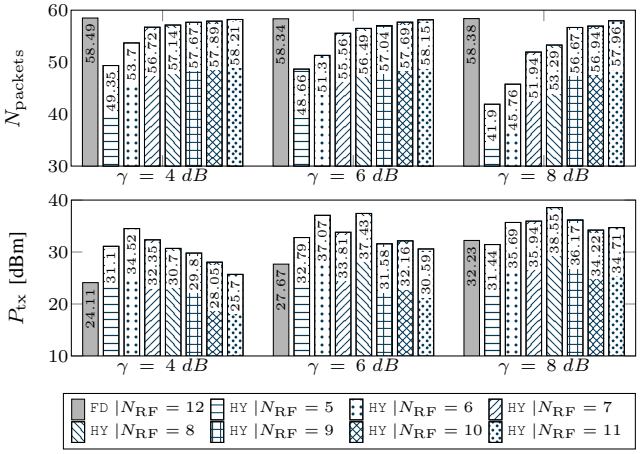

Figure 1: Evaluation of the number of decoded packets and transmit power for $N_{\mathrm{tx}} = 12$ when γ and $N_{\mathrm{tx}}^{\mathrm{RF}}$ are varied.

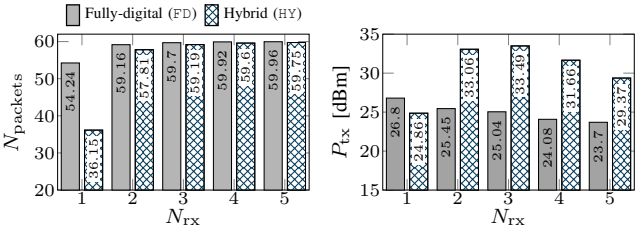

Figure 2: Evaluation of the number of decoded packets and transmit power when N_{rx} is varied.

number of RF chains in the hybrid precoder, interference management becomes more challenging at the transmitter. Thus, we observe that in general, the hybrid precoder requires more transmit power P_{tx} to attain a similar performance. As more RF chains are added, the required transmit power decreases as interference can be more effectively mitigated. It is also worth noting an apparently abnormal behavior that, for instance, occurs when $\gamma = 6$ dB for $N_{\mathrm{tx}}^{\mathrm{RF}} = 7$ and $N_{\mathrm{tx}}^{\mathrm{RF}} = 8$. Observe that P_{tx} is higher when $N_{\mathrm{tx}}^{\mathrm{RF}} = 8$ than when $N_{\mathrm{tx}}^{\mathrm{RF}} = 7$. However, N_{packets} is larger by (approximately) one unit when $N_{\mathrm{tx}}^{\mathrm{RF}} = 8$. The reason is that some users experiencing high interference cannot be served when $N_{\mathrm{tx}}^{\mathrm{RF}} = 7$. Nevertheless, when an additional RF chain is incorporated, the number of degrees of freedom increases and oftentimes a subset of the uncatered users can be served at the expense of boosting the transmit power. The maximum value of N_{packets} is 60 as we consider one transmitted message per user. Due to the highly interfering scenario we have considered, not even the fully-digital precoder with $N_{\mathrm{rand}} = 500$ can guarantee 100% successful reception.

2) Impact of N_{rx}: The objective of this configuration is to observe the performance improvement of N_{packets} and the importance of the multi-antenna architecture at the receiver. We consider that $\gamma = 5$ dB and $N_{\mathrm{iter}} = 4$. Since we vary N_{rx}, the number of randomization N_{rand} should scale with the dimensionality of $\mathbf{H}_k, \mathbf{F}, \{\mathbf{m}_i\}_{i=1}^{G}, \{\mathbf{w}_k\}_{k=1}^{K}$. Thus, for this scenario, we select $N_{\mathrm{rand}} = 400 + 300\,(N_{\mathrm{tx}} + N_{\mathrm{rx}} - 11)$ with $N_{\mathrm{tx}} = 12$ and $N_{\mathrm{rx}} = \{1, 2, 3, 4, 5\}$. For the hybrid precoder,

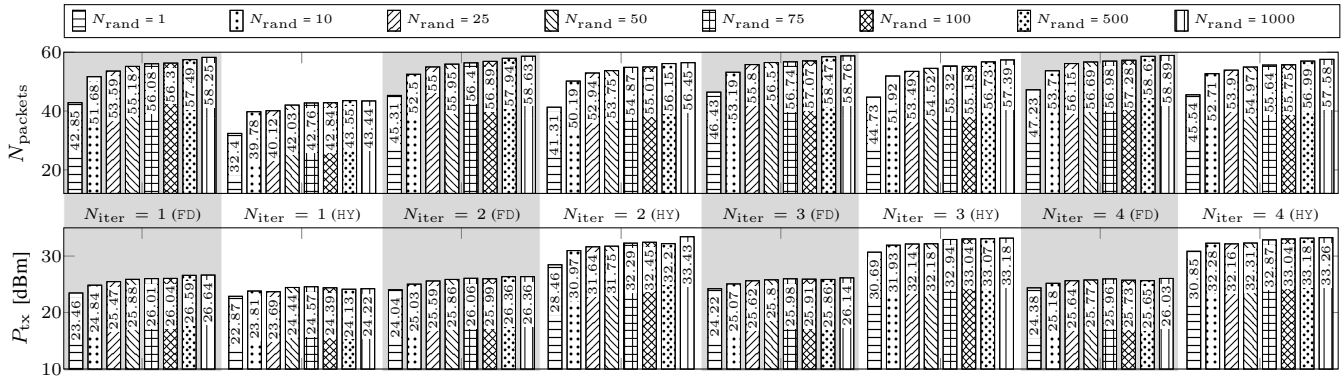

Figure 3: Evaluation of the number of decoded packets and transmit power for $N_{\text{tx}} = 12$ when N_{iter} and N_{rand} are varied.

we assume that $N_{\text{RF}} = 8$. On the other hand, for the fully-digital version $N_{\text{tx}} = N_{\text{tx}}^{\text{RF}}$. The results in Fig. 2 demonstrate that, with only $N_{\text{rx}} = 2$ antennas at the receiver, it is possible to mitigate the interference and improve N_{packets} considerably. The gain is more noticeable for the hybrid precoder as N_{packets} improves by 60%. For the fully-digital precoder, there is also a moderate gain of 9%. Moreover, the average transmit power per successfully received message improves by 12.9% and 16.8% for the digital and hybrid precoders, respectively. It is evident from this scenario that, at the transmitter side, N_{packets} cannot be further improved when the receivers operate with a single omnidirectional antenna (i.e., $N_{\text{rx}} = 1$), as interference and desired signals are equally amplified. However, when $N_{\text{rx}} = 2$, the receivers can enforce limited selectivity by rejecting the unwanted interference to a certain extent, thereby improving N_{packets}. Finally, we observe that N_{packets} for both types of precoders are very similar when $N_{\text{rx}} \geq 2$ although the consumed power differs in $6 - 8$ dBm.

3) Impact of N_{rand} and N_{iter}: The objective of this setting is to analyze the performance sensitivity of the fully-digital and hybrid precoders to the selection of N_{rand} and N_{iter}. To this purpose, we consider $N_{\text{rx}} = 2$ and $\gamma = 5$ dB. For the fully-digital precoder, we assume that $N_{\text{tx}} = N_{\text{tx}}^{\text{RF}} = 12$. On the other hand, the hybrid precoder is endowed with $N_{\text{tx}}^{\text{RF}} = 8$ and $N_{\text{tx}} = 12$. We evaluate the performance variation when $N_{\text{iter}} = \{1, 2, 3, 4, 5\}$ and $N_{\text{rand}} = \{1, 10, 25, 50, 75, 100, 500, 1000\}$. The results in terms of N_{packets} and P_{tx} for both types of precoder are shown in Fig. 3. We observe that in the fully-digital precoder case, N_{rand} is more influential than N_{iter} since N_{packets} improves noticeably when N_{rand} is augmented, whereas a small improvement can be observed between the cases $N_{\text{iter}} = 1$ and $N_{\text{iter}} = 2$. Conversely, for the hybrid precoder, N_{iter} promotes performance gap reduction with respect to the fully-digital implementation. The fully-digital precoder converges faster since only $\{\mathbf{m}_i\}_{i=1}^{G}$ and $\{\mathbf{w}_k\}_{k=1}^{K}$ are optimized. In the hybrid precoder case, we need to design $\mathbf{F}$, $\{\mathbf{m}_i\}_{i=1}^{G}$ and $\{\mathbf{w}_k\}_{k=1}^{K}$ with even more limiting constraints (finite-resolution constant-modulus phase shifts), thus requiring more iterations to obtain an stable solution.

Generation of co-channel users: In order to gain more understanding on the kind of scenario we are dealing with, we show in Fig. 4 the histogram of channel correlations for *(i)* users that belong to the same group (intra-cluster) and *(ii)* users that belong to different groups (inter-cluster). In the first case, the average channel correlation is 0.24 whereas in the second case is 0.10. The mean angles of departure $\{\bar{\theta}_i^{\text{AoD}}\}_{i=1}^{G}$ for the multicast groups are distributed in the range $[-80°, 80°]$ with angular spread $\sigma_{\text{AoD}} = 30°$. The mean angles of arrival $\{\bar{\theta}_k^{\text{AoA}}\}_{k=1}^{K}$ for each receiver are uniformly distributed in the range $[-360°, 360°]$ with angular spread of $\sigma_{\text{AoA}} = 60°$. Thus, for a given user k' that belongs to group $G_{i'}$, the paths will have angles of departure and arrival in the ranges $\bar{\theta}_{i'}^{\text{AoD}} \pm \sigma_{\text{AoD}}$ and $\bar{\theta}_{i'}^{\text{AoA}} \pm \sigma_{\text{AoD}}$, respectively. To shed more light on this aspect, Fig. 5 shows a particular channel realization when $N_{\text{tx}} = 8$, $N_{\text{tx}}^{\text{RF}} = 4$, $N_{\text{rx}} = 2$, $K = 4$, $G = 4$, $\bar{\theta}_1^{\text{AoD}} = -60°$, $\bar{\theta}_2^{\text{AoD}} = -20°$, $\bar{\theta}_3^{\text{AoD}} = 20°$, $\bar{\theta}_4^{\text{AoD}} = 60°$ and $\sigma_{\text{AoD}} = 5°$. Due to existence of multiple paths, the transmit and receive beams are not fully aligned as expected in line-of-sight scenarios. Thus, each of the users orients their receive power in specific directions that are coherent with the most meaningful beams of the transmitter beam-pattern. Also, note that secondary lobes at the receiver have been shaped to minimize amplification of interfering signals.

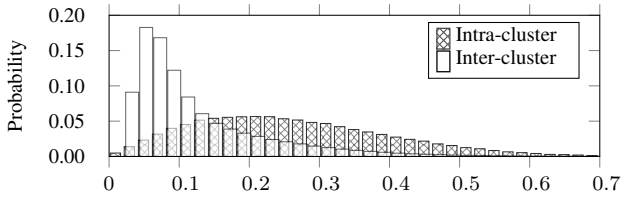

Figure 4: Evaluation of the number of decoded packets and transmit power for $N_{\text{tx}} = 12$ when N_{iter} and N_{rand} are varied.

VI. Discussion

Co-channel users: We have considered a very challenging scenario throughout our simulations in order to examine the operational limits of our design. We can observe from Fig. 4 that intra-cluster and inter-cluster users are not easily separable as a subset of them have similar channel correlations. In our scenarios, this is determined by the selection of $\{\bar{\theta}_i^{\text{AoD}}\}_{i=1}^{G}$, $\{\bar{\theta}_k^{\text{AoA}}\}_{k=1}^{K}$, σ_{AoD} and σ_{AoA}. We notice that highly correlated

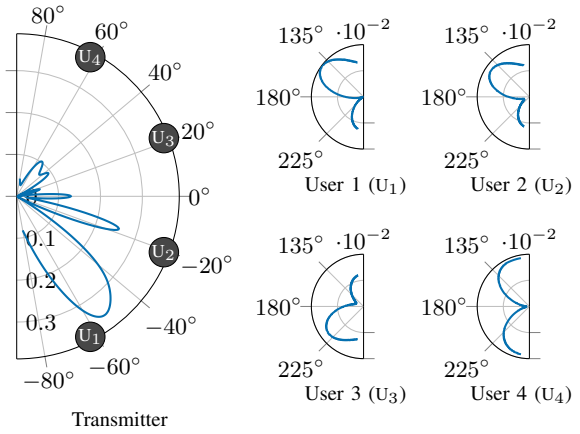

Figure 5: Radiation patterns

users (co-located users) belonging to different groups were the most challenging to cater, specifically for the hybrid precoder whose beamforming flexibility is limited.

Hybrid precoder design: Different from the majority of works in hybrid precoding (either multi-user or multicast), the proposed design has no knowledge of the optimal fully-digital precoder (as in e.g., [19]). Thus, our proposed design is not obtained as an approximation of the optimal fully-digital implementation. Without an optimal reference, the design becomes more challenging.

Initial points: We have considered naive initializations for the optimization parameters. We leave for future work the exploitation of AoA/AoD to infer more befitting initializations and thus improve the performance of the scheme.

Fully-digital precoder design: The fully-digital implementation is obtained by assigning $\mathbf{F} = \mathbf{I}$ and then optimizing alternately over $\{\mathbf{m}_i\}_{i=1}^{G}$ and $\{\mathbf{w}_k\}_{k=1}^{K}$.

Algorithm convergence: There is no theoretical evidence supporting the convergence of Algorithm 1, essentially due to the non-convexity of the problem. However, the proposed scheme exhibits an stable behavior for both digital and hybrid precoders since the solutions do not vary significantly as N_{iter} and N_{rand} increase beyond a certain limit.

Computational complexity: Neglecting the complexity owing to randomization and obviating the insignificant complexity increase due to the inclusion of slack parameters, the computational complexity of the proposed scheme when $N_{\text{iter}} = 1$ is $\mathcal{O}\left(\left(N_{\text{tx}}^{\text{RF}} N_{\text{tx}}\right)^6 + K\left(N_{\text{tx}}^{\text{RF}} N_{\text{tx}}\right)^2\right) + \mathcal{O}\left(G^3\left(N_{\text{tx}}^{\text{RF}}\right)^6 + KG\left(N_{\text{tx}}^{\text{RF}}\right)^2\right) + \mathcal{O}\left(K\left(N_{\text{rx}}\right)^6 + K\left(N_{\text{rx}}\right)^4\right)$.

VII. Conclusion

In this paper, we investigated the optimization of multi-group multicast hybrid precoders in mmWave systems. Our proposed solution is based on the alternating optimization, semidefinite relaxation and Cholesky matrix factorization, where the digital precoder, analog phase shifts, and receive combiners are optimized sequentially in an iterative manner. Furthermore, our formulation allows the employment of an arbitrary number of phase shifts. It was corroborated through extensive simulations that the hybrid precoder can indeed attain similar performance as its fully-digital counterpart, even in very challenging scenarios with high inter-cluster user correlation. In addition, we demonstrate that having receivers with two antennas suffices to improve the number of decoded packets. Thus, our proposed design achieves up to 60% gain.

References

[1] G. H. Sim and J. Widmer, "Finite Horizon Opportunistic Multicast Beamforming," *IEEE Transactions on Wireless Communications*, vol. 16, no. 3, March 2017.

[2] S. Naribole and E. Knightly, "Scalable Multicast in Highly-Directional 60-GHz WLANs," *IEEE/ACM Transactions on Networking*, vol. 25, no. 5, pp. 2844–2857, October 2017.

[3] H. Park, S. Park, T. Song, and S. Pack, "An Incremental Multicast Grouping Scheme for mmWave Networks with Directional Antennas," *IEEE Communications Letters*, vol. 17, no. 3, pp. 616–619, March 2013.

[4] N. D. Sidiropoulos, T. N. Davidson, and Z. Luo, "Transmit Beamforming for Physical-Layer Multicasting," *IEEE Transactions on Signal Processing*, vol. 54, no. 6, pp. 2239–2251, June 2006.

[5] M. X. Goemans and D. P. Williamson, "Improved Approximation Algorithms for Maximum Cut and Satisfiability Problem Using Semi-Definite Programming," *Journal of the Association for Computing Machinery*, vol. 42, no. 6, pp. 1115–1145, November 1995.

[6] E. Karipidis, N. D. Sidiropoulos, and Z. Luo, "Quality of Service and Max-Min Fair Transmit Beamforming to Multiple Cochannel Multicast Groups," *IEEE Transactions on Signal Processing*, vol. 56, no. 3, pp. 1268–1279, March 2008.

[7] E. Karipidis, N. D. Sidiropoulos, and Z. Q. Luo, "Transmit Beamforming of Multiple Co-Channel Multicast Group," in *IEEE CAMSAP*, December 2005, pp. 109–112.

[8] N. Bornhorst and M. Pesavento, "An Iterative Convex Approximation Approach for Transmit Beamforming in Multi-Group Multicasting," in *IEEE SPAWC*, June 2011, pp. 426–430.

[9] L. Tran, M. F. Hanif, and M. Juntti, "A Conic Quadratic Programming Approach to Physical Layer Multicasting for Large-Scale Antenna Arrays," *IEEE Sig. Proc. Lett.*, vol. 21, no. 1, pp. 114–117, January 2014.

[10] O. T. Demir and T. E. Tuncer, "Multi-Group Multicast Beamforming for Simultaneous Wireless Information and Power Transfer," in *EUSIPCO*, August 2015, pp. 1356–1360.

[11] A. Schad and M. Pesavento, "Max-min Fair Transmit Beamforming for Multi-Group Multicasting," in *WSA*, March 2012, pp. 115–118.

[12] D. Christopoulos, S. Chatzinotas, and B. Ottersten, "Weighted Fair Multicast Multigroup Beamforming Under Per-antenna Power Constraints," *IEEE Transaction on Signal Processing*, vol. 62, no. 19, pp. 5132–5142, October 2014.

[13] M. Sadeghi, E. Björnson, E. G. Larsson, C. Yuen, and T. L. Marzetta, "Max-Min Fair Transmit Precoding for Multi-Group Multicasting in Massive MIMO," *IEEE Transactions on Wireless Communications*, vol. 17, no. 2, pp. 1358–1373, February 2018.

[14] M. Dai and B. Clerckx, "Hybrid Precoding for Physical Layer Multicasting," *IEEE Communication Letters*, vol. 20, no. 2, pp. 228–231, February 2016.

[15] M. Sadeghi, L. Sanguinetti, and C. Yuen, "Hybrid Precoding for Multi-Group Physical Layer Multicasting," in *EW*, May 2018, pp. 1–6.

[16] J. Huang, Z. Cheng, E. Chen, and M. Tao, "Low-Complexity Hybrid Analog/Digital Beamforming for Multicast Transmission in mmWave Systems," in *IEEE ICC*, May 2017, pp. 1–6.

[17] O. T. Demir and T. E. Tuncer, "Antenna Selection and Hybrid Beamforming for Simultaneous Wireless Information and Power Transfer in Multi-Group Multicasting Systems," *IEEE Transactions on Wireless Communications*, vol. 15, no. 10, pp. 6948–6962, October 2016.

[18] A. Alkhateeb, G. Leus, and R. W. Heath, "Limited Feedback Hybrid Precoding for Multi-User Millimeter Wave Systems," *IEEE Transaction on Wireless Communications*, vol. 14, no. 11, pp. 6481–6494, Nov. 2015.

[19] X. Yu, J. C. Shen, J. Zhang, and K. B. Letaief, "Hybrid precoding design in millimeter wave mimo systems: An alternating minimization approach," in *IEEE GLOBECOM*, December 2015, pp. 1–6.

[20] W. K. Ma, P. C. Ching, and Z. Ding, "Semidefinite Relaxation Based Multiuser Detection for M-Ary PSK Multiuser Systems," *IEEE Transactions on Signal Processing*, vol. 52, no. 10, pp. 2862–2872, Oct. 2004.

C

PUBLICATION III.
FAIRNESS-AWARE HYBRID PRECODING FOR MMWAVE NOMA UNICAST/MULTICAST TRANSMISSIONS IN INDUSTRIAL IOT

Fairness-Aware Hybrid Precoding for mmWave NOMA Unicast/Multicast Transmissions in Industrial IoT

Luis F. Abanto-Leon, and Gek Hong (Allyson) Sim
Secure Mobile Networking (SEEMOO) Lab, Technische Universität Darmstadt, Germany
{labanto, asim}@seemoo.tu-darmstadt.de

***Abstract*—This paper investigates dual-layer non-orthogonally superimposed transmissions for industrial internet of things (IoT) millimeter-wave communications. Essentially, the overlayer is a ubiquitous multicast signal devised to serve all the devices in coverage with a common message, i.e., critical control packet. The underlayer is a composite signal that consists of private unicast messages. Due to safety implications, it is critical that all devices can decode the multicast information. To ensure this requirement, we jointly optimize the *hybrid precoder*, *analog combiners*, *power allocation*, and *fairness*. Specifically, we incorporate a power splitting constraint between the two overlaid signals and enforce supplementary per-device constraints to guarantee multicast fairness. Performance is evaluated in terms of the spectral efficiency, multicast fairness, and bit error rate, thus corroborating the feasibility of our proposed scheme.**

***Index Terms*—fairness, hybrid precoding, unicast, multicast, non-orthogonal multiple access, industrial IoT, mmWave.**

I. Introduction

In factories, multiple industrial devices (e.g., sensors, actuators, programmable logic devices, robotic arms) are inherently hyper-connected via hard-wiring to ensure redundancy, safety and precise coordination among the different phases of a manufacturing process. Nevertheless, wired connections hinder extensive automation deployment and constrain the mechanics of mobile robotics. Considering the rapid densification of industrial devices, wired connections become less appealing for factories of the future (i.e., Industry 4.0). Thus, wireless information transmission is a viable alternative for these environments. However, guaranteeing high-performance in terms of fairness, spectral efficiency and reliability is a challenging task.

A. Background and Motivation

Recent studies emphasize the importance of integrating non-orthogonal multiple access (NOMA) with the next-generation wireless technologies, e.g., massive multiple-input multiple-output (mMIMO) and millimeter-wave (mmWave) [1], [2]. NOMA can concurrently serve multiple devices within the same radio resource via non-orthogonal superposition of signals in power or code domain (e.g., [3], [4]), thus improving the spectral efficiency. By interweaving mMIMO, mmWave and NOMA, the expected next-generation networks throughput demands can be fulfilled while enabling simultaneous coexistence of heterogeneous connectivities. Owing to recent progress in mmWave technology, the mmWave spectrum is regarded as a plausible candidate to replace wires in industrial sectors. As a matter of fact, a measurement campaign reported that mmWave communications is feasible in industrial environments [5]. Furthermore, mmWave spectrum does not only provide high data rates (due to wide-band availability) but also characterizes for requiring antennas with a small footprint that can be easily embedded onto industrial devices and machinery.

Due to high fabrication costs, hardware complexity and power consumption, mmWave fully-digital precoders are unaffordable. In contrast, more power-efficient hybrid (digital-analog) precoders have emerged as a functional solution, where a high-dimensional analog precoder (consisting of a low-cost phase shifts network) is connected in cascade with a low-dimensional digital precoder [6], [7]. Essentially, mmWave communications has become a tangible technology due to advancements in hybrid architectures.

In this paper, we foresee an industrial scenario where a next generation Node B (gNodeB) transmits common multicast control beacons with superlative importance (e.g., critical safety packets, coordination messages) alongside less relevant private unicast information to each device (e.g., software or routine updates). To this aim, we propose the integration of NOMA, massive MIMO and mmWave. Specifically, NOMA is harnessed to transmit two overlaid signals (i.e., multicast and unicast) with different priorities. Further, mmWave provides wide-band spectrum that is efficiently exploited by massive MIMO. Thus, this integration can be leveraged to serve numerous industrial devices with a variety of data rate requirements while improving the spectral efficiency of the system.

B. Related Work

Power-domain NOMA (P-NOMA) is a comprehensive class of multiple-access technology capable of enhancing the spectrum utilization by means of superposing multiple signals with distinct power levels in the same time-frequency radio resource [8] (e.g., layered-division multiplexing (LDM) [9], multi-user superposition transmission (MUST) [3]). Although promising, the deployment of P-NOMA in practical systems has been consistently neglected due to the implementation complexity for successive interference cancellation (SIC). Nevertheless, due to novel advancements in signal processing and silicon technology, P-NOMA has reemerged in digital terrestrial television (e.g., [9]) and wireless mobile communications (e.g., [3], [4]) domains as a feasible recourse to meet the ever-increasing data rate demands. For instance, [10] leverages LDM to transmit superposed broadcast/unicast signals in single-frequency networks. The authors of [11] investigate energy efficiency in

MUST systems, where a base station with hybrid precoder conveys information to single-antenna receivers clustered in pairs. In [12], dual-layer LDM broadcast/unicast transmissions with quality of service constraints (QoS) is researched, considering a system with fully-digital precoders and single-antenna receivers. The authors in [13] investigate the design of overlaid LDM unicast/multicast precoders with the aim of maximizing the sum-capacity in a scenario with a hybrid transmitter and multi-antenna users. In [14], LDM broadcast/unicast transmissions with fully-digital transmitters and backhaul capacity constraints is investigated. In [15], [16], a similar idea to that described in [12] is proposed, where two data layers are superposed. While the multicast and unicast data streams are originated independently in [12], in [15], [16] the two data streams are interrelated. The unicast data for each user is split into common and private parts. Thus, one layer carries a common message consisting of the multicast information and the unicast common parts whereas the remaining layer conveys the unicast private messages only. Through this procedure, unicast inter-user interference (IUI) can be partially decoded and removed at each receiver (by exploiting the common unicast parts), thus further boosting the spectral efficiency.

Although mentioned in a few prior works, transmit power splitting among unicast and multicast signals is not considered in the formulations. For instance, in [12], explicit unicast and multicast QoS inequality constraints were imposed, thus removing the necessity of designing the power sharing between the signals. In [13], this aspect was not considered, causing undesirable power allocation and information irrecoverability at the receivers. On the other hand, multicast fairness at each receiver has neither been researched in non-orthogonally overlaid multicast/unicast transmissions.

C. Our Contributions

We study the spectral efficiency maximization problem in dual-layer LDM multicast/unicast systems, while considering hybrid precoders and analog combiners, subject to multicast fairness and transmit power constraints. To the best of our knowledge, *we are the first to prioritize the multicast signal (over unicast) in dual-layer LDM multicast/unicast transmissions by means of a power-splitting mechanism while guaranteeing multicast fairness at each receiver*. These features are highly relevant for industrial IoT wireless networks to ensure successful decoding of the control signals. Specifically, we consider power splitting to allow the multicast signal to be received with higher power (than the aggregate unicast signal), thus ensuring proper operation of the SIC decoder. Also, to guarantee ubiquitous multicast service (i.e., delivery of critical control packets), we incorporate fairness constraints that guarantee decodability of the multicast information at each receiver, thus promoting reliability. Further, we assume a hybrid precoder at the transmitter and analog combiners at each receiver, where finite-resolution phase shifts are adopted. We propose two solutions for the problem described. Our first scheme, PLDM−1, designs independently the multicast precoder from the unicast precoders In the second approach,

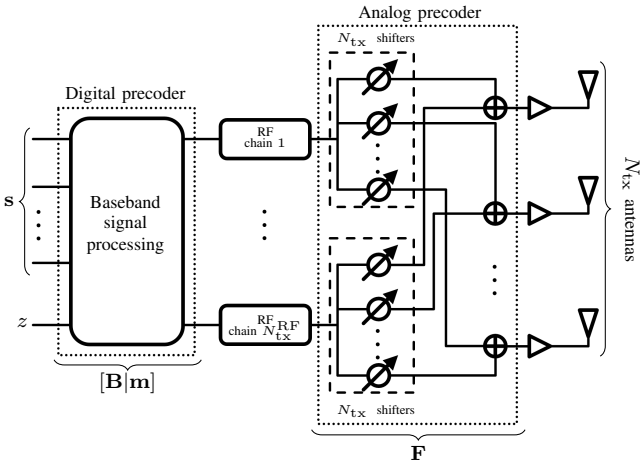

Figure 1: Dual-layer unicast-multicast LDM system

PLDM−2, the multicast precoder is obtained as a conic combination of the unicast precoding vectors. Thus, in PLDM−1 each type of signal (multicast or unicast) is transmitted through a different precoder with distinct spatial radiation pattern. Contrastingly, PLDM−2 repurposes the same precoder to multiplex the multicast and unicast signals with different powers. As a result, the two signals exhibit the the same spatial radiation pattern but with different power signatures.

Our paper is organized as follows. In Section II, we describe the system model whereas in Section III, we formulate the problem above mentioned. In Section IV, our proposed solution is described in detail. Section V is devoted for simulation results. Section VI discusses relevant implementation aspects while Section VII summarizes our conclusions.

II. System Model

We assume a mmWave system, where a gNodeB serves K devices in the downlink. The transmitted signal consists of two non-orthogonal layers that overlap with different power levels[1]. The *primary layer* is a multicast signal that transports a shared high-priority packet intended for all the devices in coverage. The *secondary layer* is a composite signal that contains multiple unicast messages, each intended for a distinct device. The gNodeB is equipped with a hybrid transmitter consisting of N_{tx} transmit antennas and $N_{\mathrm{tx}}^{\mathrm{RF}} \leq N_{\mathrm{tx}}$ radio frequency (RF) chains as shown in Fig. 1. Essentially, a hybrid precoder is formed by a high-dimensional network of low-resolution constant-modulus phase shifters (analog precoder) that perform elementary beamsteering at the RF frequency. Interconnected in cascade, a low-dimensional mixed-signal constituent (digital precoder) operates at the baseband frequency performing more sophisticated beamforming [6], [17]. Each receiver possesses a single RF chain with N_{rx} antennas, which enables analog receive beamforming. In addition, without loss of generality,

[1]We only discuss herein PLDM−1. By redefining $\mathbf{x} = \mathbf{FB}\,[\mathbf{I}|\mathbf{u}]\,[\mathbf{s}|z]^T$, PLDM−2 can be derived through a similar procedure. The elements of $\mathbf{u} \in \mathbb{R}^{K\times 1}$ represent the weights to be optimized. Thus, $\mathbf{m} = \mathbf{Bu}$.

we assume that $N_{\text{tx}}^{\text{RF}} = K$. The downlink signal is represented by $\mathbf{x} = \mathbf{F}[\mathbf{B}|\mathbf{m}][\mathbf{s}|z]^T$, where $\mathbf{F} = [\mathbf{f}_1, \mathbf{f}_2, \ldots, \mathbf{f}_K] \in \mathbb{C}^{N_{\text{tx}} \times K}$ is the analog precoder whereas $\mathbf{B} = [\mathbf{b}_1, \mathbf{b}_2, \ldots, \mathbf{b}_K] \in \mathbb{C}^{K \times K}$ and $\mathbf{m} \in \mathbb{C}^{K \times 1}$ represent the unicast and multicast digital precoders, respectively. Also, $\mathbf{s} = [s_1, s_2, \ldots, s_K]^T \in \mathbb{C}^{K \times 1}$ denotes the unicast data symbols for the K devices and $z \in \mathbb{C}$ represents the common multicast symbol, with $\mathbb{E}\{\mathbf{s}\mathbf{s}^H\} = \mathbf{I}$ and $\mathbb{E}\{z^H z\} = 1$. Under the assumption of narrowband flat-fading, the signal received by the k-th device is given by

$$y_k = \underbrace{\mathbf{w}_k^H \mathbf{H}_k \mathbf{F} \mathbf{m} z}_{\text{common multicast signal}} + \underbrace{\mathbf{w}_k^H \mathbf{H}_k \mathbf{F} \mathbf{b}_k s_k}_{\text{unicast signal for device } k} + \underbrace{\mathbf{w}_k^H \mathbf{H}_k \mathbf{F} \sum_{j \neq k} \mathbf{b}_j s_j}_{\text{interference at device } k} + \underbrace{\mathbf{w}_k^H \mathbf{n}_k}_{\text{noise}}, \tag{1}$$

where $\mathbf{w}_k \in \mathbb{C}^{N_{\text{rx}} \times 1}$ represents the analog combiner of the k-th device, $\mathbf{H}_k \in \mathbb{C}^{N_{\text{rx}} \times N_{\text{tx}}}$ denotes the downlink channel between the gNodeB and the k-th device, whereas $\mathbf{n}_k \sim \mathcal{CN}(\mathbf{0}, \sigma^2 \mathbf{I})$ denotes additive white Gaussian noise. At each receiver, the multicast symbol is decoded first by treating the aggregate unicast signals as interference. Subsequently, the multicast signal is reconstructed and then subtracted from y_k (by employing the decoded multicast symbol and the channel $\mathbf{H}_k$). As a consequence, the remaining byproduct consists solely of unicast components and noise, from where each receiver k can decode its intended symbol s_k. Thus, the signal–to–interference–plus–noise ratio (SINR) of the multicast and unicast signals are respectively defined as

$$\tilde{\gamma}_k = \frac{\left|\mathbf{w}_k^H \mathbf{H}_k \mathbf{F} \mathbf{m}\right|^2}{\sum_j \left|\mathbf{w}_k^H \mathbf{H}_k \mathbf{F} \mathbf{b}_j\right|^2 + \sigma^2 \left\|\mathbf{w}_k\right\|_2^2} \tag{2}$$

$$\gamma_k = \frac{\left|\mathbf{w}_k^H \mathbf{H}_k \mathbf{F} \mathbf{b}_k\right|^2}{\sum_{j \neq k} \left|\mathbf{w}_k^H \mathbf{H}_k \mathbf{F} \mathbf{b}_j\right|^2 + \sigma^2 \left\|\mathbf{w}_k\right\|_2^2}. \tag{3}$$

III. Problem Formulation

Aiming at maximizing the aggregate multicast and unicast spectral efficiency, the optimization problem is formulated as

$$\mathcal{P}: \max_{\substack{\{\mathbf{w}_k\}_{k=1}^K, \\ \{\mathbf{f}_k\}_{k=1}^K, \\ \{\mathbf{b}_k\}_{k=1}^K, \mathbf{m}, \Delta}} \quad \sum_k \log_2(1 + \tilde{\gamma}_k) + \log_2(1 + \gamma_k) - C\Delta \tag{4a}$$

$$\text{s.t.} \quad |\tilde{\gamma}_k - \gamma_{\min}| \leq \Delta, \forall k \in \mathcal{K}, \tag{4b}$$

$$\tilde{\gamma}_1 \geq \tilde{\gamma}_2 \geq \cdots \geq \tilde{\gamma}_K \geq \tilde{\gamma}_1, \tag{4c}$$

$$\|\mathbf{F}\mathbf{m}\|_2^2 / \sum_k \|\mathbf{F}\mathbf{b}_k\|_2^2 \geq \beta, \tag{4d}$$

$$\|\mathbf{F}\mathbf{m}\|_2^2 + \sum_k \|\mathbf{F}\mathbf{b}_k\|_2^2 \leq P_{\text{tx}}, \tag{4e}$$

$$[\mathbf{F}]_{q,r} \in \mathcal{F}, q \in \mathcal{Q}, r \in \mathcal{R}, \tag{4f}$$

$$[\mathbf{w}_k]_n \in \mathcal{W}, n \in \mathcal{N}, \forall k \in \mathcal{K}, \tag{4g}$$

$$\Delta \geq 0, \tag{4h}$$

where (4b) confines the multicast SINRs to a narrow interval around a predefined threshold $\gamma_{\min}$ (with deviation Δ), thus ensuring the control packet decoding. Constraint (4c) binds all the multicast SINRs together in order to promote fairness. Constraint (4d) splits the power among multicast and unicast signals (in the ratio of $\beta \geq 1$ to 1) with the purpose of enforcing higher priority on the multicast information and securing SIC decoding. Constraint (4e) restricts the transmit power to P_{tx} while (4f)-(4g) enforce the limitations of analog beamforming, i.e., only a small number of L_{tx} (at the analog precoder) and L_{rx} (at the analog combiners) constant-modulus phase shifts are allowed. Finally, (4g) enforces positiveness on Δ. Under sufficient power P_{tx} (and large positive C) then $\Delta \to 0$, since (4b) can be satisfied with equality. However, when P_{tx} is insufficient, Δ increases such that every $\tilde{\gamma}_k$ is at most at Δ from $\gamma_{\min}$ while simultaneously enforcing fairness via (4c). Every element $[\mathbf{F}]_{q,r}$ of the analog precoder is constrained to a feasible set $\mathcal{F} = \left\{1/\sqrt{N_{\text{tx}}}, \ldots, 1/\sqrt{N_{\text{tx}}} e^{j\frac{2\pi(L_{\text{tx}}-1)}{L_{\text{tx}}}}\right\}$, where $q \in \mathcal{Q} = \{1, \ldots, N_{\text{tx}}\}$ and $r \in \mathcal{R} = \{1, \ldots, N_{\text{tx}}^{\text{RF}}\}$. Similarly, every element $[\mathbf{w}_k]_n$ of the k-th analog combiner is restricted to $\mathcal{W} = \left\{1/\sqrt{N_{\text{rx}}}, \ldots, 1/\sqrt{N_{\text{rx}}} e^{j\frac{2\pi(L_{\text{rx}}-1)}{L_{\text{rx}}}}\right\}$, $n \in \mathcal{N} = \{1, \ldots, N_{\text{rx}}\}$.

Remark: Note that (4a) aims to jointly maximize the sum-capacity of multicast and unicast signals. While maximization of the latter term is widely accepted, optimizing the multicast sum-capacity is non-standard. However, in our case the multicast term in (4a) is linked to (4b)-(4c), thus enforcing the multicast SINRs to be equal and proximate to $\gamma_{\min}$. Thus, the combined action of (4a)-(4c) promotes multicast sum-capacity maximization and fairness improvement.

IV. Proposed Solution

We recast (4) as (5) without loss of optimality

$$\mathcal{P}_0: \max_{\substack{\{\mathbf{w}_k\}_{k=1}^K, \{\mathbf{f}_k\}_{k=1}^K, \\ \{p_k\}_{k=1}^K, \{\mathbf{v}_k\}_{k=1}^K, \mathbf{m}, \Delta}} \quad \sum_k \tilde{\gamma}_k + \gamma_k - C\Delta \tag{5a}$$

$$\text{s.t.} \quad |\tilde{\gamma}_k - \gamma_{\min}| \leq \Delta, \forall k \in \mathcal{K}, \tag{5b}$$

$$\tilde{\gamma}_1 \geq \tilde{\gamma}_2 \geq \cdots \geq \tilde{\gamma}_K \geq \tilde{\gamma}_1, \tag{5c}$$

$$\|\mathbf{F}\mathbf{m}\|_2^2 / \sum_k p_k \|\mathbf{F}\mathbf{v}_k\|_2^2 \geq \beta, \tag{5d}$$

$$\|\mathbf{F}\mathbf{m}\|_2^2 + \sum_k p_k \|\mathbf{F}\mathbf{v}_k\|_2^2 \leq P_{\text{tx}}, \tag{5e}$$

$$[\mathbf{F}]_{q,r} \in \mathcal{F}, q \in \mathcal{Q}, r \in \mathcal{R}, \tag{5f}$$

$$[\mathbf{w}_k]_n \in \mathcal{W}, n \in \mathcal{N}, \forall k \in \mathcal{K}, \tag{5g}$$

$$\|\mathbf{v}_k\|_2^2 = 1, \forall k \in \mathcal{K}, \tag{5h}$$

$$p_k \geq 0, \forall k \in \mathcal{K}, \tag{5i}$$

$$\Delta \geq 0, \forall k \in \mathcal{K}, \tag{5j}$$

where (4a) is transformed harnessing $\sum_k \log_2(1 + \gamma_k) \to \sum_k \gamma_k$ (refer to Appendix). Also, p_k is the power associated to the unit-power vector $\mathbf{v}_k$, such that $\mathbf{b}_k = \sqrt{p_k}\mathbf{v}_k$. Due to expressions involving multiplicative coupling (i.e., (5a)-(5e)) and non-convex domains (i.e., (5f)-(5g)), $\mathcal{P}_0$ is challenging to solve. Except for the convex constraints (5h)-(5j), (5a)-(5g) are non-convex. In order to approach (5), we adopt a sequential optimization scheme that can only guarantee local optimality. Hence, $\mathcal{P}_0$ is decomposed into smaller sub-problems $\mathcal{P}_1$ and $\mathcal{P}_2$ that are independently and alternately optimized.

A. Optimization of $\mathbf{w}_k$, $\mathbf{f}_k$ and $\mathbf{v}_k$

We optimize $\{\mathbf{w}_k\}_{k=1}^K$, $\{\mathbf{f}_k\}_{k=1}^K$ and $\{\mathbf{v}_k\}_{k=1}^K$ to maximize the unicast sum-capacity while momentaneously disregarding the multicast constituent. Therefore, (5b)-(5c) and (5j) are not considered in $\mathcal{P}_1$. Moreover, since $\mathbf{m}$ and $\{p_k\}_{k=1}^K$ are optimized in $\mathcal{P}_2$, we can further suppress (5d)-(5e) and (5i)-(5j) since $\mathbf{m}$ and $\{p_k\}_{k=1}^K$ can be finely tuned to satisfy such constraints in a latter stage. Thus, we define

$$\mathcal{P}_1: \max_{\{\mathbf{w}_k\}_{k=1}^K,\{\mathbf{f}_k\}_{k=1}^K,\{\mathbf{v}_k\}_{k=1}^K} \quad \sum_k \gamma_k \tag{6a}$$

$$\text{s.t.} \quad [\mathbf{F}]_{q,r} \in \mathcal{F}, q \in \mathcal{Q}, r \in \mathcal{R}, \tag{6b}$$

$$[\mathbf{w}_k]_n \in \mathcal{W}, n \in \mathcal{N}, \forall k \in \mathcal{K}, \tag{6c}$$

$$\|\mathbf{v}_k\|_2^2 = 1, \forall k \in \mathcal{K}. \tag{6d}$$

Since (6a) entails coupling of parameters and (6b)-(6c) are defined over non-convex sets, $\mathcal{P}_1$ is non-convex. On the other hand, the objective function $\sum_k \gamma_k$ is a sum of fractional programs and therefore NP-complete. Although not guaranteeing optimality, a generally accepted practice is to express a sum of fractional programs in the substractive form [11]. Thus, we define the surrogate problem

$$\widetilde{\mathcal{P}}_1: \max_{\{\mathbf{w}_k\}_{k=1}^K,\{\mathbf{f}_k\}_{k=1}^K,\{\mathbf{v}_k\}_{k=1}^K} \quad \sum_k p_k \left|\mathbf{w}_k^H \mathbf{H}_k \mathbf{F} \mathbf{v}_k\right|^2 - \psi \sum_k \sigma^2 - \psi \underbrace{\sum_k \sum_{j \neq k} p_j \left|\mathbf{w}_k^H \mathbf{H}_k \mathbf{F} \mathbf{v}_j\right|^2}_{\text{aggregate IUI of all } K \text{ devices}} \tag{7a}$$

$$\text{s.t.} \quad [\mathbf{F}]_{q,r} \in \mathcal{F}, q \in \mathcal{Q}, r \in \mathcal{R}, \tag{7b}$$

$$[\mathbf{w}_k]_n \in \mathcal{W}, n \in \mathcal{N}, \forall k \in \mathcal{K}, \tag{7c}$$

$$\|\mathbf{v}_k\|_2^2 = 1, \forall k \in \mathcal{K}, \tag{7d}$$

which is obtained by subtracting the denominator from the numerator (with $\|\mathbf{w}_k\|_2^2 = 1$ due to (6c)). We optimize $\widetilde{\mathcal{P}}_1$ by first maximizing $\sum_k p_k \left|\mathbf{w}_k^H \mathbf{H}_k \mathbf{F} \mathbf{v}_k\right|^2$ (in $\widetilde{\mathcal{P}}_{1,1}$) and subsequently minimizing the aggregate IUI $\sum_k \sum_{j \neq k} p_j \left|\mathbf{w}_k^H \mathbf{H}_k \mathbf{F} \mathbf{v}_j\right|^2$ (in $\widetilde{\mathcal{P}}_{1,2}$), in an alternate manner. For the same reasons mentioned above, $\widetilde{\mathcal{P}}_1$, $\widetilde{\mathcal{P}}_{1,1}$ and $\widetilde{\mathcal{P}}_{1,2}$ are also non-convex.

A.1 Design of $\mathbf{w}_k$ and $\mathbf{f}_k$

Disregarding the interference term in $\widetilde{\mathcal{P}}_1$, we maximize the aggregate power of the desired unicast signals at each receiver

$$\widetilde{\mathcal{P}}_{1,1}: \max_{\{\mathbf{w}_k\}_{k=1}^K,\{\mathbf{f}_k\}_{k=1}^K} \quad \sum_k p_k \left|\mathbf{w}_k^H \mathbf{H}_k \mathbf{F} \mathbf{v}_k\right|^2 \tag{8a}$$

$$\text{s.t.} \quad [\mathbf{F}]_{q,r} \in \mathcal{F}, q \in \mathcal{Q}, r \in \mathcal{R}, \tag{8b}$$

$$[\mathbf{w}_k]_n \in \mathcal{W}, n \in \mathcal{N}, \forall k \in \mathcal{K}. \tag{8c}$$

Without knowledge of $\{\mathbf{v}_k\}_{k=1}^K$, and since $N_{\text{tx}}^{\text{RF}} \leq K$ we are in the position of maximizing the RF-to-RF channel gain $|h_k|^2 = \left|\mathbf{w}_k^H \mathbf{H}_k \mathbf{f}_k\right|^2$ for each device k, where $\mathbf{F} = [\mathbf{f}_1, \mathbf{f}_2, \ldots, \mathbf{f}_K]$. Thus, we define K sub-problems

$$\widetilde{\mathcal{P}}_{1,1}^{(k)}: \max_{\mathbf{w}_k,\mathbf{f}_k} \quad \left|\mathbf{w}_k^H \mathbf{H}_k \mathbf{f}_k\right|^2 \tag{9a}$$

$$\text{s.t.} \quad [\mathbf{F}]_{q,r} \in \mathcal{F}, q \in \mathcal{Q}, r \in \mathcal{R}, \tag{9b}$$

$$[\mathbf{w}_k]_n \in \mathcal{W}, n \in \mathcal{N}, \forall k \in \mathcal{K}, \tag{9c}$$

that can be solved in parallel. The channel $\mathbf{H}_k$ is decomposed via singular value decomposition, i.e., $\mathbf{H}_k = [\mathbf{l}_k | \mathbf{L}_k] \, \mathbf{\Lambda}_k \, [\mathbf{r}_k | \mathbf{R}_k]^H$, where $\mathbf{l}_k$ and $\mathbf{r}_k$ are the left and right singular vectors corresponding to the largest singular value [10] [13]. Then, $\mathbf{w}_k$ and $\mathbf{f}_k$ are selected such that $[\mathbf{w}_k]_n = \operatorname{argmin}_{\phi \in \mathcal{W}} \left|\phi - [\mathbf{l}_k]_n\right|^2 = \operatorname{argmax}_{\phi \in \mathcal{W}} \Re\mathfrak{e}\left\{\phi^* \, [\mathbf{l}_k]_n\right\}$ and $[\mathbf{f}_k]_l = \operatorname{argmin}_{\phi \in \mathcal{F}} \left|\phi - [\mathbf{r}_k]_l\right|^2 = \operatorname{argmax}_{\phi \in \mathcal{F}} \Re\mathfrak{e}\left\{\phi^* \, [\mathbf{r}_k]_l\right\}$, $n \in \mathcal{N}$, $q \in \mathcal{Q}$, $\forall k \in \mathcal{K}$, thus satisfying (9b)-(9c). Essentially, ϕ is chosen from $\mathcal{W}$ or $\mathcal{F}$, such that its phase is the closest to the phase of $[\mathbf{l}_k]_n$ or $[\mathbf{f}_k]_l$, respectively.

A.2 Design of $\mathbf{v}_k$

Upon suppressing the first term in $\widetilde{\mathcal{P}}_1$, we minimize the aggregate inter-user interference via

$$\widetilde{\mathcal{P}}_{1,2}: \min_{\{\mathbf{v}_k\}_{k=1}^K} \quad \sum_k \sum_{j \neq k} p_j \left|\mathbf{w}_k^H \mathbf{H}_k \mathbf{F} \mathbf{v}_j\right|^2 \tag{10a}$$

$$\text{s.t.} \quad \|\mathbf{v}_k\|_2^2 = 1, \forall k \in \mathcal{K}. \tag{10b}$$

By harnessing zero-forcing (ZF) beamforming [12], the unicast precoding vectors $\mathbf{b}_k = p_k \mathbf{v}_k$ are obtained. As a result, the IUI can be removed to a great extent. To this purpose, we denote the effective baseband channel of device k as $\mathbf{h}_k^{\text{eff}} = \mathbf{w}_k^H \mathbf{H}_k \mathbf{F}$. Then, we obtain a set of unit-norm precoders $\{\mathbf{v}_k\}_{k=1}^K$ (by normalizing the ZF vectors $\{\mathbf{b}_k\}_{k=1}^K$), which minimize $\sum_k \sum_{j \neq k} \left|\mathbf{h}_k^{\text{eff}} \mathbf{b}_j\right|^2 = \sum_k \sum_{j \neq k} p_j \left|\mathbf{w}_k^H \mathbf{H}_k \mathbf{F} \mathbf{v}_j\right|^2$ since $\mathbf{h}_k^{\text{eff}} \mathbf{b}_j \approx 0, \forall j \neq k$. For sufficiently large N_{tx}, the IUI term in (10) is negligible. Therefore, $\tilde{\gamma}_k \approx \left|\mathbf{h}_k^{\text{eff}} \mathbf{m}\right|^2 / \left(p_k \left|g_k\right|^2 + \sigma^2\right)$ and $\gamma_k \approx p_k \left|g_k\right|^2 / \sigma^2$, where $g_k = \mathbf{h}_k^{\text{eff}} \mathbf{v}_k$ and $\|\mathbf{w}_k\|_2^2 = 1$.

B. Optimization of $\mathbf{m}$ and p_k

We optimize the multicast precoder and unicast powers,

$$\mathcal{P}_2: \max_{\{p_k\}_{k=1}^K,\mathbf{m},\Delta} \quad \sum_k \tilde{\gamma}_k + \gamma_k - C\Delta \tag{11a}$$

$$\text{s.t.} \quad |\tilde{\gamma}_k - \gamma_{\min}| \leq \Delta, \forall k \in \mathcal{K}, \tag{11b}$$

$$\tilde{\gamma}_1 \geq \tilde{\gamma}_2 \geq \cdots \geq \tilde{\gamma}_K \geq \tilde{\gamma}_1, \tag{11c}$$

$$\|\mathbf{F}\mathbf{m}\|_2^2 / \sum_k p_k \|\mathbf{F}\mathbf{v}_k\|_2^2 \geq \beta, \tag{11d}$$

$$\|\mathbf{F}\mathbf{m}\|_2^2 + \sum_k p_k \|\mathbf{F}\mathbf{v}_k\|_2^2 \leq P_{\text{tx}}, \tag{11e}$$

$$p_k \geq 0, \forall k \in \mathcal{K}, \tag{11f}$$

$$\Delta \geq 0. \tag{11g}$$

The objective function (11a) is constructed as the sum of two quadratic-over-linear expressions, which are non-convex. Similarly, (11b)-(11d) are of the same nature. On the other hand, (11e)-(11g) are convex. To facilitate optimization, we introduce two sets of auxiliary parameters $\{\mu_k\}_{k=1}^K$, $\{\upsilon_k\}_{k=1}^K$ and define the following problem

$$\widetilde{\mathcal{P}}_2: \max_{\substack{\{p_k\}_{k=1}^K,\{\mu_k\}_{k=1}^K,\\ \{\upsilon_k\}_{k=1}^K,\mathbf{m},\Delta}} \quad \sum_k \mu_k + \upsilon_k - C\Delta \tag{12a}$$

$$\text{s.t.} \quad \left|\mathbf{h}_k^{\text{eff}} \mathbf{m}\right|^2 / \left(p_k \left|g_k\right|^2 + \sigma^2\right) \geq \mu_k, \tag{12b}$$

$$p_k \left|g_k\right|^2 / \sigma^2 \geq \upsilon_k, \tag{12c}$$

$$\|\mathbf{F}\mathbf{m}\|_2^2 / \sum_k p_k \|\mathbf{F}\mathbf{v}_k\|_2^2 \geq \beta, \tag{12d}$$

$$\|\mathbf{F}\mathbf{m}\|_2^2 + \sum_k p_k \|\mathbf{F}\mathbf{v}_k\|_2^2 \leq P_{\text{tx}}, \tag{12e}$$

$$\mu_1 \geq \mu_2 \geq \cdots \geq \mu_K \geq \mu_1, \tag{12f}$$

$$\mu_k \leq \gamma_{\min} + \Delta, \tag{12g}$$

$$\mu_k \geq \gamma_{\min} - \Delta, \tag{12h}$$

$$\upsilon_k \geq 0, \tag{12i}$$

$$p_k \geq 0, \tag{12j}$$

$$\Delta \geq 0, \tag{12k}$$

The objective function (12a) defines the maximization of a linear function over μ_k and υ_k, therefore it is convex. Constraints (12c) and (12e)-(12k) are convex, whereas (12b) and (12d) are non-convex. In order to convexify $\widetilde{\mathcal{P}}_2$, we linearize the non-convex constraints (12b) and (12d) around a feasible point $\left(\mathbf{m}^{(t)}, p_1^{(t)}, \cdots, p_K^{(t)}\right)$. Thus, the convexified versions of (12b) and (12d) are shown in (13) and (14), respectively[2]. As a result, we optimize $\widetilde{\mathcal{P}}_2^{(t)}$ iteratively over a number of N_{iter_2} iterations. In (15), we show the vectorized form of $\widetilde{\mathcal{P}}_2$ after linearization,

$$\widetilde{\mathcal{P}}_2^{(t)}: \max_{\substack{\mathbf{m},\mathbf{p},\\ \boldsymbol{\mu},\boldsymbol{\upsilon},\Delta}} \quad \mathbf{1}^T\boldsymbol{\mu} + \mathbf{1}^T\boldsymbol{\upsilon} - C\Delta \tag{15a}$$

$$\text{s.t.} \quad 2\mathfrak{Re}\Big\{\text{diag}\left(\mathbf{A}\mathbf{p}^{(t)} + \mathbf{d}\right)\left(\mathbf{I} \otimes \mathbf{m}^{(t)\,H}\right)\mathbf{C}\left(\mathbf{1} \otimes \mathbf{m}\right)\Big\}$$

$$- \text{diag}\left(\mathbf{A}\mathbf{p} + \mathbf{d}\right)\left(\mathbf{I} \otimes \mathbf{m}^{(t)\,H}\right)\mathbf{C}\left(\mathbf{1} \otimes \mathbf{m}^{(t)}\right) -$$

$$\text{diag}\left(\mathbf{A}\mathbf{p}^{(t)} + \mathbf{d}\right)\text{diag}\left(\mathbf{A}\mathbf{p}^{(t)} + \mathbf{d}\right)\boldsymbol{\mu} \succcurlyeq \mathbf{0}, \tag{15b}$$

$$\left(\mathbf{A} \odot \left(\text{diag}\left(\mathbf{d}\right)\right)^{-1}\right)\mathbf{p} \succcurlyeq \boldsymbol{\upsilon}, \tag{15c}$$

$$2\mathfrak{Re}\left\{\left(\mathbf{c}^T\mathbf{p}^{(t)}\mathbf{m}^{(t)\,H}\mathbf{F}^H\mathbf{F}\mathbf{m}\right)\right\} -$$

$$\mathbf{c}^T\mathbf{p}\mathbf{m}^{(t)\,H}\mathbf{F}^H\mathbf{F}\mathbf{m}^{(t)} - \left(\mathbf{c}^T\mathbf{p}^{(t)}\right)^2\beta \geq 0, \tag{15d}$$

$$\|\mathbf{F}\mathbf{m}\|_2^2 + \sum_k p_k \|\mathbf{F}\mathbf{v}_k\|_2^2 \leq P_{\text{tx}}, \tag{15e}$$

$$\left(\mathbf{I} - \widetilde{\mathbf{I}}\right)\boldsymbol{\mu} \succcurlyeq \mathbf{0}, \tag{15f}$$

$$\boldsymbol{\mu} \preccurlyeq \left(\gamma_{\min} + \Delta\right)\mathbf{1}, \tag{15g}$$

$$\boldsymbol{\mu} \succcurlyeq \left(\gamma_{\min} - \Delta\right)\mathbf{1}, \tag{15h}$$

$$\boldsymbol{\upsilon} \succcurlyeq \mathbf{0}, \tag{15i}$$

$$\mathbf{p} \succcurlyeq \mathbf{0}, \tag{15j}$$

$$\Delta \geq 0. \tag{15k}$$

where $\mathbf{A} = \text{diag}\left(|g_1|^2, \ldots, |g_K|^2\right)$, $\mathbf{p} = [p_1, \ldots, p_K]^T$, $\mathbf{d} = \sigma^2\mathbf{1}$, $\mathbf{C} = \text{diag}\left(\left\|\mathbf{h}_1^{\text{eff}}\right\|_2^2, \ldots, \left\|\mathbf{h}_K^{\text{eff}}\right\|_2^2\right)$, $\mathbf{I}$ is the identity matrix, $\widetilde{\mathbf{I}}$ is obtained by cyclically shifting all the columns of $\mathbf{I}$ to the left only once, $\mathbf{c} = \left[\|\mathbf{F}\mathbf{v}_1\|_2^2, \ldots, \|\mathbf{F}\mathbf{v}_K\|_2^2\right]^T$, $\boldsymbol{\mu} = [\mu_1, \ldots, \mu_K]^T$ and $\boldsymbol{\upsilon} = [\upsilon_1, \ldots, \upsilon_K]^T$. Also, $\otimes$ denotes the Kronecker product, whereas $\odot$ represents component-wise multiplication. This formulation can be efficiently approached by convex optimization solvers. In our case, we use `CVX` and `SDPT3`.

[2]When computing the gradients of real-valued expressions with respect to complex parameters (for linearization), we have employed the Wirtinger derivatives [18].

V. Simulation Results

Throughout the simulations, we consider the geometric channel model with $L = 8$ propagation paths (to depict the highly reflective industrial environment [5]), where the azimuth angles of departure and arrival are uniformly distributed over $[-\pi; \pi]$. Also, $N_{\text{tx}} = 64$, $L_{\text{tx}} = 32$, $N_{\text{rx}} = 4$, $L_{\text{rx}} = 4$ and $K = 6$. The maximum transmit power, the power splitting parameter, and the multicast SINR target are $P_{\text{tx}} = 1$W, $\beta = 3$, $\gamma_{\min} = 5$dB, respectively. We denote our two proposed schemes by `PLDM-1` and `PLDM-2` as mentioned in Section I-C. In addition, we include the outcomes of [9], which we denote by `PLDM-0`. The results depicting spectral efficiency (SE) performance have been averaged over 1000 simulations. Fig. 2 shows the aggregate SE of the system, which is the sum of the unicast and multicast components, considering all the receivers. In terms of aggregate SE, the three schemes perform similarly. This a consequence of employing highly optimized precoders, where each expends the same amount of power P_{tx} that is distributed among the two signals in different proportions.

In Fig. 3, the SE of the multicast and unicast signals is displayed. The multicast SE per device is expected to be $\rho = \log_2\left(1 + 10^{\gamma_{\min}/10}\right) = 2.057$ bps/Hz. Further, when all devices are considered the *aggregate multicast SE* should be $\rho \times K = 12.344$ bps/Hz. This target is more tightly achieved by `PLDM-2`. Notice that both `PLDM-1` and `PLDM-2` are capable of prioritizing the multicast signal over the unicast counterpart so as to satisfy (5b). Nevertheless, `PLDM-1` can provide higher multicast SE than `PLDM-2` for low P_{tx}/σ^2. As P_{tx}/σ^2 increases, additional usable power becomes available for both signals to boost the SE. Thus, as the multicast signal approaches its target $\gamma_{\min}$, it is progressively induced to a state where the SE saturates and the unicast SE gains more relevance. This behavior is attained through (5a), (5b) and (5j). On the contrary, in `PLDM-0` the unicast SE is higher than the multicast SE for low P_{tx}/σ^2, which is unsuitable. This undesirable behavior on data prioritization is obtained even though a weighted max-min approach was considered in [13], aiming to emphasize the multicast importance.

In order to assess multicast fairness, Fig. 4 shows the SE for all devices within a confidence interval of 95%, where the shaded area delimitates the upper and lower bounds. We observe that `PLDM-1` outperforms `PLDM-2` at prioritizing multicast information for low P_{tx}/σ^2. Notice that once the target is reached, the SE of `PLDM-1` remains in the upper region of the desired threshold with some variability. On the other hand, `PLDM-2` is capable of maintaining a high multicast SE fairness among all the devices with negligible variance. For the sake of comparison, the results of `PLDM-0` are included.

$$2\mathfrak{Re}\left\{\left(p_k^{(t)}\,|g_k|^2 + \sigma^2\,\|\mathbf{w}_k\|_2^2\right)\mathbf{m}^{(t)\,H}\mathbf{h}_k^{\text{eff}\,H}\mathbf{h}_k^{\text{eff}}\mathbf{m}\right\} - \left|\mathbf{h}_k^{\text{eff}}\mathbf{m}^{(t)}\right|^2\left(p_k\,|g_k|^2 + \sigma^2\,\|\mathbf{w}_k\|_2^2\right) - \mu_k\left(p_k^{(t)}\,|g_k|^2 + \sigma^2\,\|\mathbf{w}_k\|_2^2\right)^2 \geq 0. \tag{13}$$

$$2\mathfrak{Re}\left\{\left(\sum_k p_k^{(t)}\,\|\mathbf{F}\mathbf{v}_k\|_2^2\right)\mathbf{m}^{(t)\,H}\mathbf{F}^H\mathbf{F}\mathbf{m}\right\} - \left(\sum_k p_k\,\|\mathbf{F}\mathbf{v}_k\|_2^2\right)\mathbf{m}^{(t)\,H}\mathbf{F}^H\mathbf{F}\mathbf{m}^{(t)} - \beta\left(\sum_k p_k^{(t)}\,\|\mathbf{F}\mathbf{v}_k\|_2^2\right) \geq 0. \tag{14}$$

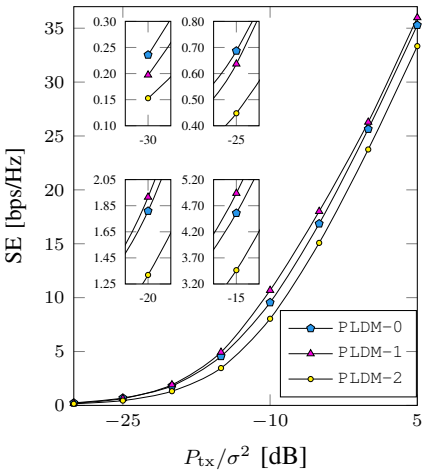

Figure 2: Overall SE of the system

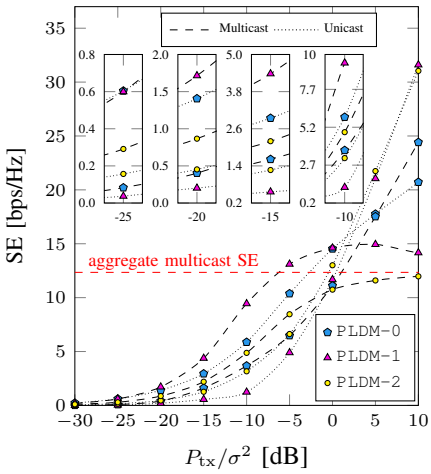

Figure 3: Disaggregated SE of the system

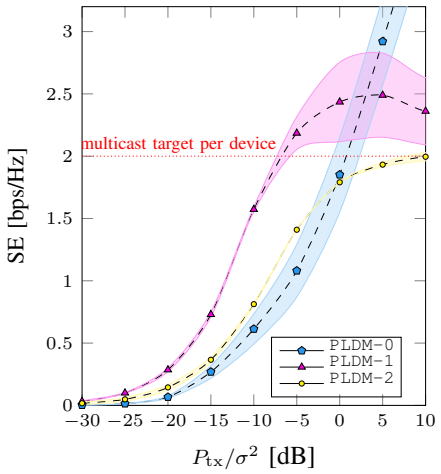

Figure 4: Multicast SE per device

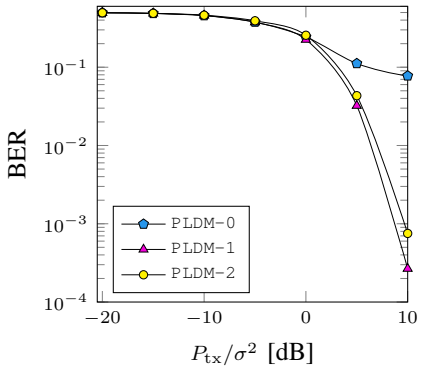

(a) Aggregate

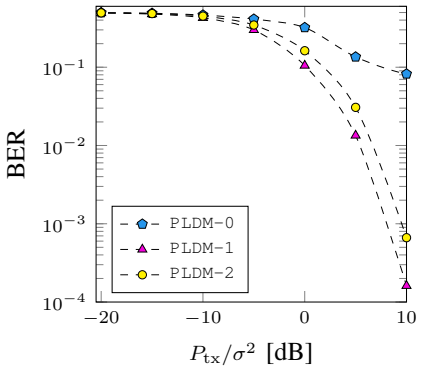

(b) Multicast

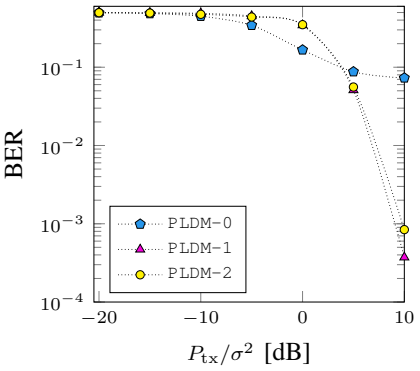

(c) Unicast

Figure 5: Bit Error Rate Performance

Fig. 5 shows the bit error rate (BER) performance averaged over 10^6 simulations, where the unicast and multicast symbols were obtained from a 4-QAM constellation. Since the multicast prioritization mechanism proposed in [13] does not work as expected, SIC cannot operate properly thus severely degrading the BER. We swapped (where necessary) the decoding order between unicast and multicast information to favor PLDM−0. On the other hand, PLDM−1 and PLDM−2 perform very similarly with a slight advantage of the former.

VI. Discussion

Unicast/multicast dichotomy: Although the power splitting mechanism promotes the prioritization of the multicast signal, the multicast SINR and SE are not always higher than that of the unicast signal. This is advantageous since unicast transmissions can support higher order modulation in high SNR regime.

Multicast SINR threshold: Having a deterministic $\gamma_{\min}$ is justified since beacon control packets are usually of fixed size and a target SINR that allows successful decoding of the message can be derived.

PLDM−1 vs PLDM−2: Recall that in PLDM−1, $\mathbf{x} = \mathbf{F}\,[\mathbf{B}|\mathbf{m}]\,[\mathbf{s}|z]^T = \mathbf{FBs} + \mathbf{F}\mathbf{m}z$. In PLDM−2, if $\mathbf{m} = \mathbf{Bu}$ then $\mathbf{x} = \mathbf{FBs} + \mathbf{FBu}z = \mathbf{FB}\,[\mathbf{s} + \mathbf{u}z]$, where $\mathbf{u} = [u_1, \cdots, u_K]^T \succcurlyeq 0$. Realize that u_k defines the ratio of energy between the unicast symbol s_k and the multicast symbol z, for the k-th device. Thus, PLDM−2 has only one set of nearly-orthogonal digital unicast precoding vectors $\{\mathbf{b}_k\}_{k=1}^K$ that are matched to the channel of each device. As a result, the multicast packet and the k-th unicast information are conveyed simultaneously through the k-th precoding vector $\mathbf{b}_k$ with different powers (since $\mathbf{m} = \mathbf{Bu}$). On the contrary, PLDM−1 is devised as non-orthogonally overlaid unicast and multicast precoders. Therefore, the spatial radiation patterns of $\{\mathbf{b}_k\}_{k=1}^K$ and $\mathbf{m}$ do not necessary match.

PLDM−0: In [13], the authors attempted to prioritize multicast information by assigning (in the objective function) a higher weighting factor to the multicast minimum SINR. However, the formulation proposed therein did not allow to enforce such condition as observed in the simulations results.

Initialization: In order to solve $\widetilde{\mathcal{P}}_2^{(t)}$ we need an initial feasible point for $\left\{p_k^{(0)}\right\}_{k=1}^K$ and $\mathbf{m}^{(0)}$. In this paper we selected, $p_k^{(0)} =$

$\frac{P_{\text{tx}}}{2\sum_k \|\mathbf{F}\mathbf{v}_k\|_2^2}$, $\forall k \in \mathcal{K}$ and a randomly generated $\mathbf{m}$ such that $\left\|\mathbf{F}\mathbf{m}^{(0)}\right\|_2^2 = \frac{P_{\text{tx}}}{2}$.

VII. Conclusion

In this paper, we investigated the joint optimization of hybrid precoding, fairness, and power splitting in NOMA-LDM superimposed transmissions for industrial IoT scenarios. We proposed two solutions: one of them regarded as the superposition of two distinct precoders with different spatial and power signatures. The second approach is designed as a purely power-domain NOMA scheme. We included a power sharing constraint to support the SIC decoder task at the receiver. In addition, simulations show that both proposed schemes are capable of providing a high degree of fairness among all the devices, which is relevant for the dissemination of critical control messages in this kind of scenarios.

VIII. Acknowledgment

This research was in part funded by the Deutsche Forschungsgemeinschaft (DFG) within the B5G-Cell project as part of the SFB 1053 MAKI.

Appendix

Let us define the function $g : \mathcal{Z} \to \mathbb{R}_0^+$ that maps any 4-tuple $(\mathbf{w}_k, \mathbf{H}_k, \mathbf{F}, \mathbf{b}_k) \in \mathcal{Z}$ to γ_k, where $\mathcal{Z}$ is a subspace of $\mathbb{C}^{N_{\text{rx}}\times 1} \times \mathbb{C}^{N_{\text{rx}}\times N_{\text{tx}}} \times \mathbb{C}^{N_{\text{tx}}\times K} \times \mathbb{C}^{K\times 1}$.

Lemma: It holds true that the 4-tuple $(\mathbf{w}_k, \mathbf{H}_k, \mathbf{F}, \mathbf{b}_k) \in \mathcal{Z}$ for which $\log_2\left(g\left(\mathbf{w}_k, \mathbf{H}_k, \mathbf{F}, \mathbf{b}_k\right)\right)$ is maximal in $\mathcal{Z}$, also makes $g\left(\mathbf{w}_k, \mathbf{H}_k, \mathbf{F}, \mathbf{b}_k\right)$ maximal in $\mathcal{Z}$.

Proof: Since every $g\left(\mathbf{w}_k, \mathbf{H}_k, \mathbf{F}, \mathbf{b}_k\right) \in \mathbb{R}_0^+$, then $g\left(\mathbf{w}_k, \mathbf{H}_k, \mathbf{F}, \mathbf{b}_k\right) \geq g\left(\widehat{\mathbf{w}}_k, \widehat{\mathbf{H}}_k, \widehat{\mathbf{F}}, \widehat{\mathbf{b}}_k\right) \Leftrightarrow \log_2\left(g\left(\mathbf{w}_k, \mathbf{H}_k, \mathbf{F}, \mathbf{b}_k\right)\right) \geq \log_2\left(g\left(\widehat{\mathbf{w}}_k, \widehat{\mathbf{H}}_k, \widehat{\mathbf{F}}, \widehat{\mathbf{b}}_k\right)\right)$, due to $\log_2(\cdot)$ being monotonically increasing in $\mathbb{R}_0^+$. Thus, for every $\left(\widehat{\mathbf{w}}_k, \widehat{\mathbf{H}}_k, \widehat{\mathbf{F}}, \widehat{\mathbf{b}}_k\right) \in \mathcal{Z}$, $g\left(\mathbf{w}_k, \mathbf{H}_k, \mathbf{F}, \mathbf{b}_k\right) \geq g\left(\widehat{\mathbf{w}}_k, \widehat{\mathbf{H}}_k, \widehat{\mathbf{F}}, \widehat{\mathbf{b}}_k\right)$. Also, for every $\left(\widehat{\mathbf{w}}_k, \widehat{\mathbf{H}}_k, \widehat{\mathbf{F}}, \widehat{\mathbf{b}}_k\right) \in \mathcal{Z}, \log_2\left(g\left(\mathbf{w}_k, \mathbf{H}_k, \mathbf{F}, \mathbf{b}_k\right)\right) \geq \log_2\left(g\left(\widehat{\mathbf{w}}_k, \widehat{\mathbf{H}}_k, \widehat{\mathbf{F}}, \widehat{\mathbf{b}}_k\right)\right)$. Therefore, the 4-tuple $(\mathbf{w}_k, \mathbf{H}_k, \mathbf{F}, \mathbf{b}_k) \in \mathcal{Z}$ that maximizes $\log_2\left(g\left(\mathbf{w}_k, \mathbf{H}_k, \mathbf{F}, \mathbf{b}_k\right)\right)$, also maximizes $g\left(\mathbf{w}_k, \mathbf{H}_k, \mathbf{F}, \mathbf{b}_k\right)$ and these two inequalities are equivalent.

References

[1] Z. Ding, P. Fan, and H. V. Poor, "Random Beamforming in Millimeter-Wave NOMA Networks," *IEEE Access*, pp. 7667–7681, February 2017.

[2] Z. Ding, L. Dai, R. Schober, and H. V. Poor, "NOMA Meets Finite Resolution Analog Beamforming in Massive MIMO and Millimeter-Wave Networks," *IEEE Communications Letters*, vol. 21, no. 8, pp. 1879–1882, August 2017.

[3] 3GPP, "3GPP TR 36.859: Study on Downlink Multiuser Superposition Transmission (MUST) for LTE (Release 13)," 2015.

[4] H. Nikopour and H. Baligh, "Sparse Code Multiple Access," in *IEEE PIMRC*, September 2013, pp. 332–336.

[5] A. Loch, C. Cano, G. H. Sim, A. Asadi, and X. Vilajosana, "A Channel Measurement Campaign for mmWave Communication in Industrial Settings," *CoRR*, vol. abs/1903.10502, 2019. [Online]. Available: http://arxiv.org/abs/1903.10502

[6] L. F. Abanto-Leon, M. Hollick, and G. H. Sim, "Hybrid Precoding for Multi-Group Multicasting in mmWave Systems," in *IEEE GLOBECOM*, December 2019.

[7] L. F. Abanto-Leon and G. H. Sim, "Learning-based Max-Min Fair Hybrid Precoding for mmWave Multicasting," in *IEEE ICC*, June 2020.

[8] P. P. Bergmans and T. M. Cover, "Cooperative Broadcasting," *IEEE Transactions on Information Theory*, vol. 20, no. 3, pp. 317–324, May 1974.

[9] L. Zhang, W. Li, Y. Wu, X. Wang, S. Park, H. M. Kim, J. Lee, P. Angueira, and J. Montalban, "Layered-Division-Multiplexing: Theory and Practice," *IEEE Transactions on Broadcasting*, vol. 62, pp. 216–232, March 2016.

[10] D. Kim, F. Khan, C. V. Rensburg, Z. Pi, and S. Yoon, "Superposition of Broadcast and Unicast in Wireless Cellular Systems," *IEEE Communications Magazine*, vol. 46, no. 7, pp. 110–117, July 2008.

[11] W. Hao, M. Zeng, Z. Chu, and S. Yang, "Energy-Efficient Power Allocation in Millimeter Wave Massive MIMO With Non-Orthogonal Multiple Access," *IEEE Wireless Communications Letters*, vol. 6, no. 6, pp. 782–785, December 2017.

[12] J. Zhao, O. Simeone, D. Gunduz, and D. Gomez-Barquero, "Non-Orthogonal Unicast and Broadcast Transmission via Joint Beamforming and LDM in Cellular Networks," in *IEEE GLOBECOM*, December 2016, pp. 1–6.

[13] J. Wang, H. Xu, B. Zhu, L. Fan, and A. Zhou, "Hybrid Beamforming Design for mmWave Joint Unicast and Multicast Transmission," *IEEE Communications Letters*, vol. 22, no. 10, pp. 2012–2015, October 2018.

[14] E. Chen, M. Tao, and Y. Liu, "Joint Base Station Clustering and Beamforming for Non-Orthogonal Multicast and Unicast Transmission With Backhaul Constraints," *IEEE Transactions on Wireless Communications*, vol. 17, no. 9, pp. 6265–6279, September 2018.

[15] Y. Mao, B. Clerckx, and V. O. K. Li, "Rate-Splitting for Multi-Antenna Non-Orthogonal Unicast and Multicast Transmission," in *IEEE SPAWC*, June 2018, pp. 1–5.

[16] ——, "Rate-Splitting for Multi-Antenna Non-Orthogonal Unicast and Multicast Transmission: Spectral and Energy Efficiency Analysis," *IEEE Transactions on Communications*, vol. 67, no. 12, pp. 8754–8770, December 2019.

[17] T. E. Bogale, L. B. Le, A. Haghighat, and L. Vandendorpe, "On the Number of RF Chains and Phase Shifters, and Scheduling Design With Hybrid Analog–Digital Beamforming," *IEEE Transactions on Wireless Communications*, vol. 15, no. 5, pp. 3311–3326, May 2016.

[18] A. Hjorungnes and D. Gesbert, "Complex-Valued Matrix Differentiation: Techniques and Key Results," *IEEE Transactions on Signal Processing*, vol. 55, no. 6, pp. 2740–2746, June 2007.

D

PUBLICATION IV.
SEQUENTIAL PARAMETRIC OPTIMIZATION FOR RATE-SPLITTING PRECODING IN NON-ORTHOGONAL UNICAST AND MULTICAST TRANSMISSIONS

Sequential Parametric Optimization for Rate-Splitting Precoding in Non-Orthogonal Unicast and Multicast Transmissions

Luis F. Abanto-Leon[†], Matthias Hollick[†], Bruno Clerckx[‡], Gek Hong (Allyson) Sim[†],
[†]Secure Mobile Networking (SEEMOO) Lab, Technical University of Darmstadt, Germany
[‡]Imperial College London, United Kingdom
Email: [†]{labanto,asim,mhollick}@seemoo.tu-darmstadt.de, [‡]b.clerckx@imperial.ac.uk

***Abstract*—This paper investigates rate-splitting (RS) precoding for non-orthogonal unicast and multicast (NOUM) transmissions using fully-digital and hybrid precoders. We study the nonconvex weighted sum-rate (WSR) maximization problem subject to a multicast requirement. We propose `FALCON`, an approach based on sequential parametric optimization, to solve the aforementioned problem. We show that `FALCON` converges to a local optimum without requiring judicious selection of an initial feasible point. Besides, we show through simulations that by leveraging RS, hybrid precoders can attain nearly the same performance as their fully-digital counterparts under certain specific settings.**

***Index Terms*—parametric optimization, SDP, unicast, multicast, non-orthogonal multiple access, rate-splitting.**

I. Introduction

The upsurge of wireless applications and the increasing omnipresence of internet-of-things (IoT) devices are expected to exacerbate the scarcity of radio resources. Moreover, recent requirements to support multiple services simultaneously (e.g., concurrent unicast and multicast) will further aggravate the situation. This state of affairs has invigorated research on non-orthogonal unicast and multicast (NOUM) transmissions and millimeter-wave. On the one hand, NOUM has been envisaged as a recourse for improving spectral efficiency due to its capability of providing concurrent services in the same radio frequency resources. Specifically, NOUM has encountered outstanding solutions through layered-division-multiplexing (LDM) [1] and rate-splitting (RS) [2]. On the other hand, usage of the underexploited millimeter-wave spectrum is a promising solution to alleviate the scarcity of radio resources. However, the adoption of (traditional) fully-digital precoders at high frequencies is challenging owing to prohibitive fabrication costs and excessive power consumption. Consequently, the more power-efficient hybrid precoders have emerged as a functional solution to overcome such difficulties.

II. Motivation

Inspired by the exceptional spectral efficiency achieved by fully-digital precoders in RS-NOUM [2], [3], and the predominant use of hybrid precoders in millimeter-wave communications, we investigate the weighted sum-rate (WSR) maximization problem with both fully-digital and hybrid precoders in millimeter-wave RS-NOUM systems. Further, the body of work on WSR maximization with RS precoding leverages weighted minimum mean square error (`WMMSE`) [2], [4]–[6] as a prevailing means of solution. In this paper, we propose `FALCON`, which is based on sequential parametric optimization and compared to `WMMSE`. Our contributions are:

- We propose `FALCON`, a fast convergence algorithm for solving the nonconvex WSR maximization problem. Our approach leverages semidefinite programming (SDP) and successive convex approximations (SCA). Specifically, we exploit sub-level/super-level sets and establish parametric convex upper bounds that can be contracted iteratively [7]. We show that `FALCON` converges to a local optimum of the nonconvex WSR maximization problem. Further, `FALCON` does not rely on judicious selection of initial feasible points (as `WMMSE` does) in order to guarantee high performance.
- We use `FALCON` and `WMMSE` with both RS-NOUM and LDM-NOUM systems. We realize that the former outperforms the latter due to the capability of RS to partially decode interference and partially treat remaining interference as noise. We compare RS-NOUM against the optimal dirty paper coding, thus revealing a small optimality gap between the two schemes.
- We find that, under specific settings, quantizing the hybrid precoder phase shifts with 4 bits is sufficient to achieve the same performance as fully-digital implementations. Further, in scenarios wherein users have channels with a low degree of correlation, such performance can be attained with 2 bits.
- We show, through simulations, that `FALCON` is less prone than `WMMSE` to return infeasible solutions due to its non-dependency on initial feasible points. Nevertheless, `FALCON` has higher computational complexity per iteration.

III. Related Work

NOUM has been studied under LDM in [1], [8]–[14]. Specifically, [1], [8], [9] investigate the design of fully-digital precoders for transmit power minimization with unicast and multicast quality-of-service (QoS) requirements. A fairness-aware hybrid precoder is proposed in [10], [15]. Energy efficiency with fully-digital precoders is investigated in [11], [12] whereas a similar setting with backhaul constraints is considered in [13], [14]. On the other hand, NOUM with RS has only been researched with fully-digital precoders in [2], [3], wherein the `WMMSE` approach is proposed for WSR maximization. Relevant literature on other aspects of RS includes [4], [5], [16]–[20]. *Although both LDM and RS are power-domain non-orthogonal schemes, the superiority of RS resides in its capability to partially decode interference. This*

is achieved by embedding fragments of unicast information in the multicast signal, that the receivers can decode and remove.

IV. System Model: RS for NOUM Transmissions

We consider a system where a next-generation Node B (gNodeB) serves K single-antenna users indexed by $\mathcal{K} = \{1,\dots,K\}$. The gNodeB is equipped with a hybrid transmitter composed of N_{tx} transmit antennas and $N_{\mathrm{tx}}^{\mathrm{RF}}$ radio frequency (RF) chains, where $K \leq N_{\mathrm{tx}}^{\mathrm{RF}} \leq N_{\mathrm{tx}}$. Without loss of generality, we assume $N_{\mathrm{tx}}^{\mathrm{RF}} = K$. The gNodeB transmits in a non-orthogonal manner a multicast message $W^{(\mathrm{m})}$ (intended to all the users) and K unicast messages $W_1^{(\mathrm{u})},\dots,W_K^{(\mathrm{u})}$ (each targeting a particular user). Every unicast message is decomposed into two components as $W_k^{(\mathrm{u})} \triangleq \left(W_k^{(\mathrm{u,c})}, W_k^{(\mathrm{u,p})}\right)$, where $W_k^{(\mathrm{u,c})}$ and $W_k^{(\mathrm{u,p})}$ are referred as the common and private parts, respectively. The multicast message along with the unicast common parts are jointly encoded into a common macro-stream as $\left\{W_1^{(\mathrm{u,c})},\dots,W_K^{(\mathrm{u,c})},W^{(\mathrm{m})}\right\} \mapsto \widetilde{\mathbf{z}} = [\widetilde{z}_1,\widetilde{z}_2,\dots]^T$. The unicast private parts are encoded into independent streams as $W_k^{(\mathrm{u,p})} \mapsto \widetilde{\mathbf{s}}_k = \left[\widetilde{s}_{k,1},\widetilde{s}_{k,2},\dots\right]^T$, $\forall k \in \mathcal{K}$. The encoded streams are processed by the baseband digital precoder $[\mathbf{B}|\mathbf{m}] = [\mathbf{b}-1,\dots,\mathbf{b}_K,\mathbf{m}] \in \mathbb{C}^{K\times(K+1)}$ of the hybrid transmitter. Let z and $\mathbf{s} = [s_1,\dots,s_K]^T$ denote the instantaneous symbol and vector symbol of the common macro-stream and private streams, respectively, such that $\mathbb{E}\left\{\left[\mathbf{s}^T|z\right]^H\left[\mathbf{s}^T|z\right]\right\} = \mathbf{I}$. Thus, the downlink signal is $\mathbf{x} = \mathbf{F}\left[\mathbf{B}|\mathbf{m}\right]\left[\mathbf{s}^T|z\right]^T \in \mathbb{C}^{N_{\mathrm{tx}}\times 1}$, where $\mathbf{F} = [\mathbf{f}_1,\dots,\mathbf{f}_K] \in \mathbb{C}^{N_{\mathrm{tx}}\times K}$ represents the RF analog precoder of the hybrid transmitter. Under flat fading, the signal received by the k-th user is

$$y_k = \underbrace{\mathbf{h}_k^H\mathbf{F}\mathbf{m}z}_{\substack{\text{common signal}\\ y_k^{(\mathrm{c})}}} + \underbrace{\mathbf{h}_k^H\mathbf{F}\mathbf{b}_k s_k}_{\substack{\text{private signal for user } k\\ y_k^{(\mathrm{p})}}} + \underbrace{\mathbf{h}_k^H\mathbf{F}\textstyle\sum_{j\neq k}\mathbf{b}_j s_j}_{\substack{\text{interference at user } k\\ y_k^{(\mathrm{i})}}} + \underbrace{n_k}_{\text{noise}}, \quad (1)$$

where $n_k \sim \mathcal{CN}\left(0,\sigma^2\right)$ denotes additive white Gaussian noise and $\mathbf{h}_k \in \mathbb{C}^{N_{\mathrm{tx}}\times 1}$ represents the channel between the gNodeB and the k-th user. Because the users have a single antenna, they are not capable of performing spatial demultiplexing to separate the two data streams. In order to distinguish and decode both signals, the users rely on successive interference cancellation (SIC), which consists in detecting and decoding one signal after the other, as explained in the following. First, each user k decodes the common macro-stream symbol z, in term $y_k^{(\mathrm{c})}$, by treating the rest of signals as noise. Subsequently, the common signal $y_k^{(\mathrm{c})}$ is reconstructed and subtracted from y_k. At this point, the remaining byproduct $\tilde{y}_k = y_k - y_k^{(\mathrm{c})}$ consists solely of private unicast components $\left\{y_k^{(\mathrm{p})}, y_k^{(\mathrm{i})}\right\}$ and noise n_k, from where user k decodes symbol s_k. Thus, the signal–to–interference–plus–noise ratio (SINR) of the common macro-stream and private streams are denoted by $\mathrm{SINR}_k^{(\mathrm{c})}$ and $\mathrm{SINR}_k^{(\mathrm{p})}$, respectively.

$$\mathrm{SINR}_k^{(\mathrm{c})} = \frac{\left|\mathbf{h}_k^H\mathbf{F}\mathbf{m}\right|^2}{\sum_{j\in\mathcal{K}}\left|\mathbf{h}_k^H\mathbf{F}\mathbf{b}_j\right|^2+\sigma^2} \quad \mathrm{SINR}_k^{(\mathrm{p})} = \frac{\left|\mathbf{h}_k^H\mathbf{F}\mathbf{b}_k\right|^2}{\sum_{j\neq k}\left|\mathbf{h}_k^H\mathbf{F}\mathbf{b}_j\right|^2+\sigma^2}$$

RS principle: Based on the expressions above, the achievable rates are $R_k^{(\mathrm{c})} = \log_2\left(1+\mathrm{SINR}_k^{(\mathrm{c})}\right)$ and $R_k^{(\mathrm{p})} = \log_2\left(1+\mathrm{SINR}_k^{(\mathrm{p})}\right)$. We define $\bar{R}^{(\mathrm{c})}$ as the maximal rate at which all users can successfully decode the common symbol z. Thus, the common macro-stream is to be encoded at a rate $\bar{R}^{(\mathrm{c})} \leq R_{\min}^{(\mathrm{c})}$, where $R_{\min}^{(\mathrm{c})} = \min_{k\in\mathcal{K}}\left\{R_1^{(\mathrm{c})},\dots,R_K^{(\mathrm{c})}\right\}$. Since z results from jointly encoding multiple messages, let C_0 denote the fraction of $\bar{R}^{(\mathrm{c})}$ conveying the multicast message $W^{(\mathrm{m})}$, and C_k the fraction of $\bar{R}^{(\mathrm{c})}$ transmitting the unicast common part $W_k^{(\mathrm{u,c})}$, subject to $C_0 + \sum_{k\in\mathcal{K}} C_k = \bar{R}^{(\mathrm{c})}$. Upon decoding the streams $\widetilde{\mathbf{z}}$ and $\widetilde{\mathbf{s}}_k$, user k acquires $W_1^{(\mathrm{u,c})},\dots,W_K^{(\mathrm{u,c})},W^{(\mathrm{m})}$ and $W_k^{(\mathrm{u,p})}$, from where the unicast message $W_k^{(\mathrm{u})}$ can be reassembled. The common parts $W_{j\neq k}^{(\mathrm{u,c})}$ decoded by user k are used for interference decoding, thus improving the SINR. The aggregate unicast rate of user k is $R_k^{(\mathrm{u})} = C_k + \log_2\left(1+\mathrm{SINR}_k^{(\mathrm{p})}\right)$.

V. Problem Formulation

The QoS-constrained WSR maximization problem is

$$\begin{aligned}
\mathcal{P}: \max_{C_0,C_k,\mathbf{F},\mathbf{b}_k,\mathbf{m}} \quad & \textstyle\sum_{k\in\mathcal{K}}\mu_k\left(C_k+\log_2\left(1+\mathrm{SINR}_k^{(\mathrm{p})}\right)\right) && \text{(2a)}\\
\text{s.t.} \quad & C_0 + \textstyle\sum_{j\in\mathcal{K}} C_j = \bar{R}^{(\mathrm{c})}, && \text{(2b)}\\
& C_0 \geq C_0^{\mathrm{th}}, && \text{(2c)}\\
& C_k \geq 0, \forall k\in\mathcal{K}, && \text{(2d)}\\
& \|\mathbf{F}\mathbf{m}\|_2^2 + \textstyle\sum_{k\in\mathcal{K}}\|\mathbf{F}\mathbf{b}_k\|_2^2 \leq P_{\mathrm{tx}}, && \text{(2e)}\\
& [\mathbf{F}]_{n_1,n_2} \in \mathcal{F}, n_1\in\mathcal{N}_1, n_2\in\mathcal{N}_2, && \text{(2f)}
\end{aligned}$$

where $\mu_k > 0$ in (2a) is the weight assigned to the k-th unicast rate and (2b) enforces the sum of *rate fractions* to be $\bar{R}^{(\mathrm{c})}$. The constraint (2c) imposes a minimum QoS requirement C_0^{th}, necessary for decoding the multicast message whereas (2d) imposes a non-negativity restriction on the rates C_k. The constraint (2e) restricts the transmit power to P_{tx} while (2f) enforces the limitations of analog beamforming. Concretely, every phase shift $[\mathbf{F}]_{n_1,n_2}$ is constrained to the feasible set $\mathcal{F} = \left\{\delta_{\mathrm{tx}},\dots,\delta_{\mathrm{tx}}\exp\left(j\frac{2\pi(L_{\mathrm{tx}}-1)}{L_{\mathrm{tx}}}\right)\right\}$, where L_{tx} is the number of allowed constant-modulus phase shifts, $\delta_{\mathrm{tx}} = \sqrt{1/N_{\mathrm{tx}}^{\mathrm{RF}}}$, $n_1 \in \mathcal{N}_1 = \{1,\dots,N_{\mathrm{tx}}\}$ and $n_2 \in \mathcal{N}_2 = \{1,\dots,N_{\mathrm{tx}}^{\mathrm{RF}}\}$.

A. WSR maximization using fully-digital precoders

In this case, $\mathbf{F} = \mathbf{I}$ thereby transforming the hybrid precoder into a fully-digital precoder, where the number of antennas and RF chains are the same. Note that this assumption removes the nonconvex constraint (2f). As a result, $\mathcal{P}$ and $\mathcal{Q}_2$ (shown in Section V-B) become equivalent.

B. WSR maximization using hybrid precoders

The hybrid precoder consists of a coupled architecture between an analog component $\mathbf{F}$ and a digital component $[\mathbf{B}|\mathbf{m}]$. This structure poses a difficulty in obtaining an optimal solution for $\mathcal{P}$. Therefore, we design the hybrid precoder by means of two suboptimal methods that prove to have high performance when compared to the fully-digital precoder (as evidenced in Section VII). These suboptimal methods consist of two stages: in *Stage 1* we design the analog precoder whereas in *Stage 2* we optimize the rate-splitting and digital precoders.

Stage 1 *(Analog precoder design):* To design the RF analog precoder $\mathbf{F} = [\mathbf{f}_1,\dots,\mathbf{f}_K]$, two methods are devised with the goal of maximizing the effective RF-to-RF channel gain of every user. *Notice that* $\mathbf{F}$ *is optimized only once as it is*

matched to the channels $\{\mathbf{h}_k\}_{k=1}^K$, which are deemed invariant for a number of channel uses.

Codebook-based (CB): This method designs $\mathbf{F}$ in a column-wise manner using a codebook $\mathcal{V}$ by means of

$$\mathcal{Q}_{1,k}: \mathbf{f}_k = \underset{\mathbf{v}}{\operatorname{argmax}} \left|\mathbf{h}_k^H \mathbf{v}\right|^2 \text{ s.t. } \mathbf{v} \in \mathcal{V} \backslash \bar{\mathcal{V}}, \forall k \in \mathcal{K}, \quad (3)$$

where $\bar{\mathcal{V}}$ is formed by all the columns of $\mathcal{V}$ that have already been assigned to some user. Initially, $\bar{\mathcal{V}} = \emptyset$ and for each user the number of elements of $\bar{\mathcal{V}}$ is increased by one.

Projection-based (PB): This methods designs $\mathbf{F}$ in an element-wise manner, given the set of phase shifts $\mathcal{F}$, via

$$\mathcal{Q}_{1,k}: \mathbf{f}_k = \underset{\mathbf{r}_k}{\operatorname{argmax}} \left|\mathbf{h}_k^H \mathbf{r}_k\right|^2 \text{ s.t. } [\mathbf{r}_k]_n \in \mathcal{F}, n \in \mathcal{N}_1, \forall k \in \mathcal{K}. \quad (4)$$

First, the unconstrained version of $\mathcal{Q}_{1,k}$ is solved, whose solution collapses to the matched filter (i.e., a vector parallel to $\mathbf{h}_k$). Then, such vector is projected onto the set $\mathcal{F}$, thus yielding $\mathbf{f}_k$, i.e., $[\mathbf{f}_k]_n = \operatorname{argmax}_{\phi \in \mathcal{F}} \operatorname{Re}\left\{\phi \, [\mathbf{h}_k]_n^*\right\}$.

***Stage 2** (Rate-splitting and digital precoder design):* With the analog precoder $\mathbf{F}$ designed, the problem that optimizes C_0, $\{C_k\}_{k=1}^K$, $\{\mathbf{b}_k\}_{k=1}^K$, $\mathbf{m}$ is given by

$$\begin{aligned}
\mathcal{Q}_2: \max_{C_0, C_k, \mathbf{b}_k, \mathbf{m}} \quad & \textstyle\sum_{k\in\mathcal{K}} \mu_k \left(C_k + \log_2\left(1 + \mathrm{SINR}_k^{(\mathrm{p})}\right)\right) && (5a)\\
\text{s.t.} \quad & C_0 + \textstyle\sum_{j\in\mathcal{K}} C_j \le \log_2\left(1 + \mathrm{SINR}_k^{(\mathrm{c})}\right), \forall k \in \mathcal{K}, && (5b)\\
& C_0 \ge C_0^{\mathrm{th}}, && (5c)\\
& C_k \ge 0, \forall k \in \mathcal{K}, && (5d)\\
& \|\mathbf{F}\mathbf{m}\|_2^2 + \textstyle\sum_{k\in\mathcal{K}} \|\mathbf{F}\mathbf{b}_k\|_2^2 \le P_{\mathrm{tx}}, && (5e)
\end{aligned}$$

where (2b) has been equivalently recast as (5b) since $\bar{R}^{(\mathrm{c})} \le R_{\min}^{(\mathrm{c})}$. This nonconvex problem has been approached via the WMMSE method proposed in [2], [3], [5], which is shown to converge to a local optimum.

VI. Proposed Solution: FALCON

To solve $\mathcal{Q}_2$, we propose FALCON, which does not require judicious selection of an initial feasible point. Our approach stems from exploiting level sets and the establishment of convex upper bounds that can be contracted iteratively. Thus, assuming that $\mathbf{g}_k = \mathbf{F}^H \mathbf{h}_k$, we equivalent recast $\mathcal{Q}_2$ as

$$\begin{aligned}
\widetilde{\mathcal{Q}}_2: \max_{\substack{C_0, C_k, \mathbf{b}_k, \mathbf{m}\\ r_k, t_k, z_k, q_k}} \quad & \textstyle\sum_{k\in\mathcal{K}} \mu_k \left(C_k + \log_2\left(r_k\right)\right) && (6a)\\
\text{s.t.} \quad & \left|\mathbf{g}_k^H \mathbf{b}_k\right|^2 \ge \left(r_k - 1\right) t_k, \forall k \in \mathcal{K}, && (6b)\\
& \textstyle\sum_{j\neq k} \left|\mathbf{g}_k^H \mathbf{b}_j\right|^2 + \sigma^2 \le t_k, \forall k \in \mathcal{K}, && (6c)\\
& C_0 + \textstyle\sum_{j\in\mathcal{K}} C_j \le \log_2\left(z_k\right), \forall k \in \mathcal{K}, && (6d)\\
& \left|\mathbf{g}_k^H \mathbf{m}\right|^2 \ge \left(z_k - 1\right) q_k, \forall k \in \mathcal{K}, && (6e)\\
& \textstyle\sum_{j\in\mathcal{K}} \left|\mathbf{g}_k^H \mathbf{b}_j\right|^2 + \sigma^2 \le q_k, \forall k \in \mathcal{K}, && (6f)\\
& r_k \ge 1, \forall k \in \mathcal{K}, && (6g)\\
& z_k \ge 1, \forall k \in \mathcal{K}, && (6h)\\
& C_0 \ge C_0^{\mathrm{th}}, && (6i)\\
& C_k \ge 0, \forall k \in \mathcal{K}, && (6j)\\
& \|\mathbf{F}\mathbf{m}\|_2^2 + \textstyle\sum_{k\in\mathcal{K}} \|\mathbf{F}\mathbf{b}_k\|_2^2 \le P_{\mathrm{tx}}. && (6k)
\end{aligned}$$

In (6a), $1+\mathrm{SINR}_k^{(\mathrm{p})}$ is lower-bounded by r_k whereas, in (6c), the denominator of $\mathrm{SINR}_k^{(\mathrm{p})}$ is upper-bounded by t_k. By combining these two relations, we obtain (6b). The constraints (6d), (6e) and (6f) are obtained in a similar manner.

***Proposition 1*:** The formulations $\mathcal{Q}_2$ and $\widetilde{\mathcal{Q}}_2$ are equivalent.

Proof: We prove the equivalence by contradiction. Let $r_{k'}^\star$, $t_{k'}^\star$, $z_{k'}^\star$, $q_{k'}^\star$ denote the values of the variables for user k' at the optimum. Let us assume that at the optimum, constraint (6c) for user k' is inactive. Under this assumption, there must exist an strictly smaller $\tilde{t}_{k'} < t_{k'}^\star$ for which (6c) attains equality. This implies that there must also exist a strictly larger $\tilde{r}_{k'} > r_{k'}^\star$ that satisfies (6b), thus producing a larger objective (6a). This result contradicts the premise that we have obtained an optimal solution. Similar relations can be derived for (6d), (6e), (6f), thus corroborating the equivalence of $\mathcal{Q}_2$ and $\widetilde{\mathcal{Q}}_2$. ■

$$\begin{aligned}
\widehat{\mathcal{Q}}_2: \max_{\substack{C_0, C_k, \mathbf{B}_k, \mathbf{M},\\ r_k, t_k, z_k, q_k}} \quad & \textstyle\sum_{k\in\mathcal{K}} \mu_k \left(C_k + \log_2\left(r_k\right)\right) && (7a)\\
\text{s.t.} \quad & r_k t_k - t_k - \mathrm{Tr}\left(\mathbf{G}_k \mathbf{B}_k\right) \le 0, \forall k \in \mathcal{K}, && (7b)\\
& \textstyle\sum_{j\neq k} \mathrm{Tr}\left(\mathbf{G}_k \mathbf{B}_j\right) + \sigma^2 - t_k \le 0, \forall k \in \mathcal{K}, && (7c)\\
& C_0 + \textstyle\sum_{j\in\mathcal{K}} C_j \le \log_2\left(z_k\right), \forall k \in \mathcal{K}, && (7d)\\
& z_k q_k - q_k - \mathrm{Tr}\left(\mathbf{G}_k \mathbf{M}\right) \le 0, \forall k \in \mathcal{K}, && (7e)\\
& \textstyle\sum_{j\in\mathcal{K}} \mathrm{Tr}\left(\mathbf{G}_k \mathbf{B}_j\right) + \sigma^2 - q_k \le 0, \forall k \in \mathcal{K}, && (7f)\\
& \mathrm{Tr}\left(\mathbf{F}^H \mathbf{F} \mathbf{M}\right) + \textstyle\sum_{k\in\mathcal{K}} \mathrm{Tr}\left(\mathbf{F}^H \mathbf{F} \mathbf{B}_k\right) \le P_{\mathrm{tx}}, && (7g)\\
& \mathbf{B}_k \succeq 0, \forall k \in \mathcal{K}, && (7h)\\
& \mathbf{M} \succeq 0, && (7i)\\
& C_0 \ge C_0^{\mathrm{th}}, && (7j)\\
& C_k \ge 0, \forall k \in \mathcal{K}, && (7k)\\
& r_k \ge 1, \forall k \in \mathcal{K}, && (7l)\\
& z_k \ge 1, \forall k \in \mathcal{K}. && (7m)
\end{aligned}$$

Via semidefinite programming, $\widetilde{\mathcal{Q}}_2$ is transformed into $\widehat{\mathcal{Q}}_2$, where $\mathbf{G}_k = \mathbf{g}_k \mathbf{g}_k^H$, and the rank-one constraints on $\mathbf{B}_k = \mathbf{b}_k \mathbf{b}_k^H$, $\mathbf{M} = \mathbf{m}\mathbf{m}^H$ have been neglected. With the exception of constraints (7b), (7e), which contain quasi-concave functions of the form xy, the rest of expressions in $\widehat{\mathcal{Q}}_2$ constitute a convex problem. In order to circumvent these constraints we resort to the inequality $\frac{\gamma}{2}x^2 + \frac{1}{2\gamma}y^2 \ge xy$, which arises from the arithmetic-geometric mean of γx^2 and $\frac{1}{\gamma}y^2$, for $\gamma > 0$ [7]. Upon applying this upper estimate to (7b), (7e), we obtain $\overline{\mathcal{Q}}_2$.

$$\begin{aligned}
\overline{\mathcal{Q}}_2: \max_{\substack{C_0, C_k, \mathbf{B}_k, \mathbf{M},\\ r_k, t_k, z_k, q_k, \alpha_k, \beta_k}} \quad & \textstyle\sum_{k\in\mathcal{K}} \mu_k \left(C_k + \log_2\left(r_k\right)\right) && (8a)\\
\text{s.t.} \quad & \frac{\alpha_k}{2} r_k^2 + \frac{1}{2\alpha_k} t_k^2 - t_k - \mathrm{Tr}\left(\mathbf{G}_k \mathbf{B}_k\right) \le 0, \forall k \in \mathcal{K}, && (8b)\\
& \frac{\beta_k}{2} z_k^2 + \frac{1}{2\beta_k} q_k^2 - q_k - \mathrm{Tr}\left(\mathbf{G}_k \mathbf{M}\right) \le 0, \forall k \in \mathcal{K}, && (8c)\\
& \alpha_k > 0, \beta_k > 0, \forall k \in \mathcal{K}, && (8d)\\
& \textstyle\sum_{j\neq k} \mathrm{Tr}\left(\mathbf{G}_k \mathbf{B}_j\right) + \sigma^2 - t_k \le 0, \forall k \in \mathcal{K}, && (8e)\\
& C_0 + \textstyle\sum_{j\in\mathcal{K}} C_j \le \log_2\left(z_k\right), \forall k \in \mathcal{K}, && (8f)\\
& \textstyle\sum_{j\in\mathcal{K}} \mathrm{Tr}\left(\mathbf{G}_k \mathbf{B}_j\right) + \sigma^2 - q_k \le 0, \forall k \in \mathcal{K}, && (8g)\\
& \mathrm{Tr}\left(\mathbf{F}^H \mathbf{F} \mathbf{M}\right) + \textstyle\sum_{k\in\mathcal{K}} \mathrm{Tr}\left(\mathbf{F}^H \mathbf{F} \mathbf{B}_k\right) \le P_{\mathrm{tx}}, && (8h)\\
& \mathbf{B}_k \succeq 0, \forall k \in \mathcal{K}, && (8i)\\
& \mathbf{M} \succeq 0, && (8j)\\
& C_0 \ge C_0^{\mathrm{th}}, && (8k)\\
& C_k \ge 0, \forall k \in \mathcal{K}, && (8l)\\
& r_k \ge 1, \forall k \in \mathcal{K}, && (8m)\\
& z_k \ge 1, \forall k \in \mathcal{K}. && (8n)
\end{aligned}$$

***Proposition 2*:** When $\gamma = y/x$, $\overline{\mathcal{Q}}_2$ and $\widehat{\mathcal{Q}}_2$ are equivalent.

Proof: The geometric mean equates the arithmetic mean when the two constituents are equal, which occurs at $\gamma = y/x$. ■

Note that $\overline{\mathcal{Q}}_2$ is still nonconvex. However, we have removed the complicated constraints (7b), (7e) by incorporating auxiliary variables α_k and β_k. Notice that if α_k and β_k are fixed, $\overline{\mathcal{Q}}_2$ is convex. Therefore, we are in the position of tailoring an algorithm to solve $\overline{\mathcal{Q}}_2$. By harnessing *Proposition 2*, we propose Algorithm 1, wherein the upper estimates of $r_k t_k$ and $z_k q_k$ are contracted iteratively by updating α_k and β_k (i.e., `lines 3,4`). Although Algorithm 1 solves $\overline{\mathcal{Q}}_2$, a solution to $\overline{\mathcal{Q}}_2$ may not be feasible to $\widehat{\mathcal{Q}}_2$ or $\widetilde{\mathcal{Q}}_2$ due to omission of the rank-one constraints and the use of upper estimates. In the following, we clarify these aspects.

***Proposition 3*:** The solutions to $\overline{\mathcal{Q}}_2^{(i)}$ have at most rank one.

Proof: Let $\overline{\mathcal{Q}}_2^{(i)}$ denote the i-th iteration of $\overline{\mathcal{Q}}_2$. Let the Lagrangian with respect to $\mathbf{M}$ be defined as $\mathcal{L}_{\mathbf{M}} = \sum_{k\in\mathcal{K}} \xi_k \left(\frac{\beta_k}{2} z_k^2 + \frac{1}{2\beta_k} q_k^2 - q_k - \mathrm{Tr}\left(\mathbf{G}_k \mathbf{M}\right) \right) + \sum_{k\in\mathcal{K}} \pi_k \big(z_k q_k - q_k - \mathrm{Tr}\left(\mathbf{G}_k \mathbf{M}\right) \big) + \epsilon \left(\mathrm{Tr}\left(\mathbf{F}^H \mathbf{F} \mathbf{M}\right) + \sum_{k\in\mathcal{K}} \mathrm{Tr}\left(\mathbf{F}^H \mathbf{F} \mathbf{B}_k\right) - P_{\mathrm{tx}} \right) - \mathrm{Tr}\left(\mathbf{S}\mathbf{M}\right)$, where $\xi_k \geq 0$, $\pi_k \geq 0$, $\epsilon \geq 0$, $\mathbf{S} \succcurlyeq \mathbf{0}$ are the dual variables. From the stationarity condition, we obtain $\mathbf{S} = \epsilon(\mathbf{F}^H\mathbf{F}) - \sum_{k\in\mathcal{K}}(\xi_k + \pi_k)\mathbf{G}_k \succcurlyeq \mathbf{0}$. Since $\mathbf{F}^H\mathbf{F}$ is positive definite, the equivalent relation $\epsilon\mathbf{I} - \sum_{k\in\mathcal{K}}(\xi_k+\pi_k)(\mathbf{F}^H\mathbf{F})^{-1}\mathbf{G}_k \succcurlyeq \mathbf{0}$ holds if $\epsilon \geq \lambda_{\max}(\mathbf{T})$, where $\lambda_{\max}$ is the principal eigenvalue of $\mathbf{T} = \sum_{k\in\mathcal{K}}(\xi_k+\pi_k)(\mathbf{F}^H\mathbf{F})^{-1}\mathbf{G}_k \succcurlyeq \mathbf{0}$. When $\epsilon > \lambda_{\max}$, the matrix $\mathbf{S}$ is positive definite and therefore $\mathrm{rank}(\mathbf{S}) = N_{\mathrm{RF}}^{\mathrm{tx}}$. Due to the complementary slackness condition, this implies that $\mathbf{M} = \mathbf{0}$. However, replacing $\mathbf{M} = \mathbf{0}$ in $\overline{\mathcal{Q}}_2^{(i)}$ yields $C_0 = 0$, which violates (2c). Therefore this solution is not feasible. When $\epsilon = \lambda_{\max}$ then $\mathbf{S} \succcurlyeq \mathbf{0}$. Consequently, $\mathrm{rank}(\mathbf{S}) = N_{\mathrm{RF}}^{\mathrm{tx}} - 1$ and $\mathrm{rank}(\mathbf{M}) = 1$, which satisfies the assertion. For the unicast precoders $\mathbf{B}_k$, similar relations can be derived. However, $\mathbf{B}_k = \mathbf{0}$ does not violate any constraint. In particular, $\mathbf{B}_k = \mathbf{0}$ can be optimal for a particular instance, specifically when the user weight μ_k is small compared to other weights. ■

***Proposition 4*:** The sequence of objective function values produced by the update method in Algorithm 1 converges.

Proof: Let Ω_i denote the optimum of $\overline{\mathcal{Q}}_2^{(i)}$. Also, let $f(\Omega_i)$ be the objective function of $\overline{\mathcal{Q}}_2^{(i)}$ evaluated at the optimum Ω_i. Note that if we evaluate $f(\Omega_{i+1})$, all the constraints are still satisfied. This implies that an optimal solution to $\overline{\mathcal{Q}}_2^{(i)}$ is feasible to $\overline{\mathcal{Q}}_2^{(i+1)}$. Further, the update method (i.e., `line 4`) renders $f(\Omega_{i+1}) \geq f(\Omega_i)$, thus generating a monotonically non-decreasing sequence of objective function values. Moreover, since $\overline{\mathcal{Q}}_2$ is limited by a power constraint, the non-decreasing sequence will be bounded and therefore guarantees convergence. ■

***Proposition 5*:** $\overline{\mathcal{Q}}_2$ satisfies the KKT conditions of $\mathcal{Q}_2$.

Proof: A solution Ω_i to $\overline{\mathcal{Q}}_2^{(i)}$ will always be feasible to $\widehat{\mathcal{Q}}_2$ as the inequalities of $\overline{\mathcal{Q}}_2^{(i)}$ are tighter. Because a solution Ω_i with rank-one $\mathbf{M}^{(i)}$, $\mathbf{B}_k^{(i)}$, $\forall k \in \mathcal{K}$ can be found in $\overline{\mathcal{Q}}_2^{(i)}$, Ω_i is also feasible to $\widetilde{\mathcal{Q}}_2$ and $\mathcal{Q}_2$. Invoking the results in Proposition 3.2 of [7], we state that the sequence of solutions $\{\Omega_i\}$ converges to a regular point $\Omega_i^\star$ that is a KKT point of $\widetilde{\mathcal{Q}}_2$ and $\mathcal{Q}_2$. ■

Based on the propositions above, we show that via FALCON the feasible set of $\overline{\mathcal{Q}}_2$ converges to the feasible set of $\mathcal{Q}_2$. Further, by iteratively solving $\overline{\mathcal{Q}}_2^{(i)}$ the solutions Ω_i converge to a local optimum of the nonconvex problem $\mathcal{Q}_2$.

Algorithm 1: Rate-splitting and precoding via FALCON

Input: $\{\mathbf{h}_k\}_{k=1}^K$, $\{\mu_k\}_{k=1}^K$, C_0^{th}.
Output: $\mathbf{F}$, $\{\mathbf{b}_k\}_{k=1}^K$, $\mathbf{m}$, C_0, $\{C_k\}_{k=1}^K$
Execute:
1: Design the analog precoder $\mathbf{F}$ by solving $\mathcal{Q}_{1,k}$, $\forall k \in \mathcal{K}$.
2: Initialize $\alpha_k^{(i)} = 1$ and $\beta_k^{(i)} = 1$, $i = 0$, $\forall k \in \mathcal{K}$.
repeat
3: Solve $\overline{\mathcal{Q}}_2^{(i)}$ employing $\alpha_k^{(i)}$ and $\beta_k^{(i)}$.
4: Update $\alpha_k^{(i+1)} = t_k^{(i)}/r_k^{(i)}$, $\beta_k^{(i+1)} = q_k^{(i)}/z_k^{(i)}$, $\forall k \in \mathcal{K}$.
5: Update $i = i + 1$.
until stopcriterion.

Table I: Feasibility response of fully-digital precoders.

Case	Parameters configuration	FALCON	WMMSE (%)														
			$P_{\mathrm{m}}^{(0)} = 0.70P_{\mathrm{tx}}$			$P_{\mathrm{m}}^{(0)} = 0.80P_{\mathrm{tx}}$			$P_{\mathrm{m}}^{(0)} = 0.90P_{\mathrm{tx}}$			$P_{\mathrm{m}}^{(0)} = 0.95P_{\mathrm{tx}}$			$P_{\mathrm{m}}^{(0)} = 0.99P_{\mathrm{tx}}$		
	$[N_{\mathrm{tx}}, K, C_0^{\mathrm{th}}]$	(%)	MRT	ZF	SLNR	MRT	ZF	SLNR	MRT	ZF	SLNR	MRT	ZF	SLNR	MRT	ZF	SLNR
A	[4,2,2.5]	**100**	38	55	54	63	63	63	75	77	73	83	83	78	**84**	83	80
B	[6,3,2.0]	**100**	36	49	68	51	63	70	70	80	77	81	83	81	**87**	87	83
C	[8,4,1.5]	**96**	53	67	86	69	73	89	80	85	93	83	85	93	91	92	**94**

Table II: Feasibility response of hybrid precoders.

Case	Parameters configuration	FALCON	WMMSE (%)														
			$P_{\mathrm{m}}^{(0)} = 0.70P_{\mathrm{tx}}$			$P_{\mathrm{m}}^{(0)} = 0.80P_{\mathrm{tx}}$			$P_{\mathrm{m}}^{(0)} = 0.90P_{\mathrm{tx}}$			$P_{\mathrm{m}}^{(0)} = 0.95P_{\mathrm{tx}}$			$P_{\mathrm{m}}^{(0)} = 0.99P_{\mathrm{tx}}$		
	$[N_{\mathrm{tx}}, K, C_0^{\mathrm{th}}]$	(%)	MRT	ZF	SLNR	MRT	ZF	SLNR	MRT	ZF	SLNR	MRT	ZF	SLNR	MRT	ZF	SLNR
A	[4,2,2.5]	**100**	54	58	69	82	77	68	82	82	78	87	87	84	**87**	87	87
B	[6,3,2.0]	**100**	63	54	62	70	72	67	79	79	76	84	83	81	**88**	87	85
C	[8,4,1.5]	**96**	74	81	79	85	85	86	93	94	91	93	95	94	**96**	96	96

VII. Simulation Results

In this section, we compare FALCON and WMMSE. In the scenarios evaluated in Section VII-A, Section VII-B, Section VII-C we employ the more versatile projection-based hybrid precoder whereas in Section VII-D we compare the two types of hybrid precoders. Throughout the simulations, we have considered $P_{\mathrm{tx}} = 50$ dBm and $\sigma^2 = 30$ dBm as in [2]. In addition, for all scenarios involving different precoders and techniques, we have used the same stopping criterion (see Algorithm 1). Specifically, the techniques are executed for a maximum of $N_{\mathrm{iter}} = 60$ iterations or until an increment of less than $\epsilon = 0.0001$ is attained (by the objective function).

A. Feasibility response

We evaluate the performance of FALCON and WMMSE with RS-NOUM, in terms of the feasible solutions count. We examine different configurations of $[N_{\mathrm{tx}}, K, C_0^{\mathrm{th}}]$ assuming equal weights $\mu_1 = \cdots = \mu_K = 1$ with fully-digital and hybrid precoders. We employ the geometric Saleh-Valenzuela channel model [21]. Since WMMSE requires an initial feasible point, we assess three types of initialization methods. The initial multicast precoder $\mathbf{m}^{(0)}$ is obtained via singular value decomposition (SVD) of the aggregate channel [3], [19] whereas the initial unicast precoders $\mathbf{b}_k^{(0)}$ are the MRT, ZF or SLNR precoding vectors. The initial multicast and unicast powers (for the initial feasible point) are computed as $P_{\mathrm{m}}^{(0)} = \left\|\mathbf{F}\mathbf{m}^{(0)}\right\|_2^2$ and $P_{\mathrm{u},k}^{(0)} = \left\|\mathbf{F}\mathbf{b}_k^{(0)}\right\|_2^2 = \frac{P_{\mathrm{tx}} - P_{\mathrm{m}}^{(0)}}{K}$, $\forall k \in \mathcal{K}$. We evaluate several values of $P^{(0)} = \{0.70P_{\mathrm{tx}}, 0.80P_{\mathrm{tx}}, 0.90P_{\mathrm{tx}}, 0.95P_{\mathrm{tx}}, 0.99P_{\mathrm{tx}}\}$ with $L_{\mathrm{tx}} = 16$ different phase shifts for the projection-based hybrid

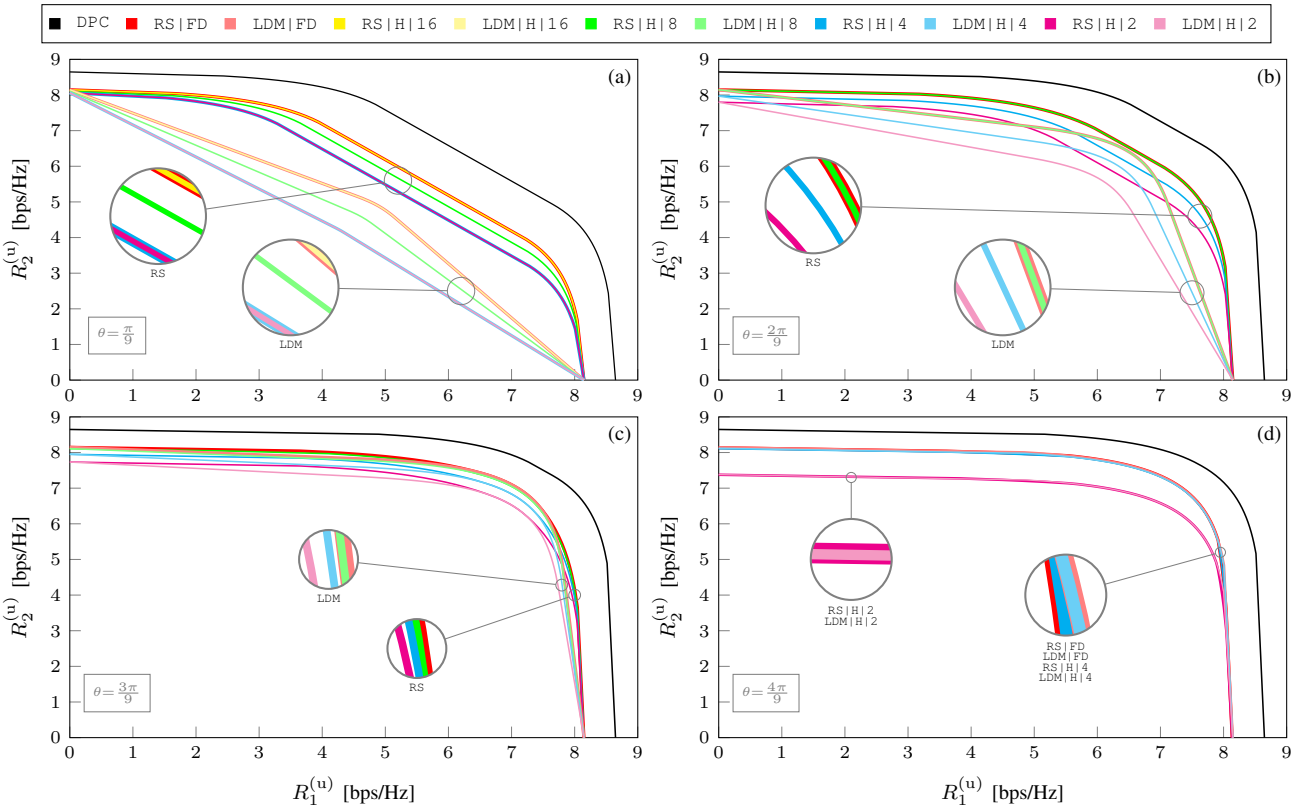

Figure 1: Two-user rate region for fully-digital (FD) and hybrid (H) precoders.

precoder. Table I and Table II show the results for the fully-digital and hybrid precoders. Note that FALCON is superior to WMSSE in delivering a larger number of feasible solutions without requiring complicated initialization. Throughout the different configurations, FALCON returns a feasible solution in at least 96% of the cases whereas the performance of WMMSE is inferior. In the WMMSE case, the same value of $P^{(0)}$ leads to different feasibility responses for distinct $[N_{\text{tx}}, K, C_0^{\text{th}}]$. In certain cases, the hybrid precoder attains more feasible solutions that the fully-digital precoder. This occurs due to the strong dependence of WMMSE on the initial feasible point, which is also influenced by the analog precoder $\mathbf{F}$. Nevertheless, this outcome does not imply that both precoders provide the same rate value, as clarified in the next scenario.

B. Convergence

We compare the convergence of FALCON and WMMSE for a random realization of Case C in Table I, which is the most favorable scenario for WMMSE. Fig. 2a shows the evolution of the unicast rates when $P_{\text{m}}^{(0)} = 0.90P_{\text{tx}}$. We observe that FALCON converges $2-3$ times faster than WMMSE for hybrid and fully-digital precoders. Since the performance of WMMSE relies on a initial point, in Fig. 2b we evaluate more cases for the fully-digital precoder using MRT (in [5] it is shown that MRT with SVD leads to faster convergence in high SNR regime as in this case). In Fig. 2b, although $P_{\text{m}}^{(0)} = 0.80P_{\text{tx}}$ produces faster convergence among other choices, it does not

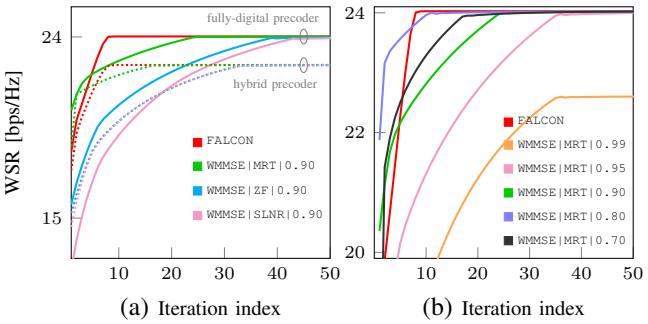

Figure 2: Convergence of FALCON and WMMSE.

surpass FALCON, which only requires 8 iterations to attain convergence. Further, from Table I, using $P_{\text{m}}^{(0)} = 0.80P_{\text{tx}}$ only produces 69% of feasible solutions. Also, note that while $P_{\text{m}}^{(0)} = 0.99P_{\text{tx}}$ produces a feasible solution in 94% of the cases, this choice makes WMMSE converge to a less optimal point. Finding performant initial feasible points for WMMSE is impractical as either infeasibility certificates are returned or the convergence is impacted. In particular, we observe that WMMSE experiences the following trade-off: *large initial power allocation for $P_{\text{m}}^{(0)}$ leads to higher likelihood of producing feasible solutions but causes extremely slow convergence (optimality may even be affected) while small initial power allocations may produce faster convergence but increases the likelihood of resulting in infeasible solutions.*

C. Two-user rate region

We evaluate the performance of RS-NOUM and LDM-NOUM using FALCON with fully-digital (FD) and projection-based hybrid (H) precoders considering the same settings as in [2], namely $K = 2$, $N_{\text{tx}} = 4$, $C_0^{\text{th}} = 0.5$ bps/Hz and channels $\mathbf{h}_1 = [1, 1, 1, 1]^H$, $\mathbf{h}_2 = \left[1, e^{j\theta}, e^{j2\theta}, e^{j3\theta}\right]^H$. For the hybrid precoder, we assume that $N_{\text{tx}}^{\text{RF}} = K = 2$ with four degrees of quantization, $L_{\text{tx}} = \{2, 4, 8, 16\}$. To solve the LDM case via FALCON, we enforce $C_k = 0$, $\forall k \in \mathcal{K}$. Fig. 1a shows the case when the channels are highly correlated ($\theta = \pi/9$). We observe that RS outperforms LDM due to its capability to manage interference, in particular in this challenging scenario. We also note that for RS and LDM, the hybrid precoder with $L_{\text{tx}} = 16$ (i.e., 4 bits) has the same performance as a fully-digital precoder. The performance when $L_{\text{tx}} = 2$ and $L_{\text{tx}} = 4$ is the same due to quantization that has produced the same analog precoder. Through Fig. 1b, Fig. 1c, Fig. 1d, the channel correlation among users is reduced by increasing θ. As expected, LDM approaches the performance of RS as interference becomes less detrimental. Interestingly, the phase resolution of the hybrid precoder becomes less relevant as the correlation between channels decreases. For instance, in Fig. 1d with $L_{\text{tx}} = 4$ (i.e., 2 bits) the hybrid and fully-digital precoders attain the same performance.

D. Comparing hybrid precoder designs

We compare the performance of FALCON in RS-NOUM with the two hybrid precoder designs described in Section V-B. In this scenario, we assume that $N_{\text{tx}} = 8$, $C_0^{\text{th}} = 1.5$ (as in Case C of Table I and Table II) for various number of users $K = \{2, 3, 4, 5, 6\}$. For the PB hybrid (PB-H) precoder we assume that $L_{\text{tx}} = 16$. For CB hybrid (CB-H) precoder, we form the codebook $\mathcal{V}$ with 128 codewords, where N_{tx} codewords are mutually orthogonal obtained from the discrete Fourier matrix of size N_{tx} and 120 codewords pseudo-randomly generated. Fig. 3 shows that PB-H outperforms CB-H through all values of K. In addition, we include FALCON and WMMSE using fully-digital precoders. For WMMSE, we have assumed $P_{\text{m}}^{(0)} = 0.80 P_{\text{tx}}$ because in Section VII-B we showed that this initial value does not affect performance substantially while allowing high convergence speed (although the feasibility ratio is conditioned).

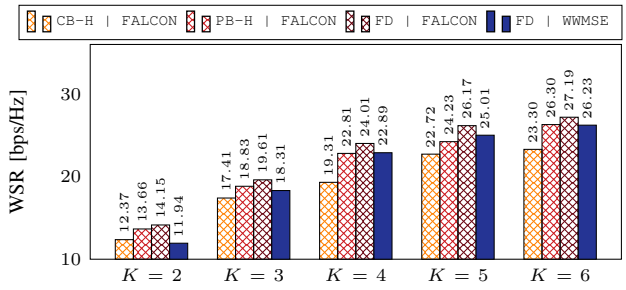

Figure 3: Performance comparison of hybrid precoders

E. Computational complexity

The computational complexity per iteration of WMMSE and FALCON with fully-digital (FD) or hybrid (H) precoders is shown in Table III. The complexity of designing the analog component $\mathbf{F}$ has been considered negligible due to simple inner products involved. Since the complexity per iteration is not representative of the convergence behavior of a scheme, we show in Table IV the time required for convergence and the feasibility ratio. We evaluate FALCON and WMMSE using fully-digital precoders for the same scenario described in Section VII-D. We observe that while FALCON has higher computational complexity per iteration (see Table III), it converges up to 100% times faster (in terms of the execution time) and in addition, it returns more feasible solutions than WMMSE.

Table III: Computational complexity per iteration

Description	Notation	Complexity
Weights of WWMSE with FD design	$\mathcal{C}^{(\text{w})}_{\text{FD-WMMSE}}$	$\mathcal{O}\left(K^2 N_{\text{tx}}\right)$
Precoders of WWMSE with FD design	$\mathcal{C}^{(\text{p})}_{\text{FD-WMMSE}}$	$\mathcal{O}\left(K^{3.5}\left[N_{\text{tx}}\right]^{3.5}\right)$
Weights of WWMSE with H design	$\mathcal{C}^{(\text{w})}_{\text{H-WMMSE}}$	$\mathcal{O}\left(K^2 N_{\text{tx}}^{\text{RF}}\right)$
Precoders of WWMSE with H design	$\mathcal{C}^{(\text{p})}_{\text{H-WMMSE}}$	$\mathcal{O}\left(K^{3.5}\left[N_{\text{tx}}^{\text{RF}}\right]^{3.5}\right)$
FALCON with FD design	$\mathcal{C}_{\text{FD-FALCON}}$	$\mathcal{O}\left(K^3\left[N_{\text{tx}}\right]^6\right)$
FALCON with H design	$\mathcal{C}_{\text{H-FALCON}}$	$\mathcal{O}\left(K^3\left[N_{\text{tx}}^{\text{RF}}\right]^6\right)$

Table IV: Convergence time

Scheme	Number of users				
	$K = 6$	$K = 5$	$K = 4$	$K = 3$	$K = 2$
FALCON	93.6s|91%	40.1s|93%	33.8s|96%	31.7s|100%	37.5s|100%
WWMSE	116.9s|67%	75.9s|82%	66.3s|75%	45.1s|79%	31.4s|62%

VIII. Conclusion

We have investigated non-orthogonal unicast multicast transmissions by means of rate-splitting with fully-digital and hybrid precoders. We considered the weighted sum-rate maximization problem with a minimum multicast QoS requirement. We proposed FALCON based on sequential parametric optimization, which is shown to outperform WMMSE under a variety of scenarios. We showed that FALCON converges to local optimum of the nonconvex problem. Although FALCON has higher complexity per iteration than WMMSE, it converges faster within a few iterations and does not require an initial feasible point, which impacts performance. Further, FALCON is a viable option for designing hybrid precoders with rate-splitting since the complexity scales with the number of RF chains, which in general, is relatively small. In addition, for the two-user case, we noticed that a quantization scheme with 4 bits is sufficient for guaranteeing performance equal to that of a fully-digital precoder. Moreover, as the user channels become less correlated, the quantization granularity of the analog precoder is less relevant.

Acknowledgment

This research is funded by the Deutsche Forschungsgemeinschaft (DFG) within the B5G-Cell project in SFB 1053

MAKI, and the LOEWE initiative (Hesse, Germany) within the emergenCITY centre.

REFERENCES

[1] J. Zhao, O. Simeone, D. Gunduz, and D. Gomez-Barquero, "Non-Orthogonal Unicast and Broadcast Transmission via Joint Beamforming and LDM in Cellular Networks," in *IEEE GLOBECOM*, December 2016, pp. 1–6.

[2] Y. Mao, B. Clerckx, and V. O. K. Li, "Rate-Splitting for Multi-Antenna Non-Orthogonal Unicast and Multicast Transmission," in *IEEE SPAWC*, June 2018, pp. 1–5.

[3] ——, "Rate-Splitting for Multi-Antenna Non-Orthogonal Unicast and Multicast Transmission: Spectral and Energy Efficiency Analysis," *IEEE Transactions on Communications*, vol. 67, no. 12, pp. 8754–8770, December 2019.

[4] H. Joudeh and B. Clerckx, "A Rate-Splitting Approach to Robust Multiuser MISO Transmission," in *IEEE ICASSP*, 2016, pp. 3436–3440.

[5] ——, "Sum-Rate Maximization for Linearly Precoded Downlink Multiuser MISO Systems With Partial CSIT: A Rate-Splitting Approach," *IEEE Transactions on Communications*, vol. 64, no. 11, pp. 4847–4861, November 2016.

[6] S. S. Christensen, R. Agarwal, E. D. Carvalho, and J. M. Cioffi, "Weighted Sum-Rate Maximization Using Weighted MMSE for MIMO-BC Beamforming Design," *IEEE Transactions on Wireless Communications*, vol. 7, no. 12, pp. 4792–4799, December 2008.

[7] A. Beck, A. Ben-Tal, and L. Tetruashvili, "A Sequential Parametric Convex Approximation Method with Applications to Nonconvex Truss Topology Design Problems," *Journal of Global Optimization*, vol. 47, no. 1, pp. 29–51, July 2010.

[8] J. Zhao, D. Gündüz, O. Simeone, and D. Gómez-Barquero, "Non-Orthogonal Unicast and Broadcast Transmission via Joint Beamforming and LDM in Cellular Networks," *IEEE Transactions on Broadcasting*, pp. 1–13, June 2019.

[9] Y. Liu, C. Lu, M. Tao, and J. Wu, "Joint Multicast and Unicast Beamforming for the MISO Downlink Interference Channel," in *IEEE SPAWC*, July 2017, pp. 1–5.

[10] L. F. Abanto-Leon and G. H. Sim, "Fairness-Aware Hybrid Precoding for mmWave NOMA Unicast/Multicast Transmissions in Industrial IoTs," in *IEEE ICC*, June 2020.

[11] Y. Li, M. Xia, and Y. Wu, "Energy-Efficient Precoding for Non-Orthogonal Multicast and Unicast Transmission via First-Order Algorithm," *IEEE Transactions on Wireless Communications*, vol. 18, no. 9, pp. 4590–4604, September 2019.

[12] O. Tervo, L. Tran, S. Chatzinotas, M. Juntti, and B. Ottersten, "Energy-Efficient Joint Unicast and Multicast Beamforming with Multi-Antenna User Terminals," in *IEEE SPAWC*, July 2017, pp. 1–5.

[13] E. Chen and M. Tao, "Backhaul-Constrained Joint Beamforming for Non-Orthogonal Multicast and Unicast Transmission," in *IEEE GLOBECOM*, December 2017, pp. 1–6.

[14] E. Chen, M. Tao, and Y. Liu, "Joint Base Station Clustering and Beamforming for Non-Orthogonal Multicast and Unicast Transmission With Backhaul Constraints," *IEEE Transactions on Wireless Communications*, vol. 17, no. 9, pp. 6265–6279, September 2018.

[15] L. F. Abanto-Leon, M. Hollick, and G. H. Sim, "BEAMWAVE: Cross-Layer Beamforming and Scheduling for Superimposed Transmissions in Industrial IoT mmWave Networks," in *Wireless Optimization*, October 2021.

[16] O. Tervo, L. Tran, S. Chatzinotas, B. Ottersten, and M. Juntti, "Multigroup Multicast Beamforming and Antenna Selection with Rate-Splitting in Multicell Systems," in *IEEE SPAWC*, 2018, pp. 1–5.

[17] H. Chen, D. Mi, Z. Chu, P. Xiao, and R. Tafazolli, "Rate-Splitting for Multigroup Multicast Beamforming in Multicarrier Systems," in *IEEE SPAWC*, 2018, pp. 1–5.

[18] X. Su, L. Li, H. Yin, and P. Zhang, "Robust Power- and Rate-Splitting-Based Transceiver Design in K -User MISO SWIPT Interference Channel Under Imperfect CSIT," *IEEE Communications Letters*, vol. 23, no. 3, pp. 514–517, March 2019.

[19] Y. Mao, B. Clerckx, and V. O. K. Li, "Rate-splitting Multiple Access for Downlink Communication Systems: Bridging, Generalizing, and Outperforming SDMA and NOMA," *EURASIP Journal on Wireless Communications and Networking*, vol. 1, no. 133, May 2018.

[20] M. Dai and B. Clerckx, "Multiuser Millimeter Wave Beamforming Strategies With Quantized and Statistical CSIT," *IEEE Transactions on Wireless Communications*, vol. 16, no. 11, pp. 7025–7038, November 2017.

[21] T. S. Rappaport, R. W. Heath, R. C. Daniels, and J. N. Murdock, *Millimeter Wave Wireless Communications*. New York: Pearson Education, 2015.

E

PUBLICATION V.
HYDRAWAVE: MULTI-GROUP MULTICAST HYBRID PRECODING AND LOW-LATENCY SCHEDULING FOR UBIQUITOUS INDUSTRY 4.0 MMWAVE COMMUNICATIONS

HydraWave: Multi-Group Multicast Hybrid Precoding and Low-Latency Scheduling for Ubiquitous Industry 4.0 mmWave Communications

Luis F. Abanto-Leon, Matthias Hollick, and Gek Hong (Allyson) Sim
Secure Mobile Networking (SEEMOO) Lab, Technichal University of Darmstadt, Germany

***Abstract*—Industry 4.0 anticipates massive interconnectivity of industrial devices (e.g., sensors, actuators) to support factory automation and production. Due to the rigidity of wired connections to harmonize with automation, wireless information transfer has attracted substantial attention. However, existing solutions for the manufacturing sector face critical issues in coping with the key performance demands: *ultra-low latency, high throughput, and high reliability*. Besides, recent advancements in wireless millimeter-wave technology advocates hybrid precoding with affordable hardware and outstanding spatial multiplexing performance. Thus, we present `HYDRAWAVE` — a new paradigm that contemplates the joint design of *group scheduling* and *hybrid precoding* for multi-group multicasting to support ubiquitous low-latency communications. Our hybrid precoder, based on semidefinite relaxation and Cholesky matrix factorization, facilitates the robust design of the constant-modulus phase shifts rendering formidable performance at a fraction of the power required by fully-digital precoders. Further, our novel group scheduling formulation minimizes the number of scheduling windows while accounting for the channel correlation of the co-scheduled multicast receivers. Compared to exhaustive search, which renders the optimal scheduling at high overhead, `HYDRAWAVE` incurs only 9.5% more delay. Notoriously, `HYDRAWAVE` attains up to 102% gain when compared to the other benchmarked schemes.**

***Index Terms*—hybrid precoding, multi-group multicasting, low-latency, Industry 4.0, millimeter-wave, scheduling.**

I. Introduction

The industrial revolution, Industry 4.0, fosters smart factories of the future where the components in a production chain—such as industrial equipment, logistics, products, and processes—are inherently interconnected. Given the hyper-connected vision of Industry 4.0, wired connections become less attractive because they (*i*) hinder automation by constraining the movement of industrial robotics and (*ii*) slow down mechanics. To overcome this obstacle, in recent years, significant effort has been dedicated to leveraging the benefits of wireless communications solutions for the manufacturing sector (e.g., 6TiSCH, ZigBee). However, the adoption of these technologies is either limited or has not been consolidated due to the uncertainty on their capability to offer performance similar to optical fiber and guarantee the critical requirements of industrial applications: *ultra-high throughput and ultra-low latency with emphasis on high reliability* [1].

Owing to recent advancements in wireless millimeter-wave (mmWave) technology, the mmWave spectrum is regarded as a solution to wire replacement in industrial/manufacturing sectors. In addition to providing multi-Gbps rates due to wideband availability, mmWave frequencies characterize for requiring antennas with a small footprint that can be easily embedded onto miniature machinery/devices. A measurement campaign conducted in an industrial environment has concluded that mmWave communications is feasible and effortlessly implementable in such environments [2]. Nevertheless, the research on wireless and (in particular) mmWave technology for the industrial context is still at its infancy.

The industrial sectors can profoundly benefit from mmWave multicast beamforming to deliver common information to industrial equipment (e.g., sensors and actuators) for the distributed organization of production. In such setting, instead of sequentially transmitting unicast streams from a transmitter to each receiver (Fig. 1a), multicasting to a group of devices (Fig. 1b) can boost the spectral efficiency and offer lower latency. Moreover, if the transmitter is equipped with multiple radio frequency (RF) chains, multi-group multicasting can be enabled thus making possible to serve several groups of devices concurrently while further leveraging the gains in terms of spectral efficiency and latency (Fig. 1c).

We envision a heterogeneous hyper-connected Industry 4.0 with *(i) anchored receivers* (e.g., sensors, actuators, programmable logic devices) that perform tasks locally and *(ii) mobile receivers* (e.g., robots) that carry out tasks at various locations. Specifically, multiple *anchored receivers* from different multicast groups can be found sharing the same space, thus increasing the difficulty of spatial multiplexing (Fig. 1b). In addition, due to mobility (e.g. robots), numerous *mobile receivers* with different information needs may temporarily change their location to carry out specific tasks, thus either altering the density of devices at different phases of the production chain or generating a variable degree of interference.

Fully-digital precoders with a massive amount of antennas and RF chains are a tangible technology at sub-6GHz frequencies. However, in mmWave, these precoders are still not affordable due to hardware complexity and high power consumption. As a result, substantial effort has been oriented to *(i)* improve the architectures design (e.g., [3], [4]) and *(ii)* develop accurate channel estimation methods (e.g., [5], [6]) for hybrid precoders, aiming at facilitating physical-layer hybrid precoding with high signal-to-interference-plus-noise ratio (SINR). In industrial scenarios, the number of multicast groups is expected to be large in comparison to the number of RF chains, generating thereby the necessity for scheduling. Further, depending on how the groups are co-scheduled, the achievable performance of the precoder will be impacted. As a result, a scrupulous design that considers the joint optimization of scheduling, hybrid precoder (at the transmitter) and analog combiners (at receivers) is required to comply with the requirements of industrial applications. To this end,

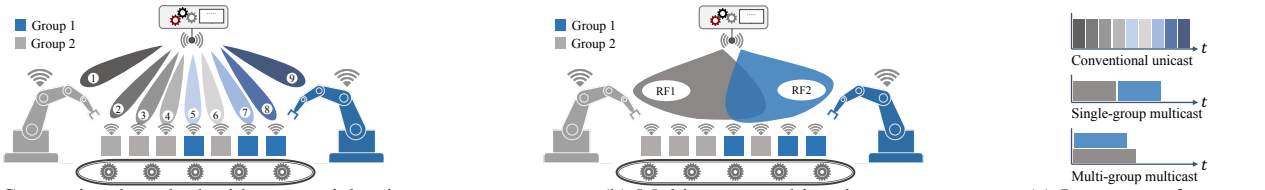

(a) Conventional method with sequential unicast (b) Multi-group multicasting (c) Latency performance

Figure 1: Comparison of mmWave unicast, conventional and proposed multi-group multicasting methods in Industry 4.0.

we propose HYDRAWAVE, a versatile scheme that devises an *agile scheduler* and a *robust multi-group multicast precoder with analog combiners*, capable of providing *high throughput, low latency, and high reliability* (which is guaranteed through service ubiquitousness).

Table I: Literature on multicasting

Type	Scheduling with PHY abstraction	PHY design w/o scheduling		PHY design w/ scheduling	
		Fully-digital	Hybrid	Fully-digital	Hybrid
SGM	[7]–[9]	[10]–[14]	[12], [15], [16]	[17], [18]	–
MGM	–	[19]–[26]	[27]–[30]	–	–

As shown in Table I, the literature on single-group multicasting (SGM) focus on either pure scheduling with physical-layer (PHY) abstraction [7]–[9] or physical-layer beamforming/precoding with [17], [18] and without scheduling [10]–[16], ignoring the interference aspect in multi-group multicast scenarios. On the other hand, the body of research on multi-group multicasting (MGM) focuses mostly on fully-digital precoder designs without scheduling tailored for sub-6GHz frequencies [19]–[26], which are not appropriate for mmWave. As a result, the more practical and cost-efficient hybrid precoders [27]–[29] have attracted substantial attention. Nevertheless, these solutions are either (*i*) constrained in application due to simplified assumptions [21], [28] or (*ii*) unimplementable in the existing multi-antenna hardware due to customized designs [27], [29]. In [30], MGM is investigated with hybrid precoders and finite resolution phase shifts but the scheduling aspect is not considered. The joint problem of *group scheduling* and *precoding* for multi-group multicasting has been studied for neither fully-digital nor hybrid precoders. The following summarizes our contributions:

- We introduce three propositions that support the design of precoders that ensure low-latency and high reliability. *Proposition 1* renders insights on the (approximate) inverse relation between SINR and latency. *Proposition 2* leverages on this result, and reveals that latency minimization is promoted when maximizing the minimum equalized SINR (e-SNR). This exposes a relevant relation with the max-min MGM problem. *Proposition 3* supports our formulation of optimal joint group scheduling and precoding for the multi-group multicast problem, with emphasis on latency minimization and high reliability.
- Due to the complexity of solving the problem related to *Proposition 3* (which requires exhaustive search), we devise a novel group scheduling formulation with a two-fold objective: *(i)* minimizing the number of scheduling windows and *(ii)* reducing channel correlation between the co-scheduled receivers. To attain the latter objective, we introduce a metric called *aggregate inter-group correlation* that is shown to be highly suitable for forming the co-scheduled multicast groups. As a result, we only need to solve the problem associated with *Proposition 2* (which is comparatively simpler) for every window of the resultant scheduling thus reducing the complexity.
- The problem associated with *Proposition 2* is non-convex. Due to the NP-hardness of this problem, we propose an alternate optimization scheme where the analog and digital components of the hybrid precoder (at the transmitter), and the analog combiners (at each receiver) are optimized sequentially. We recast each sub-problem as a semidefinite relaxation (SDR) program in order to convexify the non-convex expressions.
- We propose a versatile approach based on Cholesky matrix factorization, capable of handling an arbitrary number of phase rotations at both the analog component of the hybrid precoder (at the transmitter) and the analog combiners (at the receivers) with outstanding performance.
- Compared to prior art on multi-group multicast precoding, we consider receivers with multiple antennas, which can be adopted at mmWave frequencies owing to the small antenna footprints.
- Through extensive simulations, we evaluate the performance of our hybrid precoder and compare it against fully-digital and fully-analog implementations. Further, we also assess our proposed HYDRAWAVE (joint group scheduling and precoding) and compare it in terms of *latency* against three competing approaches: single-group multicasting (SING), random scheduling (RAND) and exhaustive search (XHAUS). We show through simulations that HYDRAWAVE can attain gains up to 102% and 60% when compared against RAND and SING, respectively, while remaining within 9.5% optimality of XHAUS.

II. Related Work

In SGM scheduling with physical-layer abstraction [7]–[9], the transmitter adjusts the gains of single-lobe switched beams to improve the SNR at the receivers. These works mainly focus on achieving high throughput with minimum delay for all the multicast receivers. Concerning SGM physical-layer precoding (hybrid/fully-digital and with/without scheduling), researchers have studied the quality-of-service (QoS) and max-min fairness problems [10]–[15], [17], [18]. Under these two categories, the QoS [19]–[23], [27], [28] and max-min fairness [22]–[26], [29] problems have also been researched for the MGM case. Fully-digital precoders are highly versatile for

interference mitigation due to the availability of numerous RF chains. However, these designs consumes excessive power and require expensive hardware (particularly for mmWave). To address these issues, the use of analog-digital architectures (i.e., hybrid precoders) have received considerable attention. Hybrid precoders are constituted by a low-dimensional digital precoder that allows interference management and a high-dimensional network of phase shifters, with an arbitrary set of phase rotations that facilitates beamsteering. These designs do not have the same versatility as fully-digital implementations but are more energy-efficient and practical. Nevertheless, the existing hybrid precoder solutions (in general, multicast and multi-user unicast designs) are restricted in usage due to either (*i*) simplified assumptions in phase rotations selection or (*i*) unimplementability owing to customized hardware. Specifically, the solution propounded in [29] requires a especially connected network of phase shifters for optimal operation. On the other hand, in [21], [28], the usage is constrained to only four different phase shifts. In [27], the analog phase shifters are replaced by high-resolution lens arrays with adjustable power, thus circumventing the actual problem of phase selection.

A work that focuses on a problem slightly related to ours is [31], where the authors study user selection and MGM precoding with fully-digital transmitters and single-antenna receivers. In [31], specific users for each multicast group are selected in order to maximize the sum-rate. Contrastingly, in our case we deal with group selection for which we devise a metric (i.e., IGC) that depicts the mean channel vector correlation among the receivers of each group. Also, in our case, the objective is to design the precoders aiming at the minimization of the transmission latency.

III. Multi-Group Multicast System Model

We consider a mmWave system where a next generation Node B (gNodeB) equipped with a hybrid precoder aims to schedule G_T multicast groups comprising a total of K_T receivers. The sets of receivers and groups are denoted by $\mathcal{K} = \{1, 2, \ldots, K_T\}$ and $\mathcal{I} = \{1, 2, \ldots, G_T\}$, respectively. In addition, $\mathcal{G}_i$ represents the set of receivers in multicast group $i \in \mathcal{I}$. The number of receivers in the i-th multicast group is represented by $|\mathcal{G}_i|$. As in [22], we assume that $\mathcal{G}_i \cap \mathcal{G}_{i'} = \{\emptyset\}, \forall i \neq i'$. The hybrid precoder at the gNodeB exhibits a sub-connected architecture, which consists of N_{tx} transmit antennas and $N_{\text{tx}}^{\text{RF}}$ RF chains. Thus, each RF chain is connected to a sub-array of $L_{\text{tx}} = N_{\text{tx}}/N_{\text{tx}}^{\text{RF}}$ antennas [3]. Due to capacity constraints, each receiver is equipped with purely analog combiners that consist of N_{rx} antennas and a single RF chain, i.e, $N_{\text{rx}}^{\text{RF}} = 1$ and $L_{\text{rx}} = N_{\text{rx}}$. Since, in general $G_T \geq N_{\text{tx}}^{\text{RF}}$, scheduling is necessary because $N_{\text{tx}}^{\text{RF}}$ determines the maximum number of data streams (or groups) that can be spatially multiplexed.

We define T_s as the number of scheduling windows, wherein mutually exclusive subsets of multicast groups are served, as shown in Fig 2. The admissible range of scheduling windows, T_s, depends on both $N_{\text{tx}}^{\text{RF}}$ and G_T. Specifically, $\lceil \frac{G_T}{N_{\text{tx}}^{\text{RF}}} \rceil \leq T_s \leq G_T$ is maximum when exactly one multicast group is served per scheduling window. Also, T_s is minimum

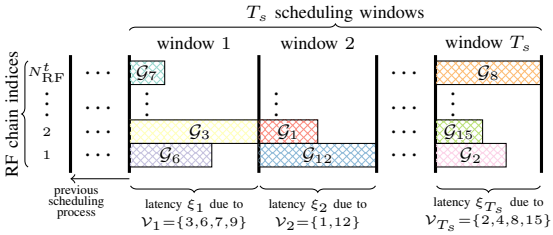

Figure 2: Multicast groups scheduling: Multicast groups 1 and 12 have been jointly scheduled during window $t = 2$.

when the gNodeB operates at maximal utilization, serving $N_{\text{tx}}^{\text{RF}}$ multicast groups simultaneously during every window (except for at most one window, if $G_T \mod N_{\text{tx}}^{\text{RF}} \neq 0$). Let $\mathcal{V}_t$ denote an ordered set containing the indices of the co-scheduled groups within window t. In addition, $\mathcal{U}_t$ denotes the set of receivers catered during window t, i.e. $\mathcal{U}_t = \{k \mid k \in \mathcal{G}_i, i \in \mathcal{V}_t\}$. Similarly, $\{\mathcal{V}_t\}_{t=1}^{T_s}$ and $\{\mathcal{U}_t\}_{t=1}^{T_s}$ denote the collection of $\mathcal{V}_t$ and $\mathcal{U}_t$ for all scheduling windows, respectively. Since every multicast group is served only once within T_s windows, then $\mathcal{V}_t \cap \mathcal{V}_{t' \neq t} = \{\emptyset\}$, $\mathcal{U}_t \cap \mathcal{U}_{t' \neq t} = \{\emptyset\}$. Due to the multicast nature of the system, every receiver $k \in \mathcal{G}_i$ requires the same length-B_i bit stream $\mathbf{b}_i = [b_{i_1}, \ldots b_{i_{B_i}}]^T$. Thus, the amount of bits required by receiver k is $B_k = B_i, \forall k \in \mathcal{G}_i$. At the transmitter, each bit stream $\mathbf{b}_i$ is encoded at a suitable rate π_i that allows successful decoding at every intended receiver. As a result, G_T symbol streams $\tilde{\mathbf{s}}_i = [\tilde{s}_{i_1}, \tilde{s}_{i_2}, \ldots]^T$ $(i \in \mathcal{I})$ with symbol-wise average unit power are produced, i.e., $\mathbb{E}\{\tilde{\mathbf{s}}_i \tilde{\mathbf{s}}_i^H\} = \mathbf{I}$. The symbol streams are arranged in a matrix $\mathbf{S} = \left[\tilde{\mathbf{s}}_1, \ldots, \tilde{\mathbf{s}}_{G_T}\right]^T$ that is zero-padded where necessary, as the length of each stream $\tilde{\mathbf{s}}_i$ depends on B_i and π_i. Specifically, the non-zero entries of $\mathbf{S}$ represent the effective data that needs to be delivered to all the groups (within T_s scheduling windows). Let $\hat{\mathbf{S}}_t = \mathbf{V}_t \mathbf{S}$ denote the $|\mathcal{V}_t|$ symbol streams transmitted during the t-th scheduling window, where $\mathbf{V}_t \in \{0, 1\}^{|\mathcal{V}_t| \times G_T}$ is a binary scheduling matrix that filters the symbol streams from $\mathbf{S}$. The *transmission latency* associated to the delivery of $\hat{\mathbf{S}}_t$ is defined as $\xi_t = \max_{i \in \mathcal{V}_t} \frac{B_i}{\pi_i}$, which represent the minimal time interval required by the devices in all the multicast groups $i \in \mathcal{V}_t$ to receive the intended data.

For any window t, the analog and digital precoders of the hybrid transmitter are denoted by $\mathbf{F}_t \in \mathbb{C}^{N_{\text{tx}} \times N_{\text{tx}}^{\text{RF}}}$ and $\mathbf{M}_t \in \mathbb{C}^{N_{\text{tx}}^{\text{RF}} \times |\mathcal{V}_t|}$, respectively. Any element (q, r) of the analog precoder is a phase rotation with constant modulus. Thus, $[\mathbf{F}_t]_{q,r} \in \mathcal{F}$, where $q \in \mathcal{Q} = \{(r-1)L_{\text{tx}} + l \mid 1 \leq l \leq L_{\text{tx}}\}$, $r \in \mathcal{R} = \{1, \ldots, N_{\text{tx}}^{\text{RF}}\}$, and $\mathcal{F} = \left\{\sqrt{\delta_F} \ldots, \sqrt{\delta_F} e^{j \frac{2\pi(D_F - 1)}{D_F}}\right\}$. D_F denotes the number of different phase shifts allowed at the transmitter, and δ_F is a scaling factor. The combiner of the k-th receiver is denoted by $\mathbf{w}_k \in \mathbb{C}^{N_{\text{rx}} \times 1}$, where $[\mathbf{w}_k]_l \in \mathcal{W}$, $l \in \mathcal{L} = \{1, \ldots, N_{\text{rx}}\}$, $\mathcal{W} = \left\{\sqrt{\delta_W}, \ldots, \sqrt{\delta_W} e^{j \frac{2\pi(D_W - 1)}{D_W}}\right\}$, D_W is the number of phase shifts allowed at the analog combiner, and δ_W is a scaling factor. The instantaneous downlink signal is represented by $\mathbf{x}_t = \mathbf{F}_t \mathbf{M}_t \tilde{\mathbf{s}}$, where $\tilde{\mathbf{s}} = \left[\tilde{s}_{1_c}, \ldots, \tilde{s}_{|\mathcal{V}_t|_c}\right]^T \in \mathbb{C}^{|\mathcal{V}_t| \times 1}$ sweeps through every column c of $\hat{\mathbf{S}}_t$ extracting the multicast symbols to be delivered during window t. The received signal at the

k-th device is denoted by $y_k = \mathbf{w}_k^H \mathbf{H}_k \mathbf{x}_t$, where $\mathbf{H}_k \in \mathbb{C}^{N_{\text{rx}} \times N_{\text{tx}}}$ denotes the channel between the device and the gNodeB, whereas $\mathbf{n}_k \sim \mathcal{CN}(\mathbf{0}, \sigma^2 \mathbf{I})$ denotes additive white Gaussian noise. Assuming a flat-fading channel, y_k is given by

$$y_k = \underbrace{\mathbf{w}_k^H \mathbf{H}_k \mathbf{F}_t \mathbf{M}_t \mathbf{s}_{i_t}}_{\text{desired multicast signal}} + \underbrace{\mathbf{w}_k^H \mathbf{H}_k \sum_{j_t=1, j_t \neq i_t}^{|\mathcal{V}_t|} \mathbf{F}_t \mathbf{M}_t \mathbf{s}_{j_t}}_{\text{interference}} + \underbrace{\mathbf{w}_k^H \mathbf{n}_k}_{\text{noise}}, \quad (1)$$

where $i_t \in \{1, 2, \ldots, |\mathcal{V}_t|\}$ is a relative index to denote the elements of $\mathcal{V}_t$. Also, $\mathbf{s}_{i_t} = \tilde{\mathbf{s}} - \mathbf{s}_{j_t}$ is a vector that contains zeros except for the i_t-th position, which stores the i_t-th element of $\tilde{\mathbf{s}}$. Thus, the SINR at receiver k is defined as

$$\text{SINR}_k = \frac{\left| \mathbf{w}_k^H \mathbf{H}_k \mathbf{F}_t \mathbf{M}_t \mathbf{e}_{i_t} \right|^2}{\sum_{j_t=1, j_t \neq i_t}^{|\mathcal{V}_t|} \left| \mathbf{w}_k^H \mathbf{H}_k \mathbf{F}_t \mathbf{M}_t \mathbf{e}_{j_t} \right|^2 + \sigma^2 \left\| \mathbf{w}_k \right\|_2^2}, \quad (2)$$

where $\mathbf{e}_{i_t}$ stores a 1 in the i_t-th position if $k \in \mathcal{V}_t\{i_t\}$ or 0 otherwise. Based on [32], the achievable rate π is approximated by the modified Shannon capacity,

$$\pi = \min\{C, C_{\max}\}, \quad (3)$$

where $C = \log_2(1 + \beta \cdot \text{SINR})$, $C_{\max}$ is the capacity limit and $\beta = 0.5$ represents the SINR loss [32]. In (1) and (2), we have dropped the subscript t when referring to $\mathbf{w}_k$ because only the combiners of the scheduled receivers need to be designed.

Remark: $\mathbf{V}_t$ is obtained from $\mathcal{V}_t = \{v_1^t, v_2^t, \ldots\}$. For instance, if v_a^t ($a \in \{1, 2, \ldots, |\mathcal{V}_t|\}$) is in the z-th position in $\mathcal{V}_t$, then the element in the z-th row and v_a^t-th column of $\mathbf{V}_t$ is set to 1.

IV. Scheduling Criteria for Multicasting

Note that T_s is not necessarily related to the overall transmission latency $\xi = \sum_{t=1}^{T_s} \xi_t$. Each bit stream $\mathbf{b}_i$ is to be transmitted at an optimal rate π_i that not only should provide service ubiquitousness (data decoding at every intended receiver) but also should minimize the transmission latency of the co-scheduled groups. Encoding every $\mathbf{b}_i \in \mathcal{V}_t$ at a high rate will promote low latency ξ_t, but it will require superior SINR at every receiver $k \in \mathcal{G}_i (i \in \mathcal{V}_t)$ to ensure successful decoding. Nevertheless, under constrained transmit and receive power, a high SINR at every receiver cannot be guaranteed, compromising thereby the service ubiquitousness. On the other hand, transmitting at very low rate improves data decodability for a larger number of receivers (ubiquitousness enhancement) at the expense of increasing latency. In light of this observation, we realize that the optimal rate needs to be carefully devised to *(i)* improve the ubiquitousness and *(ii)* minimize the latency. However, the optimal rate depends on the SINR, which can only be determined once the scheduling, precoder and combiners have been designed. This calls for a meticulous design of the hybrid precoder, analog combiners, and scheduling in order to attain ubiquitous multi-group multicast service with low latency. In the following, we present three propositions that will guide our design of $\{\mathcal{V}_t\}_{t=1}^{T_s}$, $\{\mathbf{F}_t\}_{t=1}^{T_s}$, $\{\mathbf{M}_t\}_{t=1}^{T_s}$, $\{\mathbf{w}_k\}_{k=1}^{K_T}$ to attain the desired objectives.

Proposition 1: Let $1 \leq t' \leq T_s$ be a window with defined $\mathcal{V}_{t'}$, $\mathbf{F}_{t'}$, $\mathbf{M}_{t'}$, $\{\mathbf{w}_k\}_{k \in \mathcal{U}_{t'}}$, then the transmission latency $\xi_{t'|\mathcal{V}_{t'}, \mathbf{F}_{t'}, \mathbf{M}_{t'}, \{\mathbf{w}_k\}_{k \in \mathcal{U}_{t'}}}$ is approximately inversely proportional to the minimum regularized SINR (r-SINR) among all the co-scheduled receivers.

We assume that for a certain window t', the sets $\mathcal{V}_{t'}$ and $\mathcal{U}_{t'}$ have been determined. Moreover, we consider that $\mathbf{F}_{t'}$ and $\mathbf{M}_{t'}$ at the transmitter, and $\{\mathbf{w}_k\}_{k \in \mathcal{U}_{t'}}$ for each scheduled receiver, have been designed. Under these assumptions, the SINR at any receiver is obtained via (2). The maximal rate $\pi_{k|\mathcal{V}_{t'}, \mathbf{F}_{t'}, \mathbf{M}_{t'}, \mathbf{w}_k}$ at which receiver $k \in \mathcal{G}_i, (i \in \mathcal{V}_{t'})$ can successfully decode is given by (3). Thus, the minimal latency associated to receiver $k \in \mathcal{G}_i\,(i \in \mathcal{V}_{t'})$ is $\xi_{k|\mathcal{V}_{t'}, \mathbf{F}_{t'}, \mathbf{M}_{t'}, \mathbf{w}_k} = \frac{B_i}{\pi_{k|\mathcal{V}_{t'}, \mathbf{F}_{t'}, \mathbf{M}_{t'}, \mathbf{w}_k}}$. Since every receiver $k \in \mathcal{G}_i\,(i \in \mathcal{V}_{t'})$ requires the same information, the optimal rate at which $\mathbf{b}_i$ can be encoded while guaranteeing successful reception at every receiver, is determined by $\pi_{i|\mathcal{V}_{t'}, \mathbf{F}_{t'}, \mathbf{M}_{t'}, \{\mathbf{w}_k\}_{k \in \mathcal{U}_{t'}}} = \min_{k \in \mathcal{G}_i} \pi_{k|\mathcal{V}_{t'}, \mathbf{F}_{t'}, \mathbf{M}_{t'}, \mathbf{w}_k}$. The latency associated to multicast group $i \in \mathcal{V}_{t'}$ is denoted by $\xi_{i|\mathcal{V}_{t'}, \mathbf{F}_{t'}, \mathbf{M}_{t'}, \{\mathbf{w}_k\}_{k \in \mathcal{U}_{t'}}}$, and the latency owing to all multicast groups scheduled during window t' is defined as $\xi_{t'|\mathcal{V}_{t'}, \mathbf{F}_{t'}, \mathbf{M}_{t'}, \{\mathbf{w}_k\}_{k \in \mathcal{U}_{t'}}} = \max_{i \in \mathcal{V}_{t'}} \xi_{i|\mathcal{V}_{t'}, \mathbf{F}_{t'}, \mathbf{M}_{t'}, \{\mathbf{w}_k\}_{k \in \mathcal{U}_{t'}}}$, which can also be expressed as

$$\xi_{t'}^{\star} = \xi_{t'|\mathcal{U}_{t'}, \mathbf{F}_{t'}, \mathbf{M}_{t'}, \{\mathbf{w}_k\}_{k \in \mathcal{U}_{t'}}} = \max_{k \in \mathcal{U}_{t'}} \left\{ \frac{B_k}{\pi_{k|\mathcal{U}_{t'}, \mathbf{F}_{t'}, \mathbf{M}_{t'}, \mathbf{w}_k}} \right\} \quad (4)$$

As shown in Appendix A, the transmission latency is approximately inversely proportional to the minimum r-SINR among all the receivers $k \in \mathcal{U}_{t'}$, i.e.,

$$\xi_{t'}^{\star} \approx^{-1} \min_{k \in \mathcal{U}_{t'}} \left\{ \left(1 + \beta \cdot \text{SINR}_{k|\mathcal{V}_{t'}, \mathbf{F}_{t'}, \mathbf{M}_{t'}, \mathbf{w}_k}\right)^{\frac{1}{B_k}} \right\}, \quad (5)$$

where $(1+\beta \cdot \text{SINR}_{k|\mathcal{V}_{t'}, \mathbf{F}_{t'}, \mathbf{M}_{t'}, \mathbf{w}_k})^{\frac{1}{B_k}}$ is termed r-SINR. Further, (5) reveals a crucial relation between latency and SINR, which we exploit to design optimal precoders and combiners.

Proposition 2: Let t' be a window with defined $\mathcal{V}_{t'}$, then the minimization of transmission latency $\xi_{t'|\mathcal{V}_{t'}}$ is equivalent to designing $\mathbf{F}_{t'}, \mathbf{M}_{t'}, \{\mathbf{w}_k\}_{k \in \mathcal{U}_{t'}}$ such that the minimum equalized SINR (e-SINR) of all co-scheduled receivers is maximized.

To minimize the latency associated to $\mathcal{V}_{t'}$, the optimization problem that devises optimal $\mathbf{F}_{t'}, \mathbf{M}_{t'}, \{\mathbf{w}_k\}_{k \in \mathcal{U}_{t'}}$ is

$$\min_{\substack{\mathbf{F}_{t'} \in \Omega_F \\ \mathbf{M}_{t'} \in \Omega_M \\ \{\mathbf{w}_k\}_{k \in \mathcal{U}_{t'}} \in \Omega_W}} \xi_{t'|\mathcal{U}_{t'}} \leftrightarrow \max_{\substack{\mathbf{F}_{t'} \in \Omega_F \\ \mathbf{M}_{t'} \in \Omega_M \\ \{\mathbf{w}_k\}_{k \in \mathcal{U}_{t'}} \in \Omega_W}} \min_{k \in \mathcal{U}_{t'}} \frac{\text{SINR}_{k|\mathcal{V}_{t'}}}{B_k}, \quad (6)$$

where $\frac{\text{SINR}_{k|\mathcal{V}_{t'}}}{B_k}$ is e-SINR. Also, Ω_F, Ω_M, and Ω_W are the feasible sets for the analog precoder, digital precoder and analog combiners, respectively. A more detailed derivation of this expression is available in Appendix B.

Proposition 3: The minimization of the overall transmission latency of the system is equivalent to simultaneously maximizing the minimum e-SINR of the co-scheduled receivers at every scheduling window.

It follows from *Proposition 2* that, in order to minimize the overall latency, the latency associated to every scheduling window t must also be minimum. Thus,

$$\min_{\substack{\{\mathbf{F}_t\}_{t=1}^{T_s} \in \Omega_F \\ \{\mathbf{M}_t\}_{t=1}^{T_s} \in \Omega_M \\ \{\mathbf{w}_k\}_{k=1}^{K_T} \in \Omega_W \\ \{\mathcal{V}_t\}_{t=1}^{T_s} \in \Omega_{V(T_s)} \\ T_s \in \Omega_T}} \boldsymbol{\xi} \leftrightarrow \max_{\substack{\{\mathbf{F}_t\}_{t=1}^{T_s} \in \Omega_F \\ \{\mathbf{M}_t\}_{t=1}^{T_s} \in \Omega_M \\ \{\mathbf{w}_k\}_{k=1}^{K_T} \in \Omega_W \\ \{\mathcal{V}_t\}_{t=1}^{T_s} \in \Omega_{V(T_s)} \\ T_s \in \Omega_T}} \bigwedge_{t=1}^{T_s} \min_{k \in \mathcal{U}_t} \left\{ \frac{\text{SINR}_{k|\mathcal{V}_t}}{B_k} \right\}, \quad (7)$$

where $\boldsymbol{\xi} = [\xi_1, \ldots, \xi_{T_s}]^T$. Besides, $\Omega_{V(T_s)}$ denotes the feasible set of all the scheduling combinations for a given T_s, whereas $\Omega_T \equiv \left[\lceil G_T/N_{\text{tx}}^{\text{RF}} \rceil, G_T\right]$ defines the feasible set of T_s. Since the feasible sets Ω_F, Ω_M, Ω_W, $\Omega_{V(T_s)}$, and Ω_T are non-convex (discussed in Section V), (7) is difficult to solve. Moreover, $\{\mathbf{F}_t\}_{t=1}^{T_s}$, $\{\mathbf{M}_t\}_{t=1}^{T_s}$, and $\{\mathbf{w}_k\}_{k=1}^{K_T}$ are mutually coupled as observed in (2). Furthermore, the number of potential scheduling combinations grows combinatorially with G_T and $N_{\text{tx}}^{\text{RF}}$.

A straightforward but intractable solution to (7) is exhaustive search (XHAUS), whereby every scheduling pattern $\{\mathcal{V}_t\}_{t=1}^{T_s} \in \Omega_{V(T_s)}$ for every value $T_s \in \Omega_T$ is created. Then, for each pattern, the precoder and combiners are to be designed according to (6) while keeping the best-performing scheduling. A simpler approach consists in randomly associating the groups (RAND) and then solving (6). It is evident that for any scheduling choice, we are required to solve (6) for every window. Thus, in the following, we propose an approach based on semidefinite relaxation and Cholesky matrix factorization to design near-optimal hybrid precoders and analog combiners.

V. Proposed Joint Design of Hybrid Precoder and Analog Combiners

Given $\mathcal{V}_t$, a suitable hybrid precoder and analog combiners for window t can be designed based on (6). Thus, the latency ξ_t is minimized when

$$\mathcal{P}_0: \max_{\substack{\mathbf{F}_t, \mathbf{M}_t, \\ \{\mathbf{w}_k\}_{k\in\mathcal{U}_t}}} \quad \min_{k\in\mathcal{U}_t} \frac{\frac{1}{B_k}\left|\mathbf{w}_k^H \mathbf{H}_k \mathbf{F}_t \mathbf{M}_t \mathbf{e}_{i_t}\right|^2}{\sum\limits_{\substack{j_t=1 \\ j_t\neq i_t}}^{|\mathcal{V}_t|} \left|\mathbf{w}_k^H \mathbf{H}_k \mathbf{F}_t \mathbf{M}_t \mathbf{e}_{j_t}\right|^2 + \sigma^2 \|\mathbf{w}_k\|_2^2} \tag{8a}$$

$$\text{s.t.} \quad \|\mathbf{F}_t \mathbf{M}_t\|_{\text{F}}^2 \leq P_{\text{tx}}^{\max}, \tag{8b}$$

$$\|\mathbf{w}_k\|_2^2 \leq P_{\text{rx}}^{\max}, k \in \mathcal{U}_t, \tag{8c}$$

$$[\mathbf{F}_t]_{q,r} \in \mathcal{F}, q \in \mathcal{Q}, r \in \mathcal{R}, \tag{8d}$$

$$[\mathbf{w}_k]_l \in \mathcal{W}, l \in \mathcal{L}, \tag{8e}$$

where (8a) aims at maximizing the minimum e-SINR, (8b) restricts the transmit power of the hybrid precoder, whereas (8c) limits the receive power of each receiver. On the other hand, (8d) and (8e) enforce the phase shifts of the analog precoder $\mathbf{F}_t$ and analog combiners $\{\mathbf{w}_k\}_{k\in\mathcal{U}_t}$ to have constant modulus. Furthermore, (8a) is non-convex since it is as a fractional program of quadratic forms with coupled parameters. The constraints (8d) and (8e) are non-convex since $[\mathbf{F}_t]_{q,r}$ and $[\mathbf{w}]_l$ belong to the non-convex sets $\mathcal{F}$ and $\mathcal{W}$, respectively. Thus, (8c) is also non-convex. Besides, (8b) is non-convex due to the coupling between $\mathbf{F}_t$ and $\mathbf{M}_t$, and the existence of (8d). As a result, $\mathcal{P}_0$ is a non-convex program with non-convex constrains. Note that (8) can be recast as (9),

$$\mathcal{P}_0: \max_{\substack{\alpha, \mathbf{F}, \mathbf{M}, \\ \{\mathbf{w}_k\}_{k=1}^K}} \quad \alpha \tag{9a}$$

$$\text{s.t.} \quad \frac{1}{B_k} \frac{\left|\mathbf{w}_k^H \mathbf{H}_k \mathbf{F} \mathbf{M} \mathbf{e}_i\right|^2}{\sum\limits_{j\neq i} \left|\mathbf{w}_k^H \mathbf{H}_k \mathbf{F} \mathbf{M} \mathbf{e}_j\right|^2 + \sigma^2 \|\mathbf{w}_k\|_2^2} \geq \alpha, \tag{9b}$$

$$\|\mathbf{F}\mathbf{M}\|_{\text{F}}^2 \leq P_{\text{tx}}^{\max}, \tag{9c}$$

$$\|\mathbf{w}_k\|_2^2 \leq P_{\text{rx}}^{\max}, \forall k \in \mathcal{U}_t, \tag{9d}$$

$$[\mathbf{F}]_{q,r} \in \mathcal{F}, q \in \mathcal{Q}, r \in \mathcal{R}, \tag{9e}$$

$$[\mathbf{w}_k]_l \in \mathcal{W}, l \in \mathcal{L}, \tag{9f}$$

$$\alpha \geq 0. \tag{9g}$$

For notation simplification, we assume that $G = |\mathcal{V}_t|$ and $K = |\mathcal{U}_t|$. In addition, we also drop the subscript t when referring to $\mathbf{F}_t$ and $\mathbf{M}_t$. Note that $\mathcal{P}_0$ is challenging to solve due to parameter coupling and non-convexity of the feasible sets. In fact, for the particular case when $\mathbf{F} = \mathbf{I}$ and $\mathbf{w}_k = 1$, $\mathcal{P}_0$ was shown to be NP-hard [10]. In this paper, we resort to alternate optimization [33] to solve (9). Thus, $\mathbf{F}$, $\mathbf{M}$, and $\{\mathbf{w}_k\}_{k=1}^K$ are sequentially optimized in an iterative manner.

A. Optimization of $\mathbf{F}$

Given $\mathbf{M}$ and $\{\mathbf{w}_k\}_{k=1}^K$, α and $\mathbf{F}$ are optimized as follows,

$$\mathcal{P}_1: \max_{\alpha, \mathbf{F}} \quad \alpha \tag{10a}$$

$$\text{s.t.} \quad \alpha B_k \sum_{j\neq i} \left|\mathbf{w}_k^H \mathbf{H}_k \mathbf{F} \mathbf{M} \mathbf{e}_j\right|^2 + \alpha B_k \sigma^2 \|\mathbf{w}_k\|_2^2 - \left|\mathbf{w}_k^H \mathbf{H}_k \mathbf{F} \mathbf{M} \mathbf{e}_i\right|^2 \leq 0, \forall k \in \mathcal{U}_t, \tag{10b}$$

$$\|\mathbf{F}\mathbf{M}\|_{\text{F}}^2 \leq P_{\text{tx}}^{\max}, \tag{10c}$$

$$[\mathbf{F}]_{q,r} \in \mathcal{F}, q \in \mathcal{Q}, r \in \mathcal{R}, \tag{10d}$$

$$\alpha \geq 0. \tag{10e}$$

Due to the sub-connected architecture of the analog precoder, $\mathbf{F}$ is sparse. Thus, we can express $\mathbf{F}\mathbf{M} = \text{diag}(\mathbf{f})\widetilde{\mathbf{M}}$, where $\widetilde{\mathbf{M}} = \mathbf{M} \otimes \mathbf{1}_{L_{\text{tx}}}$, and $\mathbf{f} \in \mathbb{C}^{N_{\text{tx}}\times 1}$ is a vector that contains the non-zero elements of $\mathbf{F}$. In addition, $\mathbf{F}\mathbf{M}\mathbf{e}_i = \text{diag}\left(\widetilde{\mathbf{M}}\mathbf{e}_i\right)\mathbf{f}$. Thus, (10) is equivalent to

$$\mathcal{P}_1: \max_{\alpha, \mathbf{f}} \quad \alpha \tag{11a}$$

$$\text{s.t.} \quad \alpha B_k \sum_{j\neq i} \mathbf{f}^H \mathbf{b}_{k,j} \mathbf{b}_{k,j}^H \mathbf{f} - \mathbf{f}^H \mathbf{b}_{k,i} \mathbf{b}_{k,i}^H \mathbf{f} + \alpha B_k \sigma^2 \|\mathbf{w}_k\|_2^2 \leq 0, \forall k \in \mathcal{U}_t, \tag{11b}$$

$$\|\mathbf{L}\mathbf{f}\|_2^2 \leq P_{\text{tx}}^{\max}, \tag{11c}$$

$$[\mathbf{f}]_n \in \mathcal{F}, n \in \mathcal{N}, \tag{11d}$$

$$\alpha \geq 0, \tag{11e}$$

where $\mathbf{b}_{k,i} = \text{diag}\left(\widetilde{\mathbf{M}}\mathbf{e}_i\right)^H \mathbf{H}^H \mathbf{w}_k^H$, $\mathbf{L} = \left(\widetilde{\mathbf{M}}^T \otimes \mathbf{1}_{N_{\text{tx}}}\right) \odot (\mathbf{1}_G \otimes \mathbf{I}_{N_{\text{tx}}\times N_{\text{tx}}})$, $\mathcal{N} = \{1, 2, \ldots, N_{\text{tx}}\}$. Realize that (11d) is non-convex due the combinatorial selection of phase shifts $[\mathbf{f}]_n$ from $\mathcal{F}$. Similarly, (11b) and (11c) are non-convex as they depend on $\mathbf{f}$, whereas (11e) is linear. In order to approach $\mathcal{P}_1$, our strategy consists of three stages. In the first stage (Stage A_1), we recast $\mathcal{P}_1$ as an SDR program to convexify (11b), (11c), and (11d), thus resulting in $\mathcal{P}_{\text{SDR},1}$ in (12). After convexification, the only non-convex constraint that remains in $\mathcal{P}_{\text{SDR},1}$ is (12b). To find a near-optimal solution, we resort to the bisection method in the second stage (Stage A_2). In the third stage (Stage A_3), we use Cholesky factorization and randomization to recover $\mathbf{f}$ from $\mathbf{Y}$.

Stage A_1 (*Transformation of $\mathcal{P}_1$ to SDR*):

$$\mathcal{P}_{\text{SDR},1}: \max_{\alpha, \mathbf{Y}} \quad \alpha \tag{12a}$$

$$\text{s.t.} \quad \alpha B_k \text{Tr}\left(\mathbf{B}_{k,\setminus i}\mathbf{Y}\right) - \text{Tr}\left(\mathbf{B}_{k,i}\mathbf{Y}\right) + \alpha B_k \sigma^2 \|\mathbf{w}_k\|_2^2 \leq 0, \forall k \in \mathcal{U}_t, \tag{12b}$$

$$\mathrm{Tr}\left(\mathbf{DY}\right) \leq P_{\mathrm{tx}}^{\max}, \tag{12c}$$

$$\mathrm{diag}\left(\mathbf{Y}\right) = \delta_F \mathbf{1}_{N_{\mathrm{tx}}}, \tag{12d}$$

$$\mathbf{Y} \succcurlyeq 0, \tag{12e}$$

$$\alpha \geq 0, \tag{12f}$$

where $\mathbf{Y} = \mathbf{f}\mathbf{f}^H$, $\mathbf{D} = \mathbf{L}^H\mathbf{L}$, $\mathbf{B}_{k,\setminus i} = \sum_{j\neq i} \mathbf{b}_{k,j}\mathbf{b}_{k,j}^H$ and $\mathbf{B}_{k,i} = \mathbf{b}_{k,i}\mathbf{b}_{k,i}^H$ are positive semi-definite matrices.

Stage $\mathbf{A_2}$ (*Bisection search for* $\mathcal{P}_{\mathrm{SDR},1}$): Notice that (12b) is quasi-convex on $\mathbf{Y}$ and α because for any $\alpha \geq 0$, (12b) collapses to a convex constraint. Thus, we resort to the bisection search method [10], [23], [34], where we define an initial interval $\left[\alpha_L^{(0)}, \alpha_U^{(0)}\right]$ for α. Then, we progressively update the interval depending on the returned solutions for $\mathbf{Y}$. A natural lower bound is $\alpha_L^{(0)} = 0$. An upper bound $\alpha_U^{(0)}$ can be obtained by assigning the total power to the weakest receiver $k \in \mathcal{U}_t$. Thus, from (12b) we obtain $\alpha_U^{(0)} = \min_{k\in\mathcal{U}_t} \frac{\mathrm{Tr}\left(\mathbf{B}_{k,i}\mathbf{Y}\right)}{B_k\sigma^2\|\mathbf{w}_k\|_2^2}$. Further, since $\mathbf{B}_{k,i}$ and $\mathbf{Y}$ are positive semidefinite, $\mathrm{Tr}\left(\mathbf{B}_{k,i}\mathbf{Y}\right) \leq \mathrm{Tr}\left(\mathbf{B}_{k,i}\right)\mathrm{Tr}\left(\mathbf{Y}\right)$ holds [35]. Also, $\mathrm{Tr}\left(\mathbf{Y}\right) = \mathrm{Tr}\left(\mathbf{f}\mathbf{f}^H\right) = N_{\mathrm{tx}}^{\mathrm{RF}}$. Therefore, $\alpha_U^{(0)} = \min_{k\in\mathcal{U}_t} \frac{N_{\mathrm{tx}}^{\mathrm{RF}}\mathrm{Tr}\left(\mathbf{B}_{k,i}\right)}{B_k\sigma^2\|\mathbf{w}_k\|_2^2}$. With the initial interval defined, at every iteration ℓ we set $\alpha^{(\ell)} = \frac{\alpha_L^{(\ell)}+\alpha_U^{(\ell)}}{2}$ and solve $\mathcal{P}_{\mathrm{SDR},1}^{(\ell)}$ for $\mathbf{Y}$ with the given $\alpha^{(\ell)}$. At each iteration ℓ, we update the lower and upper bounds in the following manner. If $\mathcal{P}_{\mathrm{SDR},1}^{(\ell)}$ is feasible, then $\alpha_L^{(\ell+1)} = \alpha^{(\ell)}$. Otherwise, $\alpha_U^{(\ell+1)} = \alpha^{(\ell)}$. Through this procedure, an ϵ-suboptimal solution can be obtained within $N_{\mathrm{bis}_1} = \log_2\left(\frac{1}{\epsilon}\left(\alpha_U^{(0)} - \alpha_L^{(0)}\right)\right)$ iterations.

Stage $\mathbf{A_3}$ (*Recovery of* $\mathbf{f}$): Let $\widehat{\mathbf{Y}}$ represent an ϵ-suboptimal solution to (12). When $\widehat{\mathbf{Y}}$ is rank-1, an optimal solution $\mathbf{Y}^\star = \widehat{\mathbf{Y}}$ has been found to (12). Thus, $\mathbf{f}^\star$ can be recovered straightforwardly by means of eigen-decomposition. Otherwise, we resort to a procedure inspired by [36].

Stage A$_{3\text{-}1}$: Any element (n_1, n_2) of $\mathbf{Y}$ can be represented as $[\mathbf{Y}]_{n_1,n_2} = [\mathbf{f}]_{n_1}[\mathbf{f}]_{n_2}^*$. If we define a vector $\mathbf{u} \in \mathbb{C}^{N_{\mathrm{tx}}\times 1}$ such that $\|\mathbf{u}\|_2^2 = \mathbf{u}^H\mathbf{u} = 1$, we can express $[\mathbf{Y}]_{n_1,n_2}$ in terms of $\mathbf{u}$, i.e., $[\mathbf{Y}]_{n_1,n_2} = \left([\mathbf{f}]_{n_1}\mathbf{u}^T\right)\left([\mathbf{f}]_{n_2}^*\mathbf{u}^*\right)$. Moreover, if we define $\mathbf{q}_n = [\mathbf{f}]_n\mathbf{u}$, $\mathbf{Y}$ can be recast as $\mathbf{Y} = \mathbf{Q}^T\mathbf{Q}^*$ with $\mathbf{Q} = [\mathbf{q}_1, \ldots, \mathbf{q}_{N_{\mathrm{tx}}}]$.

Stage A$_{3\text{-}2}$: By means of Cholesky factorization, we can decompose $\widehat{\mathbf{Y}}$ as $\widehat{\mathbf{Y}} = \widehat{\mathbf{Q}}^T\widehat{\mathbf{Q}}^*$, where $\widehat{\mathbf{Q}} = [\widehat{\mathbf{q}}_1, \ldots, \widehat{\mathbf{q}}_{N_{\mathrm{tx}}}]$. In *Stage A$_{3\text{-}1}$*, we assumed that every $\mathbf{q}_n$ is originated from the same vector $\mathbf{u}$. Thus, we need to find both $\mathbf{f}$ and $\mathbf{u}$ that satisfy $\mathbf{q}_n = [\mathbf{f}]_n\mathbf{u}, \forall n \in \mathcal{N}$. Since such vectors $\mathbf{f}$ and $\mathbf{u}$ may not exist, we aim at finding approximate $\widehat{\mathbf{u}}$ and $\widehat{\mathbf{f}}$, such that $\widehat{\mathbf{q}}_n \approx \left[\widehat{\mathbf{f}}\right]_n\widehat{\mathbf{u}}, \forall n \in \mathcal{N}$. Mathematically, this is expressed as

$$\widehat{\mathcal{P}}_{\mathrm{LS},1}: \min_{\widehat{\mathbf{u}},\widehat{\mathbf{f}}} \sum_{n=1}^{N_{\mathrm{tx}}} \left\|\widehat{\mathbf{q}}_n - \left[\widehat{\mathbf{f}}\right]_n\widehat{\mathbf{u}}\right\|_2^2 \tag{13a}$$

$$\text{s.t.} \quad \|\widehat{\mathbf{u}}\|_2^2 = 1, \tag{13b}$$

$$\left[\widehat{\mathbf{f}}\right]_n \in \mathcal{F}, \forall n \in \mathcal{N}, \tag{13c}$$

where we find $\widehat{\mathbf{u}}$ and $\widehat{\mathbf{f}}$ with the least error in the 2-norm sense.

Stage A$_{3\text{-}3}$: Minimizing simultaneously both $\widehat{\mathbf{u}}$ and $\widehat{\mathbf{f}}$ is challenging. Thus, we generate a random vector $\widehat{\mathbf{u}}$, such that $\|\mathbf{u}\|_2^2 = 1$. Therefore, we solve

$$\widehat{\mathcal{P}}_{\mathrm{LS},2}: \min_{\left[\widehat{\mathbf{f}}\right]_n\in\mathcal{F},\forall n\in\mathcal{N}} \sum_{n=1}^{N_{\mathrm{tx}}} \left\|\widehat{\mathbf{q}}_n - \left[\widehat{\mathbf{f}}\right]_n\widehat{\mathbf{u}}\right\|_2^2 \tag{14}$$

By expanding (14), we obtain

$$\widehat{\mathcal{P}}_{\mathrm{LS},2}: \max_{\left[\widehat{\mathbf{f}}\right]_n\in\mathcal{F},\forall n\in\mathcal{N}} \sum_{n=1}^{N_{\mathrm{tx}}} \Re\mathfrak{e}\left(\left[\widehat{\mathbf{f}}\right]_n\widehat{\mathbf{q}}_n^H\widehat{\mathbf{u}}\right). \tag{15}$$

Note that (15) can be decomposed into N_{tx} parallel subproblems. Further, since $z_n = \widehat{\mathbf{q}}_n^H\widehat{\mathbf{u}}$ is known in $\widehat{\mathcal{P}}_{\mathrm{LS},2}$, we select $\left[\widehat{\mathbf{f}}\right]_n$ such that the real part is maximized. This is equivalent to choosing $\left[\widehat{\mathbf{f}}\right]_n$ with the closest phase to z_n^*. Therefore, among the phase rotations in $\mathcal{F}$, we choose the closest to z_n^*. To improve $\widehat{\mathbf{f}}$, we generate N_{rand_1} vectors $\widehat{\mathbf{u}}_v$ with $\|\mathbf{u}_v\|_2^2 = 1$ ($v = 1, \ldots, N_{\mathrm{rand}_1}$), and for each we find its corresponding $\widehat{\mathbf{f}}_v$. Then, we select $\mathbf{f}^\dagger$ among N_{rand_1} candidates that provides the largest minimum e-SINR, i.e., $\mathbf{f}^\dagger = \arg_{\widehat{\mathbf{f}}_1,\ldots,\widehat{\mathbf{f}}_{N_{\mathrm{rand}_1}}} \max\min_{k\in\mathcal{U}_t} \frac{\mathrm{SINR}_k}{B_k}$. Finally, $\mathbf{f}^\dagger$ is reshaped to obtain $\mathbf{F}^\dagger = \mathrm{reshape}\left(\mathbf{f}^\dagger\right)$. The function $\mathrm{reshape}(\cdot)$ reverses the effect of $\mathrm{vec}(\cdot)$.

B. Optimization of $\mathbf{M}$

Assuming that $\mathbf{F}$ and $\{\mathbf{w}_k\}_{k=1}^K$ are known, (9) collapses to

$$\mathcal{P}_2: \max_{\alpha,\mathbf{M}} \ \alpha \tag{16a}$$

$$\text{s.t.} \ \alpha B_k \sum_{j\neq i}\left|\mathbf{w}_k^H\mathbf{H}_k\mathbf{F}\mathbf{M}\mathbf{e}_j\right|^2 + \alpha B_k\sigma^2\|\mathbf{w}_k\|_2^2 - \left|\mathbf{w}_k^H\mathbf{H}_k\mathbf{F}\mathbf{M}\mathbf{e}_i\right|^2 \leq 0, \forall k \in \mathcal{U}_t, \tag{16b}$$

$$\|\mathbf{F}\mathbf{M}\|_{\mathrm{F}}^2 \leq P_{\mathrm{tx}}^{\max}, \tag{16c}$$

$$\alpha \geq 0. \tag{16d}$$

We can equivalently express $\mathcal{P}_2$ as,

$$\mathcal{P}_2: \max_{\alpha,\mathbf{m}} \ \alpha \tag{17a}$$

$$\text{s.t.} \ \alpha B_k \sum_{j\neq i}\mathbf{m}^H\mathbf{c}_{k,j}\mathbf{c}_{k,j}^H\mathbf{m} - \mathbf{m}^H\mathbf{c}_{k,i}\mathbf{c}_{k,i}^H\mathbf{m} + \alpha B_k\sigma^2\|\mathbf{w}_k\|_2^2 \leq 0, \forall k \in \mathcal{U}_t, \tag{17b}$$

$$\|(\mathbf{I}\otimes\mathbf{F})\,\mathbf{m}\|_2^2 \leq P_{\mathrm{tx}}^{\max}, \tag{17c}$$

$$\alpha \geq 0, \tag{17d}$$

$$\tag{17e}$$

where $\mathbf{c}_{k,i} = \left(\mathbf{e}_i \otimes \left(\mathbf{F}^H\mathbf{H}_k^H\mathbf{w}_k\right)\right)$ and $\mathbf{m} = \mathrm{vec}\left(\mathbf{M}\right)$. Following a similar procedure as before, the SDR form of (17) is

$$\mathcal{P}_{\mathrm{SDR},2}: \max_{\alpha,\mathbf{Z}} \quad \alpha \tag{18a}$$

$$\text{s.t.} \quad \alpha B_k\mathrm{Tr}\left(\mathbf{C}_{k,\setminus i}\mathbf{Z}\right) - \mathrm{Tr}\left(\mathbf{C}_{k,i}\mathbf{Z}\right) + \alpha B_k\sigma^2\|\mathbf{w}_k\|_2^2 \leq 0, \forall k \in \mathcal{U}_t, \tag{18b}$$

$$\mathrm{Tr}\left(\mathbf{J}\mathbf{Z}\right) \leq P_{\mathrm{tx}}^{\max}, \tag{18c}$$

$$\mathbf{Z} \succcurlyeq 0, \tag{18d}$$

$$\alpha \geq 0, \tag{18e}$$

where $\mathbf{Z} = \mathbf{m}\mathbf{m}^H$, $\mathbf{J} = (\mathbf{I}\otimes\mathbf{F})^H(\mathbf{I}\otimes\mathbf{F})$, $\mathbf{C}_{k,\setminus i} = \sum_{j\neq i}\mathbf{c}_{k,j}\mathbf{c}_{k,j}^H$ and $\mathbf{C}_{k,i} = \mathbf{c}_{k,i}\mathbf{c}_{k,i}^H$. As in Stage A$_2$, we use the bisection method to approach (18). In this case, $\alpha_L^{(0)} = 0$ and $\alpha_U^{(0)} = \min_{k\in\mathcal{U}_t}\frac{P_{\mathrm{tx}}^{\max}\mathrm{Tr}\left(\mathbf{C}_{k,i}\right)}{B_k\sigma^2\|\mathbf{w}_k\|_2^2}$. The process is repeated for N_{bis_2} iterations. At the end of the bisection procedure, we obtain $\widehat{\mathbf{Z}}$ from which $\widehat{\mathbf{m}}$ is estimated. If $\widehat{\mathbf{Z}}$ is rank-1, then an optimal solution $\mathbf{Z}^\star = \widehat{\mathbf{Z}}$ has been found to (18). Otherwise, we generate N_{rand_2} candidates according to $\widehat{\mathbf{m}}_v \sim \mathcal{CN}\left(\mathbf{0}, \widehat{\mathbf{Z}}\right)$ ($v = 1, \ldots, N_{\mathrm{rand}_2}$) and retain the best-performing candidate $\mathbf{m}^\dagger = \arg_{\widehat{\mathbf{m}}_1,\ldots,\widehat{\mathbf{m}}_{N_{\mathrm{rand}_2}}} \max\min_{k\in\mathcal{U}_t}\frac{\mathrm{SINR}_k}{B_k}$ [37], [38]. Finally, $\mathbf{m}^\dagger$ is reshaped to obtain $\mathbf{M}^\dagger$.

C. Optimization of $\{\mathbf{w}_k\}_{k=1}^K$

Now, we assume that $\mathbf{F}$ and $\mathbf{M}$ are given. Therefore, we optimize the analog combiners $\{\mathbf{w}_k\}_{k=1}^K$ as shown in (19)

$$\mathcal{P}_3: \max_{\alpha,\{\mathbf{w}_k\}_{k=1}^K} \quad \alpha \tag{19a}$$

$$\text{s.t.} \quad \alpha B_k \sum_{j\neq i} \left|\mathbf{w}_k^H \mathbf{H}_k \mathbf{F}\mathbf{M}\mathbf{e}_j\right|^2 + \alpha B_k \sigma^2 \left\|\mathbf{w}_k\right\|_2^2 - \left|\mathbf{w}_k^H \mathbf{H}_k \mathbf{F}\mathbf{M}\mathbf{e}_i\right|^2 \leq 0, \forall k \in \mathcal{U}_t, \tag{19b}$$

$$\|\mathbf{w}_k\|_2^2 \leq P_{\text{rx}}^{\max}, \forall k \in \mathcal{U}_t, \tag{19c}$$

$$[\mathbf{w}_k]_l \in \mathcal{W}, l \in \mathcal{L}, \tag{19d}$$

$$\alpha \geq 0. \tag{19e}$$

We observe that each combiner can be optimized independently since any variation of $\mathbf{w}_k$ will only affect the SINR of the k-th receiver. Therefore, we solve K sub-problems $\mathcal{P}_3^{(k)}$ in parallel. The SDR form of $\mathcal{P}_3^{(k)}$ is

$$\mathcal{P}_{\text{SDR},3}^{(k)}: \max_{\alpha,\mathbf{W}_k} \quad \alpha \tag{20a}$$

$$\text{s.t.} \quad \alpha B_k \text{Tr}\left(\widetilde{\mathbf{P}}_{k,\setminus i}\mathbf{W}_k\right) - \text{Tr}\left(\mathbf{P}_{k,i}\mathbf{W}_k\right), \tag{20b}$$

$$\text{Tr}\left(\mathbf{W}_k\right) \leq P_{\text{rx}}^{\max}, \tag{20c}$$

$$\text{diag}\left(\mathbf{W}_k\right) = \delta_W \mathbf{1}_{N_{\text{rx}}}, \tag{20d}$$

$$\mathbf{W}_k \succcurlyeq 0, \tag{20e}$$

$$\alpha \geq 0, \tag{20f}$$

where $\mathbf{W}_k = \mathbf{w}_k\mathbf{w}_k^H$, $\mathbf{P}_{k,i} = \mathbf{H}_k\mathbf{F}\mathbf{M}\mathbf{e}_i\mathbf{e}_i^H\mathbf{M}^H\mathbf{F}^H\mathbf{H}_k$ and $\widetilde{\mathbf{P}}_{k,\setminus i} = \sum_{j\neq i}\mathbf{P}_{k,j} + B_k\sigma^2\mathbf{I}$. Since the combiners $\mathbf{w}_k$ are analog, we follow the same procedure used to optimize $\mathbf{F}$. In this case, the lower bound is $\alpha_{L_k}^{(0)} = 0$ whereas the upper bound $\alpha_{U_k}^{(0)} = \lambda_{\max}\left(\mathbf{P}_{k,i}\widetilde{\mathbf{P}}_{k,\setminus i}^{-1}\right)$ is the maximum eigenvalue of matrix $\mathbf{P}_{k,i}\widetilde{\mathbf{P}}_{k,\setminus i}^{-1}$. The bisection process is repeated for N_{bis_3} iterations as explained in Stage A_2, upon whose completion $\widehat{\mathbf{W}}_k$ is obtained. If $\widehat{\mathbf{W}}_k$ is rank-1, then $\mathbf{W}_k^\star = \widehat{\mathbf{W}}_k$ is also optimal to (20). Otherwise we generate N_{rand_3} candidates $\widehat{\mathbf{w}}_{k,v}$ ($v = 1, \ldots, N_{\text{rand}_3}$) for each $\widehat{\mathbf{w}}_k$ as discussed in Stage A_3, and select the best-performing $\mathbf{w}_k^\dagger = \arg_{\widehat{\mathbf{w}}_{k,1},\ldots,\widehat{\mathbf{w}}_{k,N_{\text{rand}_3}}} \max \frac{\text{SINR}_k}{B_k}$.

To further refine $\mathbf{F}$, $\mathbf{M}$, $\{\mathbf{w}_k\}_{k=1}^K$, we sequentially solve $\mathcal{P}_{\text{SDR},1}$, $\mathcal{P}_{\text{SDR},2}$ and $\left\{\mathcal{P}_{\text{SDR},3}^{(k)}\right\}_{k=1}^K$ for a number of N_{iter} iterations. Also, since the number of bits B_i to be transmitted can be arbitrarily large, we use normalized values $\widetilde{B}_i$ in the range $[0, 1]$, only for optimization purposes. Also, the scaling factors δ_F and δ_W, in Section III, are chosen such that $\|\mathbf{F}\|_{\text{F}}^2 = N_{\text{tx}}^{\text{RF}}$ and $\|\mathbf{w}_k\|_2^2 = P_{\text{rx}}^{\max}$. Thus, $\delta_F = N_{\text{tx}}^{\text{RF}}/N_{\text{tx}}$ and $\delta_W = P_{\text{rx}}^{\max}/N_{\text{rx}}$.

VI. Proposed Scheduling Algorithm

Given that scheduling plays a key role in ensuring minimum latency, in this section, we propose a novel scheduling formulation that aims to minimize both, the number of scheduling windows and the aggregate inter-group correlation (IGC). We model the scheduling problem as a Boolean program,

$$\mathcal{S}: \min_{\{\mu_{i,i}\}_{i=1}^{G_T},\{\tau_{i,j,l}\}} \underbrace{\sum_{i=1}^{G_T}\mu_{i,i}}_{\text{first term}} + \omega \underbrace{\sum_{i=1}^{G_T-1}\sum_{j\geq i}^{G_T-1}\sum_{l>j}^{G_T}\rho_{j,l}\cdot\tau_{i,j,l}}_{\text{second term: aggregate IGC}} \tag{21a}$$

$$\text{s.t.} \quad \sum_{i\leq j<l}\rho_{j,l}\cdot\tau_{i,j,l} \leq \lambda\cdot\mu_{i,i}, \forall i, \tag{21b}$$

$$\sum_{i\leq j}\mu_{i,j} = 1, \forall j, \tag{21c}$$

$$\sum_{j\geq i}\mu_{i,j} \leq N_{\text{tx}}^{\text{RF}}, \forall i, \tag{21d}$$

$$\mu_{i,j} \leq \mu_{i,i}, \forall i < j, \tag{21e}$$

$$\mu_{i,j} + \mu_{i,l} \leq 1 + \tau_{i,j,l}, \forall i \leq j < l, \tag{21f}$$

$$\mu_{i,j} \in \{0, 1\}, \tag{21g}$$

$$\tau_{i,j,l} \in \{0, 1\}. \tag{21h}$$

Each binary variable $\mu_{i,j}$ assumes the value of 1 if multicast group j is scheduled in the i-th window (or 0 otherwise). The binary variable $\tau_{i,j,l}$ is 1 if any two multicast groups j and l have been co-scheduled during the i-th window. Also, we define $\rho_{j,l} = \frac{\left|\mathbf{h}_j^H\mathbf{h}_l\right|}{\|\mathbf{h}_j\|_2\|\mathbf{h}_l\|_2}$ as the inter-group correlation (IGC) between groups j and l, where $\mathbf{h}_j = \frac{1}{|\mathcal{G}_j|}\sum_{k\in\mathcal{G}_j}\text{vec}\left(\mathbf{H}_k\right)$ is the mean channel vector of all receivers k in group j. The first term in (21a) represents the number of scheduling windows, whereas the second term is the aggregate IGC, which is computed in a pair-wise manner and accumulated as a penalization. If there exist more than a solution that yields the same optimal amount of scheduling windows, the second term penalizes the candidates that exhibit large aggregate IGC. Realize that by minimizing the aggregate IGC, we attempt to produce scheduling patterns wherein receivers of different co-scheduled groups are the least correlated (on average), thereby enhancing the SINR and latency. For every window i, (21b) restricts the aggregate IGC of the co-scheduled groups to remain below λ, which is the maximum threshold. Also, (21c) enforces every group j to be scheduled once, whereas (21d) restricts the number of groups per window to be at most $N_{\text{tx}}^{\text{RF}}$. Without loss of generality, (21e) and the condition $i < j$ imposed on (21a)–(21d) reduce the search space and therefore the complexity. Further, (21f) binds the variables $\mu_{i,j}$ and $\tau_{i,j,l}$ and ensures consistency among them. Finally, (21g) and (21h) declare $\mu_{i,i}$ and $\tau_{i,j,l}$ as Boolean. In (21a), ω is chosen such that the first and second term have equal weights on average.

VII. Numerical Results

This section sheds light on the performance of our proposed scheme HYDRAWAVE (joint group scheduling and precoding). We focus on two performance metrics: *minimum e-SINR* and *latency*. First, to gain insights into the effectiveness of our hybrid precoder design, we evaluate its performance against fully-digital and fully-analog implementations, in which we leave out the scheduling aspect. Next, we investigate the impact of different scheduling algorithms on the total latency, which additionally accounts for the beam-switching delay between the scheduling windows.

HYDRAWAVE: our proposed scheduling and precoding scheme.
SING: single-group multicasting scheduling serves only one multicast group per scheduling window.
RAND: random scheduling selects stochastically an allocation pattern among all possible combinations.
XHAUS: exhaustive search finds the best scheduling policy that minimizes latency among all the possibilities.

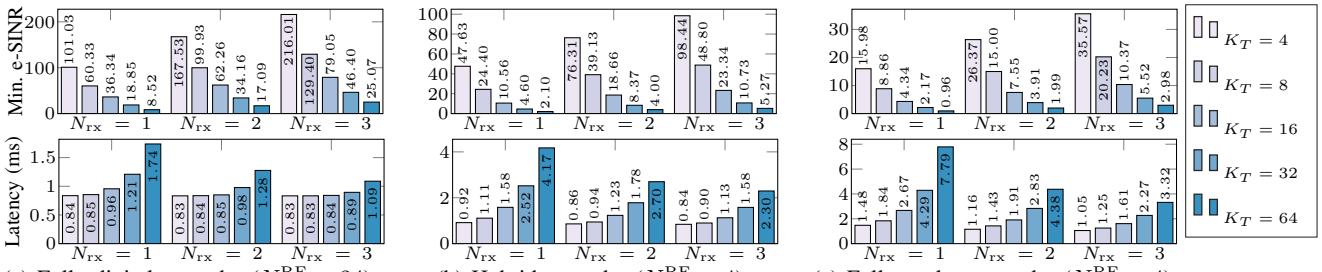

(a) Fully-digital precoder ($N_{\text{tx}}^{\text{RF}} = 24$) (b) Hybrid precoder ($N_{\text{tx}}^{\text{RF}} = 4$) (c) Fully-analog precoder ($N_{\text{tx}}^{\text{RF}} = 4$)

Figure 3: Evaluation of e-SINR and latency for different precoders

In simulations, we consider the geometric channel model with $N_{\text{paths}} = 6$ propagation paths between the transmitter and each receiver [39], [40], considering the high density of reflecting surfaces in an industrial environment. The receivers are divided equally among all the multicast groups. The numerical results show the average performance over 100 channel realizations. Table II summarizes the parameters setting.

Table II: Simulations configuration

Parameter	Notation & Value
Number of antennas at the transmitter	$N_{\text{tx}} = 24$ (with $L_{\text{tx}} = 6$)
Number of antennas at the receiver	$N_{\text{rx}} = \{1, 2, 3\}$
Number of RF chains at the transmitter	$N_{\text{tx}}^{\text{RF}} = 4$
Number of shifts at the transmitter	$D_F = 16$
Number of phase shifts at the receivers	$D_W = 4$
Maximum transmit power	$P_{\text{tx}}^{\max} = 20$ dBm (100 mW)
Maximum receive power	$P_{\text{rx}}^{\max} = 0$ dBm (1 mW)
Noise power	$\sigma^2 = 10$ dBm
Number of multicast groups	$G_T = 4$
Number of receivers	$K_T = \{4, 8, 16, 32, 64\}$
Bit-stream length	$B_1 = B_2 = B_3 = B_4 = 4$ Mbits
Number of bisection procedures	$N_{\text{bis}_1} = N_{\text{bis}_2} = N_{\text{bis}_3} = 10$
Number of randomizations	$N_{\text{rand}_1} = 5 \cdot N_{\text{tx}}$ $N_{\text{rand}_2} = 100 \cdot \lvert\mathcal{G}_t\rvert$ $N_{\text{rand}_3} = 20 \cdot N_{\text{rx}}$
Number of sequential iterations	$N_{\text{iter}} = 3$

1) Performance of Hybrid Precoder without Scheduling: We compare the performance of the proposed hybrid precoder design against a fully-digital implementation, which can be obtained as a particular case of our formulation when $N_{\text{tx}}^{\text{RF}} = N_{\text{tx}}$, $L_{\text{tx}} = 1$ and $\mathbf{F} = \mathbf{I}$. Similarly, we also consider a fully-analog precoder that can be obtained when $\mathbf{M} = \mathbf{I}$. In this scenario, we consider a single window t' with a defined scheduling $\mathcal{V}_{t'}$, where two multicast groups are concurrently served. The performance of this scenario is shown in Fig. 3 and is essentially related to *Proposition 2*. We observe that, for a given number of receivers K_T, the minimum e-SINR improves with an increasing number of receive antennas N_{rx}, because the beam-steering capability of each receiver is augmented. Further, for a given N_{rx}, as the number of receivers K_T increases, the e-SINR reduces since the total power is distributed accordingly. In terms of latency, (calculated with (4)), the fully-digital precoder outperforms the hybrid and fully-analog precoders as it is endowed with a larger amount of RF chains that allows enhanced interference reduction, thus promoting higher data rates. However, due to excessive power consumption and hardware costs of fully-digital precoders in mmWave frequencies, the hybrid precoder is a promising candidate with low power consumption and high performance. For instance, if $P_{\text{RF}} = 250$ mW [41] and $P_{\text{PS}} = 30$ mW [42] represent the power consumed by a single RF chain and a single 4-bit-resolution phase shifter ($D_F = 16$), the instantaneous power consumed by the hybrid and digital precoders are $P_{\text{hyb}} = P_{\text{tx}}^{\max} + N_{\text{tx}}^{\text{RF}} P_{\text{RF}} + N_{\text{tx}} P_{\text{PS}} = 1.82$ W and $P_{\text{dig}} = P_{\text{tx}}^{\max} + N_{\text{tx}}^{\text{RF}} P_{\text{RF}} = 6.10$ W, respectively. This reveals an improvement of 235% on energy consumption and $44\% - 232\%$ on energy efficiency (results excluded due to space limitation).

2) Performance of Hybrid Precoder with Scheduling: Fig. 4 illustrates the performance of HYDRAWAVE, SING, RAND, and XHAUS. In our scheduling formulation in (21), λ controls the maximum tolerable aggregate IGC. Thus, in the fully-digital precoder case, a larger λ can be supported due to the versatility of the precoder to manage interference. On the other hand, due to the limited amount of RF chains, the values of λ used with the hybrid and analog precoders need to be comparatively smaller. We observe that, in terms of latency, the fully-digital precoder outperforms the hybrid and fully-analog implementations. Further, for any precoder type with a small number of receivers (e.g., $K_T = 16$), SING produces the greatest latency while XHAUS is optimal (according to *Proposition 3*). On the other hand, RAND exhibits an intermediate performance between SING and XHAUS. As the number of receivers increases (e.g., $K_T = 64$), the performance gap between SING and XHAUS reduces considerably because interference becomes more complex to manage, thus yielding SING optimal in some realizations. On the contrary, RAND deteriorates since the impact of scheduling becomes more relevant in the presence of higher interference. When considering a switching delay of $\delta_{\text{SW}} = 0.5$ ms between consecutive windows [7], similar behavior can be observed except for SING being heavily penalized due to the incapability of spatial multiplexing. Furthermore, we include the performance of HYDRAWAVE with different values of λ. In Fig. 4, λ_{opt} is obtained upon evaluating several λ and bisecting the search space until negligible variation is observed. For the fully-digital precoder, HYDRAWAVE attains near-optimality when $K_T = 16$. Also, its performance remains within 11% of the optimal value for $K_T = \{32, 64\}$ when $\delta_{\text{SW}} = 0.0$, and within 9% when $\delta_{\text{SW}} = 0.5$ ms. In the hybrid and fully-analog cases, the performance of HYDRAWAVE remains in the range $1.5 - 9.5\%$ and $3.4 - 11.7\%$ of the optimal XHAUS, respectively. In the hybrid precoder case, HYDRAWAVE exhibits gains up 32% higher than SING and up to 102% compared to RAND when $\delta_{\text{SW}} = 0$. When $\delta_{\text{SW}} = 0.5$, the gains are up to 60% and 59%, respectively. While finding λ_{opt} could be time-consuming, we

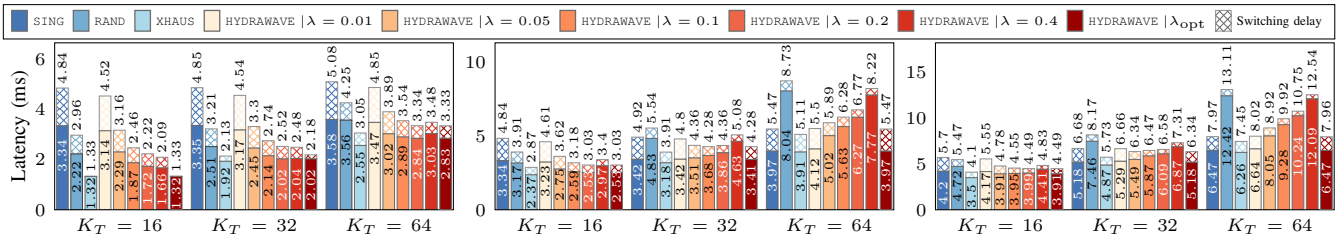

(a) Fully-digital precoder (b) Hybrid precoder (c) Fully-analog precoder

Figure 4: Latency performance of different scheduling schemes with fully-digital, hybrid, and fully-analog precoders.

notice that for a reasonable value of $\lambda = \{0.05, 0.1\}$ the fully-digital and hybrid precoders behave remarkably compared to XHAUS while outperforming SING and RAND.

VIII. Discussion and Future Work

Optimization Parameters: Finding λ_{opt} is challenging as it depends on the channel between the transmitter and receivers, as well as on the total interference. In order to circumvent this problem, a system could be trained using deep-learning to map the inputs to a suitable value of λ. Other possible options are data clustering and multivariate regression.

Hybrid Precoder Design: Compared to most approaches on hybrid precoding (multi-user or multicast) in the literature, in this paper, the hybrid precoder is not obtained as an approximation of the optimal digital implementation. We design the precoder without any knowledge of the digital implementation. We presume that the performance of the hybrid precoder can be further boosted if a better initialization scheme is explored.

Hybrid Precoder Complexity: The worst-case complexity of the hybrid precoder design, when using standard interior-point methods is $N_{\text{bis}_1}\mathcal{O}\left(G^3N_{\text{tx}}^6 + KGN_{\text{tx}}^2\right) + N_{\text{bis}_2}\mathcal{O}\left(\left(GN_{\text{tx}}^{\text{RF}}\right)^6 + K\left(GN_{\text{tx}}^{\text{RF}}\right)^2\right) + KN_{\text{bis}_3}\mathcal{O}\left(N_{\text{rx}}^6 + N_{\text{rx}}^2\right)$.

Optimal Scheduler: Finding the optimal scheduler is intrinsically of combinatorial nature. Alternative relaxations of $0-1$ parameters in *Proposition 3* based on log, exp, and arctan functions could be further explored.

IX. Conclusion

We investigated the joint optimization of scheduling and multi-group multicast hybrid precoders to achieve ubiquitous low-latency mmWave communications in Industry 4.0 settings. We proposed a scheme based on alternate optimization, semidefinite relaxation and Cholesky matrix factorization to design the hybrid precoder. Also, we presented a novel scheduling formulation that takes into account the number of RF chains at the transmitter while minimizes the number of scheduling windows and channel correlation among the co-scheduled receivers. We corroborated through simulations that in terms of SINR the hybrid precoder can attain outstanding performance with a few number of RF chains. In terms of latency performance, the proposed HYDRAWAVE is capable of performing within 9.5% of the optimal XHAUS while exhibiting noticeable advantage over SING and RAND.

X. Acknowledgment

The research is funded by the Deutsche Forschungsgemeinschaft (DFG) within the B5G-Cell project in SFB 1053 MAKI.

Appendix A
Derivation of Proposition 1

Let $C_k^\star = C_{k|\mathcal{V}_{t'},\mathbf{F}_{t'},\mathbf{M}_{t'},\mathbf{w}_k}$, $\text{SINR}_k^\star = \text{SINR}_{k|\mathcal{V}_{t'},\mathbf{F}_{t'},\mathbf{M}_{t'},\mathbf{w}_k}$ and $\xi_{t'}^\star = \xi_{t'|\mathcal{U}_{t'},\mathbf{F}_{t'},\mathbf{M}_{t'},\{\mathbf{w}_k\}_{k\in\mathcal{U}_{t'}}}$. From (4), the transmission latency $\xi_{t'}^\star$ with known $\mathcal{U}_{t'}, \mathbf{F}_{t'}, \mathbf{M}_{t'}, \{\mathbf{w}_k\}_{k\in\mathcal{U}_{t'}}$ is defined as

$$\xi_{t'}^\star = \max_{k\in\mathcal{U}_{t'}}\left\{\frac{B_k}{\min\left\{C_k^\star, C_{\max}\right\}}\right\} \tag{A.1a}$$

$$= \max_{k\in\mathcal{U}_{t'}}\left\{\max\left\{\frac{B_k}{C_k^\star}, \frac{B_k}{C_{\max}}\right\}\right\} \tag{A.1b}$$

$$= \frac{1}{\min\limits_{k\in\mathcal{U}_{t'}}\left\{\min\left\{\frac{C_k^\star}{B_k}, \frac{C_{\max}}{B_k}\right\}\right\}} \tag{A.1c}$$

$$= \frac{1}{\min\limits_{k\in\mathcal{U}_{t'}}\left\{\frac{\log_2(1+\beta\cdot\text{SINR}_k^\star)}{B_k}, \frac{C_{\max}}{B_k}\right\}} \tag{A.1d}$$

$$= \frac{1}{\log_2\left(\min\limits_{k\in\mathcal{U}_{t'}}\left\{(1+\beta\cdot\text{SINR}_k^\star)^{\frac{1}{B_k}}, 2^{\frac{C_{\max}}{B_k}}\right\}\right)}. \tag{A.1e}$$

Because (A.1c) involves extremizations of the same type, they can be combined. When $|\mathcal{V}_t| > 1$, in general $1+\beta\cdot\text{SINR}_k^\star \leq 2^{C_{\max}}$, due to interference and restricted transmit/receive power. Further, since $\log_2(\cdot)$ is monotonically increasing, then,

$$\xi_{t'}^\star \asymp^{-1} \min_{k\in\mathcal{U}_{t'}}\left\{(1+\beta\cdot\text{SINR}_k^\star)^{\frac{1}{B_k}}\right\}. \tag{A.2}$$

Appendix B
Derivation of Proposition 2

Let $\xi_{t'}^\star = \xi_{t'|\mathcal{U}_{t'}}$ and $\text{SINR}_k^\star = \text{SINR}_{k|\mathcal{U}_{t'}}$ represent the latency during window t' and the SINR of receiver $k \in \mathcal{U}_{t'}$, respectively when solely $\mathcal{U}_t$ is known. Thus, $\mathbf{F}_{t'}, \mathbf{M}_{t'}, \{\mathbf{w}_k\}_{k\in\mathcal{U}_{t'}}$ are be designed in order to minimize (A.1c), i.e.,

$$\min_{\substack{\mathbf{F}_{t'}\in\Omega_F,\mathbf{M}_{t'}\in\Omega_M\\ \{\mathbf{w}_k\}_{k\in\mathcal{U}_{t'}}\in\Omega_W}} \frac{1}{\min\limits_{k\in\mathcal{U}_{t'}}\left\{\min\left\{\frac{C_k^\star}{B_k}, \frac{C_{\max}}{B_k}\right\}\right\}}, \tag{B.1}$$

which is equivalent to

$$\overset{(B.1)}{=} \max_{\substack{\mathbf{F}_{t'}\in\Omega_F,\mathbf{M}_{t'}\in\Omega_M\\ \{\mathbf{w}_k\}_{k\in\mathcal{U}_{t'}}\in\Omega_W}} \min_{k\in\mathcal{U}_{t'}}\left\{\min\left\{\frac{C_k^\star}{B_k}, \frac{C_{\max}}{B_k}\right\}\right\} \tag{B.2a}$$

$$\overset{(B.1)}{=} \max_{\substack{\mathbf{F}_{t'}\in\Omega_F,\mathbf{M}_{t'}\in\Omega_M\\ \{\mathbf{w}_k\}_{k\in\mathcal{U}_{t'}}\in\Omega_W}} \min_{k\in\mathcal{U}_{t'}}\left\{\frac{C_k^\star}{B_k}\right\} \tag{B.2b}$$

$$\overset{(B.1)}{=} \max_{\substack{\mathbf{F}_{t'}\in\Omega_F,\mathbf{M}_{t'}\in\Omega_M\\ \{\mathbf{w}_k\}_{k\in\mathcal{U}_{t'}}\in\Omega_W}} \min_{k\in\mathcal{U}_{t'}}\left\{\frac{\log_2\left(1+\beta\cdot\text{SINR}_k^\star\right)}{B_k}\right\} \tag{B.2c}$$

$$\overset{(B.1)}{=} \max_{\substack{\mathbf{F}_{t'}\in\Omega_F,\mathbf{M}_{t'}\in\Omega_M\\ \{\mathbf{w}_k\}_{k\in\mathcal{U}_{t'}}\in\Omega_W}} \min_{k\in\mathcal{U}_{t'}}\left\{\frac{\text{SINR}_k^\star}{B_k}\right\} \tag{B.2d}$$

$$\overset{(B.1)}{=} \max_{\substack{\mathbf{F}_{t'}\in\Omega_F,\mathbf{M}_{t'}\in\Omega_M \\ \{\mathbf{w}_k\}_{k\in\mathcal{U}_{t'}}\in\Omega_W}} \min_{i\in\mathcal{V}_{t'}} \min_{k\in\mathcal{G}_i} \left\{ \frac{\mathrm{SINR}_k^\star}{B_k} \right\}, \tag{B.2e}$$

where (B.2a) collapses to (B.2b) because $C_{\max}$ does not depend on $\mathbf{F}_{t'}, \mathbf{M}_{t'}, \{\mathbf{w}_k\}_{k\in\mathcal{U}_{t'}}$. In (B.2c), since $\log_2\left(1+\beta\cdot\mathrm{SINR}_k^\star\right)$ is an injective mapping of $\mathrm{SINR}_k^\star$, it is equivalent to (B.2d). Further, (B.2e) is an alternative notation for (B.2d).

REFERENCES

[1] B. Martinez, C. Cano, and X. Vilajosana, "A Square Peg in a Round Hole: The Complex Path for Wireless in the Manufacturing Industry," *IEEE Communications Magazine*, vol. 57, no. 4, pp. 109–115, Apr. 2019.

[2] A. Loch, C. Cano, G. H. Sim, A. Asadi, and X. Vilajosana, "A Channel Measurement Campaign for mmWave Communication in Industrial Settings." [Online]. Available: https://arxiv.org/abs/1903.10502

[3] X. Song, T. Kühne, and G. Caire, "Fully-Connected vs. Sub-Connected Hybrid Precoding Architectures for mmWave MU-MIMO," *CoRR*, Nov. 2019. [Online]. Available: https://arxiv.org/pdf/1904.10276.pdf

[4] D. Zhang, Y. Wang, X. Li, and W. Xiang, "Hybridly Connected Structure for Hybrid Beamforming in mmWave Massive MIMO Systems," *IEEE Transactions on Communications*, vol. 66, no. 2, pp. 662–674, Feb. 2018.

[5] A. Alkhateeb, O. E. Ayach, G. Leus, and R. W. Heath, "Channel Estimation and Hybrid Precoding for Millimeter Wave Cellular Systems," *IEEE Journal of Selected Topics in Signal Processing*, vol. 8, no. 5, pp. 831–846, Oct. 2014.

[6] Z. Marzi, D. Ramasamy, and U. Madhow, "Compressive Channel Estimation and Tracking for Large Arrays in mm-Wave Picocells," *IEEE Journal of Selected Topics in Signal Processing*, vol. 10, no. 3, pp. 514–527, Apr. 2016.

[7] H. Zhang, Y. Jiang, K. Sundaresan, S. Rangarajan, and B. Zhao, "Wireless Multicast Scheduling With Switched Beamforming Antennas," *IEEE/ACM Transactions on Networking*, vol. 20, no. 5, pp. 1595–1607, Oct. 2012.

[8] K. Sundaresan, K. Ramachandran, and S. Rangarajan, "Optimal Beam Scheduling for Multicasting in Wireless Networks," in *ACM Mobicom*, 2009, pp. 205–216.

[9] G. H. Sim and J. Widmer, "Finite Horizon Opportunistic Multicast Beamforming," *IEEE Transactions on Wireless Communications*, vol. 16, no. 3, pp. 1452–1465, Mar. 2017.

[10] N. D. Sidiropoulos, T. N. Davidson, and Z. Luo, "Transmit Beamforming for Physical-Layer Multicasting," *IEEE Transactions on Signal Processing*, vol. 54, no. 6, pp. 2239–2251, Jun. 2006.

[11] L. Tran, M. F. Hanif, and M. Juntti, "A Conic Quadratic Programming Approach to Physical Layer Multicasting for Large-Scale Antenna Arrays," *IEEE Signal Processing Letters*, vol. 21, no. 1, pp. 114–117, Jan. 2014.

[12] J. Choi, "Iterative Methods for Physical-Layer Multicast Beamforming," *IEEE Transactions on Wireless Communications*, vol. 14, no. 9, pp. 5185–5196, Sept. 2015.

[13] M. Bengtsson and B. Ottersten, "Optimal and Suboptimal Transmit Beamforming," in *Handbook of Antennas in Wireless Communications*, L. C. Godara, Ed., CRC Press, Aug. 2001, ch. 18.

[14] B. Gopalakrishnan and N. D. Sidiropoulos, "High Performance Adaptive Algorithms for Single-Group Multicast Beamforming," *IEEE Transactions on Signal Processing*, vol. 63, no. 16, pp. 4373–4384, Aug 2015.

[15] M. Dai and B. Clerckx, "Hybrid Precoding for Physical Layer Multicasting," *IEEE Communications Letters*, vol. 20, no. 2, Feb. 2016.

[16] L. F. Abanto-Leon and G. H. Sim, "Learning-based Max-Min Fair Hybrid Precoding for mmWave Multicasting," in *IEEE ICC*, Jun. 2020.

[17] E. Aryafar, M. A. Khojastepour, K. Sundaresan, S. Rangarajan, and E. Knightly, "ADAM: An Adaptive Beamforming System for Multicasting in Wireless LANs," *IEEE/ACM Transactions on Networking*, vol. 21, no. 5, pp. 1595–1608, Oct. 2013.

[18] L. Zhou, Z. Xu, W. Jiang, and W. Luo, "Joint Multicast Beamforming and User Scheduling in Large-scale Antenna Systems," *IET Communications*, vol. 12, no. 11, pp. 1307–1314, Jul. 2018.

[19] E. Karipidis, N. D. Sidiropoulos, and Z. Q. Luo, "Transmit Beamforming of Multiple Co-Channel Multicast Group," in *IEEE CAMSAP*, Dec. 2005, pp. 109–112.

[20] N. Bornhorst and M. Pesavento, "An Iterative Convex Approximation Approach for Transmit Beamforming in Multi-Group Multicasting," in *IEEE SPAWC*, Jun. 2011, pp. 426–430.

[21] O. T. Demir and T. E. Tuncer, "Multi-group Multicast Beamforming for Simultaneous Wireless Information and Power Transfer," in *EUPSICO*, Aug. 2015, pp. 1356–1360.

[22] E. Karipidis, N. D. Sidiropoulos, and Z. Luo, "Quality of Service and Max-Min Fair Transmit Beamforming to Multiple Cochannel Multicast Groups," *IEEE Transactions on Signal Processing*, vol. 56, no. 3, pp. 1268–1279, Mar. 2008.

[23] Y. Gao and M. Schubert, "Group-oriented Beamforming for Multi-stream Multicasting based on Quality-of-service Requirements," in *IEEE CAMSAP*, Dec. 2005, pp. 193–196.

[24] A. Schad and M. Pesavento, "Max-min Fair Transmit Beamforming for Multi-Group Multicasting," in *WSA*, Mar. 2012, pp. 115–118.

[25] D. Christopoulos, S. Chatzinotas, and B. Ottersten, "Weighted Fair Multicast Multigroup Beamforming Under Per-antenna Power Constraints," *IEEE Transactions on Signal Processing*, vol. 62, no. 19, pp. 5132–5142, Oct. 2014.

[26] M. Sadeghi, E. Björnson, E. G. Larsson, C. Yuen, and T. L. Marzetta, "Max-Min Fair Transmit Precoding for Multi-Group Multicasting in Massive MIMO," *IEEE Transactions on Wireless Communications*, vol. 17, no. 2, pp. 1358–1373, Feb. 2018.

[27] J. Huang, Z. Cheng, E. Chen, and M. Tao, "Low-Complexity Hybrid Analog/Digital Beamforming for Multicast Transmission in mmWave Systems," in *IEEE ICC*, May. 2017, pp. 1–6.

[28] O. T. Demir and T. E. Tuncer, "Antenna Selection and Hybrid Beamforming for Simultaneous Wireless Information and Power Transfer in Multi-Group Multicasting Systems," *IEEE Transactions on Wireless Communications*, vol. 15, no. 10, pp. 6948–6962, Oct. 2016.

[29] M. Sadeghi, L. Sanguinetti, and C. Yuen, "Hybrid Precoding for Multi-Group Physical Layer Multicasting," in *EW*, May. 2018, pp. 1–6.

[30] L. F. Abanto-Leon, M. Hollick, and G. H. Sim, "Hybrid Precoding for Multi-Group Multicasting in mmWave Systems," in *IEEE GLOBECOM*, Dec. 2019.

[31] D. Christopoulos, S. Chatzinotas, and B. Ottersten, "Multicast Multigroup Precoding and User Scheduling for Frame-Based Satellite Communications," *IEEE Transactions on Wireless Communications*, vol. 14, no. 9, pp. 4695–4707, Sept. 2015.

[32] M. R. Akdeniz, Y. Liu, M. K. Samimi, S. Sun, S. Rangan, T. S. Rappaport, and E. Erkip, "Millimeter Wave Channel Modeling and Cellular Capacity Evaluation," *IEEE Journal on Selected Areas in Communications*, vol. 32, no. 6, pp. 1164–1179, Jun. 2014.

[33] I. Csiszár and G. Tusnády, "Information Geometry and Alternating Minimization Procedures," *Statistics & Decisions: Supplement Issues*, vol. 1, pp. 205–237, 1984.

[34] A. Wiesel, Y. C. Eldar, and S. Shamai, "Linear Precoding via Conic Optimization for Fixed MIMO Receivers," *IEEE Transactions on Signal Processing*, vol. 54, no. 1, pp. 161–176, Jan. 2006.

[35] Z. P. Yang and X. X. Feng, "A Note on the Trace Inequality for Products of Hermitian Matrix Power," *Journal of Inequalities in Pure and Applied Mathematics*, vol. 3, no. 5, Jul. 2002.

[36] W. K. Ma, P. C. Ching, and Z. Ding, "Semidefinite Relaxation Based Multiuser Detection for M-Ary PSK Multiuser Systems," *IEEE Transactions on Signal Processing*, vol. 52, no. 10, pp. 2862–2872, Oct. 2004.

[37] Z. Luo, N. D. Sidiropoulos, P. Tseng, and S. Zhang, "Approximation Bounds for Quadratic Optimization with Homogeneous Quadratic Constraints," *SIAM Journal on Optimization*, vol. 18, no. 1, pp. 1–28, Feb. 2007.

[38] S. Zhang and Y. Huang, "Complex Quadratic Optimization and Semidefinite Programming," *SIAM Journal on Optimization*, vol. 16, no. 3, pp. 871–890, Jan. 2006.

[39] A. A. M. Saleh and R. Valenzuela, "A Statistical Model for Indoor Multipath Propagation," *IEEE Journal on Selected Areas in Communications*, vol. 5, no. 2, pp. 128–137, Feb. 1987.

[40] R. W. Heath, N. González-Prelcic, S. Rangan, W. Roh, and A. M. Sayeed, "An Overview of Signal Processing Techniques for Millimeter Wave MIMO Systems," *IEEE Journal of Selected Topics in Signal Processing*, vol. 10, no. 3, pp. 436–453, Apr. 2016.

[41] X. Gao, L. Dai, S. Han, C. I, and R. W. Heath, "Energy-Efficient Hybrid Analog and Digital Precoding for MmWave MIMO Systems With Large Antenna Arrays," *IEEE Journal on Selected Areas in Communications*, vol. 34, no. 4, pp. 998–1009, Apr. 2016.

[42] R. Méndez-Rial, C. Rusu, N. González-Prelcic, A. Alkhateeb, and R. W. Heath, "Hybrid MIMO Architectures for mmWave Communications: Phase Shifters or Switches?" *IEEE Access*, vol. 4, pp. 247–267, 2016.

F

PUBLICATION VI.
BEAMWAVE: CROSS-LAYER BEAMFORMING AND SCHEDULING FOR SUPERIMPOSED TRANSMISSIONS IN INDUSTRIAL IOT MMWAVE NETWORKS

BEAMWAVE: Cross-layer Beamforming and Scheduling for Superimposed Transmissions in Industrial IoT mmWave Networks

Luis F. Abanto-Leon, and Matthias Hollick, and Gek Hong (Allyson) Sim

Secure Mobile Networking Lab, Technische Universität Darmstadt, Germany

{labanto, mhollick, asim}@seemoo.tu-darmstadt.de

***Abstract*—The omnipresence of IoT devices in Industry 4.0 is expected to foster higher reliability, safety, and efficiency. However, interconnecting a large number of wireless devices without jeopardizing the system performance proves challenging. To address the requirements of future industries, we investigate the cross-layer design of beamforming and scheduling for layered-division multiplexing (LDM) systems in millimeter-wave bands. Scheduling is crucial as the devices in industrial settings are expected to proliferate rapidly. Also, highly performant beamforming is necessary to ensure scalability. By adopting LDM, multiple transmissions can be non-orthogonally superimposed. Specifically, we consider a *superior-importance control multicast message* required to be ubiquitous to all devices and *inferior-importance private unicast messages* targeting a subset of scheduled devices. Due to NP-hardness, we propose `BEAMWAVE`, which decomposes the problem into *beamforming* and *scheduling*. Through simulations, we show that `BEAMWAVE` attains near-optimality and outperforms other competing schemes.**

***Index Terms*—cross-layer, beamforming, scheduling, unicast, multicast, layered-division multiplexing, industrial IoT, mmWave.**

I. Introduction

Industry 4.0 envisions automated factories with a massive number of interconnected industrial internet-of-things (IoT) devices [1], such as sensors, actuators, programmable logic devices, and access points. Such degree of interconnectivity is expected to facilitate ultra-precise control and seamless coordination, thus enabling extremely efficient and dependable manufacturing processes [2]. In the existing industrial settings, the majority of stationary devices are interconnected through redundant wired connections to guarantee communications with high reliability. However, with the upsurge of devices in smart industries, wired solutions will encounter the following problems: *(i)* intricate implementation complexity to interconnect a massive number of devices, *(ii)* increased operational costs due to hard-wiring, *(iii)* limited maneuverability of articulated robots, and *(iv)* communication infeasibility with autonomous mobile freight transport. In contrast, wireless solutions can substantially simplify the deployment complexity and reduce maintenance costs while promoting the adoption of more flexible mechanics and mobile apparatus. *Thus, the transformation from wired to wireless infrastructure is an appealing strategy towards the evolution of industries.*

By harnessing *millimeter-wave* (mmWave) and *massive multiple-input multiple-output* (mMIMO), high spectral efficiency has been demonstrated (e.g., [3], [4]). Specifically, mmWave is an attractive substitute for the saturated sub-6 GHz spectrum due to broad bandwidth availability. Also, because of the shorter wavelength, mmWave requires miniature antennas that can be easily embedded onto small industrial devices. Further, mmWave exhibits high spatial reuse due to severe path-loss and sparse propagation, making it ideal for short-range communications in extremely dense scenarios such as the industrial settings. Besides, owing to increased degrees of freedom, mMIMO renders extraordinary interference mitigation [5], [6] that enables augmented spectral efficiency and exceptional multiplexing capability, which are desirable features to support the future industrial landscape.

In factories of the future, industrial devices will require two types of information: *shared safety/control messages* (multicast signal) and *private messages* (unicast signals). Such a requirement could be addressed by orthogonal multiple access (OMA) schemes, wherein multicast and unicast signals would be transmitted in disjoint time or frequency resources. Nevertheless, with the anticipated escalation, OMA schemes will struggle to accommodate a large number of devices in orthogonal resources. Thus, *non-orthogonal multiple access* (NOMA) schemes are envisaged as a remedy to cope with the scarcity of radio resources. In particular, NOMA can boost the spectral efficiency by admitting superposed transmissions in the power or code domain. Among the plethora of NOMA variants [7], layered-division multiplexing (LDM) has been recognized as a promising candidate to meet the growing spectrum demands. LDM is a power-domain NOMA scheme capable of conveying multiple layers of information simultaneously while using the same time-frequency resources. By harnessing LDM in industrial settings, multicast and unicast information can be disseminated concurrently without resorting to OMA schemes such as time/frequency-division multiplexing (T/FDM).

Several NOMA schemes have recently been intertwined with mmWave and mMIMO, showing remarkable synergy in many use cases (e.g., [8]–[10]). Also, preliminary studies on the usage of NOMA [11] and mmWave [12] for smart industries have shown favorable results. Based on this evidence, it is expected that by jointly leveraging mmWave, mMIMO and LDM, the stringent requirements of future industrial ecosystems can be fulfilled. However, the synthesis of these technologies poses challenges that require further study when considered in the context of Industry 4.0.

Challenges: The following summarizes relevant aspects that need to be considered in the envisaged industrial landscape.

- The maximum number of devices that can be simultaneously served with individual signals is limited by the number of radio frequency (RF) chains at the transmitter (e.g., base station). Hence, with the forecasted rapid escalation of devices in industrial sectors [13], the problem aggravates. Most existing works on beamforming consider sufficient RF chains to serve all devices, thus rendering scheduling unnecessary. *However, as networks densify, scheduling will be pivotal in exerting substantial improvement in the system performance. Thus, considering the cross-layer optimization of beamforming and scheduling is of utmost importance.*
- Multicast and unicast transmissions give rise to conflicting objectives. From the multicast perspective, the transmitter consumes lesser power while the spectral efficiency improves when the devices have correlated channels. From the unicast perspective, we observe the opposite effect, i.e., correlated channels yield low spectral efficiency while demanding higher power. *As a result, selecting a suitable set of devices (i.e., scheduling) in superimposed multicast-unicast LDM systems requires special consideration.*
- Problems dealing with cross-layer optimization of beamforming and scheduling are challenging to solve due its inherent nature of involving integer and continuous variables.

Research problem: Due to safety reasons, the superior-importance multicast signal (e.g., control messages) is not subject to scheduling but is required to be ubiquitous to all IoT devices. Contrastingly, the inferior-importance unicast signals (e.g., software updates) are conveyed to only a specific subset of devices (i.e., scheduling) subject to RF chains availability. As a result, two superimposed beamformers are designed. One beamformer transmits the control signal to all devices. The second beamformer caters a selected subset of devices with private unicast signals, where the selection of devices is inspired by the max-min criterion.

Related work: Beamforming in LDM systems has been studied for *(i)* transmit power minimization [8], [14], [15], *(ii)* energy efficiency improvement [16], *(iii)* joint beamforming and base station clustering [17], [18], *(iv)* sum-rate maximization [19], *(v)* simultaneous wireless information and power transfer (SWIPT) [20], [21], and *(vi)* fairness improvement [22]. *To the best of our knowledge, the cross-layer optimization problem for joint design of beamforming and scheduling in LDM systems has not been studied before. Further, the combination of mmWave, mMIMO and LDM has neither been studied in industrial settings.*

Contributions: Our contributions are the following.

- We formulate a NP-hard problem ($\mathcal{P}$) that jointly optimizes *beamforming* and *scheduling* for multicast-unicast LDM transmissions, where we impose a signal-to-interference-plus-noise ratio (SINR) constraint on the multicast signal to ensure that every IoT device correctly decodes the ubiquitous safety message.
- To solve problem $\mathcal{P}$ we propose `BEAMWAVE`, which decomposes $\mathcal{P}$ into two problems $\mathcal{S}$ and $\mathcal{D}$. We propose a novel scheduling scheme $\mathcal{S}$ based on new pair-wise metrics, `PAWN`, `ROOK`, `KING`, that we devise to guide the decision. Essentially, these metrics represent the discordance of co-scheduling two devices together. To solve $\mathcal{D}$, we devise an approach based on the convex-concave procedure (CCP). Through simulations, we show that the proposed `BEAMWAVE` can attain near-optimality when compared to an exhaustive search approach.
- We motivate the need for scheduling in LDM systems, specially when the number of RF chains is insufficient to serve a significantly larger number of devices (which is expected in future industrial settings). In addition, we apply our proposed scheduler $\mathcal{S}$ to T/FDM systems to find the set of devices co-scheduled in the same time or frequency resource. Through simulations, we show the importance of scheduling when compared to more trivial schemes such as random selection.

II. System Model

We assume a system, where a next-generation Node B (gNodeB) serves K devices indexed by $\mathcal{K} = \{1, \cdots, K\}$. The gNodeB transmits a signal composed of two non-orthogonal layers. The *primary layer* is a multicast signal that conveys a shared control message intended for every device $k \in \mathcal{K}$. The *secondary layer* is a composite signal consisting of multiple unicast messages intended for a subset of devices $\mathcal{K}' \subseteq \mathcal{K}$, where $K' = |\mathcal{K}'|$. Thus, K' *dual-layer* devices are catered with simultaneous unicast and multicast transmissions, whereas $K - K'$ *single-layer* devices are served with multicast information only. The gNodeB possesses a precoder (i.e., *transmit beamformer*) consisting of N_{tx} antennas and $N_{\text{tx}}^{\text{RF}} << N_{\text{tx}}$ RF chains. Without loss of generality, we assume that $N_{\text{tx}}^{\text{RF}} = K'$. Besides, each IoT device in the system is equipped with a single RF chain (i.e., $N_{\text{rx}}^{\text{RF}} = 1$) and N_{rx} antennas.

The downlink signal from the gNodeB is denoted by $\mathbf{x} = [\mathbf{B}|\mathbf{m}]\left[\mathbf{s}^T|z\right]^T$. The unicast and multicast precoders are represented by $\mathbf{B} \in \mathbb{C}^{N_{\text{tx}} \times K'}$ and $\mathbf{m} \in \mathbb{C}^{N_{\text{tx}} \times 1}$, respectively. In addition, $\mathbf{s} \in \mathbb{C}^{K' \times 1}$ denotes the unicast symbols for the *dual-layer* devices while $z \in \mathbb{C}$ is the shared multicast symbol intended for all K devices, with $\mathbb{E}\left\{\left[\mathbf{s}^T, z\right]^H \left[\mathbf{s}^T, z\right]\right\} = \mathbf{I}$. More specifically, $\mathbf{B} = \widetilde{\mathbf{B}}\mathbf{U}$ where $\widetilde{\mathbf{B}} = [\mathbf{b}_1, \ldots, \mathbf{b}_K] \in \mathbb{C}^{N_{\text{tx}} \times K}$ and $\mathbf{U} \in \mathbb{B}^{K \times K'}$ is a binary matrix. Also, $\mathbf{s} = \mathbf{U}^T\widetilde{\mathbf{s}}$ where $\widetilde{\mathbf{s}} = [s_1, \ldots, s_K]^T \in \mathbb{C}^{K \times 1}$. Concretely, the matrix $\mathbf{U}$ selects the *dual-layer* devices that will be served with both unicast and multicast signals. Thus, it must hold that $\mathbf{1}^T\mathbf{U}\mathbf{1} = K'$, $\mathbf{U}\mathbf{1} \preccurlyeq \mathbf{1}$ and $\mathbf{U}^T\mathbf{1} \preccurlyeq \mathbf{1}$. As a result, $\mathbf{U}\mathbf{U}^T = \text{diag}\left([\mu_1, \cdots, \mu_K]\right)$ is a square matrix whose k-th diagonal element is 1 when k is a *dual-layer* device (i.e., $\mu_k = \left[\mathbf{U}\mathbf{U}^T\right]_{k,k} = 1$, if $k \in \mathcal{K}'$). Otherwise, $\mu_k = \left[\mathbf{U}\mathbf{U}^T\right]_{k,k} = 0$ when k is a *single-layer* device. Assuming flat fading, the signal received by device $k \in \mathcal{K}$ is given by

$$y_k = \underbrace{\mathbf{w}_k^H\mathbf{H}_k\mathbf{m}z}_{y_k^{\text{M}}\text{: multicast signal}} + \underbrace{\mathbf{w}_k^H\mathbf{H}_k\sum_{j\in\mathcal{K}'}\mathbf{b}_j s_j}_{y_k^{\text{U}}\text{: aggregate unicast signal}} + \underbrace{\mathbf{w}_k^H\mathbf{n}_k}_{\eta_k\text{:noise}}, \tag{1}$$

where $\mathbf{w}_k^H\mathbf{H}_k\sum_{j\in\mathcal{K}\setminus\mathcal{K}'}\mu_j\mathbf{b}_j s_j = 0$ since $\mu_j = 0$, $\forall j \in \mathcal{K}\setminus\mathcal{K}'$. Besides, $\mathbf{w}_k \in \mathbb{C}^{N_{\text{rx}} \times 1}$ represents the combiner (i.e., *receive beamformer*) of the k-th device, $\mathbf{n}_k \sim \mathcal{CN}\left(\mathbf{0}, \sigma^2\mathbf{I}\right)$ symbolizes circularly symmetric Gaussian noise whereas $\mathbf{H}_k \in \mathbb{C}^{N_{\text{rx}} \times N_{\text{tx}}}$

denotes the channel between the gNodeB and the k-th device, defined as

$$\mathbf{H}_k = \sqrt{\frac{N_{\rm rx} N_{\rm tx}}{L_k}} \sum_{l=1}^{L_k} \rho_k^{(l)} \mathbf{a}_{\rm rx}\left(\psi_k^{(l)}\right) \mathbf{a}_{\rm tx}\left(\phi_k^{(l)}\right)^H. \tag{2}$$

Here, L_k is the number of paths in $\mathbf{H}_k$, whereas $\psi_k^{(l)}$ and $\phi_k^{(l)}$ represent the angle of arrival (AoA) and angle of departure (AoD) of the l-th path in $\mathbf{H}_k$, respectively. The array vector responses at the k-th device and gNodeB, in the directions of $\psi_k^{(l)}$ and $\phi_k^{(l)}$, are respectively defined as $\mathbf{a}_{\rm rx}\left(\psi_k^{(l)}\right) = \frac{1}{\sqrt{N_{\rm rx}}}\left[1, \cdots, e^{-j(N_{\rm rx}-1)\frac{2\pi}{\lambda} d\cos(\psi_k^{(l)})}\right]^T$ and $\mathbf{a}_{\rm tx}\left(\phi_k^{(l)}\right) = \frac{1}{\sqrt{N_{\rm tx}}}\left[1, \cdots, e^{-j(N_{\rm tx}-1)\frac{2\pi}{\lambda} d\cos(\phi_k^{(l)})}\right]^T$. Also, $\frac{d}{\lambda} = 0.5$ and $\rho_k^{(l)}$ is the complex gain of the l-th path in $\mathbf{H}_k$, which is represented as a random variable following a complex Gaussian distribution $\mathcal{CN}(0,1)$.

Due to the superposed structure of the transmitted signal, successive interference cancellation (SIC) is performed by the *dual-layer* devices in order to extract multicast and unicast information. Every device $k \in \mathcal{K}$ decodes the multicast symbol first by treating the aggregate unicast signal as noise. In addition, if k is a *dual-layer* device (i.e., $k \in \mathcal{K}'$), then the device applies SIC decoding. Essentially, the k-th device reconstructs the multicast signal $y_k^{\rm M}$ using the decoded symbol z, and then subtracts $y_k^{\rm M}$ from y_k. Thereupon, the remaining byproduct consists solely of unicast components ($y_k^{\rm U}$) and noise (η_k), from where the *dual-layer* device can decode its intended symbol s_k. The SINR of the multicast and unicast signals at the k-th device are respectively defined as

$$\text{SINR}_k^{\rm M} = \frac{\left|\mathbf{w}_k^H \mathbf{H}_k \mathbf{m}\right|^2}{\sum_{j\in\mathcal{K}'} \left|\mathbf{w}_k^H \mathbf{H}_k \mathbf{b}_j\right|^2 + \sigma^2 \left\|\mathbf{w}_k\right\|_2^2}, \forall k \in \mathcal{K}, \tag{3}$$

$$\text{SINR}_k^{\rm U} = \frac{\left|\mathbf{w}_k^H \mathbf{H}_k \mathbf{b}_k\right|^2}{\sum_{j\neq k, j\in\mathcal{K}'} \left|\mathbf{w}_k^H \mathbf{H}_k \mathbf{b}_j\right|^2 + \sigma^2 \left\|\mathbf{w}_k\right\|_2^2}, \forall k \in \mathcal{K}'. \tag{4}$$

III. Problem Formulation

We present a joint formulation that encompasses the optimization of *(i)* scheduling, *(ii)* precoders and *(iii)* combiners,

$$\begin{aligned}
\mathcal{P}: \max_{\substack{\mathbf{W},\mathbf{m},\\ \widetilde{\mathbf{B}},\boldsymbol{\mu}}} \quad & \min_{k\in\mathcal{K}} \frac{\left|\mathbf{w}_k^H \mathbf{H}_k \mathbf{b}_k\right|^2 g(\mu_k)}{\sum_{j\neq k, j\in\mathcal{K}} \left|\mathbf{w}_k^H \mathbf{H}_k \mathbf{b}_j\right|^2 \mu_j + \sigma^2 \left\|\mathbf{w}_k\right\|_2^2} \\
\text{s.t.} \quad & \text{C}_1: \frac{\left|\mathbf{w}_k^H \mathbf{H}_k \mathbf{m}\right|^2}{\sum_{j\in\mathcal{K}} \left|\mathbf{w}_k^H \mathbf{H}_k \mathbf{b}_j\right|^2 \mu_j + \sigma^2 \left\|\mathbf{w}_k\right\|_2^2} \geq \gamma_{\min}, \forall k \in \mathcal{K}, \\
& \text{C}_2: \sum_{k\in\mathcal{K}} \left\|\mathbf{b}_k\right\|_2^2 \mu_k + \left\|\mathbf{m}\right\|_2^2 \leq P_{\rm tx}, \\
& \text{C}_3: \sum_{k\in\mathcal{K}} \mu_k = K', \\
& \text{C}_4: [\mathbf{w}_k]_l \in \mathcal{W}, l \in \mathcal{L}, \forall k \in \mathcal{K}, \\
& \text{C}_5: \mu_k \in \{0,1\},
\end{aligned}$$

where $g(\chi)$ is defined as

$$g(\chi) = \begin{cases} 1, & \text{if } \chi = 1, \\ \infty, & \text{if } \chi = 0. \end{cases}$$

and $\mathbf{W} = [\mathbf{w}_1, \cdots, \mathbf{w}_K]$, $\widetilde{\mathbf{B}} = [\mathbf{b}_1, \cdots, \mathbf{b}_K]$, $\boldsymbol{\mu} = [\mu_1, \cdots, \mu_K]$.

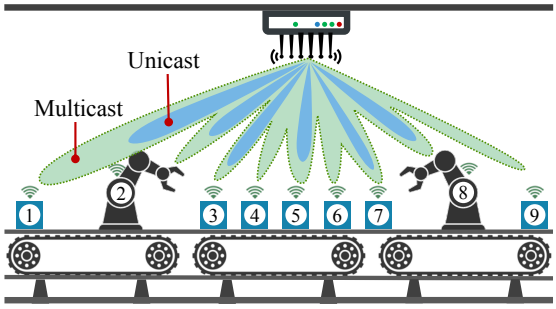

Figure 1: Multicast-unicast LDM system with $K = 9$ devices. *The multicast signal is intended for all devices whereas only a subset of $K' = 6$ devices is served with private unicast signals.*

The objective function of $\mathcal{P}$ aims to find the subset $\mathcal{K}' \subseteq \mathcal{K}$ that maximizes the minimum $\text{SINR}_k^{\rm U}$, $k \in \mathcal{K}'$. The constraint C_1 requires $\text{SINR}_k^{\rm M}$ to be above a threshold $\gamma_{\min}$ for all devices, whereas C_2 limits the transmit power to $P_{\rm tx}$. The constraint C_3 selects K' devices for *dual-layer* transmissions while C_4 enforces beamforming restrictions on the combiners. Specifically, only a small number of $L_{\rm rx}$ constant-modulus phase shifts are admitted for designing the combiners. Every phase shift $[\mathbf{w}_k]_l$ is confined to $\mathcal{W} = \left\{\delta_{\rm rx}, \ldots, \delta_{\rm rx} e^{j\frac{2\pi(L_{\rm rx}-1)}{L_{\rm rx}}}\right\}$, $l \in \mathcal{L} = \{1, \ldots, N_{\rm rx}\}$[1]. Finally, C_5 enforces the Boolean nature of μ_k. We consider limited receive power $P_{\rm rx}$ at each device. Thus, $P_{\rm rx} = \left\|\mathbf{w}_k\right\|_2^2 = \sum_{l=1}^{N_{\rm rx}} \left|[\mathbf{w}_k]_l\right|^2 = N_{\rm rx}\delta_{\rm rx}^2$, where $\delta_{\rm rx} = \sqrt{P_{\rm rx}/N_{\rm rx}}$.

To solve $\mathcal{P}$, one possibility is to adopt an exhaustive search approach (XHAUS). This procedure consists in generating every subset of devices of size K' from a total of K, thus yielding $J = \binom{K}{K'}$ possibilities for $\boldsymbol{\mu}$, i.e., $\{\boldsymbol{\mu}_1, \cdots, \boldsymbol{\mu}_J\}$. Then, $\mathcal{P}$ is solved for each of the combinations, i.e., $\left\{\mathcal{P}\left(\mathbf{W}, \mathbf{m}, \widetilde{\mathbf{B}}, \boldsymbol{\mu}_1\right), \cdots, \mathcal{P}\left(\mathbf{W}, \mathbf{m}, \widetilde{\mathbf{B}}, \boldsymbol{\mu}_J\right)\right\}$ and the choice that attains the *max-min* unicast SINR is selected as optimal. While XHAUS yields the best scheduling, it is computationally expensive. Therefore, in Section IV, we propose a scheme, wherein $\boldsymbol{\mu}$ is determined in advance by a novel scheduler. Then, $\mathbf{W}, \mathbf{m}, \widetilde{\mathbf{B}}$ are designed for the resulting selection of devices[2]. Problem $\mathcal{P}$ is illustrated in Fig. 1.

IV. BEAMWAVE: Proposed Scheme

We divide $\mathcal{P}$ into two problems: $\mathcal{S}$ (Section IV-A) and $\mathcal{D}$ (Section IV-B). First, $\mathcal{S}$ finds a subset $\mathcal{K}'$ of *dual-layer* devices, thus rendering the binary scheduling variables available. Subsequently, $\mathcal{D}$ designs the precoder and the combiners.

A. Scheduling

Selecting an optimal subset of *dual-layer* devices $\mathcal{K}'$ that leads to the maximization of the minimum unicast SINR is intrinsically of combinatorial nature. In order to circumvent the exhaustive search, we propose a novel scheduling scheme

[1]Realize that $\mathcal{W}$ consists of equally-distributed phase rotations with magnitude $\delta_{\rm rx}$, where $L_{\rm rx}$ defines the phase resolution.

[2]Notice that even for a given $\boldsymbol{\mu}'$, the problem $\mathcal{P}\left(\mathbf{W}, \mathbf{m}, \widetilde{\mathbf{B}}, \boldsymbol{\mu}'\right)$ is nonconvex and challenging to solve.

$\mathcal{S}$, which is based on the minimization of an aggregate pairwise device-specific channel metric. The objective is to find the variables $\boldsymbol{\mu}$ and $\boldsymbol{\nu}$ such that $f_{\mathcal{S}}(\boldsymbol{\nu})$ is minimized.

$$\begin{aligned}
\mathcal{S}: \min_{\boldsymbol{\mu},\boldsymbol{\nu}} \quad & f_{\mathcal{S}}(\boldsymbol{\nu}) \triangleq \sum_{j=1}^{K-1} \sum_{l=j+1}^{K} \theta_{j,l} \cdot \nu_{j,l} \\
\text{s.t.} \quad & \mathrm{Q}_1 : \mu_j \geq \nu_{j,l}, \forall j < l, \\
& \mathrm{Q}_2 : \mu_j + \mu_l \leq 1 + \nu_{j,l}, \forall j < l, \\
& \mathrm{Q}_3 : \sum_{j=1}^{K} \mu_j = K', \\
& \mathrm{Q}_4 : \mu_j \in \{0,1\}, \forall j, \\
& \mathrm{Q}_5 : \nu_{j,l} \in \{0,1\}, \forall j < l.
\end{aligned}$$

In particular, $\theta_{j,l}$ denotes a positive metric between two devices $j \in \mathcal{K}$ and $l \in \mathcal{K}$, representing the discordance of co-scheduling the two devices. The auxiliary variable $\nu_{j,l}$, assumes the value of 1, if devices j and l are co-scheduled for *dual-layer* transmissions. Otherwise, $\nu_{j,l} = 0$. As defined in $\mathcal{P}$, the variable μ_j denotes with 1 that $j \in \mathcal{K}$ is a *dual-layer* device. The constraints Q_1 and Q_2 have been included in order to bind the two sets of variables, i.e., $\boldsymbol{\mu}$ and $\boldsymbol{\nu}$. Specifically, Q_1 states that $\nu_{j,l}$ is upper-bounded by μ_j since $\nu_{j,l}$ can only be 1 when the devices j and l are co-scheduled. Similarly, Q_2 is a lower bound for $\nu_{j,l}$ in terms of μ_j and μ_l. Besides, Q_3 restricts the maximum number of *dual-layer* devices to K'. Constraints $\mathrm{Q}_4 - \mathrm{Q}_5$ denote the Boolean nature of the variables.

We denote the solution of $\mathcal{S}$ by $(\boldsymbol{\mu}^\star, \boldsymbol{\nu}^\star)$. In the following, we propose three metrics $\theta_{j,l}$ (i.e., PAWN, ROOK, KING), based on channel correlation and channel energy, which will support the scheduling decision.

CORR: Channel correlation has been extensively used for multiuser unicast scheduling in prior literature (e.g., [23]). Given any two devices j and l, CORR is computed as $\theta_{j,l} = \frac{\left|\mathbf{h}_j^H \mathbf{h}_l\right|}{\|\mathbf{h}_j\|_2 \|\mathbf{h}_l\|_2}$, where $\mathbf{h}_j = \mathrm{vec}(\mathbf{H}_j)$. Intuitively, a large value of $0 \leq \theta_{j,l} \leq 1$ implies that the two devices have correlated channels and therefore they are prone to generate more interference to each other. CORR has conventionally been used in a greedy manner, where users/devices are sequentially chosen based on the cumulative correlation with respect to the already selected devices. In contrast, herein we use CORR in combination with our proposed scheduler $\mathcal{S}$, thus allowing to find the best set $\mathcal{K}'$ of *dual-layer* devices that renders the least aggregate pair-wise channel correlation in the sense of $f_{\mathcal{S}}(\boldsymbol{\nu})$.

PAWN: We propose this metric as a generalization of CORR, where we compute the channel correlation between all the rows of $\mathbf{H}_j$ and $\mathbf{H}_l$. For two devices j and l, the metric is expressed as $\theta_{j,l} = \sum_{n_1=1}^{N_{\mathrm{rx}}} \sum_{n_2=1}^{N_{\mathrm{rx}}} \frac{1}{N_{\mathrm{rx}}^2} \frac{\left|\mathbf{H}_j(n_1)\mathbf{H}_l^H(n_2)\right|}{\|\mathbf{H}_j(n_1)\|_2 \|\mathbf{H}_l(n_2)\|_2}$, with $\mathbf{H}_j(n)$ denoting the n-th row of $\mathbf{H}_j$. Note that for the special case of $N_{\mathrm{rx}} = 1$, CORR and PAWN are equivalent.

ROOK: We devise this metric as a combination of two components. One of the constituents leverages the channel energy difference between two devices. The second component is the metric PAWN. Thus, ROOK is defined as $\theta_{j,l} = \omega \frac{\left|\|\mathbf{H}_j\|_{\mathrm{F}}^2 - \|\mathbf{H}_l\|_{\mathrm{F}}^2\right|}{\|\mathbf{H}_j\|_{\mathrm{F}}^2 + \|\mathbf{H}_l\|_{\mathrm{F}}^2} + (1-\omega) \sum_{n_1=1}^{N_{\mathrm{rx}}} \sum_{n_2=1}^{N_{\mathrm{rx}}} \frac{1}{N_{\mathrm{rx}}^2} \frac{\left|\mathbf{H}_j(n_1)\mathbf{H}_l^H(n_2)\right|}{\|\mathbf{H}_j(n_1)\|_2 \|\mathbf{H}_l(n_2)\|_2}$ with $0 \leq \omega \leq 1$. The rationale for this metric is that devices with uncorrelated channel vectors and comparable channel energy are desirable for scheduling.

KING: We also devise this metric as a combination of two components. Specifically, we combine PAWN with the ratio between the channel energy of a device and the largest channel energy among all the devices. Thus, $\theta_{j,l} = \omega \left(\frac{\|\mathbf{H}_{\max}\|_{\mathrm{F}}^2 - \|\mathbf{H}_j\|_{\mathrm{F}}^2}{\|\mathbf{H}_{\max}\|_{\mathrm{F}}^2} + \frac{\|\mathbf{H}_{\max}\|_{\mathrm{F}}^2 - \|\mathbf{H}_l\|_{\mathrm{F}}^2}{\|\mathbf{H}_{\max}\|_{\mathrm{F}}^2} \right) + (1-\omega) \sum_{n_1=1}^{N_{\mathrm{rx}}} \sum_{n_2=1}^{N_{\mathrm{rx}}} \frac{1}{N_{\mathrm{rx}}^2} \frac{\left|\mathbf{H}_j(n_1)\mathbf{H}_l^H(n_2)\right|}{\|\mathbf{H}_j(n_1)\|_2 \|\mathbf{H}_l(n_2)\|_2}$, where $\|\mathbf{H}_{\max}\|_{\mathrm{F}}^2 = \max_{j \in \mathcal{K}} \|\mathbf{H}_j\|_{\mathrm{F}}^2$ and $0 \leq \omega \leq 1$. In contrast to ROOK, this metric measures the relative difference with respect to the largest energy, which compensates for the cases when the devices have uncorrelated channels but commensurable low energy.

Rationale: Intuitively, the aim of $\mathcal{S}$ is to place in $\mathcal{K} \backslash \mathcal{K}'$ (i.e. set of multicast-only devices) those devices that hinder more significantly the maximization of the minimum unicast SINR. This is achieved by $f_{\mathcal{S}}(\boldsymbol{\nu})$, which aims to minimize the total discordance of the co-scheduled devices. Whether such devices *(i)* have highly-correlated channels among themselves or *(ii)* have strongly attenuated channels and thus require high power, by not including them in $\mathcal{K}'$, the devices in $\mathcal{K}'$ can gain the highest profit (i.e., the minimum $\mathrm{SINR}_k^{\mathrm{U}}$, $k \in \mathcal{K}'$ is maximized).

B. Optimization of precoder and combiners

Once the scheduling variables $\boldsymbol{\mu}^\star$ are known, we replace them in $\mathcal{P}\left(\mathbf{W}, \mathbf{m}, \widetilde{\mathbf{B}}, \boldsymbol{\mu}^\star\right)$. Thus, the remaining problem optimizes the unicast and multicast precoders (at the gNodeB) and combiners (at the devices) as shown in

$$\begin{aligned}
\mathcal{D}: \max_{\mathbf{W},\mathbf{m},\mathbf{B},} \quad & f_{\mathcal{D}}(\mathbf{W},\mathbf{B}) \triangleq \min_{k \in \mathcal{K}'} \frac{\left|\mathbf{w}_k^H \mathbf{H}_k \mathbf{b}_k\right|^2}{\sum_{j \neq k, j \in \mathcal{K}'} \left|\mathbf{w}_k^H \mathbf{H}_k \mathbf{b}_j\right|^2 + \sigma^2 \|\mathbf{w}_k\|_2^2} \\
\text{s.t.} \quad & \frac{\left|\mathbf{w}_k^H \mathbf{H}_k \mathbf{m}\right|^2}{\sum_{j \in \mathcal{K}'} \left|\mathbf{w}_k^H \mathbf{H}_k \mathbf{b}_j\right|^2 + \sigma^2 \|\mathbf{w}_k\|_2^2} \geq \gamma_{\min}, \forall k \in \mathcal{K}, \\
& \sum_{k \in \mathcal{K}'} \|\mathbf{b}_k\|_2^2 + \|\mathbf{m}\|_2^2 \leq P_{\mathrm{tx}}, \\
& [\mathbf{w}_k]_l \in \mathcal{W}, l \in \mathcal{L}, \forall k \in \mathcal{K}, .
\end{aligned}$$

where $\mathbf{B} = \widetilde{\mathbf{B}}\mathbf{U}$ and $\mathbf{U}\mathbf{U}^T = \mathrm{diag}(\boldsymbol{\mu})$ as defined in Section II. Due to coupling between $\{\mathbf{b}_k\}_{k \in \mathcal{K}'}$ and $\{\mathbf{w}_k\}_{k=1}^K$, the optimization of $\mathcal{D}$ is challenging. To cope with it, we first design the combiners $\{\mathbf{w}_k\}_{k=1}^K$ based on the channels $\{\mathbf{H}_k\}_{k=1}^K$, which are assumed to be invariant for a few channel uses. Then, we jointly optimize the unicast precoders $\{\mathbf{b}_k\}_{k \in \mathcal{K}'}$ and the multicast precoder $\mathbf{m}$.

B.1 Optimization of combiners $\{\mathbf{w}_k\}_{k=1}^K$

We define $\mathcal{D}_1 \triangleq \cup_{k \in \mathcal{K}} \mathcal{D}_{1,k}$, where

$$\mathcal{D}_{1,k}: \max_{\mathbf{w}_k} \left\| \mathbf{w}_k^H \mathbf{H}_k \right\|_2^2 \quad \text{s.t.} \quad \left|[\mathbf{w}_k]_l\right| = \delta_{\mathrm{rx}}, l \in \mathcal{L}. \tag{8}$$

Problem $\mathcal{D}_1$ designs the combiners $\{\mathbf{w}_k\}_{k=1}^K$ for all IoT devices in an independent manner. Therefore, each device can self-optimize its own combiner without need of the gNodeB. This problem admits a close-form solution that can be obtained using the Lagrange multipliers method. Specifically, the solution collapses to the principal eigenvector $\mathbf{r}_{\max}$ of $\mathbf{H}_k \mathbf{H}_k^H$. Then, to enforce the constant-modulus finite-resolution phase

shifts, $\mathbf{r}_{\max}$ is projected onto $\mathcal{W}$. Therefore, for the k-th device, $\mathbf{w}_k$ is obtained via $[\mathbf{w}_k]_l = \operatorname{argmax}_{\phi\in\mathcal{W}} \Re\mathfrak{e}\left\{\phi^* [\mathbf{r}_{\max}]_l\right\}$, $\forall l \in \mathcal{L}$. The solution of $\mathcal{D}_1$ is denoted by $\mathbf{W}^\star = \left[\mathbf{w}_1^\star, \cdots, \mathbf{w}_K^\star\right]$.

B.2 Optimization of $\{\mathbf{b}_k\}_{k\in\mathcal{K}'}$ and $\mathbf{m}$

Assuming that $\mathbf{g}_k = \mathbf{H}_k^H \mathbf{w}_k^\star$, the objective function of $\mathcal{D}$ depends only on $\mathbf{B}$. Note that $f_{\mathcal{D}}(\mathbf{W}^\star, \mathbf{B})$ is the minimum of several SINRs, which can be translated as a constraint as

$$\begin{aligned}
\mathcal{D}_2: \max_{\mathbf{B},\mathbf{m},\alpha} \quad & \alpha \\
\text{s.t.} \quad & \mathrm{R}_1: \frac{\left|\mathbf{g}_k^H \mathbf{b}_k\right|^2}{\sum_{j\neq k, j\in\mathcal{K}'} \left|\mathbf{g}_k^H \mathbf{b}_j\right|^2 + \sigma^2 \left\|\mathbf{w}_k^\star\right\|_2^2} \geq \alpha, \forall k \in \mathcal{K}', \\
& \mathrm{R}_2: \frac{\left|\mathbf{g}_k^H \mathbf{m}\right|^2}{\sum_{j\in\mathcal{K}'} \left|\mathbf{g}_k^H \mathbf{b}_j\right|^2 + \sigma^2 \left\|\mathbf{w}_k^\star\right\|_2^2} \geq \gamma_{\min}, \forall k \in \mathcal{K}, \\
& \mathrm{R}_3: \sum_{k\in\mathcal{K}'} \|\mathbf{b}_k\|_2^2 + \|\mathbf{m}\|_2^2 \leq P_{\mathrm{tx}}.
\end{aligned}$$

where $\mathrm{R}_1 - \mathrm{R}_2$ are nonconvex whereas R_3 is convex.

Note that $\mathcal{D}_2$ poses a difficulty in finding a solution as it cannot be addressed by known frameworks in its current form. In the following, we propose a reformulation of the problem that allows tailoring an algorithm to solve it. In particular, we transform $\mathcal{D}_2$ into a difference-of-convex (DC) programming problem, where the objective and/or constraints are convex or DC functions. Then, by harnessing the convex-concave procedure (CCP), a local optimal solution of the resulting DC programming problem can be obtained.

Reformulation: With respect to R_1, if we bound from above the denominator with $\sum_{j\neq k, j\in\mathcal{K}'} \left|\mathbf{g}_k^H \mathbf{b}_j\right|^2 + \sigma^2 \left\|\mathbf{w}_k^\star\right\|_2^2 \leq t_k$ and the numerator from below with $\left|\mathbf{g}_k^H \mathbf{b}_k\right|^2 \geq r_k$, then R_1 can be equivalently rewritten as the intersection of the following constraints

$$\mathrm{R}_1 = \begin{cases}
\mathrm{R}_{1-1}: \underbrace{r_k}_{\text{convex}} - \underbrace{\left|\mathbf{g}_k^H \mathbf{b}_k\right|^2}_{\text{convex}} \leq 0, \forall k \in \mathcal{K}', \\
\mathrm{R}_{1-2}: \underbrace{\sum_{j\neq k, j\in\mathcal{K}'} \left|\mathbf{g}_k^H \mathbf{b}_j\right|^2 + \sigma^2 \left\|\mathbf{w}_k^\star\right\|_2^2 - t_k}_{\text{convex}} \leq 0, \forall k \in \mathcal{K}', \\
\mathrm{R}_{1-3}: \underbrace{\alpha t_k - r_k}_{\text{nonconvex}} \leq 0, \forall k \in \mathcal{K}'.
\end{cases}$$

In addition, we observe that the nonconvex constraint R_{1-3} can be recast as

$$\mathrm{R}_{1-3}: \underbrace{(\alpha + t_k)^2 - 4r_k}_{\text{convex}} - \underbrace{(\alpha - t_k)^2}_{\text{convex}} \leq 0, \forall k \in \mathcal{K}',$$

which stems from the difference of squares: $\frac{(x+y)^2-(x-y)^2}{4} = xy$. Adopting a similar procedures as for R_1 reformulation, then R_2 can be expressed as,

$$\mathrm{R}_2 = \begin{cases}
\mathrm{R}_{2-1}: \underbrace{p_k}_{\text{convex}} - \underbrace{\left|\mathbf{g}_k^H \mathbf{m}\right|^2}_{\text{convex}} \leq 0, \forall k \in \mathcal{K}, \\
\mathrm{R}_{2-2}: \underbrace{\sum_{j\in\mathcal{K}'} \left|\mathbf{g}_k^H \mathbf{b}_j\right|^2 + \sigma^2 \left\|\mathbf{w}_k^\star\right\|_2^2 - q_k}_{\text{convex}} \leq 0, \forall k \in \mathcal{K}, \\
\mathrm{R}_{2-3}: \underbrace{\gamma_{\min} q_k - p_k}_{\text{convex}} \leq 0, \forall k \in \mathcal{K}.
\end{cases}$$

Observe that R_{1-2}, R_{2-2}, R_{2-3}, R_3 are convex whereas R_{1-1}, R_{1-3}, R_{2-1} are DC functions. Thus, with the transformations above, $\mathcal{D}_2$ is now a DC programming problem.

Solution: Optimization problems that have convex or DC objective/constraints can be efficiently tackled by means of the CCP procedure, which guarantees a stationary solution of the original problem.

> The CCP procedure [24] guarantees a stationary point of a DC programming problem. The main idea of CCP is to iteratively solve a sequence of convex subproblems, each of which is constructed by replacing the concave terms with first-order Taylor approximations. Consider the DC programming problem
>
> $$\begin{aligned} \mathcal{Z}: \max_{\mathbf{z}_1,\mathbf{z}_2} \quad & f(\mathbf{z}_1, \mathbf{z}_2) \\ \text{s.t.} \quad & h_i(\mathbf{z}_1) - g_i(\mathbf{z}_2) \leq, i = 1, \cdots, I, \end{aligned}$$
>
> where $f(\mathbf{z}_1, \mathbf{z}_2)$ is concave in $\mathbf{z}_1$, $\mathbf{z}_2$ whereas $h_i(\mathbf{z}_1)$ and $g_i(\mathbf{z}_2)$ are convex in $\mathbf{z}_1$ and $\mathbf{z}_2$, respectively. To convexify $\mathcal{Z}$, the concave terms, i.e. $-g_i(\mathbf{z}_2)$, are linearized. The resulting convexified DC programming problem is therefore expressed as
>
> $$\begin{aligned} \mathcal{Z}^{(\ell)}: \max_{\mathbf{z}_1,\mathbf{z}_2} \quad & f(\mathbf{z}_1, \mathbf{z}_2) \\ \text{s.t.} \quad & h_i(\mathbf{z}_1) - \tilde{g}_i(\mathbf{z}_2) \leq, i = 1, \cdots, I, \end{aligned}$$
>
> where $\tilde{g}_i(\mathbf{z}_2) = g_i\left(\mathbf{z}_2^{(\ell-1)}\right) + \nabla_{\mathbf{z}_2}^T g_i\left(\mathbf{z}_2^{(\ell-1)}\right)\left(\mathbf{z}_2 - \mathbf{z}_2^{(\ell-1)}\right)$ denotes a linearized version of $g_i(\mathbf{z}_2)$ around a given point $\mathbf{z}_2^{(\ell-1)}$. Since every instance of the resulting problem $\mathcal{Z}^{(\ell)}$ is convex, it can be solved using general-purpose solvers via interior-point methods. The process is repeated iteratively, each time refining the initial point $\mathbf{z}_2^{(\ell-1)} \leftarrow \mathbf{z}_2$ until a stop criterion is satisfied. Let N_{conv} be the maximum number of iterations that $\mathcal{Z}^{(\ell)}$ can be solved, and let $\epsilon \geq 0$ be a small number (e.g., $\epsilon = 0.001$). Thus, the iterative process stops when $\ell = N_{\text{conv}}$ or $\left|f(\mathbf{z}_1, \mathbf{z}_2) - f\left(\mathbf{z}_1^{(\ell-1)}, \mathbf{z}_2^{(\ell-1)}\right)\right| \leq \epsilon$. Further, to guarantee convergence, an initial feasible point (i.e., when $\ell = 0$) is required, which we discuss in Appendix A.

According to the CCP procedure described above, to solve $\mathcal{D}_2$, we need solve the convex problem $\mathcal{D}_2^{(\ell)}$ iteratively until a stop criterion is met. Thus, for a given iteration ℓ, the convex problem $\mathcal{D}_2^{(\ell)}$ is defined as

$$\mathcal{D}_2^{(\ell)}: \max_{\substack{\mathbf{B},\mathbf{m},\alpha \\ \mathbf{r},\mathbf{t},\mathbf{p},\mathbf{q}}} \alpha \quad \text{s.t.} \quad \mathrm{R}_{1-1}{}^{(\ell)}, \mathrm{R}_{1-2}, \mathrm{R}_{1-3}{}^{(\ell)}, \mathrm{R}_{2-1}{}^{(\ell)}, \mathrm{R}_{2-2}, \mathrm{R}_{2-3}, \mathrm{R}_3.$$

$$\mathrm{R}_{1-1}{}^{(\ell)}: r_k + \left|\mathbf{g}_k^H \mathbf{b}_k^{(l-1)}\right|^2 - 2\Re\mathfrak{e}\left\{\mathbf{b}_k^{(l-1)H} \mathbf{g}_k \mathbf{g}_k^H \mathbf{b}_k\right\} \leq 0, \forall k \in \mathcal{K}',$$

$$\mathrm{R}_{1-3}{}^{(\ell)}: (\alpha + t_k)^2 - 4r_k + \left(\alpha^{(l-1)} - t_k^{(l-1)}\right)^2 - 2\left(\alpha^{(l-1)} - t_k^{(l-1)}\right)(\alpha - t_k) \leq 0,$$

$$\mathrm{R}_{2-1}{}^{(\ell)}: p_k + \left|\mathbf{g}_k^H \mathbf{m}^{(l-1)}\right|^2 - 2\Re\mathfrak{e}\left\{\mathbf{m}^{(l-1)H} \mathbf{g}_k \mathbf{g}_k^H \mathbf{m}\right\} \leq 0, \forall k \in \mathcal{K}.$$

At the completion of each iteration ℓ, the obtained solutions $\mathbf{B}$, $\mathbf{m}$, α, $\mathbf{t}$ are passed to $\mathbf{B}^{(\ell)}$, $\mathbf{m}^{(\ell)}$, $\alpha^{(\ell)}$, $\mathbf{t}^{(\ell)}$, which are used as the new initializations for the subsequent iteration $\ell + 1$. The solution of this stage is $\mathbf{B}^\star$ and $\mathbf{m}^\star$. For completeness, we summarize in *Algorithm* the complete optimization procedure of $\mathcal{S}$ and $\mathcal{D}$.

Algorithm: BEAMWAVE optimization

Input: $\{\mathbf{H}_k\}_{k=1}^{K}$, $\gamma_{\min}$, N_{conv}, ϵ

Execute:

1: Find $\boldsymbol{\mu}^{\star}$ by solving the scheduling problem $\mathcal{S}$.
2: Design the combiners $\{\mathbf{w}_k^{\star}\}_{k=1}^{K}$ for all devices by solving problem $\mathcal{D}_{1,k}$, $\forall k \in \mathcal{K}$.
3: Design the multicast precoder $\mathbf{m}^{\star}$ and the unicast precoders $\{\mathbf{b}_k^{\star}\}_{k\in\mathcal{K}'}$ by solving $\mathcal{D}_2^{(\ell)}$.

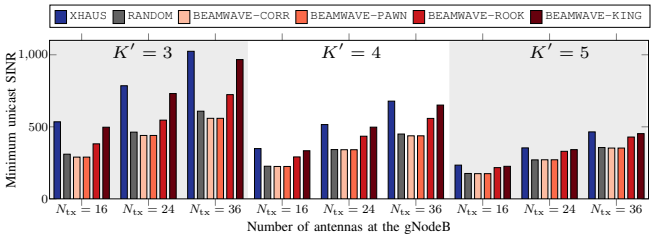

Figure 2: Achievable minimum unicast SINR for varying N_{tx} at the gNodeB.

V. Simulation Results

Throughout the simulations, we consider the geometric channel model defined in (2), with $L = L_1 = \cdots = L_K = 3$ propagation paths. This assumption is compliant with the results of a measurement campaign in an industrial environment [12], where the number of propagation paths is usually between 1 to 3. The angles of arrival are uniformly distributed as $\psi_k^{(l)} \in [-\pi; \pi]$ whereas the angles of departure are distributed as $\phi_k^{(l)} \in [-\pi/3; \pi/3]$. The power assigned to the combiners is $P_{\text{rx}} = 0$ dBm, the noise power is $\sigma^2 = 10$ dBm, and the multicast QoS requirement is $\gamma_{\min} = 4$ (~ 6 dB). Also, $\omega = 0.5$, $N_{\text{conv}} = 20$ and $\epsilon = 0.001$. The results in this section show the average performance over 100 simulations. For the selected settings, in all the channel realizations, we have obtained feasible solutions. To solve the optimization problems, we have used CVX. Specifically, CVX and GUROBI were used to solve the integer linear program $\mathcal{S}$. The convex problem $\mathcal{D}_2^{(\ell)}$ was solved by means of CVX and SDPT3. In the following, we examine scenarios, in which we evaluate the performance of BEAMWAVE.

A. Minimum unicast SINR for various N_{tx}

Fig. 2 depicts the impact of different N_{tx} configurations on the minimum unicast SINR when the total number of devices in the system is $K = 6$ and the number of *dual-layer* devices $K' = \{3, 4, 5\}$ varies. In this case, we have assumed that the IoT devices are equipped with a single antenna, i.e., $N_{\text{rx}} = 1$ and the gNodeB can transmit with a maximum power $P_{\text{tx}} = 35$ dBm.

As a general trend, we observe that increasing the number of *dual-layer* devices K' decreases the minimum unicast SINR. This occurs because the limited power P_{tx} at the gNodeB is divided into a greater number of scheduled devices, thus reducing the individual allocation of power for each *dual-layer* device. Also, serving more *dual-layer* devices translates to producing more interference, thus impacting the SINR. On the contrary, increasing N_{tx} improves the minimum unicast SINR. Essentially, a larger N_{tx} reduces the beamwidth that can be produced by the antenna array at the gNodeB, thus allowing to form more directional transmissions with reduced interference.

Another general trend in Fig. 2 is that XHAUS (exhaustive search) exhibits the highest performance in all configurations as it schedules the optimum subset of K' *dual-layer* devices. By leveraging the channel correlation, BEAMWAVE-CORR[3] only performs slightly better than RANDOM. Thus, scheduling decisions based solely on the channel correlation are insufficient to devise an optimal scheduler for LDM systems. On the contrary, BEAMWAVE-ROOK and BEAMWAVE-KING, which additionally include channel energy information, clearly outperform RANDOM. These two schemes achieve up to 60.38% and 77.68% higher SINR, respectively, compared to RANDOM. Noteworthily, throughout all the results in Fig. 2, BEAMWAVE-ROOK and BEAMWAVE-KING perform at worst 30.4% and 14.13% below XHAUS, respectively.

B. Minimum unicast SINR for various N_{rx}

Fig. 3 shows the impact of varying N_{rx} and L_{rx} on the minimum unicast SINR when $K = 6$, $K' = 5$, $N_{\text{tx}} = 16$, and $P_{\text{tx}} = 35$ dBm. In this setting, the IoT devices have a single RF chain that is connected to N_{rx} antennas. As a result, the devices are not capable of implementing any type of linear processing for interference mitigation but can perform constrained beamsteering due to constraint C_4 in $\mathcal{P}$.

In all subfigures in Fig. 3, we observe that the minimum unicast SINR improves as the number of receive antennas increases. With larger N_{rx}, the devices can shape more directional reception patterns to mitigate undesired signals. In particular, up to 60% gain can be achieved with $L_{\text{rx}} = 4$ when varying N_{tx} from 1 to 2. Also, since augmenting L_{rx} results in higher-resolution phase shifts, we observe performance improvement through Fig. 3a to Fig. 3d. In particular, gains up to 16.00%, 30.70% and 49.47% are achieved when increasing L_{rx} from 2 to 4, 4 to 8 and 8 to 16, respectively.

By comparing the performance of the proposed scheduling schemes under all assessed settings, the scheme that attains superior performance is BEAMWAVE-KING. In particular, BEAMWAVE-KING is outperformed by at most 5.60% when compared to the optimal highly complex XHAUS.

C. Spectral efficiency

In this scenario we consider $N_{\text{rx}} = 1$, $N_{\text{tx}} = 32$, , $P_{\text{tx}} = 45$ dBm and a varying number of devices $K = \{8, 12, 16, 20, 24, 28, 32, 36\}$. In particular, the number of scheduled *dual-layer* devices changes according to $K' = K/4$. In Fig. 4, we show the unicast spectral efficiency (SE) attained by BEAMWAVE. Due to the exponential growth in the number of scheduling combinations, the results with XHAUS are not

[3]As mentioned in Section IV-A, when $N_{\text{rx}} = 1$, PAWN and CORR result in the same value. For this reason, we observe that BEAMWAVE-CORR and BEAMWAVE-PAWN attain the same performance.

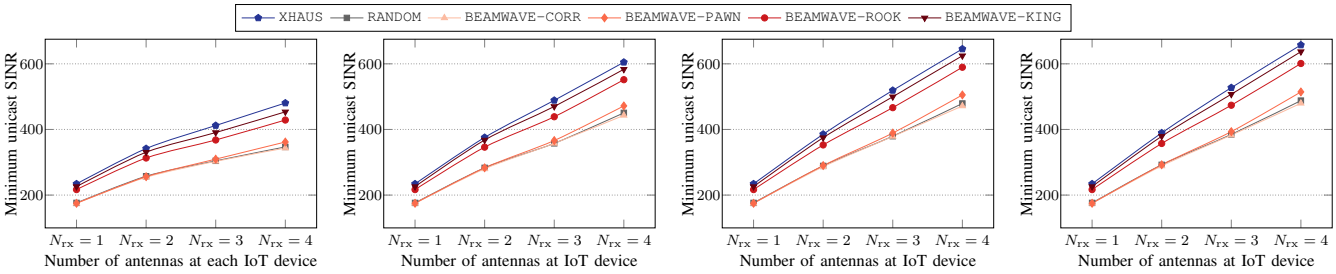

(a) $L_{\text{rx}} = 2$ (b) $L_{\text{rx}} = 4$ (c) $L_{\text{rx}} = 8$ (d) $L_{\text{rx}} = 16$

Figure 3: Achievable minimum SINR for varying N_{rx} and L_{rx} at each IoT device.

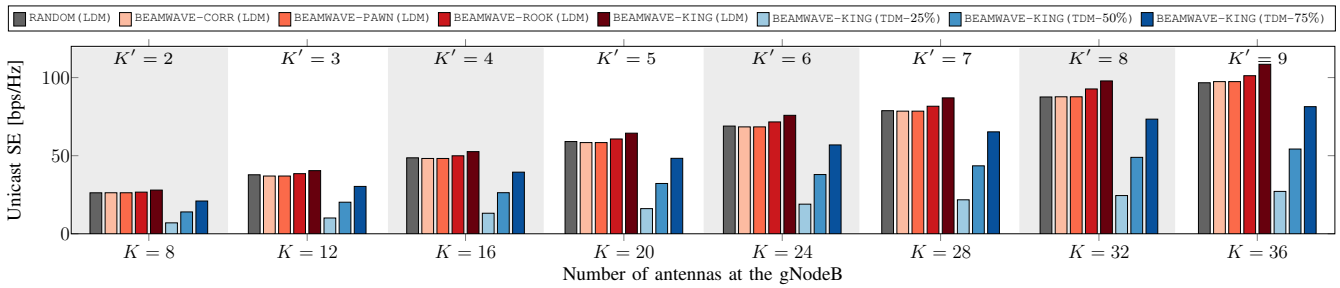

Figure 4: Spectral efficiency performance for varying K and $K' = K/4$.

presented in this scenario. However, BEAMWAVE-KING is taken as reference as it was shown in previous scenarios that its performance is at most 14.13% below the optimality of XHAUS. Further, we also use our proposed scheduler with T/FDM systems.

Note that while RANDOM scheduling performs as equally well as BEAMWAVE for small K' (since the generated interference is low), we observe that when K' is large (e.g., $K' = 16$) there is a significant performance gap. This shows that scheduling exerts a critical task, specially in LDM systems which generate additional inter-layer interference between unicast and multicast signals. Besides, we observe that LDM outperforms TDM, where the time allotted for unicast transmissions is 25%, 50% and 75% of the total available[4]. The remaining time is used for transmitting the multicast signal. Specifically, in the TDM case, we have also used BEAMWAVE to make the selection of unicast devices that yields the *max-min* SINR.

D. Computational complexity

In Table I, we show the complexity of the benchmarked schemes. In particular, $\mathcal{C}_{\mathcal{S}}$ is the complexity of the proposed scheduler, where $M = \frac{K(K+1)}{2}$ is the number of $0-1$ variables and $C = K^2 - K + 1$ is the number of constraints. As a reference, we have used the runtime of Vaidya's algorithm for the linear program, which GUROBI solves via the branch and bound (BnB) procedure. The complexity $\mathcal{C}_{\mathcal{D}_{1,k}}$ stems from the singular value decomposition (SVD) used to obtain the principal eigenvector, as described in Section IV-B1. Also, $\mathcal{C}_{\mathcal{D}_2}$ is derived based on the complexity required by interior point methods. Finally, $\mathcal{C}_{\text{XHAUS}}$, $\mathcal{C}_{\text{BEAMWAVE}}$ and $\mathcal{C}_{\text{RANDOM}}$ denote the overall complexities of the schemes XHAUS, BEAMWAVE and RANDOM respectively.

Table I: Computational complexity

Notation	Complexity
$\mathcal{C}_{\mathcal{S}}$	$\mathcal{O}\left(2^M (M+C)^{1.5} M\right)$
$\mathcal{C}_{\mathcal{D}_{1,k}}$	$\mathcal{O}\left(N_{\text{rx}}^3\right)$
$\mathcal{C}_{\mathcal{D}_2}$	$N_{\text{conv}} \cdot \mathcal{O}\left(\left(N_{\text{tx}} K' (K+K')\right)^{3.5}\right)$
$\mathcal{C}_{\text{RANDOM}}$	$\mathcal{C}_{\mathcal{D}_2} + K \cdot \mathcal{C}_{\mathcal{D}_{1,k}}$
$\mathcal{C}_{\text{BEAMWAVE}}$	$\mathcal{C}_{\mathcal{D}_2} + K \cdot \mathcal{C}_{\mathcal{D}_{1,k}} + \mathcal{C}_{\mathcal{S}}$
$\mathcal{C}_{\text{XHAUS}}$	$\binom{K}{K'} \cdot \mathcal{C}_{\mathcal{D}_2} + K \cdot \mathcal{C}_{\mathcal{D}_{1,k}}$

VI. Conclusions

In this paper we investigated the cross-layer optimization of beamforming and scheduling for mmWave LDM systems, aiming to support future Industry 4.0 scenarios. In particular, through the adoption of LDM, multiple signal layers can be transmitted simultaneously using the same radio resources. For smart factory settings, we assumed that a superior-importance safety/control multicast message is required to be ubiquitous to all the devices in the system. In addition, due to insufficient RF chains, inferior-importance private unicast information is simultaneously transmitted to a selected group of scheduled devices with the aim of maximizing the minimum SINR. Due to NP-hardness of the problem, we proposed

[4]In the TDM case, the IoT devices are served in two time windows. In the first window, with duration T_m, all IoT devices in $\mathcal{K}$ are served with the multicast control signal. In the second window, with duration T_u, a subset of devices $\mathcal{K}'$ are served with unicast signals (e.g., software updates), such that $T_m + T_u = 1$. In our simulations, we have varied $T_u = \{0.25, 0.50, 0.75\}$.

BEAMWAVE which partitions the problem into *(i)* beamforming and *(ii)* scheduling. For device scheduling, we proposed a novel formulation, where we devised three metrics based on channel features, namely PAWN, ROOK, and KING to guide the selection decision. Further, we designed a precoder (i.e., transmit beamformer) with remarkable performance adopting the convex-concave procedure. We showed that our proposed scheme attains high spectral efficiency and outperforms orthogonal multiplexing schemes such as T/FDM.

ACKNOWLEDGMENT

The research is in part funded by the Deutsche Forschungsgemeinschaft (DFG) within the B5G-Cell project in SFB 1053 MAKI and by the LOEWE initiative (Hesse, Germany) within the emergenCITY center.

REFERENCES

[1] X. Chen, *Massive Access for Cellular Internet of Things Theory and Technique*. Berlin, Germany: Springer, 2019.

[2] L. F. Abanto-Leon, M. Hollick, and G. H. Sim, "HydraWave: Multi-group Multicast Hybrid Precoding and Low-Latency Scheduling for Ubiquitous Industry 4.0 mmWave Communications," in *IEEE WoWMoM*, 2020, pp. 98–107.

[3] E. Björnson, L. V. der Perre, S. Buzzi, and E. G. Larsson, "Massive MIMO in Sub-6 GHz and mmWave: Physical, Practical, and Use-Case Differences," *IEEE Wireless Communications*, vol. 26, no. 2, pp. 100–108, April 2019.

[4] L. N. Ribeiro, S. Schwarz, M. Rupp, and A. L. F. de Almeida, "Energy Efficiency of mmWave Massive MIMO Precoding With Low-Resolution DACs," *IEEE Journal of Selected Topics in Signal Processing*, vol. 12, no. 2, pp. 298–312, April 2018.

[5] E. G. Larsson, O. Edfors, F. Tufvesson, and T. L. Marzetta, "Massive MIMO for Next Generation Wireless Systems," *IEEE Communications Magazine*, vol. 52, no. 2, pp. 186–195, February 2014.

[6] E. Björnson, J. Hoydis, and L. Sanguinetti, "Massive MIMO Has Unlimited Capacity," *IEEE Transactions on Wireless Communications*, vol. 17, no. 1, pp. 574–590, January 2018.

[7] Y. Liu, Z. Qin, M. Elkashlan, Z. Ding, A. Nallanathan, and L. Hanzo, "Nonorthogonal Multiple Access for 5G and Beyond," *Proceedings of the IEEE*, vol. 105, no. 12, pp. 2347–2381, December 2017.

[8] J. Zhao, O. Simeone, D. Gunduz, and D. Gomez-Barquero, "Non-Orthogonal Unicast and Broadcast Transmission via Joint Beamforming and LDM in Cellular Networks," in *IEEE GLOBECOM*, December 2016, pp. 1–6.

[9] X. Chen, Z. Zhang, C. Zhong, R. Jia, and D. W. K. Ng, "Fully Non-Orthogonal Communication for Massive Access," *IEEE Transactions on Communications*, vol. 66, no. 4, pp. 1717–1731, April 2018.

[10] Z. Ding, P. Fan, and H. V. Poor, "Random Beamforming in Millimeter-Wave NOMA Networks," *IEEE Access*, vol. 5, pp. 7667–7681, February 2017.

[11] 3GPP, "Technical Specification Group Services and System Aspects," 3rd Generation Partnership Project (3GPP), Technical Report (TR) 21.916, 03 2020, version 0.4.0. [Online]. Available: www.3gpp.org/ftp/Specs/archive/21_series/21.916

[12] A. Loch, C. Cano, G. H. Sim, A. Asadi, and X. Vilajosana, "A Channel Measurement Campaign for mmWave Communication in Industrial Settings," *IEEE Transactions on Wireless Communications*, September 2020.

[13] M. R. Palattella, M. Dohler, A. Grieco, G. Rizzo, J. Torsner, T. Engel, and L. Ladid, "Internet of Things in the 5G Era: Enablers, Architecture, and Business Models," *IEEE Journal on Selected Areas in Communications*, vol. 34, no. 3, pp. 510–527, March 2016.

[14] J. Zhao, D. Gündüz, O. Simeone, and D. Gómez-Barquero, "Non-Orthogonal Unicast and Broadcast Transmission via Joint Beamforming and LDM in Cellular Networks," *IEEE Transactions on Broadcasting*, vol. 66, no. 2, pp. 216–228, June 2020.

[15] Y. Liu, C. Lu, M. Tao, and J. Wu, "Joint Multicast and Unicast Beamforming for the MISO Downlink Interference Channel," in *IEEE SPAWC*, July 2017, pp. 1–5.

[16] Y. Li, M. Xia, and Y. Wu, "Energy-Efficient Precoding for Non-Orthogonal Multicast and Unicast Transmission via First-Order Algorithm," *IEEE Transactions on Wireless Communications*, vol. 18, no. 9, pp. 4590–4604, September 2019.

[17] E. Chen and M. Tao, "Backhaul-Constrained Joint Beamforming for Non-Orthogonal Multicast and Unicast Transmission," in *IEEE GLOBECOM*, December 2017, pp. 1–6.

[18] E. Chen, M. Tao, and Y. Liu, "Joint Base Station Clustering and Beamforming for Non-Orthogonal Multicast and Unicast Transmission With Backhaul Constraints," *IEEE Transactions on Wireless Communications*, vol. 17, no. 9, pp. 6265–6279, September 2018.

[19] J. Wang, H. Xu, B. Zhu, L. Fan, and A. Zhou, "Hybrid Beamforming Design for mmWave Joint Unicast and Multicast Transmission," *IEEE Communications Letters*, vol. 22, no. 10, pp. 2012–2015, October 2018.

[20] W. Hao, G. Sun, Z. Chu, P. Xiao, Z. Zhu, S. Yang, and R. Tafazolli, "Beamforming Design in SWIPT-Based Joint Multicast-Unicast mmWave Massive MIMO With Lens-Antenna Array," *IEEE Wireless Communications Letters*, vol. 8, no. 4, pp. 1124–1128, August 2019.

[21] W. Hao, G. Sun, F. Zhou, D. Mi, J. Shi, P. Xiao, and V. C. M. Leung, "Energy-Efficient Hybrid Precoding Design for Integrated Multicast-Unicast Millimeter Wave Communications With SWIPT," *IEEE Transactions on Vehicular Technology*, vol. 68, no. 11, pp. 10 956–10 968, November 2019.

[22] L. F. Abanto-Leon and G. H. Sim, "Fairness-Aware Hybrid Precoding for mmWave NOMA Unicast/Multicast Transmissions in Industrial IoT," in *IEEE ICC*, June 2020, pp. 1–7.

[23] T. Yoo, N. Jindal, and A. Goldsmith, "Multi-Antenna Downlink Channels with Limited Feedback and User Selection," *IEEE Journal on Selected Areas in Communications*, vol. 25, no. 7, pp. 1478–1491, September 2007.

[24] T. Lipp and S. Boyd, "Variations and Extension of the Convex–Concave Procedure," *Optimization and Engineering*, vol. 17, no. 2, pp. 263–287, June 2016.

[25] W. Hao, M. Zeng, Z. Chu, and S. Yang, "Energy-Efficient Power Allocation in Millimeter Wave Massive MIMO With Non-Orthogonal Multiple Access," *IEEE Wireless Communications Letters*, vol. 6, no. 6, pp. 782–785, December 2017.

APPENDIX A
INITIAL FEASIBLE POINT FOR $\mathcal{D}_2$

In order to find $\mathbf{B}^{(0)}$, $\mathbf{m}^{(0)}$, $\alpha^{(0)}$, $\mathbf{t}^{(0)}$ we proceed as follows. First, let us define a as the power of the multicast precoder $\mathbf{m}$, such that $\mathbf{m} = \sqrt{a}\widehat{\mathbf{m}}$, $\|\widehat{\mathbf{m}}\|_2^2 = 1$. Similarly, we define a_k as the power of the unicast precoder $\mathbf{b}_k$, $k \in \mathcal{K}'$ such that $\mathbf{b}_k = \sqrt{a_k}\widehat{\mathbf{b}}_k$, $\left\|\widehat{\mathbf{b}}_k\right\|_2^2 = 1$. Now, we let $\left\{\widehat{\mathbf{b}}_k\right\}_{k\in\mathcal{K}'}$ be the zero-forcing precoders [25]. On the other hand, we let $\widehat{\mathbf{m}}$ be the principal eigenvector of the aggregate channels of all users. Thus, we define

$$\mathcal{D}_2^{\text{ini}}: \min_{\{a_k\}_{k\in\mathcal{K}'},a} \quad \sum_{k\in\mathcal{K}'}\sum_{j\neq k, j\in\mathcal{K}'} a_j \left|h_{k,j}\right|^2$$
$$\text{s.t.} \quad \frac{a\left|h_k\right|^2}{\sum_{j\in\mathcal{K}'} a_j\left|h_{k,j}\right|^2 + \sigma^2\left\|\mathbf{w}_k^\star\right\|_2^2} \geq \gamma_{\min}, \forall k \in \mathcal{K},$$
$$\sum_{k\in\mathcal{K}'} a_k\left\|\widehat{\mathbf{b}}_k\right\|_2^2 + a\left\|\widehat{\mathbf{m}}\right\|_2^2 \leq P_{\text{tx}},$$

where $h_{k,j} = \mathbf{g}_k^H\widehat{\mathbf{b}}_j$ and $h_k = \mathbf{g}_k^H\mathbf{m}$. Note that $\mathcal{D}_2^{\text{ini}}$ is a linear programming problem. Also, observe that any feasible solution for $\mathcal{D}_2^{\text{ini}}$ will be feasible for $\mathcal{D}_2$. In particular, the objective function of $\mathcal{D}_2^{\text{ini}}$ minimizes the total unicast interference perceived by all IoT devices (i.e., sum of all terms in the denominator of R_1 in $\mathcal{D}_2$). Once $\mathcal{D}_2^{\text{ini}}$ is solved, we obtain a solution $\left(\{a_k^\star\}_{k\in\mathcal{K}'}, a^\star\right)$. Harnessing this outcome, we obtain the initial feasible points for $\mathcal{D}_2^{(0)}$ by defining $\mathbf{b}_k^{(0)} = a_k^\star\widehat{\mathbf{b}}_k$, $\mathbf{m}^{(0)} = a^\star\widehat{\mathbf{m}}$, $t_k^{(0)} = \sum_{j\neq k, j\in\mathcal{K}'} a_j^\star\left|h_{k,j}\right|^2 + \sigma^2\left\|\mathbf{w}_k^\star\right\|_2^2$, $\alpha^{(0)} = \min_{k\in\mathcal{K}'} \frac{a_k^\star\left|h_{k,k}\right|^2}{\sum_{j\neq k, j\in\mathcal{K}'} a_j^\star\left|h_{k,j}\right|^2 + \sigma^2\left\|\mathbf{w}_k^\star\right\|_2^2}$.

G

PUBLICATION VII.
RADIORCHESTRA: PROACTIVE MANAGEMENT OF MILLIMETER-WAVE SELF-BACKHAULED SMALL CELLS VIA JOINT OPTIMIZATION OF BEAMFORMING, USER ASSOCIATION, RATE SELECTION, AND ADMISSION CONTROL

RadiOrchestra: Proactive Management of Millimeter-wave Self-backhauled Small Cells via Joint Optimization of Beamforming, User Association, Rate Selection, and Admission Control

Luis F. Abanto-Leon†, Arash Asadi†, Andres Garcia-Saavedra‡, Gek Hong (Allyson) Sim†, Matthias Hollick†
†Technische Universität Darmstadt, Germany, ‡NEC Laboratories Europe GmbH
†{labanto, aasadi, asim, mhollick}@seemoo.tu-darmstadt.de, ‡andres.garcia.saavedra@neclab.eu

***Abstract*—Millimeter-wave self-backhauled small cells are a key component of next-generation wireless networks. Their dense deployment will increase data rates, reduce latency, and enable efficient data transport between the access and backhaul networks, providing greater flexibility not previously possible with optical fiber. Despite their high potential, operating dense self-backhauled networks optimally is an open challenge, particularly for radio resource management (RRM). This paper presents, RadiOrchestra, a holistic RRM framework that models and optimizes beamforming, rate selection as well as user association and admission control for self-backhauled networks. The framework is designed to account for practical challenges such as hardware limitations of base stations (e.g., computational capacity, discrete rates), the need for adaptability of backhaul links, and the presence of interference. Our framework is formulated as a nonconvex mixed-integer nonlinear program, which is challenging to solve. To approach this problem, we propose three algorithms that provide a trade-off between complexity and optimality. Furthermore, we derive upper and lower bounds to characterize the performance limits of the system. We evaluate the developed strategies in various scenarios, showing the feasibility of deploying practical self-backhauling in future networks.**

***Index Terms*—radio resource management, self-backhauling, millimeter-wave, beamforming, scheduling,**

I. Introduction

Network *densification*, through the deployment of small cells, is indispensable to meet the increasing user demands for emerging wireless services [1]. Small cells are realized by low-cost radio access nodes, known as small base stations (SBSs), that provide wireless connectivity to undersized geographical areas [2]. SBSs are strategically installed in close proximity to the end users, bolstering the quality of experience and improving the radio access network (RAN) performance. *In this way, dense small cell deployments are expected to increase data rates, maintain low latency, extend coverage and support a large number of users, thereby enabling the rollout of a wide range of new services.*

As small cell deployments become denser, more efficient forms of backhauling data traffic between SBSs and the core network will be needed [3]. Optical fiber has been the predominant means for this task, but its installation and maintenance are costly. Self-backhauling, standardized under the name of *integrated access and backhaul* (IAB) [4], is an innovative technology that promises to reduce costs by sharing the wireless spectrum in time/frequency/space between RAN and backhaul links [5]. Small cells with self-backhauling capabilities benefit from a tight integration of access and backhaul functions, leading to high reconfigurability and facilitating self-adaptation to a wide range of cases.

Self-backhauled small cells require wide bandwidth to cope with the growing access-backhaul traffic. The millimeter-wave spectrum offers the necessary bandwidth to meet this requirement but it poses challenges, e.g., limited transmission range. Fortunately, recent advances in beamforming [6] have overcome the physical drawbacks of millimeter-waves by taking advantage of the small antennas size that have enabled large antenna arrays. *Thus, millimeter-wave self-backhauled small cell networks, realized by multi-antenna SBSs, will play a key role in next-generation wireless networks. Their dense deployment will reduce costs and enable efficient transport of massive data traffic between access and backhaul networks. In addition, the flexibility of millimeter-wave self-backhauled small cells will provide higher adaptability in various topologies and network conditions, previously not possible with fiber.*

Despite consensus on the potential of millimeter-wave self-backhauling, designing an optimal system remains an open research challenge [7], which requires efficient radio resource management (RRM) across the access and backhaul networks. To date, the body of work in this area often overlooks practical challenges inherent to realistic wireless communications systems, such as discrete modulations and coding schemes (MCSs), or low computing capabilities of SBSs. *Our work is motivated by the absence of holistic RRM frameworks providing a realistic model and a practical solution for millimeter-wave self-backhauled small cells deployments.* In the following, we introduce these challenges and put them in perspective with the literature.

Challenge 1: Scalable self-backhauling design. The majority of prior works relies on point-to-point links, e.g., [8], [9], between macro base station (MBS) and SBSs, which is unscalable in dense SBS deployments. The scalability issue is addressed in a handful of works, e.g., [10], [11] assume that SBSs are capable of multi-layer successive interference cancellation (SIC). While this assumption simplifies traffic transport, it involves heavy computational tasks (i.e., SIC) not suited for SBSs. *Thus, to keep SBS economical for the operators, it is necessary to reduce the computational burden*

Table I: Categorization of related work

Approach	Solution	Spectrum	Network	Access network					Backhaul network				
				Topology	Beamforming	User association	Rate selection	Admission control	Topology	Link	Medium	Beamforming	Rate selection
[20], [21]	Joint	Sub-6GHz	Single-SBS	Unicast	✓	✗	✓	✓	N/A	N/A	N/A	N/A	N/A
[22]–[25]	Joint	Sub-6GHz	Multi-SBS	Unicast	✓	Many	✗	✗	N/A	N/A	N/A	N/A	N/A
[26], [27]	Decoupled	Sub-6GHz	Single-SBS	Multicast	✓	✗	✗	✓	N/A	N/A	N/A	N/A	N/A
[28]	Joint	Millimeter-wave	Multi-SBS	Unicast	3D	Many	✗	✗	N/A	N/A	N/A	N/A	N/A
[8], [29]	Joint	Millimeter-wave	Multi-SBS	N/A	N/A	N/A	N/A	N/A	Unicast	Adaptive	Wireless	2D	✗
[30]	Joint	Sub-6GHz	Multi-SBS	Multicast	2D	Many	✗	✗	Unicast	Fixed	Wired	✗	✗
[31], [32]	Joint	Sub-6GHz	Multi-SBS	Both	2D	Many	✗	✗	Unicast	Fixed	Wired	✗	✗
[9], [12]	Decoupled	Sub-6GHz	Multi-SBS	Unicast	2D	✗	✗	✓	Unicast	Unbounded	Wired	✗	✗
[13]	Joint	Sub-6GHz	Multi-SBS	Unicast	2D	One	✗	✓	Unicast	Fixed	Wireless	✗	✗
[17]	Decoupled	Millimeter-wave	Multi-SBS	Unicast	3D	Many	✗	✗	Unicast	Adaptive	Wireless/TDM	3D	✗
[18]	Decoupled	Sub-6GHz	Multi-SBS	Unicast	2D	One	✗	✓	Unicast	Adaptive	Wireless/SDM	2D	✗
[10]	Decoupled	Sub-6GHz	Multi-SBS	Unicast	2D	Many	✗	✗	Multicast	Adaptive/SIC	Wireless/SDM	2D	✗
[15]	Joint	Sub-6GHz	Multi-SBS	Unicast	2D	One	✗	✓	Unicast	Adaptive	Wireless/SDM	2D	✗
[14], [16]	Joint	Sub-6GHz	Multi-SBS	Multicast	2D	✗	✗	✗	Unicast	Fixed	Wireless	✗	✗
[33]	Joint	Sub-6GHz	Multi-SBS	Unicast	2D	One	✗	✓	Unicast	Adaptive	Wireless/SDM	2D	✗
[19]	Joint	Sub-6GHz	Multi-SBS	Unicast	2D	Many	✗	✗	Multicast	Adaptive	Wireless/TDM	2D	✗
[11]	Joint	Sub-6GHz	Multi-SBS	Unicast	2D	✗	✗	✗	Unicast	Adaptive/SIC	Wireless/SDM	2D	✗
Proposed	Joint	Millimeter-wave	Multi-SBS	Unicast	3D	Many	✓	✓	Multicast	Adaptive	Wireless/SDM	3D	✓

The connection between the MBS and SBSs is called backhaul link, which is a convention in small cells literature. However, in a cloud-RAN context, MBSs are called central processors or BBUs, SBSs are called RRHs, and the connection between MBS and SBSs are called fronthaul links. In Table I, we have considered both kinds of nomenclatures since the problems originated from these two contexts are essentially the same.

of SBSs by developing practical backhauling mechanisms.

Challenge 2: Adaptive backhaul capacity. Although self-backhauling relies on wireless media, whose capacity is inherently highly variable due to noise and interference, the assumption of unlimited or fixed capacity prevails in many prior works, e.g., [9], [12]–[14]. *However, it is necessary to consider the capacity limitation of backhaul links as well as their variability in real systems.*

Challenge 3: User association. It is conventionally assumed that users are served by a single SBS [13], [15] or by all SBSs within a given range [9], [12]. While these assumptions simplify the problem formulation and solution, they are neither realistic nor optimal. *Thus, a general scheme is needed where users are associated to multiple SBSs in a flexible manner without considering extremes cases.*

Challenge 4: Admission control. Many works assume that all users can be served simultaneously [14], [16], [17], which is unrealistic due to limitations in power, number of antennas or RF chains. *Admission control (or user scheduling) is crucial to guarantee the quality of service requirements for at least a subset of admitted users, thereby circumventing unfeasibility issues.*

Challenge 5: Discrete data rates. It is usually assumed that data rates are continuous-valued, e.g., [8], [10], [17]–[19]. However, in practice they are limited to a number of possible choices, i.e., finite set of MCSs. *It is critical to consider the discreteness of rates since results obtained from solving problems for continuous values cannot be easily applied to real systems and are not expected to work properly.*

In contrast to prior art, we propose a comprehensive RRM framework that includes the challenges mentioned above, allowing us to more realistically validate millimeter-wave self-backhauled small cell deployments. Our approach makes the following novel contributions.

Contribution 1: In Section II, we address *Challenge 1* by proposing a simple yet effective *clustering mechanism for SBSs and users* that results in multiple non-overlapping *virtual cells* or *clusters*. This allows us to exploit multigroup multicast beamforming for backhaul traffic transmissions. Our clustering approach simplifies the backhaul design and reduces hardware/computational requirements at the sending and receiving nodes.

Contribution 2: In Section II-A and Section II-B we model *Challenge 2*, *Challenge 3*, *Challenge 4*, *Challenge 5* considering the access-backhaul interdependencies between MBS, SBSs and users. In Section II-C, we include these challenges in our formulation to jointly optimize *beamforming, user association, rate selection, admission control in the access network* and *beamforming, rate selection in the backhaul network* for maximizing the access network downlink weighted sum-rate. We cast the problem as a nonconvex mixed-integer nonlinear program (MINLP), which to the best of our knowledge, has not been investigated before.

Contribution 3: To tackle the nonconvex MINLP, we propose three formulations and their corresponding algorithms. In Section IV, we recast the nonconvex MINLP as a mixed-integer second-order cone program (MISOCP), which can be solved optimally. Due to the large number of integral variables, the cost of solving the MISOCP via branch-and-cut (BnC) techniques is prohibitive. To cope with this issue, in Section VI we propose a formulation solved via an iterative algorithm that tackles a SOCP at every instance. In Section VII, a much simpler SOCP formulation further decreases the complexity by reducing the number of variables, and optimizing only the beamformers gains. In particular, the complexity of the latter algorithm with respect to the former decreases roughly by a factor equal to the third power of the number of antennas at the SBS.

Contribution 4: In Section V, we derive an upper bound to provide insights on the performance gaps and trade-offs of RadiOrchestra. We also provide a simple lower bound marking the oerformance. We note that the upper bound is a novel problem itself that has not been investigated before.

Contribution 5: In Section VIII, we examine RadiOrchestra exhaustively under several scenarios including transmit power, number of clusters, and channel estimation errors.

There is a plethora of literature on self-backhauling for sub-6GHz spectrum, e.g., [19], [32], [33], which assume signals properties that do not work for millimeter-wave. Many works have focused on the design of either the backhaul, e.g., [8], [29], [34], [35] or the access network, e.g., [27], [28] alone. However, the growth that mobile networks are experiencing

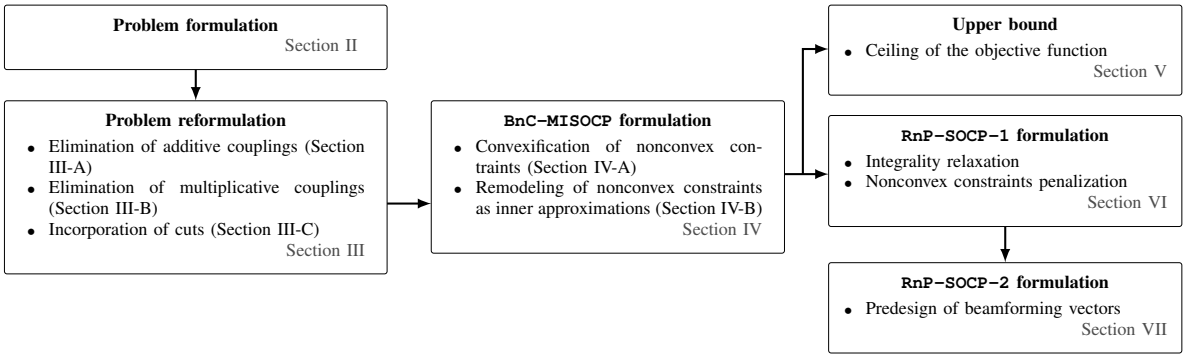

Figure 1: Overview of the steps to formulate and solve the problem in RadiOrchestra.

calls for heterogeneous networks with wireless backhauling, which require joint optimization. Considering linear antenna arrays, many works have optimized beamforming, e.g., [18], [33]. However, planar arrays are capable of 3D beamforming and hence are more suitable for dense deployments. The joint optimization of beamforming and user association *(Challenge 3)*, admission *(Challenge 4)*, or rate selection *(Challenge 5)*, generally requires solving complex nonconvex MINLPs. Thus, many works facing these challenges split the problem into stages and solve them separately. For instance, the integer variables are eliminated first by assuming a given set of scheduled users, e.g., [17], [18]. Then, the nonconvex functions are linearized and the problem is solved in the continuous domain. Although simpler to solve, variable decoupling affects optimality due to interdependencies removal. To meet the continuously growing demands, resources have to be exploited more optimally. Therefore, RRM problems need to be solved as a whole, without relying on variable partitioning which translates to inefficient radio resource usage.

After a scrupulous study of the state of the art, we found that the works most related to ours are [10], [19]. Like us, the authors of [10] assumed a multicast topology in the backhaul network, with a MBS transmitting multiple signals to various SBSs using multigroup multicasting beamforming (each signal carrying the data of a user). Since a single SBS may serve several users, SBSs are therefore required to decode many signal layers via SIC, which entails heavy computational burden for low-cost SBSs. Further, the decoding order of signals is known to affect the performance, leading to potential high decoding errors and making SIC impractical, which was not evaluated in [10]. The authors of [19] considered multiple SBS groups served in a multicast manner using time division multiplexing (TDM), i.e., each group at a time. However, as the number of clusters grows, the multiplexing time generates longer latency that is unavoidable as SBSs need to transmit coordinately to users, making it less practical. In addition, these works do not consider discrete rates, admission control, millimeter-wave spectrum and 3D beamforming. For completeness, we summarize in Table I the related literature on RRM for small cells.

Overview: Not surprisingly, the inherent couplings among all the different parameters of the system result in a complex problem which is difficult to address. However, our framework helps to realize the true potential of self-backhauled mobile networks, in particular in the presence of real-world constraints. To the best of our knowledge, this is the first work that has modeled an integrated access-backhaul system with such practical constraints and proposed solutions to assess its performance. The investigated problem is unique and hence existing solutions are not applicable to it. In the following, we provide an overview of the steps taken to solve our problem, from a systems design perspective as well as the mathematical treatment.

Systems aspect. 3GPP specifications for 5G leave several design choices to the operators such as spectrum allocation of backhaul and access. We leveraged these degrees of freedom to reduce the complexity of the problem while maintaining a realistic setup. The wireless nature of the access and backhaul links, coupled with the dense deployment of SBSs and users, creates a very complex interference environment. In RadiOrchestra, we choose an out-of-band system where backhaul and access links use different frequency bands, thus disentangling the interference between the two networks. Conventionally, the MBS sends individual backhaul signals to each SBS thus producing interference, which is handled via (point-to-point) unicast beamforming. In dense deployments this solution does not scale well due to the need to multiplex various data streams. Thus, we propose a clustering strategy where the MBS divides the SBSs into *clusters*, which are served simultaneously via (point-to-multipoint) multigroup multicast beamforming. This has three advantages: (i) Enhancing the scalability of self-backhauling by avoiding point-to-point transmissions which cause higher interference; (ii) Eliminating the need for heavy signal processing (e.g., SIC operation) at SBSs [10], [11]; (iii) Reducing hardware requirements and costs since MBS becomes more cost-efficient only requiring as many RF chains as SBS clusters, which is far less than the point-to-point topology (i.e., dedicated RF-chain per link).

Problem formulation and solution. Considering our design choices above, we model the system and propose solutions in a series of steps that are demonstrated in Fig. 1. We formulate a RRM problem for integrated access-backhaul networks considering real-world constraints, which results in a nonconvex MINLP with entangled variables (see **Section II**). We adopt a series of procedures to simplify the structure of the nonconvex

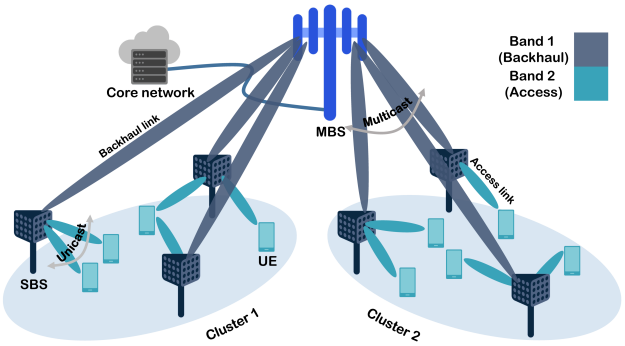

Figure 2: Self-backhauled SBSs grouped into clusters. The backhaul exploits multigroup multicast beamforming for data sharing whereas the access network is based on distributed unicast beamforming.

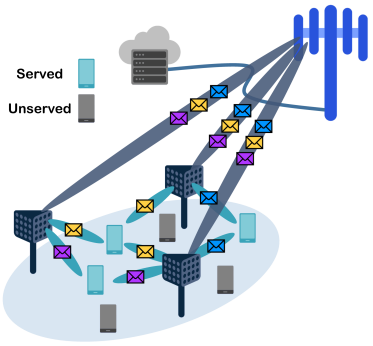

Figure 3: SBS clustering allows to merge data of all the served users into one stream, minimizing interference and simplifying data decoding at the SBSs.

MINLP without altering its optimality. Thus, we *(i)* improve its tractability by eliminating additive binary couplings and multiplicative mixed-integer couplings, and *(ii)* reduce the search space by adding cuts. Although the problem structure is greatly simplified after these procedures, it still remains a nonconvex MINLP. However, its more amenable layout allows us to tailor algorithms for its solution (see **Section III**). We transform some of the nonconvex constraints into equivalent (convex) SOC constraints and remodel others as convex inner SOC approximations. As a result, we recast the nonconvex MINLP into a MISOCP, which can be solved optimally (see **Section IV**). Although solving the proposed MISOCP guarantees an optimal solution, it requires a considerable amount of time due to the numerous integral variables. To deal with that, which translates to more branches evaluations by the BnC method, we propose a reformulation based on relaxation and penalization of the integral variables that only requires to solve iteratively a SOCP, and is guaranteed to attain a local optimum (see **Section VI**). To further simplify the computational burden and expedite the solving time, we offer a much simpler reformulation that reduces the number of continuous variables, where we predesign the access and backhaul beamforming vectors and only optimize their gains. As a result, we only solve a low-complexity SOCP problem iteratively (see **Section VII**). Finally, we derive an upper bound for the problem, which we use to characterize the performance of the developed algorithms (see **Section V**).

II. System Model and Problem Formulation

We consider that data is transported from the core network to the user equipments (UEs) via a MBS and a deployment of SBSs as shown in Fig. 2. The SBSs are connected to the MBS through wireless backhaul links. We assume an out-of-band full-duplex access-backhaul system, i.e., the backhaul network (connecting SBSs to the MBS) and the access network (connecting UEs to SBSs) operate simultaneously employing orthogonal bands. In the following, we detail the modeling assumptions.

Backhaul model: We rely on an advantageous clustering approach, where we divide the SBSs into L non-overlapping *virtual cells or clusters*, each formed by B SBSs (as in distributed antenna systems). In this way, data streams sent from the MBS to a SBS cluster contain the aggregate content for all the served UEs in that cluster, as shown in Fig. 3. The SBSs are deployed in a planned fashion and grouped based on their proximity. The antenna arrays are oriented towards the cluster center, as shown in Fig. 4.

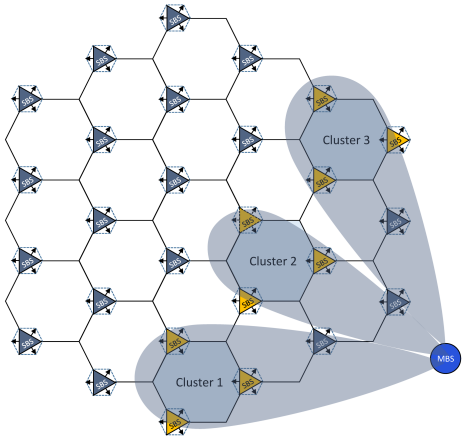

Figure 4: SBS distribution and clustering with a MBS transmitting multicast streams to three different clusters.

Access model: Each UE is pre-associated to a SBS cluster, based on the geographical distance or a given operator policy. Without loss of generality, we assume that each cluster has U UEs. Thus, SBSs in a cluster transmit collaboratively to UEs only within that cluster. However, not all SBSs are necessarily involved in serving a particular UE, and not all UEs may be served. The information for all the served UEs is co-processed by all SBSs, thus allowing to handle interference more efficiently.

Channel model: The backhaul links operate over a bandwidth $W_{\mathrm{BW}}^{\mathrm{backhaul}}$ and we assume line-of-sight (LOS) connectivity since the MBS and SBSs are usually strategically installed in the planning phase. Besides, the access network operates over a bandwidth $W_{\mathrm{BW}}^{\mathrm{access}}$ and its channels (i.e., between SBSs and UEs) exhibit multipath scattering containing both line-of-sight (LOS) and Non-line-of-sight (NLOS) components. Both access and backhaul channels are modeled according to [36].

Optimization model: In line with the related literature, we assume that the MBS has knowledge of the access channels between the SBSs and UEs. In particular, 3GPP specifies

channel training procedures in the access network that we can rely upon. In addition, the MBS also knows the backhaul channels, i.e., between itself and the SBSs. This knowledge is even simpler to acquire than the access channels since backhaul links are rather static with small variability. In summary, the MBS collects knowledge of all the wireless channels and, accordingly, optimizes all the radio resources of the system.

For the sake of clarity, variables and parameters used in the following sections are summarized in Table II.

Table II: Parameters and variables of the system

Parameters and Variables	Notation
Number of transmit antennas at the MBS and SBSs	$N_{\text{tx}}^{\text{MBS}}$, $N_{\text{tx}}^{\text{SBS}}$
Maximum transmit power at the MBS and SBSs	$P_{\text{tx}}^{\text{MBS}}$, $P_{\text{tx}}^{\text{SBS}}$
Number of clusters in the system	L
Number of UEs per cluster	U
Number of SBSs per cluster	B
Number of predefined rate/SINR values	J^{UE}, J^{SBS}
Bandwidth of the access and backhaul networks	$W_{\text{BW}}^{\text{access}}$, $W_{\text{BW}}^{\text{backhaul}}$
Set of clusters	$\mathcal{L} = \{1, \cdots, L\}$
Set of SBSs	$\mathcal{B} = \bigcup_{l \in \mathcal{L}} \mathcal{B}_l$
Set of UEs	$\mathcal{U} = \bigcup_{l \in \mathcal{L}} \mathcal{U}_l$
Set of predefined rate/SINR values at SBSs	$\mathcal{J}^{\text{SBS}}$
Set of predefined rate/SINR values at UEs	$\mathcal{J}^{\text{UE}}$
Set of UEs in the l-th cluster	$\mathcal{U}_l$
Set of SBSs in the l-th cluster	$\mathcal{B}_l$
Channel between the MBS and SBS b	$\mathbf{g}_b$
Channel between SBS b and UE u	$\mathbf{h}_{b,u}$
Multicast precoder from the MBS to SBS cluster $\mathcal{B}_l$	$\mathbf{m}_l$
Unicast precoder from SBS b to UE u	$\mathbf{w}_{b,u}$
Binary variable for UE rate/SINR selection	$\alpha_{u,j}$
Binary variable for SBS rate/SINR selection	$\beta_{l,j}$
Binary variable for UE association	$\kappa_{b,u}$

A. Backhaul Network: Multicast Transmissions from MBS to SBSs

In the backhaul network, two important aspects are dealt with. First, *rate selection*, i.e. choosing appropriate data rates at which the MBS transmits information to the SBSs. Second, *beamforming*, i.e. adjusting the amplitude and phases of the signals at the MBS to guarantee the selected rates.

Beamforming: The MBS is equipped with a planar array of $N_{\text{tx}}^{\text{MBS}}$ transmit antennas operating on Band 1 used for communication with the SBSs, which have $N_{\text{rx}}^{\text{SBS}} = 1$ receive antenna. The MBS transmits as many streams as clusters. Every stream contains the aggregate data for the served UEs in their respective clusters (see Fig. 3). The instantaneous multicast symbol for the SBSs in cluster $\mathcal{B}_l$ is denoted by z_l, with $\mathbb{E}[z_l] = 0$ and $\mathbb{E}\left[|z_l|_2^2\right] = 1$. The beamforming vector conveying z_l is denoted by $\mathbf{m}_l$. The composite signal transmitted from the MBS to all SBS clusters is given by $\mathbf{x}^{\text{MBS}} = \sum_{l \in \mathcal{L}} \mathbf{m}_l z_l$. The received signal at SBS $b \in \mathcal{B}_l$ is expressed as

$$\begin{aligned} y_b^{\text{SBS}} &= \mathbf{g}_b^H \mathbf{x}^{\text{MBS}} + n_b \\ &= \underbrace{\mathbf{g}_b^H \mathbf{m}_l z_l}_{\text{signal for SBS } b} + \underbrace{\sum_{l' \in \mathcal{L}, l' \neq l} \mathbf{g}_b^H \mathbf{m}_{l'} z_{l'}}_{\text{interference}} + \underbrace{n_b}_{\text{noise}}, \end{aligned} \tag{1}$$

where $\mathbf{g}_b$ is the channel between SBS $b \in \mathcal{B}_l$ and the MBS whereas $n_b \sim \mathcal{CN}\left(0, \sigma_{\text{SBS}}^2\right)$ symbolizes circularly symmetric Gaussian noise. The signal-to-interference-plus-noise ratio (SINR) at SBS b is

$$\text{SINR}_b^{\text{SBS}} = \frac{\left|\mathbf{g}_b^H \mathbf{m}_l\right|^2}{\sum_{l' \in \mathcal{L}, l' \neq l} \left|\mathbf{g}_b^H \mathbf{m}_{l'}\right|^2 + \sigma_{\text{SBS}}^2}. \tag{2}$$

Since all SBSs within a cluster receive the same common information (i.e. aggregate UE content), the effective rate/SINR per cluster is determined by the SBS with the worst conditions. As a result, a more sensible means of quantifying the maximal SINR per cluster is the following $\widetilde{\text{SINR}}_l^{\text{SBS}} = \min_{b \in \mathcal{B}_l} \left\{\text{SINR}_b^{\text{SBS}}\right\}, \forall l \in \mathcal{L}$.

REMARK: *This system is known as multigroup multicast beamforming [37] and has been studied for transmissions from a MBS/SBS to multiple clusters of UEs. We exploit that same idea to transmit data streams from the MBS to the SBSs. We assume that the number of streams that the MBS can handle is sufficient to serve all SBS clusters, i.e.* $N_{\text{streams}}^{\text{MBS}} \geq L$.

Rate Selection: In practical wireless communications systems, the set of eligible data rates is finite [38, pp. 64]. These predefined rates are uniquely identified by their associated CQI index, and each corresponds to a specific MCS. In addition, for each rate, a minimum received SINR is required in order to ensure a target block error rate (BLER) [39]. While the rates and MCSs are standardized, the corresponding target SINRs are usually vendor- and equipment-specific. We consider the target SINRs in [40], which are shown in Table III (in linear scale) and approximately exhibit increments of twice the previous rate starting from $R_1^{\text{SBS}} = 0.2344$ bps/Hz.

Table III: Rates and target SINR values

Coding rate	Rate R_j^{SBS} [bps/Hz]	SINR Γ_j^{SBS}
120/1024 (QPSK)	0.2344	0.2159
308/1024 (QPSK)	0.6016	0.6610
602/1024 (QPSK)	1.1758	1.7474
466/1024 (QAM)	2.7305	10.6316
948/1024 (QAM)	5.5547	95.6974

In order to assign R_j^{SBS} to the l-th SBS cluster, it is required that $\widetilde{\text{SINR}}_l^{\text{SBS}} \geq \Gamma_j^{\text{SBS}}$, $j \in \mathcal{J}^{\text{SBS}}$, where $\mathcal{J}^{\text{SBS}}$ represent the set of possible rates. To represent the rate assignment, we introduce the binary variables $\beta_{l,j} \in \{0, 1\}$ with $\beta_{l,j} = 1$ denoting that the SBSs in $\mathcal{B}_l$ are allocated R_j^{SBS}. We assume that all SBS clusters are served, which is ensured through $\sum_{j \in \mathcal{J}^{\text{SBS}}} \beta_{l,j} = 1, \forall l \in \mathcal{L}$ and $N_{\text{streams}}^{\text{MBS}} \geq L$. Thus, to guarantee the predefined target BLER for cluster $\mathcal{B}_l$, it must hold that $\widetilde{\text{SINR}}_l^{\text{SBS}} \geq \sum_{j \in \mathcal{J}^{\text{SBS}}} \beta_{l,j} \Gamma_j^{\text{SBS}}$.

B. Access Network: Distributed Unicast Transmissions from SBSs to UEs

In the access network, four pivotal aspects are addressed. First, *admission control*, i.e. deciding which UEs are served. Second, *rate selection*, i.e. choosing data rates for the served UEs. Third, *user association*, i.e. determining which subset of SBSs transmit to a served UE. Fourth, *beamforming*.

Beamforming and User Association: Each SBS is equipped with a planar array of $N_{\text{tx}}^{\text{SBS}}$ transmit antennas operating on Band 2 and used for communication with the UEs, which have $N_{\text{rx}}^{\text{UE}} = 1$ receive antenna. A SBS $b \in \mathcal{B}_l$ serving a subset of UEs in $\mathcal{U}_l$ transmits multiple unicast signals simultaneously, each signal targeting a specific UE. The instantaneous unicast symbol for UE $u \in \mathcal{U}_l$ is denoted by $s_{l,u}$, with $\mathbb{E}[s_{l,u}] = 0$ and $\mathbb{E}\left[|s_{l,u}|_2^2\right] = 1$. In addition, the beamforming vector from SBS $b \in \mathcal{B}_l$ transmitting $s_{l,u}$ to UE $u \in \mathcal{U}_l$ is denoted by $\mathbf{w}_{b,u}$. Therefore, the composite signal that SBS b in $\mathcal{B}_l$ sends to the UEs in $\mathcal{U}_l$ is represented by $\mathbf{x}_b^{\text{SBS}} = \sum_{u \in \mathcal{U}_l} \mathbf{w}_{b,u} s_{l,u} \kappa_{b,u}$,

$$y_u^{\mathrm{UE}} = \underbrace{\sum_{b\in\mathcal{B}_l} \mathbf{h}_{b,u}^H \mathbf{w}_{b,u} s_{l,u} \kappa_{b,u}}_{\text{signal for UE } u \text{ in cluster } \mathcal{U}_l} + \underbrace{\sum_{b\in\mathcal{B}_l} \sum_{\substack{u'\in\mathcal{U}_l \\ u'\neq u}} \mathbf{h}_{b,u}^H \mathbf{w}_{b,u'} s_{l,u'} \kappa_{b,u'}}_{\text{interference originated in cluster } \mathcal{U}_l} + \underbrace{\sum_{\substack{l'\in\mathcal{L} \\ l'\neq l}} \sum_{b'\in\mathcal{B}_{l'}} \sum_{u'\in\mathcal{U}_{l'}} \mathbf{h}_{b',u}^H \mathbf{w}_{b',u'} s_{l',u'} \kappa_{b',u'}}_{\text{aggregate interference originated in clusters } \mathcal{U}_{l'\neq l}} + \underbrace{n_u}_{\text{noise}} \tag{3}$$

$$\mathrm{SINR}_u^{\mathrm{UE}} = \frac{\left| \sum_{b\in\mathcal{B}_l} \mathbf{h}_{b,u}^H \mathbf{w}_{b,u} \kappa_{b,u} \right|^2}{\sum\limits_{\substack{u'\in\mathcal{U}_l \\ u'\neq u}} \left| \sum_{b\in\mathcal{B}_l} \mathbf{h}_{b,u}^H \mathbf{w}_{b,u'} \kappa_{b,u'} \right|^2 + \sum\limits_{\substack{l'\in\mathcal{L} \\ l'\neq l}} \sum_{u'\in\mathcal{U}_{l'}} \left| \sum_{b'\in\mathcal{B}_{l'}} \mathbf{h}_{b',u}^H \mathbf{w}_{b',u'} \kappa_{b',u'} \right|^2 + \sigma_{\mathrm{UE}}^2}. \tag{4}$$

$$\begin{aligned}
\mathcal{P}' : \max_{\mathbf{m}_l, \mathbf{w}_{b,u}, \alpha_{u,j}, \beta_{l,j}, \kappa_{b,u}} \quad & R_{\mathrm{w-sum}}^{\mathrm{access}}(\boldsymbol{\alpha}) \equiv \sum_{l\in\mathcal{L}} \sum_{u\in\mathcal{U}_l} \omega_u \sum_{j\in\mathcal{J}^{\mathrm{UE}}} \alpha_{u,j} R_j^{\mathrm{UE}} \\
\text{s.t.} \quad & \mathrm{C}_1 : \alpha_{u,j} = \{0,1\}, \forall l \in \mathcal{L}, u \in \mathcal{U}_l, j \in \mathcal{J}^{\mathrm{UE}}, \\
& \mathrm{C}_2 : \sum_{j\in\mathcal{J}^{\mathrm{UE}}} \alpha_{u,j} \leq 1, \forall l \in \mathcal{L}, u \in \mathcal{U}_l, \\
& \mathrm{C}_3 : \sum_{l\in\mathcal{L}} \|\mathbf{m}_l\|_2^2 \leq P_{\mathrm{tx}}^{\mathrm{MBS}}, \\
& \bar{\mathrm{C}}_4 : \sum_{u\in\mathcal{U}_l} \|\mathbf{w}_{b,u}\kappa_{b,u}\|_2^2 \leq P_{\mathrm{tx}}^{\mathrm{SBS}}, \forall l \in \mathcal{L}, b \in \mathcal{B}_l, \\
& \bar{\mathrm{C}}_5 : \mathrm{SINR}_u^{\mathrm{UE}} \geq \sum_{j\in\mathcal{J}^{\mathrm{UE}}} \alpha_{u,j} \Gamma_j^{\mathrm{UE}}, \forall l \in \mathcal{L}, u \in \mathcal{U}_l, \\
& \mathrm{C}_6 : \kappa_{b,u} = \{0,1\}, \forall l \in \mathcal{L}, b \in \mathcal{B}_l, u \in \mathcal{U}_l, \\
& \mathrm{C}_7 : \sum_{u\in\mathcal{U}_l} \kappa_{b,u} \leq N_{\mathrm{streams}}^{\mathrm{SBS}}, \forall l \in \mathcal{L}, b \in \mathcal{B}_l, \\
& \mathrm{C}_8 : \sum_{u\in\mathcal{U}_l} \kappa_{b,u} \geq 1, \forall l \in \mathcal{L}, b \in \mathcal{B}_l, \\
& \mathrm{C}_9 : \sum_{b\in\mathcal{B}_l} \kappa_{b,u} \leq B_{\max} \sum_{j\in\mathcal{J}^{\mathrm{UE}}} \alpha_{u,j}, \forall l \in \mathcal{L}, u \in \mathcal{U}_l, \\
& \mathrm{C}_{10} : \sum_{b\in\mathcal{B}_l} \kappa_{b,u} \geq B_{\min} \sum_{j\in\mathcal{J}^{\mathrm{UE}}} \alpha_{u,j}, \forall l \in \mathcal{L}, u \in \mathcal{U}_l, \\
& \mathrm{C}_{11} : \beta_{l,j} = \{0,1\}, \forall l \in \mathcal{L}, j \in \mathcal{J}^{\mathrm{SBS}}, \\
& \mathrm{C}_{12} : \sum_{j\in\mathcal{J}^{\mathrm{SBS}}} \beta_{l,j} = 1, \forall l \in \mathcal{L}, \\
& \mathrm{C}_{13} : W_{\mathrm{BW}}^{\mathrm{access}} \sum_{u\in\mathcal{U}_l} \sum_{j\in\mathcal{J}^{\mathrm{UE}}} \alpha_{u,j} R_j^{\mathrm{UE}} \leq W_{\mathrm{BW}}^{\mathrm{backhaul}} \sum_{j\in\mathcal{J}^{\mathrm{SBS}}} \beta_{l,j} R_j^{\mathrm{SBS}}, \forall l \in \mathcal{L}, \\
& \mathrm{C}_{14} : \sum_{u\in\mathcal{U}_l} \sum_{j\in\mathcal{J}^{\mathrm{UE}}} \alpha_{u,j} = U_{\mathrm{served}}, \forall l \in \mathcal{L}, \\
& \bar{\mathrm{C}}_{15} : \widetilde{\mathrm{SINR}}_l^{\mathrm{SBS}} \geq \sum_{j\in\mathcal{J}^{\mathrm{SBS}}} \beta_{l,j} \Gamma_j^{\mathrm{SBS}}, \forall l \in \mathcal{L},
\end{aligned}$$

where $\kappa_{b,u}$ is a binary variable that is 1 when SBS $b \in \mathcal{B}_l$ serves UE $u \in \mathcal{U}_l$ and 0 otherwise. A served UE $u \in \mathcal{U}_l$ receives its information from at least $B_{\min} = 1$ and at most $B_{\max} = B$ SBSs in $\mathcal{B}_l$. The signal received by UE u in $\mathcal{U}_l$ is given by (3), where $n_u \sim \mathcal{CN}\left(0, \sigma_{\mathrm{UE}}^2\right)$ and $\mathbf{h}_{b,u}$ represents the channel between SBS b and UE u. Every UE perceives interference from within its own cluster and from neighboring clusters. The SINR at UE u in $\mathcal{U}_l$ is defined by (4). When $\kappa_{b,u} = 0$, no information is sent to the UE. The effective beamforming vector is $\kappa_{b,u} \cdot \mathbf{w}_{b,u}$, which becomes a zero-vector for unserved UEs, thus accomplishing the association between UEs and SBSs.

Rate Selection and Admission Control: Similarly to Section II-A, the rate assigned to a served UE can only be one within a set of predefined values. To depict the rate selection for the UEs, we introduce the binary variables $\alpha_{u,j} \in \{0,1\}$. These variables perform the dual task of admission control and rate selection, which is ensured by $\sum_{j\in\mathcal{J}^{\mathrm{UE}}} \alpha_{u,j} \leq 1, \forall l \in \mathcal{L}, u \in \mathcal{U}_l$, where $\mathcal{J}^{\mathrm{UE}}$ represents the set of possible rate values. A UE u is served when $\sum_{j\in\mathcal{J}^{\mathrm{UE}}} \alpha_{u,j} = 1$, meaning that one rate has been assigned. Otherwise, when $\sum_{j\in\mathcal{J}^{\mathrm{UE}}} \alpha_{u,j} = 0$, the UE is not served. We denote the rates and target SINRs for UEs with R_j^{UE} and Γ_j^{UE}, respectively. To assign R_j^{UE} to UE u, it is required that $\mathrm{SINR}_u^{\mathrm{UE}} \geq \Gamma_j^{\mathrm{UE}}$, $j \in \mathcal{J}^{\mathrm{UE}}$, for which we assume the same values shown in Table III in Section III. Further, not all UEs shall be admitted since each SBS can support up to $N_{\mathrm{streams}}^{\mathrm{SBS}}$ streams simultaneously.

C. Problem Formulation

We investigate the problem of joint optimization of *beamforming*, *user association*, *rate selection*, *admission control*

Proposition 1. Due to existence of $\mathrm{C}_1 - \mathrm{C}_2$, constraint $\bar{\mathrm{C}}_5$ can be equivalently rewritten as

$$\mathrm{C}_5 : \mathrm{SINR}_u^{\mathrm{UE}} \geq \alpha_{u,j}\Gamma_j^{\mathrm{UE}}, \forall l \in \mathcal{L}, u \in \mathcal{U}_l, j \in \mathcal{J}^{\mathrm{UE}}.$$

Proof: Because of C_2*, there is at most one variable at a time that is* 1*. As a result, the SINR constraints can be decomposed into multiple constraints, each being related to only one binary variable.* □

Proposition 2. Due to existence of C_6, constraints $\bar{\mathrm{C}}_4 - \mathrm{C}_5$ can be equivalently rewritten as C_{17}, C_{18}, C_{19}, C_{20}, $\bar{\mathrm{C}}_{21}$, where

$$\bar{\mathrm{C}}_4 - \mathrm{C}_5 = \begin{cases} \mathrm{C}_{17} : p_{b,u} \geq 0, \forall l \in \mathcal{L}, b \in \mathcal{B}_l, u \in \mathcal{U}_l, \\ \mathrm{C}_{18} : \sum_{u \in \mathcal{U}_l} p_{b,u} \leq P_{\mathrm{tx}}^{\mathrm{SBS}}, \forall l \in \mathcal{L}, b \in \mathcal{B}_l, \\ \mathrm{C}_{19} : p_{b,u} \leq \kappa_{b,u} P_{\mathrm{tx}}^{\mathrm{SBS}}, \forall l \in \mathcal{L}, b \in \mathcal{B}_l, u \in \mathcal{U}_l, \\ \mathrm{C}_{20} : \left\| \left[2\mathbf{w}_{b,u}^H, \kappa_{b,u} - p_{b,u} \right] \right\|_2 \leq \kappa_{b,u} + p_{b,u}, \forall l \in \mathcal{L}, b \in \mathcal{B}_l, u \in \mathcal{U}_l, \\ \bar{\mathrm{C}}_{21} : \dfrac{\left| \sum_{b \in \mathcal{B}_l} \mathbf{h}_{b,u}^H \mathbf{w}_{b,u} \right|^2}{\sum_{\substack{u' \in \mathcal{U}_l \\ u' \neq u}} \left| \sum_{b \in \mathcal{B}_l} \mathbf{h}_{b,u}^H \mathbf{w}_{b,u'} \right|^2 + \sum_{\substack{l' \in \mathcal{L} \\ l' \neq l}} \sum_{u' \in \mathcal{U}_{l'}} \left| \sum_{b' \in \mathcal{B}_{l'}} \mathbf{h}_{b',u}^H \mathbf{w}_{b',u'} \right|^2 + \sigma_{\mathrm{UE}}^2} \geq \alpha_{u,j}\Gamma_j^{\mathrm{UE}}, \forall l \in \mathcal{L}, u \in \mathcal{U}_l, j \in \mathcal{J}^{\mathrm{UE}}, \end{cases}$$

Proof: See Appendix A. □

Proposition 3. Due to existence of C_1, constraint $\bar{\mathrm{C}}_{21}$ can be rewritten as C_{21}, where

$$\mathrm{C}_{21} : \sum_{l' \in \mathcal{L}} \sum_{u' \in \mathcal{U}_{l'}} \left| \sum_{b' \in \mathcal{B}_{l'}} \mathbf{h}_{b',u}^H \mathbf{w}_{b',u'} \right|^2 + \sigma_{\mathrm{UE}}^2 \leq \left(1 + \Gamma_j^{\mathrm{UE}^{-1}}\right) \left| \sum_{b \in \mathcal{B}_l} \mathbf{h}_{b,u}^H \mathbf{w}_{b,u} \right|^2 + \left(1 - \alpha_{u,j}\right)^2 Q_u^2, \forall l \in \mathcal{L}, u \in \mathcal{U}_l, j \in \mathcal{J}^{\mathrm{UE}},$$

and $Q_u^2 = P_{\mathrm{tx}}^{\mathrm{SBS}} \sum_{l' \in \mathcal{L}} \sum_{b' \in \mathcal{B}_{l'}} \|\mathbf{h}_{b',u}\|_2^2 + \sigma_{\mathrm{UE}}^2$ is an upper bound for the left-hand side (LHS) term of C_{21}.
Proof: See Appendix B. □

in the access network and *beamforming*, *rate selection* in the backhaul network aiming to maximize the weighted sum-rate at the access network (i,e., for the UEs), which is formulated as $\mathcal{P}'$ in the previous page.

In $\mathcal{P}'$, $R_{\mathrm{w-sum}}^{\mathrm{access}}(\boldsymbol{\alpha})$ denotes the weighted sum-rate achieved by all UEs in the access network. Besides, ω_u represents the weight associated to UE u, which can be adjusted by the network operator to assign different priorities, for instance, to balance fairness among UEs. Formally, the objective function is expressed as $R_{\mathrm{w-sum}}^{\mathrm{access}}(\boldsymbol{\alpha}) \equiv W_{\mathrm{BW}}^{\mathrm{access}} \sum_{l \in \mathcal{L}} \sum_{u \in \mathcal{U}_l} \omega_u \sum_{j \in \mathcal{J}^{\mathrm{UE}}} \alpha_{u,j} R_j^{\mathrm{UE}}$. However, since $W_{\mathrm{BW}}^{\mathrm{access}}$ is constant, we have redefined it as $R_{\mathrm{w-sum}}^{\mathrm{access}}(\boldsymbol{\alpha}) \equiv \sum_{l \in \mathcal{L}} \sum_{u \in \mathcal{U}_l} \omega_u \sum_{j \in \mathcal{J}^{\mathrm{UE}}} \alpha_{u,j} R_j^{\mathrm{UE}}$ without altering the nature of the problem.

Constraints C_1, C_2, $\bar{\mathrm{C}}_4$, $\bar{\mathrm{C}}_5$, C_6, C_7, C_8, C_9, C_{10}, C_{14} are related to the access network, C_3, C_{11}, C_{12}, $\bar{\mathrm{C}}_{15}$ are related to the backhaul network whereas C_{13} is related to both networks. Constraints $\mathrm{C}_1 - \mathrm{C}_2$ depict the rate selection for all UEs, constraint C_3 restricts the transmit power of the MBS, constraint $\bar{\mathrm{C}}_4$ restricts the transmit power of the SBSs, constraint $\bar{\mathrm{C}}_5$ guarantees that the unicast SINR is larger than the corresponding target SINR (specified in Table III), constraints $\mathrm{C}_6 - \mathrm{C}_8$ ensure that each SBS serves at least one UE but cannot serve more UEs than the number of streams it can handle, constraints $\mathrm{C}_9 - \mathrm{C}_{10}$ ensure that each admitted UE is served by at least $B_{\min}$ and by at most $B_{\max}$ SBSs, constraints $\mathrm{C}_{11} - \mathrm{C}_{12}$ guarantee a rate selection for every SBS cluster, constraint C_{13} guarantees that the total access throughput in a cluster does not exceed the throughput of the corresponding serving backhaul link, C_{14} ensures that there are U_{served} served UEs per cluster, constraint $\bar{\mathrm{C}}_{15}$ guarantees that the SINR per SBS cluster is larger than the selected target SINR (specified in Table III).

REMARK: *In the strict sense, the integrality constraints (i.e.,* C_1*,* C_6*,* C_{11}*) make* $\mathcal{P}'$ *nonconvex. Nevertheless, in the MINLP literature, a MINLP is referred to as nonconvex if it remains nonconvex even after excluding the integral variables. Otherwise, it is called convex [41]. In general, both convex and nonconvex MINLPs are NP-hard but the latter ones are more challenging to solve. Specifically,* $\mathcal{P}'$ *is a nonconvex MINLP and the nonconvexity nature is conferred by the constraints* $\bar{\mathrm{C}}_4$*,* $\bar{\mathrm{C}}_5$*,* $\bar{\mathrm{C}}_{15}$*.*

III. Proposed Problem Reformulation

In this section, we propose a series of transformations to simplify the nonconvex constraints $\bar{\mathrm{C}}_4$, $\bar{\mathrm{C}}_5$, $\bar{\mathrm{C}}_{15}$. The resulting reformulation $\mathcal{P}$ (shown in Section III-D) is used in Section IV, Section VI, Section VII, where we propose three algorithms: `BnC-MISOCP`, `RnP-SOCP-1` and `RnP-SOCP-2`.

A. Eliminating Additive Coupling between Binary Variables

To deal with the additive coupling of the binary variables at the right-hand side (RHS) of $\bar{\mathrm{C}}_5$ (i.e. sum of variables), we separate $\bar{\mathrm{C}}_5$ into multiple equivalent constraints, as described in *Proposition 1*.

B. Eliminating the Multiplicative Coupling between Continuous and Binary Variables

To deal with the multiplicative coupling between the unicast beamforming vectors and binary variables (in the form $\mathbf{w}_{b,u}\kappa_{b,u}$) in $\bar{\mathrm{C}}_4 - \mathrm{C}_5$, we reformulate such interdependencies as equivalent additive couplings, which are simpler to handle, as described in *Proposition 2*. In addition, note that $\mathrm{C}_{17} - \mathrm{C}_{20}$ are convex, whereas $\bar{\mathrm{C}}_{21}$ is a nonconvex mixed-integer nonlinear constraint. To circumvent the involved structure $\bar{\mathrm{C}}_{21}$, we remodel it (without loss of optimality) harnessing the *big-M* method [42], which allows to remove the multiplicative tie

Proposition 4. Due to existence of C_{11}, constraint $\bar{\mathrm{C}}_{15}$ can be equivalently recast as C_{15}, where

$$\mathrm{C}_{15}: \sum_{l' \in \mathcal{L}} \left|\mathbf{g}_b^H \mathbf{m}_{l'}\right|^2 + \sigma_{\mathrm{SBS}}^2 \leq \left(1+\Gamma_j^{\mathrm{SBS}^{-1}}\right) \left|\mathbf{g}_b^H \mathbf{m}_l\right|^2 + \left(1-\beta_{l,j}\right)^2 Q_b^2, \forall l \in \mathcal{L}, b \in \mathcal{B}_l, j \in \mathcal{J}^{\mathrm{SBS}},$$

and $Q_b^2 = P_{\mathrm{tx}}^{\mathrm{MBS}} \left\|\mathbf{g}_b\right\|_2^2 + \sigma_{\mathrm{SBS}}^2$ is an upper bound for the LHS term of C_{15}.

Proof: The proof is along the same lines as the procedures adopted in Proposition 1, Proposition 2 and Proposition 3. Therefore, it is omitted. □

Proposition 5. The nonconvex constraints $\mathrm{C}_{21} - \mathrm{C}_{22}$ can be equivalently expressed as SOC constraints $\mathrm{C}_{23} - \mathrm{C}_{25}$, i.e.,

$$\mathrm{C}_{21} - \mathrm{C}_{22} = \begin{cases} \mathrm{C}_{23}: \left\| \left[\bar{\mathbf{h}}_u^H \mathbf{W}, \sigma_{\mathrm{UE}}\right] \right\|_2 \leq \sqrt{1+\Gamma_j^{\mathrm{UE}^{-1}}} \mathsf{Re}\left\{\mathbf{h}_u^H \mathbf{w}_u\right\} + \left(1-\alpha_{u,j}\right) Q_u, \forall l \in \mathcal{L}, u \in \mathcal{U}_l, j \in \mathcal{J}^{\mathrm{UE}}, \\ \mathrm{C}_{24}: \mathsf{Re}\left\{\mathbf{h}_u^H \mathbf{w}_u\right\} \geq \alpha_{u,j} \sqrt{\Gamma_j^{\mathrm{UE}}} \sigma_{\mathrm{UE}}, \forall l \in \mathcal{L}, u \in \mathcal{U}_l, j \in \mathcal{J}^{\mathrm{UE}}, \\ \mathrm{C}_{25}: \mathsf{Im}\left\{\mathbf{h}_u^H \mathbf{w}_u\right\} = 0, \forall l \in \mathcal{L}, u \in \mathcal{U}_l, j \in \mathcal{J}^{\mathrm{UE}}. \end{cases}$$

Proof: See Appendix C. □

Proposition 6. The nonconvex constraints $\mathrm{C}_{15} - \mathrm{C}_{16}$ can be recast as the more conservative SOC constraints $\mathrm{C}_{26} - \mathrm{C}_{27}$, where

$$\mathrm{C}_{15} - \mathrm{C}_{16} = \begin{cases} \mathrm{C}_{26}: \left\| \left[\mathbf{g}_b^H \mathbf{M}, \sigma_{\mathrm{SBS}}\right] \right\|_2 \leq \sqrt{1+\Gamma_j^{\mathrm{SBS}^{-1}}} \mathsf{Re}\left\{\mathbf{g}_b^H \mathbf{m}_l\right\} + \left(1-\beta_{l,j}\right) Q_b, \forall l \in \mathcal{L}, b \in \mathcal{B}_l, j \in \mathcal{J}^{\mathrm{SBS}}, \\ \mathrm{C}_{27}: \mathsf{Re}\left\{\mathbf{g}_b^H \mathbf{m}_l\right\} \geq \beta_{l,j} \sqrt{\Gamma_j^{\mathrm{SBS}}} \sigma_{\mathrm{SBS}}, \forall l \in \mathcal{L}, b \in \mathcal{B}_l, j \in \mathcal{J}^{\mathrm{SBS}}. \end{cases}$$

Proof: See Appendix D. □

between the beamformers and binary variables, as described in *Proposition 3*. Finally, because constraint $\bar{\mathrm{C}}_{15}$ has a similar structure as $\bar{\mathrm{C}}_5$, we can reformulate it in an equivalent manner, as described in *Proposition 4*.

C. Adding Cuts to Tighten the Feasible Set

To reduce the number of branches to be evaluated by MINLP solvers, we include valid inequalities (cuts) for certain constraints involving integer variables. Thus, we add the constraints C_{16} and C_{22}, defined as

$$\mathrm{C}_{16}: \left|\mathbf{g}_b^H \mathbf{m}_l\right|^2 \geq \beta_{l,j} \Gamma_j^{\mathrm{SBS}} \sigma_{\mathrm{SBS}}^2, \forall l \in \mathcal{L}, b \in \mathcal{B}_l, j \in \mathcal{J}^{\mathrm{SBS}},$$

$$\mathrm{C}_{22}: \left| \sum_{b \in \mathcal{B}_l} \mathbf{h}_{b,u}^H \mathbf{w}_{b,u} \right|^2 \geq \alpha_{u,j} \Gamma_j^{\mathrm{UE}} \sigma_{\mathrm{UE}}^2, \forall l \in \mathcal{L}, u \in \mathcal{U}_l, j \in \mathcal{J}^{\mathrm{UE}}.$$

Note that C_{16} is a lower bound for the multicast SINR numerator, which becomes tight when the interference term is zero. This constraint is always satisfied when $\beta_{l,j}$ are binary thus reducing the feasible set and tightening the problem relaxation when the binary variables are recast as real values (as in the proposed algorithms in Section VI and Section VII). Adding C_{16} does not change the nature of the problem nor affects its optimality. Similarly, C_{22} is a lower bound for the unicast SINR numerator.

D. Redefining the Problem

After applying the transformations in Section III-A, Section III-B and Section III-C, the nonconvex constraints $\bar{\mathrm{C}}_4$, $\bar{\mathrm{C}}_5$, $\bar{\mathrm{C}}_{15}$ have been replaced by the convex constraints C_{17}, C_{18}, C_{19}, C_{20} and the nonconvex constraints C_{15}, C_{21}. In addition, the nonconvex constraints C_{16}, C_{22} have been added to contract the feasible set. Collecting these outcomes, we define $\mathcal{P}$ as

$$\begin{aligned} \mathcal{P}: \max_{\substack{\mathbf{m}_l, \mathbf{w}_{b,u}, p_{b,u}, \\ \alpha_{u,j}, \beta_{l,j}, \kappa_{b,u}}} \quad & \text{convex: } R_{\mathrm{w-sum}}^{\mathrm{access}}(\boldsymbol{\alpha}) \\ \text{s.t.} \quad & \text{convex: } \mathrm{C}_2 - \mathrm{C}_3, \mathrm{C}_7 - \mathrm{C}_{10}, \mathrm{C}_{12} - \mathrm{C}_{14}, \\ & \qquad \mathrm{C}_{17} - \mathrm{C}_{20}, \\ & \text{nonconvex: } \mathrm{C}_{15} - \mathrm{C}_{16}, \mathrm{C}_{21} - \mathrm{C}_{22}, \\ & \text{binary: } \mathrm{C}_1, \mathrm{C}_6, \mathrm{C}_{11}. \end{aligned}$$

REMARK: *Notice that $\mathcal{P}$ is also a nonconvex MINLP and has the same optimal solution as $\mathcal{P}'$ since the introduced transformations do not affect the original feasible set. However, the structure of $\mathcal{P}$ is simpler, thus allowing us to tailor algorithms for solving the problem more efficiently.*

IV. BNC-MISOCP: Proposed MISOCP Formulation

In this section, we recast $\mathcal{P}$ as a MISOCP by transforming the nonconvex constraints into convex ones. We remodel $\mathrm{C}_{21} - \mathrm{C}_{22}$ as convex constraints and replace $\mathrm{C}_{15} - \mathrm{C}_{16}$ with convex inner surrogates.

A. Transforming Nonconvex Constraints into Convex Constraints

To deal with the nonconvex constraints $\mathrm{C}_{21} - \mathrm{C}_{22}$, we recast them as convex conic constraints as they have hidden convexity. To simplify notation, we first rewrite $\mathrm{C}_{21} - \mathrm{C}_{22}$ as

$$\begin{aligned} \mathrm{C}_{21}: \left|\bar{\mathbf{h}}_u^H \mathbf{W}\right|^2 + \sigma_{\mathrm{UE}}^2 \leq & \left(1+\Gamma_j^{\mathrm{UE}^{-1}}\right) \left|\mathbf{h}_u^H \mathbf{w}_u\right|^2 \\ & + \left(1-\alpha_{u,j}\right)^2 Q_u^2, \forall l \in \mathcal{L}, u \in \mathcal{U}_l, j \in \mathcal{J}^{\mathrm{UE}}, \\ \mathrm{C}_{22}: \alpha_{u,j} \Gamma_j^{\mathrm{UE}} \sigma_{\mathrm{UE}}^2 \leq & \left|\mathbf{h}_u^H \mathbf{w}_u\right|^2, \forall l \in \mathcal{L}, u \in \mathcal{U}_l, j \in \mathcal{J}^{\mathrm{UE}}, \end{aligned}$$

where $\left|\sum_{b \in \mathcal{B}_l} \mathbf{h}_{b,u}^H \mathbf{w}_{b,u}\right|^2 = \left|\mathbf{h}_u^H \mathbf{w}_u\right|^2, u \in \mathcal{U}_l$ and $\sum_{l' \in \mathcal{L}} \sum_{u' \in \mathcal{U}_{l'}} \left|\sum_{b' \in \mathcal{B}_{l'}} \mathbf{h}_{b',u}^H \mathbf{w}_{b',u'}\right|^2 = \left|\bar{\mathbf{h}}_u^H \mathbf{W}\right|^2$. In particular, $\mathbf{h}_u = \left[\mathbf{h}_{b_1,u}^H, \cdots, \mathbf{h}_{b_B,u}^H\right]^H$ and $\mathbf{w}_u = \left[\mathbf{w}_{b_1,u}^H, \cdots, \mathbf{w}_{b_B,u}^H\right]^H$, denote respectively the channels and beamforming vectors from all SBS in the same cluster that UE u is located. Further, $\bar{\mathbf{h}}_u$ denotes the channel between UE u and all SBSs in the system whereas $\mathbf{W}$ is a block diagonal matrix collecting all beamforming vectors between SBSs and UEs. After applying these changes, we are in the position of expressing the nonconvex constraints $\mathrm{C}_{21} - \mathrm{C}_{22}$ as exactly equivalent SOC constraints, as described in *Proposition 5*.

B. Recasting Nonconvex Constraints as Convex Inner Approximations

To circumvent the nonconvex constraints C_{15}, C_{16}, we replace them by convex surrogates. Assuming that $\mathbf{M} = [\mathbf{m}_1, \cdots, \mathbf{m}_L]$, we express C_{15} as

$$\mathrm{C}_{15}: \left\|\mathbf{g}_b^H \mathbf{M}\right\|_2^2 + \sigma_{\mathrm{SBS}}^2 \leq \left(1 + \Gamma_j^{\mathrm{SBS}^{-1}}\right) \left|\mathbf{g}_b^H \mathbf{m}_l\right|^2 + (1-\beta_{l,j})^2 Q_b^2, \forall l \in \mathcal{L}, b \in \mathcal{B}_l, j \in \mathcal{J}^{\mathrm{SBS}}.$$

Using this expression, we reformulate $\mathrm{C}_{15} - \mathrm{C}_{16}$ as convex inner SOC approximations, as stated in *Proposition 6*. If constraints $\mathrm{C}_{26} - \mathrm{C}_{27}$ are satisfied, then $\mathrm{C}_{15} - \mathrm{C}_{16}$ are automatically guaranteed because the feasible set of $\mathrm{C}_{26} - \mathrm{C}_{27}$ is contained in that of $\mathrm{C}_{15} - \mathrm{C}_{16}$. Therefore, they are called inner approximations.

C. Summarizing the Changes

After applying the transformations above, we define the following problem,

$$\mathcal{P}_0: \max_{\substack{\mathbf{m}_l, \mathbf{w}_{b,u}, p_{b,u}, \\ \alpha_{u,j}, \beta_{l,j}, \kappa_{b,u}}} \quad \text{convex: } R_{\mathrm{w-sum}}^{\mathrm{access}}(\boldsymbol{\alpha})$$
$$\text{s.t.} \quad \text{convex: } \mathrm{C}_2 - \mathrm{C}_3, \mathrm{C}_7 - \mathrm{C}_{10}, \mathrm{C}_{12} - \mathrm{C}_{14}, \mathrm{C}_{17} - \mathrm{C}_{20}, \mathrm{C}_{23} - \mathrm{C}_{27},$$
$$\text{binary: } \mathrm{C}_1, \mathrm{C}_6, \mathrm{C}_{11},$$

which is an inner approximation of problem $\mathcal{P}$ due to convexification of its original feasible set upon replacing $\mathrm{C}_{15} - \mathrm{C}_{16}$ by $\mathrm{C}_{26} - \mathrm{C}_{27}$. Thus, any feasible solution to $\mathcal{P}_0$ will also be feasible to $\mathcal{P}'$ and $\mathcal{P}$. Here, $\mathcal{P}_0$ has $N_v = 2LN_{\mathrm{tx}}^{\mathrm{MBS}} + 2LBUN_{\mathrm{tx}}^{\mathrm{SBS}} + 2LBU + LJ^{\mathrm{SBS}} + LUJ^{\mathrm{UE}}$ variables, $N_l = 3L + 2LU + 3LB + 2LBU + 3LUJ^{\mathrm{UE}} + LBJ^{\mathrm{SBS}}$ linear constraints and $N_c = 1 + LBU + LUJ^{\mathrm{UE}} + LBJ^{\mathrm{SBS}}$ convex constraints. The complexity is $\mathcal{O}\left(N_s (N_v)^3 (N_l + N_c)\right)$, where N_s is the total number of evaluations needed by the mixed-integer (MIP) solver.

REMARK: *Note that $\mathcal{P}_0$ is a convex MINLP, and as such it can be solved optimally by MIP solvers which exploit BnC techniques to prune infeasible solutions thus reducing the search space of the problem. Although BnC techniques can explore the binary space more efficiently and are faster than exhaustive search, they may still require a considerable amount of time to find the optimum, specially when the number of integral variables is large as in $\mathcal{P}_0$. Thus, in order to expedite this process, we propose suboptimal algorithms in Section VI and Section VII based on integrality relaxation and penalization.*

V. PROPOSED BOUNDS

We derive an *upper bound* and a *lower bound* for $\mathcal{P}_0$. The upper bound is defined as a MISOCP whereas the lower bound is a system- and problem-specific rate value. When not possible to obtain a solution for $\mathcal{P}_0$ (due to high time complexity), the upper and lower bounds will be used as benchmarks for the developed algorithms in Section VI and Section VII.

Upper Bound (`UB`): While the weighted sum-rate is a mechanism to balance rates, i.e., to give higher priorities to the least favored UEs, the actual aggregate rate in the network is given by the sum-rate $R_{\mathrm{sum}}^{\mathrm{access}}(\boldsymbol{\alpha}) = W_{\mathrm{BW}}^{\mathrm{access}} \sum_{l \in \mathcal{L}} \sum_{u \in \mathcal{U}_l} \sum_{j \in \mathcal{J}^{\mathrm{UE}}} \alpha_{u,j} R_j^{\mathrm{UE}}$ (without the weights). Thus, note that $R_{\mathrm{sum}}^{\mathrm{access}}(\boldsymbol{\alpha})$ is related to constraint C_{13}, which ensures that the access sum-rate per cluster does not exceed the rate of the serving backhaul link. Therefore, the access sum-rate $R_{\mathrm{sum}}^{\mathrm{access}}(\boldsymbol{\alpha})$ is bounded from above by the backhaul sum-rate, defined as $R_{\mathrm{sum}}^{\mathrm{backhaul}}(\boldsymbol{\beta}) \triangleq W_{\mathrm{BW}}^{\mathrm{backhaul}} \sum_{l \in \mathcal{L}} \sum_{j \in \mathcal{J}^{\mathrm{SBS}}} \beta_{l,j} R_j^{\mathrm{SBS}}$, i.e., $R_{\mathrm{sum}}^{\mathrm{access}}(\boldsymbol{\alpha}) \leq R_{\mathrm{sum}}^{\mathrm{backhaul}}(\boldsymbol{\beta})$. Since the backhaul sum-rate depends only on $\mathbf{m}_l$ and $\beta_{l,j}$, the upper bound is given by

$$\mathcal{P}_{\mathrm{UB}}: \max_{\mathbf{m}_l, \beta_{l,j}} \; R_{\mathrm{sum}}^{\mathrm{backhaul}}(\boldsymbol{\beta}) \quad \text{s.t.} \quad \mathrm{C}_3, \mathrm{C}_{11}, \mathrm{C}_{12}, \mathrm{C}_{26}, \mathrm{C}_{27},$$

which is a MISOCP that can be solved optimally. *The upper bound essentially maximizes the backhaul network throughput without considering the access network requirements.* Note that $\mathcal{P}_{\mathrm{UB}}$ has $N_v = LJ^{\mathrm{SBS}} + 2LN_{\mathrm{tx}}^{\mathrm{MBS}}$ variables, $N_l = L + LBJ^{\mathrm{SBS}}$ linear constraints and $N_c = 1 + LBJ^{\mathrm{SBS}}$ convex constraints. Thus, its complexity is $\mathcal{O}\left(N_s (N_v)^3 (N_l + N_c)\right)$, where N_s represents the total number of evaluations needed by the MIP solver.

REMARK: *$\mathcal{P}_{\mathrm{UB}}$ can be interpreted as joint multigroup multicast beamforming and rate selection, which has not been investigated before. A similar problem was studied in [43] but with continuous rates. Although we do not investigate this new problem alone but in conjunction with the additional access network constraints, we believe it is important to highlight its novelty as it represents the discrete counterpart of the aforementioned problem thus filling a gap in the existing literature and opening new avenues of research.*

Lower Bound (`LB`): The lower bound is based on the analysis of $\mathcal{P}_0$. From constraint C_{13}, a number of U_{served} UEs per cluster needs to be served. In the worst case, these UEs are allocated the lowest rate possible, which based on Table III, corresponds to $R_1^{\mathrm{UE}} = 0.2344$ bps/Hz. With L clusters, the minimum sum-rate at the access network is defined as $R_{\mathrm{sum-min}}^{\mathrm{access}} = R_1^{\mathrm{UE}} \cdot W_{\mathrm{BW}}^{\mathrm{access}} \cdot U_{\mathrm{served}} \cdot L$ bps. We underline that this bound corresponds to the worst possible case in which the UEs are minimally served while still satisfying the system constraints.

VI. `RnP-SOCP-1`: PROPOSED SOCP FORMULATION

This formulation is derived from problem $\mathcal{P}_0$. We propose a relax-and-penalize SOCP algorithm denoted by `RnP-SOCP-1`, which iteratively optimizes a SOCP. To cope with the integrality constraints C_1, C_6, C_{11}, we replace them with the intersection of two continuous sets [44], as described in *Proposition 7*.

Proposition 7. The constraints C_1, C_6, C_{11} can be equivalently expressed as,

$$\mathrm{C}_1 = \begin{cases} \mathrm{X}_1: 0 \leq \alpha_{u,j} \leq 1, \\ \mathrm{Z}_1: \sum_{l,u,j} \alpha_{u,j} - \alpha_{u,j}^2 \leq 0, \end{cases}$$
$$\mathrm{C}_6 = \begin{cases} \mathrm{X}_2: 0 \leq \kappa_{b,u} \leq 1, \\ \mathrm{Z}_2: \sum_{l,b,u} \kappa_{b,u} - \kappa_{b,u}^2 \leq 0, \end{cases}$$
$$\mathrm{C}_{11} = \begin{cases} \mathrm{X}_3: 0 \leq \beta_{l,j} \leq 1, \\ \mathrm{Z}_3: \sum_{l,j} \beta_{l,j} - \beta_{l,j}^2 \leq 0. \end{cases}$$

Proof: It is straightforward to see that X_1 and Z_1 intersect only at $\{0, 1\}$. Thus, we omit further details. □

Notice that constraints $\mathrm{X}_1 - \mathrm{X}_3$ are convex whereas $\mathrm{Z}_1 - \mathrm{Z}_3$ are nonconvex. Considering *Proposition 7*, we define

$$\widetilde{\mathcal{P}}_1 : \max_{\boldsymbol{\Theta}\in\mathscr{D}} \quad R(\boldsymbol{\alpha},\boldsymbol{\beta},\boldsymbol{\kappa}) \triangleq R^{\text{access}}_{\text{w-sum}}(\boldsymbol{\alpha}) \underbrace{-\lambda_\alpha f_\alpha(\boldsymbol{\alpha}) - \lambda_\beta f_\beta(\boldsymbol{\beta}) - \lambda_\kappa f_\kappa(\boldsymbol{\kappa})}_{\text{nonconvex DC functions}} \tag{7}$$

$$\begin{aligned}
&f_\alpha(\boldsymbol{\alpha}) \triangleq p_\alpha(\boldsymbol{\alpha}) + q_\alpha(\boldsymbol{\alpha}), && p_\alpha(\boldsymbol{\alpha}) \triangleq \sum_{l\in\mathcal{L}}\sum_{u\in\mathcal{U}_l}\sum_{j\in\mathcal{J}^{\text{UE}}} \alpha_{u,j}, && q_\alpha(\boldsymbol{\alpha}) \triangleq -\sum_{l\in\mathcal{L}}\sum_{u\in\mathcal{U}_l}\sum_{j\in\mathcal{J}^{\text{UE}}} \alpha_{u,j}^2,\\
&f_\beta(\boldsymbol{\beta}) \triangleq p_\beta(\boldsymbol{\beta}) + q_\beta(\boldsymbol{\beta}), && p_\beta(\boldsymbol{\beta}) \triangleq \sum_{l\in\mathcal{L}}\sum_{j\in\mathcal{J}^{\text{SBS}}} \beta_{l,j}, && q_\beta(\boldsymbol{\beta}) \triangleq -\sum_{l\in\mathcal{L}}\sum_{j\in\mathcal{J}^{\text{SBS}}} \beta_{l,j}^2,\\
&f_\kappa(\boldsymbol{\kappa}) \triangleq p_\kappa(\boldsymbol{\kappa}) + q_\kappa(\boldsymbol{\kappa}), && p_\kappa(\boldsymbol{\kappa}) \triangleq \sum_{l\in\mathcal{L}}\sum_{b\in\mathcal{B}_l}\sum_{u\in\mathcal{U}_l} \kappa_{b,u}, && q_\kappa(\boldsymbol{\kappa}) \triangleq -\sum_{l\in\mathcal{L}}\sum_{b\in\mathcal{B}_l}\sum_{u\in\mathcal{U}_l} \kappa_{b,u}^2.
\end{aligned}$$

$$\widetilde{\mathcal{P}}_1^{(t)} : \max_{\boldsymbol{\Theta}\in\mathscr{D}} \quad \tilde{R}^{(t)}(\boldsymbol{\alpha},\boldsymbol{\beta},\boldsymbol{\kappa}) \triangleq R^{\text{access}}_{\text{w-sum}}(\boldsymbol{\alpha}) - \lambda_\alpha \tilde{f}_\alpha^{(t)}(\boldsymbol{\alpha}) - \lambda_\beta \tilde{f}_\beta^{(t)}(\boldsymbol{\beta}) - \lambda_\kappa \tilde{f}_\kappa^{(t)}(\boldsymbol{\kappa}) \tag{8}$$

$$\tilde{f}_\alpha^{(t)}(\boldsymbol{\alpha}) \triangleq p_\alpha(\boldsymbol{\alpha}) + \tilde{q}_\alpha^{(t)}(\boldsymbol{\alpha}), \qquad \tilde{f}_\beta^{(t)}(\boldsymbol{\beta}) \triangleq p_\beta(\boldsymbol{\beta}) + \tilde{q}_\beta^{(t)}(\boldsymbol{\beta}), \qquad \tilde{f}_\kappa^{(t)}(\boldsymbol{\kappa}) \triangleq p_\kappa(\boldsymbol{\kappa}) + \tilde{q}_\kappa^{(t)}(\boldsymbol{\kappa}).$$

$$\mathcal{P}_1 : \max_{\boldsymbol{\Theta}} \quad R^{\text{access}}_{\text{w-sum}}(\boldsymbol{\alpha}) \quad \text{s.t.} \quad \underbrace{\boldsymbol{\Theta}\in\mathscr{D}}_{\text{convex}}, \underbrace{\text{Z}_1 - \text{Z}_3}_{\text{nonconvex}}$$

which is equivalent to $\mathcal{P}_0$. Here, $\boldsymbol{\Theta} = (\mathbf{M}, \mathbf{W}, \mathbf{p}, \boldsymbol{\alpha}, \boldsymbol{\beta}, \boldsymbol{\kappa})$ groups all the optimization variables and $\mathscr{D}$ denotes the feasible set spanned by the convex constraints $\text{X}_1 - \text{X}_3, \text{C}_2 - \text{C}_3, \text{C}_7 - \text{C}_{10}, \text{C}_{12} - \text{C}_{14}, \text{C}_{17} - \text{C}_{20}, \text{C}_{23} - \text{C}_{27}$. Although $\mathcal{P}_1$ is a nonconvex MINLP, its nonconvexity is only due to simple polynomial constraints $\text{Z}_1 - \text{Z}_3$, which belong to the class of difference of convex (DC) functions.

Since $\mathcal{P}_1$ is challenging to solve optimally, we aim to obtain a locally optimal solution. To find a solution for $\mathcal{P}_1$, we devise an algorithm based on the minorization-maximization (MM) principle. To cope with $\text{Z}_1 - \text{Z}_3$, we include them as penalty terms in the objective function [45]. Thus, we define $\widetilde{\mathcal{P}}_1$ in (7) where $\lambda_\alpha \geq 0$, $\lambda_\beta \geq 0$, $\lambda_\kappa \geq 0$. Whenever $\boldsymbol{\alpha}$, $\boldsymbol{\beta}$, $\boldsymbol{\kappa}$ are not binary, the functions $f_\alpha(\boldsymbol{\alpha})$, $f_\beta(\boldsymbol{\beta})$, $f_\kappa(\boldsymbol{\kappa})$ are positive. By including them in the objective, they can be used as a measure of the degree of satisfaction of the binary constraints, with λ_α, λ_β, λ_κ representing penalty factors. Problems $\mathcal{P}_1$ and $\widetilde{\mathcal{P}}_1$ are related in the following sense. If *Proposition 8* is satisfied, $\mathcal{P}_1$ and $\widetilde{\mathcal{P}}_1$ become equivalent [45], [46].

Proposition 8. The optimization problems $\mathcal{P}_1$ and $\widetilde{\mathcal{P}}_1$ are equivalent for sufficiently large values of λ_α, λ_β, λ_κ, in which case both problems attain the same optimal value and solution.
Proof: See Appendix E. □

To solve $\widetilde{\mathcal{P}}_1$, the complication is in the objective since $f_\alpha(\boldsymbol{\alpha})$, $f_\beta(\boldsymbol{\beta})$, $f_\kappa(\boldsymbol{\kappa})$ are nonconvex DC functions. Thus, we apply first-order approximations to $q_\alpha(\boldsymbol{\alpha})$, $q_\beta(\boldsymbol{\beta})$, $q_\kappa(\boldsymbol{\kappa})$, and define

$$\begin{aligned}
\tilde{q}_\alpha^{(t)}(\boldsymbol{\alpha}) &\triangleq q_\alpha\left(\boldsymbol{\alpha}^{(t-1)}\right) + \nabla_{\boldsymbol{\alpha}} q_\alpha^T\left(\boldsymbol{\alpha}^{(t-1)}\right)\left(\boldsymbol{\alpha} - \boldsymbol{\alpha}^{(t-1)}\right),\\
\tilde{q}_\beta^{(t)}(\boldsymbol{\beta}) &\triangleq q_\beta\left(\boldsymbol{\beta}^{(t-1)}\right) + \nabla_{\boldsymbol{\beta}} q_\beta^T\left(\boldsymbol{\beta}^{(t-1)}\right)\left(\boldsymbol{\beta} - \boldsymbol{\beta}^{(t-1)}\right),\\
\tilde{q}_\kappa^{(t)}(\boldsymbol{\kappa}) &\triangleq q_\kappa\left(\boldsymbol{\kappa}^{(t-1)}\right) + \nabla_{\boldsymbol{\kappa}} q_\kappa^T\left(\boldsymbol{\kappa}^{(t-1)}\right)\left(\boldsymbol{\kappa} - \boldsymbol{\kappa}^{(t-1)}\right),
\end{aligned}$$

where $\tilde{q}_\alpha^{(t)}(\boldsymbol{\alpha}) \geq q_\alpha(\boldsymbol{\alpha})$, $\tilde{q}_\beta^{(t)}(\boldsymbol{\beta}) \geq q_\beta(\boldsymbol{\beta})$, $\tilde{q}_\kappa^{(t)}(\boldsymbol{\kappa}) \geq q_\kappa(\boldsymbol{\kappa})$ are outer linear approximations for $q_\alpha(\boldsymbol{\alpha})$, $q_\beta(\boldsymbol{\beta})$, $q_\kappa(\boldsymbol{\kappa})$, respectively.

Here, $\boldsymbol{\alpha}^{(t-1)}$, $\boldsymbol{\beta}^{(t-1)}$, $\boldsymbol{\kappa}^{(t-1)}$ denote a feasible solution (i.e. reference point for linearization) whereas $\nabla_{\mathbf{x}}$ represents the derivative with respect to variable $\mathbf{x}$. Using the MM principle and constructing a sequence of surrogate functions $\tilde{q}_\alpha^{(t)}(\boldsymbol{\alpha})$, $\tilde{q}_\beta^{(t)}(\boldsymbol{\beta})$, $\tilde{q}_\kappa^{(t)}(\boldsymbol{\kappa})$ at every iteration t, we solve problem $\widetilde{\mathcal{P}}_1^{(t)}$ defined in (8), which is a SOCP where $\tilde{f}_\alpha^{(t)}(\boldsymbol{\alpha}) \geq f_\alpha(\boldsymbol{\alpha})$, $\tilde{f}_\beta^{(t)}(\boldsymbol{\beta}) \geq f_\beta(\boldsymbol{\beta})$, $\tilde{f}_\kappa^{(t)}(\boldsymbol{\kappa}) \geq f_\kappa(\boldsymbol{\kappa})$. In particular, problem $\widetilde{\mathcal{P}}_1^{(t)}$ is convex and can be solved using interior-point methods. By solving $\widetilde{\mathcal{P}}_1^{(t)}$ iteratively, we show in *Proposition 9* and *Proposition 10*, that $\widetilde{\mathcal{P}}_1^{(t)}$ is a global lower bound of $\widetilde{\mathcal{P}}_1$ and the obtained solution is a KKT point.

Proposition 9. Problem $\widetilde{\mathcal{P}}_1^{(t)}$ is a global lower bound for $\widetilde{\mathcal{P}}_1$ since $\tilde{R}^{(t)}(\boldsymbol{\alpha},\boldsymbol{\beta},\boldsymbol{\kappa}) \leq R(\boldsymbol{\alpha},\boldsymbol{\beta},\boldsymbol{\kappa})$.
Proof: See Appendix F. □

Proposition 10. Starting from a feasible point $\boldsymbol{\Theta}^{(0)} = \left(\cdot,\cdot,\cdot,\boldsymbol{\alpha}^{(0)},\boldsymbol{\beta}^{(0)},\boldsymbol{\kappa}^{(0)}\right)$, the sequence of solutions $\boldsymbol{\Theta}^{(t)} = \left(\mathbf{M}^{(t)},\mathbf{W}^{(t)},\mathbf{p}^{(t)},\boldsymbol{\alpha}^{(t)},\boldsymbol{\beta}^{(t)},\boldsymbol{\kappa}^{(t)}\right)$, for $t \geq 1$, obtained by iteratively solving $\widetilde{\mathcal{P}}_1^{(t)}$ constitutes a sequence of enhanced points for $\widetilde{\mathcal{P}}_1$, which converges to a KKT point.
Proof: See Appendix G. □

To solve $\widetilde{\mathcal{P}}_1^{(t)}$, a feasible point $\boldsymbol{\Theta}^{(0)}$ is needed to guarantee convergence as explained in *Proposition 10*. We generate random initial feasible points and test them for feasibility, as described in [47]. We use the best of these points as the initial $\boldsymbol{\Theta}^{(0)}$, and iteratively solve $\widetilde{\mathcal{P}}_1^{(t)}$ as shown in Algorithm 1.

Algorithm 1: Optimization of $\mathcal{P}_1$

Step 1:	Define N_{iter}, δ, λ_α, λ_β, λ_κ.
Step 2:	Find an initial point $\boldsymbol{\Theta}^{(0)} = \left(\cdot,\cdot,\cdot,\boldsymbol{\alpha}^{(0)},\boldsymbol{\beta}^{(0)},\boldsymbol{\kappa}^{(0)}\right)$ using $\{0,1\}$ values.
Step 3:	Initialize $t = 1$.
Step 4:	Solve $\mathcal{P}_1^{(t)}$ using $\boldsymbol{\Theta}^{(t-1)}$.
Step 5:	Assign $\boldsymbol{\Theta}^{(t)} \leftarrow \boldsymbol{\Theta}^{(t-1)}$.
Step 6:	Update the iteration index t by one, i.e. $t = t + 1$.
Step 7:	Verify if the stop criterion is attained. Otherwise, return to *Step 4*.

We stop the iterative process when a criterion has been met, i.e., $t = N_{\text{iter}}$ or $\tilde{R}^{(t)}(\boldsymbol{\alpha},\boldsymbol{\beta},\boldsymbol{\kappa}) - \tilde{R}^{(t-1)}(\boldsymbol{\alpha},\boldsymbol{\beta},\boldsymbol{\kappa}) \leq \delta$. The computational complexity of $\widetilde{\mathcal{P}}_1^{(t)}$ is similar to that of one evaluation of $\mathcal{P}_0$. In particular, $N_v = 2LN_{\text{tx}}^{\text{MBS}} +$

$$(\mathrm{C}_3)\ \mathrm{L}_1 : \sum_{l\in\mathcal{L}} t_l^2 \le P_{\mathrm{tx}}^{\mathrm{MBS}},$$

$$(\mathrm{C}_{20})\ \mathrm{L}_2 : \left\| \left[2\widehat{\mathbf{w}}_{b,u}^H v_{b,u}, \kappa_{b,u} - p_{b,u} \right] \right\|_2 \le \kappa_{b,u} + p_{b,u}, \forall l \in \mathcal{L}, b \in \mathcal{B}_l, u \in \mathcal{U}_l,$$

$$(\mathrm{C}_{23})\ \mathrm{L}_3 : \left\| [\mathbf{S}_b \mathbf{v}, \sigma_{\mathrm{UE}}] \right\|_2 \le \sqrt{1+\Gamma_j^{\mathrm{UE}\,-1}}\, \mathsf{Re}\left\{ \sum_{b\in\mathcal{B}_l} c_{b,u} v_{b,u} \right\} + (1-\alpha_{u,j})\, Q_u, \forall l \in \mathcal{L}, u \in \mathcal{U}_l, j \in \mathcal{J}^{\mathrm{UE}},$$

$$(\mathrm{C}_{24})\ \mathrm{L}_4 : \mathsf{Re}\left\{ \sum_{b\in\mathcal{B}_l} c_{b,u} v_{b,u} \right\} \ge \alpha_{u,j} \sqrt{\Gamma_j^{\mathrm{UE}}} \sigma_{\mathrm{UE}}, \forall l \in \mathcal{L}, u \in \mathcal{U}_l, j \in \mathcal{J}^{\mathrm{UE}},$$

$$(\mathrm{C}_{25})\ \mathrm{L}_5 : \mathsf{Im}\left\{ \sum_{b\in\mathcal{B}_l} c_{b,u} v_{b,u} \right\} = 0, \forall l \in \mathcal{L}, u \in \mathcal{U}_l, j \in \mathcal{J}^{\mathrm{UE}}.$$

$$(\mathrm{C}_{26})\ \mathrm{L}_6 : \left\| [\mathbf{R}_b \mathbf{t}, \sigma_{\mathrm{SBS}}] \right\|_2 \le \sqrt{1+\Gamma_j^{\mathrm{SBS}\,-1}}\, r_{b,l} t_l + (1-\beta_{l,j})\, Q_b, \forall l \in \mathcal{L}, b \in \mathcal{B}_l, j \in \mathcal{J}^{\mathrm{SBS}},$$

$$(\mathrm{C}_{27})\ \mathrm{L}_7 : r_{b,l} t_l \ge \beta_{l,j} \sqrt{\Gamma_j^{\mathrm{SBS}}} \sigma_{\mathrm{SBS}}, \forall l \in \mathcal{L}, b \in \mathcal{B}_l, j \in \mathcal{J}^{\mathrm{SBS}},$$

$2LBUN_{\mathrm{tx}}^{\mathrm{SBS}} + 2LBU + LJ^{\mathrm{SBS}} + LUJ^{\mathrm{UE}}$ variables, $N_l = 3L + 2LU + 3LB + 2LJ^{\mathrm{SBS}} + 4LBU + 5LUJ^{\mathrm{UE}} + LBJ^{\mathrm{SBS}}$ linear constraints and $N_c = 1 + LBU + LUJ^{\mathrm{UE}} + LBJ^{\mathrm{SBS}}$ convex constraints. Therefore, the complexity is $\mathcal{O}\left(N_{\mathrm{iter}}(N_v)^3(N_l+N_c)\right)$, where N_{iter} is the number of iterations.

VII. RnP-SOCP-2: Proposed SOCP Formulation

This formulation is derived from problem $\mathcal{P}_1$. We propose an alternative relax-and-penalize SOCP algorithm, denoted by RnP-SOCP-2, whose main characteristic is the reduced number of optimization variables compared to RnP-SOCP-1, thus allowing to obtain solutions faster. To decrease the large number of optimization variables in $\mathcal{P}_1$, (essentially dominated by the number of antennas at the MBS and SBSs) we adopt a simpler approach in which instead of optimizing high-dimensional beamforming vectors, we only optimize their gains.

In particular, we define the variables $v_{b,u}$ and t_l as the gains (i.e., amplitude and phase) of predefined unicast (i.e., access) and multicast (i.e., backhaul) beamforming vectors $\widehat{\mathbf{w}}_{b,u}$ and $\widehat{\mathbf{m}}_l$, respectively, such that $\mathbf{m}_l = t_l \widehat{\mathbf{m}}_l$, $\mathbf{w}_{b,u} = v_{b,u}\widehat{\mathbf{w}}_{b,u}$, $\|\widehat{\mathbf{m}}_l\|_2^2 = 1$, $\|\widehat{\mathbf{w}}_{b,u}\|_2^2 = 1$. We design the unit-norm unicast beamforming vectors $\widehat{\mathbf{w}}_{b,u}$ using the zero-forcing (ZF) criterion. On the other hand, the unit-norm multicast beamforming vectors $\widehat{\mathbf{m}}_l$ are obtained experimentally upon evaluating the upper bound $\mathcal{P}_{\mathrm{UB}}$ for multiple realizations with varying degrees of shadowing and small-scale fading, and then taking the average of all these beamforming vectors. This procedure allows us to obtain a fair estimation of the multicast beamforming vectors because the SBSs are stationary and therefore the MBS-SBS channels geometry do not change substantially. Thus, the constraints that are affected by $\mathbf{m}_l = t_l\widehat{\mathbf{m}}_l$, $\mathbf{w}_{b,u} = v_{b,u}\widehat{\mathbf{w}}_{b,u}$ are C_3, C_{20},$\mathrm{C}_{23}-\mathrm{C}_{27}$ which are redefined at the top of this page, where $\mathbf{S}_b$ is a block diagonal matrix containing the combinations of beamformers $\widehat{\mathbf{w}}_{b,u}$ and channels for UE u, $c_{b,u} = \mathbf{h}_{b,u}^H \widehat{\mathbf{w}}_{b,u}$, $\mathbf{R}_b = \mathrm{diag}\left(\mathbf{g}_b^H \widehat{\mathbf{M}}\right)$, $r_{b,l} = \mathsf{Re}\left\{\mathbf{g}_b^H \widehat{\mathbf{m}}_l\right\}$.

After applying these changes, we define,

$$\mathcal{P}_2 : \max_{\boldsymbol{\Theta}} \quad R_{\mathrm{w-sum}}^{\mathrm{access}}(\boldsymbol{\alpha}) \quad \text{s.t.} \quad \underbrace{\boldsymbol{\Theta} \in \mathscr{D}}_{\text{convex}}, \underbrace{\mathrm{Z}_1 - \mathrm{Z}_3}_{\text{nonconvex}},$$

where $\boldsymbol{\Theta} = (\mathbf{t}, \mathbf{v}, \mathbf{p}, \boldsymbol{\alpha}, \boldsymbol{\beta}, \boldsymbol{\kappa})$ with $\mathscr{D}$ denoting the feasible set spanned by the constraints $\mathrm{L}_1 - \mathrm{L}_7, \mathrm{X}_1 - \mathrm{X}_3, \mathrm{C}_2, \mathrm{C}_7 - \mathrm{C}_{10}, \mathrm{C}_{12} - \mathrm{C}_{14}, \mathrm{C}_{17} - \mathrm{C}_{19}$. In a similar manner as with $\widetilde{\mathcal{P}}_1$, we define $\widetilde{\mathcal{P}}_2$, and thereupon its linearized version as $\widetilde{\mathcal{P}}_2^{(t)}$, which can be solved via Algorithm 1. $\widetilde{\mathcal{P}}_2^{(t)}$ is a SOCP program with $N_v = 2L + 4LBU + LJ^{\mathrm{SBS}} + LUJ^{\mathrm{UE}}$ decision variables, which roughly represent half of that used in BnC-MISOCP and RnP-SOCP-1 (for the evaluated settings). In addition, $\widetilde{\mathcal{P}}_2^{(t)}$ has $N_l = 3L + 2LU + 3LB + 2LBU + 3LUJ^{\mathrm{UE}} + LBJ^{\mathrm{SBS}}$ linear constraints and $N_c = 1 + LBU + LUJ^{\mathrm{UE}} + LBJ^{\mathrm{SBS}}$ convex constraints. Thus, the complexity of RnP-SOCP-2 is $\mathcal{O}\left(N_{\mathrm{iter}}(N_v)^3(N_l+N_c)\right)$, with N_{iter} denoting the number of iterations. Further, we note that RnP-SOCP-2 exhibits reduced complexity compared to RnP-SOCP-1.

VIII. Simulation Results

We evaluate the performance of RadiOrchestra in different scenarios with varying conditions. Throughout all simulations, we consider the following default parameters, unless specified otherwise. The carrier frequency is $f_c = 41$ GHz (V-band in FR2) with $W_{\mathrm{BW}}^{\mathrm{access}} = W_{\mathrm{BW}}^{\mathrm{backhaul}} = 100$ MHz bandwidth [36]. The channel models are UMa LOS for the backhaul and UMi LOS/NLOS for the access [36], which include path-loss, shadowing and small-scale fading. In the system, there are $L = 5$ clusters each having $B = 3$ SBSs and $U = 20$ UEs, thus making a total of $B_{\mathrm{total}} = 15$ SBSs and $U_{\mathrm{total}} = 100$ UEs. The MBS has a maximum transmit power of $P_{\mathrm{tx}}^{\mathrm{MBS}} = 36$ dBm and is equipped with a 16×4 antenna array ($N_{\mathrm{tx}}^{\mathrm{MBS}} = 64$) whereas the SBSs can transmit at a maximum power of $P_{\mathrm{tx}}^{\mathrm{SBS}} = 14$ dBm and have smaller 4×4 arrays ($N_{\mathrm{tx}}^{\mathrm{SBS}} = 16$). We assume that SBSs can support up to four UEs ($N_{\mathrm{streams}}^{\mathrm{SBS}} = 4$) simultaneously, and there are $U_{\mathrm{served}} = 4$ UEs served concurrently (i.e., in one slot) in each cluster. Further, all UEs have the same priority, i.e., $\omega_u = \frac{1}{L*U}$ and $\sum_{l\in\mathcal{L}} \sum_{u\in\mathcal{U}_l} \omega_u = 1$. In Table IV, we show the parameters for each scenario. The algorithms have been implemented using CVX and MOSEK on a computer with 16GB RAM and a Intel Core i7-6700 processor.

Scenario $\mathbf{S_1}$: Optimality gap and computational complexity. We benchmark the algorithms considering a small

Table IV: Simulation settings

Scenario	Backhaul network						Access network				
	$N_{\text{tx}}^{\text{MBS}}$	$P_{\text{tx}}^{\text{MBS}}$ [dBm]	L	B	B_{total}	χ_{backhaul}	$P_{\text{tx}}^{\text{SBS}}$ [dBm]	U	U_{total}	U_{served}	χ_{access}
S_1	64	$9, 12, \ldots, 27$	2	3	6	0	$6, 10, 14$	6	12	3	0
S_2	$16, 32, 48, 64$	$15, 18, \ldots, 36$	$1, 2, \ldots, 6$	3	$3, 6, \ldots, 18$	0	–	–	–	–	–
	64	$15, 18, \ldots, 36$	5	$1, 2, \ldots, 6$	$5, 10, \ldots, 30$	0	–	–	–	–	–
S_3	64	$15, 18, \ldots, 36$	5	3	15	0	$0, 2, \ldots, 14$	20	100	4	0
S_4	64	$18, 27, 36$	$2, 3, \ldots, 6$	3	$6, 9, \ldots, 18$	0	14	20	100	4	0
S_5	64	36	5	3	15	$[0, 1]$	14	20	100	4	$[0, 1]$
S_6	64	36	5	3	15	0	14	20	100	4 (slotted)	0

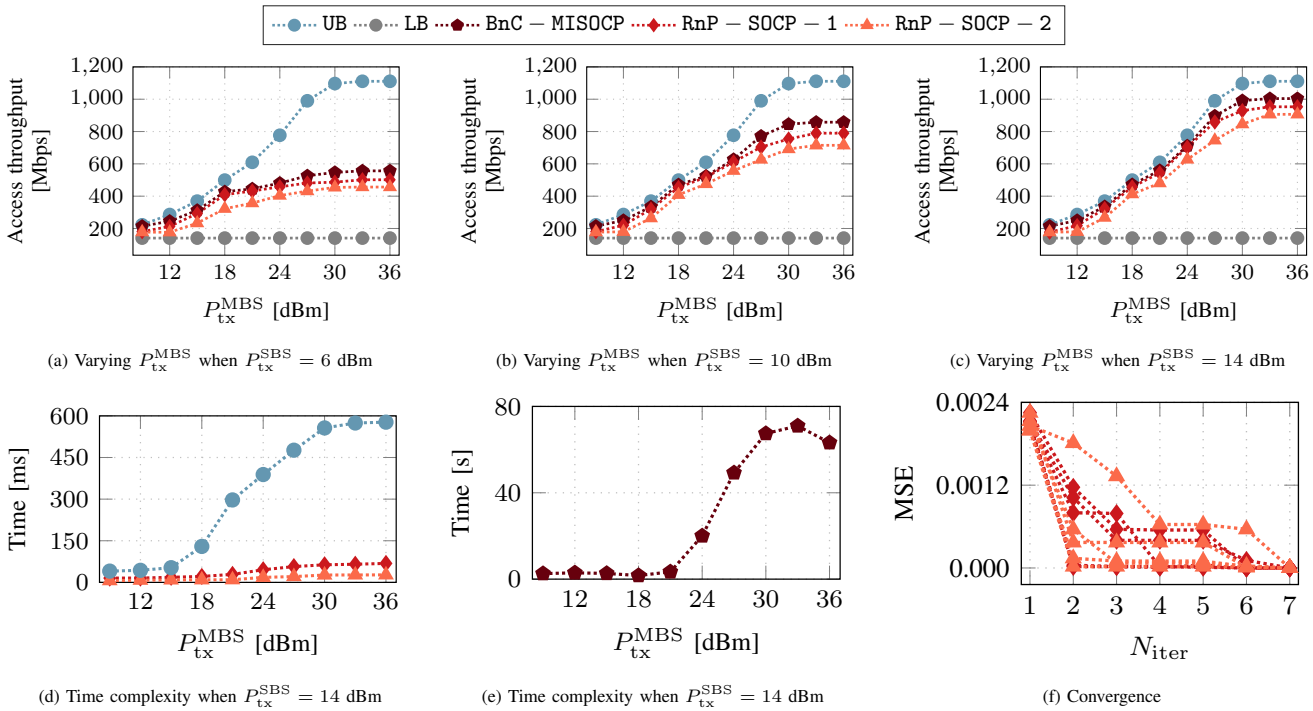

(a) Varying $P_{\text{tx}}^{\text{MBS}}$ when $P_{\text{tx}}^{\text{SBS}} = 6$ dBm

(b) Varying $P_{\text{tx}}^{\text{MBS}}$ when $P_{\text{tx}}^{\text{SBS}} = 10$ dBm

(c) Varying $P_{\text{tx}}^{\text{MBS}}$ when $P_{\text{tx}}^{\text{SBS}} = 14$ dBm

(d) Time complexity when $P_{\text{tx}}^{\text{SBS}} = 14$ dBm

(e) Time complexity when $P_{\text{tx}}^{\text{SBS}} = 14$ dBm

(f) Convergence

Figure 5: Evaluation of Scenario S_1. *We notice the small performance gap of `RnP-SOCP-1` and `RnP-SOCP-2` with respect to `BnC-MISOCP`, which is reasonable considering that their time complexities are smaller by 3 orders of magnitude. Because CVX needs to parse the mathematical model into a suitable structure for MOSEK, the results showing time complexity consider the raw solving time while neglecting the parsing time. Besides, we note that `UB` can be used for quick benchmarking when the access throughput bottleneck is originated by the backhaul network. In addition, we note that `LB` is loose as it is agnostic to the network conditions but provides an idea of the worst-case scenario without solving any problem. It becomes valuable when evaluating cases wherein the transmit power at the MBS or SBSs are limited as in Fig. 5a because under such conditions the lowest rates will very likely be allocated.*

setting, with the purpose of obtaining an optimal solution for `BnC-MISOCP` within a reasonable amount of time and compare its performance against that of `RnP-SOCP-1` and `RnP-SOCP-2`. Fig. 5a, Fig. 5b, Fig. 5c show the access throughput with various MBS and SBSs transmit powers. In particular, `RnP-SOCP-1` and `RnP-SOCP-2` are 5.1% and 9.7% below `BnC-MISOCP` when $P_{\text{tx}}^{\text{SBS}} = 14$ dBm (see Fig. 5c). Also, `UB` becomes tighter with increasing $P_{\text{tx}}^{\text{SBS}}$, e.g., within only 9.6% with respect to `BnC-MISOCP` in Fig. 5c. This occurs because `UB` only considers the backhaul throughput optimization, which depends on $P_{\text{tx}}^{\text{MBS}}$. Thus, as long as the bottleneck is originated in the access network (due to low transmit power at the SBSs), `UB` will not capture such limitations. With higher $P_{\text{tx}}^{\text{SBS}}$, as shown in Fig. 5c, the access throughput limitation is removed and is shifted to the backhaul network, where $P_{\text{tx}}^{\text{MBS}}$ is varied from a low to a high transmit power. As a result, in Fig. 5c the access throughput limitation is dominated by $P_{\text{tx}}^{\text{MBS}}$, where we recognize a high degree of similarity between `UB` and `BnC-MISOCP`. Therefore, `UB` can be used as a tight bound to evaluate the performance of the system whenever the SBSs can transmit at sufficiently high power.

On the other hand, Fig. 5d and Fig. 5e provide the time complexities when $P_{\text{tx}}^{\text{SBS}} = 14$ (as in Fig. 5c) showing that `RnP-SOCP-1` and `RnP-SOCP-2` are roughly 1000 and 2000 times computationally faster than `BnC-MISOCP`, respectively. Similarly, the time complexity of `UB` is approximately 100 times lighter than that of `BnC-MISOCP`. This huge difference is because the complexity of `BnC-MISOCP` is combinatorial, i.e., collapsing to exhaustive search in the worst case. Although this case may not be reached in practice, `BnC-MISOCP` requires to solve multiple convex problems to prune the infeasible branches and thus abridge the search process. However, `RnP-SOCP-1` and `RnP-SOCP-2` circumvent this issue by relaxing the binary variables, penalizing them and solving the problem in the continuous domain, which explains their reduced complexity. Besides, `UB` has a small number of optimization variables compared to `BnC-MISOCP`, explaining

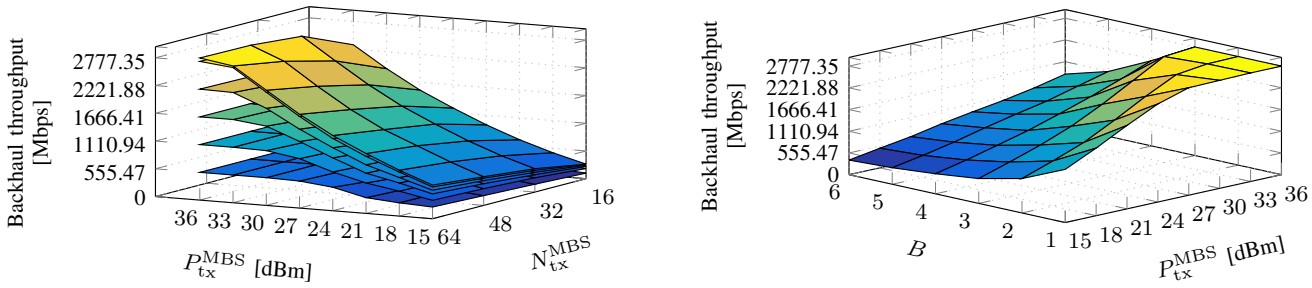

(a) Backhaul throughput for varying $P_{\text{tx}}^{\text{MBS}}$, $N_{\text{tx}}^{\text{MBS}}$ and L when $B = 3$.

(b) Backhaul throughput for varying B and $N_{\text{tx}}^{\text{MBS}}$ when $L = 5$.

Figure 6: Evaluation of Scenario S_2. *We note that* UB *can be used to evaluate multiple network configurations, thus providing insights of potentially optimal operations points that can be adopted in the planning phase of the network.*

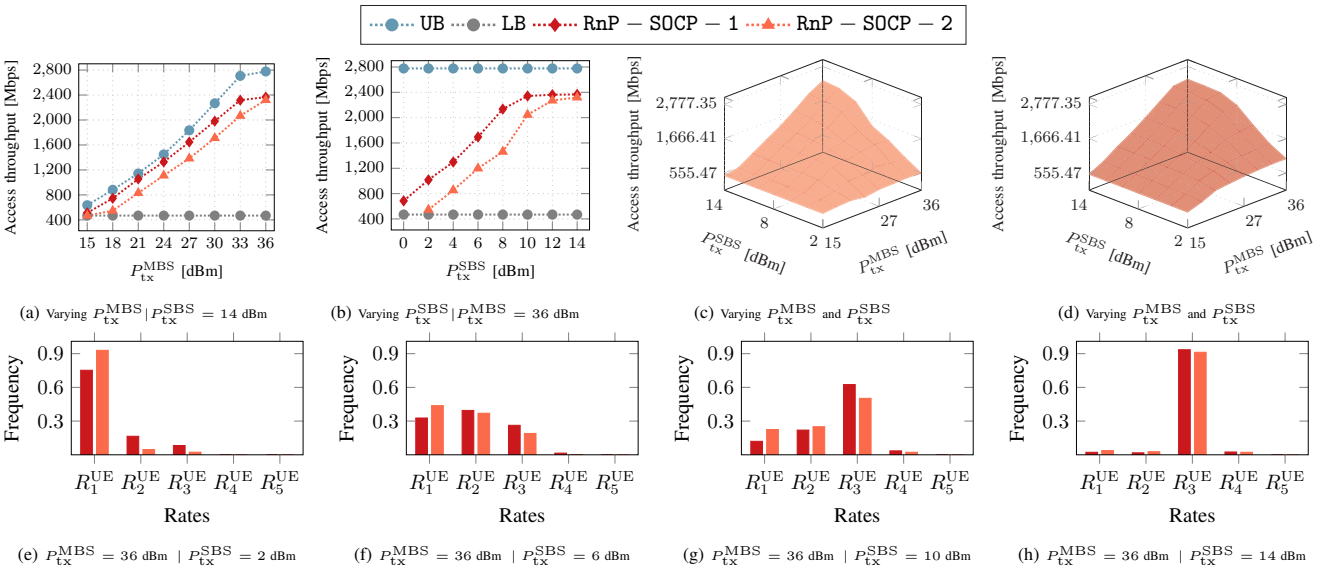

(a) Varying $P_{\text{tx}}^{\text{MBS}} | P_{\text{tx}}^{\text{SBS}} = 14$ dBm

(b) Varying $P_{\text{tx}}^{\text{SBS}} | P_{\text{tx}}^{\text{MBS}} = 36$ dBm

(c) Varying $P_{\text{tx}}^{\text{MBS}}$ and $P_{\text{tx}}^{\text{SBS}}$

(d) Varying $P_{\text{tx}}^{\text{MBS}}$ and $P_{\text{tx}}^{\text{SBS}}$

(e) $P_{\text{tx}}^{\text{MBS}} = 36$ dBm | $P_{\text{tx}}^{\text{SBS}} = 2$ dBm

(f) $P_{\text{tx}}^{\text{MBS}} = 36$ dBm | $P_{\text{tx}}^{\text{SBS}} = 6$ dBm

(g) $P_{\text{tx}}^{\text{MBS}} = 36$ dBm | $P_{\text{tx}}^{\text{SBS}} = 10$ dBm

(h) $P_{\text{tx}}^{\text{MBS}} = 36$ dBm | $P_{\text{tx}}^{\text{SBS}} = 14$ dBm

Figure 7: Evaluation of Scenario S_3. *We note that maximizing the access throughput is highly dependent on both backhaul and access network parameters, which highlights the importance of jointly optimizing them.*

its faster solving time. Note that the time complexities grow with increasing $P_{\text{tx}}^{\text{MBS}}$ because a higher $P_{\text{tx}}^{\text{MBS}}$ enables the allocation of a wider range of rates thus needing more evaluations, specially by BnC-MISOCP and UB. Further, Fig. 5f shows the convergence of RnP-SOCP-1 and RnP-SOCP-2 for 5 different realizations. Here, we measured the error of the binary variables with respect to their rounded versions and computed the mean squared error (MSE), showing that after 6 or 7 iterations the error converges to zero, i.e., the relaxed binary variables values become integer.

Scenario S_2: Upper bound as a means of network planning. Since UB is much simpler to solve than BnC-MISOCP (as shown in Fig. 5d and Fig. 5e), we can use UB in larger settings to examine multiple configurations of number of antennas, transmit power, number of clusters and cluster size. From the planning perspective, these results are valuable as they allow us to choose suitable operation points for the network. In Fig. 6a, we show the backhaul throughput (i.e., the objective of UB) for various combinations of $P_{\text{tx}}^{\text{MBS}}$, $N_{\text{tx}}^{\text{MBS}}$, L, where the bottommost and uppermost layers represent $L = 1$ (one cluster) and $L = 6$ (six clusters), respectively. We observe that the backhaul throughput improves with increasing number of antennas and transmit power because more antennas enhance the multiplexing capability while a higher power allows transmitting at higher rates. However, when the number of clusters grows from $L = 5$ to $L = 6$, the throughput saturates showing marginal improvement because the scenario becomes more interference limited (due to more SBSs deployed). *We realize that with* $N_{\text{tx}}^{\text{MBS}} = 64$ *antennas,* $P_{\text{tx}}^{\text{MBS}} = 36$ *dBm transmit power and* $L = 5$ *clusters, the backhaul network can be operated at its full capacity*. In Fig. 6a, we considered $B = 3$, but we validate such decision in Fig. 6b, where we illustrate the backhaul throughput for various combinations of $P_{\text{tx}}^{\text{MBS}}$ and B when $L = 5$. We note that the throughput decreases when the cluster size increases from $B = 1$ to $B = 6$ because, to reach more SBSs, higher MBS power is consumed but also more interference is generated due to more SBSs scattered. However, a larger SBS cluster is preferred because *(i)* more UEs can be served (each SBS can serve a limited number of UEs) and *(ii)* UEs can be allocated higher rates by being connected to more SBSs. With $B = 3$, still the maximum backhaul throughput can be achieved.

Scenario S_3: Impact of the transmit power. Fig. 7a, Fig. 7b, Fig. 7c and Fig. 7d illustrate how the variation of transmit

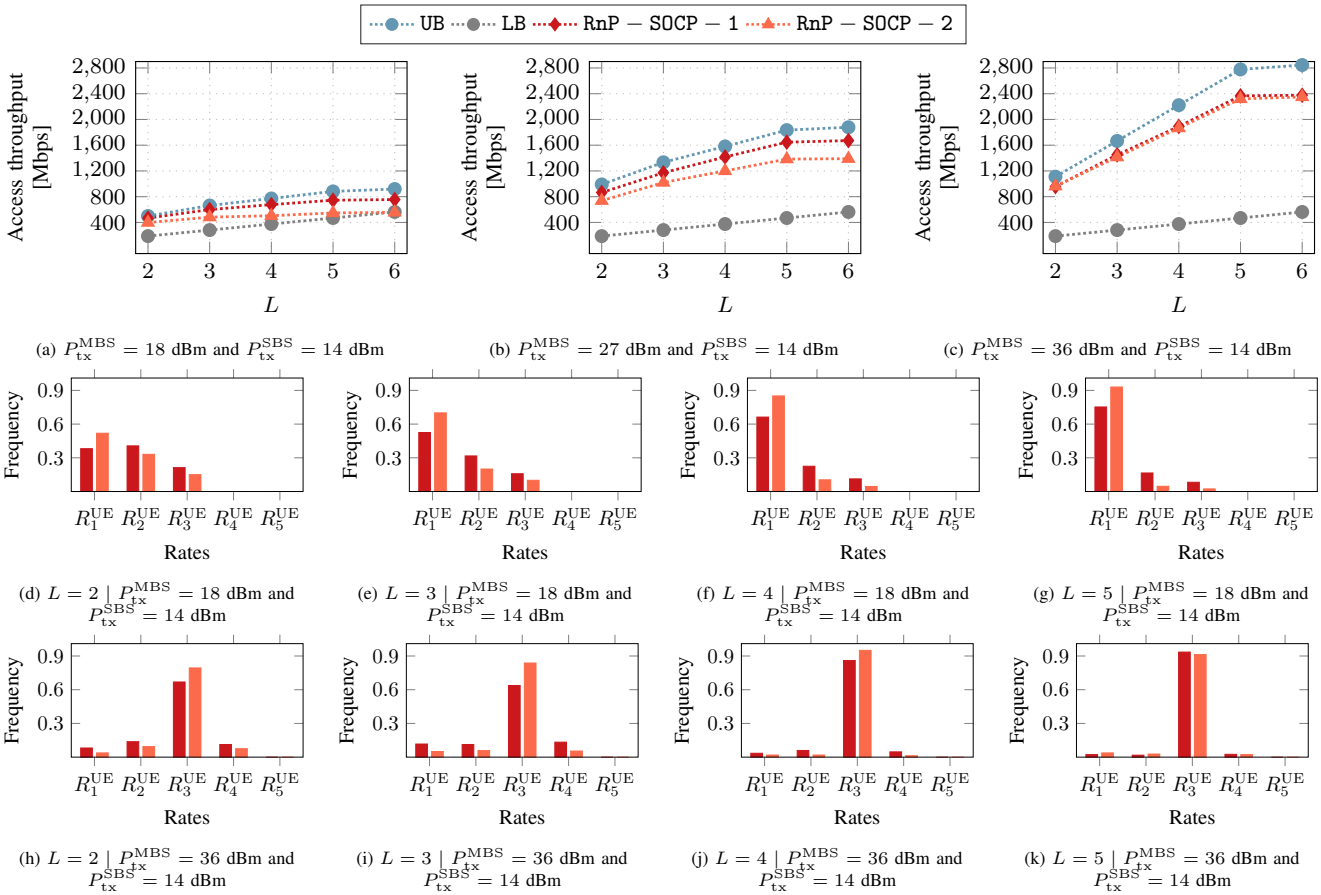

Figure 8: Evaluation of Scenario S_4. *We note that the overall access throughput can be expanded with more clusters (i.e., more SBSs and UEs). However, this improvement may saturate beyond a number of clusters due to more interference or insufficient transmit power.*

power at the MBS and SBSs impacts the access network throughput. Fig. 7a shows the case when $P_{tx}^{SBS} = 14$ dBm and P_{tx}^{MBS} is varied. As observed, the access throughput improves as the MBS increases its transmit power, which is logical since the backhaul capacity is naturally expanded with higher power. Similarly, Fig. 7b shows the case when $P_{tx}^{MBS} = 36$ dBm and P_{tx}^{SBS} is varied. We note that the access throughput improves as the SBSs increase their transmit power. This occurs because higher SBSs power enables UEs to be assigned higher rates. We observe in Fig. 7a and Fig. 7b that when $P_{tx}^{MBS} = 36$ dBm and $P_{tx}^{SBS} = 14$, both `RnP-SOCP-1` and `RnP-SOCP-2` achieve nearly the same performance although `RnP-SOCP-2` grows at a slower rate. This slower improvement stems from the fact that the beamforming vectors for `RnP-SOCP-2` are predesigned and only their gains can be optimized, thus allowing for less flexibility compared to `RnP-SOCP-1`. Thus, their performance meet only in the presence of high MBS/SBSs transmit power. At this point, the gap compared to `UB` is 14.8% and 16.5% for `RnP-SOCP-1` and `RnP-SOCP-2`, respectively. Fig. 7c and Fig. 7d show the effect of varying both P_{tx}^{SBS} and P_{tx}^{MBS}. In Fig. 7e, Fig. 7f, Fig. 7g, Fig. 7h, we show the allocation of UE rates when $P_{tx}^{MBS} = 36$ and P_{tx}^{SBS} is varied gradually from a low to a high power. At lower P_{tx}^{SBS} as in Fig. 7e, the UEs are mainly assigned the lowest rates. As P_{tx}^{SBS} becomes higher, it becomes possible to allocate higher rates to the UEs, as observed in Fig. 7h.

Scenario S_4: Impact of the number of clusters. Fig. 8a, Fig. 8b, Fig. 8c show the access throughput when $P_{tx}^{SBS} = 14$ dBm and the number of clusters is varied from $L = 2$ to $L = 6$ for different P_{tx}^{MBS} values. The access throughput improves with increasing L because more clusters translates to more served UEs (there are U_{served} UEs per cluster), and hence the higher aggregate rate. Besides, higher P_{tx}^{MBS} also improves the access throughput because it boosts the backhaul network capacity. In particular, we observe throughput saturation when increasing from $L = 5$ to $L = 6$, which is consistent with the behavior observed in Fig. 6a where the backhaul network throughput was evaluated. Further, we note that `RnP-SOCP-1` outperforms `RnP-SOCP-2` when $P_{tx}^{MBS} = \{18, 27\}$ dBm. However, for sufficiently high $P_{tx}^{MBS} = 36$ dBm, the performance of both are comparable. Besides, we examine the UE rate allocation in Fig. 8d, Fig. 8e, Fig. 8f and Fig. 8g assuming $P_{tx}^{MBS} = 18$ dBm, $P_{tx}^{SBS} = 14$ dBm. We observe that when the number of clusters is small, e.g. $L = 2$ (see Fig. 8d), the rates assigned to the UEs span a wider range compared to the case when $L = 5$ (see Fig. 8g). The reason for this behavior is that more interference is generated in the backhaul network with $L = 5$ than with $L = 2$. In particular, with $L = 2$, only two signals are transmitted whereas with $L = 5$, five different signals are sent from the MBS, thus

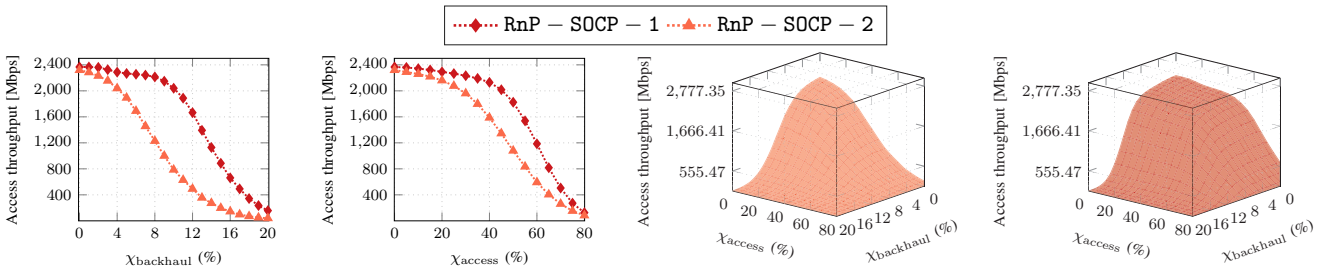

(a) Imprecise backhaul channel (b) Imprecise access channel (c) Imprecise channels (d) Imprecise channels

Figure 9: Evaluation of Scenario S_5. *We have used the model* $\mathbf{c} = \sqrt{1-\chi^2}\hat{\mathbf{c}} + \chi\mathbf{p}$ *to emulate imprecise channel conditions, where* $\mathbf{c}$ *is the estimated channel,* $\hat{\mathbf{c}}$ *is the exact access/backhaul channel (but unknown),* $\chi \in [0,1]$ *is the degree at which the perturbation contaminates the channel, and* $\mathbf{p} \sim \left(\mathbf{0}, \|\hat{\mathbf{c}}\|_2^2 \mathbf{I}/K\right)$ *is a random perturbation, where* K *is the length of* $\hat{\mathbf{c}}$*. We note the importance of careful provision of the backhaul network because it is the link with highest importance delivering data to the UEs. A potential disruption affecting this link causes a degradation of the whole network whereas impairments in the individual access links do not have a significant impact on the overall network performance. We underline a fundamental difference regarding the impact of imperfect CSI in system models assuming discrete or continuous rates. While CSI variations affect both systems, it has more detrimental consequences in the discrete-rate case. For instance, in continuous-rate models, a CSI variation will produce a SINR different from the expected thus also affecting the rate. However, the resulting rate will still be feasible for the model due to being continuous. On the contrary, in discrete-rate models, if the SINR is below the required target, the data will not be decoded by the SBS/UE thus causing the resulting rate to drop to zero.*

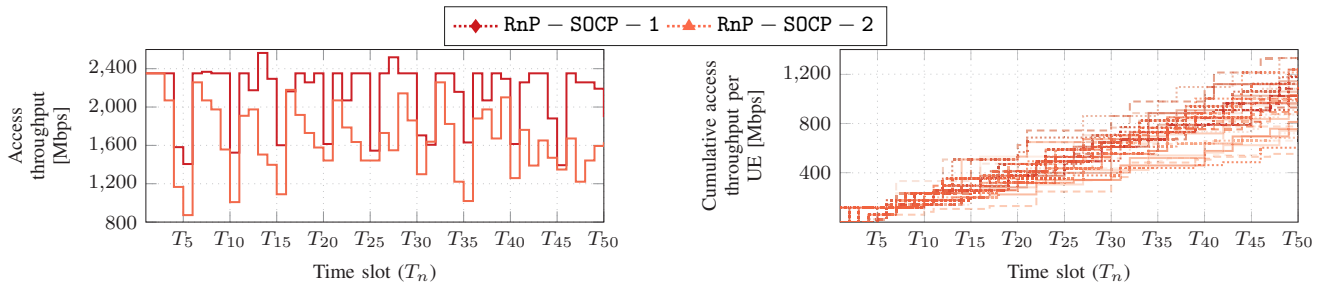

(a) Serving $U_{\text{served}} = 4$ UEs per cluster per slot. (b) Displaying the individual rates of all UEs in cluster $\mathcal{U}_1$.

Figure 10: Evaluation of Scenario S_6. *We observe that it is possible to serve all UEs in a system by allocating them in multiple slots, showing that RadiOrchestra is scalable. In addition, the UE rates can be adapted to enforce different priorities based on any network policy of the operator. In this example, we aimed at improving fairness among UEs.*

generating more interference at the receiving SBSs. In Fig. 8h, Fig. 8i, Fig. 8j and Fig. 8k we also examine the UE rates assuming $P_{\text{tx}}^{\text{MBS}} = 36$ dBm, $P_{\text{tx}}^{\text{SBS}} = 14$ dBm. In this case, the backhaul network has sufficiently high power. As a result, throughout Fig. 8h, Fig. 8i, Fig. 8j and Fig. 8k, the distribution of rates remains more or less similar.

Scenario S_5: Impact of imprecise channel estimation. Fig. 9a shows the access throughput when the access channels are estimated perfectly but the backhaul channels inaccurately. Here, the channel energy variation is represented by ξ_{backhaul}. Although backhaul channels are generally static due to fixed positions of MBS and SBS, it is important to test the network against estimation errors that may arise due to hardware miscalibration or impairments. We observe that as the degree of error in the backhaul channels increases, the access throughput is affected more severely due to information that cannot be decoded by the SBSs and therefore not relayed to the UEs. Further, `RnP-SOCP-1` is more robust than `RnP-SOCP-2` to dealing with such imprecisions because `RnP-SOCP-2` only optimizes the beamformers gains, making it less robust to perturbations. With `RnP-SOCP-1` and `RnP-SOCP-2`, the throughput decreases 4.2% and 18.4%, respectively when the channel energy varies within $\xi_{\text{backhaul}} = 5\%$, and 10.1% and 58.5%, respectively when the channel energy varies within $\xi_{\text{backhaul}} = 10\%$. Fig. 9b shows the access throughput when the access channels are estimated inaccurately but the backhaul channels perfectly, and the error energy is represented by ξ_{access}. The access channel may be inaccurately estimated due to UE mobility, feedback quantization or unmanaged interference from other networks.

We note that the access throughput with `RnP-SOCP-1` and `RnP-SOCP-2` only suffers a decay of 9.9% and 31.6%, respectively, even when the access channels change within $\xi_{\text{access}} = 40\%$, which is much less compared to the case in Fig. 9a. The reason for this outcome is that a disruption in an access link may cause only a single UE not being able to decode its information (since its SINR may decrease). In contrast, a disruption in a backhaul link may cause many SBSs in a cluster to be automatically unsupplied, thus making them unable to deliver data to the UEs. In addition, the multicast topology of the backhaul network is more susceptible to channel variations, since the link with the weakest condition limits the data rate for the whole SBS cluster. On the other hand, Fig. 9c and Fig. 9d show the access throughput performance when both the access and backhaul channels contain estimation errors.

Scenario S_6: Time-slotted evaluation. We have evaluated the access throughput considering that all UEs have the same priorities. However, the UE priorities (weights) can be

adjusted, for instance, to balance the cumulative throughput so that all UEs experience a similar degree of fairness over time. To realize this, we evaluate the algorithms in a slotted manner. Assuming $L = 5$, $U = 20$, $U_{\text{served}} = 4$, the network needs 5 slots to allocate the 100 UEs, i.e., in each slot, 20 UEs are simultaneously served with 4 UEs per cluster. In Fig. 10a, we show the access throughput for `RnP-SOCP-1` and `RnP-SOCP-2` during 50 slots of equal duration $T = T_n - T_{n-1}$ and assuming that the channel is estimated every 5 slots, i.e., once all the UEs have been served, a new UE scheduling with a different channel is considered. In particular, in every cluster, in time slot T_1, 4 UEs out of 20 are chosen; in slot T_2, 4 out of 16 are chosen; in slot T_3, 4 out of 12 are chosen, in slot T_4, 4 out of 8, and in slot T_5 the remaining 4 UEs are served. In slot T_6, the weights are updated based on the cumulative rate the UEs have experienced according to $w_u^{(n)} = \frac{1}{T\sum_{i=1}^{n} r_u^{(i-1)}}$ (up to normalization), where $r_u^{(i)}$ is the rate of UE u in slot T_i. In slot T_6, another 4 UEs out of 20 are chosen (possibly a different UE batch than in slot T_1). The process continues in this manner, updating the weights every 5 slots. In Fig. 10b, we show the individual cumulative throughput for all 20 UEs in cluster $\mathcal{U}_1$. We realize that the throughput experienced by the UEs tend to be similar as the deviation from each other is small, which is achieved due to the adaption of weights.

IX. Conclusions

Self-backhauling millimeter-wave networks are a key enabler for dense deployments by virtue of reducing costs (not needing fiber links) and facilitating higher flexibility through usage of wireless links. However, designing efficient and practical solutions for such systems are extremely complex due to the intertwined nature of backhaul and radio access networks that are not straightforward to model, and intrinsically result in complex problems with coupled optimization variables that are challenging to solve. In this paper, RadiOrchestra demonstrated how to tame this complexity with a series of design choices in the system, and providing mathematical formulation and optimization of radio resources. We proposed three formulations and their respective algorithms, `BnC-MISOCP`, `RnP-SOCP-1` and `RnP-SOCP-2`, to jointly optimize beamforming, user association, rate selection and admission control with the aim of maximizing the access network throughput. Our complexity analysis showed that `RnP-SOCP-1` and `RnP-SOCP-2` are less complex than `BnC-MISOCP` while the simulation results illustrated that their performance remained within 16.5% of the upper bound. We believe this attractive complexity-performance trade-off is key to potential adaptation of RadiOrchestra in future systems. RadiOrchestra can be extended in several directions. In RadiOrchestra we considered that both the access and backhaul networks operate over a fixed bandwidth. However, to make the approach more flexible and therefore capable of dealing with unbalanced channel conditions, bandwidth optimization could be incorporated as an additional degree of freedom. Another direction is expanding RadiOrchestra to be robust against channel imprecisions at both the access and backhaul networks to ultimately preserve the integrity of data. While current networks are centralized, enabling distributed optimization algorithms is desirable due to lower latency. Thus, a possible direction of expanding RadiOrchestra is to parallelize the optimization to let each SBS cluster optimize the resources without a central coordinator.

Acknowledgment

The research is in part funded by the Deutsche Forschungsgemeinschaft (DFG) within the B5G-Cell project in SFB 1053 MAKI, by the LOEWE initiative (Hesse, Germany) within the emergenCITY center, and by the European Commission through Grant No. 101017109 (DAEMON project).

References

[1] X. Ge, S. Tu, G. Mao, C.-X. Wang, and T. Han, "5G Ultra-Dense Cellular Networks," *IEEE Wireless Communications*, vol. 23, no. 1, pp. 72–79, 2016.

[2] J. An, K. Yang, J. Wu, N. Ye, S. Guo, and Z. Liao, "Achieving Sustainable Ultra-Dense Heterogeneous Networks for 5G," *IEEE Communications Magazine*, vol. 55, no. 12, pp. 84–90, 2017.

[3] N. Wang, E. Hossain, and V. K. Bhargava, "Backhauling 5G Small Cells: A Radio Resource Management Perspective," *IEEE Wireless Communications*, vol. 22, no. 5, pp. 41–49, 2015.

[4] 3GPP, "5G; NR; Integrated Access and Backhaul (IAB) Electromagnetic Compatibility (EMC)," 3rd Generation Partnership Project (3GPP), Technical Specification (TS) 38.175, 11 2020, version 16.0.0.

[5] G. Americas, "Innovations in 5G Backhaul Technologies," White Paper, 06 2020.

[6] E. G. Larsson, O. Edfors, F. Tufvesson, and T. L. Marzetta, "Massive MIMO for Next Generation Wireless Systems," *IEEE Communications Magazine*, vol. 52, no. 2, pp. 186–195, 2014.

[7] M. Polese, M. Giordani, T. Zugno, A. Roy, S. Goyal, D. Castor, and M. Zorzi, "Integrated Access and Backhaul in 5G mmWave Networks: Potential and Challenges," *IEEE Communications Magazine*, vol. 58, no. 3, pp. 62–68, 2020.

[8] S. Hur, T. Kim, D. J. Love, J. V. Krogmeier, T. A. Thomas, and A. Ghosh, "Millimeter Wave Beamforming for Wireless Backhaul and Access in Small Cell Networks," *IEEE Trans. Commun.*, vol. 61, no. 10, pp. 4391–4403, 2013.

[9] C. Pan, H. Zhu, N. J. Gomes, and J. Wang, "Joint Precoding and RRH Selection for User-Centric Green MIMO C-RAN," *IEEE Trans. Wireless Commun.*, vol. 16, no. 5, pp. 2891–2906, 2017.

[10] E. Chen, M. Tao, and N. Zhang, "User-Centric Joint Access-Backhaul Design for Full-Duplex Self-Backhauled Wireless Networks," *IEEE Trans. Commun.*, vol. 67, no. 11, pp. 7980–7993, 2019.

[11] L. Lei, E. Lagunas, S. Chatzinotas, and B. Ottersten, "NOMA Aided Interference Management for Full-Duplex Self-Backhauling HetNets," *IEEE Communications Letters*, vol. 22, no. 8, pp. 1696–1699, 2018.

[12] X. Huang, G. Xue, R. Yu, and S. Leng, "Joint Scheduling and Beamforming Coordination in Cloud Radio Access Networks With QoS Guarantees," *IEEE Transactions on Vehicular Technology*, vol. 65, no. 7, pp. 5449–5460, 2016.

[13] T. H. L. Dinh, M. Kaneko, E. H. Fukuda, and L. Boukhatem, "Energy Efficient Resource Allocation Optimization in Fog Radio Access Networks With Outdated Channel Knowledge," *IEEE Trans. Green Commun. Netw.*, vol. 5, no. 1, pp. 146–159, 2021.

[14] H. T. Nguyen, H. D. Tuan, T. Q. Duong, H. V. Poor, and W.-J. Hwang, "Nonsmooth Optimization Algorithms for Multicast Beamforming in Content-Centric Fog Radio Access Networks," *IEEE Trans. Signal Process.*, vol. 68, pp. 1455–1469, 2020.

[15] L. Chen, F. R. Yu, H. Ji, B. Rong, X. Li, and V. C. M. Leung, "Green Full-Duplex Self-Backhaul and Energy Harvesting Small Cell Networks With Massive MIMO," *IEEE J. Sel. Topics Signal Process.*, vol. 34, no. 12, pp. 3709–3724, 2016.

[16] Y. Chen, S. He, Y. Huang, J. Ren, and L. Yang, "Robust Multigroup Multicast Beamforming Design for Backhaul-Limited Cloud Radio Access Network," *IEEE Signal Processing Letters*, vol. 26, no. 1, pp. 189–193, 2019.

[17] G. Kwon and H. Park, "Joint User Association and Beamforming Design for Millimeter Wave UDN With Wireless Backhaul," *IEEE J. Sel. Topics Signal Process.*, vol. 37, no. 12, pp. 2653–2668, 2019.

[18] T. K. Vu, M. Bennis, S. Samarakoon, M. Debbah, and M. Latva-aho, "Joint Load Balancing and Interference Mitigation in 5G Heterogeneous

Networks," *IEEE Trans. Wireless Commun.*, vol. 16, no. 9, pp. 6032–6046, 2017.

[19] B. Hu, C. Hua, J. Zhang, C. Chen, and X. Guan, "Joint Fronthaul Multicast Beamforming and User-Centric Clustering in Downlink C-RANs," *IEEE Trans. Wireless Commun.*, vol. 16, no. 8, pp. 5395–5409, 2017.

[20] Y. Cheng, A. Philipp, and M. Pesavento, "Dynamic Rate Adaptation and Multiuser Downlink Beamforming Using Mixed Integer Conic Programming," in *EURASIP European Signal Processing Conference (EUSIPCO)*, 2012, pp. 824–828.

[21] Y. Cheng and M. Pesavento, "Joint Discrete Rate Adaptation and Downlink Beamforming Using Mixed Integer Conic Programming," *IEEE Trans. Signal Process.*, vol. 63, no. 7, pp. 1750–1764, 2015.

[22] Y. Cheng, M. Pesavento, and A. Philipp, "Joint Network Optimization and Downlink Beamforming for CoMP Transmissions Using Mixed Integer Conic Programming," *IEEE Trans. Signal Process.*, vol. 61, no. 16, pp. 3972–3987, 2013.

[23] D. H. N. Nguyen, L. B. Le, and T. Le-Ngoc, "Optimal Dynamic Point Selection for Power Minimization in Multiuser Downlink CoMP," *IEEE Trans. Wireless Commun.*, vol. 16, no. 1, pp. 619–633, 2017.

[24] M. Sanjabi, M. Razaviyayn, and Z.-Q. Luo, "Optimal Joint Base Station Assignment and Beamforming for Heterogeneous Networks," *IEEE Trans. Signal Process.*, vol. 62, no. 8, pp. 1950–1961, 2014.

[25] H. Ghauch, M. M. U. Rahman, S. Imtiaz, C. Qvarfordt, M. Skoglund, and J. Gross, "User Assignment in C-RAN Systems: Algorithms and Bounds," *IEEE Trans. Wireless Commun.*, vol. 17, no. 6, pp. 3889–3902, 2018.

[26] S. X.-Y. Ni and A. M.-C. So, "Mixed-Integer Semidefinite Relaxation of Joint Admission Control and Beamforming: An SOC-Based Outer Approximation Approach with Provable Guarantees," in *IEEE SPAWC*, 2018, pp. 1–5.

[27] A. Bandi, M. R. B. Shankar, S. Chatzinotas, and B. Ottersten, "Joint User Grouping, Scheduling, and Precoding for Multicast Energy Efficiency in Multigroup Multicast Systems," *IEEE Trans. Wireless Commun.*, vol. 19, no. 12, pp. 8195–8210, 2020.

[28] A. Alizadeh and M. Vu, "Load Balancing User Association in Millimeter Wave MIMO Networks," *IEEE Trans. Wireless Commun.*, vol. 18, no. 6, pp. 2932–2945, 2019.

[29] A. Pizzo and L. Sanguinetti, "Optimal Design of Energy-Efficient Millimeter Wave Hybrid Transceivers for Wireless Backhaul," in *International Symposium on Modeling and Optimization in Mobile, Ad Hoc, and Wireless Networks (WiOpt)*, 2017, pp. 1–8.

[30] M. Tao, E. Chen, H. Zhou, and W. Yu, "Content-Centric Sparse Multicast Beamforming for Cache-Enabled Cloud RAN," *IEEE Trans. Wireless Commun.*, vol. 15, no. 9, pp. 6118–6131, 2016.

[31] E. Chen, M. Tao, and Y.-F. Liu, "Joint Base Station Clustering and Beamforming for Non-Orthogonal Multicast and Unicast Transmission With Backhaul Constraints," *IEEE Trans. Wireless Commun.*, vol. 17, no. 9, pp. 6265–6279, 2018.

[32] H. H. M. Tam, H. D. Tuan, D. T. Ngo, T. Q. Duong, and H. V. Poor, "Joint Load Balancing and Interference Management for Small-Cell Heterogeneous Networks With Limited Backhaul Capacity," *IEEE Trans. Wireless Commun.*, vol. 16, no. 2, pp. 872–884, 2017.

[33] B. Hu, C. Hua, C. Chen, and X. Guan, "Joint Beamformer Design for Wireless Fronthaul and Access Links in C-RANs," *IEEE Trans. Wireless Commun.*, vol. 17, no. 5, pp. 2869–2881, 2018.

[34] D. Yuan, H.-Y. Lin, J. Widmer, and M. Hollick, "Optimal and Approximation Algorithms for Joint Routing and Scheduling in Millimeter-Wave Cellular Networks," *IEEE/ACM Trans. Netw.*, vol. 28, no. 5, pp. 2188–2202, 2020.

[35] A. Ortiz, A. Asadi, G. H. Sim, D. Steinmetzer, and M. Hollick, "SCAROS: A Scalable and Robust Self-Backhauling Solution for Highly Dynamic Millimeter-Wave Networks," *IEEE J. Sel. Areas Commun.*, vol. 37, no. 12, pp. 2685–2698, 2019.

[36] 3GPP, "Study on Channel Model for Frequencies from 0.5 to 100 GHz," 3rd Generation Partnership Project (3GPP), Technical Report (TR) 38.901, 2017, version 14.00.

[37] N. Bornhorst, M. Pesavento, and A. B. Gershman, "Distributed Beamforming for Multi-Group Multicasting Relay Networks," *IEEE Trans. Signal Process.*, vol. 60, no. 1, pp. 221–232, 2012.

[38] 3GPP, "5G; NR; Physical Layer Procedures for Data," 3rd Generation Partnership Project (3GPP), Technical Specification (TS) 38.214, 2020, version 16.2.0.

[39] K. K. Leung and W. Li-Chun, "Integrated Link Adaptation and Power Control to Improve Error and Throughput Performance in Broadband Wireless Packet Networks," *IEEE Trans. Wireless Commun.*, vol. 1, no. 4, pp. 619–629, 2002.

[40] R. Kovalchukov, D. Moltchanov, Y. Gaidamaka, and E. Bobrikova, "An Accurate Approximation of Resource Request Distributions in Millimeter Wave 3GPP New Radio Systems," in *Internet of Things, Smart Spaces, and Next Generation Networks and Systems*, O. Galinina, S. Andreev, S. Balandin, and Y. Koucheryavy, Eds. Cham: Springer International Publishing, 2019, pp. 572–585.

[41] N. V. Sahinidis, "Mixed-integer Nonlinear Programming 2018," *Optim. Eng.*, vol. 20, no. 2, p. 301–306, 2019.

[42] G. B. Dantzig, "Programming in a Linear Structure," 1948, uSA, Washington D.C.

[43] D. Christopoulos, S. Chatzinotas, and B. Ottersten, "Multicast Multigroup Precoding and User Scheduling for Frame-Based Satellite Communications," *IEEE Trans. Wireless Commun.*, vol. 14, no. 9, pp. 4695–4707, 2015.

[44] E. Che, H. D. Tuan, and H. H. Nguyen, "Joint Optimization of Cooperative Beamforming and Relay Assignment in Multi-User Wireless Relay Networks," *IEEE Trans. Wireless Commun.*, vol. 13, no. 10, pp. 5481–5495, 2014.

[45] J. Nocedal and S. Wright, *Numerical Optimization*. New York, USA: Springer-Verlag, 2006.

[46] A. H. Phan, H. D. Tuan, H. H. Kha, and D. T. Ngo, "Nonsmooth Optimization for Efficient Beamforming in Cognitive Radio Multicast Transmission," *IEEE Trans. Signal Process.*, vol. 60, no. 6, pp. 2941–2951, 2012.

[47] A. Bandi, M. R. B. Shankar, S. Chatzinotas, and B. Ottersten, "A Joint Solution for Scheduling and Precoding in Multiuser MISO Downlink Channels," *IEEE Trans. Wireless Commun.*, vol. 19, no. 1, pp. 475–490, 2020.

[48] M. Bengtsson and B. Ottersten, "Optimal and Suboptimal Transmit Beamforming," in *Handbook of Antennas in Wireless Communications*, L. C. Godara, Ed., CRC Press, 2001.

[49] H. Chen, A. B. Gershman, and S. Shahbazpanahi, "Distributed Peer-to-Peer Beamforming for Multiuser Relay Networks," in *IEEE International Conference on Acoustics, Speech and Signal Processing (ICASSP)*, 2009, pp. 2265–2268.

[50] B. R. Marks and G. P. Wright, "A General Inner Approximation Algorithm for Nonconvex Mathematical Programs," *Operations Research*, vol. 26, no. 4, pp. 681–683, 1978.

APPENDIX A: PROOF OF PROPOSITION 2

In constraints $\bar{\mathrm{C}}_4$ and C_5, the beamformer $\mathbf{w}_{b,u}$ and binary variable $\kappa_{b,u}$ are tied. This leads to obtain zero-beamformers for unserved UEs. To ensure the same effect after removing the multiplicative coupling between $\mathbf{w}_{b,u}$ and $\kappa_{b,u}$, additional constraints are required. First, we define the auxiliary variable $p_{b,u}$ representing the power of the beamformer from SBS b to UE u, which leads us to declare the following constraint, $\mathrm{C}_{17}: p_{b,u} \geq 0, \forall l \in \mathcal{L}, b \in \mathcal{B}_l, u \in \mathcal{U}_l$. Considering, the newly introduced variable, constraint $\bar{\mathrm{C}}_4$ is redefined as $\mathrm{C}_{18}: \sum_{u \in \mathcal{U}_l} p_{b,u} \leq P_{\mathrm{tx}}^{\mathrm{SBS}}, \forall l \in \mathcal{L}, b \in \mathcal{B}_l$. In addition, the power $p_{b,u}$ of a beamformer needs to be zero for unserved UEs and positive for served UEs, which is enforced via $\mathrm{C}_{19}: p_{b,u} \leq \kappa_{b,u} P_{\mathrm{tx}}^{\mathrm{SBS}}, \forall l \in \mathcal{L}, b \in \mathcal{B}_l, u \in \mathcal{U}_l$. To connect the beamformer $\mathbf{w}_{b,u}$ and its power $p_{b,u}$, we define $\|\mathbf{w}_{b,u}\|_2^2 \leq \kappa_{b,u} p_{b,u}$, which ensures that the beamformer is a zero-vector when $\kappa_{b,u} = 0$. Note that $\|\mathbf{w}_{b,u}\|_2^2 \leq \kappa_{b,u} p_{b,u}$ is nonconvex but it can be recast as a SOC constraint as shown in the following. Using the difference of squares, the product $\kappa_{b,u} p_{b,u}$ is equivalent to $\kappa_{b,u} p_{b,u} = \frac{(\kappa_{b,u}+p_{b,u})^2 - (\kappa_{b,u}-p_{b,u})^2}{4}$, which allows us to rearrange $\|\mathbf{w}_{b,u}\|_2^2 \leq \kappa_{b,u} p_{b,u}$ as a new constraint $\mathrm{C}_{20}: \left\| \left[2\mathbf{w}_{b,u}^H, \kappa_{b,u} - p_{b,u} \right] \right\|_2 \leq \kappa_{b,u} + p_{b,u}, \forall l \in \mathcal{L}, b \in \mathcal{B}_l, u \in \mathcal{U}_l$. After these changes, $\mathbf{w}_{b,u}$ and $\kappa_{b,u}$ have been decoupled while still guaranteeing the same effect as if coupled. Thus, the product $\mathbf{w}_{b,u}\kappa_{b,u}$ can be replaced by $\mathbf{w}_{b,u}$ upon including $\mathrm{C}_{17} - \mathrm{C}_{20}$. The, constraint $\bar{\mathrm{C}}_{21}$ is obtained after replacing $\mathbf{w}_{b,u}\kappa_{b,u}$ by $\mathbf{w}_{b,u}$ in C_5.

$$\mathrm{C}_{21}: \sum_{l'\in\mathcal{L}}\sum_{u'\in\mathcal{U}_{l'}}\Big|\sum_{b'\in\mathcal{B}_{l'}}\mathbf{h}_{b',u}^H\mathbf{w}_{b',u'}\Big|^2+\sigma_{\mathrm{UE}}^2\le\left(1+\Gamma_j^{\mathrm{UE}^{-1}}\right)\Big|\sum_{b\in\mathcal{B}_l}\mathbf{h}_{b,u}^H\mathbf{w}_{b,u}\Big|^2+(1-\alpha_{u,j})^2Q_u^2,\forall l\in\mathcal{L},u\in\mathcal{U}_l,j\in\mathcal{J}^{\mathrm{UE}}.$$

$$\mathrm{C}_{21}-\mathrm{C}_{22}=\begin{cases}\mathrm{C}_{23}:\left\|\left[\bar{\mathbf{h}}_u^H\mathbf{W},\sigma_{\mathrm{UE}}\right]\right\|_2\le\sqrt{1+\Gamma_j^{\mathrm{UE}^{-1}}}\mathsf{Re}\left\{\mathbf{h}_u^H\mathbf{w}_u\right\}+(1-\alpha_{u,j})Q_u,\forall l\in\mathcal{L},u\in\mathcal{U}_l,j\in\mathcal{J}^{\mathrm{UE}},\\ \mathrm{C}_{24}:\mathsf{Re}\left\{\mathbf{h}_u^H\mathbf{w}_u\right\}\ge\alpha_{u,j}\sqrt{\Gamma_j^{\mathrm{UE}}}\sigma_{\mathrm{UE}},\forall l\in\mathcal{L},u\in\mathcal{U}_l,j\in\mathcal{J}^{\mathrm{UE}},\\ \mathrm{C}_{25}:\mathsf{Im}\left\{\mathbf{h}_u^H\mathbf{w}_u\right\}=0,\forall l\in\mathcal{L},u\in\mathcal{U}_l,j\in\mathcal{J}^{\mathrm{UE}}.\end{cases}$$

APPENDIX B: PROOF OF PROPOSITION 3

We follow a similar procedure as in [20].We exchange positions between the SINR denominator and the right-hand side (RHS) of $\bar{\mathrm{C}}_{21}$. Then, we add $\left|\sum_{b\in\mathcal{B}_l}\mathbf{h}_{b,u}^H\mathbf{w}_{b,u}\right|^2$ to both sides, thus yielding

$$\bar{\mathrm{C}}_{21}:\left(1+{\alpha_{u,j}}^{-1}\Gamma_j^{\mathrm{UE}^{-1}}\right)\Big|\sum_{b\in\mathcal{B}_l}\mathbf{h}_{b,u}^H\mathbf{w}_{b,u}\Big|^2\ge\sum_{l'\in\mathcal{L}}\sum_{u'\in\mathcal{U}_{l'}}\Big|\sum_{b'\in\mathcal{B}_{l'}}\mathbf{h}_{b',u}^H\mathbf{w}_{b',u'}\Big|^2+\sigma_{\mathrm{UE}}^2,\forall l\in\mathcal{L},u\in\mathcal{U}_l,j\in\mathcal{J}^{\mathrm{UE}}.$$

To deal with this nonconvex constraint, we first derive expressions for its two cases.

$$\begin{aligned}&\textcircled{1}\ \alpha_{u,j}=0\Rightarrow\ \sum_{l'\in\mathcal{L}}\sum_{u'\in\mathcal{U}_{l'}}\Big|\sum_{b'\in\mathcal{B}_{l'}}\mathbf{h}_{b',u}^H\mathbf{w}_{b',u'}\Big|^2\\&\qquad+\sigma_{\mathrm{UE}}^2\le\infty,\forall l\in\mathcal{L},u\in\mathcal{U}_l,j\in\mathcal{J}^{\mathrm{UE}},\\&\textcircled{2}\ \alpha_{u,j}=1\Rightarrow\ \sum_{l'\in\mathcal{L}}\sum_{u'\in\mathcal{U}_{l'}}\Big|\sum_{b'\in\mathcal{B}_{l'}}\mathbf{h}_{b',u}^H\mathbf{w}_{b',u'}\Big|^2+\sigma_{\mathrm{UE}}^2\le\\&\qquad\left(1+\Gamma_j^{\mathrm{UE}^{-1}}\right)\Big|\sum_{b\in\mathcal{B}_l}\mathbf{h}_{b,u}^H\mathbf{w}_{b,u}\Big|^2,\forall l\in\mathcal{L},\\&\qquad u\in\mathcal{U}_l,j\in\mathcal{J}^{\mathrm{UE}}.\end{aligned}$$

In case $\textcircled{1}$, the inequality is satisfied by default. Besides, it is possible to find an upper bound Q_u^2 for $\sum_{l'\in\mathcal{L}}\sum_{u'\in\mathcal{U}_{l'}}\left|\sum_{b'\in\mathcal{B}_{l'}}\mathbf{h}_{b',u}^H\mathbf{w}_{b',u'}\right|^2+\sigma_{\mathrm{UE}}^2$ to prevent using ∞. By harnessing the *big-M* method, we can equivalently combine the two cases into C_{21}, shown at the top of this page. The upper bound $Q_u^2=P_{\mathrm{tx}}^{\mathrm{SBS}}\sum_{l'\in\mathcal{L}}\sum_{b'\in\mathcal{B}_{l'}}\left\|\mathbf{h}_{b',u}\right\|_2^2+\sigma_{\mathrm{UE}}^2$ is obtained by maximizing the LHS of C_{21}.

APPENDIX C: PROOF OF PROPOSITION 5

Assuming that $\mathbf{x}=\left[\bar{\mathbf{h}}_u^H\mathbf{W},\sigma_{\mathrm{UE}}\right]$, constraint C_{21} can be expressed as

$$\|\mathbf{x}\|_2^2\le\left(1+\Gamma_j^{\mathrm{UE}^{-1}}\right)\left|\mathbf{h}_u^H\mathbf{w}_u\right|^2+(1-\alpha_{u,j})^2Q_u^2,\forall l\in\mathcal{L},u\in\mathcal{U}_l,j\in\mathcal{J}^{\mathrm{UE}}.$$

Taking the square root at both sides and applying the Jensen's inequality to the RHS expression, we obtain

$$\sqrt{\left(1+\Gamma_j^{\mathrm{UE}^{-1}}\right)\left|\mathbf{h}_u^H\mathbf{w}_u\right|^2+(1-\alpha_{u,j})^2Q_u^2}\le\sqrt{1+\Gamma_j^{\mathrm{UE}^{-1}}}\left|\mathbf{h}_u^H\mathbf{w}_u\right|+(1-\alpha_{u,j})Q_u.$$

When $\alpha_{u,j}=1$, the inequality is tight, because the RHS and LHS of the expression above become equivalent, i.e., $\|\mathbf{x}\|_2\le\sqrt{1+\Gamma_j^{\mathrm{UE}^{-1}}}\left|\mathbf{h}_u^H\mathbf{w}_u\right|$. When $\alpha_{u,j}=0$, the inequality still remains valid, i.e. $\|\mathbf{x}\|_2\le\sqrt{1+\Gamma_j^{\mathrm{UE}^{-1}}}\left|\mathbf{h}_u^H\mathbf{w}_u\right|+Q_u$, because Q_u is an upper bound for $\|\mathbf{x}\|_2$. As a result, the following expression is equivalent to C_{21}

$$\|\mathbf{x}\|_2\le\sqrt{1+\Gamma_j^{\mathrm{UE}^{-1}}}\left|\mathbf{h}_u^H\mathbf{w}_u\right|+(1-\alpha_{u,j})Q_u,\forall l\in\mathcal{L},u\in\mathcal{U}_l,j\in\mathcal{J}^{\mathrm{UE}}.$$

Notice that the beamforming vectors are invariant to phase shift. In particular, $\mathbf{w}_u$ and $\mathbf{w}_ue^{j\theta_u}$ yield the same received SINR at the UE u. Thus, it is possible to choose a phase $e^{j\theta_u}$ such that $\mathbf{h}_u^H\mathbf{w}_u$ becomes purely real and nonnnegative [48, ch. 18]. Therefore, the following holds

$$\|\mathbf{x}\|_2\le\sqrt{1+\Gamma_j^{\mathrm{UE}^{-1}}}\left|\mathbf{h}_u^H\mathbf{w}_u\right|+(1-\alpha_{u,j})Q_u\triangleq\begin{cases}\|\mathbf{x}\|_2\le\sqrt{1+\Gamma_j^{\mathrm{UE}^{-1}}}\mathsf{Re}\left\{\mathbf{h}_u^H\mathbf{w}_u\right\}+(1-\alpha_{u,j})Q_u,\\ \mathsf{Re}\left\{\mathbf{h}_u^H\mathbf{w}_u\right\}\ge0,\\ \mathsf{Im}\left\{\mathbf{h}_u^H\mathbf{w}_u\right\}=0.\end{cases}$$

Similarly, constraint C_{22} can be expressed as

$$\alpha_{u,j}\sqrt{\Gamma_j^{\mathrm{UE}}}\sigma_{\mathrm{UE}}\le\left|\mathbf{h}_u^H\mathbf{w}_u\right|\triangleq\begin{cases}\alpha_{u,j}\sqrt{\Gamma_j^{\mathrm{UE}}}\sigma_{\mathrm{UE}}\le\mathsf{Re}\left\{\mathbf{h}_u^H\mathbf{w}_u\right\}\\ \mathsf{Re}\left\{\mathbf{h}_u^H\mathbf{w}_u\right\}\ge0,\\ \mathsf{Im}\left\{\mathbf{h}_u^H\mathbf{w}_u\right\}=0.\end{cases}$$

Combining the results above, constraints $\mathrm{C}_{21}-\mathrm{C}_{22}$ are remodeled as $\mathrm{C}_{23}-\mathrm{C}_{25}$, shown at the top of this page.

APPENDIX D: PROOF OF PROPOSITION 6

Note that $\left|\mathbf{g}_b^H\mathbf{m}_l\right|\ge\mathsf{Re}\left\{\mathbf{g}_b^H\mathbf{m}_l\right\}$ always holds true. The inequality becomes tight when the phase of $\mathbf{g}_b^H\mathbf{m}_l$ is zero [37], [49]. This is, in general, not true unless there is a single SBS per cluster. Using this conservative relation, we replace $\mathrm{C}_{15}-\mathrm{C}_{16}$ by $\mathrm{C}_{26}-\mathrm{C}_{27}$, which are defined as

$$\begin{aligned}&\mathrm{C}_{26}:\left\|\mathbf{g}_b^H\mathbf{M}\right\|_2^2+\sigma_{\mathrm{SBS}}^2\le\left(1+\Gamma_j^{\mathrm{SBS}^{-1}}\right)\mathsf{Re}\left\{\mathbf{g}_b^H\mathbf{m}_l\right\}^2\\&\qquad+(1-\beta_{l,j})^2Q_b^2,\forall l\in\mathcal{L},b\in\mathcal{B}_l,j\in\mathcal{J}^{\mathrm{SBS}},\\&\mathrm{C}_{27}:\beta_{l,j}\Gamma_j^{\mathrm{SBS}}\sigma_{\mathrm{SBS}}^2\le\mathsf{Re}\left\{\mathbf{g}_b^H\mathbf{m}_l\right\}^2,\forall l\in\mathcal{L},b\in\mathcal{B}_l,j\in\mathcal{J}^{\mathrm{SBS}},\end{aligned}$$

where $Q_b^2=P_{\mathrm{tx}}^{\mathrm{MBS}}\left\|\mathbf{g}_b\right\|_2^2+\sigma_{\mathrm{SBS}}^2$. However, these inequalities can be recast as the following convex SOC constraints

$$\begin{aligned}&\mathrm{C}_{26}:\left\|\left[\mathbf{g}_b^H\mathbf{M},\sigma_{\mathrm{SBS}}\right]\right\|_2\le\sqrt{1+\Gamma_j^{\mathrm{SBS}^{-1}}}\mathsf{Re}\left\{\mathbf{g}_b^H\mathbf{m}_l\right\}\\&\qquad+(1-\beta_{l,j})Q_b,\forall l\in\mathcal{L},b\in\mathcal{B}_l,j\in\mathcal{J}^{\mathrm{SBS}},\\&\mathrm{C}_{27}:\beta_{l,j}\sqrt{\Gamma_j^{\mathrm{SBS}}}\sigma_{\mathrm{SBS}}\le\mathsf{Re}\left\{\mathbf{g}_b^H\mathbf{m}_l\right\},\forall l\in\mathcal{L},b\in\mathcal{B}_l,j\in\mathcal{J}^{\mathrm{SBS}},\end{aligned}$$

where the Jensen's inequality has been applied to C_{26}.

APPENDIX E: PROOF OF PROPOSITION 8

We define the Lagrange dual function of $\mathcal{P}_1$ as $\phi\left(\lambda_\alpha,\lambda_\beta,\lambda_\kappa\right)=\max_{\boldsymbol{\Theta}\in\mathscr{D}}L\left(\boldsymbol{\alpha},\boldsymbol{\beta},\boldsymbol{\kappa},\lambda_\alpha,\lambda_\beta,\lambda_\kappa\right)$, where $L\left(\boldsymbol{\alpha},\boldsymbol{\beta},\boldsymbol{\kappa},\lambda_\alpha,\lambda_\beta,\lambda_\kappa\right)=R_{\mathrm{w-sum}}^{\mathrm{access}}\left(\boldsymbol{\alpha}\right)-\lambda_\alpha f_\alpha\left(\boldsymbol{\alpha}\right)-\lambda_\beta f_\beta\left(\boldsymbol{\beta}\right)-\lambda_\kappa f_\kappa\left(\boldsymbol{\kappa}\right)$. In addition, we define

$$\begin{aligned}\text{primal}:\ p^*&=\max_{\boldsymbol{\Theta}\in\mathscr{D}}\min_{\lambda_\alpha,\lambda_\beta,\lambda_\kappa\ge0}L\left(\boldsymbol{\alpha},\boldsymbol{\beta},\boldsymbol{\kappa},\lambda_\alpha,\lambda_\beta,\lambda_\kappa\right)\\&=\max\left(\mathcal{P}_1\right).\\\text{dual}:\ d^*&=\min_{\lambda_\alpha,\lambda_\beta,\lambda_\kappa\ge0}\max_{\boldsymbol{\Theta}\in\mathscr{D}}L\left(\boldsymbol{\alpha},\boldsymbol{\beta},\boldsymbol{\kappa},\lambda_\alpha,\lambda_\beta,\lambda_\kappa\right)\end{aligned}$$

$$= \min_{\lambda_\alpha,\lambda_\beta,\lambda_\kappa \geq 0} \phi\left(\lambda_\alpha,\lambda_\beta,\lambda_\kappa\right).$$

According to the weak duality theorem, the following holds

$$p^* \leq \min_{\lambda_\alpha,\lambda_\beta,\lambda_\kappa \geq 0} \phi\left(\lambda_\alpha,\lambda_\beta,\lambda_\kappa\right). \tag{E.1}$$

Note that $f_\alpha\left(\boldsymbol{\alpha}\right) \geq 0$, $f_\beta\left(\boldsymbol{\beta}\right) \geq 0$, $f_\kappa\left(\boldsymbol{\kappa}\right) \geq 0$, for $\boldsymbol{\Theta} \in \mathscr{D}$. Thus, the Lagrangian $L\left(\boldsymbol{\alpha},\boldsymbol{\beta},\boldsymbol{\kappa},\lambda_\alpha,\lambda_\beta,\lambda_\kappa\right)$ is monotonically decreasing with respect to λ_α, λ_β, λ_κ when $\boldsymbol{\Theta} \in \mathscr{D}$. Further, this means that $\phi\left(\lambda_\alpha,\lambda_\beta,\lambda_\kappa\right)$ is monotonically decreasing with respect to λ_α, λ_β, λ_κ and is bounded by the optimal value of $\mathcal{P}_1$. We distinguish the following two cases.

Case 1: Suppose that $f_\alpha\left(\boldsymbol{\alpha}_0\right) = 0, f_\beta\left(\boldsymbol{\beta}_0\right) = 0, f_\kappa\left(\boldsymbol{\kappa}_0\right) = 0$ for some $\lambda_{\alpha_0} < \infty$, $\lambda_{\beta_0} < \infty$, $\lambda_{\kappa_0} < \infty$, implying that $\boldsymbol{\alpha}_0$, $\boldsymbol{\beta}_0$, $\boldsymbol{\kappa}_0$ are binary. Therefore, $\boldsymbol{\alpha}_0$, $\boldsymbol{\beta}_0$, $\boldsymbol{\kappa}_0$ are also feasible to $\mathcal{P}_1$. Replacing this solution in the primal problem, we obtain $L\left(\boldsymbol{\alpha}_0,\boldsymbol{\beta}_0,\boldsymbol{\kappa}_0,\lambda_{\alpha_0},\lambda_{\beta_0},\lambda_{\kappa_0}\right) = R^{\text{access}}_{\text{w}-\text{sum}}\left(\boldsymbol{\alpha}_0\right) \leq p^*$. Now, considering the dual problem and (E.1), we have that $\phi\left(\lambda_{\alpha_0},\lambda_{\beta_0},\lambda_{\kappa_0}\right) = L\left(\boldsymbol{\alpha}_0,\boldsymbol{\beta}_0,\boldsymbol{\kappa}_0,\lambda_{\alpha_0},\lambda_{\beta_0},\lambda_{\kappa_0}\right) = R^{\text{access}}_{\text{w}-\text{sum}}\left(\boldsymbol{\alpha}_0\right) \geq p^*$, which implies that $p^* = d^*$, i.e. strong duality holds. Based on the previous result, we realize that

$$\phi\left(\lambda_{\alpha_0},\lambda_{\beta_0},\lambda_{\kappa_0}\right) = \min_{\lambda_\alpha,\lambda_\beta,\lambda_\kappa \geq 0} \phi\left(\lambda_\alpha,\lambda_\beta,\lambda_\kappa\right),$$
$$\phi\left(\lambda_\alpha,\lambda_\beta,\lambda_\kappa\right) = p^*, \forall \lambda_\alpha \geq \lambda_{\alpha_0}, \forall \lambda_\beta \geq \lambda_{\beta_0}, \forall \lambda_\kappa \geq \lambda_{\kappa_0},$$

which means that for any $\lambda_\alpha, \lambda_\beta, \lambda_\kappa$, such that $\lambda_{\alpha_0} < \lambda_\alpha < \infty, \lambda_{\beta_0} < \lambda_\beta < \infty, \lambda_{\kappa_0} < \lambda_\kappa < \infty$, problems $\mathcal{P}_1$ and $\widetilde{\mathcal{P}}_1$ share the same optimal value an optimal solution. Thus, $\mathcal{P}_1$ can be solved by means of $\widetilde{\mathcal{P}}_1$ for appropriately chosen large values of $\lambda_\alpha, \lambda_\beta, \lambda_\kappa$.

Case 2: Suppose that $f_\alpha\left(\boldsymbol{\alpha}_0\right) > 0, f_\beta\left(\boldsymbol{\beta}_0\right) > 0, f_\kappa\left(\boldsymbol{\kappa}_0\right) > 0$, for $\lambda_{\alpha_0} > 0$, $\lambda_{\beta_0} > 0$, $\lambda_{\kappa_0} > 0$, implying that some elements of $\boldsymbol{\alpha}_0$, $\boldsymbol{\beta}_0$, $\boldsymbol{\kappa}_0$ take values between 0 and 1. From the dual problem, we have that $\phi\left(\lambda_{\alpha_0},\lambda_{\beta_0},\lambda_{\kappa_0}\right) \to -\infty$. However, this contradicts the weak duality theorem, which states that $\phi\left(\lambda_\alpha,\lambda_\beta,\lambda_\kappa\right)$ is bounded from below by the primal solution, which is at worst zero. Thus, this case is not valid.

Appendix F: Proof of Proposition 9

Note that $q_\alpha\left(\boldsymbol{\alpha}\right)$, $q_\beta\left(\boldsymbol{\beta}\right)$, $q_\kappa\left(\boldsymbol{\kappa}\right)$ are concave. Therefore, their first-order approximations $\tilde{q}^{(t)}_\alpha\left(\boldsymbol{\alpha}\right)$, $\tilde{q}^{(t)}_\beta\left(\boldsymbol{\beta}\right)$, $\tilde{q}^{(t)}_\kappa\left(\boldsymbol{\kappa}\right)$ satisfy $q_\alpha\left(\boldsymbol{\alpha}\right) \leq \tilde{q}^{(t)}_\alpha\left(\boldsymbol{\alpha}\right)$, $q_\beta\left(\boldsymbol{\beta}\right) \leq \tilde{q}^{(t)}_\beta\left(\boldsymbol{\beta}\right)$, $q_\kappa\left(\boldsymbol{\kappa}\right) \leq \tilde{q}^{(t)}_\kappa\left(\boldsymbol{\kappa}\right)$. Now, we define

$$\begin{aligned} g_1\left(\boldsymbol{\alpha},\boldsymbol{\beta},\boldsymbol{\kappa}\right) &\triangleq R^{\text{access}}_{\text{w}-\text{sum}}\left(\boldsymbol{\alpha}\right) - \lambda_\alpha p_\alpha\left(\boldsymbol{\alpha}\right) - \lambda_\beta p_\beta\left(\boldsymbol{\beta}\right) \\ &\quad - \lambda_\kappa p_\kappa\left(\boldsymbol{\kappa}\right), \\ g_2\left(\boldsymbol{\alpha},\boldsymbol{\beta},\boldsymbol{\kappa}\right) &\triangleq \lambda_\alpha q_\alpha\left(\boldsymbol{\alpha}\right) + \lambda_\beta q_\beta\left(\boldsymbol{\beta}\right) + \lambda_\kappa q_\kappa\left(\boldsymbol{\kappa}\right), \\ \tilde{g}^{(t)}_2\left(\boldsymbol{\alpha},\boldsymbol{\beta},\boldsymbol{\kappa}\right) &\triangleq \lambda_\alpha \tilde{q}^{(t)}_\alpha\left(\boldsymbol{\alpha}\right) + \lambda_\beta \tilde{q}^{(t)}_\beta\left(\boldsymbol{\beta}\right) + \lambda_\kappa \tilde{q}^{(t)}_\kappa\left(\boldsymbol{\kappa}\right). \end{aligned}$$

Considering the expressions above, the objective function of $\widetilde{\mathcal{P}}_1$ can be rewritten as $R\left(\boldsymbol{\alpha},\boldsymbol{\beta},\boldsymbol{\kappa}\right) = g_1\left(\boldsymbol{\alpha},\boldsymbol{\beta},\boldsymbol{\kappa}\right) - g_2\left(\boldsymbol{\alpha},\boldsymbol{\beta},\boldsymbol{\kappa}\right)$ whereas the objective of $\widetilde{\mathcal{P}}^{(t)}_1$ can be rewritten as $\tilde{R}^{(t)}\left(\boldsymbol{\alpha},\boldsymbol{\beta},\boldsymbol{\kappa}\right) = g_1\left(\boldsymbol{\alpha},\boldsymbol{\beta},\boldsymbol{\kappa}\right) - \tilde{g}^{(t)}_2\left(\boldsymbol{\alpha},\boldsymbol{\beta},\boldsymbol{\kappa}\right)$. Since $g_2\left(\boldsymbol{\alpha},\boldsymbol{\beta},\boldsymbol{\kappa}\right) \leq \tilde{g}^{(t)}_2\left(\boldsymbol{\alpha},\boldsymbol{\beta},\boldsymbol{\kappa}\right)$ then $\tilde{R}^{(t)}\left(\boldsymbol{\alpha},\boldsymbol{\beta},\boldsymbol{\kappa}\right)$ is a lower bound for the objective of $\widetilde{\mathcal{P}}_1$, i.e. $\tilde{R}^{(t)}\left(\boldsymbol{\alpha},\boldsymbol{\beta},\boldsymbol{\kappa}\right) \leq R\left(\boldsymbol{\alpha},\boldsymbol{\beta},\boldsymbol{\kappa}\right)$. Further, the equality holds when $\boldsymbol{\alpha} = \boldsymbol{\alpha}^{(t-1)}$, $\boldsymbol{\beta} = \boldsymbol{\beta}^{(t-1)}$, $\boldsymbol{\kappa} = \boldsymbol{\kappa}^{(t-1)}$ showing the bound tightness.

Appendix G: Proof of Proposition 10

Realize that $\boldsymbol{\Theta}^{(t-1)}$ is a feasible point for $\widetilde{\mathcal{P}}^{(t)}_1$ whereas $\boldsymbol{\Theta}^{(t)}$ is its optimal solution. For iteration t, we have that $R\left(\boldsymbol{\alpha},\boldsymbol{\beta},\boldsymbol{\kappa}\right) \geq \tilde{R}^{(t)}\left(\boldsymbol{\alpha},\boldsymbol{\beta},\boldsymbol{\kappa}\right)$ and $R\left(\boldsymbol{\alpha}^{(t-1)},\boldsymbol{\beta}^{(t-1)},\boldsymbol{\kappa}^{(t-1)}\right) = \tilde{R}^{(t)}\left(\boldsymbol{\alpha}^{(t-1)},\boldsymbol{\beta}^{(t-1)},\boldsymbol{\kappa}^{(t-1)}\right)$. Using these relations,

$$\begin{aligned} R\left(\boldsymbol{\alpha}^{(t)},\boldsymbol{\beta}^{(t)},\boldsymbol{\kappa}^{(t)}\right) &\geq \tilde{R}^{(t)}\left(\boldsymbol{\alpha}^{(t)},\boldsymbol{\beta}^{(t)},\boldsymbol{\kappa}^{(t)}\right) \\ &\geq \tilde{R}^{(t)}\left(\boldsymbol{\alpha}^{(t-1)},\boldsymbol{\beta}^{(t-1)},\boldsymbol{\kappa}^{(t-1)}\right), \\ &= R\left(\boldsymbol{\alpha}^{(t-1)},\boldsymbol{\beta}^{(t-1)},\boldsymbol{\kappa}^{(t-1)}\right), \end{aligned}$$

which shows that $\left(\boldsymbol{\alpha}^{(t)},\boldsymbol{\beta}^{(t)},\boldsymbol{\kappa}^{(t)}\right)$ is more optimal for $\mathcal{P}_1$ than $\left(\boldsymbol{\alpha}^{(t-1)},\boldsymbol{\beta}^{(t-1)},\boldsymbol{\kappa}^{(t-1)}\right)$. Further, $R\left(\boldsymbol{\alpha}^{(t)},\boldsymbol{\beta}^{(t)},\boldsymbol{\kappa}^{(t)}\right) \geq R\left(\boldsymbol{\alpha}^{(t-1)},\boldsymbol{\beta}^{(t-1)},\boldsymbol{\kappa}^{(t-1)}\right)$ implies that $\left(\mathbf{M}^{(t)},\mathbf{W}^{(t)},\mathbf{p}^{(t)}\right)$ is equally or more optimal for $\mathcal{P}_1$ than $\left(\mathbf{M}^{(t-1)},\mathbf{W}^{(t-1)},\mathbf{p}^{(t-1)}\right)$ due to linkage with C_{20}, $\text{C}_{23} - \text{C}_{24}$. Thus, $\boldsymbol{\Theta}^{(t)} = \left(\mathbf{M}^{(t)},\mathbf{W}^{(t)},\mathbf{p}^{(t)},\boldsymbol{\alpha}^{(t)},\boldsymbol{\beta}^{(t)},\boldsymbol{\kappa}^{(t)}\right)$ is more befitting for $\mathcal{P}_1$ than $\boldsymbol{\Theta}^{(t-1)}$. As a result, the sequence of points $\left\{\boldsymbol{\Theta}^{(t)}\right\}$ constitutes a sequence of enhanced points for $\mathcal{P}_1$. In addition, $\left\{\boldsymbol{\Theta}^{(t)}\right\}$ is bounded because $\tilde{R}^{(t)}\left(\boldsymbol{\alpha},\boldsymbol{\beta},\boldsymbol{\kappa}\right)$ is upper-bounded by $R\left(\boldsymbol{\alpha},\boldsymbol{\beta},\boldsymbol{\kappa}\right)$, and $R\left(\boldsymbol{\alpha},\boldsymbol{\beta},\boldsymbol{\kappa}\right)$ is upper-bounded by the multicast rate, which is ultimately constrained by the maximum transmit power from the MBS. By Cauchy's theorem, there must exist a convergent subsequence $\left\{\boldsymbol{\Theta}^{(t_n)}\right\}$ such that

$$\lim_{n\to\infty}\left[R\left(\boldsymbol{\alpha}^{(t_n)},\boldsymbol{\beta}^{(t_n)},\boldsymbol{\kappa}^{(t_n)}\right) - R\left(\boldsymbol{\alpha}^\star,\boldsymbol{\beta}^\star,\boldsymbol{\kappa}^\star\right)\right] = 0, \tag{G.1}$$

where $\boldsymbol{\Theta}^\star = \left(\mathbf{M}^\star,\mathbf{W}^\star,\mathbf{p}^\star,\boldsymbol{\alpha}^\star,\boldsymbol{\beta}^\star,\boldsymbol{\kappa}^\star\right)$ is a limit point for $\left\{\boldsymbol{\Theta}^{(t_n)}\right\}$. Thus, for each iteration t, there exists some n such that $t_n \leq t \leq t_{n+1}$. From (G.1) we obtain

$$\begin{aligned} \epsilon^{(t_n)} &= \lim_{n\to\infty}\left[R\left(\boldsymbol{\alpha}^{(t_n)},\boldsymbol{\beta}^{(t_n)},\boldsymbol{\kappa}^{(t_n)}\right) - R\left(\boldsymbol{\alpha}^\star,\boldsymbol{\beta}^\star,\boldsymbol{\kappa}^\star\right)\right] = 0, \\ \epsilon^{(t_{n+1})} &= \lim_{n\to\infty}\left[R\left(\boldsymbol{\alpha}^{(t_{n+1})},\boldsymbol{\beta}^{(t_{n+1})},\boldsymbol{\kappa}^{(t_{n+1})}\right) - R\left(\boldsymbol{\alpha}^\star,\boldsymbol{\beta}^\star,\boldsymbol{\kappa}^\star\right)\right] = 0, \\ \epsilon^{(t)} &= \lim_{n\to\infty}\left[R\left(\boldsymbol{\alpha}^{(t)},\boldsymbol{\beta}^{(t)},\boldsymbol{\kappa}^{(t)}\right) - R\left(\boldsymbol{\alpha}^\star,\boldsymbol{\beta}^\star,\boldsymbol{\kappa}^\star\right)\right], \end{aligned}$$

showing that $\epsilon^{(t_n)} \leq \epsilon^{(t)} \leq \epsilon^{(t_{n+1})}$ and $\lim_{t\to\infty} R\left(\boldsymbol{\alpha}^{(t)},\boldsymbol{\beta}^{(t)},\boldsymbol{\kappa}^{(t)}\right) = R\left(\boldsymbol{\alpha}^\star,\boldsymbol{\beta}^\star,\boldsymbol{\kappa}^\star\right)$. Therefore, each accumulation point $\boldsymbol{\Theta}^\star = \left(\mathbf{M}^\star,\mathbf{W}^\star,\mathbf{p}^\star,\boldsymbol{\alpha}^\star,\boldsymbol{\beta}^\star,\boldsymbol{\kappa}^\star\right)$ is a KKT point [32], [50].

Luis F. Abanto-Leon received the MSc. degree in Communications Engineering in 2015 from Tohoku University, Japan. From November 2018, he is a PhD student at Technische Universität (TU) Darmstadt in the Department of Computer Science. His research interests are mathematical programming and signal processing for radio resource management in millimeter-wave wireless networks.

Arash Asadi is a research group leader at TU Darmstadt, where he leads the Wireless Communication and Sensing Lab (WISE). His research is focused on wireless communication and sensing and its application in Beyond-5G/6G networks. He is a recipient of several awards, including Athena Young Investigator award from TU Darmstadt and outstanding PhD and master thesis awards from UC3M. Some of his papers on D2D communication have appeared in IEEE COMSOC best reading topics on D2D communication and IEEE COMSOC Tech Focus.

Andres Garcia-Saavedra Andres Garcia-Saavedra received his PhD degree from the University Carlos III of Madrid (UC3M) in 2013. He then joined Trinity College Dublin (TCD), Ireland, as a research fellow until 2015. Currently, he is a Principal Researcher at NEC Laboratories Europe. His research interests lie in the application of fundamental mathematics to real-life wireless communication systems.

Gek Hong (Allyson) Sim is currently a Post-Doctoral Researcher with the Department of Computer Science, Technische Universität Darmstadt, Germany. She received the bachelor's degree (Eng.) in telecommunication and the first master's degree in engineering science from Multimedia University, Malaysia, in 2007 and 2011, respectively. She was awarded master's and Ph.D. degrees in telematics engineering from the University Carlos III Madrid in 2012 and 2015, respectively. Her research interests include multicast scheduling, precoding, and MAC layer optimization for millimeter-wave networks.

Matthias Hollick received the Ph.D. degree from Technische Universität (TU) Darmstadt in 2004. He is currently the Head of the Secure Mobile Networking Lab, Department of Computer Science, TU Darmstadt, Germany. He has been researching and teaching at TU Darmstadt, Universidad Carlos III de Madrid, and the University of Illinois at Urbana–Champaign. His research focus is on resilient, secure, privacy-preserving, and quality-of-service-aware communication for mobile and wireless systems and networks.

H

PUBLICATION VIII.
RADIO RESOURCE MANAGEMENT DESIGN FOR RSMA: OPTIMIZATION OF BEAMFORMING, USER ADMISSION, AND DISCRETE/CONTINUOUS RATES WITH IMPERFECT SIC

Radio Resource Management Design for RSMA: Optimization of Beamforming, User Admission, and Discrete/Continuous Rates with Imperfect SIC

Luis F. Abanto-Leon[†], Aravindh Krishnamoorthy[‡], Andres Garcia-Saavedra[§], Gek Hong Sim[†], Robert Schober[‡], and Matthias Hollick[†]
[†]Secure Mobile Networking Lab, Technische Universität Darmstadt, Germany
[‡]Friedrich-Alexander-Universität Erlangen-Nürnberg, Germany [§]NEC Laboratories Europe, Germany

Abstract—This paper investigates the radio resource management (RRM) design for multiuser rate-splitting multiple access (RSMA), accounting for various characteristics of practical wireless systems, such as the use of discrete rates, the inability to serve all users, and the imperfect successive interference cancellation (SIC). Specifically, failure to consider these characteristics in RRM design may lead to inefficient use of radio resources. Therefore, we formulate the RRM of RSMA as optimization problems to maximize respectively the weighted sum rate (WSR) and weighted energy efficiency (WEE), and jointly optimize the beamforming, user admission, discrete/continuous rates, accounting for imperfect SIC, which result in nonconvex mixed-integer nonlinear programs that are challenging to solve. Despite the difficulty of the optimization problems, we develop algorithms that can find high-quality solutions. We show via simulations that carefully accounting for the aforementioned characteristics, can lead to significant gains. Precisely, by considering that transmission rates are discrete, the transmit power can be utilized more intelligently, allocating just enough power to guarantee a given discrete rate. Additionally, we reveal that user admission plays a crucial role in RSMA, enabling additional gains compared to random admission by facilitating the servicing of selected users with mutually beneficial channel characteristics. Furthermore, provisioning for possibly imperfect SIC makes RSMA more robust and reliable.

Index Terms—Beamforming, user admission, discrete rates, rate splitting, imperfect SIC, spectral efficiency, energy efficiency.

1 Introduction

Rate-splitting multiple access (RSMA) has emerged as a promising technology capable of outperforming non-orthogonal multiple access (NOMA) and space-division multiple access (SDMA), owing to its superior ability to cope with multiuser interference [1]–[3]. To date, several studies have demonstrated in various use cases [4] the higher capabilities of RSMA compared to SDMA and NOMA, thus positioning RSMA as a formidable multiple access candidate with enormous potential to meet the stringent connectivity requirements of next-generation wireless communications systems [5]. A key element to ensure high RSMA performance is the radio resource management (RRM) design. The RRM for RSMA systems has focused chiefly on the beamforming and power allocation design, which have been investigated for a plethora of use cases and for different design goals, such as fairness, sum secrecy rate (SSR), sum rate (SR), weighted SR (WSR), and weighted energy efficiency (WEE) maximization. For instance, the authors of [6] studied the beamforming design for WSR maximization in joint radar and communications, whereas the authors of [7] developed cooperative beamforming strategies to maximize the WSR in visible light communications. Also, the authors of [8], [9] investigated the beamforming design for WSR maximization in non-orthogonal unicast and multicast (NOUM) systems. The beamforming design for rate fairness maximization in cooperative relaying networks was investigated in [10]. Driven by the same goal, the joint design of beamforming and the phase shifts of an intelligent reflecting surface was studied in [11]. Beamforming and artificial noise design for maximization of the secrecy rate fairness was investigated in [12]. Besides, the beamforming design for WEE maximization in unmanned aerial vehicle networks was studied in [13]. The authors of [14], [15] investigated the beamforming design for maximization of respectively the WSR and WEE, whereas the authors of [16] designed the beamforming for simultaneous WSR and WEE maximization. Power allocation was investigated for SR, SSR, and rate fairness maximization in [17]–[19], [20], and [21], respectively. The body of work on beamforming and power allocation design of RSMA continues to grow and show promising results. However, the literature has failed to investigate several critical characteristics of practical wireless systems, i.e., rate discretization, user admission, and imperfect successive interference cancellation (SIC).

Concerning the first characteristic, most of the literature, assumed continuous rates modeled by Shannon's capacity formula, e.g., [1]–[4], [6], [7], [11]–[21]. This assumption contrasts with the predominant use of discrete rates in practical wireless systems and raises questions as to whether RSMA's gains will remain valid when discrete rates are accounted for. Transmission rates in wireless systems are determined by the choice of a modulation and coding scheme (MCS), as specified by 3GPP [22], leading to a finite set of discrete rates. Employing Shannon's capacity formula is mathematically more tractable than assuming discrete rates, hence its wide adoption. However, it renders continuous-valued rate upper bounds that cannot be achieved in practice. A naive solution to this problem is to project the continuous rates onto the discrete domain, i.e., round them to the closest feasible discrete rate [23]. However, this may lead

to performance degradation. Therefore, rate discretization must be properly accounted for in the RRM design to exploit the full potential of RSMA. An early study in [24] investigated the impact of beamforming and discrete rates on the SR of RSMA, and showed that RSMA outperforms SDMA for discrete rates. However, the proposed design does not consider predefined MCSs, since the authors assumed continuous rates and customized the MCSs to achieve a SR close to the ensemble average, obtained over multiple channel realizations. A few works investigated the impact of beamforming and discrete rates on the performance of SDMA. For instance, joint beamforming and discrete rate allocation design was investigated in [25], [26] for SR maximization and in [27] for WSR maximization. However, these results are not applicable to RSMA, since RSMA is a more general framework that includes SDMA as a special case.

Concerning the second characteristic, access policies in wireless systems typically restrict the number of users served per time slot, e.g., due to the availability of a limited number of radio frequency chains. This characteristic is especially limiting for SDMA, which requires one RF chain per served user. In contrast, RSMA can support more users than RF chains are available since RSMA can exploit the multicast signal to aggregate information for several users. However, in this case, RSMA degrades severely as the number of users increases since the multicast signal must be delivered to all supported users. This condition becomes a limitation in RSMA and raises the need for selective user admission. The impact of user admission on performance has not yet been studied for RSMA, but has been studied for SDMA and NOMA. For instance, the joint beamforming and user admission design for SDMA was investigated in [28] to minimize the transmit power, and in [29] to maximize the SR and rate fairness. The authors of [30] developed joint beamforming and user admission strategies for SDMA to maximize the number of users served. Driven by the same goal, the authors of [31] designed the power and subchannel allocation for NOMA. Besides, the joint design of beamforming, user admission, and discrete rate allocation for SR maximization of SDMA was investigated in [32]. However, the solutions developed in the preceding studies are not valid for RSMA. Specifically, user admission for RSMA differs significantly from that for SDMA and NOMA, as RSMA delivers information to users via superimposed multicast and unicast precoders. Unicast precoders benefit from users with uncorrelated channels because interference is easier to mitigate, whereas the multicast precoder benefits from users with correlated channels as this facilitates transmitting shared information. Therefore, given these conflicting objectives, it is important to include the user admission in the RRM design of RSMA.

Finally, as the last key characteristic, it is important to account for imperfect SIC. Specifically, the performance of RSMA is highly dependent on the success of SIC. In practice, SIC is generally not perfect, which causes unmanaged self-interference that can compromise performance. Despite the importance of accounting for imperfect SIC in the RRM design of RSMA, SIC has been assumed to be perfect in most of the RSMA literature, with few exceptions. For instance, the authors of [33] investigated the beamforming and subcarrier allocation design for SR maximization taking into account imperfect SIC. However, the proposed design assumed continuous rates and did not consider user admission. The impact of imperfect SIC on the SR of RSMA was investigated in [34], where the authors derived bounds for power allocation but did not take user admission and discrete rates into account. Besides, NOMA can also be affected by imperfect SIC and, therefore, a number of works have investigated its impact in this context. In particular, for NOMA, the impact of imperfect SIC and power allocation was studied in [35]–[37] for SR maximization, and in [38] for EE maximization.

Motivated by the above discussion, we expect that the performance of RSMA systems can be significantly improved if the aforementioned characteristics are accounted for. Thus, we propose to account for discrete rates, user admission, and imperfect SIC during RRM design in order to maximize the performance of RSMA in practical systems. To the best of the authors' knowledge, RRM design for RSMA systems considering these characteristics has not been investigated yet. Due to the widespread adoption of Shannon's capacity formula for RRM design, we also investigate the integration of continuous rates, user admission, and imperfect SIC, which has also not been studied before for RSMA systems. We adopt the maximization of the WSR and WEE as design objectives. This paper makes the following contributions:

- We formulate two novel RRM problems to maximize respectively the WSR and WEE of RSMA by jointly optimizing the beamforming, user admission, and private and common discrete rates, while accounting for imperfect SIC. The resulting WSR and WEE problems, denoted by $\mathcal{P}'_{\mathrm{DWSR}}$ and $\mathcal{P}'_{\mathrm{DWEE}}$ in Section 3.1, are nonconvex mixed-integer nonlinear programs (MINLPs) and are difficult to solve. In addition, we formulate problems $\mathcal{Q}'_{\mathrm{CWSR}}$ and $\mathcal{Q}'_{\mathrm{CWEE}}$ in Section 4.1, which represent the continuous-rate counterparts of $\mathcal{P}'_{\mathrm{DWSR}}$ and $\mathcal{P}'_{\mathrm{DWEE}}$, and are also nonconvex MINLPs.
- In Section 3.2, we propose an optimal mixed-integer second-order cone program (`OPT-MISOCP`) algorithm, which tackles the nonconvexities of $\mathcal{P}'_{\mathrm{DWSR}}$ and $\mathcal{P}'_{\mathrm{DWEE}}$ through a series of convex transformations. Specifically, instead of treating $\mathcal{P}'_{\mathrm{DWSR}}$ and $\mathcal{P}'_{\mathrm{DWEE}}$ as general nonconvex MINLPs, `OPT-MISOCP` approximates $\mathcal{P}'_{\mathrm{DWSR}}$ and $\mathcal{P}'_{\mathrm{DWEE}}$ as convex MINLPs $\mathcal{P}_{\mathrm{DWSR}}$ and $\mathcal{P}_{\mathrm{DWEE}}$, respectively, which can be solved in a globally optimal manner. However, circumventing the nonconvexities of $\mathcal{P}'_{\mathrm{DWSR}}$ and $\mathcal{P}'_{\mathrm{DWEE}}$ poses the risk of shrinking their feasible set, possibly resulting in a loss of optimality. Therefore, we derive an upper bound to evaluate the corresponding loss in performance and show via simulations that the globally optimal solutions for $\mathcal{P}_{\mathrm{DWSR}}$ and $\mathcal{P}_{\mathrm{DWEE}}$ result in near-optimal solutions for $\mathcal{P}'_{\mathrm{DWSR}}$ and $\mathcal{P}'_{\mathrm{DWEE}}$ with negligible degradation. In addition, the proposed `OPT-MISOCP` algorithm features customized cutting planes that reduce the runtime by a factor of $3-20$ without impacting performance.
- In Section 4.2, we solve $\mathcal{Q}'_{\mathrm{CWSR}}$ and $\mathcal{Q}'_{\mathrm{CWEE}}$ based on binary enumeration and convex transformations. In particular, we employ enumeration to list all possible user admission combinations, thus resulting in multiple

subproblems. To solve each subproblem, we devise an optimal successive convex approximation with semidefinite relaxation (OPT-SCA-SDR) algorithm, which finds a Karush-Kuhn-Tucker (KKT) point. In addition, to comply with the finite set of discrete rates, the continuous rates obtained by OPT-SCA-SDR are projected, i.e., rounded to the closest feasible discrete rates.

- Our simulations show that RSMA designed for discrete rates achieves gains of up to 89.7% (WSR) and 21.5% (WEE) compared to projecting continuous rates. Also, user admission proves crucial for RSMA as it yields additional gains of up to 15.3% (WSR) and 11.4% (WEE) compared to random user admission when discrete rates are considered. Furthermore, accounting for imperfect SIC prevents severe performance degradation by mitigating the impact of self-interference. Overall, our simulation results reveal that accounting for characteristics of practical wireless systems in RRM of RSMA leads to improved exploitation of the radio resources, and therefore to higher spectral efficiency (SE) and energy efficiency (EE).

The remainder of this paper is organized as follows. In Section 2, we present the system model. In Section 3, considering discrete rates, we formulate and solve the RRM as optimization problems for maximization of the WSR and WEE, respectively, while in Section 4, we do the same for continuous rates. Simulation results are presented in Section 5. Finally, we summarize our conclusions in Section 6.

Notation: In this paper, $|a|$ and the $\|\mathbf{a}\|_2$ represent the absolute value of scalar a and the ℓ_2-norm of vector $\mathbf{a}$, respectively. $\mathbf{A}^{\mathrm{T}}$, $\mathbf{A}^{\mathrm{H}}$, $\mathrm{Rank}\,(\mathbf{A})$, $\mathrm{Tr}\,(\mathbf{A})$, and $\mathfrak{Re}\{\mathbf{A}\}$ and $\mathfrak{Im}\{\mathbf{A}\}$ denote the transpose, Hermitian transpose, rank, trace, and real and imaginary part of matrix $\mathbf{A}$, respectively. $\mathbf{A} \succcurlyeq \mathbf{0}$ indicates that $\mathbf{A}$ is a positive semidefinite matrix. $\mathbb{C}^{N\times M}$ denotes the space of $N \times M$ complex-valued matrices. $\mathbf{I}$ is the identity matrix, $j \triangleq \sqrt{-1}$ is the imaginary unit, and $\mathbb{E}\{\cdot\}$ denotes statistical expectation.

2 System Model

In this section, we present the system model for the considered RRM optimization problems.

2.0.1 System Architecture: We consider the downlink cellular system shown in Fig. 1a, where a base station (BS) is equipped with an antenna array with N_{tx} elements, which can consume a maximum transmit power of $P_{\mathrm{tx}}^{\max}$. There are U single-antenna user equipments (UEs), and the BS admits only K UEs, where $K \leq U$. We index the UEs with the elements of set $\mathcal{U}$, such that $|\mathcal{U}| = U$. The UEs are distributed within a 120° sector and are located at a maximum distance D_{BS} from the BS. The BS estimates the channel state information (CSI) using uplink pilots exploiting channel reciprocity. The RRM optimizer at the BS uses the CSI and other system parameters, such as the maximum transmit power, to maximize the WSR or WEE.

2.0.2 RSMA Principle: In this section, we revisit the RSMA principle excluding the UE admission phase for ease of presentation. As shown in Fig. 1b, every UE has a corresponding message denoted by $\widetilde{W}_u$, $u \in \mathcal{U}$, but only K UEs out of U are served. Thus, we assume that K UEs are preselected for downlink transmission, and denote this set of UEs by $\mathcal{U}'$, such that $|\mathcal{U}'| = K$, and by UE_u the u-th UE in

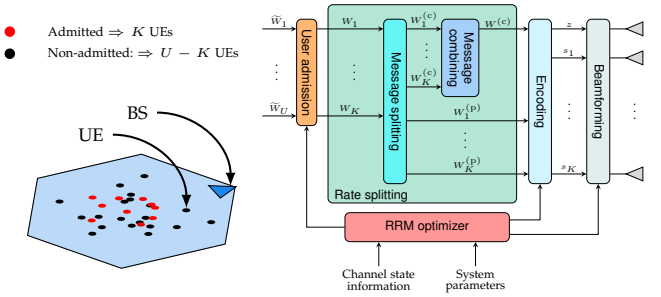

(a) System model (b) RSMA with integrated RRM optimizer

Figure 1: System model and RSMA with integrated RRM optimizer. In the system, K out of U UEs are admitted for downlink transmission. The message for the admitted UEs is precoded via rate splitting and transmitted over the air.

$\mathcal{U}'$. Now, every UE in $\mathcal{U}'$ is served with a message denoted by W_u, $u \in \mathcal{U}'$, which is decomposed into two parts as $W_u \triangleq \left(W_u^{(\mathrm{p})}, W_u^{(\mathrm{c})}\right)$, where $W_u^{(\mathrm{p})}$ and $W_u^{(\mathrm{c})}$ are respectively referred to as the private and common portions of W_u. The private portion of UE_u is encoded into a symbol $s_u \in \mathbb{C}$ that is transmitted at a rate $R_u^{(\mathrm{p})}$ in an unicast manner. On the other hand, the common portions $W_u^{(\mathrm{c})}$ of all UEs are combined and encoded into a symbol $s_0 \in \mathbb{C}$, which is transmitted at a rate $R^{(\mathrm{c})}$ in a multicast manner to all UEs. The symbols are assumed to be statistically independent, such that $\mathbb{E}\left\{\mathbf{s}^{\mathrm{H}}\mathbf{s}\right\} = \mathbf{I}$ and $\mathbf{s} = \left[s_0, s_1, \ldots, s_K\right]^{\mathrm{T}} \in \mathbb{C}^{(K+1)\times 1}$. The rate portion of $R^{(\mathrm{c})}$ corresponding to UE_u is denoted by C_u, such that $R^{(\mathrm{c})} = \sum_u C_u$. As a result, UE_u is served with an overall rate of $R_u^{(\mathrm{p})} + C_u$. Every UE recovers $W_u^{(\mathrm{c})}$ and $W_u^{(\mathrm{p})}$ after decoding s_0 and s_u, respectively, which allows to reassemble message W_u. In addition, each UE_u acquires the common parts $W_{i\neq u}^{(\mathrm{c})}$, corresponding to the other UEs, which are used for interference decoding and cancellation. Thus, by adjusting the partitioning ratio of the common and private portions, $W_u^{(\mathrm{p})}$ and $W_u^{(\mathrm{c})}$, of the messages, RSMA can seamlessly bridge the two extremes of fully treating interference as noise and fully decoding it [3].

2.0.3 Discrete and Continuous Rates: Practical wireless systems, as defined, e.g., in cellular standards, support only a finite set of data rates [22, p. 64]. These predefined rates are identified by their channel quality indicator (CQI) and correspond to specific MCSs. For each rate, a target SINR is required to ensure a given block error rate (BLER) [39]. The rates and MCSs are typically standardized, e.g., by 3GPP. However, the target SINRs are specific to the equipment in use. We denote with J the total number of available MCSs supported by the system and with $\mathcal{J} = \{1, \ldots, J\}$ the set that indexes them. Hence, for a given discrete rate R_j, $j \in \mathcal{J}$, there is a corresponding target SINR Γ_j that must be met to guarantee that rate. In addition, we assume that $\mathcal{J}$ is an ordered set, such that $R_{j+1} > R_j$ and $\Gamma_{j+1} > \Gamma_j$. Thus, if an UE achieves an SINR of $\overline{\Gamma}$, the BS can allocate any discrete rate $\overline{R}_{\mathrm{dis}} \triangleq \left\{R_j \mid \Gamma_j \leq \overline{\Gamma}, j \in \mathcal{J}\right\}$ to the UE. On the contrary, when Shannon's capacity formula is used for rate allocation, the BS assigns continuous rate $\overline{R}_{\mathrm{con}} \triangleq \log_2\left(1 + \overline{\Gamma}\right)$.

3 Problem Formulation and Proposed Algorithm for Discrete-Rate RSMA

In this section, we formulate and solve the WSR and WEE maximization problems to optimize the beamforming, user admission, and discrete rates for imperfect SIC. For ease of presentation, we summarize the most important parameters and decision variables in Table 1.

Table 1: Parameters and decision variables of the considered system.

Parameters and Decision Variables	Notation
Number of antennas at the BS	N_{tx}
Number of UEs	U
Number of admitted UEs	K
Number of discrete rates	J
Channel between the BS and UE_u	$\mathbf{h}_u$
Noise power	σ^2
Weight of UE_u	ω_u
Dynamic power consumption of the circuitry	P_{dyn}
Static power consumption of the circuitry	P_{sta}
Conversion efficiency of the power amplifier	η_{eff}
Common rate of UE_u	C_u
Private precoder for UE_u	$\mathbf{w}_u$
Common precoder for all admitted UEs	$\mathbf{m}$
Binary variable for private rate selection	$\alpha_{u,j}$
Binary variable for common rate selection	κ_j
Binary variable for UE admission	χ_u
Binary variable for private precoder design	μ_u
Binary variable for common precoder design	ψ

3.1 Problem Formulation

We consider two objectives, namely, WSR and WEE maximization, and define the corresponding optimization problems $\mathcal{P}'_{\text{DWSR}}$ and $\mathcal{P}'_{\text{DWEE}}$, shown at the bottom of this page. Specifically, ω_u is the weight associated with UE_u, which can be set by the network operator, e.g., to improve rate fairness. Besides, we define $\mathbf{W} = [\mathbf{w}_1, \ldots, \mathbf{w}_U]$, $\mathbf{c} = [C_1, \ldots, C_U]$, $\boldsymbol{\chi} = [\chi_1, \ldots, \chi_U]$, $\boldsymbol{\mu} = [\mu_1, \ldots, \mu_U]$, $\boldsymbol{\alpha} = [\alpha_{1,1}, \ldots, \alpha_{U,J}]$, and $\boldsymbol{\kappa} = [\kappa_1, \ldots, \kappa_J]$. In addition, η_{eff} represents the amplifier efficiency and $P_{\text{cir}} = N_{\text{tx}} P_{\text{dyn}} + P_{\text{sta}}$ is the power consumed by the circuitry at the BS, where P_{dyn} and P_{sta} denote the dynamic and static parts, respectively [16]. Next, we discuss the constraints of the above optimization problems.

3.1.1 User admission: To indicate whether a given UE_u is admitted, we introduce constraint $\overline{\mathrm{C}}_1 : \chi_u \in \{0,1\}, \forall u \in \mathcal{U}$, i.e., $\chi_u = 1$ indicates that the BS serves UE_u, and $\chi_u = 0$ otherwise. Further, we have $\overline{\mathrm{C}}_2 : \sum_{u\in\mathcal{U}} \chi_u = K$ as the number of admitted UEs is K. An admitted UE can receive its message via the common signal only, the private signal only, or both. To indicate whether an admitted UE_u is served via the private signal, we introduce $\overline{\mathrm{C}}_3 : \mu_u \in \{0,1\}, \forall u \in \mathcal{U}$, i.e., $\mu_u = 1$ indicates that UE_u is served via the private signal, and $\mu_u = 0$ otherwise. We also include $\overline{\mathrm{C}}_4 : \mu_u \le \chi_u, \forall u \in \mathcal{U}$, to ensure that non-admitted UEs are not served by a private signal. Naturally, non-admitted UEs are also not served by the common signal but this is handled by constraint $\overline{\mathrm{C}}_{12}$, discussed in Section 3.1.5. Lastly, we introduce $\overline{\mathrm{C}}_5 : \psi \in \{0,1\}$ to denote whether the common signal is used.

3.1.2 Beamforming: The BS employs a private precoder $\mathbf{w}_u\mu_u \in \mathbb{C}^{N_{\text{tx}}\times 1}$ to precode symbol s_u, and a common precoder $\mathbf{m}\psi \in \mathbb{C}^{N_{\text{tx}}\times 1}$ to precode symbol s_0. The private precoder is $\mathbf{0}$ when UE_u is not admitted. Thus, the downlink signal of the BS is given by $\mathbf{x} = \sum_{u\in\mathcal{U}} \mathbf{w}_u\mu_u s_u + \mathbf{m}\psi s_0$. To account for the transmit power limitation of the BS, the precoders must satisfy $\overline{\mathrm{C}}_6 : \sum_{u\in\mathcal{U}} \|\mathbf{w}_u\mu_u\|_2^2 + \|\mathbf{m}\psi\|_2^2 \le P_{\text{tx}}^{\max}$.

3.1.3 Imperfect SIC: The signal received by UE_u is expressed as $y_u = \mathbf{h}_u^{\mathrm{H}}\mathbf{x} + \eta_u$, which is equivalent to

$$y_u = \underbrace{\mathbf{h}_u^{\mathrm{H}}\mathbf{m}\psi s_0}_{\substack{\text{common signal}\\ y_u^{(\mathrm{c})}}} + \underbrace{\mathbf{h}_u^{\mathrm{H}}\mathbf{w}_u\mu_u s_u}_{\substack{\text{private signal}\\ y_u^{(\mathrm{p})}}} + \underbrace{\textstyle\sum_{i\neq u}\mathbf{h}_u^{\mathrm{H}}\mathbf{w}_i\mu_i s_i}_{\substack{\text{interference}\\ y_u^{(\mathrm{int})}}} + \underbrace{\eta_u}_{\text{noise}}, \tag{1}$$

where $y_u^{(\mathrm{c})}$ is the received common signal, $y_u^{(\mathrm{p})}$ is the received private signal, and $y_u^{(\mathrm{int})}$ is the interference at UE_u. Further, $\eta_u \sim \mathcal{CN}(0, \sigma^2)$ denotes additive white Gaussian noise, and $\mathbf{h}_u \in \mathbb{C}^{N_{\text{tx}}\times 1}$ represents the channel between the BS and UE_u. An admitted UE_u utilizes SIC in order to recover its message from y_u. Specifically, UE_u decodes first the common symbol s_0 by treating signals $y_u^{(\mathrm{p})}$ and $y_u^{(\mathrm{int})}$ as noise. Next, UE_u reconstructs the received common signal $y_u^{(\mathrm{c})}$ and subtracts it from y_u, yielding $y_u^{\text{SIC}} = y_u^{(\mathrm{p})} + y_u^{(\mathrm{int})} + \eta_u$, based on which it decodes its private symbol s_u. However, removal of $y_u^{(\mathrm{c})}$ is not perfect in practice, which can be caused, e.g., by hardware impairments [34], [35]. Therefore, the signal after imperfect SIC can be expressed as $y_u^{\text{iSIC}} = \Delta_{\text{SIC}} y_u^{(\mathrm{c})} + y_u^{(\mathrm{p})} + y_u^{(\mathrm{int})} + \eta_u$,

$$\begin{aligned}
\mathcal{P}'_{\text{DWSR}}: \mathcal{P}'_{\text{DWEE}}: \max_{\mathbf{W},\mathbf{m},\mathbf{c},\boldsymbol{\chi},\boldsymbol{\mu},\boldsymbol{\alpha},\boldsymbol{\kappa},\psi} \quad & \begin{cases} f_{\text{DWSR}}(\mathbf{c},\boldsymbol{\alpha}) \triangleq \sum_{u\in\mathcal{U}} \omega_u \big(\sum_{j\in\mathcal{J}} \alpha_{u,j} R_j + C_u\big) & \text{(linear)} \\ f_{\text{DWEE}}(\mathbf{W},\mathbf{m},\mathbf{c},\boldsymbol{\mu},\boldsymbol{\alpha},\psi) \triangleq \frac{\sum_{u\in\mathcal{U}} \omega_u \big(\sum_{j\in\mathcal{J}} \alpha_{u,j} R_j + C_u\big)}{\frac{1}{\eta_{\text{eff}}}\big(\sum_{u\in\mathcal{U}} \|\mathbf{w}_u\mu_u\|_2^2 + \|\mathbf{m}\psi\|_2^2\big) + P_{\text{cir}}} & \text{(nonconvex)} \end{cases} \\
\text{s.t.} \quad & \overline{\mathrm{C}}_1 : \chi_u \in \{0,1\}, \forall u \in \mathcal{U}, && \text{(binary)} \\
& \overline{\mathrm{C}}_2 : \textstyle\sum_{u\in\mathcal{U}} \chi_u = K, && \text{(linear)} \\
& \overline{\mathrm{C}}_3 : \mu_u \in \{0,1\}, \forall u \in \mathcal{U}, && \text{(binary)} \\
& \overline{\mathrm{C}}_4 : \mu_u \le \chi_u, \forall u \in \mathcal{U}, && \text{(linear)} \\
& \overline{\mathrm{C}}_5 : \psi \in \{0,1\}, && \text{(binary)} \\
& \overline{\mathrm{C}}_6 : \textstyle\sum_{u\in\mathcal{U}} \|\mathbf{w}_u\mu_u\|_2^2 + \|\mathbf{m}\psi\|_2^2 \le P_{\text{tx}}^{\max}, && \text{(nonconvex)} \\
& \overline{\mathrm{C}}_7 : \alpha_{u,j} \in \{0,1\}, \forall u \in \mathcal{U}, j \in \mathcal{J}, && \text{(binary)} \\
& \overline{\mathrm{C}}_8 : \textstyle\sum_{j\in\mathcal{J}} \alpha_{u,j} = \mu_u, \forall u \in \mathcal{U}, && \text{(linear)} \\
& \overline{\mathrm{C}}_9 : \mathsf{SINR}_u^{(\mathrm{p})} \ge \textstyle\sum_{j\in\mathcal{J}} \alpha_{u,j}\Gamma_j, \forall u \in \mathcal{U}, && \text{(nonconvex)} \\
& \overline{\mathrm{C}}_{10} : \kappa_j \in \{0,1\}, \forall j \in \mathcal{J}, && \text{(binary)} \\
& \overline{\mathrm{C}}_{11} : \textstyle\sum_{j\in\mathcal{J}} \kappa_j = \psi, && \text{(linear)} \\
& \overline{\mathrm{C}}_{12} : \mathsf{SINR}_u^{(\mathrm{c})} \ge \chi_u \textstyle\sum_{j\in\mathcal{J}} \kappa_j\Gamma_j, \forall u \in \mathcal{U}, && \text{(nonconvex)} \\
& \overline{\mathrm{C}}_{13} : C_u \ge 0, \forall u \in \mathcal{U}, && \text{(linear)} \\
& \overline{\mathrm{C}}_{14} : C_u \le \chi_u \textstyle\sum_{j\in\mathcal{J}} \kappa_j R_j, \forall u \in \mathcal{U}, && \text{(nonconvex)} \\
& \overline{\mathrm{C}}_{15} : \textstyle\sum_{u\in\mathcal{U}} C_u = \sum_{j\in\mathcal{J}} \kappa_j R_j, && \text{(linear)} \\
& \overline{\mathrm{C}}_{16} : \textstyle\sum_{j\in\mathcal{J}} \alpha_{u,j} R_j + C_u \ge R_{\min}\chi_u, \forall u \in \mathcal{U}, && \text{(linear)}
\end{aligned}$$

where $0 \leq \Delta_{\mathrm{SIC}} \leq 1$ is the percentage of the common signal that is not canceled, i.e., $\Delta_{\mathrm{SIC}} = 0$ implies perfect SIC. As a result, the SINRs of the common and private signals at UE_u are $\mathsf{SINR}_u^{(\mathrm{c})} = \frac{\left|\mathbf{h}_u^{\mathrm{H}}\mathbf{m}\psi\right|^2}{\sum_{i\in\mathcal{U}}|\mathbf{h}_u^{\mathrm{H}}\mathbf{w}_i\mu_i|^2+\sigma^2}$ and $\mathsf{SINR}_u^{(\mathrm{p})} = \frac{\left|\mathbf{h}_u^{\mathrm{H}}\mathbf{w}_u\mu_u\right|^2}{|\Delta_{\mathrm{SIC}}\mathbf{h}_u^{\mathrm{H}}\mathbf{m}\psi|^2+\sum_{i\neq u}|\mathbf{h}_u^{\mathrm{H}}\mathbf{w}_i\mu_i|^2+\sigma^2}$, respectively. The exact value of Δ_{SIC} is usually not known by the BS. Therefore, it must be set properly to avoid performance degradation, and thus guarantee the target SINRs that enable the allocated rates. Typical values for Δ_{SIC} are in the range of 4% and 10% [35].

3.1.4 Rate selection for the private signals: An UE_u receiving a private signal at a rate R_j, can only decode the message if $\mathsf{SINR}_u^{(\mathrm{p})} \geq \Gamma_j$, where Γ_j is the target SINR that guarantees R_j (for numerical values, see Table 2 in Section 5). To depict the assignment of private rates, we introduce constraint $\overline{\mathrm{C}}_7 : \alpha_{u,j} \in \{0,1\}, \forall u \in \mathcal{U}, j \in \mathcal{J}$, where $\alpha_{u,j} = 1$ indicates that UE_u is served by a private signal transmitted at rate R_j. In addition, we include $\overline{\mathrm{C}}_8 : \sum_{j\in\mathcal{J}} \alpha_{u,j} = \mu_u, \forall u \in \mathcal{U}$, to ensure that a rate is allocated to UE_u, if it is served by the private signal. Further, to associate the discrete rates and their corresponding target SINRs, we include $\overline{\mathrm{C}}_9 : \mathsf{SINR}_u^{(\mathrm{p})} \geq \sum_{j\in\mathcal{J}} \alpha_{u,j}\Gamma_j, \forall u \in \mathcal{U}$, which ensures for UE_u a private rate of $\sum_{j\in\mathcal{J}} \alpha_{u,j}R_j$ if $\mu_u = 1$. Note that $\mu_u = 0$ does not indicate that UE_u is not admitted since UE_u can also be served by the common signal if $C_u > 0$.

3.1.5 Rate selection for the common signal: An admitted UE_u can only decode the common message transmitted at rate R_j, if $\mathsf{SINR}_u^{(\mathrm{c})} \geq \Gamma_j$. To this end, we introduce constraint $\overline{\mathrm{C}}_{10} : \kappa_j \in \{0,1\}, j \in \mathcal{J}$, where $\kappa_j = 1$ indicates that rate R_j is selected. We include $\overline{\mathrm{C}}_{11} : \sum_{j\in\mathcal{J}} \kappa_j = \psi$ to allow for the possibility that the common rate is zero (see constraint $\overline{\mathrm{C}}_5$). To unify user admission and the allocation of the common rate, we add $\overline{\mathrm{C}}_{12} : \mathsf{SINR}_u^{(\mathrm{c})} \geq \chi_u \sum_{j\in\mathcal{J}} \kappa_j\Gamma_j, \forall u \in \mathcal{U}$, which results in the common rate $\sum_{j\in\mathcal{J}} \kappa_j R_j$ for all admitted UEs. Although the rate portions C_u are not continuous, they have very fine granularity because rate splitting is capable of dividing the messages W_u into portions of any size. Thus, we treat C_u as continuous-valued by adding $\overline{\mathrm{C}}_{13} : C_u \geq 0, \forall u \in \mathcal{U}$. To keep consistency with user admission, we include $\overline{\mathrm{C}}_{14} : C_u \leq \chi_u \sum_{j\in\mathcal{J}} \kappa_j R_j, \forall u \in \mathcal{U}$, to enforce $C_u = 0$ for non-admitted UEs or when the common rate is zero (see constraints $\overline{\mathrm{C}}_5, \overline{\mathrm{C}}_{11}$). Moreover, we add $\overline{\mathrm{C}}_{15} : \sum_u C_u = \sum_{j\in\mathcal{J}} \kappa_j R_j$ to guarantee that the sum of all common portions C_u is equal to the overall common rate. Finally, we enforce a minimum rate $R_{\min}$ per admitted UE by including constraint $\overline{\mathrm{C}}_{16} : \sum_{j\in\mathcal{J}} \alpha_{u,j}R_j + C_u \geq R_{\min}\chi_u$.

REMARK 1: *Problems $\mathcal{P}'_{\mathrm{DWSR}}$ and $\mathcal{P}'_{\mathrm{DWEE}}$ are nonconvex MINLPs, which are challenging to solve. Specifically, the nonconvexity is due to constraints $\overline{\mathrm{C}}_6$, $\overline{\mathrm{C}}_9$, $\overline{\mathrm{C}}_{12}$, $\overline{\mathrm{C}}_{14}$ and the objective function $f_{\mathrm{DWEE}}(\mathbf{W}, \mathbf{m}, \mathbf{c}, \boldsymbol{\mu}, \boldsymbol{\alpha}, \psi)$, which contain quotients of quadratic functions and multiplicative couplings. Further, a simple strategy to obtain the SDMA versions of $\mathcal{P}'_{\mathrm{DWSR}}$ and $\mathcal{P}'_{\mathrm{DWEE}}$ is to set $\psi = 0$ because RSMA includes SDMA as a special case.*

3.2 Proposed Algorithm

We propose the `OPT-MISOCP` algorithm to solve the nonconvex MINLPs $\mathcal{P}'_{\mathrm{DWSR}}$ and $\mathcal{P}'_{\mathrm{DWEE}}$. Instead of treating $\mathcal{P}'_{\mathrm{DWSR}}$ and $\mathcal{P}'_{\mathrm{DWEE}}$ as general nonconvex MINLPs, we propose a sequence of transformations to overcome the nonconvexities, thereby transforming the nonconvex MINLPs $\mathcal{P}'_{\mathrm{DWSR}}$ and $\mathcal{P}'_{\mathrm{DWEE}}$ to the convex MISOCPs $\mathcal{P}_{\mathrm{DWSR}}$ and $\mathcal{P}_{\mathrm{DWEE}}$, respectively, whose global optima can be found using branch-and-bound (BnB) and interior-point methods (IPMs). Specifically, BnB is used for decomposing the binary variables of the MISOCP, whereas IPMs are used for solving the underlying SOCPs. In the following, we describe the proposed algorithm for $\mathcal{P}'_{\mathrm{DWSR}}$ and then we extend it to $\mathcal{P}'_{\mathrm{DWEE}}$.

3.2.1 Circumventing Integer Multiplicative Couplings: To cope with the multiplicative coupling between binary variables in constraints $\overline{\mathrm{C}}_{12}$, $\overline{\mathrm{C}}_{14}$, appearing in the form of $\chi_u\kappa_j$, we transform such products into the intersection of linear combinations. We introduce new variables $\pi_{u,j} = \chi_u\kappa_j$, and equivalently rewrite constraints $\overline{\mathrm{C}}_{12}$, $\overline{\mathrm{C}}_{14}$ as constraints $\overline{\mathrm{D}}_1 - \overline{\mathrm{D}}_6$, shown at the top of the next page (cf. **Appendix A**).

3.2.2 Circumventing Mixed-Integer Multiplicative Couplings: To deal with the mixed-integer multiplicative couplings in constraints $\overline{\mathrm{C}}_6$, $\overline{\mathrm{C}}_9$, $\overline{\mathrm{D}}_5$, appearing in the form of $\mathbf{w}_u\mu_u$ and $\mathbf{m}\psi$, we reformulate such products as linear relations without altering the nature of the problem. Thus, constraints $\overline{\mathrm{C}}_6, \overline{\mathrm{C}}_9, \overline{\mathrm{D}}_5$ are equivalently rewritten as constraints $\overline{\mathrm{E}}_1 - \overline{\mathrm{E}}_5$, shown at the top of the next page (cf. **Appendix B**).

3.2.3 Circumventing Integer Additive Couplings: The additive couplings of binary variables in $\overline{\mathrm{E}}_4$, $\overline{\mathrm{E}}_5$, which appear in the form $\sum_{j\in\mathcal{J}} \alpha_{u,j}\Gamma_j$ and $\sum_{j\in\mathcal{J}} \pi_{u,j}\Gamma_j$, pose a difficulty for subsequent convexification since multiple binary variables and their corresponding target SINRs are combined. However, since the couplings are linear and sum to at most one, we can handle them by expanding them into several constraints (i.e., as multiple choice constraints), such that each of the resulting constraints depends on one binary variable only. Thus, constraints $\overline{\mathrm{E}}_4$, $\overline{\mathrm{E}}_5$ are equivalently recast as $\overline{\mathrm{F}}_1$, $\overline{\mathrm{F}}_2$, shown at the top of the next page (cf. **Appendix C**).

3.2.4 Reformulating the SINR Constraints via the Big-M Method: To deal with the disjunctiveness caused by the binary variables, which lead to different SINR requirements for the admitted and non-admitted UEs, in $\overline{\mathrm{F}}_1$, $\overline{\mathrm{F}}_2$, we merge these two cases into a single one via the Big-M method. Thus, by defining $\overline{\mathbf{W}}_u = [\Delta_{\mathrm{SIC}}\mathbf{m}, \mathbf{w}_1, \ldots, \mathbf{w}_{u-1}, \mathbf{w}_{u+1}, \ldots, \mathbf{w}_U]$ and $L_{\max,u}^2 = \|\mathbf{h}_u\|_2^2 P_{\mathrm{tx}}^{\max} + \sigma^2$, we recast constraints $\overline{\mathrm{F}}_1$, $\overline{\mathrm{F}}_2$ as $\overline{\mathrm{G}}_1, \overline{\mathrm{G}}_2$, shown at the top of the next page (cf. **Appendix D**).

3.2.5 Convexifying the Private SINR Constraints: Although constraint $\overline{\mathrm{G}}_1$ is nonconvex due to being a difference of convex (DC) functions, it can be convexified without changing its feasible set. In fact, constraint $\overline{\mathrm{G}}_1$ can be expressed as $\overline{\mathrm{H}}_1$, $\overline{\mathrm{H}}_2$, $\overline{\mathrm{H}}_3$, shown at the top of the next page (cf. **Appendix E**).

3.2.6 Convexifying the Common SINR Constraints: The nonconvex constraint $\overline{\mathrm{G}}_2$ can be replaced by the inner convex approximations $\bar{\mathrm{I}}_1$, $\bar{\mathrm{I}}_2$, shown at the top of the next page, which may shrink the original feasible set (cf. **Appendix F**).

3.2.7 Adding Cutting Planes to Tighten the Feasible Domain: To reduce the search complexity caused by BnB branching for the binary variables, we add problem-specific cutting planes, which do not impact optimality (cf. **Appendix G**). We add cuts $\overline{\mathrm{J}}_1$ to tighten the feasible set, which can help

$$\overline{\mathrm{C}}_{12}, \overline{\mathrm{C}}_{14} \Leftrightarrow \begin{cases} \overline{\mathrm{D}}_1 : \pi_{u,j} \in \{0,1\}, \forall u \in \mathcal{U}, j \in \mathcal{J}, & \text{(binary)} \\ \overline{\mathrm{D}}_2 : \pi_{u,j} \leq \chi_u, \forall u \in \mathcal{U}, j \in \mathcal{J}, \ \overline{\mathrm{D}}_3 : \pi_{u,j} \leq \kappa_j, \forall u \in \mathcal{U}, j \in \mathcal{J}, & \text{(linear)} \\ \overline{\mathrm{D}}_4 : \pi_{u,j} \geq \chi_u + \kappa_j - 1, \forall u \in \mathcal{U}, j \in \mathcal{J}, & \text{(linear)} \\ \overline{\mathrm{D}}_5 : \frac{\left|\mathbf{h}_u^{\mathrm{H}} \mathbf{m} \psi\right|^2}{\sum_{i \in \mathcal{U}} |\mathbf{h}_u^{\mathrm{H}} \mathbf{w}_i \mu_i|^2 + \sigma^2} \geq \sum_{j \in \mathcal{J}} \pi_{u,j} \Gamma_j, \forall u \in \mathcal{U}, & \text{(nonconvex)} \\ \overline{\mathrm{D}}_6 : C_u \leq \sum_{j \in \mathcal{J}} \pi_{u,j} R_j, \forall u \in \mathcal{U}. & \text{(linear)} \end{cases}$$

$$\overline{\mathrm{C}}_6, \overline{\mathrm{C}}_9, \overline{\mathrm{D}}_5 \Leftrightarrow \begin{cases} \overline{\mathrm{E}}_1 : \|\mathbf{w}_u\|_2^2 \leq \mu_u P_{\mathrm{tx}}^{\max}, \forall u \in \mathcal{U}, \ \overline{\mathrm{E}}_2 : \|\mathbf{m}\|_2^2 \leq \psi P_{\mathrm{tx}}^{\max}, \ \overline{\mathrm{E}}_3 : \sum_{u \in \mathcal{U}} \|\mathbf{w}_u\|_2^2 + \|\mathbf{m}\|_2^2 \leq P_{\mathrm{tx}}^{\max}, & \text{(convex)} \\ \overline{\mathrm{E}}_4 : \frac{\left|\mathbf{h}_u^{\mathrm{H}} \mathbf{w}_u\right|^2}{\Delta_{\mathrm{SIC}}^2 |\mathbf{h}_u^{\mathrm{H}} \mathbf{m}|^2 + \sum_{i \neq u, i \in \mathcal{U}} |\mathbf{h}_u^{\mathrm{H}} \mathbf{w}_i|^2 + \sigma^2} \geq \sum_{j \in \mathcal{J}} \alpha_{u,j} \Gamma_j, \forall u \in \mathcal{U}, & \text{(nonconvex)} \\ \overline{\mathrm{E}}_5 : \frac{\left|\mathbf{h}_u^{\mathrm{H}} \mathbf{m}\right|^2}{\sum_{i \in \mathcal{U}} |\mathbf{h}_u^{\mathrm{H}} \mathbf{w}_i|^2 + \sigma^2} \geq \sum_{j \in \mathcal{J}} \pi_{u,j} \Gamma_j, \forall u \in \mathcal{U}. & \text{(nonconvex)} \end{cases}$$

$$\overline{\mathrm{E}}_4, \overline{\mathrm{E}}_4 \Leftrightarrow \begin{cases} \overline{\mathrm{F}}_1 : \frac{\left|\mathbf{h}_u^{\mathrm{H}} \mathbf{w}_u\right|^2}{\Delta_{\mathrm{SIC}}^2 |\mathbf{h}_u^{\mathrm{H}} \mathbf{m}|^2 + \sum_{i \neq u, i \in \mathcal{U}} |\mathbf{h}_u^{\mathrm{H}} \mathbf{w}_i|^2 + \sigma^2} \geq \alpha_{u,j} \Gamma_j, \forall u \in \mathcal{U}, j \in \mathcal{J}, & \text{(nonconvex)} \\ \overline{\mathrm{F}}_2 : \frac{\left|\mathbf{h}_u^{\mathrm{H}} \mathbf{m}\right|^2}{\sum_{i \in \mathcal{U}} |\mathbf{h}_u^{\mathrm{H}} \mathbf{w}_i|^2 + \sigma^2} \geq \pi_{u,j} \Gamma_j, \forall u \in \mathcal{U}, j \in \mathcal{J}. & \text{(nonconvex)} \end{cases}$$

$$\overline{\mathrm{F}}_1, \overline{\mathrm{F}}_2 \Leftrightarrow \begin{cases} \overline{\mathrm{G}}_1 : \left\| \left[\mathbf{h}_u^{\mathrm{H}} \overline{\mathbf{W}} u, \sigma\right] \right\|_2^2 \leq \frac{1}{\Gamma_j} \left|\mathbf{h}_u^{\mathrm{H}} \mathbf{w}_u\right|^2 + (1 - \alpha_{u,j}) L_{\max,u}^2, \forall u \in \mathcal{U}, j \in \mathcal{J}, & \text{(nonconvex)} \\ \overline{\mathrm{G}}_2 : \left\| \left[\mathbf{h}_u^{\mathrm{H}} \mathbf{W}, \sigma\right] \right\|_2^2 \leq \frac{1}{\Gamma_j} \left|\mathbf{h}_u^{\mathrm{H}} \mathbf{m}\right|^2 + (1 - \pi_{u,j}) L_{\max,u}^2, \forall u \in \mathcal{U}, j \in \mathcal{J}. & \text{(nonconvex)} \end{cases}$$

$$\overline{\mathrm{G}}_1 \Leftrightarrow \begin{cases} \overline{\mathrm{H}}_1 : \mathfrak{Re}\left\{\mathbf{h}_u^{\mathrm{H}} \mathbf{w}_u\right\} \geq 0, \forall u \in \mathcal{U}, \ \overline{\mathrm{H}}_2 : \mathfrak{Im}\left\{\mathbf{h}_u^{\mathrm{H}} \mathbf{w}_u\right\} = 0, \forall u \in \mathcal{U}, & \text{(linear)} \\ \overline{\mathrm{H}}_3 : \left\| \left[\mathbf{h}_u^{\mathrm{H}} \overline{\mathbf{W}} u, \sigma\right] \right\|_2 \leq \frac{1}{\sqrt{\Gamma_j}} \mathfrak{Re}\left\{\mathbf{h}_u^{\mathrm{H}} \mathbf{w}_u\right\} + (1 - \alpha_{u,j}) L_{\max,u}, \forall u \in \mathcal{U}, j \in \mathcal{J}. & \text{(convex)} \end{cases}$$

$$\overline{\mathrm{G}}_2 \Leftrightarrow \begin{cases} \overline{\mathrm{I}}_1 : \mathfrak{Re}\left\{\mathbf{h}_u^{\mathrm{H}} \mathbf{m}\right\} \geq 0, \forall u \in \mathcal{U}, & \text{(linear)} \\ \overline{\mathrm{I}}_2 : \left\| \left[\mathbf{h}_u^{\mathrm{H}} \mathbf{W}, \sigma\right] \right\|_2 \leq \frac{1}{\sqrt{\Gamma_j}} \mathfrak{Re}\left\{\mathbf{h}_u^{\mathrm{H}} \mathbf{m}\right\} + (1 - \pi_{u,j}) L_{\max,u}, \forall u \in \mathcal{U}, j \in \mathcal{J}. & \text{(convex)} \end{cases}$$

accelerating the optimization. In addition, we include $\overline{\mathrm{J}}_2$ as an upper bound of the sum-rate, which facilitates early stopping:

$$\overline{\mathrm{J}}_1 : \mathfrak{Re}\left\{\mathbf{h}_u^{\mathrm{H}} \mathbf{w}_u\right\} \geq \sigma \sum_{j \in \mathcal{J}} \alpha_{u,j} \sqrt{\Gamma_j}, \forall u \in \mathcal{U}, \quad \text{(linear)}$$

$$\overline{\mathrm{J}}_2 : \sum_{u \in \mathcal{U}} \Big(\sum_{j \in \mathcal{J}} \alpha_{u,j} R_j + C_u \Big) \leq (K+1) R_J. \quad \text{(linear)}$$

REMARK 2: *In our simulations, a remarkable improvement in runtime was observed with the addition of $\overline{\mathrm{J}}_1$ and $\overline{\mathrm{J}}_2$, which accelerated the optimization $3-20$ times compared to the case without them.*

3.2.8 Outlining the Algorithm and Its Extension to Solve $\mathcal{P}'_{\mathrm{DWEE}}$: Recapitulating the results above, problem $\mathcal{P}'_{\mathrm{DWSR}}$ is recast as

$$\mathcal{P}_{\mathrm{DWSR}} : \max_{\boldsymbol{\Theta}} f_{\mathrm{DWSR}}(\mathbf{c}, \boldsymbol{\alpha}) \text{ s.t. } \boldsymbol{\Theta} \in \mathcal{C},$$

where $\boldsymbol{\Theta} = (\mathbf{W}, \mathbf{m}, \mathbf{c}, \boldsymbol{\chi}, \boldsymbol{\mu}, \boldsymbol{\alpha}, \boldsymbol{\kappa}, \boldsymbol{\pi}, \psi)$ and $\mathcal{C}$ is the feasible set of $\boldsymbol{\Theta}$ defined by $\overline{\mathrm{C}}_1 - \overline{\mathrm{C}}_5, \overline{\mathrm{C}}_7, \overline{\mathrm{C}}_8, \overline{\mathrm{C}}_{10}, \overline{\mathrm{C}}_{11}, \overline{\mathrm{C}}_{13}, \overline{\mathrm{C}}_{15}, \overline{\mathrm{C}}_{16}, \overline{\mathrm{D}}_1 - \overline{\mathrm{D}}_4, \overline{\mathrm{D}}_6, \overline{\mathrm{E}}_1 - \overline{\mathrm{E}}_3, \overline{\mathrm{H}}_1 - \overline{\mathrm{H}}_3, \overline{\mathrm{I}}_1, \overline{\mathrm{I}}_2, \overline{\mathrm{J}}_1, \overline{\mathrm{J}}_2$. Analogous to $\mathcal{P}'_{\mathrm{DWSR}}$, we recast problem $\mathcal{P}'_{\mathrm{DWEE}}$ as

$$\mathcal{P}_{\mathrm{DWEE}} : \min_{\boldsymbol{\Theta}} \frac{\frac{1}{\eta_{\mathrm{eff}}} \left(\sum_{u \in \mathcal{U}} \|\mathbf{w}_u\|_2^2 + \|\mathbf{m}\|_2^2 \right) + P_{\mathrm{cir}}}{\sum_{u \in \mathcal{U}} \omega_u \left(\sum_{j \in \mathcal{J}} \alpha_{u,j} R_j + C_u \right)} \text{ s.t. } \boldsymbol{\Theta} \in \mathcal{C},$$

where we have transformed the maximization of $f_{\mathrm{DWEE}}(\mathbf{W}, \mathbf{m}, \mathbf{c}, \boldsymbol{\mu}, \boldsymbol{\alpha}, \psi)$ into the minimization of its reciprocal $\frac{1}{f_{\mathrm{DWEE}}(\mathbf{W}, \mathbf{m}, \mathbf{c}, \boldsymbol{\mu}, \boldsymbol{\alpha}, \psi)}$. In addition, we have removed the mixed-integer couplings from the objective function, as described in Section 3.2.2. As a result, the objective function of $\mathcal{P}_{\mathrm{DWEE}}$ is convex. Note that $\mathcal{P}_{\mathrm{DWSR}}$ and $\mathcal{P}_{\mathrm{DWEE}}$ are MISOCPs, which can be solved globally optimal via BnB and IPMs with off-the-shelf solvers, such as `MOSEK` and `GUROBI`, as the problems are convex in the continuous variables.

REMARK 3: *Due to the inner convexification of the feasible sets of $\mathcal{P}'_{\mathrm{DWSR}}$ ($\mathcal{P}'_{\mathrm{DWEE}}$) in Section 3.2.6, a globally optimal solution for $\mathcal{P}_{\mathrm{DWSR}}$ ($\mathcal{P}_{\mathrm{DWEE}}$) is feasible for $\mathcal{P}'_{\mathrm{DWSR}}$ ($\mathcal{P}'_{\mathrm{DWEE}}$) but not necessarily globally optimal for $\mathcal{P}'_{\mathrm{DWSR}}$ ($\mathcal{P}'_{\mathrm{DWEE}}$). However, such solution is found to be near-optimal for $\mathcal{P}'_{\mathrm{DWSR}}$ ($\mathcal{P}'_{\mathrm{DWEE}}$), as shown in Section 5.1, where we compare $\mathcal{P}_{\mathrm{DWSR}}$ against an upper bound of $\mathcal{P}'_{\mathrm{DWSR}}$, showing a negligible performance loss.*

3.2.9 Computational Complexity: Problems $\mathcal{P}_{\mathrm{DWSR}}$ and $\mathcal{P}_{\mathrm{DWEE}}$ involve $N_v = (U+1)N_{\mathrm{tx}} + U$ continuous variables and $N_c = 5UJ + 7U + 4$ linear and convex constraints. The dimension of the underlying SOCP is $N_d = 2JN_{\mathrm{tx}}U^2 + U^2 + 3UJ + 7U + 2UN_{\mathrm{tx}} + 2N_{\mathrm{tx}}$ for fixed values of the binary variables. Therefore, the complexities of problems $\mathcal{P}_{\mathrm{DWSR}}$ and $\mathcal{P}_{\mathrm{DWEE}}$ is $\mathcal{O}\left(N_p N_c^{0.5} N_v^2 N_d\right)$, where N_p is the number of solutions evaluated by the BnB solver. The worst-case for N_p is given by $N_p^{\mathrm{all}} = J^U + \sum_{k=0}^{K} \binom{U}{k} J^{k+1}$. In practice, $N_p \ll N_p^{\mathrm{all}}$ since BnB methods are capable of pruning infeasible and suboptimal branches, thus reducing the search complexity.

4 Problem Formulation and Proposed Algorithm for Continuous-Rate RSMA

In this section, we formulate and solve the WSR and WEE maximization problems for RSMA to optimize the beamforming, user admission, and continuous rates, while accounting for imperfect SIC.

4.1 Problem Formulation

We consider again WSR and WEE maximization as objectives, as in Section 3.1. Thus, we define the corresponding optimization problems $\mathcal{Q}'_{\mathrm{CWSR}}$ and $\mathcal{Q}'_{\mathrm{CWEE}}$, shown at the top of the next page. To account for continuous rates, we have applied the following changes to problems $\mathcal{P}'_{\mathrm{DWSR}}$ and $\mathcal{P}'_{\mathrm{DWEE}}$ in Section 3.1. First, we have eliminated binary

$$\begin{aligned}
\mathcal{Q}'_{\mathrm{CWSR}}:\ \mathcal{Q}'_{\mathrm{CWEE}}: \max_{\mathbf{W},\mathbf{m},\mathbf{c},\boldsymbol{\chi},\psi}\ & \begin{cases} f'_{\mathrm{CWSR}}\left(\mathbf{W},\mathbf{m},\mathbf{c}\right) \triangleq \sum_{u\in\mathcal{U}}\omega_u\big(\log_2\left(1+\mathsf{SINR}_u^{(\mathrm{p})}\right)+C_u\big) & \text{(nonconvex)} \\ f'_{\mathrm{CWEE}}\left(\mathbf{W},\mathbf{m},\mathbf{c}\right) \triangleq \frac{\sum_{u\in\mathcal{U}}\omega_u\left(\log_2\left(1+\mathsf{SINR}_u^{(\mathrm{p})}\right)+C_u\right)}{\frac{1}{\eta_{\mathrm{eff}}}\left(\sum_{u\in\mathcal{U}}\|\mathbf{w}_u\chi_u\|_2^2+\|\mathbf{m}\psi\|_2^2\right)+P_{\mathrm{cir}}} & \text{(nonconvex)} \end{cases} \\
\text{s.t.}\quad & \overline{\mathrm{C}}_1: \chi_u\in\{0,1\}, \forall u\in\mathcal{U}, && \text{(binary)} \\
& \overline{\mathrm{C}}_2: \textstyle\sum_{u\in\mathcal{U}}\chi_u = K, && \text{(linear)} \\
& \overline{\mathrm{C}}_5: \psi\in\{0,1\}, && \text{(binary)} \\
& \overline{\mathrm{C}}_6: \textstyle\sum_{u\in\mathcal{U}}\|\mathbf{w}_u\chi_u\|_2^2+\|\mathbf{m}\psi\|_2^2 \le P_{\mathrm{tx}}^{\max}, && \text{(nonconvex)} \\
& \overline{\mathrm{C}}_{13}: C_u\ge 0, \forall u\in\mathcal{U}, && \text{(linear)} \\
& \overline{\mathrm{C}}_{17}: C_u \le \psi\chi_u S_{\max}, \forall u\in\mathcal{U}, && \text{(linear)} \\
& \overline{\mathrm{C}}_{18}: \textstyle\sum_{i\in\mathcal{U}} C_i \le \log_2\left(1+\mathsf{SINR}_u^{(\mathrm{c})}\right)+(1-\chi_u)S_{\max}, \forall u\in\mathcal{U}, && \text{(nonconvex)} \\
& \overline{\mathrm{C}}_{19}: \log_2\left(1+\mathsf{SINR}_u^{(\mathrm{p})}\right)+C_u \ge R_{\min}\chi_u, \forall u\in\mathcal{U}. && \text{(nonconvex)}
\end{aligned}$$

$$\begin{aligned}
\mathcal{Q}_{\mathrm{CWSR}_n}:\ \max_{\mathbf{W},\mathbf{m},\mathbf{c}}\ & f_{\mathrm{CWSR}_n}\left(\mathbf{W},\mathbf{m},\mathbf{c}\right) && \text{(nonconvex)} \\
\text{s.t.}\quad & \overline{\mathrm{C}}_6: \textstyle\sum_{u\in\mathcal{U}'_n}\|\mathbf{w}_u\|_2^2+\|\mathbf{m}\|_2^2 \le P_{\mathrm{tx}}^{\max}, && \text{(convex)} \\
& \overline{\mathrm{C}}_{13}: C_u\ge 0, \forall u\in\mathcal{U}'_n, && \text{(linear)} \\
& \overline{\mathrm{C}}_{18}: \textstyle\sum_{i\in\mathcal{U}'_n} C_i \le \log_2\left(1+\frac{\left|\mathbf{h}_u^{\mathrm{H}}\mathbf{m}\right|^2}{\sum_{i\in\mathcal{U}'_n}\left|\mathbf{h}_u^{\mathrm{H}}\mathbf{w}_i\right|^2+\sigma^2}\right), \forall u\in\mathcal{U}'_n, && \text{(nonconvex)} \\
& \overline{\mathrm{C}}_{19}: \log_2\left(1+\frac{\left|\mathbf{h}_u^{\mathrm{H}}\mathbf{w}_u\right|^2}{\Delta_{\mathrm{SIC}}^2\left|\mathbf{h}_u^{\mathrm{H}}\mathbf{m}\right|^2+\sum_{i\neq u,i\in\mathcal{U}'_n}\left|\mathbf{h}_u^{\mathrm{H}}\mathbf{w}_i\right|^2+\sigma^2}\right)+C_u \ge R_{\min}, \forall u\in\mathcal{U}'_n, && \text{(nonconvex)} \\
& \overline{\mathrm{C}}_{20}: \|\mathbf{m}\|_2^2 \le \psi_0 P_{\mathrm{tx}}^{\max}, && \text{(convex)}
\end{aligned}$$

variables $\boldsymbol{\alpha},\boldsymbol{\kappa}$ used for discrete rate selection. Second, we have reduced the number of binary variables by dropping $\boldsymbol{\mu}$ and only use $\boldsymbol{\chi}$ since $\boldsymbol{\mu}=\boldsymbol{\chi}$, as rates are continuous. Hence, we could remove constraints $\overline{\mathrm{C}}_3,\overline{\mathrm{C}}_4,\overline{\mathrm{C}}_7-\overline{\mathrm{C}}_{12}$ and employ Shannon's capacity formula to redefine constraints $\overline{\mathrm{C}}_{14},\overline{\mathrm{C}}_{15},\overline{\mathrm{C}}_{16}$. Specifically, we have replaced constraint $\overline{\mathrm{C}}_{14}$ with $\overline{\mathrm{C}}_{17}: C_u\le\psi\chi_u S_{\max},\forall u\in\mathcal{U}$, and constraint $\overline{\mathrm{C}}_{15}$ with $\overline{\mathrm{C}}_{18}: \sum_{i\in\mathcal{U}} C_i \le \log_2\left(1+\mathsf{SINR}_u^{(\mathrm{c})}\right)+(1-\chi_u)S_{\max},\forall u\in\mathcal{U}$, where $S_{\max}=\max_{u\in\mathcal{U}}\log_2\left(1+\frac{P_{\mathrm{tx}}^{\max}}{\sigma^2}\left\|\mathbf{h}_u\right\|_2^2\right)$ is an upper bound for the common rate. Note that $\overline{\mathrm{C}}_{18}$ is tighter when $\chi_u=1$, and therefore the sum of the common rates is bounded by the minimum common rate of all admitted UEs. Finally, we have replaced $\overline{\mathrm{C}}_{16}$ with $\overline{\mathrm{C}}_{19}: \log_2\left(1+\mathsf{SINR}_u^{(\mathrm{p})}\right)+C_u \ge R_{\min}\chi_u,\forall u\in\mathcal{U}$, and also redefined the objective functions using Shannon's capacity formula as $f'_{\mathrm{CWSR}}\left(\mathbf{W},\mathbf{m},\mathbf{c}\right)\triangleq\sum_{u\in\mathcal{U}}\omega_u\big(\log_2\left(1+\mathsf{SINR}_u^{(\mathrm{p})}\right)+C_u\big)$ and $f'_{\mathrm{CWEE}}\left(\mathbf{W},\mathbf{m},\mathbf{c}\right)\triangleq\frac{\sum_{u\in\mathcal{U}}\omega_u\left(\log_2\left(1+\mathsf{SINR}_u^{(\mathrm{p})}\right)+C_u\right)}{\frac{1}{\eta_{\mathrm{eff}}}\left(\sum_{u\in\mathcal{U}}\|\mathbf{w}_u\chi_u\|_2^2+\|\mathbf{m}\psi\|_2^2\right)+P_{\mathrm{cir}}}$.

REMARK 4: *Problems $\mathcal{Q}'_{\mathrm{CWSR}}$, $\mathcal{Q}'_{\mathrm{CWEE}}$ are nonconvex MINLPs, and compared to $\mathcal{P}'_{\mathrm{CWSR}}$, $\mathcal{P}'_{\mathrm{CWEE}}$, they assume continuous rates. In addition, their structure is more complex than that of $\mathcal{P}'_{\mathrm{CWSR}}$, $\mathcal{P}'_{\mathrm{CWEE}}$, as they involve multiplicative couplings of continuous variables, which were not present in $\mathcal{P}'_{\mathrm{CWSR}}$, $\mathcal{P}'_{\mathrm{CWEE}}$.*

4.2 Proposed Algorithm

To solve $\mathcal{Q}'_{\mathrm{CWSR}}$ and $\mathcal{Q}'_{\mathrm{CWEE}}$, we leverage successive convex approximation (SCA), semidefinite relaxation (SDR), and binary enumeration. In particular, we enumerate all combinations of admitted UEs and then solve the underlying nonconvex subproblem for each combination via the proposed `OPT-SCA-SDR` algorithm, which finds a KKT point by exploiting SCA and SDR. In the following, we describe the proposed algorithm by considering $\mathcal{Q}'_{\mathrm{CWSR}}$ and then we extend it to $\mathcal{Q}'_{\mathrm{CWEE}}$.

4.2.1 Enumerating the Binary Variables: Let N be the total number of combinations of admitted UEs and $\mathcal{N}=\{1,\ldots,N\}$ the set collecting them. Considering a given combination $n\in\mathcal{N}$, problem $\mathcal{Q}'_{\mathrm{CWSR}}$ reduces to $\mathcal{Q}_{\mathrm{CWSR}_n}$, shown at the top of this page. In particular, $f_{\mathrm{CWSR}_n}\left(\mathbf{W},\mathbf{m},\mathbf{c}\right)\triangleq\sum_{u\in\mathcal{U}'_n}\omega_u\Big(\log_2\Big(1+\frac{\left|\mathbf{h}_u^{\mathrm{H}}\mathbf{w}_u\right|^2}{\Delta_{\mathrm{SIC}}^2\left|\mathbf{h}_u^{\mathrm{H}}\mathbf{m}\right|^2+\sum_{i\neq u,i\in\mathcal{U}'_n}\left|\mathbf{h}_u^{\mathrm{H}}\mathbf{w}_i\right|^2+\sigma^2}\Big)+C_u\Big)$, and $\mathcal{U}'_n\subseteq\mathcal{U}$ denotes the set of admitted UEs in combination n, such that $\mu_u=1,\forall u\in\mathcal{U}'_n$ and $|\mathcal{U}'_n|=K$. For notational simplicity, we reset the UE indices in $\mathcal{U}'_n$, such that $\mathcal{U}'_n=\{1,\ldots,K\}$. Here, constraint $\overline{\mathrm{C}}_{20}$ is included to eliminate the coupling $\mathbf{m}\psi_0$ in an analogous manner as in Section 3.2.2 for constraint E_1. We have not included C_{17} because it is implied by $\overline{\mathrm{C}}_{18},\overline{\mathrm{C}}_{20}$ when ψ_0 is given. We adopt $\psi_0=1$ for RSMA and $\psi_0=0$ for SDMA.

4.2.2 Transforming the Problem via Sublevel and Superlevel Sets: We introduce nonnegative variables $\boldsymbol{\gamma}\in\mathbb{R}_+^K,\boldsymbol{\rho}\in\mathbb{R}_+^K,\boldsymbol{\lambda}\in\mathbb{R}_+^K,\boldsymbol{\tau}\in\mathbb{R}_+^K$, and $\beta\in\mathbb{R}_+$ to define sublevel and superlevel sets, thereby transforming problem $\mathcal{Q}_{\mathrm{CWSR}_n}$ into $\widetilde{\mathcal{Q}}_{\mathrm{CWSR}_n}$. In **Appendix H**, we show that $\mathcal{Q}_{\mathrm{CWSR}_n}$ and $\widetilde{\mathcal{Q}}_{\mathrm{CWSR}_n}$ are equivalent. Specifically, we bound the private SINRs from below via $\frac{\left|\mathbf{h}_u^{\mathrm{H}}\mathbf{w}_u\right|^2}{\Delta_{\mathrm{SIC}}^2\left|\mathbf{h}_u^{\mathrm{H}}\mathbf{m}\right|^2+\sum_{i\neq u,i\in\mathcal{U}'_n}\left|\mathbf{h}_u^{\mathrm{H}}\mathbf{w}_i\right|^2+\sigma^2}\ge\gamma_u-1$. Also, we bound the interference at each UE from above by including $\Delta_{\mathrm{SIC}}^2\left|\mathbf{h}_u^{\mathrm{H}}\mathbf{m}\right|^2+\sum_{i\neq u,i\in\mathcal{U}'_n}\left|\mathbf{h}_u^{\mathrm{H}}\mathbf{w}_i\right|^2+\sigma^2\le\rho_u$. Following the same idea, we include $\frac{\left|\mathbf{h}_u^{\mathrm{H}}\mathbf{m}\right|^2}{\sum_{i\in\mathcal{U}'_n}\left|\mathbf{h}_u^{\mathrm{H}}\mathbf{w}_i\right|^2+\sigma^2}\ge\tau_u-1$ and $\sum_{i\in\mathcal{U}'_n}\left|\mathbf{h}_u^{\mathrm{H}}\mathbf{w}_i\right|^2+\sigma^2\le\lambda_u$ to bound the common SINRs and the interference. Furthermore, we bound the objective function from below, such that $f_{\mathrm{CWSR}_n}\left(\mathbf{W},\mathbf{m},\mathbf{c}\right)\ge\beta$, thus defining a new objective function $f_{\mathrm{CWSR}_n}\left(\beta\right)\triangleq\beta$. Upon applying these transformations to $\mathcal{Q}_{\mathrm{CWSR}_n}$, we obtain problem $\widetilde{\mathcal{Q}}_{\mathrm{CWSR}_n}$, shown at the top of the next page.

4.2.3 Leveraging Semidefinite Programming: By employing semidefinite programming and introducing positive semidefinite variables $\mathbf{W}_u\in\mathbb{C}^{N_{\mathrm{tx}}\times N_{\mathrm{tx}}}$ and $\mathbf{M}\in\mathbb{C}^{N_{\mathrm{tx}}\times N_{\mathrm{tx}}}$, which replace $\mathbf{w}_u\mathbf{w}_u^{\mathrm{H}}$ and $\mathbf{m}\mathbf{m}^{\mathrm{H}}$, respectively, constraints $\overline{\mathrm{C}}_6,\overline{\mathrm{C}}_{20},\overline{\mathrm{K}}_1,\overline{\mathrm{K}}_2,\overline{\mathrm{K}}_4,\overline{\mathrm{K}}_5$ can be equivalently reformulated to

$$\widetilde{\mathcal{Q}}_{\mathrm{CWSR}_n}: \max_{\mathbf{W},\mathbf{m},\mathbf{c},\boldsymbol{\gamma},\boldsymbol{\rho},\boldsymbol{\lambda},\boldsymbol{\tau},\beta} \quad f_{\mathrm{CWSR}_n}(\beta) \triangleq \beta$$
$$\text{s.t.} \quad \overline{\mathrm{K}}_1: \left|\mathbf{h}_u^{\mathrm{H}}\mathbf{w}_u\right|^2 \geq (\gamma_u-1)\rho_u, \forall u \in \mathcal{U}_n', \quad \text{(nonconvex)}$$
$$\overline{\mathrm{K}}_2: \Delta_{\mathrm{SIC}}^2\left|\mathbf{h}_u^{\mathrm{H}}\mathbf{m}\right|^2 + \textstyle\sum_{i\neq u, i\in\mathcal{U}_n'}\left|\mathbf{h}_u^{\mathrm{H}}\mathbf{w}_i\right|^2 + \sigma^2 \leq \rho_u, \forall u \in \mathcal{U}_n', \quad \text{(convex)}$$
$$\overline{\mathrm{K}}_3: \beta - \textstyle\sum_{u\in\mathcal{U}_n'}\omega_u\left(\log_2(\gamma_u)+C_u\right) \leq 0, \quad \text{(convex)}$$
$$\overline{\mathrm{K}}_4: \left|\mathbf{h}_u^{\mathrm{H}}\mathbf{m}\right|^2 \geq (\tau_u-1)\lambda_u, \forall u \in \mathcal{U}_n', \quad \text{(nonconvex)}$$
$$\overline{\mathrm{K}}_5: \textstyle\sum_{i\in\mathcal{U}_n'}\left|\mathbf{h}_u^{\mathrm{H}}\mathbf{w}_i\right|^2 + \sigma^2 \leq \lambda_u, \forall u \in \mathcal{U}_n', \quad \text{(convex)}$$
$$\overline{\mathrm{K}}_6: \textstyle\sum_{i\in\mathcal{U}_n'} C_i - \log_2(\tau_u) \leq 0, \forall u \in \mathcal{U}_n', \quad \text{(convex)}$$
$$\overline{\mathrm{K}}_7: R_{\min} - \log_2(\gamma_u) - C_u \leq 0, \forall u \in \mathcal{U}_n', \quad \text{(convex)}$$
$$\overline{\mathrm{K}}_8: \beta \geq 0, \quad \text{(linear)}$$
$$\overline{\mathrm{C}}_6, \overline{\mathrm{C}}_{13}, \overline{\mathrm{C}}_{20}.$$

$$\overline{\mathrm{C}}_6, \overline{\mathrm{C}}_{20}, \overline{\mathrm{K}}_1, \overline{\mathrm{K}}_2, \overline{\mathrm{K}}_4, \overline{\mathrm{K}}_5 \Leftrightarrow \begin{cases} \overline{\mathrm{L}}_1: \textstyle\sum_{u\in\mathcal{U}_n'}\mathrm{Tr}(\mathbf{W}_u) + \mathrm{Tr}(\mathbf{M}) \leq P_{\mathrm{tx}}^{\max}, \ \overline{\mathrm{L}}_2: \mathrm{Tr}(\mathbf{M}) \leq \psi_0 P_{\mathrm{tx}}^{\max}, & \text{(linear)} \\ \overline{\mathrm{L}}_3: (\gamma_u-1)\rho_u - \mathbf{h}_u^{\mathrm{H}}\mathbf{W}_u\mathbf{h}_u \leq 0, \forall u \in \mathcal{U}_n', & \text{(nonconvex)} \\ \overline{\mathrm{L}}_4: \Delta_{\mathrm{SIC}}^2\mathbf{h}_u^{\mathrm{H}}\mathbf{M}\mathbf{h}_u + \textstyle\sum_{i\neq u, i\in\mathcal{U}_n'}\mathbf{h}_u^{\mathrm{H}}\mathbf{W}_i\mathbf{h}_u + \sigma^2 \leq \rho_u, \forall u \in \mathcal{U}_n', & \text{(linear)} \\ \overline{\mathrm{L}}_5: (\tau_u-1)\lambda_u - \mathbf{h}_u^{\mathrm{H}}\mathbf{M}\mathbf{h}_u \leq 0, \forall u \in \mathcal{U}_n', & \text{(nonconvex)} \\ \overline{\mathrm{L}}_6: \textstyle\sum_{i\in\mathcal{U}_n'}\mathbf{h}_u^{\mathrm{H}}\mathbf{W}_i\mathbf{h}_u + \sigma^2 \leq \lambda_u, \forall u \in \mathcal{U}_n', & \text{(linear)} \\ \overline{\mathrm{L}}_7: \mathbf{W}_u \succcurlyeq 0, \forall u \in \mathcal{U}_n', & \text{(linear)} \\ \overline{\mathrm{L}}_8: \mathbf{M} \succcurlyeq 0, & \text{(linear)} \\ \overline{\mathrm{L}}_9: \mathrm{Rank}(\mathbf{W}_u) \leq 1, \forall u \in \mathcal{U}_n', \ \overline{\mathrm{L}}_{10}: \mathrm{Rank}(\mathbf{M}) \leq \psi_0. & \text{(nonconvex)} \end{cases}$$

$$\overline{\mathrm{L}}_3, \overline{\mathrm{L}}_5 \Leftrightarrow \begin{cases} \overline{\mathrm{M}}_1: \frac{\bar{\Omega}_{1,u}^{(t)}}{2}\gamma_u^2 + \frac{1}{2\bar{\Omega}_{1,u}^{(t)}}\rho_u^2 - \rho_u - \mathbf{h}_u^{\mathrm{H}}\mathbf{W}_u\mathbf{h}_u \leq 0, \forall u \in \mathcal{U}_n', & \text{(convex)} \\ \overline{\mathrm{M}}_2: \frac{\bar{\Omega}_{2,u}^{(t)}}{2}\tau_u^2 + \frac{1}{2\bar{\Omega}_{2,u}^{(t)}}\lambda_u^2 - \lambda_u - \mathbf{h}_u^{\mathrm{H}}\mathbf{M}\mathbf{h}_u \leq 0, \forall u \in \mathcal{U}_n', & \text{(convex)} \end{cases}$$

$$\overline{\mathrm{L}}_9, \overline{\mathrm{L}}_{10} \Leftrightarrow \left\{\overline{\mathrm{M}}_3: \zeta_0\mathbf{I} - \mathbf{T}_0^{(t)^{\mathrm{H}}}\mathbf{M}\mathbf{T}_0^{(t)} \succcurlyeq \mathbf{0}, \ \ \overline{\mathrm{M}}_4: \zeta_u\mathbf{I} - \mathbf{T}_u^{(t)^{\mathrm{H}}}\mathbf{W}_u\mathbf{T}_u^{(t)} \succcurlyeq \mathbf{0}, \forall u \in \mathcal{U}_n', \quad \text{(convex)}\right.$$

$\overline{\mathrm{L}}_1 - \overline{\mathrm{L}}_{10}$, shown at the top of the next page. In doing so, the nonconvexity of constraints $\overline{\mathrm{K}}_1, \overline{\mathrm{K}}_4$ are circumvented in part as the quadratic terms on the left-hand side are linearized. The newly introduced variables also affect constraints $\overline{\mathrm{K}}_2, \overline{\mathrm{K}}_5$, $\overline{\mathrm{C}}_6, \overline{\mathrm{C}}_{20}$. The positive semidefiniteness of $\mathbf{W}_u$ and $\mathbf{M}$ are specified by $\overline{\mathrm{L}}_7$, $\overline{\mathrm{L}}_8$, whereas $\overline{\mathrm{L}}_9, \overline{\mathrm{L}}_{10}$ allow for the private and common signals to be used or not. Considering the equivalence between $\overline{\mathrm{C}}_6, \overline{\mathrm{C}}_{20}, \overline{\mathrm{K}}_1, \overline{\mathrm{K}}_2, \overline{\mathrm{K}}_4, \overline{\mathrm{K}}_5$ and $\overline{\mathrm{L}}_1 - \overline{\mathrm{L}}_{10}$, we define problem

$$\widehat{\mathcal{Q}}_{\mathrm{CWSR}_n}: \max_{\widehat{\mathbf{W}},\mathbf{M},\mathbf{c},\boldsymbol{\gamma},\boldsymbol{\rho},\boldsymbol{\lambda},\boldsymbol{\tau},\beta} \quad f_{\mathrm{CWSR}_n}(\beta)$$
$$\text{s.t.} \quad \overline{\mathrm{C}}_{13}, \overline{\mathrm{K}}_3, \overline{\mathrm{K}}_6 - \overline{\mathrm{K}}_8, \overline{\mathrm{L}}_1 - \overline{\mathrm{L}}_{10},$$

where $\widehat{\mathbf{W}} = (\mathbf{W}_1, \ldots, \mathbf{W}_K)$. We note that $\widehat{\mathcal{Q}}_{\mathrm{CWSR}_n}$ is equivalent to $\widetilde{\mathcal{Q}}_{\mathrm{CWSR}_n}$ and $\mathcal{Q}_{\mathrm{CWSR}_n}$ since the feasible set and objective function are not affected by the applied transformation of the constraints.

4.2.4 Addressing the Nonconvex Constraints: To cope with the nonconvex constraints $\overline{\mathrm{L}}_3, \overline{\mathrm{L}}_5, \overline{\mathrm{L}}_9, \overline{\mathrm{L}}_{10}$, we adopt an iterative approach whereby we sequentially approximate these constraints by convex approximations.

• *Quasi-convex constraints:* To circumvent the quasi-convex constraints $\overline{\mathrm{L}}_3, \overline{\mathrm{L}}_5$, we replace them with the inner convex approximations $\overline{\mathrm{M}}_1, \overline{\mathrm{M}}_3$, shown at the top of this page, where t is the iteration index, and $\bar{\Omega}_{1,u}^{(t)}$, $\bar{\Omega}_{2,u}^{(t)}$, $u \in \mathcal{U}_n'$, are parameters adapted iteratively. In recasting $\overline{\mathrm{L}}_3, \overline{\mathrm{L}}_5$ as $\overline{\mathrm{M}}_1, \overline{\mathrm{M}}_2$, we have employed the arithmetic-geometric mean inequality, which states that $ab \leq \frac{a^2}{2} + \frac{b^2}{2}$ for $a, b \in \mathbb{R}_+$. By introducing a new parameter $\Phi \in \mathbb{R}_+$ and applying transformations $a \leftarrow \sqrt{\Phi}a$ and $b \leftarrow \sqrt{\frac{1}{\Phi}}b$, we obtain inequality $ab \leq \frac{\Phi}{2}a^2 + \frac{1}{2\Phi}b^2$, which becomes tight when $\Phi = \frac{b}{a}$ [40]. Note that $\frac{\Phi}{2}a^2 + \frac{1}{2\Phi}b^2$ is a convex overestimate of ab, which decouples a and b, allowing to circumvent the nonconvexity of the product ab. Exploiting this observation, we introduce parameter $\bar{\Omega}_{1,u}^{(t)}$ and apply the parameterized inequality to the product $\gamma_u\rho_u$ in $\overline{\mathrm{L}}_3$, such that $\gamma_u\rho_u \leq \frac{\bar{\Omega}_{1,u}^{(t)}}{2}\gamma_u^2 + \frac{1}{2\bar{\Omega}_{1,u}^{(t)}}\rho_u^2$. We proceed in a similar manner with constraint $\overline{\mathrm{L}}_5$ by introducing $\Omega_{2,u}^{(t)}$, which yields $\tau_u\lambda_u \leq \frac{\bar{\Omega}_{2,u}^{(t)}}{2}\tau_u^2 + \frac{1}{2\bar{\Omega}_{2,u}^{(t)}}\lambda_u^2$. Next, we replace products $\gamma_u\rho_u$ and $\tau_u\lambda_u$ with their respective convex overestimates, $\frac{\bar{\Omega}_{1,u}^{(t)}}{2}\gamma_u^2 + \frac{1}{2\bar{\Omega}_{1,u}^{(t)}}\rho_u^2$ and $\frac{\bar{\Omega}_{2,u}^{(t)}}{2}\tau_u^2 + \frac{1}{2\bar{\Omega}_{2,u}^{(t)}}\lambda_u^2$, thus yielding $\overline{\mathrm{M}}_1, \overline{\mathrm{M}}_2$. In each iteration t, we update the parameters according to $\bar{\Omega}_{1,u}^{(t)} = \frac{\rho_u^{(t-1)}}{\gamma_u^{(t-1)}}$ and $\bar{\Omega}_{2,u}^{(t)} = \frac{\lambda_u^{(t-1)}}{\tau_u^{(t-1)}}$ making it possible to sequentially adapt the convex approximation. Upon replacing $\overline{\mathrm{L}}_3, \overline{\mathrm{L}}_5$ with $\overline{\mathrm{M}}_1, \overline{\mathrm{M}}_2$ in problem $\widehat{\mathcal{Q}}_{\mathrm{CWSR}_n}$, and then solving it, an optimal solution to this modified problem will be feasible for $\widehat{\mathcal{Q}}_{\mathrm{CWSR}_n}$, $\widetilde{\mathcal{Q}}_{\mathrm{CWSR}_n}$, and $\mathcal{Q}_{\mathrm{CWSR}_n}$ since the feasible set of $\overline{\mathrm{M}}_1, \overline{\mathrm{M}}_2$ is contained in that of $\overline{\mathrm{L}}_3, \overline{\mathrm{L}}_5$. However, the solution will not necessarily be globally optimal for $\widehat{\mathcal{Q}}_{\mathrm{CWSR}_n}$, $\widetilde{\mathcal{Q}}_{\mathrm{CWSR}_n}$, and $\mathcal{Q}_{\mathrm{CWSR}_n}$ due to the possible reduction of the feasible set caused by the inner convexification in $\overline{\mathrm{M}}_1, \overline{\mathrm{M}}_2$.

• *Rank constraints:* In order to cope with rank constraints $\overline{\mathrm{L}}_9, \overline{\mathrm{L}}_{10}$, we adopt the iterative method proposed in [41], which is described as follows. We first reformulate $\overline{\mathrm{L}}_9$, $\overline{\mathrm{L}}_{10}$ as $\overline{\mathrm{M}}_3$, $\overline{\mathrm{M}}_4$, shown at the top of this page. Then, we

$$R_{u,n}^{\mathrm{proj}} = \left\{ R_j \mid j = \arg\min_{i \in \mathcal{J}} \overline{\mathsf{SINR}}_{u,n}^{(\mathrm{p})} - \Gamma_i, \overline{\mathsf{SINR}}_{u,n}^{(\mathrm{p})} \geq \Gamma_i \right\} \tag{2}$$

$$\overline{C}_{u,n}^{\mathrm{proj}} = \left\{ \frac{\overline{C}_{u,n}}{\sum_{u \in \mathcal{U}_n'} \overline{C}_{u,n}} R_j \mid j = \arg\min_{i \in \mathcal{J}} \left\{ \min_{u \in \mathcal{U}_n'} \overline{\mathsf{SINR}}_{u,n}^{(\mathrm{c})} \right\} - \Gamma_i, \left\{ \min_{u \in \mathcal{U}_n'} \overline{\mathsf{SINR}}_{u,n}^{(\mathrm{c})} \right\} \geq \Gamma_i \right\} \tag{3}$$

penalize the objective function by adding cost function $\sum_{u \in \mathcal{U}_n' \cup \{0\}} p_u^{(t)} \zeta_u$, which promotes rank minimization and enforces $\mathbf{M}$ and $\mathbf{W}_u$ to have rank at most one, as shown in **Appendix I**. The ζ_u, $\forall u \in \mathcal{U}_n' \cup \{0\}$, are slack variables and $p_u^{(t)} \in \mathbb{R}_+$, $\forall u \in \mathcal{U}_n' \cup \{0\}$, represent the penalty weights in iteration t. Matrices $\overline{\mathbf{M}}^{(t-1)}$ and $\overline{\mathbf{W}}_u^{(t-1)}$ are the respective solutions for $\mathbf{M}$ and $\mathbf{W}_u$, obtained in iteration $t-1$. Also, $\mathbf{T}_0^{(t)} \in \mathbb{C}^{N_{\mathrm{tx}} \times (N_{\mathrm{tx}}-1)}$ is formed by the eigenvectors of the $N_{\mathrm{tx}}-1$ smallest eigenvalues of $\overline{\mathbf{M}}^{(t-1)}$, whereas $\mathbf{T}_u^{(t)} \in \mathbb{C}^{N_{\mathrm{tx}} \times (N_{\mathrm{tx}}-1)}$ is formed by the eigenvectors of the $N_{\mathrm{tx}}-1$ smallest eigenvalues of $\overline{\mathbf{W}}_u^{(t-1)}$.

4.2.5 Outlining the Algorithm and Its Extension to Solve $\mathcal{Q}'_{\mathrm{CWEE}}$: The transformation of constraints $\overline{\mathrm{L}}_3, \overline{\mathrm{L}}_5, \overline{\mathrm{L}}_9, \overline{\mathrm{L}}_{10}$ into $\overline{\mathrm{M}}_1 - \overline{\mathrm{M}}_4$, leads to the following problem

$$\begin{aligned} \bar{\mathcal{Q}}_{\mathrm{CWSR}_n}^{(t)} : \max_{\substack{\widehat{\mathbf{W}}, \mathbf{M}, \mathbf{c}, \boldsymbol{\gamma}, \boldsymbol{\rho}, \\ \boldsymbol{\lambda}, \boldsymbol{\tau}, \boldsymbol{\zeta}, \beta}} \quad & f_{\mathrm{CWSR}_n}(\beta) - \textstyle\sum_{u \in \mathcal{U}_n' \cup \{0\}} p_u^{(t)} \zeta_u \\ \text{s.t.} \quad & \overline{\mathrm{C}}_{13}, \overline{\mathrm{K}}_3, \overline{\mathrm{K}}_6 - \overline{\mathrm{K}}_8, \overline{\mathrm{L}}_1, \overline{\mathrm{L}}_2, \\ & \overline{\mathrm{L}}_4, \overline{\mathrm{L}}_6 - \overline{\mathrm{L}}_8, \overline{\mathrm{M}}_1 - \overline{\mathrm{M}}_4. \end{aligned}$$

On the other hand, to solve $\mathcal{Q}'_{\mathrm{CWEE}}$, we introduce the following problem

$$\begin{aligned} \bar{\mathcal{Q}}_{\mathrm{CWEE}_n}^{(t)} : \max_{\substack{\widehat{\mathbf{W}}, \mathbf{M}, \mathbf{c}, \boldsymbol{\gamma}, \boldsymbol{\rho}, \\ \boldsymbol{\lambda}, \boldsymbol{\tau}, \boldsymbol{\zeta}, \beta, \theta, \delta}} \quad & f_{\mathrm{CWEE}_n}(\theta) - \textstyle\sum_{u \in \mathcal{U}_n' \cup \{0\}} p_u^{(t)} \zeta_u \\ \text{s.t.} \quad & \overline{\mathrm{C}}_{13}, \overline{\mathrm{K}}_3, \overline{\mathrm{K}}_6 - \overline{\mathrm{K}}_8, \overline{\mathrm{L}}_1, \overline{\mathrm{L}}_2, \overline{\mathrm{L}}_4, \\ & \overline{\mathrm{L}}_6 - \overline{\mathrm{L}}_8, \overline{\mathrm{M}}_1 - \overline{\mathrm{M}}_4, \overline{\mathrm{N}}_1 - \overline{\mathrm{N}}_3, \end{aligned}$$

where we employed the same procedure as described in Section 4.2.1 to Section 4.2.4. Compared to $\bar{\mathcal{Q}}_{\mathrm{CWSR}_n}^{(t)}$, problem $\bar{\mathcal{Q}}_{\mathrm{CWEE}_n}^{(t)}$ features variables θ and δ, convex constraints $\overline{\mathrm{N}}_1 : \sum_{u \in \mathcal{U}_n'} \mathrm{Tr}(\mathbf{W}_u) + \mathrm{Tr}(\mathbf{M}) \leq \eta_{\mathrm{eff}} \delta$, $\overline{\mathrm{N}}_2 : \frac{\bar{\Omega}_3^{(t)}}{2} \theta^2 + \frac{1}{2\bar{\Omega}_3^{(t)}} \delta^2 + \theta P_{\mathrm{cir}} \leq \beta$ and $\overline{\mathrm{N}}_3 : \theta \geq 0$, and parameter $\bar{\Omega}_3^{(t)}$. In particular, θ is used to bound the objective function $f_{\mathrm{CWEE}_n}(\mathbf{W}, \mathbf{m}, \mathbf{c})$ from below. Variable δ is used to bound the transmit power efficiency from above, thereby yielding constraint $\overline{\mathrm{N}}_1$. The introduction of δ and θ in the objective function leads to a multiplicative coupling $\theta\delta$, which is dealt with in the same manner as in Section 4.2.4, yielding $\overline{\mathrm{N}}_2$. Also, $\overline{\mathrm{N}}_3$ is added to ensure the positiveness of the objective function. Parameter $\bar{\Omega}_3^{(t)}$ is updated as $\bar{\Omega}_3^{(t)} = \frac{\delta^{(t-1)}}{\theta^{(t-1)}}$ and the objective function is penalized by $\sum_{u \in \mathcal{U}_n' \cup \{0\}} p_u^{(t)} \zeta_u$.

Problems $\bar{\mathcal{Q}}_{\mathrm{CWSR}_n}^{(t)}$ and $\bar{\mathcal{Q}}_{\mathrm{CWEE}_n}^{(t)}$ are convex and can be solved optimally via IPMs. Both are solved iteratively, improving the objective function in each iteration until a stop criterion is met, i.e., the difference of the objective function values between successive iterations is less than a threshold ϵ or the number of iterations exceeds N_{iter}. In **Appendix J**, we show that $\bar{\mathcal{Q}}_{\mathrm{CWSR}_n}^{(t)}$ and $\bar{\mathcal{Q}}_{\mathrm{CWEE}_n}^{(t)}$ converges to a KKT point. Also, by increasing the penalty weights $p_u^{(t)}$, variables ζ_u decrease in each iteration, leading to $\zeta_u \to 0$ and $\sum_{u \in \mathcal{U}_n' \cup \{0\}} p_u^{(t)} \zeta_u \to 0$. This causes $\mathbf{M}$ and $\mathbf{W}_u$ to have at most rank one, since the $N_{\mathrm{tx}}-1$ smallest eigenvalues of these matrices are progressively squeezed to zero. Assuming that $\bar{\mathcal{Q}}_{\mathrm{CWSR}_n}^{(t)}$ converge in iteration $t^\star$, we have that $\mathbf{M} \approx \overline{\mathbf{M}}^{(t^\star-1)}$, where $\mathbf{M}$ is the solution in iteration $t^\star$. Via eigendecomposition of $\mathbf{M}$, we have $\mathbf{M} = \widetilde{\mathbf{R}}_0 \boldsymbol{\Sigma}_0 \widetilde{\mathbf{R}}_0^{\mathrm{H}}$, such that $\widetilde{\mathbf{R}}_0 \widetilde{\mathbf{R}}_0^{\mathrm{H}} = \mathbf{I}$, $\boldsymbol{\Sigma}_0 = \mathrm{diag}(\sigma_{0,1}, \ldots, \sigma_{0,N_{\mathrm{tx}}})$, and $\widetilde{\mathbf{R}}_0 = [\mathbf{r}_0 | \mathbf{R}_0]$. Therefore, $\mathbf{T}_0^{(t^\star)^{\mathrm{H}}} \mathbf{M} \mathbf{T}_0^{(t^\star)} = \mathbf{T}_0^{(t^\star)^{\mathrm{H}}} [\mathbf{r}_0 | \mathbf{R}_0] \boldsymbol{\Sigma}_0 [\mathbf{r}_0 | \mathbf{R}_0]^{\mathrm{H}} \mathbf{T}_0^{(t^\star)}$, which can be further reduced to $\mathbf{T}_0^{(t^\star)^{\mathrm{H}}} \mathbf{M} \mathbf{T}_0^{(t^\star)} = [\mathbf{0} | \mathbf{I}] \boldsymbol{\Sigma}_0 [\mathbf{0} | \mathbf{I}]^{\mathrm{H}} = \mathrm{diag}(\sigma_{0,2}, \ldots, \sigma_{0,N_{\mathrm{tx}}})$, since $\mathbf{T}_0^{(t^\star)^{\mathrm{H}}} \mathbf{r}_0 \approx \mathbf{0}$ and $\mathbf{T}_0^{(t^\star)^{\mathrm{H}}} \mathbf{R}_0 \approx \mathbf{I}$. Considering these outcomes and $\overline{\mathrm{M}}_3$, we obtain $\zeta_0 \mathbf{I} \succcurlyeq \mathrm{diag}(\sigma_{0,2}, \ldots, \sigma_{0,N_{\mathrm{tx}}})$, which leads to $\sigma_{0,2}, \ldots, \sigma_{0,N_{\mathrm{tx}}} \to 0$ as $\zeta_0 \to 0$. Because $\sigma_{0,1}$ is not affected by this procedure, $\sigma_{0,1}$ can be different from zero or even zero, i.e., $\mathbf{M}$ can be at most rank-one. Following the same reasoning, we can obtain equivalent results for $\mathbf{T}_u^{(t^\star)^{\mathrm{H}}} \mathbf{W}_u \mathbf{T}_u^{(t^\star)}$, $\forall u \in \mathcal{U}_n'$. The solutions that satisfy $\overline{\mathrm{L}}_9, \overline{\mathrm{L}}_{10}$ are recovered via eigendecomposition of $\mathbf{M}$ and $\mathbf{W}_u$, i.e., $\mathbf{m} = \sqrt{\sigma_{0,1}} \mathbf{r}_0$ and $\mathbf{w}_u = \sqrt{\sigma_{u,1}} \mathbf{r}_u$, where $\sigma_{u,1}$ and $\mathbf{r}_u$ are the largest eigenvalue and principal eigenvector of $\mathbf{W}_u$, respectively. The same analysis can be applied to $\bar{\mathcal{Q}}_{\mathrm{CWEE}_n}^{(t)}$ as the constraints are the same.

4.2.6 Projecting the Continuous Rates: Due to the use of Shannon's capacity formula, the rates obtained by solving $\bar{\mathcal{Q}}_{\mathrm{CWSR}_n}^{(t)}$ and $\bar{\mathcal{Q}}_{\mathrm{CWEE}_n}^{(t)}$ are continuous. To meet the MCS specifications, these rates are projected, i.e., approximated to the closest feasible discrete rates. Thus, the best solution with projected rates is given by $f_{\mathrm{CWSR}}^{\mathrm{proj}}(\mathbf{W}, \mathbf{m}, \mathbf{c}) \triangleq \max_{n \in \mathcal{N}} \sum_{u \in \mathcal{U}_n'} \omega_u \left(R_{u,n}^{\mathrm{proj}} + C_{u,n}^{\mathrm{proj}} \right)$ and $f_{\mathrm{CWEE}}^{\mathrm{proj}}(\mathbf{W}, \mathbf{m}, \mathbf{c}) \triangleq \max_{n \in \mathcal{N}} \frac{\sum_{u \in \mathcal{U}} \omega_u \left(\log_2 \left(1 + \overline{\mathsf{SINR}}_{u,n}^{(\mathrm{p})} \right) + \overline{C}_{u,n} \right)}{\frac{1}{\eta_{\mathrm{eff}}} \left(\sum_{u \in \mathcal{U}} \|\overline{\mathbf{w}}_{u,n}\|_2^2 + \|\overline{\mathbf{m}}_n\|_2^2 \right) + P_{\mathrm{cir}}}$, where $R_{u,n}^{\mathrm{proj}}$ and $\overline{C}_{u,n}^{\mathrm{proj}}$ are defined in (2) and (3), shown at the top of this page, whereas R_j, Γ_j were introduced in Section 2. In particular, $\overline{\mathsf{SINR}}_{u,n}^{(\mathrm{p})}$ and $\overline{\mathsf{SINR}}_{u,n}^{(\mathrm{c})}$ are respectively the highest discrete private and common SINRs that can be achieved by UE_u in $\mathcal{U}_n'$, which are mapped to their respective discrete rates $R_{u,n}^{\mathrm{proj}}$ and $\overline{C}_{u,n}^{\mathrm{proj}}$. Besides, $\overline{C}_{u,n}$, $\overline{\mathbf{w}}_{u,n}$, and $\overline{\mathbf{m}}_n$ are the common rate portion of UE_u, the private precoder of UE_u, and the common precoder of the n-th combination $\mathcal{U}_n'$, respectively. After evaluating all N combinations of admitted UEs, we pick the combination that achieves the highest objective function value.

4.2.7 Computational Complexity: The computational complexities of solving $\mathcal{Q}_{\mathrm{CWSR}}$ and $\mathcal{Q}_{\mathrm{CWEE}}$ are similar, which is given by $\mathcal{O}\left(N_q N_c^{0.5} N_v^2 N_d\right)$, where $N_q = 2\binom{K}{U}$ is the total number of combinations of admitted UEs, $N_c = 9K + 6$ is the total number of constraints, $N_v = 2KN_{\mathrm{tx}} + 9N_{\mathrm{tx}} + 2K + 11$ is the number of decision variables, and $N_d = N_{\mathrm{tx}}^2 K^3 + N_{\mathrm{tx}}^2 K^2 + 5KN_{\mathrm{tx}}^2 + K^3 + 3N_{\mathrm{tx}}^2 + K^2 + 2K + 1$ is the dimension of the SDP program.

Table 2: Rates and target SINRs for various CQIs.

CQI (j)	1	2	3	4	5	6	7	8	9	10	11	12	13	14	15
Modulation	QPSK						16QAM			64QAM					
Coding rate	0.0762	0.1172	0.1885	0.3008	0.4385	0.5879	0.3691	0.4785	0.6016	0.4551	0.5537	0.6504	0.7539	0.8525	0.9258
Rate (R_j) [bps/Hz]	0.1523	0.2344	0.3770	0.6016	0.8770	1.1758	1.4766	1.9141	2.4063	2.7305	3.3223	3.9023	4.5234	5.1152	5.5547
Target SINR (Γ_j)	0.1128	0.2159	0.3892	0.6610	1.0962	1.7474	2.8113	4.3321	7.0081	10.6316	16.6648	25.8345	38.4503	60.0620	95.6974

Table 3: Simulation parameters.

Scenario	Objective	$P_{\text{tx}}^{\max}$ [dBm]	σ^2 [dBm]	N_{tx}	U	K	Δ_{SIC}	η_{eff}	P_{dyn} [dBm]	P_{sta} [dBm]	Weights	Channels
I	WSR	$40, 50$	30	4	2	2	0	–	–	–	Various [3]	Deterministic [3]
II	WSR	$40, 45, 50$	30	4	2	2	0	–	–	–	Various [3]	Deterministic [3]
III	WSR	$30, 40, 50$	30	4	2	2	$[0, 1]$	–	–	–	Various [3]	Deterministic [3]
IV	WEE	$30, 40$	30	4	2	2	0	0.35	33	38	Various [3]	Deterministic [3]
V	WSR	40	3GPP [44]	16	$2, \ldots, 6$	U	0	–	–	–	Uniform	3GPP [42]
VI	WSR	$10, \ldots, 40$	3GPP [44]	16	6	3	0	–	–	–	Uniform	3GPP [42]
VII	WEE	40	3GPP [44]	16	$2, \ldots, 6$	U	0	0.35	33	38	Uniform	3GPP [42]
VIII	WEE	$10, \ldots, 40$	3GPP [44]	16	6	3	0	0.35	33	38	Uniform	3GPP [42]

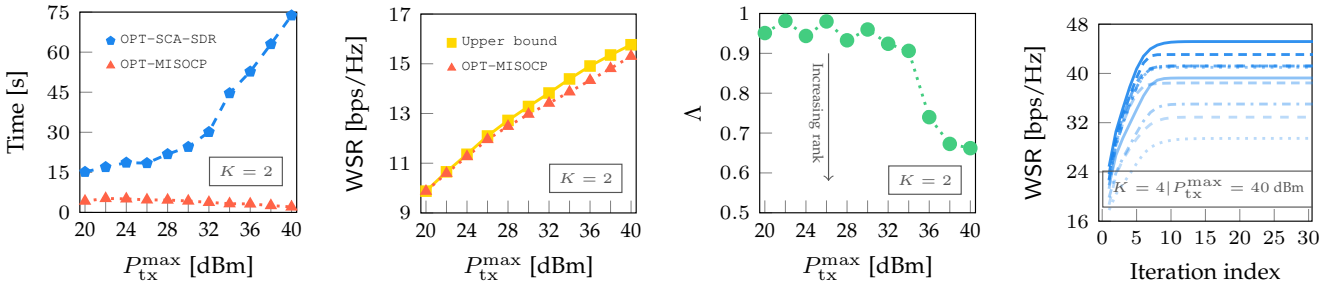

(a) Average runtime of OPT-SCA-SDR and OPT-MISOCP for $U = 4$, $K = 2$, and uncorrelated channels.

(b) Average WSR of OPT-MISOCP and upper bound for $U = 4$, $K = 2$, and uncorrelated channels.

(c) Average 'rank-oneness' of the upper bound for $U = 4$, $K = 2$, and uncorrelated channels.

(d) Convergence of OPT-SCA-SDR for 10 channel realizations, $U = K = 4$, and uncorrelated channels.

Figure 2: Analysis of time complexity, optimality, and convergence.

5 Simulation Results

We evaluate the WSR and WEE for several configurations, varying the number of UEs, number of admitted UEs, and transmit powers. We consider two cases, namely, two-user settings (**Scenario I** to **Scenario IV**) and multiuser settings (**Scenario V** to **Scenario VIII**). For the first set of scenarios, we adopt deterministic channels and do not include user admission to gain insight regarding the impact of discrete rates, which is done by modifying constraint $\overline{\text{C}}_2$ as $\sum_{u\in\mathcal{U}} \chi_u \leq K$. In particular, we consider a system consisting of a BS with $N_{\text{tx}} = 4$ antennas and $U = 2$ UEs with channels $\mathbf{h}_1 = [1, 1, 1, 1]^{\text{H}}$, $\mathbf{h}_2 = \left[1, e^{j\phi}, e^{j2\phi}, e^{j3\phi}\right]^{\text{H}}$, where $\phi = \left\{\frac{\pi}{9}, \frac{2\pi}{9}, \frac{3\pi}{9}, \frac{4\pi}{9}\right\}$ controls the similarity of the channels of the UEs, whereas the noise power is set to $\sigma^2 = 30$ dBm, as in [3]. For the second set of scenarios, we adopt UMi line-of-sight (LOS)/non-LOS (NLOS) channels [42] with carrier frequency $f_{\text{c}} = 41$ GHz, $N_{\text{p}} = 4$ paths, bandwidth BW $= 100$ MHz, noise figure NF $= 5$ dB, and noise power $\sigma^2 = -174 + \text{NF} + 10\log_{10}(\text{BW/Hz})$ dBm. For this case, we consider two types of channels, i.e., correlated and uncorrelated, in order to assess the performance for different channel conditions. The uncorrelated and correlate channels model the cases when the UEs are distributed across the entire sector of 120° and within a narrower sector of 10°, respectively. Also, we consider $J = 15$ MCSs with target SINRs corresponding to 10% BLER [43], as shown in Table 2.

For the optimization of $\bar{\mathcal{Q}}_{\text{CWSR}_n}^{(t)}$ and $\bar{\mathcal{Q}}_{\text{CWEE}_n}^{(t)}$, we initialize the variables γ_u, ρ_u, τ_u, λ_u, δ_u, θ_u, $\forall u \in \mathcal{U}$, as $\gamma_u^{(0)} = 1$, $\rho_u^{(0)} = 1$, $\tau_u^{(0)} = 1$, $\lambda_u^{(0)} = 1$, $\delta_u^{(0)} = 1$, $\theta_u^{(0)} = 1$. In addition, we initialize the penalty factor p_u as $p_u^{(0)} = 0.01$, $\forall u \in \mathcal{U}$, which is updated in each iteration t as $p_u^{(t+1)} = \min\left\{p_{\text{inc}} \cdot p_u^{(t)}, p_{\max}\right\}$, where $p_{\text{inc}} = 4$ and $p_{\max} = 1000$. As for the stopping criterion, we consider the threshold $\epsilon = 0.0001$ and the maximum number of iterations $N_{\text{iter}} = 120$. The simulation results depict the average over $N_{\text{ch}} = 100$ channel realizations assuming $R_{\min} = R_1$ (see Table 2), unless specified otherwise. The maximum distance between the BS and UEs is $D_{\text{BS}} = 60$ m. The formulated optimization problems are solved using CVX and MOSEK. The parameter settings employed in the considered scenarios are specified in Table 3. Furthermore, we compare the following algorithms.

- **OPT-MISOCP:** As proposed in Section 3.2 for discrete rates. By setting $\psi = 0$, it reduces to SDMA.
- **OPT-SCA-SDR:** As proposed in Section 4.2 for continuous rates. By setting $\psi = 0$, it reduces to SDMA.
- **RND-MISOCP:** Variant of OPT-MISOCP, which assumes random user admission.
- **RND-SCA-SDR:** Variant of OPT-SCA-SDR, which assumes random user admission.
- **PR-OPT-SCA-SDR:** Obtained from OPT-SCA-SDR upon projecting the rates, as shown in (2) and (3).
- **PR-RND-SCA-SDR:** Obtained from RND-SCA-SDR upon projecting the rates, as shown in (2) and (3).

5.1 Complexity, Optimality, and Convergence

In this section, we quantify the runtime complexity of OPT-MISOCP and OPT-SCA-SDR, evaluate the optimality of OPT-MISOCP with respect to an upper bound, and analyze the convergence of OPT-SCA-SDR. For the results shown in Fig. 2, we consider the WSR problem with uncorrelated channels for $U = 4$, $K = \{2, 4\}$, weights $\omega_1 = \cdots = \omega_4 = 1$, and $N_{\text{ch}} = 10$ channel realizations.

Runtime complexity: We compare the runtime complexity

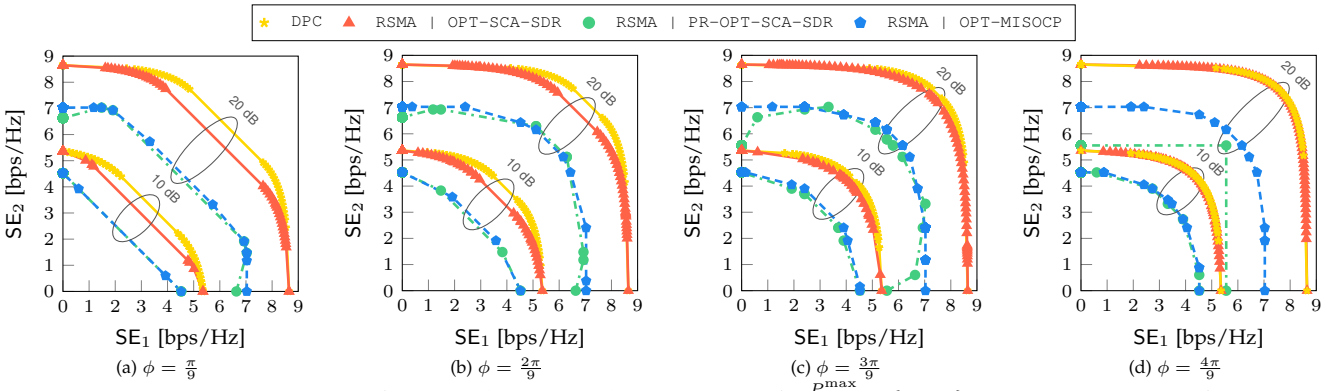

(a) $\phi = \frac{\pi}{9}$ (b) $\phi = \frac{2\pi}{9}$ (c) $\phi = \frac{3\pi}{9}$ (d) $\phi = \frac{4\pi}{9}$

Figure 3: (*Scenario I*) Two-user SE region of RSMA with discrete and continuous rates for $\frac{P_{\text{tx}}^{\max}}{\sigma^2} = \{10, 20\}$ dB. *Since* OPT-SCA-SDR *does not account for rate saturation, it continues upgrading the private rates, not necessarily leading to improved performance upon rate projection. In contrast,* OPT-MISOCP *considers that the rates are bounded and discrete, promoting more appropriate usage of power. Specifically,* OPT-MISOCP *uses the surplus of power to upgrade weaker private or common signals, preventing severe rate saturation of other signals.*

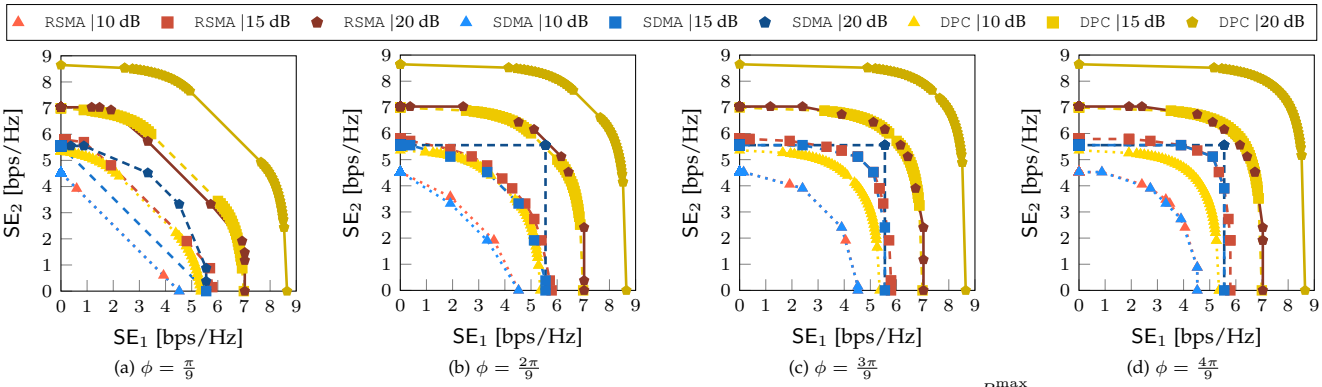

(a) $\phi = \frac{\pi}{9}$ (b) $\phi = \frac{2\pi}{9}$ (c) $\phi = \frac{3\pi}{9}$ (d) $\phi = \frac{4\pi}{9}$

Figure 4: (*Scenario II*) Two-user SE region of RSMA and SDMA with discrete rates using OPT-MISOCP for $\frac{P_{\text{tx}}^{\max}}{\sigma^2} = \{10, 15, 20\}$ dB. *The advantage of RSMA stems from its capability of using the surplus of power to transmit the common signal, even in scenarios with highly uncorrelated channels, which SDMA is unable to do.*

of OPT-MISOCP and OPT-SCA-SDR. In Fig. 2a, we observe that for the considered parameters, OPT-MISOCP is $4 - 36$ times faster than OPT-SCA-SDR since the former exploits BnB, which circumvents the need of an exhaustive search. In contrast, OPT-SCA-SDR considers all possible combinations of admitted UEs. Furthermore, OPT-SCA-SDR is an iterative scheme, which needs to solve multiple instances of the problem until a stop criterion is met. We notice that OPT-SCA-SDR needs more time to converge as the transmit power increases. In particular, higher transit powers facilitate higher WSRs, and therefore more iterations are needed before the stopping criterion is satisfied. On the other hand, the runtime of OPT-MISOCP remains constant and even slightly decreases for higher transmit powers. This is due to constraint J_2, introduced in Section 3.2.7, which allows early stopping.

REMARK 5: *We observed that for small numbers of UEs, e.g., $U = \{4, 5\}$,* OPT-MISOCP *has an affordable runtime. However, as U increases beyond these values, the runtime of* OPT-MISOCP *grows substantially, as more binary variables are involved. To keep* OPT-MISOCP *affordable, it can be combined with a simple subcarrier allocation policy to avoid co-processing multiple UEs simultaneously and allowing for parallelization.*

***Scenario I**: Two-User SE Region for Continuous/Discrete RSMA Rates*

Optimality: We compare the WSR performance of OPT-MISOCP to an upper bound that we devise using SDR to demonstrate that OPT-MISOCP can yield near-optimal solutions for $\mathcal{P}'_{\text{DWSR}}$. This upper bound is used to analyze the impact of the convexification procedure used in OPT-MISOCP. Since the upper bound has a larger feasible set due to the rank-one relaxation, it finds solutions that yield higher objective function values than OPT-MISOCP. However, such solutions are not necessarily feasible for problem $\mathcal{P}_{\text{DWSR}}$. In Fig. 2b, we observe that the performance gap between OPT-MISOCP and the upper bound is generally small, although it slightly increases to 3% for higher transmit powers. To explain this result, we show in Fig. 2c, the ratio of the principal eigenvalue to the sum of all eigenvalues, which we denote by Λ, i.e., Λ portrays the 'rank-oneness' of the upper bound solutions. Specifically, it is defined as $\Lambda = \frac{1}{\min\{1,\text{Rank}(\mathbf{X}_0)\}+\sum_{u\in\mathcal{U}}\min\{1,\text{Rank}(\mathbf{X}_u)\}} \frac{\sum_{u\in\mathcal{U}\cup\{0\}}\hat{\lambda}_{\max,u}}{\sum_m \hat{\lambda}_{m,u}}$, where $\hat{\lambda}_{m,u}$ is the m-th eigenvalue of $\mathbf{X}_u \succcurlyeq \mathbf{0}$, $u \in \mathcal{U} \cup \{0\}$. Here, $\mathbf{X}_u$ is the private precoder for UE_u and $\mathbf{X}_0$ is the precoder for the common signal, obtained by the upper bound. Λ reveals that the upper bound solutions have ranks higher than one, and therefore are not feasible for problem $\mathcal{P}_{\text{DWSR}}$, thus explaining the performance gap.

Convergence: In Fig. 2d, we show the convergence of OPT-SCA-SDR for $N_{\text{ch}} = 10$ channel realizations.

In Fig. 3, we compare the SE of RSMA with discrete and continuous rates to investigate the impact of rate discretization. For all considered cases, OPT-MISOCP and PR-OPT-SCA-SDR exhibit similar performance when

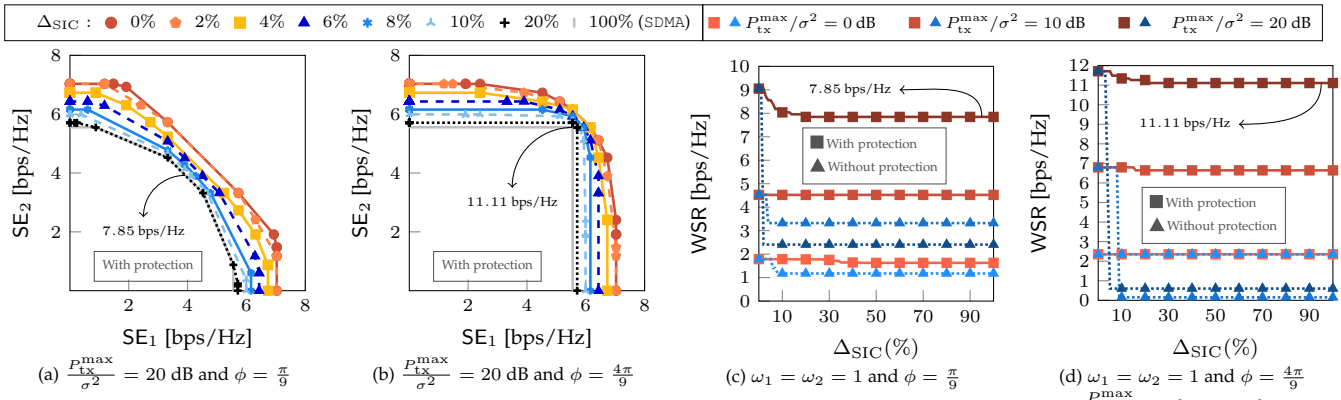

(a) $\frac{P_{\text{tx}}^{\max}}{\sigma^2} = 20$ dB and $\phi = \frac{\pi}{9}$ (b) $\frac{P_{\text{tx}}^{\max}}{\sigma^2} = 20$ dB and $\phi = \frac{4\pi}{9}$ (c) $\omega_1 = \omega_2 = 1$ and $\phi = \frac{\pi}{9}$ (d) $\omega_1 = \omega_2 = 1$ and $\phi = \frac{4\pi}{9}$

Figure 5: (*Scenario III*) Two-user SE region of RSMA with discrete rates and imperfect SIC using OPT-MISOCP for $\frac{P_{\text{tx}}^{\max}}{\sigma^2} = \{0, 10, 20\}$ dB and various Δ_{SIC} values. *Accounting for potentially imperfect SIC has an enormous performance benefit. In the worst case, RSMA collapses to SDMA, still providing outstanding performance compared to the case without protection. In the presence of large unmanaged residuals of the common signal, due to an imperfect SIC, the private rates cannot be guaranteed, thus collapsing to zero due to the inability to fulfill the target SINRs required for successful message decoding.*

$\frac{P_{\text{tx}}^{\max}}{\sigma^2} = 10$ dB. This occurs because the rates obtained by OPT-SCA-SDR are small due to the low transmit power, and therefore projection does not have a significant impact. However, the performance gap between them can become large when $\frac{P_{\text{tx}}^{\max}}{\sigma^2} = 20$ dB due to the higher rates achieved, which can lead to more noticeable projection losses. For instance, the difference is negligible in Fig. 3a, whereas it is more evident in Fig. 3c. The reason is that the channels become less correlated as ϕ increases, making the common rate less relevant for OPT-SCA-SDR. This causes OPT-SCA-SDR to be noticeably impacted by rate projection, as the private rates may experience heavy saturation while the common rate remains small. Fig. 3d shows an extreme case with low channel correlation, which causes OPT-SCA-SDR to opt for SDMA. In this case, the loss due to projection is higher than in Fig. 3b and Fig. 3c since the common rate is zero, and the private rates saturate at R_J (see Table 2). On the other hand, OPT-MISOCP can prevent rate saturation losses as it takes the rate discretization into account, and expends its surplus of power to improve the common rate. For reference, we have included dirty paper coding (DPC), which is capacity-achieving for continuous rates [45]. We observe that the proposed OPT-SCA-SDR can approach the performance of DPC, especially in Fig. 3d, thus demonstrating that the proposed OPT-SCA-SDR produces high-quality solutions.

***Scenario II**: Two-User SE Region with Discrete Rates for RSMA and SDMA*

In Fig. 4, we compare the SE of RSMA and SDMA using discrete rates to elucidate the performance gap between them for different transmit powers. In Fig. 4a, RSMA and SDMA have nearly the same performance when $\frac{P_{\text{tx}}^{\max}}{\sigma^2} = 10$ dB, however, RSMA outperforms SDMA when $\frac{P_{\text{tx}}^{\max}}{\sigma^2} = \{15, 20\}$ dB. SDMA is unable to cope well with high channel correlation, showing little improvement even as the transmit power increases. In contrast, RSMA can take advantage of high channel correlation to achieve considerable improvement. In Fig. 4b to Fig. 4d, RSMA outperforms SDMA by a small margin when $\frac{P_{\text{tx}}^{\max}}{\sigma^2} = \{10, 15\}$ dB as the channels are less correlated, thus making the transmission of the common signal more expensive. However, RSMA clearly outperforms SDMA when $\frac{P_{\text{tx}}^{\max}}{\sigma^2} = 20$ dB since SDMA saturates (i.e., UEs are served at rate $R_J = 5.5547$ bps/Hz), whereas RSMA can still improve as it can use the surplus of power to support a common signal.

***Scenario III**: Two-User SE Region with Imperfect SIC for RSMA*

In Fig. 5, we evaluate the SE of RSMA for various levels of protection against imperfect SIC as well as without protection. When we consider protection, we assume a given $\Delta_{\text{SIC}} \neq 0\%$, which is taken into account for the optimization. Therefore, the BS guarantees the allocated rates for the UEs up to the selected value of Δ_{SIC}. When we neglect protection, we assume $\Delta_{\text{SIC}} = 0\%$ for the optimization even though the UEs may suffer from imperfect SIC. Therefore, the allocated rates may not be guaranteed. In Fig. 5a and Fig. 5b, protection against imperfect SIC is considered. We observe that endowing RSMA with a higher robustness against imperfect SIC, i.e., larger Δ_{SIC}, produces a more noticeable decrease in the SE because the private SINRs are optimized to deal with additional interference due to $\Delta_{\text{SIC}} \neq 0\%$ (see Section 3.1.3). Also, we observe that values up to $\Delta_{\text{SIC}} = 4\%$ do not affect the SE performance substantially while providing adequate protection. However, RSMA almost collapses to SDMA when $\Delta_{\text{SIC}} = 20\%$, as the common rates become very small. In fact, RSMA smartly switches to SDMA for values larger than $\Delta_{\text{SIC}} = 20\%$ since the high protection against imperfect SIC prevents enhancement of the private SINRs. The results for SDMA are identical to those for RSMA with $\Delta_{\text{SIC}} = 100\%$. In Fig. 5c and Fig. 5d, we evaluate the impact of not accounting for imperfect SIC on the WSR performance, where we consider the same scenarios in Fig. 5a and Fig. 5b, and equal weights, i.e., $\omega_1 = \omega_2 = 1$. In Fig. 5c, the impact of imperfect SIC is small when $\frac{P_{\text{tx}}^{\max}}{\sigma^2} = 0$ dB because information is predominantly transmitted via the common signal which is not affected by imperfect SIC. When $\frac{P_{\text{tx}}^{\max}}{\sigma^2} = \{10, 20\}$ dB, the common and private rates increase since higher MCSs can be selected. This also implies that potential unmanaged residuals of the common signal may cause the private rates to collapse more noticeably, e.g., the SE drops from 7.85 bps/Hz to 2.41 bps/Hz (when $\frac{P_{\text{tx}}^{\max}}{\sigma^2} = 20$ dB) and from 4.52 bps/Hz to 3.32 bps/Hz (when $\frac{P_{\text{tx}}^{\max}}{\sigma^2} = 10$ dB). However, the system performs well when protection against imperfect SIC is considered. In particular, for high Δ_{SIC}, RSMA transitions to SDMA thereby avoiding further private SINRs

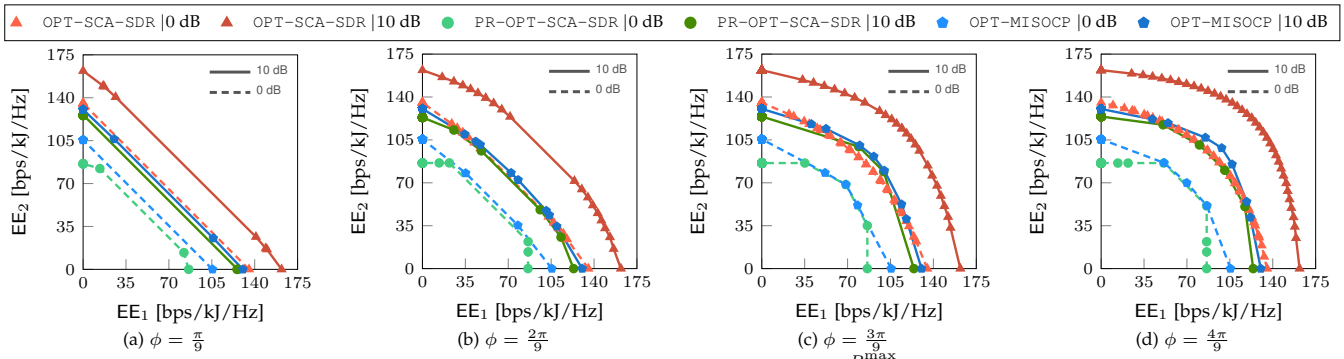

Figure 6: (*Scenario IV*) Two-user EE region of RSMA with discrete and continuous rates for $\frac{P_{\text{tx}}^{\max}}{\sigma^2} = \{0, 10\}$ dB, $\eta_{\text{eff}} = 0.35$, $P_{\text{dyn}} = 33$ dBm, and $P_{\text{sta}} = 38$ dBm. *As it uses the transmit power more judiciously,* `OPT-MISOCP` *has a notable advantage over* `PR-OPT-SCA-SDR`*, ensuring high discrete rates with minimal power consumption, leading to improved EE. In contrast,* `PR-OPT-SCA-SDR` *is not aware of rate discretization, and therefore the precoders have larger powers than necessary, which impacts the EE upon rate projection.*

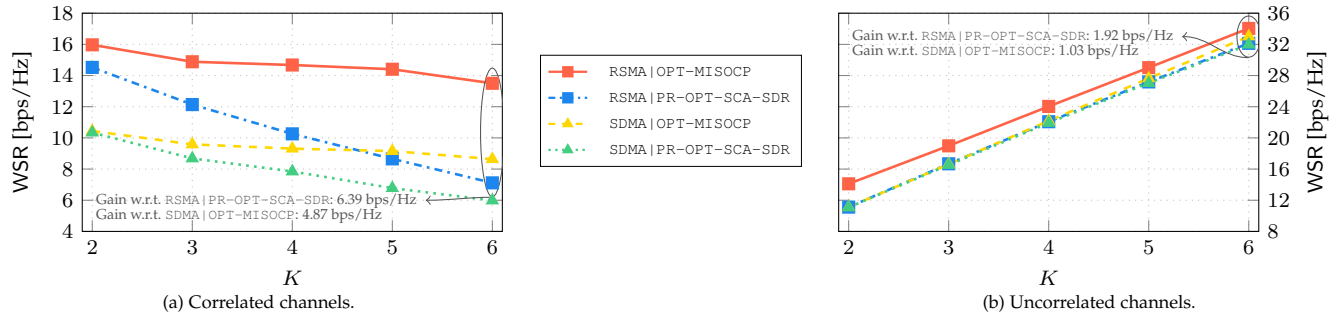

(a) Correlated channels.

(b) Uncorrelated channels.

Figure 7: (*Scenario V*) WSR of RSMA and SDMA as a function of the number of admitted UEs. *In Fig. 7a,* `RSMA | OPT-MISOCP` *has an advantage of* 6.39 *bps/Hz* (↑ 89.7% *gain) and* 4.87 *bps/Hz* (↑ 56.3% *gain) with respect to* `RSMA | PR-OPT-SCA-SDR` *and* `SDMA | OPT-MISOCP`*, respectively, when* $U = 6$*. In Fig. 7b,* `RSMA | OPT-MISOCP` *has an advantage of* 1.92 *bps/Hz* (↑ 5.9% *gain) and* 1.03 *bps/Hz* (↑ 3.1% *gain) compared to* `RSMA | PR-OPT-SCA-SDR` *and* `SDMA | OPT-MISOCP`*, respectively, when* $K = 6$*.*

degradation. In Fig. 5d, we observe the same trend as in Fig. 5c, although the degradation due to imperfect SIC is more conspicuous when protection against imperfect SIC is neglected. This occurs because the channels are highly uncorrelated, making the private rates even more prominent than in Fig. 5c, with the consequent potential risk of much larger degradation in case of SIC failure.

Scenario IV*: Two-User EE Region with Continuous/Discrete Rates for RSMA*

In Fig. 6, we compare the EE of RSMA with continuous and discrete rates to investigate the impact of rate discretization. In Fig. 6a to Fig. 6d, the EE of both `OPT-MISOCP` and `PR-OPT-SCA-SDR` improve when $P_{\text{tx}}^{\max}$ increases from 0 dB to 10 dB, as a higher transmit power allows to find an improved EE operating point with a better trade-off between the achieved rates and the expended power. When $\frac{P_{\text{tx}}^{\max}}{\sigma^2} = 0$ dB (dashed lines), `OPT-MISOCP` surpasses `PR-OPT-SCA-SDR` showing gains as large as 18 bps/kJ/Hz, particularly when the UE weights are not equal. When $\frac{P_{\text{tx}}^{\max}}{\sigma^2} = 10$ dB (solid lines), `OPT-MISOCP` also outperforms `PR-OPT-SCA-SDR` although the gap is smaller. The reason for this effect is that `OPT-MISOCP` can better exploit the limited transmit power when $\frac{P_{\text{tx}}^{\max}}{\sigma^2} = 0$ dB as it is able to handle discrete rates, whereas `PR-OPT-SCA-SDR` wastes power yielding rates higher than necessary, thus incurring a loss after projection. However, when $\frac{P_{\text{tx}}^{\max}}{\sigma^2} = 10$ dB, the power limitation is alleviated, and therefore `PR-OPT-SCA-SDR` can reduce the performance gap with respect to `OPT-MISOCP`. We oserve that as channels become less correlated, the EE of `OPT-MISOCP` and `PR-OPT-SCA-SDR` improve because interference can be handled more effectively and with less transmit power.

Scenario V*: Impact of the Number of Admitted UEs on WSR Performance*

In Fig. 7, we compare the WSR of RSMA and SDMA when the number admitted UEs varies. In Fig. 7a, we consider correlated channels, for which we observe that an increasing number of UEs leads to WSR degradation. This occurs because the UEs are located in close proximity of each other, exacerbating interference for every additional UE admitted. We observe that `RSMA | OPT-MISOCP` has a noticeable advantage over `SDMA | OPT-MISOCP` since it can exploit the channel similarity via the common signal. We observe a similar behavior for `RSMA | PR-OPT-SCA-SDR` and `SDMA | PR-OPT-SCA-SDR` although the difference between them decreases as U increases. Also, not considering rate discretization can severely affect `RSMA | PR-OPT-SCA-SDR`, reducing its performance to the extent of being outperformed by `SDMA | OPT-MISOCP` when $U = \{5, 6\}$. In Fig. 7b, we consider uncorrelated channels, for which we observe that increasing the number of UEs leads to an improved WSR. This is expected as interference is more easily dealt with in this case. Also, `RSMA | PR-OPT-SCA-SDR` and `SDMA | PR-OPT-SCA-SDR` achieve the same performance because RSMA does not devise a common signal. However, `RSMA | OPT-MISOCP` surpasses `SDMA | OPT-MISOCP` as it is able to exploit the surplus of power to devise the common signal. Besides, `SDMA | OPT-MISOCP` performs slightly better than `RSMA | PR-OPT-SCA-SDR` as it avoids projection losses.

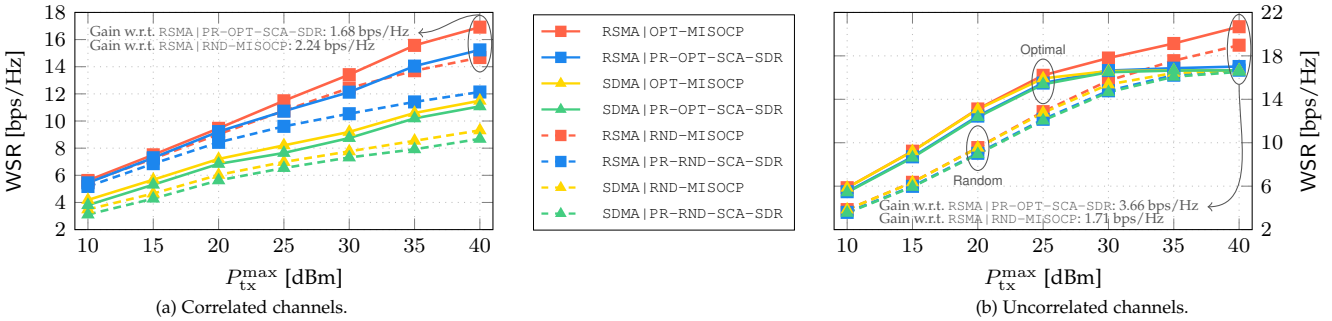

(a) Correlated channels. (b) Uncorrelated channels.

Figure 8: (*Scenario VI*) WSR of RSMA and SDMA with optimal and random UE admission as a function of the transmit power. *In Fig. 8a,* `RSMA|OPT-MISOCP` *has an advantage of* 1.68 *bps/Hz* (↑ 10.9% *gain) and* 2.24 *bps/Hz* (↑ 15.3% *gain) with respect to* `RSMA|PR-OPT-SCA-SDR` *and* `RSMA|RND-MISOCP`*, respectively, when* $P_{\text{tx}}^{\max} = 40$ *dBm. In Fig. 8b,* `RSMA|OPT-MISOCP` *has an advantage of* 3.66 *bps/Hz* (↑ 21.6% *gain) with respect to* `RSMA|PR-OPT-SCA-SDR` *and* 1.71 *bps/Hz* (↑ 8.9% *gain) with respect to* `RSMA|RND-MISOCP`*, when* $P_{\text{tx}}^{\max} = 40$ *dBm.*

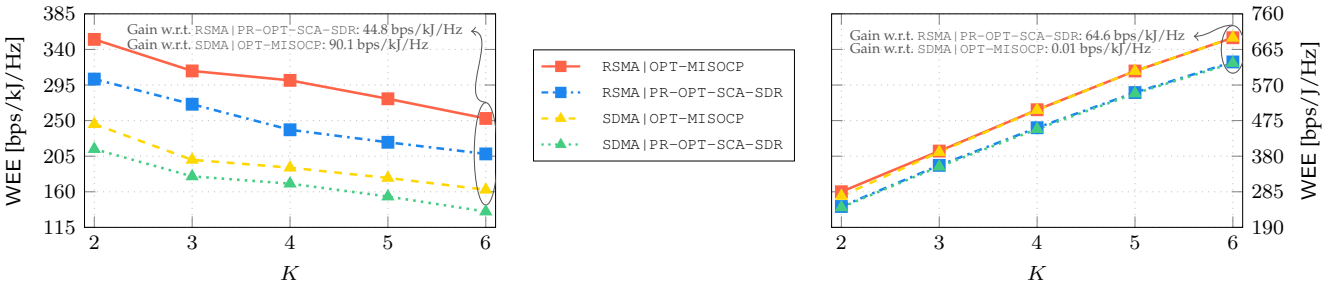

(a) Correlated channels. (b) Uncorrelated channels.

Figure 9: (*Scenario VII*) WEE of RSMA and SDMA as a function of the number of admitted UEs. *In Fig. 9a,* `RSMA|OPT-MISOCP` *outperforms* `RSMA|OPT-PR-SCA-SDR` *and* `SDMA|OPT-MISOCP` *by* 44.8 *bps/kJ/Hz* (↑ 21.5% *gain) and* 90.1 *bps/kJ/Hz* (↑ 55.4% *gain), respectively, when* $K = 6$*. In Fig. 9b,* `RSMA|OPT-MISOCP` *outperforms* `RSMA|OPT-PR-SCA-SDR` *by* 64.6 *bps/kJ/Hz* (↑ 10.2% *gain), when* $K = 6$*.*

***Scenario VI**: Impact of the Transmit Power on the WSR Performance*

In Fig. 8, we evaluate the WSR as a function of the transmit power. In Fig. 8a, we consider correlated channels, for which optimal admission leads to a consistently higher WSR compared to random admission of UEs. Besides, RSMA outperforms SDMA in all cases due to the high channel similarity. Specifically, the performance gap widens as the transmit power increases since higher rates can be allocated to the common signal, whereas SDMA is hampered by high interference. We also observe that `RSMA|OPT-MISOCP` outperforms `RSMA|PR-OPT-SCA-SDR` for all considered cases, whereas `RSMA|RND-MISOCP` performs similarly to `RSMA|PR-OPT-SCA-SDR` even though `RSMA|RND-MISOCP` does not control which UEs are admitted. In Fig. 8b, we consider uncorrelated channels, where optimal admission also facilitates additional gains for both RSMA and SDMA compared to random admission, particularly when the transmit power is more constrained. Besides, `SDMA|OPT-MISOCP` performs marginally better than `RSMA|PR-OPT-SCA-SDR` because the latter collapses to SDMA due to the low channel correlation, thereby experiencing severe saturation upon rate projection. On the other hand, the gains due to optimal UE admission tend to diminish for higher transmit powers. For high transmit powers, `RSMA|RND-MISOCP` surpasses `RSMA|PR-OPT-SCA-SDR` as the former accounts for rate discretization, thus avoiding losses due to rate projection.

***Scenario VII**: Impact of the Number of Admitted UEs on WEE Performance*

In Fig. 9, we compare the WEE of RSMA and SDMA as a function of the number of admitted UEs. In Fig. 9a, we consider correlated channels, for which RSMA and SDMA experience a WEE degradation as the number of admitted UEs increases. This occurs because the transmit power needs to be distributed among more UEs, thus affecting the SINRs and the allocated rates. However, RSMA attains a higher performance than SDMA since RSMA is capable of harnessing the high channel similarity. Further, we observe that `RSMA|OPT-MISOCP` and `SDMA|OPT-MISOCP` respectively outperform `RSMA|PR-OPT-SCA-SDR` and `SDMA|PR-OPT-SCA-SDR` by at least 20%. In Fig. 9b, we consider uncorrelated channels, for which RSMA collapses to SDMA in most cases, since the common rate is very small or zero due to a low channel correlation. Furthermore, the common rate improves marginally when the number of UEs increases, as it requires a substantially larger transmit power. Specifically, as the number of UEs increases, utilizing the common signal becomes less energy-efficient. We observe that `RSMA|OPT-MISOCP` outperforms `RSMA|PR-OPT-SCA-SDR` for all considered values of K.

***Scenario VIII**: Impact of the Transmit Power on the WEE Performance*

In Fig. 10, we evaluate the WEE as a function of the transmit power. In Fig. 10a, we consider correlated channels, for which RSMA outperforms SDMA as it can exploit the high channel correlation. We also observe that optimal admission performs significantly better than random admission, as it allows to select UEs with mutually beneficial channel characteristics that promote EE gains. In addition, increasing the transmit power boosts the WEE as improved operating points can be found. However, this increment saturates after a certain point, as the power required to reach higher rates becomes too costly for a marginal gain in WEE. Besides, `RSMA|RND-MISOCP` performs similarly to `RSMA|PR-OPT-SCA-SDR` since its ability to handle discrete rates compensates indirectly for the random selection

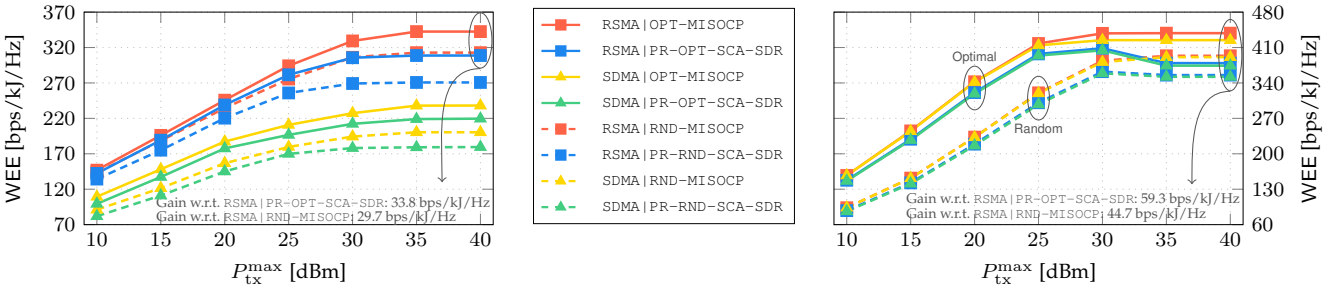

(a) Correlated channels.

(b) Uncorrelated channels.

Figure 10: (*Scenario VIII*) WEE of RSMA and SDMA with optimal and random UE admission as a function of the transmit power. *In Fig. 10a,* `RSMA|OPT-MISOCP` *outperforms* `RSMA|OPT-PR-SCA-SDR` *and* `RSMA|RND-MISOCP` *by* 33.8 *bps/kJ/Hz (↑* 10.9% *gain) and* 29.7 *bps/kJ/Hz (↑* 9.5% *gain), respectively, when* $P_{\text{tx}}^{\max} = 40$ *dBm. In Fig. 10b,* `RSMA|OPT-MISOCP` *outperforms* `RSMA|OPT-PR-SCA-SDR` *and* `RSMA|RND-MISOCP` *by* 59.3 *bps/kJ/Hz (↑* 15.6% *gain) and* 44.7 *bps/kJ/Hz (↑* 11.4% *gain), respectively, when* $P_{\text{tx}}^{\max} = 40$ *dBm.*

of UEs. In Fig. 10b, we consider uncorrelated channels, for which we observe that optimal UE admission can lead to substantial gains. Also, `RSMA|OPT-MISOCP` and `SDMA|OPT-MISOCP` outperform `RSMA|OPT-PR-SCA-SDR` and `RSMA|RND-PR-SCA-SDR`, respectively. Moreover, `RSMA|OPT-PR-SCA-SDR` and `SDMA|OPT-PR-SCA-SDR` experience a WEE degradation for larger values of the transmit power because of rate saturation.

6 Conclusions

In this paper, two new RRM problems were proposed to investigate the SE and EE of RSMA, taking into account characteristics of practical wireless systems, namely the use of discrete rates in contrast to the widely embraced continuous rates, the need for selective UE admission instead of ubiquitously serving all UEs, and imperfect SIC in lieu of ideal SIC. In particular, we investigated the maximization of the WSR and WEE of RSMA as optimization problems and jointly optimized the beamforming, the UE admission, and the allocation of discrete rates, while accounting for an imperfect SIC. Furthermore, given the widespread adoption of Shannon's capacity formula for SINR-rate modeling in RRM designs, we also considered the case of continuous rates. The considered RRM problems resulted in nonconvex MINLPs, which are generally difficult to solve. Nevertheless, we developed two algorithms capable of finding high-quality solutions. The first algorithm addresses the RRM with discrete rates and transforms the nonconvex MINLP into a MISOCP, which can be solved globally optimally via BnB and IPMs. This algorithm features custom cutting planes that reduce the runtime. The second algorithm addresses the RRM with continuous rates, and solves the nonconvex MINLP using binary enumeration, SDR, and SCA, converging to a KKT point. We revealed that ignoring the practical characteristics of wireless systems in RRM design can have serious repercussions on performance. Specifically, we demonstrated the importance of accounting for discrete rates in the RRM model to avoid potentially severe rate projection losses. In addition, we recognized the importance of selectivity for UE admission, which yields greater gains, as it allows to serve UEs with mutually beneficial channel characteristics that can improve the WSR or WEE. Finally, our results confirmed the benefits of accounting for imperfect SIC to guarantee the allocated rate. Our simulations show that RSMA designed for discrete rates achieves gains of up to 89.7% (WSR) and 21.5% (WEE) compared to projecting continuous rates onto the admissible set of discrete rates since projection losses are avoided. Furthermore, user admission proves crucial for RSMA as it yields additional gains of up to 15.3% (WSR) and 11.4% (WEE) compared to random user admission when discrete rates are considered.

Acknowledgment

The research is in part funded by the Deutsche Forschungsgemeinschaft (DFG) within the B5G-Cell project (210487104) in SFB 1053 MAKI and the HyRIS project (455077022), by the LOEWE initiative (Hesse, Germany) within the emergenCITY center, and by the European Commission within the DAEMON project (101017109).

References

[1] B. Clerckx, Y. Mao, E. A. Jorswieck *et al.*, "A primer on rate-splitting multiple access: Tutorial, myths, and frequently asked questions," *IEEE J. Sel. Areas Commun.*, pp. 1–44, 2023.

[2] B. Clerckx, Y. Mao, R. Schober *et al.*, "Is NOMA efficient in multi-antenna networks? A critical look at next generation multiple access techniques," *IEEE Open J. Commun. Soc.*, vol. 2, pp. 1310–1343, 2021.

[3] Y. Mao, B. Clerckx, and V. O. K. Li, "Rate-splitting multiple access for downlink communication systems: Bridging, generalizing, and outperforming SDMA and NOMA," *EURASIP J. Wirel. Commun. Netw.*, vol. 1, no. 133, May 2018.

[4] Y. Mao, O. Dizdar, B. Clerckx, R. Schober, P. Popovski, and H. V. Poor, "Rate-splitting multiple access: Fundamentals, survey, and future research trends," *IEEE Commun. Surveys Tuts.*, vol. 24, no. 4, pp. 2073–2126, 2022.

[5] Y. Liu, S. Zhang, X. Mu *et al.*, "Evolution of NOMA toward next generation multiple access (NGMA) for 6G," *IEEE J. Sel. Areas Commun.*, vol. 40, no. 4, pp. 1037–1071, 2022.

[6] C. Xu, B. Clerckx, S. Chen, Y. Mao, and J. Zhang, "Rate-splitting multiple access for multi-antenna joint radar and communications," *IEEE J. Sel. Topics Signal Process.*, vol. 15, no. 6, pp. 1332–1347, 2021.

[7] S. Naser, L. Bariah, S. Muhaidat, M. Al-Qutayri, M. Uysal, and P. C. Sofotasios, "Interference management strategies for multiuser multicell MIMO VLC systems," *IEEE Trans. Commun.*, vol. 70, no. 9, pp. 6002–6019, 2022.

[8] L. F. Abanto-Leon, M. Hollick, B. Clerckx, and G. H. Sim, "Sequential parametric optimization for rate-splitting precoding in non-orthogonal unicast and multicast transmissions," in *Proc. IEEE ICC*, 2022, pp. 1–7.

[9] Y. Mao, B. Clerckx, and V. O. K. Li, "Rate-splitting for multi-antenna non-orthogonal unicast and multicast transmission," in *Proc. IEEE SPAWC*, June 2018, pp. 1–5.

[10] H. Pang, F. Ji, L. Xu, Y. Liu, and M. Wen, "Resource allocation for RSMA-based coordinated direct and relay transmission," *IEEE Wireless Commun. Lett.*, vol. 12, no. 3, pp. 505–509, 2023.

[11] H. Fu, S. Feng, and D. W. K. Ng, "Resource allocation design for IRS-aided downlink MU-MISO RSMA systems," in *Proc. IEEE ICC Workshops*, 2021, pp. 1–6.

[12] H. Fu, S. Feng, W. Tang, Z. Wei, and D. W. K. Ng, "Secrecy outage-constrained robust resource allocation design for MU-

MISO RSMA systems," in *Proc. IEEE GLOBECOM Workshops*, 2021, pp. 1 –7.
[13] A. Rahmati, Y. Yapici, N. Rupasinghe, I. Guvenc, H. Dai, and A. Bhuyan, "Energy efficiency of RSMA and NOMA in cellular-connected mmwave UAV networks," in *Proc. ICC Workshops*, 2019, pp. 1–6.
[14] Y. Mao, B. Clerckx, and V. O. K. Li, "Rate-splitting for multi-antenna non-orthogonal unicast and multicast transmission: Spectral and energy efficiency analysis," *IEEE Trans. Commun.*, vol. 67, no. 12, pp. 8754–8770, December 2019.
[15] B. Matthiesen, Y. Mao, A. Dekorsy, P. Popovski, and B. Clerckx, "Globally optimal spectrum- and energy-efficient beamforming for rate splitting multiple access," *IEEE Trans. Signal Process.*, vol. 70, pp. 5025–5040, 2022.
[16] G. Zhou, Y. Mao, and B. Clerckx, "Rate-splitting multiple access for multi-antenna downlink communication systems: Spectral and energy efficiency tradeoff," *IEEE Trans. Wireless Commun.*, vol. 21, no. 7, pp. 4816–4828, 2022.
[17] N. Q. Hieu, D. T. Hoang, D. Niyato, and D. I. Kim, "Optimal power allocation for rate splitting communications with deep reinforcement learning," *IEEE Wireless Commun. Lett.*, vol. 10, no. 12, pp. 2820–2823, 2021.
[18] Z. Yang, M. Chen, W. Saad, and M. Shikh-Bahaei, "Optimization of rate allocation and power control for rate splitting multiple access (RSMA)," *IEEE Trans. Commun.*, vol. 69, no. 9, pp. 5988–6002, 2021.
[19] A. R. Flores and R. C. de Lamare, "Robust and adaptive power allocation techniques for rate splitting based MU-MIMO systems," *IEEE Trans. Commun.*, vol. 70, no. 7, pp. 4656–4670, 2022.
[20] T. Cai, J. Zhang, S. Yan, L. Meng, J. Sun, and N. Al-Dhahir, "Resource allocation for secure rate-splitting multiple access with adaptive beamforming," in *Proc. IEEE ICC Workshops*, 2021, pp. 1–6.
[21] N. Q. Hieu, D. T. Hoang, D. Niyato, D. N. Nguyen, D. I. Kim, and A. Jamalipour, "Joint power allocation and rate control for rate splitting multiple access networks with covert communications," *IEEE Trans. Commun.*, pp. 1–14, 2023.
[22] 3GPP, "5G; NR; Physical layer procedures for data," 3rd Generation Partnership Project (3GPP), Technical Specification (TS) 38.214, 2020, version 16.2.0.
[23] G. H. Sim and J. Widmer, "Finite horizon opportunistic multicast beamforming," *IEEE Trans. Wireless Commun.*, vol. 16, no. 3, pp. 1452–1465, 2017.
[24] O. Dizdar, Y. Mao, W. Han, and B. Clerckx, "Rate-splitting multiple access for downlink multi-antenna communications: Physical layer design and link-level simulations," in *Proc. IEEE PIMRC*, 2020, pp. 1–6.
[25] Y. Cheng, A. Philipp, and M. Pesavento, "Dynamic rate adaptation and multiuser downlink beamforming using mixed integer conic programming," in *Proc. EUSIPCO*, 2012, pp. 824–828.
[26] Y. Cheng and M. Pesavento, "Joint discrete rate adaptation and downlink beamforming using mixed integer conic programming," *IEEE Trans. Signal Process.*, vol. 63, no. 7, pp. 1750–1764, 2015.
[27] H.-T. Wai, Q. Li, and W.-K. Ma, "Discrete sum rate maximization for MISO interference broadcast channels: Convex approximations and efficient algorithms," *IEEE Trans. Signal Process.*, vol. 64, no. 16, pp. 4323–4336, 2016.
[28] S. X.-Y. Ni and A. M.-C. So, "Mixed-integer semidefinite relaxation of joint admission control and beamforming: An SOC-based outer approximation approach with provable guarantees," in *Proc. IEEE SPAWC*, 2018, pp. 1–5.
[29] A. Bandi, M. R. B. Shankar, S. Chatzinotas, and B. Ottersten, "A joint solution for scheduling and precoding in multiuser MISO downlink channels," *IEEE Trans. Wireless Commun.*, vol. 19, no. 1, pp. 475–490, 2020.
[30] E. Matskani, N. D. Sidiropoulos, Z.-Q. Luo, and L. Tassiulas, "Convex approximation techniques for joint multiuser downlink beamforming and admission control," *IEEE Trans. Wireless Commun.*, vol. 7, no. 7, pp. 2682–2693, 2008.
[31] R. Wang, W. Kang, G. Liu, R. Ma, and B. Li, "Admission control and power allocation for noma-based satellite multi-beam network," *IEEE Access*, vol. 8, pp. 33 631–33 643, 2020.
[32] L. F. Abanto-Leon, A. Asadi, A. Garcia-Saavedra, G. H. Sim, and M. Hollick, "Radiorchestra: Proactive management of millimeter-wave self-backhauled small cells via joint optimization of beamforming, user association, rate selection, and admission control," *IEEE Trans. Wireless Commun.*, pp. 1–20, 2022.
[33] X. Ou, X. Xie, H. Lu, and H. Yang, "Resource allocation in MU-MISO rate-splitting multiple access with SIC errors for URLLC services," *IEEE Trans. Commun.*, vol. 71, no. 1, pp. 229–243, 2023.
[34] G. Chopra, A. Chowdary, and A. Kumar, "Bounds on power and common message fractions for RSMA with imperfect SIC," 2022.
[35] N. Mouni, A. Kumar, and P. K. Upadhyay, "Adaptive user pairing for NOMA systems with imperfect SIC," *IEEE Wireless Commun. Lett.*, vol. 10, no. 7, pp. 1547–1551, 2021.
[36] I. A. Mahady, E. Bedeer, S. Ikki, and H. Yanikomeroglu, "Sum-rate maximization of NOMA systems under imperfect successive interference cancellation," *IEEE Commun. Lett.*, vol. 23, no. 3, pp. 474–477, 2019.
[37] X. Wang, R. Chen, Y. Xu, and Q. Meng, "Low-complexity power allocation in NOMA systems with imperfect SIC for maximizing weighted sum-rate," *IEEE Access*, vol. 7, pp. 94 238–94 253, 2019.
[38] H. Wang, Z. Zhang, and X. Chen, "Energy-efficient power allocation for non-orthogonal multiple access with imperfect successive interference cancellation," in *Proc. WCSP*, 2017, pp. 1–6.
[39] K. K. Leung and W. Li-Chun, "Integrated link adaptation and power control to improve error and throughput performance in broadband wireless packet networks," *IEEE Trans. Wireless Commun.*, vol. 1, no. 4, pp. 619–629, 2002.
[40] A. Beck, A. Ben-Tal, and L. Tetruashvili, "A sequential parametric convex approximation method with applications to nonconvex truss topology design problems," *J. Glob. Optim.*, vol. 47, no. 1, pp. 29–51, 2010.
[41] C. Sun and R. Dai, "An iterative rank penalty method for non-convex quadratically constrained quadratic programs," *SIAM J. Control Optim.*, vol. 57, no. 6, pp. 3749–3766, 2019.
[42] 3GPP, "Study on scenarios and requirements for next generation access technologies," 3rd Generation Partnership Project (3GPP), Technical Report (TR) 38.913, 05 2017, version 14.2.0.
[43] R. Kovalchukov, D. Moltchanov, Y. Gaidamaka, and E. Bobrikova, "An accurate approximation of resource request distributions in millimeter wave 3GPP new radio systems," in *Proc. NEW2AN*, O. Galinina, S. Andreev, S. Balandin, and Y. Koucheryavy, Eds. Cham: Springer International Publishing, 2019, pp. 572–585.
[44] 3GPP, "Technical specification group radio access network; V2X services based on NR; User equipment (UE) radio transmission and reception," 3rd Generation Partnership Project (3GPP), Technical Report (TR) 38.886, 2022, version 16.3.0.
[45] H. Viswanathan, S. Venkatesan, and H. Huang, "Downlink capacity evaluation of cellular networks with known-interference cancellation," *IEEE J. Sel. Areas Commun.*, vol. 21, no. 5, pp. 802–811, 2003.
[46] G. P. McCormick, "Computability of global solutions to factorable nonconvex programs: Part I – Convex underestimating problems," *Math. Program.*, vol. 10, no. 1, p. 147–175, 1976.
[47] L.-N. Tran, M. F. Hanif, A. Tolli, and M. Juntti, "Fast converging algorithm for weighted sum rate maximization in multicell MISO downlink," *IEEE Signal Process. Lett.*, vol. 19, no. 12, pp. 872–875, 2012.
[48] F. Alavi, K. Cumanan, Z. Ding, and A. G. Burr, "Robust beamforming techniques for non-orthogonal multiple access systems with bounded channel uncertainties," *IEEE Commun. Lett.*, vol. 21, no. 9, pp. 2033–2036, 2017.
[49] H. Fu, S. Feng, W. Tang, and D. W. K. Ng, "Robust secure beamforming design for two-user downlink MISO rate-splitting systems," *IEEE Trans. Wireless Commun.*, vol. 19, no. 12, pp. 8351–8365, 2020.
[50] D. Xu, X. Yu, Y. Sun, D. W. K. Ng, and R. Schober, "Resource allocation for IRS-assisted full-duplex cognitive radio systems," *IEEE Trans. Commun.*, vol. 68, no. 12, pp. 7376–7394, 2020.

Luis F. Abanto-Leon received his master's degree in communications engineering in 2015 from Tohoku University (Japan). He is currently pursuing his Ph.D. degree with Technische Universität (TU) Darmstadt, Department of Computer Science. His research focuses on optimization theory, signal processing, and algorithm design for radio resource management for 5G wireless networks.

Aravindh Krishnamoorthy (Graduate Student Member, IEEE) received the master's degree in communication and multimedia engineering from the Friedrich-Alexander University of Erlangen-Nuremberg (FAU), Germany, in 2015. He is currently pursuing the Ph.D. degree with the Institute for Digital Communications, FAU, under the sponsorship of Fraunhofer Institute for Integrated Circuits (IIS), Erlangen, Germany. He returned to academics in 2012, after a successful industrial career spanning several years in Philips Semiconductors and Ericsson. His industrial experience includes algorithm design for audio signal processing and system and algorithm design for 4th and 5th generation (4G and 5G) wireless communication systems. His current research interests include information and communication theory, probability theory, and (numerical) linear algebra. Aravindh is also an active reviewer for several IEEE journals.

Andres Garcia-Saavedra received his PhD degree from the University Carlos III of Madrid (UC3M) in 2013. He then joined Trinity College Dublin (TCD), Ireland, as a research fellow until 2015. Currently, he is a Principal Researcher at NEC Laboratories Europe. His research interests lie in the application of fundamental mathematics to real-life wireless communication systems.

Gek Hong (Allyson) Sim is a postdoctoral researcher with the Department of Computer Science, Technische Universität Darmstadt, Germany. She received the bachelor's degree in telecommunication and the first master's degree in engineering science from Multimedia University, Malaysia, in 2007 and 2011, respectively. She was awarded master's and Ph.D. degrees in telematics engineering from the University Carlos III Madrid in 2012 and 2015, respectively. Her research interests include multicast scheduling, precoding, and MAC layer optimization for millimeter-wave networks.

Robert Schober (S'98, M'01, SM'08, F'10) received the Diplom (Univ.) and the Ph.D. degrees in electrical engineering from Friedrich-Alexander University of Erlangen-Nuremberg (FAU), Germany, in 1997 and 2000, respectively. From 2002 to 2011, he was a Professor and Canada Research Chair at the University of British Columbia (UBC), Vancouver, Canada. Since January 2012 he is an Alexander von Humboldt Professor and the Chair for Digital Communication at FAU. His research interests fall into the broad areas of Communication Theory, Wireless and Molecular Communications, and Statistical Signal Processing.

Robert received several awards for his work including the 2002 Heinz Maier Leibnitz Award of the German Science Foundation (DFG), the 2004 Innovations Award of the Vodafone Foundation for Research in Mobile Communications, a 2006 UBC Killam Research Prize, a 2007 Wilhelm Friedrich Bessel Research Award of the Alexander von Humboldt Foundation, the 2008 Charles McDowell Award for Excellence in Research from UBC, a 2011 Alexander von Humboldt Professorship, a 2012 NSERC E.W.R. Stacie Fellowship, a 2017 Wireless Communications Recognition Award by the IEEE Wireless Communications Technical Committee, and the 2022 IEEE Vehicular Technology Society Stuart F. Meyer Memorial Award. Furthermore, he received numerous Best Paper Awards for his work including the 2022 ComSoc Stephen O. Rice Prize. Since 2017, he has been listed as a Highly Cited Researcher by the Web of Science. Robert is a Fellow of the Canadian Academy of Engineering, a Fellow of the Engineering Institute of Canada, and a Member of the German National Academy of Science and Engineering.

He served as Editor-in-Chief of the IEEE Transactions on Communications, VP Publications of the IEEE Communication Society (ComSoc), ComSoc Member at Large, and ComSoc Treasurer. Currently, he serves as Senior Editor of the Proceedings of the IEEE and as ComSoc President-Elect.

Matthias Hollick received the Ph.D. degree from Technische Universität (TU) Darmstadt in 2004. He is currently the Head of the Secure Mobile Networking Lab, Department of Computer Science, TU Darmstadt, Germany. He has been researching and teaching at TU Darmstadt, Universidad Carlos III de Madrid, and the University of Illinois at Urbana–Champaign. His research focus is on resilient, secure, privacy-preserving, and quality-of-service-aware communication for mobile and wireless systems and networks.

APPENDIX A: CIRCUMVENTING INTEGER MULTIPLICATIVE COUPLINGS

We introduce new variables $\pi_{u,j} = \chi_u \kappa_j$, which are binary due to $\overline{\mathrm{C}}_1, \overline{\mathrm{C}}_{10}$. Therefore, we define $\overline{\mathrm{D}}_1 : \pi_{u,j} \in \{0,1\}, \forall u \in \mathcal{U}, j \in \mathcal{J}$, and employ the McCormick envelopes to linearize the product of binary variables χ_u, κ_j [46]. The product $\chi_u \kappa_j$ can be removed if constraints $\overline{\mathrm{D}}_2 : \pi_{u,j} \leq \chi_u, \forall u \in \mathcal{U}, j \in \mathcal{J}$, $\overline{\mathrm{D}}_3 : \pi_{u,j} \leq \kappa_j, \forall u \in \mathcal{U}, j \in \mathcal{J}$, $\overline{\mathrm{D}}_4 : \pi_{u,j} \geq \chi_u + \kappa_j - 1, \forall u \in \mathcal{U}, j \in \mathcal{J}$, are added. Further, we obtain $\overline{\mathrm{D}}_5 : \frac{\left|\mathbf{h}_u^{\mathrm{H}} \mathbf{m} \psi\right|^2}{\sum_{i \in \mathcal{U}} \left|\mathbf{h}_u^{\mathrm{H}} \mathbf{w}_i \mu_i\right|^2 + \sigma^2} \geq \sum_{j \in \mathcal{J}} \pi_{u,j} \Gamma_j, \forall u \in \mathcal{U}$, and $\overline{\mathrm{D}}_6 : C_u \leq \sum_{j \in \mathcal{J}} \pi_{u,j} R_j, \forall u \in \mathcal{U}$, upon replacing $\overline{\mathrm{D}}_1$ in $\overline{\mathrm{C}}_{12}$, $\overline{\mathrm{C}}_{14}$.

APPENDIX B: CIRCUMVENTING MIXED-INTEGER MULTIPLICATIVE COUPLINGS

Let $\tilde{\mathbf{w}}_u = \mathbf{w}_u \mu_u$ be the effective precoder for UE_u. When $\mu_u = 0$, then UE_u is not served by a private signal since $\tilde{\mathbf{w}}_u = \mathbf{0}$. When $\mu_u = 1$, then UE_u is served by a private signal via precoder $\tilde{\mathbf{w}}_u = \mathbf{w}_u \neq \mathbf{0}$. We can decouple $\mathbf{w}_u$ and μ_u, while obtaining the same effect, by including constraint $\overline{\mathrm{E}}_1 : \|\mathbf{w}_u\|_2^2 \leq \mu_u P_{\mathrm{tx}}^{\max}$. In a similar manner, we can decouple $\mathbf{m}$ and ψ by including $\overline{\mathrm{E}}_2 : \|\mathbf{m}\|_2^2 \leq \psi P_{\mathrm{tx}}^{\max}$. With these changes, constraints $\overline{\mathrm{C}}_6$, $\overline{\mathrm{C}}_9$, $\overline{\mathrm{D}}_5$ can be respectively rewritten as $\overline{\mathrm{E}}_3 : \sum_{u \in \mathcal{U}} \|\mathbf{w}_u\|_2^2 + \|\mathbf{m}\|_2^2 \leq P_{\mathrm{tx}}^{\max}$, $\overline{\mathrm{E}}_4 : \frac{\left|\mathbf{h}_u^{\mathrm{H}} \mathbf{w}_u\right|^2}{\Delta_{\mathrm{SIC}}^2 \left|\mathbf{h}_u^{\mathrm{H}} \mathbf{m}\right|^2 + \sum_{i \neq u, i \in \mathcal{U}} \left|\mathbf{h}_u^{\mathrm{H}} \mathbf{w}_i\right|^2 + \sigma^2} \geq \sum_{j \in \mathcal{J}} \alpha_{u,j} \Gamma_j, \forall u \in \mathcal{U}$, and $\overline{\mathrm{E}}_5 : \frac{\left|\mathbf{h}_u^{\mathrm{H}} \mathbf{m}\right|^2}{\sum_{i \in \mathcal{U}} \left|\mathbf{h}_u^{\mathrm{H}} \mathbf{w}_i\right|^2 + \sigma^2} \geq \sum_{j \in \mathcal{J}} \pi_{u,j} \Gamma_j, \forall u \in \mathcal{U}$.

APPENDIX C: CIRCUMVENTING INTEGER ADDITIVE COUPLINGS

For a given UE_u, we distinguish the following two cases, (1) $\sum_{j \in \mathcal{J}} \alpha_{u,j} = 0$ (UE_u is not served by a private signal) and (2) $\sum_{j \in \mathcal{J}} \alpha_{u,j} = 1$ (UE_u is served by a private signal). When (1) is true, constraint $\overline{\mathrm{E}}_4$ collapses to $\mathsf{SINR}_u^{(\mathrm{p})} \geq 0$ since $\alpha_{u,j} = 0, \forall j \in \mathcal{J}$. When (1) is true, constraint $\overline{\mathrm{F}}_1$ collapses to the intersection of J constraints, i.e., $\mathsf{SINR}_u^{(\mathrm{p})} \geq 0$, $\forall j \in \mathcal{J}$, which yields $\mathsf{SINR}_u^{(\mathrm{p})} \geq 0$, and is equivalent to $\overline{\mathrm{E}}_4$. We can obtain the same equivalence between $\overline{\mathrm{E}}_4$ and $\overline{\mathrm{F}}_1$ for (2). Similarly, to prove the equivalence between $\overline{\mathrm{E}}_5$ and $\overline{\mathrm{F}}_2$, we follow a procedure along the same lines, which we omit due to space constraints.

APPENDIX D: REFORMULATING THE SINR CONSTRAINTS VIA THE BIG-M METHOD

By defining $\overline{\mathbf{W}}_u = [\Delta_{\mathrm{SIC}} \mathbf{m}, \mathbf{w}_1, \ldots, \mathbf{w}_{u-1}, \mathbf{w}_{u+1}, \ldots, \mathbf{w}_U]$, constraint $\overline{\mathrm{F}}_1$ can be expressed as $\left\|\left[\mathbf{h}_u^{\mathrm{H}} \overline{\mathbf{W}}_u, \sigma\right]\right\|_2^2 \leq \frac{1}{\alpha_{u,j} \Gamma_j} \left|\mathbf{h}_u^{\mathrm{H}} \mathbf{w}_u\right|^2, \forall u \in \mathcal{U}, j \in \mathcal{J}$, from where two cases arise: Case (1) $\alpha_{u,j} = 1 \Rightarrow \left\|\left[\mathbf{h}_u^{\mathrm{H}} \overline{\mathbf{W}}_u, \sigma\right]\right\|_2^2 \leq \frac{1}{\Gamma_j} \left|\mathbf{h}_u^{\mathrm{H}} \mathbf{w}_u\right|^2$ and Case (2) $\alpha_{u,j} = 0 \Rightarrow \left\|\left[\mathbf{h}_u^{\mathrm{H}} \overline{\mathbf{W}}_u, \sigma\right]\right\|_2^2 \leq \infty$. Notice that using ∞ is not necessary as it would suffice to find an upper bound $L_{\max,u}^2$ such that $\left\|\left[\mathbf{h}_u^{\mathrm{H}} \overline{\mathbf{W}}_u, \sigma\right]\right\|_2^2 \leq L_{\max,u}^2$. Therefore, the two cases can be integrated into a single inequality, thus redefining $\overline{\mathrm{F}}_1$ as $\overline{\mathrm{G}}_1 : \left\|\left[\mathbf{h}_u^{\mathrm{H}} \overline{\mathbf{W}}_u, \sigma\right]\right\|_2^2 \leq \frac{\left|\mathbf{h}_u^{\mathrm{H}} \mathbf{w}_u\right|^2}{\Gamma_j} + (1 - \alpha_{u,j})^2 L_{\max,u}^2, \forall u \in \mathcal{U}, j \in \mathcal{J}$, where $L_{\max,u} = \sqrt{\|\mathbf{h}_u\|_2^2 P_{\mathrm{tx}}^{\max} + \sigma^2}$. We follow a similar procedure to transform $\overline{\mathrm{F}}_2$ into $\overline{\mathrm{G}}_2$, which we omit here.

APPENDIX E: CONVEXIFYING THE PRIVATE SINR CONSTRAINTS

While $\overline{\mathrm{G}}_1$ is nonconvex in its current form, it can be transformed into a SOC constraint using Jensen's inequality, as $\left\|\left[\mathbf{h}_u^{\mathrm{H}} \overline{\mathbf{W}}_u, \sigma\right]\right\|_2 \leq \frac{\left|\mathbf{h}_u^{\mathrm{H}} \mathbf{w}_u\right|}{\sqrt{\Gamma_j}} + (1 - \alpha_{u,j}) L_{\max,u}, \forall u \in \mathcal{U}$, $j \in \mathcal{J}$. Note that this inequality and $\overline{\mathrm{G}}_1$ are not equivalent but both delimit the same feasible domain when $\alpha_{u,j} = 1$. When $\alpha_{u,j} = 0$, the inequality still holds without changing the feasible set because of the valid upper bound. Besides, since the precoders are invariant to phase shifting, $\mathbf{w}_u$ and $\mathbf{w}_u e^{j\theta_u}$ yield the same SINR. As a result, it is possible to choose a phase $e^{j\theta_u}$ such that $\mathbf{h}_u^{\mathrm{H}} \mathbf{w}_u$ becomes purely real and nonnegative. Based on this observation, $\overline{\mathrm{G}}_1$ can be equivalently expressed via constraints $\overline{\mathrm{H}}_1 : \mathfrak{Re}\left\{\mathbf{h}_u^{\mathrm{H}} \mathbf{w}_u\right\} \geq 0, \forall u \in \mathcal{U}$, $\overline{\mathrm{H}}_2 : \mathfrak{Im}\left\{\mathbf{h}_u^{\mathrm{H}} \mathbf{w}_u\right\} = 0, \forall u \in \mathcal{U}$, $\overline{\mathrm{H}}_3 : \left\|\left[\mathbf{h}_u^{\mathrm{H}} \overline{\mathbf{W}}_u, \sigma\right]\right\|_2 \leq \frac{1}{\sqrt{\Gamma_j}} \mathfrak{Re}\left\{\mathbf{h}_u^{\mathrm{H}} \mathbf{w}_u\right\} + (1 - \alpha_{u,j}) L_{\max,u}$, $\forall u \in \mathcal{U}, j \in \mathcal{J}$.

APPENDIX F: CONVEXIFYING THE COMMON SINR CONSTRAINTS

Note that $\left|\mathbf{h}_u^{\mathrm{H}} \mathbf{m}\right| \geq \mathfrak{Re}\left\{\mathbf{h}_u^{\mathrm{H}} \mathbf{m}\right\}$ always holds true. Using this relation, we replace $\overline{\mathrm{G}}_2$ with the convex constraints $\overline{\mathrm{I}}_1 : \mathfrak{Re}\left\{\mathbf{h}_u^{\mathrm{H}} \mathbf{m}\right\} \geq 0, \forall u \in \mathcal{U}$, and $\overline{\mathrm{I}}_2 : \left\|\left[\mathbf{h}_u^{\mathrm{H}} \mathbf{W}, \sigma\right]\right\|_2 \leq \frac{1}{\sqrt{\Gamma_j}} \mathfrak{Re}\left\{\mathbf{h}_u^{\mathrm{H}} \mathbf{m}\right\} + (1 - \pi_{u,j}) L_{\max,u}, \forall u \in \mathcal{U}, j \in \mathcal{J}$, where $\mathbf{W} = [\mathbf{w}_1, \ldots, \mathbf{w}_U]^{\mathrm{T}}$. To obtain $\overline{\mathrm{I}}_2$, we can follow the same procedure as in **Appendix E**.

APPENDIX G: ADDING CUTTING PLANES TO TIGHTEN THE FEASIBLE DOMAIN

From $\overline{\mathrm{E}}_4$, $\overline{\mathrm{H}}_1$, $\overline{\mathrm{H}}_2$, we obtain $\hat{\mathrm{J}}_1 : \mathfrak{Re}\left\{\mathbf{h}_u^{\mathrm{H}} \mathbf{w}_u\right\}^2 \geq \sum_{j \in \mathcal{J}} \alpha_{u,j} \Gamma_j \left(\Delta_{\mathrm{SIC}}^2 \left|\mathbf{h}_u^{\mathrm{H}} \mathbf{m}\right|^2 + \sum_{i \neq u, i \in \mathcal{U}} \left|\mathbf{h}_u^{\mathrm{H}} \mathbf{w}_i\right|^2 + \sigma^2\right), \forall u \in \mathcal{U}, j \in \mathcal{J}$. Assuming zero interference and perfect SIC (i.e., $\Delta_{\mathrm{SIC}} = 0$), we obtain a lower bound for $\mathfrak{Re}\left\{\mathbf{h}_u^{\mathrm{H}} \mathbf{w}_u\right\}$ defined as $\breve{\mathrm{J}}_1 : \mathfrak{Re}\left\{\mathbf{h}_u^{\mathrm{H}} \mathbf{w}_u\right\} \geq \sigma \sqrt{\sum_{j \in \mathcal{J}} \alpha_{u,j} \Gamma_j}, \forall u \in \mathcal{U}$. However, since the sum of all $\alpha_{u,j}$ is at most one for a given UE_u (see constraints $\overline{\mathrm{C}}_3, \overline{\mathrm{C}}_7, \overline{\mathrm{C}}_8$), then $\breve{\mathrm{J}}_1$ can be equivalently recast as $\overline{\mathrm{J}}_1 : \mathfrak{Re}\left\{\mathbf{h}_u^{\mathrm{H}} \mathbf{w}_u\right\} \geq \sigma \sum_{j \in \mathcal{J}} \alpha_{u,j} \sqrt{\Gamma_j}, \forall u \in \mathcal{U}$, thus defining a new set of cuts. Besides, $\overline{\mathrm{J}}_2$ allows to terminate early the binary variable branching. In particular, if the upper bound is achieved by some combination of admitted UEs, the algorithm has found an optimal solution, and therefore the process is stopped. Although $\overline{\mathrm{J}}_1$, $\overline{\mathrm{J}}_2$ are optional, they tighten the feasible set of binary variables and accelerate the search.

APPENDIX H: TRANSFORMING THE PROBLEM VIA SUBLEVEL AND SUPERLEVEL SETS

We show by contradiction that $\mathrm{K}_1 - \mathrm{K}_6$ are satisfied with equality at the optimum, thus corroborating that $\mathcal{Q}_{\mathrm{CWSR}_n}$ and $\widetilde{\mathcal{Q}}_{\mathrm{CWSR}_n}$ are equivalent. Note that K_7, K_8 are satisfied automatically, if $\mathrm{K}_1 - \mathrm{K}_6$ are tight. We assume that we have an optimal solution for $\widetilde{\mathcal{Q}}_{\mathrm{CWSR}_n}$ with objective function value $\beta^\star$, and denote with $\gamma_u^\star$, $\rho_u^\star$, $\tau_u^\star$, $\lambda_u^\star$, $C_u^\star$ the optimal values of γ_u, ρ_u, τ_u, λ_u, C_u corresponding to UE_u. We further assume that at the optimum, $\overline{\mathrm{K}}_2$ for UE_u is inactive, i.e., not tight, allowing for the existence of a strictly smaller $\rho_u' < \rho_u^\star$, for which $\overline{\mathrm{K}}_2$ is also satisfied. However, a smaller ρ_u' implies that there exists a larger $\gamma_u' > \gamma_u^\star$ that satisfies $\overline{\mathrm{K}}_1$,

allowing for the existence of a larger objective function value $\beta' > \beta^\star$ due to $\overline{\mathrm{K}}_3$, hence contradicting the assumption that we have found an optimum. Similarly, we can assume that $\overline{\mathrm{K}}_5$ for UE_u is inactive, allowing for the existence of $\lambda'_u < \lambda^\star_u$, for which $\overline{\mathrm{K}}_5$ is also satisfied. At the same time, this allows for the existence of $\tau'_u > \tau^\star_u$ that satisfies $\overline{\mathrm{K}}_4$, and therefore for a larger $C'_u > C^\star_u$ due to $\overline{\mathrm{K}}_6$, thus leading to a higher objective function value and contradicting the assumption that we have found an optimum. For further reading, the reader is referred to [47], where similar deductions were drawn for a different problem. The same analysis can be extended for $\mathcal{Q}_{\mathrm{CWEE}_n}$.

APPENDIX I: SOLUTIONS WITH AT MOST RANK ONE

We define the Lagrangian of $\bar{\mathcal{Q}}^{(t)}_{\mathrm{CWSR}_n}$ with respect to $\mathbf{M}$ (when $\psi = 1$, otherwise $\mathbf{M} = \mathbf{0}$) as $\bar{\mathcal{L}} = \phi_{\overline{\mathrm{L}}_1}\mathrm{Tr}(\mathbf{M}) + \phi_{\overline{\mathrm{L}}_2}\mathrm{Tr}(\mathbf{M}) + \sum_u \phi^u_{\overline{\mathrm{L}}_4}\Delta^2_{\mathrm{SIC}}\mathbf{h}^{\mathrm{H}}_u\mathbf{M}\mathbf{h}_u - \mathrm{Tr}\left(\mathbf{\Phi}_{\overline{\mathrm{L}}_8}\mathbf{M}\right) - \sum_u \phi^u_{\overline{\mathrm{M}}_2}\mathbf{h}^{\mathrm{H}}_u\mathbf{M}\mathbf{h}_u - \mathrm{Tr}\left(\mathbf{\Phi}_{\overline{\mathrm{M}}_3}\left(\zeta_0\mathbf{I} - {\mathbf{T}^{(t)}_0}^{\mathrm{H}}\mathbf{M}\mathbf{T}^{(t)}_0\right)\right) + h(\widehat{\mathbf{W}})$, where $h(\widehat{\mathbf{W}})$ represents the terms that depend on $\widehat{\mathbf{W}}$. Based on the KKT dual feasibility condition, $\phi_{\overline{\mathrm{L}}_1} \geq 0$, $\phi_{\overline{\mathrm{L}}_2} \geq 0$, $\mathbf{\Phi}_{\overline{\mathrm{L}}_8} \succcurlyeq \mathbf{0}$, $\mathbf{\Phi}_{\overline{\mathrm{M}}_3} \succcurlyeq \mathbf{0}$ are the KKT multipliers associated with constraints $\overline{\mathrm{L}}_1, \overline{\mathrm{L}}_2, \overline{\mathrm{L}}_3, \overline{\mathrm{M}}_1$, whereas $\varphi_1, \ldots, \varphi_4$, $\phi^u_{\overline{\mathrm{M}}_2}$ are the KKT multipliers associated with constraints $\overline{\mathrm{L}}_1$, $\overline{\mathrm{M}}_2$ for UE_u. By invoking the KKT stationarity condition, we take the derivative of $\bar{\mathcal{L}}$ with respect to $\mathbf{M}$ and equate it to zero, yielding $\mathbf{\Phi}_{\overline{\mathrm{L}}_8} = \mathbf{A} + c\mathbf{h}_u\mathbf{h}^{\mathrm{H}}_u$, where $\mathbf{A} = \left(\phi_{\overline{\mathrm{L}}_1} + \phi_{\overline{\mathrm{L}}_2}\right)\mathbf{I} + \mathbf{T}^{(t)}_0\mathbf{\Phi}_{\overline{\mathrm{M}}_3}{\mathbf{T}^{(t)}_0}^{\mathrm{H}}$ and $c = \sum_u \phi^u_{\overline{\mathrm{L}}_4}\Delta^2_{\mathrm{SIC}} - \phi^u_{\overline{\mathrm{M}}_2}$. From the KKT complementary slackness condition, it must hold that $\mathbf{\Phi}_{\overline{\mathrm{L}}_8}\mathbf{M} = \mathbf{0}$ and $\mathbf{\Phi}_{\overline{\mathrm{M}}_3}\left(\zeta_0\mathbf{I} - {\mathbf{T}^{(t)}_0}^{\mathrm{H}}\mathbf{M}\mathbf{T}^{(t)}_0\right) = \mathbf{0}$. Applying Sylvester's rank inequality to $\mathbf{\Phi}_{\overline{\mathrm{L}}_8}\mathbf{M} = \mathbf{0}$, we obtain that $\mathrm{Rank}\left(\mathbf{\Phi}_{\overline{\mathrm{L}}_8}\right) + \mathrm{Rank}(\mathbf{M}) \leq N_{\mathrm{tx}}$. In addition, we note that $\mathbf{\Phi}_{\overline{\mathrm{L}}_8}$ is Hermitian with $\mathrm{Rank}\left(\mathbf{\Phi}_{\overline{\mathrm{L}}_8}\right) \geq N_{\mathrm{tx}} - 1$ since $\mathbf{A}$ is positive definite. This results in two possible cases, i.e., $\mathrm{Rank}\left(\mathbf{\Phi}_{\overline{\mathrm{L}}_8}\right) = N_{\mathrm{tx}}$ and $\mathrm{Rank}\left(\mathbf{\Phi}_{\overline{\mathrm{L}}_8}\right) = N_{\mathrm{tx}} - 1$. When $\mathrm{Rank}\left(\mathbf{\Phi}_{\overline{\mathrm{L}}_8}\right) = N_{\mathrm{tx}}$ then $\mathbf{M} = \mathbf{0}$, implying that the common signal is not transmitted. Also, $\mathrm{Rank}\left(\mathbf{\Phi}_{\overline{\mathrm{L}}_8}\right) = N_{\mathrm{tx}} - 1$ for some $c < 0$, which leads to $\mathrm{Rank}(\mathbf{M}) \leq 1$. The same conclusions can be obtained for $\mathbf{W}_u$, $\forall u \in \mathcal{U}'_n$. The same procedure can be applied to $\bar{\mathcal{Q}}^{(t)}_{\mathrm{CWEE}_n}$ as the two problems are similar, which leads to the same conclusion, i.e., the ranks of $\mathbf{M}$ and $\mathbf{W}_u$, $\forall u \in \mathcal{U}'_n$ are at most one. For further reading, we refer to [41], [48]–[50], where similar problems were considered.

APPENDIX J: CONVERGENCE PROOF

Since $\widehat{\mathcal{Q}}_{\mathrm{CWSR}_n}$ and $\mathcal{Q}_{\mathrm{CWSR}_n}$ are equivalent, in this proof we employ $\widehat{\mathcal{Q}}_{\mathrm{CWSR}_n}$, which can be expressed as

$$\widehat{\mathcal{Q}}_{\mathrm{CWSR}_n}: \max_{\boldsymbol{\nu}\in\mathcal{X}} \quad f(\boldsymbol{\nu}) \quad \text{s.t.} \quad \begin{array}{l} g_i(\boldsymbol{\nu}) \leq 0,\ i \in \mathcal{V}, \\ h_j(\boldsymbol{\nu}) \leq 0,\ j \in \mathcal{W}, \\ \ell_k(\boldsymbol{\nu}) \leq 0,\ k \in \mathcal{R}, \end{array}$$

where $\boldsymbol{\nu}$ collects all the decision variables of $\widehat{\mathcal{Q}}_{\mathrm{CWSR}_n}$; $\mathcal{X}$ denotes the feasible set; $f(\boldsymbol{\nu})$ is the objective function; $g_i(\boldsymbol{\nu}) \leq 0, i \in \mathcal{V}$, represent constraints $\overline{\mathrm{L}}_3, \overline{\mathrm{L}}_5$; $h_i(\boldsymbol{\nu}) \leq 0, i \in \mathcal{W}$, represent constraints $\overline{\mathrm{L}}_9, \overline{\mathrm{L}}_{10}$; $\ell_k(\boldsymbol{\nu}) \leq 0, k \in \mathcal{R}$, represent the rest of constraints; and $\mathcal{V}, \mathcal{W}, \mathcal{R}$ are index sets. Similarly, we express $\bar{\mathcal{Q}}^{(t)}_{\mathrm{CWSR}_n}$ as

$$\bar{\mathcal{Q}}^{(t)}_{\mathrm{CWSR}_n}: \max_{\boldsymbol{\omega}\in\bar{\mathcal{X}}^{(t)}} \quad \bar{f}(\boldsymbol{\omega}) \quad \text{s.t.} \quad \begin{array}{l} G_i\left(\boldsymbol{\omega}, \Omega^{(t)}_i\right) \leq 0,\ i \in \mathcal{V}, \\ H_j(\boldsymbol{\omega}) \leq 0,\ j \in \mathcal{W}, \\ \ell_k(\boldsymbol{\omega}) \leq 0,\ k \in \mathcal{R}, \end{array}$$

where $\boldsymbol{\omega}$ collects all the decision variables of $\bar{\mathcal{Q}}^{(t)}_{\mathrm{CWSR}_n}$; $\bar{\mathcal{X}}^{(t)}$ denotes the feasible set; $\bar{f}(\boldsymbol{\omega})$ is the objective function; $G_i\left(\boldsymbol{\omega}, \Omega^{(t)}_i\right) \leq 0, i \in \mathcal{V}$, represent constraints $\overline{\mathrm{M}}_1$, $\overline{\mathrm{M}}_2$; and $H_j(\boldsymbol{\omega}) \leq 0,\ j \in \mathcal{W}$, represent constraints $\overline{\mathrm{M}}_3$, $\overline{\mathrm{M}}_4$. Let $\boldsymbol{\omega}_t$ denote the solution of $\bar{\mathcal{Q}}^{(t)}_{\mathrm{CWSR}_n}$ and let $\Omega^{(t)}_i = \Pi(\boldsymbol{\omega}_{t-1}), i \in \mathcal{V}$, be the adaptable parameters in $\overline{\mathrm{M}}_1$, $\overline{\mathrm{M}}_2$, computed as a function $\Pi(\cdot)$ of the previous solution $\boldsymbol{\omega}_{t-1}$. Since $\overline{\mathrm{M}}_1$, $\overline{\mathrm{M}}_2$ are inner approximations for $\overline{\mathrm{L}}_3$, $\overline{\mathrm{L}}_5$, i.e., $G_i\left(\boldsymbol{\omega}, \Omega^{(t)}_i\right) \geq g_i(\boldsymbol{\omega})$, then $\bar{\mathcal{X}}^{(t)} \subseteq \mathcal{X}$. Also, for sufficiently large penalty weights $p^{(t)}_u$, constraints $\overline{\mathrm{M}}_3$, $\overline{\mathrm{M}}_4$ ensure $\bar{\mathcal{X}}^{(t)} \subseteq \mathcal{X}$. Therefore, $\boldsymbol{\omega}_t$ satisfies $\widehat{\mathcal{Q}}_{\mathrm{CWSR}_n}$. Note that $\boldsymbol{\omega}_t$ also satisfies $\bar{\mathcal{Q}}^{(t+1)}_{\mathrm{CWSR}_n}$ since $\Omega^{(t)}_i$ is updated such that $G_i\left(\boldsymbol{\omega}_{t-1}, \Omega^{(t)}_i\right) = g_i(\boldsymbol{\omega}_{t-1})$. Therefore, $\boldsymbol{\omega}_t \in \bar{\mathcal{X}}^{(t)} \cap \bar{\mathcal{X}}^{(t+1)}$. This implies that $\bar{f}(\boldsymbol{\omega}_{t+1}) \geq \bar{f}(\boldsymbol{\omega}_t)$, leading to a monotonically non-decreasing sequence $\left\{\bar{f}(\boldsymbol{\omega}_t)\right\}$. Since $\bar{\mathcal{X}}^{(t)}$ is compact and $\bar{\mathcal{Q}}^{(t)}_{\mathrm{CWSR}_n}$ is limited by a power constraint, sequence $\left\{\bar{f}(\boldsymbol{\omega}_t)\right\}$ is bounded and converges. In particular, the collection of solutions for $\bar{\mathcal{Q}}^{(t)}_{\mathrm{CWSR}_n}$ define a sequence $\{\boldsymbol{\omega}_t\}$ that converges to an accumulation point $\boldsymbol{\omega}^\star$, i.e., $\boldsymbol{\omega}_t \to \boldsymbol{\omega}^\star$, which is a KKT point.

Note that $\boldsymbol{\nu}$ is included in $\boldsymbol{\omega}$ such that $\boldsymbol{\omega} = (\boldsymbol{\nu}, \boldsymbol{\zeta})$, where $\boldsymbol{\zeta}$ are the slack variables in $\overline{\mathrm{M}}_3$, $\overline{\mathrm{M}}_4$. Since $\boldsymbol{\omega}^\star$ is an accumulation point of $\{\boldsymbol{\omega}_t\}$, there exists a subsequence $\{\boldsymbol{\omega}_{m_t}\}$ such that $\boldsymbol{\omega}_{m_t} \to \boldsymbol{\omega}^\star$. Hence, it also follows that $\boldsymbol{\omega}_{m_t-1} \to \boldsymbol{\omega}^\star$. Upon convergence at $\boldsymbol{\omega}^\star = (\boldsymbol{\nu}^\star, \boldsymbol{\zeta}^\star)$, variables $\boldsymbol{\zeta}^\star = \mathbf{0}$ and therefore $\boldsymbol{\nu}^\star$ is also an accumulation point. In addition, $H_j(\boldsymbol{\omega}^\star) = h_j(\boldsymbol{\nu}^\star), j \in \mathcal{W}$, since both enforce feasible sets with ranks of at most one. Let $\mathcal{L} = \mathcal{V} \cup \mathcal{W} \cup \mathcal{R}$ such that $\mathcal{V} \cap \mathcal{W} = \{\emptyset\}$, $\mathcal{W} \cap \mathcal{R} = \{\emptyset\}$, $\mathcal{R} \cap \mathcal{V} = \{\emptyset\}$. Also, let $\mathcal{I} \supseteq \mathcal{L}$ be the set of active constraints of $\widehat{\mathcal{Q}}_{\mathrm{CWSR}_n}$ with respect to $\boldsymbol{\nu}^\star$ and let $\mathcal{I}_{m_t} \supseteq \mathcal{L}$ be the set of active constraints of $\bar{\mathcal{Q}}^{(t)}_{\mathrm{CWSR}_n}$ with respect to $\boldsymbol{\omega}_{m_t}$. Now, letting $t \to \infty$ for $\bar{\mathcal{Q}}^{(t)}_{\mathrm{CWSR}_n}$, we obtain that $G_i(\boldsymbol{\omega}_{m_t}, \Pi(\boldsymbol{\omega}_{m_t-1})) \to G_i(\boldsymbol{\omega}^\star, \Pi(\boldsymbol{\omega}^\star)) = g_i(\boldsymbol{\omega}^\star) = g_i(\boldsymbol{\nu}^\star), i \in \mathcal{V}$; $H_j(\boldsymbol{\omega}_{m_t}) \to H_j(\boldsymbol{\omega}^\star) = h_j(\boldsymbol{\omega}^\star) = h_j(\boldsymbol{\nu}^\star), j \in \mathcal{W}$; and $\ell_k(\boldsymbol{\omega}_{m_t}) \to \ell_k(\boldsymbol{\omega}^\star) = \ell_k(\boldsymbol{\nu}^\star), k \in \mathcal{R}$. These limits suggest that there exists an integer T_1 for which $\mathcal{I}_{m_t} \subseteq \mathcal{I}, \forall t > T_1$.

Similarly, we have $\nabla_{\boldsymbol{\omega}}\bar{f}(\boldsymbol{\omega}_{m_t}) \to \nabla_{\boldsymbol{\omega}}\bar{f}(\boldsymbol{\omega}^\star) = [\nabla_{\boldsymbol{\nu}} f(\boldsymbol{\nu}^\star) \quad \mathbf{0}]$; $\nabla_{\boldsymbol{\omega}} G_i(\boldsymbol{\omega}_{m_t}, \Pi(\boldsymbol{\omega}_{m_t-1})) \to \nabla_{\boldsymbol{\omega}} G_i(\boldsymbol{\omega}^\star, \Pi(\boldsymbol{\omega}^\star)) = \nabla_{\boldsymbol{\omega}} g_i(\boldsymbol{\omega}^\star) = [\nabla_{\boldsymbol{\nu}} g_i(\boldsymbol{\nu}^\star) \quad \mathbf{0}], i \in \mathcal{V}$; $\nabla_{\boldsymbol{\omega}} H_j(\boldsymbol{\omega}_{m_t}) \to \nabla_{\boldsymbol{\omega}} H_j(\boldsymbol{\omega}^\star) = [\nabla_{\boldsymbol{\nu}} h_j(\boldsymbol{\nu}^\star) \quad \mathbf{0}], j \in \mathcal{W}$; and $\nabla_{\boldsymbol{\omega}} \ell_k(\boldsymbol{\omega}_{m_t}) \to \nabla_{\boldsymbol{\omega}} \ell_k(\boldsymbol{\omega}^\star) = [\nabla_{\boldsymbol{\nu}} \ell_k(\boldsymbol{\nu}^\star) \quad \mathbf{0}], l \in \mathcal{R}$, showing that all constraint gradients of $\bar{\mathcal{Q}}^{(t)}_{\mathrm{CWSR}_n}$ converge to their corresponding ones in $\widehat{\mathcal{Q}}_{\mathrm{CWSR}_n}$. These results together with the fact that $\mathcal{I}_{m_t} \subseteq \mathcal{I}, \forall t \geq T_1$, imply that there exists an integer $T_2 > T_1$ such that $\boldsymbol{\omega}_{m_t}$ is a regular point of $\bar{\mathcal{Q}}^{(t)}_{\mathrm{CWSR}_n}$ when $t > T_2$, for which the KKT conditions are satisfied, i.e., $-\nabla_{\boldsymbol{\omega}}\bar{f}(\boldsymbol{\omega}_{m_t}) + \sum_{i\in\mathcal{V}} \mu^{m_t}_i \nabla_{\boldsymbol{\omega}} G_i(\boldsymbol{\omega}_{m_t}, \Pi(\boldsymbol{\omega}_{m_t-1})) + \sum_{j\in\mathcal{W}} \nabla_{\boldsymbol{\omega}} \mu^{m_t}_j H_j(\boldsymbol{\omega}_{m_t}) + \sum_{k\in\mathcal{R}} \nabla_{\boldsymbol{\omega}} \mu^{m_t}_k \ell_k(\boldsymbol{\omega}_{m_t}) = 0$; $\mu^{m_t}_i G_i(\boldsymbol{\omega}_{m_t}, \Pi(\boldsymbol{\omega}_{m_t-1})) = 0, i \in \mathcal{V}$; $\mu^{m_t}_j H_j(\boldsymbol{\omega}_{m_t}) = 0, j \in$

$\mathcal{W}$; and $\mu_k^{m_t}\ell_k\left(\boldsymbol{\omega}_{m_t}\right)=0, k\in\mathcal{R}$; where $\mu_l^{m_t}\geq 0, l\in\mathcal{L}$, are KKT multipliers.

Considering $t>T_2$, let $\mathbf{r}_t=\nabla_{\boldsymbol{\omega}}\bar{f}\left(\boldsymbol{\omega}_{m_t}\right)$ and let $\mathbf{D}_t$ be the matrix whose columns are the gradients of the active constraints, indexed by $\mathcal{I}$. By complementary slackness, it follows that $\mu_l^{m_t}=0, l\notin\mathcal{I}$ for $t>T_2$. Thus, the stationarity condition can be expressed in matrix form as $\mathbf{D}_t\mathbf{b}_t=\mathbf{r}_t$, where $\mathbf{b}_t$ is formed by the elements in $\{\mu_l^{m_t}\mid l\in\mathcal{I}\}$, which are positive. Similarly, we define $\mathbf{r}=\nabla_{\boldsymbol{\omega}}f\left(\boldsymbol{\omega}^\star\right)$ and $\mathbf{D}$ as the matrix whose columns are the gradients of the constraints indexed by $\mathcal{I}$. Thus we have that $\mathbf{D}_t\to\mathbf{D}$ and $\mathbf{r}_t\to\mathbf{r}$, where $\mathbf{D}_t$ and $\mathbf{D}$ are full rank for $t>T_2$ due to $\boldsymbol{\omega}_{m_t}$ being a regular point at which the set of active gradients are linearly independent, leading to $\mathbf{b}_t=\left(\mathbf{D}_t^{\mathrm{T}}\mathbf{D}_t\right)^{-1}\mathbf{D}_t^{\mathrm{T}}\mathbf{r}_t$ and $\mathbf{b}_t\to\left(\mathbf{D}^{\mathrm{T}}\mathbf{D}\right)^{-1}\mathbf{D}^{\mathrm{T}}\mathbf{r}$. Since $\mu_l^{m_t}, l\in\mathcal{L}$, are either elements from $\mathbf{r}_t$ or zero, they have a limit which we denote by $\mu_l^\star, l\in\mathcal{L}$. Thus, letting $t\to\infty$, the KKT conditions of $\bar{\mathcal{Q}}^{(t)}_{\mathrm{CWSR}_n}$ are $-\nabla_{\boldsymbol{\omega}}\bar{f}\left(\boldsymbol{\omega}^\star\right)+\sum_{i\in\mathcal{I}\cap\mathcal{V}}\nabla_{\boldsymbol{\omega}}\mu_i^\star G_i\left(\boldsymbol{\omega}^\star,\Pi\left(\boldsymbol{\omega}^\star\right)\right)+\sum_{j\in\mathcal{I}\cap\mathcal{W}}\nabla_{\boldsymbol{\omega}}\mu_j^\star H_j\left(\boldsymbol{\omega}^\star\right)+\sum_{k\in\mathcal{I}\cap\mathcal{R}}\nabla_{\boldsymbol{\omega}}\mu_k^\star\ell_k\left(\boldsymbol{\omega}^\star\right)=0$; $\mu_i^\star G_i\left(\boldsymbol{\omega}^\star,\Pi\left(\boldsymbol{\omega}^\star\right)\right)=0, i\in\mathcal{I}\cap\mathcal{V}$; $\mu_j^\star H_j\left(\boldsymbol{\omega}^\star\right)=0, j\in\mathcal{I}\cap\mathcal{W}$; and $\mu_k^\star\ell_k\left(\boldsymbol{\omega}^\star\right)=0, k\in\mathcal{I}\cap\mathcal{R}$. Since $\bar{f}\left(\boldsymbol{\omega}^\star\right)=f\left(\boldsymbol{\omega}^\star\right)$; $G_i\left(\boldsymbol{\omega}^\star,\Pi\left(\boldsymbol{\omega}^\star\right)\right)=g_i\left(\boldsymbol{\omega}^\star\right), i\in\mathcal{V}$; $H_j\left(\boldsymbol{\omega}^\star\right)=h_j\left(\boldsymbol{\omega}^\star\right), j\in\mathcal{W}$; and $\mu_l^\star=0, l\notin\mathcal{I}$, we obtain that $-\nabla_{\boldsymbol{\omega}}f\left(\boldsymbol{\omega}^\star\right)+\sum_{i\in\mathcal{V}}\nabla_{\boldsymbol{\omega}}\mu_i^\star g_i\left(\boldsymbol{\omega}^\star\right)+\sum_{j\in\mathcal{W}}\nabla_{\boldsymbol{\omega}}\mu_j^\star H_j\left(\boldsymbol{\omega}^\star\right)+\sum_{k\in\mathcal{R}}\nabla_{\boldsymbol{\omega}}\mu_k^\star\ell_k\left(\boldsymbol{\omega}^\star\right)=0$; $\mu_i^\star g_i\left(\boldsymbol{\omega}^\star\right)=0, i\in\mathcal{V}$; $\mu_j^\star h_j\left(\boldsymbol{\omega}^\star\right)=0, j\in\mathcal{W}$; and $\mu_k^\star\ell_k\left(\boldsymbol{\omega}^\star\right)=0, k\in\mathcal{R}$; which prove that $\boldsymbol{\omega}^\star$ is a KKT point as the above KKT conditions are the same for $\bar{\mathcal{Q}}^{(t)}_{\mathrm{CWSR}_n}$. We can arrive to the same conclusion for $\widehat{\mathcal{Q}}_{\mathrm{CWEE}_n}$ and $\bar{\mathcal{Q}}^{(t)}_{\mathrm{CWEE}_n}$. For further reading, we refer to [40].

ERKLÄRUNG ZUR DISSERTATIONSSCHRIFT

gemäß § 9 der Allgemeinen Bestimmungen der Promotionsordnung der Technischen Universität Darmstadt vom 12. Januar 1990 (ABI. 1990, S. 658) in der Fassung der 8. Novelle vom 1. März 2018

Hiermit versichere ich, Luis Fernando Abanto Leon, die vorliegende Dissertationsschrift ohne Hilfe Dritter und nur mit den angegebenen Quellen und Hilfsmitteln angefertigt zu haben. Alle Stellen, die Quellen entnommen wurden, sind als solche kenntlich gemacht. Eigenzitate aus vorausgehenden wissenschaftlichen Veröffentlichungen sowie die Urheberschaften der einzelnen Beiträge sind in Anlehnung an die Hinweise des Promotionsausschusses des Fachbereichs Informatik zum Thema „Kumulative Dissertation und Eigenzitate in Dissertationen“ (CR; 01.12.2022) im Kapitel „*Collaborations and My Contributions*“ auf den Seiten xvii bis xx angegeben. Diese Arbeit hat in gleicher oder ähnlicher Form noch keiner Prüfungsbehörde vorgelegen. In der abgegebenen Dissertationsschrift stimmen die schriftliche und die elektronische Fassung überein.

Darmstadt, 22. September 2023

Luis Fernando Abanto Leon